ASPECTS OF SEDIMENTOLOGICAL, STRUCTURAL AND STRATIGRAPHIC INVESTIGATIONS OF THE COLLAR STRATA OF THE VREDEFORT STRUCTURE: CONTRIBUTIONS TOWARDS AN UNDERSTANDING OF THE PRE-HISTORY AND ORIGIN OF THE STRUCTURE

Joseph James Mayer, M.Sc.

Thesis submitted to the Faculty of Science
of the Potchefstroomse Universiteit vir Christelike Hoër Onderwys
in fulfilment of the requirements for the degree of

DOCTOR OF PHILOSOPHY

in

GEOLOGY

Promoter: Prof. J. Markgraaff
Assistant Promoter: Dr. B.G. Els

POTCHEFSTROOM
1992

To the Memory of

HELENA

and my

PARENTS

ACKNOWLEDGMENTS

Deo non fortuna — Lord, Thou hast established the earth, and it abideth......

The privilege to teach sedimentology, stratigraphy and structural geology, all interdependent subdiciplines, was undoubtedly instrumental in shaping the course of the studies presented in this thesis. I therefore acknowledge my indebtedness to my Alma Mater, the Potchefstroom University for Christian Higher Education, and to those many persons attached to the former Department of Geology at this University, whose influence had had an important bearing, directly or indirectly, towards the realisation of this presentation.

A very special word of sincere thanks goes to my two study leaders Johan Markgraaff and Gerhard Els.

To my co-authors, Hans Albat and Gerhard Els, I owe my deepest gratitude. I am indebted to these gentlemen, individually, for their indispensable contributions towards the research and research papers contained in this thesis. In all undertakings we formed, as co-authors and co-workers, a mutual reinforcing team wherein responsibility to act as the senior author, for the different papers, was taken alternately.

I wish to thank the Director of the Geological Survey of South Africa for permission to include, in this thesis, a map of the Central Rand Group of the Vredefort Structure, the mapping of which was carried out under contract for the latter institution.

Lastly I thank my wife, Marié, and my children for their loving support and the endless patience shown during the final period of preparation of this thesis.

PREFACE

This thesis is, for the major part, composed of published research papers and also contains research material which originally formed part of a poster presentation. The credit for these as scientific contributions is shared by co–authors. It is therefore deemed appropriate that an exposition should be given to assist any reader/examiner of the thesis to make an assessment of the share of the author with respect to the scientific work contained in this presentation. For this reason the following statements, elucidating the individual contributions of each co–author for work shared, are hereby submitted on the pages which follow:

RE: - RESEARCH PAPERS BY ALBAT AND MAYER, AND MAYER AND ALBAT - PERMISSION FOR PAPERS TO BE INCLUDED IN A THESIS.

I, THE UNDERSIGNED, HANS MARTIN ALBAT, HEREBY GRANT FULL PERMISSION FOR RESEARCH DATA ORIGINALLY CONTAINED IN A POSTER PRESENTATION (1, LISTED BELOW) AND PUBLISHED PAPERS, OF WHICH I AM FIRST AUTHOR (2 AND 3, LISTED BELOW) AND SECOND AUTHOR (4 AND 5, LISTED BELOW), TO BE INCLUDED IN A Ph. D - THESIS, WHICH IS TO BE SUBMITTED TO THE FACULTY OF SCIENCE BY MR. J.J. MAYER:

1. ALBAT, H.M. AND MAYER, J.J. (1987). INTERRELATIONSHIPS OF STRUCTURAL ELEMENTS IN THE UPPER QUARTZITE MEMBER OF THE HOSPITAL HILL SUBGROUP IN THE SOUTH WESTERN SECTOR OF THE VREDEFORT STRUCTURE. (POSTER PRESENTATION). CONTRIBUTIONS TO INTERNATIONAL WORKSHOP ON CRYPTOEXPLOSIONS AND CATASTROPHES IN THE GEOLOGICAL RECORD, PARYS, SOUTH AFRICA.

2. ALBAT, H.M. AND MAYER, J.J. (1989). MEGASCOPIC PLANAR SHOCK FRACTURES IN THE VREDEFORT STRUCTURE: A POTENTIAL TIME MARKER? TECTONOPHYSICS, 162, 265-276.

3. ALBAT, H.M. AND MAYER, J.J. (1990). SHATTER CONES IN VREDEFORT ROCKS - IMAGINATION OR REALITY? S. AFR. J. GEOL., 93, 547-548

4. MAYER, J.J. AND ALBAT, H.M. (1988). THE TECTONO-SEDIMENTARY SETTING OF THE AREA OF THE VREDEFORT STRUCTURE DURING DEPOSITION OF THE UPPER QUARTZITE MEMBER OF THE HOSPITAL HILL SUBGROUP. S. AFR. J. GEOL., 91, 239-247.

5. MAYER, J.J. AND ALBAT, H.M. (1990). AN APPRAISAL OF THE SIGNIFICANCE OF SMALL-SCALE FOLD STRUCTURES IN THE CONTORTED BED OF THE AREA OF THE VREDEFORT STRUCTURE. S. AFR. J. GEOL., 93, 311-317.

I HEREWITH CERTIFY THAT THE COLLECTION OF THE DATA INTERPRETATION AND WRITING OF THE PUBLICATIONS LISTED ABOVE WAS A JOINT EFFORT SHARED BY BOTH AUTHORS.

Hans Martin Albat

HANS MARTIN ALBAT

JUNE 1992

Signed before me at Otjiwarongo on this 19TH day of June 1992.

Abraham Christoffel van Wyk

CLERK OF THE COURT
OTJIWARONGO

STATEMENT REGARDING THE FOLLOWING RESEARCH PAPERS:

1. Mayer, J.J., and Els, B.G. (1992). The reconstruction of palaeocurrent dispersal patterns for Turffontein strata in the Vredefort Structure in relation to a tectonic model for the area. *S. Afr. J. Geol.*, 95.

2. Els, B.G., and Mayer, J.J. (1992). Transgressive and progradational beach and nearshore facies in the late Archaean Turffontein Subgroup of the Witwatersrand Supergroup, Vredefort area, South Africa. *S. Afr. J. Geol.*, 95.

Permission to include in a thesis

I hereby confirm to have granted permission for the inclusion of the above-mentioned research papers, of which I am a co-author, in a thesis by J.J. Mayer.

Individual contributions of the co-authors

Paper no. 1: At the stage when the second author (B.G. Els) became involved in the research project, it had been in progress for some time and much of the data (tectonic dips and palaeocurrent readings) had been collected. Collection of additional data and data processing were shared by the co-authors. All versions of the manuscript and accompanying diagrams were compiled by the first author (J.J. Mayer) and informally reviewed by the second. The fundamental hypothesis, namely the proposed tectonic model for the Vredefort Structure, was individually conceived by the first author, who also individually carried out a literature search.

Paper no. 2: Some of the data used in this paper had been collected and a preliminary, general environmental interpretation had been made by the second author (J.J. Mayer), before the first author became involved in the project. Field work for the compilation of the vertical profiles, and data processing, were carried out jointly by the two authors. The various versions of the manuscript, and most of the diagrams, were compiled by the first author and informally reviewed by the second, who also compiled a number of diagrams and suggested literature pertaining to the introductory sections. The final, detailed environmental interpretation was conceived jointly by the two authors.

B.G. Els

13 June 1992.

THOMAS PEARSON CATO
Kommissaris van Ede en ... Commissioner of Oaths and
... DIRECTOR
PU vir CHO/PU for CHE 2520 POTCHEFSTROOM

RESEARCH PAPERS by Albat and Mayer, and **Mayer and Albat** - **STATEMENT** by the author of the thesis **REGARDING INDIVIDUAL CONTRIBUTIONS OF CO-AUTHORS**

I, the undersigned, Joseph James Mayer hereby declare that my share in the research and compilation of a poster presentation (1, listed below) and published papers, of which I am first author (2 to 3, listed below) and second author (4 to 5, listed below), are as follows:

1. Albat, H.M. & Mayer, J.J. (1987). Interrelationships of structural elements in the upper quartzite member of the Hospital Hill Subgroup in the southwestern sector of the Vredefort Structure (poster presentation). *Contributions to International Workshop on Cryptoexplosions and Catastrophes in the Geological Record, Parys, South Africa*
2. Albat, H.M. & Mayer, J.J. (1989). Megascopic planar shock fractures in the Vredefort Structure: a potential time marker? *Tectonophysics*, **162**, 265–276
3. Albat, H.M. & Mayer, J.J. (1990). Shatter cones in Vredefort rocks – imagination or reality ? *S. Afr. J. Geol.*, **93**, 547-548.
4. Mayer, J.J. & Albat, H.M. (1988). The tectono-sedimentary setting of the area of the Vredefort Structure during deposition of the upper quartzite member of the Hospital Hill Subgroup. *S. Afr. J. Geol.*, **91**, 239–247.
5. Mayer, J.J. & Albat, H.M. (1990). An appraisal of the significance of small-scale fold structures in the contorted bed of the area of the Vredefort Structure. *S. Afr. J. Geol.*, **93**, 311–317.

Poster presentation 1 and research paper 2: (forming the basis of Chapters 7 and 6 of this thesis)

H.M. Albat became aware of the existence of a pervading fabric of closely spaced "joints" in Witwatersrand quartzites during the course of the mapping of Witwatersrand strata and the recording of shatter cone data in the southwestern sector of the Vredefort Structure. With a view to participating and contributing towards the proceedings of the International Workshop on Cryptoexplosions and Catastrophes in the Geological record, held at Parys, South Africa in 1987, these "joints" and their relationship to shatter cones were investigated by Albat in collaboration with the second author (Mayer). The collection of structural data on Witwatersrand rocks, initially in the area of Rooderand 510 and Leeudoorns 350, and at a later stage in study areas selected to cover the entire arc of exposed Witwatersrand strata in the Vredefort Structure, was shared by the authors. The plotting and initial interpretation of these data for the poster presentation and later for the research paper were carried out by the the first author (Albat). Final conclusions on the interpretation of these "joints" as planar shock features and their significance and relationships to other features was jointly reached by the two authors after lengthy discussions. The planning, exposition, and writing of the text for the poster and the compilation of the manuscript for the published research paper was a joint effort by both authors. The first author (Albat) was responsible for the literature search and the compilation of the diagrams.

The paper in the thesis (Chapter 7), bearing the title of the original poster presentation, was compiled by the second author (Mayer) and represents an expansion of the assimilated original research material contained on the poster, supplemented by later field observations jointly carried out by both the first and second authors and by the second author (Mayer) in collaboration with colleague A.A. Bisschoff.

Paper 3 (forming the basis of Chapter 8 of this thesis)

This published "Geological Note" represents the announcement of a discovery, jointly made by both authors during fieldwork, of a discrete and perfect shatter cone from the northeastern sector of the Vredefort Structure. The compilation of the "Note" is the product of a joint effort towards an exposition of the importance of the discovery. The first author was responsible for the illustrations.

Paper 4 (forming the basis of Chapter 2 of this thesis)

Part of the data used in this paper was jointly collected by the first (Mayer) and second author (Albat). Some additional data were collected by the first author (Mayer). The interpretation of the data was the responsibility of the first author (Mayer) but results were discussed at length and final conclusions were reached jointly. The literature search, compilation of the manuscript and accompanying diagrams were made by the first author (Mayer). The second author was responsible for the photographic illustrations. The manuscript was informally reviewed by the second author (Albat).

The addendum to this paper, in the thesis, is solely attributable to the view point of the first author (Mayer)

Paper 5 (forming the basis of Chapter 3 of this thesis)

The second author (Albat) became involved in this research project at a late stage when much of the data pertaining to fold-axis orientation had already been collected. The age relationships of shatter cones, of the megascopic shock fractures and the intrusive epidiorite sills with respect to the small-scale fold structures remained open questions and were jointly investigated by the authors. The data were initially interpreted by the first author but a critical assessment of the interpretation was made by the second author (Albat), who also informally reviewed the manuscript and the diagrams compiled by the first author (Mayer). The literature search was the responsibility of the first author (Mayer) while the second author provided the photo illustrations.

The addendum to this paper in the thesis is on solely attributable the view point of the first author (Mayer)

....

J.J. Mayer

DECLARATION OF OWN WORK

I, the undersigned, hereby declare that the following chapters in this thesis, including the map and mapping of the Central Rand Group, are solely my own work:

Chapter 1: An overview of hypotheses and literature pertaining to the Vredefort Structure.

Chapter 9: The stratigraphy of the Central Rand Group in the Vredefort area – based on the map of the Central Rand Group.

Chapter 10: Summary and conclusions which give an integrated overview of the findings of the research work contained in this thesis.

....

J.J. Mayer

29/6/92

TABLE OF CONTENTS

CHAPTER 1

AN OVERVIEW OF HYPOTHESES AND LITERATURE PERTAINING TO THE VREDEFORT STRUCTURE

AN OVERVIEW OF HYPOTHESES AND LITERATURE PERTAINING TO THE VREDEFORT STRUCTURE

Introduction

The Vredefort Structure or Vredefort Dome is located roughly in the centre of the preserved Witwatersrand Basin. Although it is one of several other dome-like structures, in and around the rim of the tectonic basin, its characteristics are unmatched by any of the other structures: it differs from them in that it is roughly circular in plan; its collar strata dip steeply (for most part overturned); its core rocks, in a like manner, stand on edge; it is unique in that shatter cones, megascopic planar fractures and pseudotachylite abound its rocks; it is undoubtedly unique with regard to the presence of the high pressure phases of silica, coesite and stishovite, in rocks within its confines.

Since first recognised, much has been written with regard to this enigmatic Structure. The literature on the Vredefort Structure has become voluminous and is characterised by controversial issues with respect to the mode of origin of the Structure and the chronological sequence of events pertaining to its genesis. In this introductory chapter the main objective is to use available literature to briefly sketch the historic development of ideas relating to the two main hypotheses for the origin of the structure: the endogenic versus the exogenic (meteorite impact) modes of origin.

Towards the end of this chapter the topics of subsequent chapters are introduced and their contribution towards a better understanding of the geology, and origin of the Structure, is outlined. These chapters comprise: (i) offprints of papers published, in conjunction with a co-author, on various aspects pertaining to the Vredefort Structure, from 1988 to 1990, (see Preface); (ii) an article adapted from a poster presentation (and extended), presented in 1987, at the *International Workshop on Cryptoexplosions and Catastrophes in the Geological Record, Parys, South Africa*; (iii) manuscript copies of additional research articles on the Vredefort Structure (also in conjunction with a co-author), in press at the time of compiling this thesis; and (iv) an explanation of the stratigraphy and geology of the Central Rand Group, recently remapped in the area of the Vredefort Structure.

Development of ideas favouring an endogenous origin for the Vredefort Structure

G.W. Stow, while in the service of the Geological Survey of the Orange Free State, was probably the first geologist to notice the tilted nature of the strata in the collar of the Vredefort Structure when he visited the vicinity of the new town of Parys in 1887. He attributed the steep dip, and the altered character of the ancient sediments, to a volcanic centre somewhere near Palmietfontein 99 (Nel, 1927).

The first, however, to recognise the circular plan shape of the granite hub and the overfolded nature of the encircling belt of sediments were G.A.F. Molengraaff and D. Draper during their joint visit to the western and central portions of the Vredefort area in the early 1890's. While the circular shape and tilted to overtilted attitude of the collar strata of the Vredefort Mountain Land were fairly well comprehended from 1891 onwards, the question of whether the Archaean granite of the central hub was intrusive into to the sediments or not, was still an undecided issue at the time. To some it was obvious that the the granite was intrusive and they used this hypothesis to explain the tilting of the beds. According to Hall and Molengraaff (1925), Molengraaff at first, in 1891, regarded the Vredefort granite to be older than the sediments. Later, in 1904, he changed his mind about this because of the presence of strong contact metamorphism (the spotted hornfelses) in the lower Witwatersrand sediments near the the contact with the granite (Chapter 1, of Hall and Molengraaff, 1925).

F.H. Hatch was the first to indicate, on a map he published in 1903, that there were younger intrusive granites in the collar rocks and S.J. Shand drew the attention to the occurrence of pseudotachylite (originally spelled "pseudothacylyte") (Hall and Molengraaff, 1925). The diversity of rock types in the area, however, really only became known through the work of Drs. Hall and Molengraaff in 1922 and L.T. Nel's mapping in 1923 and 1924. By then it had been established that the granitic hub constitutes part of the Basement Complex and that the observed contact metamorphism could possibly be related to the younger granite intrusions. Hall and Molengraaff (1925) also focused the attention on the fact that pseudotachylite is found in all rocks of pre-Karoo age in the Vredefort area, with the exception of the dykes of enstatite-granophyre (presently referred to as "bronzite granophyre" dykes).

Because of the presence of the alkali granite intrusions and other igneous rocks, considered at the time to postdate the Vredefort Event, Hall and Molengraaff (1925) were led to believe that a hidden intrusive body was present under the central granite hub of the Vredefort Structure. They reasoned that this intrusion was partly responsible for the updoming of the strata and that it constituted, in conjunction with centripetal pressure, the major cause of the diastrophism. Because of the location of the outcrops of the alkali granite intrusions, and the eccentricity of their metamorphic effect, Nel (1939) argued that, if these intrusives were related to the postulated main igneous body, they could not be responsible for the doming as they are not centrally emplaced. Bailey (1926), however, maintained that only magmatic upheaval and concomitant centrifugal pressure could explain the localised intensity and symmetry of updoming. Nel (1927) therefore suggested that, if this is accepted, the younger granites at the surface may represent a branch-off from a deep-seated main mass beneath the centre of the Structure.

H.Cloos, in 1937, was evidently first to suggest that the Vredefort Structure was a diapir caused by deep subsidence and concomitant sedimentation in the area, resulting in the eventual uprising of the basement (Nel *et al.*, 1939).

On account of his studies of primary structures, such as banding in the granite-gneiss of the Vredefort hub and the orientation of feldspar phenocrysts, Willemse (1937) came to the conclusion that the Vredefort granite represents an original domelike feature in the basement. Du Toit (1954) visualised the Vredefort Structure as originating from the combined action of domal uprising and a northerly thrust. Brock and Pretorius (1964) also shared the view that the Vredefort Structure represents a pre-Witwatersand dome similar to the other domes in and around the Witwatersrand basin, and termed it a "pre-Witwatersrand structural entity".

The idea of a hidden intrusion beneath the granite-gneiss was further pursued by Maree (1944) who inferred from gravity anomalies that the Dome was underlain by a body of dense rock with an eccentric disposition with respect to the granite hub. He postulated this body to be a mafic pluton which gave off apophyses, resulting in satellites of the main body to intrude in the collar sediments.

Bisschoff (1969) accepted the idea that the hub of the Vredefort Structure was an initial dome, as proposed by Willemse (1937) and Brock and Pretorius (1964), and suggested that the final overturning of the collar strata resulted from additional doming caused by the intrusion of a central pluton. He suggested that the magmatic activity commenced with the emplacement of the basic rocks before overfolding, continued through the emplacement of the alkaline rocks, and culminated with the emplacement of the bronzite granophyre dykes after overfolding and faulting. In listing the chronology of events Bisschoff (*op. cit.*) pointed out that shatter cone formation preceded the formation of pseudotachylite.

An endogenous origin for the Vredefort Structure, in which the formation of shatter cones is explained, was proposed by Nicolaysen (1972). He considers the Vredefort Structure a cryptoexplosion structure, visualising it as a diapir which obtained release from strong lateral confinement by growing in the vertical direction. According to this model shatter cones formed when the beds were roughly vertical, or perhaps overturned, and at the time of their formation the cones did not point toward a focus, as in the reconstruction by Manton (1962, 1965) (see next section).

Simpson (1978, 1981) claims to have found shatter cone segments superimposed on fault breccias in the rim synclinorium. According to her interpretation these findings clearly indicate that shatter cone formation took place after faulting and therefore postdate the overturning of the collar. From a detailed microfabric analysis of numerous quartzite samples from the collar strata, Lilly (1981) identified two events of shock deformation in the area. He reasoned that the first and major shock event occurred when the strata were still sub-horizontal. Lilly (1981) associates the second, less intense shock, with the formation of shatter cones after the strata had been overturned. According to him the separation, in time, of the two shocks is indicated by the fact that shatter cone segments have been recorded on post-overturning fault breccias (citing Simpson, 1978), which by then had already become coherent. Lilly (*op. cit.*) proposed some type of explosive endogenic origin for the Vredefort Structure.

An interesting concept concerning the Vredefort core, was introduced as result of a geochemical and a geochronological study of the granitic hub gneisses by Slawson (1976). He proposed that the core rocks are, similar to the collar strata, turned up sharply, resulting in a deep profile of the crust being brought into view (the so-called crust-on-edge model). A geological and geophysical study of the core by Stepto (1979, 1990) substantially confirmed Slawson's proposal. From geological mapping of the basement Stepto (1990) delineated a three-fold concentric zoning comprising, the "Outer Granite Gneisses" (OGG), the "Steynskraal Formation" (SSF) and the "Inlandsee Leucogranofels" (ILG). He also concluded that a small occurrence of a massive, homogeneous, biotite-rich granite, near the centre of the structure, is a post-deformation intrusion.

Schreyer (1983) and Fricke *et al.* (1990) studied fluid inclusions and planar elements in quartz of the basement rocks of the Vredefort Structure. They showed that the filling fluid was dense CO_2 which was trapped in shock-induced planar elements in the quartz, possibly immediately after the shock event. From these studies the aforementioned earth scientists concluded that a deep-seated CO_2-rich gas explosion, rather than an impact, was responsible for the origin of the Vredefort Structure.

Winter (1987a, 1987b) postulated that the Vredefort Structure represented neither an astrobleme nor a gastrobleme. He proposed that the Witwatersrand Basin, and the Vredefort Structure, developed at a normal tectonic growth rate in a continental back-arc plate tectonic setting. Colliston (1990) also aligned himself with the idea of a tectonic origin for the Vredefort Structure which precludes any endogenous/exogenous catastrophic shock or diapiric event. He submitted a hypothesis according to which deep crustal subsurface shearing is employed to explain the configuration of the Vredefort Structure. A northwest-trending, southeast-dipping, subsurface ductile shear zone is postulated, which possibly has the crust-mantle interface as its lower boundary. Thrust displacement on this shear zone, towards the north, caused the supracrustal rocks to dome up, resulting in the asymmetry of the Structure. Corner *et al.* (1990), too, embrace a tectonic origin for the Vredefort Structure. They visualise the development of the Structure to be intimately connected with the tectonic evolution of the Kaapvaal Craton. From processed gravity and aeromagnetic data, covering the Witwatersrand basin and adjacent areas, they inferred two major structural axes. These are a northwest-trending geanticlinal arch, which they termed the Vredefort axis, and a north-northeast-trending axis of crustal downwarp constituting the long axis of the Witwatersrand basin. The Vredefort Structure lies at the intersection of these axes and, according to Corner *et al.* (1990), its origin seems to be linked to tectonic mechanisms.

Development of ideas supporting an exogenous (meteorite impact) origin for the Vredefort Structure

The recognition of meteorite impact scars probably extends back at least a century (French 1990) but the first to suggest that a sizable terrestrial structure might be linked to a meteorite impact was A. Werner who proposed such an origin for the Riess structure in 1904 (Pohl, 1987). In 1906 D.M. Barringer also convincingly argued that Meteor Crater, Arizona, was produced by the high-speed impact of a large iron meteorite (Melosh, 1989). In later years many small structures such as the Lake Botsumtwi in Ghana, Wabar crater in Arabia, the Campo del Cielo craters in Argentina and a few others, were described as meteor craters. Many of the larger craters, however, were initially described as cryptovolcanic structures, a term first used by W. Brancha and E. Fraas in 1905 for Steinheim (Melosh, 1989).

As early as 1937, Boon and Albritton proposed that the Vredefort Structure and, in fact, all cryptovolcanic structures are the scars of ancient meteorite impacts (Hargraves, 1961; Melosh, 1989). In 1947, R.A. Daly attempted to revive the idea of an extraterrestrial origin for the Vredefort Structure, but the idea was generally rejected in lieu of the tectonic/magmatic hypothesis (Truswell, 1977).

Shatter cones –In the early part of the century the linking of geological structures with meteorite impact was generally based on the presence of meteoritic iron in the vicinity of these crater-like structures. Dietz (1959), however, was the first to suggest that shatter cones occurred only at impact craters and his proposal was supported by an experiment in which E.M. Shoemaker and others produced shatter cones around small-scale impacts in dolomite (Melosh, 1989).

Although shatter cones were observed in the rocks of the Vredefort Structure by Nel (1927), he did not pay much attention to these structures and only casually mentions them in his explanation of the geology of the Vredefort map, describing them as "cone in cone" structures. Dietz, who studied the Kentland Structure in 1947 was convinced of the significance of shatter cones as reliable geological criterion for the recognition of impact structures (Melosh, 1989). According to Hargraves (1961), Dietz wrote to him and suggested that a search be made for shatter cones in the Vredefort Structure. Hargraves (*op. cit.*) found them to be very abundant and, although he did not attempt measuring their orientations systematically, he came to the conclusion that the cone axes appeared to be more or less parallel to the bedding planes of the sediments. He furthermore concluded from careful observations that the apices of the cones would point radially towards the granite hub if the beds were to be turned back to the horizontal.

In a discussion on Hargraves' paper, Brock (1961) expressed the view that it was somewhat futile to attempt to "resuscitate an idea which had long ago been discarded on structural grounds". This statement was in view of the fact that R.A. Daly was not successful in promoting such an idea in 1947. Brock (*op. cit.*) maintained that professor Daly was probably not at all serious, at the time, when he expressed the view that the Vredefort Structure originated as result of an impact because "he (professor Daly) is alleged to have said that he got a lot of quiet fun from throwing the idea to the wolves".

Dietz (1961), however, was very excited about Hargraves' discovery and urged South African geologists to study the Vredefort Ring with renewed energy, proposing that a search should be made for coesite which he thought was a co-criterion for recognising astroblemes. Quantitative data on shatter cones were effectively produced a year later by

Manton (1962). Manton recorded the azimuths and plunge of shatter cone striations of a large number of cone segments from which he stereographically produced a statistical master cone for a specific structural homogeneous area. He was able to demonstrate that the apical angles of such master cones are usually between 93^0 and 108^0 and that the apices, around the arc of the Structure, would practically all be directed to a central focal point about 13 to 14 km above the present land surface, if the strata are rotated to the horizontal.

Although the shatter cones were interpreted as high velocity shock features by Dietz (1961), Hargraves (1961) and Manton (1962), others such as Brink and Knight (1961) and Ramsay (1961) were of the opinion that they could form as result of ordinary stresses and could possibly be explained in terms of crustal tectonic mechanisms.

According to the "impactists" shatter cones formed as result of a shock wave which passed through strata lying approximately horizontal in the Vredefort area. The formation of the cones therefore dates the moment before the overturning of the collar strata. Ramsay (1961) noticed a foliation on which shatter cone segments had been superimposed in pelitic rocks of the Central Rand Group (Witwatersrand Supergroup) in a road cutting on Rooderand 510. He expressed the opinion that, if this foliation represented axial plane foliation, which developed as result of the overfolding of the strata in the Vredefort collar, then the shatter cones are post-overfolding in age. As indicated, in the previous section, both Simpson (1981) and Lilly (1981) interpreted shatter cones as post collar-deformation structures. Nicolaysen (1972) explained these structures in terms of a different physical model whereby they formed at a very late stage of collar deformation. He suggested that the cones, at the time of their formation, did not point toward a focus but pointed to the vertical. At a later point in time Nicolaysen and Reimold (1987), however, repudiated the existence of these structures as actual cones. They interpreted the geometrical pattern of striae on projections as the result of the intersection of a number of joint planes, referred to as multiple-striated joint sets (msjs).

Although Ramsay (1961) held the view that shatter cones could possibly equally well have resulted from tectonic stress, Ramsay and Huber (1987) expressed the opinion that shatter cones are characteristic of very high speed deformations with wave velocities of about 5000 $m\ s^{-1}$, caused by shock waves which could only arise from the impact of large meteoritic bodies on the Earth's surface. According to these authors explosions, which are often associated with certain types of volcanic activity, do not appear to generate shock waves of the magnitude required for the formation of shatter cones.

Albat (1988), following Manton's method of measuring shatter cones, confirmed the geometric character of the statistical master cone and established a definite relationship between shatter cones and bedding. He found the mean apical angle to be 100^0 with a small standard deviation of 7,5^0. He further demonstrated that there were two separate domains recognisable in which the angle between the bedding pole and the cone axis remained fairly constant. For domain I, in the southwestern part of the structure, the angle is more or less 65^0 and approximately 80^0 for domain II, which covers the larger part of the collar arc extending from the west to the northeast.

Pseudotachylite – Whereas shatter cones are interpreted by the supporters of the impact hypothesis as the manifestations of the moment of applied shock, before the overturning of the collar, the formation of pseudotachylite is viewed by them as the manifestation of a single event which followed. This is namely the turning up of the collar strata, the brecciation, faulting and folding of these strata as result of the rebound shock. Reimold *et al.* (1990a), however, on grounds of ^{40}Ar–^{39}Ar dating of pseudotachylite postulated that at least six pseudotachylite-forming events occurred at Vredefort between ages of (Ga) 2.25 $\pm$ 0.04 and 1.09 $\pm$ 0.10. From these they conclude that there was no single shock event, but that the pseudotachylite was generated by several local high-strain (possibly seismic-shock) events. Martini (1991) also distinguishes between what he calls the "A–" and "B–" types of pseudotachylite. He, however, proposed that the A–type, which occurs as thin veinlets and are associated with the high pressure phases of SiO_2 (see later discussion), formed during the transit of a shock wave due to an impact and preceded the thick B–type pseudotachylite and microbreccia veins, which formed a moment after the initial shock concomitant with the upturning of the collar strata.

"Bronzite" granophyre – The bronzite granophyre of the Vredefort area (formerly referred to as the enstatite granophyre) was regarded by earlier investigators as allied to pseudotachylite (Hall and Molengraaff, 1925; Nel, 1927; Willemse 1937). Field observations, however, have shown that the granophyre, which occurs as dykes and is riddled with xenoliths of quartzite and granite, cross-cuts pseudotachylite occurrences and, in fact, is free of deformation structures such as shatter cones (Bisschoff, 1969; 1971). French *et al.* (1989) and French and Nielsen (1990) interpreted the bronzite granophyre dykes, some of which occur close to the contact of the collar strata with the granite–gneiss core, as an impact-melt breccia. They base their idea on the range of chemical variation, which is similar to that observed in impact melt bodies from large and small terrestrial impact structures. The concept, however, that the bronzite granophyre postdates the Vredefort event, as indicated by the absence of pseudotachylite and shatter cones, has been questioned by Reimold *et al.* (1990b). These authors have allegedly found small pseudotachylite veins and occurrences of so-called multiple jointing, which they interpret to be associated with shatter cones, in the granophyre. According to them these findings indicate that the deformation coupled to the Vredefort event continued after the emplacement of the granophyre, suggesting an internal and possibly orogenic origin for the Vredefort Structure.

Microfabrics of quartzites and microdeformations in quartz – Although Carter (1965, 1968) concluded from microfabric studies of the quartz grains of certain quartzites from the Vredefort collar that these fabrics resulted from the passage of a shock wave, generated by meteorite impact, the phenomenon of microdeformations in the quartz grains of Vredefort quartzites, as an indicator of high-speed shock, is another controversial issue. The preservation and distribution of these features in the Vredefort Structure are apparently anomalous compared to those at known impact sites. Grieve *et al.* (1990), however, interpret this anomaly as the result of post-shock recrystallization. Reimold (1990), on the other hand, maintains that the general appearance of the vast majority of microdeformations in the quartz of Vredefort rocks is not consistent with the criteria of shock lamellae outlined by Alexopoulos *et al.* (1988). He suggested that tectonic forces at high strain rates could be the cause of the phenomena. Finally, Hart *et al.* (1991) conclude that the shock phenomena (the microdeformations) do indicate that the Vredefort Structure represents the oldest and largest known impact structure on earth. They postulate, however, that there were thermo-tectonic events which occurred both prior to and after the postulated impact event, which complicate the interpretation of its origin.

Coesite and Stishovite – Martini (1978) was able to demonstrate that coesite and stishovite are in fact present in Vredefort rocks, as had earlier been predicted by Dietz (1961). He found these polymorphs of SiO_2 to be associated with thin pseudotachylite veinlets in a sample of collar rock from the Central Rand Group in the northeastern part of the collar of the Vredefort Structure. According to Martini (1991) controversial arguments, with regard to the origin of these polymorphs of SiO_2, were put forward by some earth scientists who claim that these high-pressure phases of SiO_2 may also grow at much lower pressures than accepted and are thus not necessarily indicative of impact . Martini (*op. cit.*), however, discusses and deals convincingly with these arguments. In a follow-up study he was able to outline the field distribution of these polymorphs, in the Vredefort area, and concluded that the origin by impact remained the simplest and most realistic model to explain the origin of the Vredefort Structure.

The geochronology of the rock units in the Vredefort area

Most of the important rock units which have a bearing on the history of events in the Vredefort area have been dated and the age data are reviewed by Walraven and Elsenbroek (1991). From the data published by these authors and Reimold *et al.* (1990a), the following list of important rock units and their dates, in descending order, has been compiled:

ROCK UNIT	AGE (GA)
Mafic relics in the ILG of the core	3.5
The ILG and OLG of the core	3.0
The Dominion Group	3.0
The Ventersdorp Supergroup	2.7
Pseudotachylite	2.25 ± 4
The Transvaal Sequence	2.2 to 2.5
The Schurwedraai alkali granite and mariupolite dykes	2.2
Massive overprinting recorded in the ILG and OGG	2.0–2.1 and 2.2–2.4
The Lindequesdrift pluton and Roodekraal Complex	2163 ±31
The Losberg Complex	2041 ±41
Bronzite Granophyre	2006
The Rietfontein Complex	2004 ±
Late Central Intrusive Granite	1944 ± 92
Pseudotachylite (?)	1090 ± 10

Introduction to subsequent chapters:

The chapters constituting the main body of this thesis comprise the following research papers:

Chapter 2. The tectono-sedimentary setting of the area of the Vredefort Structure during the deposition of the upper quartzite member of the Hospital Hill Subgroup.

Chapter 3. An appraisal of the significance of small-scale fold structures in the contorted bed of the area of the Vredefort Structure.

Chapter 4. The reconstruction of palaeocurrent dispersal patterns for Turffontein strata in the Vredefort Structure in relation to a tectonic model for the area.

Chapter 5. Transgressive and progradational beach and nearshore facies in the late Archaean Turffontein subgroup of the Witwatersrand Supergroup, Vredefort area, South Africa.

Chapter 6. Megascopic planar shock fractures in the Vredefort Structure: a potential time marker.

Chapter 7. The interrelationship of structural elements in the upper quartzite member of the Hospital Hill Subgroup in the southwestern portion of the Vredefort collar.

Chapter 8. Shatter cones in Vredefort rocks – imagination or reality?

Chapter 9. The stratigraphy and geology of the Central Rand Group in the Vredefort area: An explanation of the accompanying geological map.

In these papers the principles of sedimentology, stratigraphy and structural geology form a basis of mutual support for various aspects outlined in the objectives of the papers.

A joint objective of the reconstruction of palaeocurrent patterns (Chapters 2 and 4) and of the study of the distribution pattern of small-scale folds in the contorted bed (Chapter 3) is to determine if the granite-gneiss, forming the core of the Vredefort Structure, had at any time during the history of sedimentation of the Witwatersrand strata, been a "structural entity" as proposed by Brock and Pretorius (1964).

The major objective of the paper of Chapter 3 is to confirm a tectonic origin (as opposed to a gravity-slump origin) for the contorted bed of the Hospital Hill Subgroup in the Vredefort area. This is substantiated against the background of the regional palaeoslope direction, during late Hospital Hill times, as established by palaeocurrent modes (Chapter 2). It is further suggested that the contorted bed possibly marks a tectonic event of minor thrusting which predates the episode of crustal tension during the Ventersdorp volcanic period.

Chapters 2 and 4, focus mainly on the reconstruction of the palaeodrainage patterns in the "Vredefort window" during Hospital Hill and Turffontein times. Chapter 4, however, has two additional important objectives: (i) to demonstrate that the conventional method of reconstructing palaeocurrent vectors (restoring the beds to the horizontal by rotating them about their strike axes) has an inherent shortcoming, in that the technique is based on a misconception of the large-scale nature of the Vredefort Structure; and (ii) to propose a reconstruction technique based on an empirically-derived model for the Vredefort Structure.

In Chapter 5 the undoubted existence of shallow marine conditions during mid-Turffontein times is indicated, amidst the general contrary viewpoint that the Central Rand Group comprise fluvial sediments only. Possible beach and nearshore depositional conditions are proposed for a thin marine unit in the Turffontein Subgroup.

In Chapter 6 the attention is drawn to the regional distribution pattern of densely-spaced fracture surfaces which pervade most of the quartzitic formations of the Vredefort Collar and which have hitherto been overlooked by geoscientists. Because these s–surfaces have a geometrical relationship with shatter cones, they are regarded as genetically-related phenomena and can therefore be used to demarcate a chronological boundary, which separates all geo-events predating the upturning of the collar strata from all geological episodes post-dating this event. This dictum is put to practice in Chapters 3 and 7.

In Chapter 8 the attention is focused on the fact that discrete shatter cones, although extremely rare, do exist and that the concept of the geometry of the cone, as derived statistically, is in fact valid.

Chapter 9 introduces a proposed lithostratigraphical subdivision for the Central Rand Group of the Vredefort area, based on recent mapping of this stratigraphic unit. Short descriptions of the geology of the Formations, in this Group, are given.

In the final chapter (Chapter 10) the findings of the preceding research papers are integrated into sedimentological and structural models, which should contribute to a better understanding of the complex geology of the Vredefort Structure.

REFERENCES

Albat, H.M. (1988). Shatter cone/bedding interrelationship in the Vredefort Structure: evidence for meteorite impact? *S. Afr. J. Geol.*, **91**, 106-113.

Alexopoulos, J.S., Grieve, R.A.F. & Robertson, P.B., (1988). Microscopic lamellar deformation features in quartz: discriminative characteristics of shock generated varieties. *Geology*, **16**, 796-799.

Bailey, E.B. (1926). Domes in Scotland and South Africa. *Geol. Mag.*, **43**, 481-494.

Bisschoff, A.A. (1969). *The petrology of the igneous and metamorphic rocks in the Vredefort Dome and adjoining parts of the Potchefstroom Syncline.* D.Sc. thesis (unpubl.), Univ. Pretoria, 243pp.

Bisschoff, A.A. (1971). The dioritic rocks of the Vredefort dome. *Trans. geol. Soc. S. Afr.*, **75**, 31–45.

Brink, A.B.A. and Knight, K. (1961). Discussion on 'Shatter cones in the rocks of the Vredefort Ring'. *Trans. geol. Soc. S. Afr.*, **64**, 157–158.

Brock, B.B. (1961). Discussion on 'Shatter cones in the rocks of the Vredefort Ring'. *Trans. geol. Soc. S. Afr.*, **64**, 155.

Brock, B.B. and Pretorius, D.A. (1964). Rand basin sedimentation and tectonics, pp. 549-599. In: S.H. Haughton (Ed.), *The Geology of some Ore Deposits of Southern Africa*, 1, Geol. Soc. S.Afr., Johannesburg, 625pp.

Bucher, W.H. (1963). Cryptoexplosion structures caused from without or from within the Earth ('astroblemes' or 'geoblemes')? *Amer. J. Sci.*, **261**, 597-649.

Carter, N.L. (1965). Basal quartz deformation lamellae – a criterion for recognition of impactites. *Amer.J. Sci.*, **263**, 786–806.

Carter, N.L. (1968). Dynamic deformation of quartz, pp. 453–474. In: B.M. French and N.M. Short (Eds.), *Shock Metamorphism of Natural Materials.* Mono Book, Baltimore.

Colliston, W.P. (1990). A model of compressional tectonics for the origin of the Vredefort Structure. *Tectonophysics*, **171**, 115-118.

Corner, B., Durrheim, R.J. and Nicolaysen, L.O. (1990). Relationships between the Vredefort structure and the Witwatersrand basin within the tectonic framework of the Kaapvaal craton as interpreted from regional gravity and aeromagnetic data. *Tectonophysics*, 171, 49–62.

Daly, R.A. (1947). The Vredefort ring-structure of South Africa. *J. Geol.*, **55**, 125-145.

Dietz, R.S. (1959). Shatter cones in cryptoexplosion structures (meteorite impact?). *J. Geol.*, **67**, 496–505.

Dietz, R.S. (1961). Vredefort ring-structure – Meteorite impact scar? *J. Geol.*, **69**, 499–516.

Du Toit, A.L. (1954). *The Geology of South Africa*. Oliver and Boyd, Edinburgh, 3rd ed., 611pp.

French, B. M., Orth C.J., and Quintana L.R. (1989). Iridium in the Vredefort Bronzite Granophyre: Impact melting and limits on a possible extraterrestrial component. *Proc. Lunar Planet Sci. Conf. 19th*, pp. 733–744.

French, B.M. (1990). 25 Years of the Impact-Volcanic Controversy. *Eos*,71, 411–414.

French, B.M. and Nielsen, R. (1990). Vredefort Bronzite Granophyre: chemical evidence for origin as a meteorite impact melt. *Tectonophysics*, 171, 119–138.

Fricke, A., Medenbach, O. and Schreyer, W. (1990). Fluid inclusions, planar elements and pseudotachylites in the basement rocks of the Vredefort Structure, South Africa. *Tectonophysics*, 171, 169–183.

Grieve, R.A.F., Coderre, J.M., Robertson, P.B. & Alexopoulos, J. (1990). Microscopic planar deformation features in quartz of the Vredefort Structure: Anomalous but still suggestive of an impact origin. *Tectonophysics*, 171, 185-200.

Hall, A.L. & Molengraaff, G.A.F. (1925). The Vredefort Mountain Land in southern Transvaal and northern Orange Free State. *Verh. K. Akad. Wet.*, 24, 1–183.

Hargraves, R.B. (1961). Shatter cones in the rocks of the Vredefort Ring. *Trans. geol. Soc. S. Afr.*, **64**, 147–154.

Hart, R.J., Andreoli, M.A.G., Reimold, W.U. and Tredoux, M. (1991). Aspects of the dynamic and thermal metamorphic history of the Vredefort cryptoexplosion structure: implications for its origin. *Tectonophysics*, 192, 313–331.

Lilly, P.A. (1981). Shock metamorphism in the Vredefort collar: evidence for internal shock sources. *J. geophys. Res.*, 86, 10689-10700.

Manton, W.I. (1962). *The orientation and implication of shatter cones in the Vredefort Ring structure.* M.Sc. thesis (unpubl.) Univ. Witwatersrand, Johannesburg, 167pp.

Manton, W.I. (1965). The orientation and origin of shatter cones in the Vredefort Ring. In: *Geological Problems in Lunar Research.* Ann. New York Akad. Sci., **123**, 1017-1049.

Maree, B.D. (1944). The Vredefort Structure as revealed by a gravimetric survey. *Trans. geol. Soc. S. Afr.*, **47**, 183–196.

Martini, J.E.J. (1978). Coesite and stishovite in the Vredefort Dome, South Africa. *Nature*, **272**, 715–717.

Martini, J.E.J. (1991). The nature, distribution and genesis of the coesite and stishovite associated with the pseudotachylite of the Vredefort Dome, South Africa. *Earth Planet. Sci. Lett.*, **103**, 285–300.

Melosh, H.J. (1989). *Impact Cratering A Geologic Process.* Oxford University Press, New York, 245 pp.

Nel, L.T. (1927). The geology of the country around Vredefort – An explanation of the geological map. *Spec. Publ. geol. Surv. S. Afr.*, **6**, 134pp.

Nel, L.T., Truter, F.C., Willemse, J. and Mellor, E.T. (1939). *The geology of the country around Potchefstroom and Klerksdorp.* Expl. Sheet 61 (Potchefstroom), geol. Surv. S. Afr., Dept. Min., Govt. Printer, Pretoria 156pp.

Nicolaysen, L.O. (1972). North American cryptoexplosion structures: interpreted as diapirs which obtain release from strong lateral confinement. *Mem. geol. Soc. Amer.*, **132**, 605–620.

Nicolaysen, L.O. & Reimold, W.U. (1978). Shatter cones revisited (working paper). *Contributions to International Workshop on Cryptoexplosions and Catastrophes in the Geological Record, Parys, South Africa, Section N2.*

Pohl, J. (1987). Introduction to the Riess crater. *Contributions to International Workshop on Cryptoexplosions and Catastrophes in the Geological Record, Parys, South Africa, Section N2.*

Ramsay, J.G. (1961). Discussion on 'Shatter cones in the rocks of the Vredefort Ring'. *Trans. geol. Soc. S. Afr.*, **64**, 156–157.

Ramsay, J.G. & Huber, M.I.(1987). *The techniques of modern structural geology. Volume 2: Folds and Fractures.* Academic Press, Oxford, 462 pp.

Reimold, W.U. (1990) The controversial microdeformations in quartz from the Vredefort Structure, South Africa – a discussion. *S. Afr. J. Geol.*, **93**, 645–663.

Reimold, W.U., Jessberger, E.K. and Stephan, T., Bayly, B. (1990a). ^{40}Ar–^{39}Ar dating of pseudotachylite from the Vredefort dome South Africa: a Progress report. *Tectonophysics*, **192**, 139–152.

Reimold, W.U., Horsch, H., and Durrheim, R.J. (1990b). The "Bronzite"-Granophyre from the Vredefort Structure – A detailed analytical study and reflections on the genesis of one of the Vredefort's enigmas. *Proceedings of the 20th lunar and Planetary Science Conference*, pp. 433–450.

Schreyer, W. (1983). Metamorphism and fluid inclusions in the basement of the Vredefort Dome, South Africa: guidelines to the origin of the structure. *J. Petrol.*, 24,(1), 26–47.

Simpson, C. (1978). The Structure of the rim synclinorium of the Vredefort Dome. *Trans. geol. Soc. S. Afr.*, 81, (1), 115–122.

Simpson, C. (1981). Occurrence and orientation of shatter cones in Pretoria Group quartzites in the collar of the Vredefort 'Dome': impact origin precluded. *J. geophys. Res.*, 86, 10701–10706.

Slawson, W.F. (1976). Vredefort core: a cross section of the upper crust. *Geochim. Cosmochim. Acta.*, 40, 117–121.

Stepto, D. (1979). *A geological and geophysical study of the central portion of the Vredefort Dome structure.* Ph.D. Thesis, Univ. Witwatersrand, Johannesburg, 500pp.

Stepto, D. (1990). The geology and gravity field in the central core of the Vredefort structure, *Tectonophysics*, 171, 75–103.

Truswell, J.F. (1977). *The geological evolution of South Africa.* Purnell, Cape Town, 218pp.

Walraven, F. & Elsenbroek, J.H. (1991). Geochronology of the Schurwedraai Alkali Granite and associated nepheline syenite and implications for the origin of the Vredefort structure. *S. Afr. J. Geol.*, 91, (2/3), 228–235.

Willemse, J. (1937). On the Old granite of the Vredefort region and some of its associated rocks. *Trans. geol. S. Afr.*, 40, 43–119.

Winter, H. de la R. (1987a). Vredefort Structure fits naturally into regional geology. *Contributions to International Workshop on Cryptoexplosions and Catastrophes in the Geological Record, Parys, South Africa, Section N2.*

Winter, H. de la R. (1987b). A cratonic foreland model for Witwatersrand Basin development in a continental back-arc, plate-tectonic setting. *S. Afr. J. Geol.*, 90, 409–427.

CHAPTER 2

THE TECONO-SEDIMENTARY SETTING OF THE AREA OF THE VREDEFORT STRUCTURE DURING THE DEPOSITION OF THE UPPER QUARTZITE MEMBER OF THE HOSPITAL HILL SUBGROUP

S.Afr.J.Geol.,1988.91(2).239–247

The tectono-sedimentary setting of the area of the Vredefort Structure during deposition of the upper quartzite member of the Hospital Hill Subgroup

J.J. Mayer and H.M. Albat

Department of Geology, Potchefstroom University for Christian Higher Education, Potchefstroom 2520, Republic of South Africa

Accepted 19 January 1988

Palaeocurrent data from the upper quartzite member of the Hospital Hill Subgroup reveal a relatively uniform palaeostrike for the area of the Vredefort Structure during the early part of the history of Witwatersrand sedimentation. This palaeostrike was approximately north-northeast to south-southwest for the western part of the structure and northeast to southwest for the eastern part. The direction of the palaeodeclivity, according to palaeocurrent data, was in a general southeasterly direction. No early hub existed. The tectono-sedimentary setting of the environment of early Witwatersrand sedimentation is envisaged to have been that of a continental shelf subjected to cycles of transgression and regression by a shallow sea.

Paleostroomgegewens afkomstig van die boonste kwartsietlid van die Hospitaal Heuwelsubgroep toon aan dat 'n relatiewe eenvormige paleostrekking in die gebied van die Vredefortstruktuur, tydens die vroeë deel van die geskiedenis van Witwatersrandsedimentasie, bestaan het. Hierdie paleostrekking was ongeveer noord-noordoos na suid-suidwes vir die westelike deel van die struktuur en noordoos na suidwes vir die oostelike deel. Die rigting van die paleohelling was, volgens die paleostroomgegewens, in 'n algemene suidoostelike rigting. Geen vroeë koepel het bestaan nie. Die tektono-sedimentêre ligging van die omgewing van Witwatersrandsedimentasie word voorgehou as dié van 'n kontinentale platte wat onderwerp was aan siklusse van transgressie en regressie deur 'n vlak see.

Introduction

The 2,3-2,7 G.a. (Allsopp *et al.*, 1986) Witwatersrand succession of gold-bearing, mostly shallow-water, clastic sediments, as well as the associated enigmatic Vredefort Structure, located almost centrally within the Witwatersrand Basin, are two of the best known geological features of South Africa (Figure 1). Varied and divergent hypotheses with regard to the origin of the Witwatersrand Basin and particularly the Vredefort Structure have evolved with the course of time.

With regard to the origin of the Witwatersrand Basin and sediments, early prospectors naively assigned a fluvial origin to a Witwatersrand gold-bearing conglomerate regarding it to be a tilted fossil river bed (Truswell, 1977). Later, based on the knowledge of the greater areal extent of the Witwatersrand beds, early investigators were led to believe that the Witwatersrand sediments represented a shallow marine littoral sequence (Brock & Pretorius, 1964,).

As a result of more information on the Witwatersrand depository which became available due to a heightening of prospecting activities for gold after 1932, Brock & Pretorius (1964) developed their model of a restricted tectonic basin on a craton. According to Brock & Pretorius (1964) the great thickness of shallow-water sediments, with which the basin was filled, is quite incompatible with oceans.

This model of the Witwatersrand depository, wherein the emphasis was placed on the fluvial filling of a restricted basin, has remained popular for more than a decade. The return to a view of some open marine origin, for at least the 'lower' division of the Witwatersrand succession, has now been in vogue for some time (Eriksson *et al.*, 1979; Camden-Smith, 1980; Watchorn, 1980). The subsequent closing of the basin is considered to have followed at a late stage in the lower Witwatersrand times (Watchorn, 1980; Tankard *et al.*, 1982) due to the progressive deformation of the depositional environment. According to Winter (1986) the plate-tectonic setting was that of a back arc.

With regard to the Vredefort Structure, Brock & Pretorius (1964) believed that the Witwatersrand Basin was, from the outset, crudely defined by an elliptical ring of granite domes of which the Johannesburg and Devon domes (Figure 1) were probably positive features and "the Vredefort hub, in its basin environment, can be viewed as a cratonic unit rigid enough to have influenced the shape and attitude of the adjacent rocks". The idea that the hub was a pre-existing structural entity with a presumably positive character in pre-Witwatersrand times is also

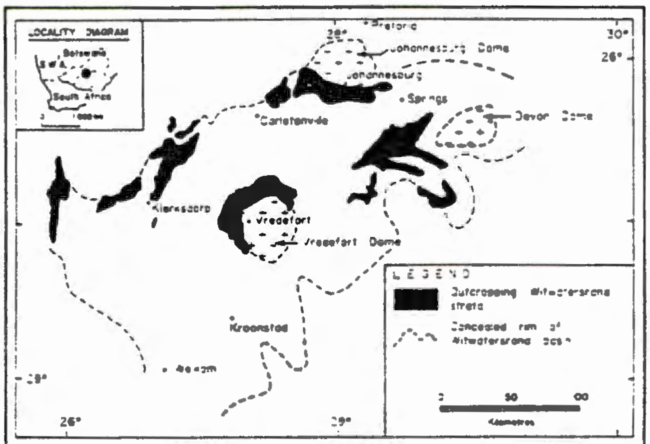

Figure 1 Simplified map showing outlines of the Witwatersrand Basin and the larger granite domes of the region as well as the Vredefort Structure (after Tankard *et al.*, 1982).

shared by other authors such as Willemse (1937), Bishopp (1941), Maree (1944), Du Toit (1954), and Bisschoff (1969). The authors mentioned above have all implicitly taken the stance that endogenetic forces were responsible for not only the origin of the Vredefort Structure, but also the deformation of the Witwatersrand Basin, and therefore, the origin of the Potchefstroom Synclinorium as such.

Diametrically opposed to this idea are the views of those who believe the Vredefort Structure to be an astrobleme. The early and tentative proposals by Daly (see Truswell, 1977) that the Vredefort Structure represented the impact scar of an enormous meteorite was revived by Dietz (1961) and supported by Hargraves (1961) and Manton (1965). These authors believe that certain shock phenomena, and in particular the so-called shatter cones which occur in Vredefort rocks, are positive manifestations of the impact origin of this structure. However, it is considered that similar features might also result from a sudden diapiric release of compressed columns of rock in the earth's crust (Nicolaysen, 1972).

The objective of this research, the results of which are presented in this paper, is threefold. Primarily the investigation of palaeocurrent patterns of the upper Hospital Hill quartzite was undertaken to determine whether the floor on which the Dominion Group lavas extruded, and on which the deposition of the Witwatersrand sediments had followed in the area of the Vredefort Structure, had any initial positive hub-like character, or whether any record of an early rising of the floor of this area is manifested by sedimentary structures which relate to the palaeoslope. Secondly, research now in progress shows a consistent pattern for the attitude of fold axes of the contorted bed over the area of the Vredefort Structure after the over-folded strata are restored to a horizontal attitude. The question of the palaeoslope during early Witwatersrand times, addressed in this paper, is therefore important as evidence for assessing the merits of the two opposing hypotheses on the origin of the contorted bed: soft sediment deformation versus tectonic deformation. Thirdly, the outcome of this study was deemed to be of importance in connection with respect to a marine origin for the sedimentary succession of the Hospital Hill quartzites in the area of the Vredefort Structure.

Primary sedimentary structures, palaeocurrent directions and general stratigraphic character of the upper quartzitic succession and associated beds of the Hospital Hill Subgroup

The spectacular Vredefort Structure is composed, for most part, of steeply dipping to overturned strata. The tilted to overfolded strata of this structure comprise Dominion lavas and Witwatersrand, Ventersdorp, and Transvaal successions, draped in a semi-circular fashion around the northwestern segment of a partially exposed hub of basement granite gneiss (Figure 2). Within the arc of exposed lower Witwatersrand rocks, surrounding the granite-gneiss core, interrupted ridges of the well developed upper quartzite of the Hospital Hill Subgroup contribute towards the topography constituting the Vredefort Mountain Land. These ridges of quartzite do not only stand out because of the grandeur of their steep dip slopes (especially noticeable in the northwestern and northern parts of the arc of collar rocks) but they are also conspicuous due to the reflective nature of their relatively pure white basal beds. Stratigraphically higher up in the succession the quartzites are notably brownish-buff in colour and microscopic evidence, as well as the physical appearance of thin argillite drapes on scoured surfaces, confirm their lesser degree of winnowing. These observations apply more notably to the southwestern sector of the Dome.

Throughout the area of the Vredefort Structure trough cross-bedding is abundantly developed as a primary sedimentary structure in the upper Hospital Hill quartzitic succession. The troughs are excellently manifested as casts on the overturned dip slopes where they show up as gently curved bulging structures. They display their contents of cross-beds in the form of 'ribbings' crossing the cylindrical-like structures (Figures 3a and 3b). The ribbings are the traces of foresets whose inclined surfaces consecutively intersect the enveloping surfaces of the troughs. Other primary sedimentary structures which occur, but show localized development, are planar cross-beds, current ripples, small oscillation ripples, and sets of interference ripples. Sedimentary deformation structures

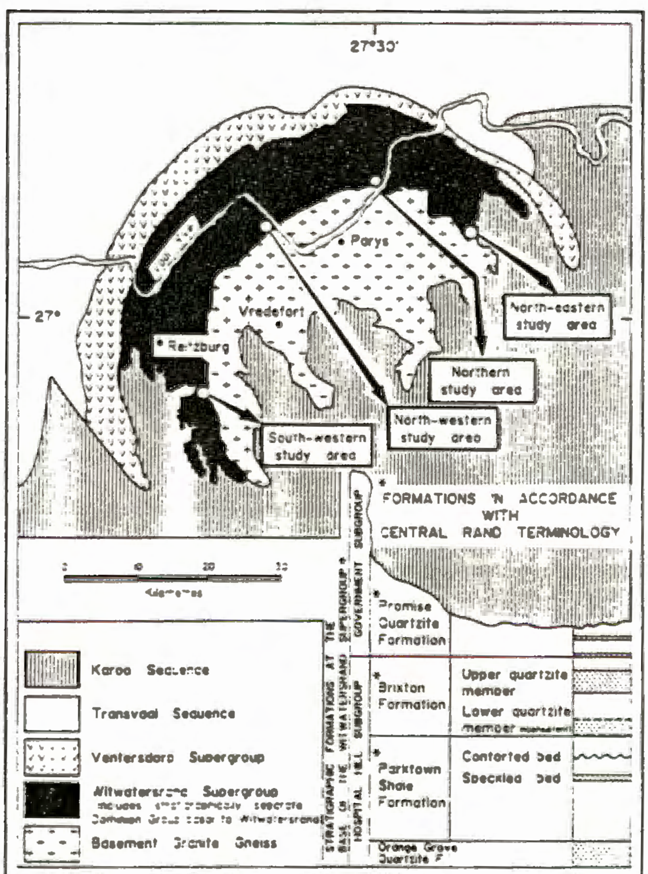

Figure 2 Map of the Vredefort Structure (after Truswell, 1977) showing distribution of study areas and stratigraphy at the base of the Witwatersrand Supergroup.

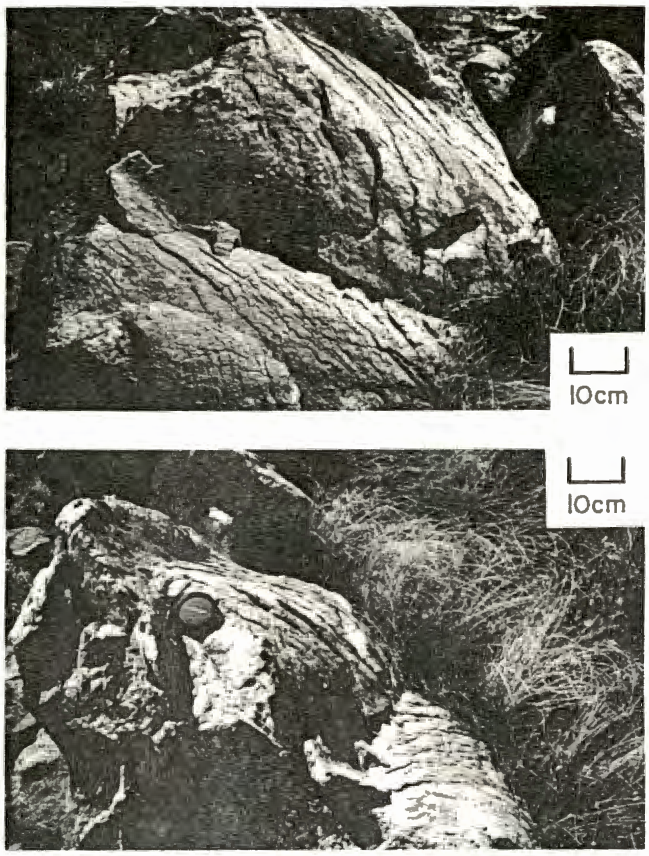

Figure 3 Casts of troughs (trough cross-bedding) upper Hospital Hill quartzite southwestern study area. Note traces of foresets crossing troughs. a.(above) Two troughs (not *in situ*) separated by a cusp. b.(below) Two troughs (*in situ*) on dipslope of overturned beds: beds dip east, trough axes plunge northeast.

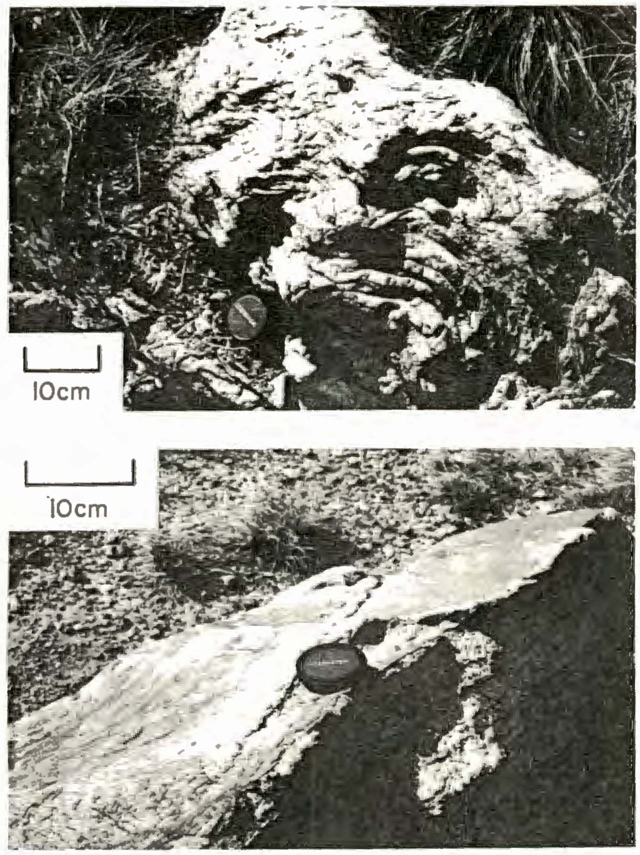

Figure 4 a.(above) Convolute folds in foresets of planar cross-beds (upper Hospital Hill quartzite, southwestern study area). Note that structures are upside down as cuspidal 'anticlines' normally point upwards. b.(below) Molds of two troughs (uninverted) separated by sharp-pointed cusp. Right-way-up strata of upper Hospital Hill quartzite (southwestern study area).

such as overturned crossbeds and convolute folding are also developed (Figure 4a).

Four localities (Figure 2), spaced over the area of the Vredefort Structure, were selected for studying primary sedimentary structures and their palaeocurrent directions. These localitiess, on the upper Hospital Hill quartzite, are referred to as the southwestern, northwestern, northern, and northeastern study areas respectively.

The southwestern study area (Leeuwdoorns 350 and adjoining Vlakspruit 1180)

The southwestern study area comprises the outcrop of the upper quartzite member of the Hospital Hill Subgroup which forms a low, but prominent ridge configured in a z-like pattern in plan on Leeuwdoorns 350 (IQ), but which extends with the normal northerly regional strike towards the adjoining farm Vlakspruit 1180 (IQ) (Figure 6). At the southern end of the outcrop on Leeuwdoorns 350 (IQ) the strata are terminated by a major fault. From this point, in a northerly direction, the consecutive outcrop segments of the z-pattern, which is due to an uncommon fold structure, are respectively presented by overturned easterly dipping strata followed by right-way-up northerly dipping strata, followed by overturned easterly dipping strata (Figure 6). The relatively short stretch of right-way-up strata, in the fold structure of this area, affords the opportunity of viewing some uninverted structures (Figure 4b). At one locality along this outcrop a solitary, but fine example of a linguoid current ripple has been preserved. The recording of palaeocurrent directions, however, was exclusively made on the inverted outcrops of the southwestern study area because these outcrops conform to the general regional strike. At the top of the arenitic succession planar crossbeds (Figure 5) and water-escape structures (Figure 4a) are developed. In order to illustrate the character of the sediments and the spatial distribution of the primary and other sedimentary structures of the upper Hospital Hill quartzite in this study area a generalized stratigraphic column is presented by Figure 7.

The column shows that, besides being preceded and succeeded by mudrocks, the sands are also interrupted by a local facies consisting of fine-grained muddy sediments and some interbedded sands. None of the contacts between the dominantly arenitic successions (weather-resistant) and the mixed mud-sand rocks or other mudrocks (less resistant) are exposed. No gravel lags or pebbles were found within the succession of beds of the arenitic sequence or the strata directly bounding thls sequence in any of the study areas.

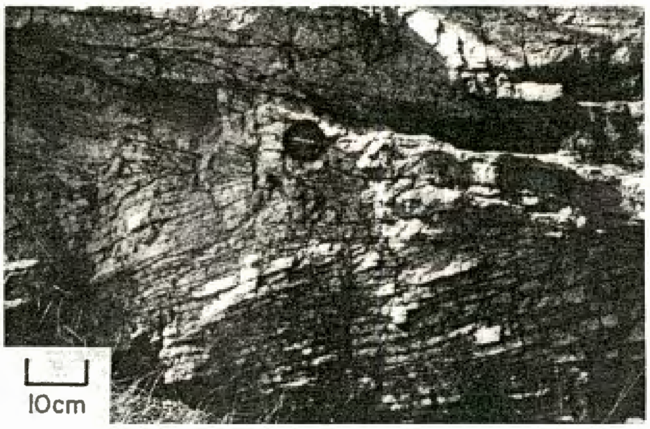

Figure 5 Planar tabular cross-bedding in Hospital Hill quartzite, southwestern study area. Set thickness ± 45 cm.

At this stage it must be pointed out that although the rocks of the study areas are described in sedimentary terms, in this paper, they in fact represent metaquartzites, hornfelses, and ferruginous slates. In addition, they also contain certain alleged shock phenomena such as shatter cones, brecciated zones filled with pseudotachylite and pseudotachylite veins. Fortunately, the thermal and shock metamorphism, to which the rocks were subjected, did not obliterate their original sedimentary character nor destroy any of the sedimentary structures they contain. It must also be noted that the broad subdivision of the generalized stratigraphic column (Figure 7), into four facies, is not intended as an accurate facies analysis. The divisions are in general substantiated by lithological differences as well as differences in the character of the primary sedimentary structures which they contain.

The lower mud facies (consistent in the Vredefort area) forms part of a thick succession of banded to laminated ironstones and is probably the product of chemical precipitation. Interbedded in this facies, in the southwestern study area at lower stratigraphic levels are bands of andalusite hornfelses which show finely laminated to graded bedding characteristics. The ironstones and mudstones outcrop sparsely and are mostly covered by alluvium.

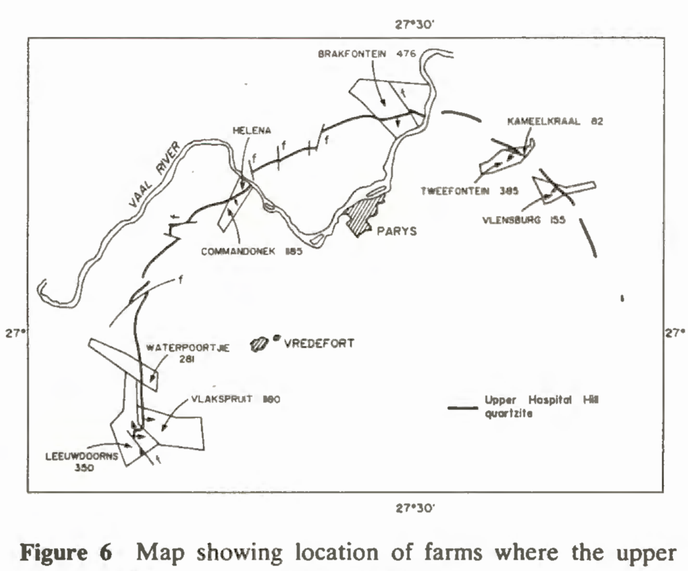

Figure 6 Map showing location of farms where the upper Hospital Hill quartzite was studied for palaeocurrent trends.

The basal or orthoquartzitic facies of the arenitic succession (consistent in the Vredefort area and responsible for the dip slopes of the upper Hospital Hill Quartzite in most areas) is characterized by white, well-winnowed sands which show well-developed trough cross-bedding and occasional small symmetrical ripple marks and sets of interference ripples. The troughs show a unimodal and exclusively mono-directional palaeocurrent pattern (Figure 7). In the southwestern and other study areas, with the exception of the northeastern study area, this facies was exclusively analysed for palaeocurrent directions (Figure 8). The arenites of this facies, which are usually fuchsite-stained, show troughs varying from a few centimetres to more than a metre in the transverse section. The trend of the palaeocurrents, obtained from the recording of trough axes and foreset geometery in this unit, is towards the core of the Vredefort Structure i.e., in an east-southeasterly direction (Figure 8a) after the overfolding of the beds is restored. In this respect the rotation of the data to restore the overfolding was carried out using the local strike of the strata as rotational axes for all study areas. From the consistent regional pattern

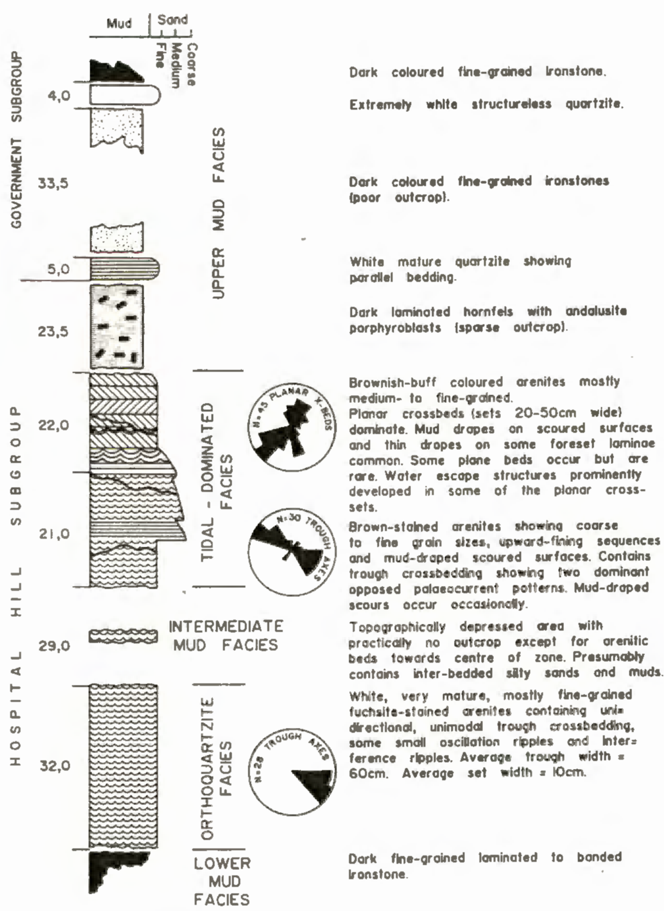

Figure 7 Generalized stratigraphic column for the upper Hospital Hill quartzite showing nature of bounding formations and sedimentary character and structures of the quartzitic sequence.

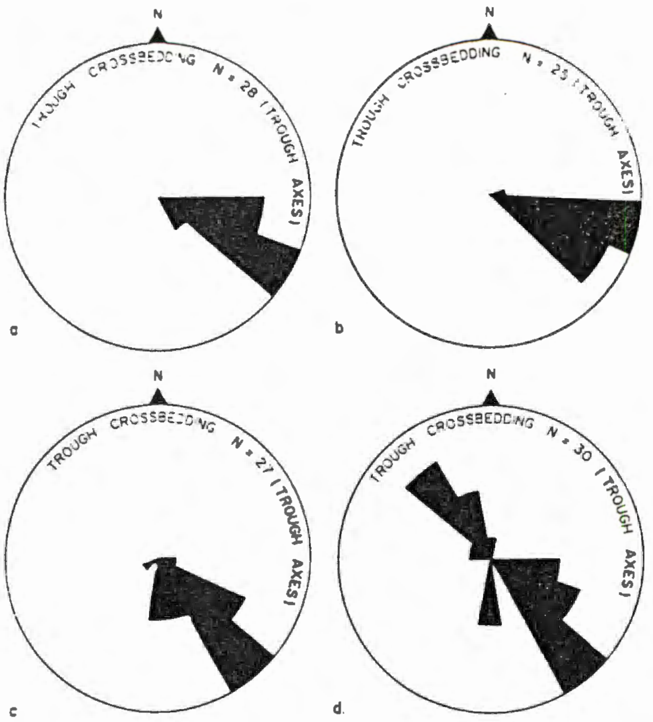

Figure 8 Rose diagrams showing palaeocurrent trends based on trough cross-bedding in different study areas. a. Southwestern study area (basal facies only). b. Northwestern study area (basal facies only). c. Northern study area (basal facies only). d. Northeastern study area (composite of basal and tidal-dominated facies).

obtained from the different study areas, it seems that this simple rotational procedure is reasonably accurate. The character of the intermediate mud facies (restricted to the southwestern sector of the Dome), which follows the basal orthoquartzite facies, is obscure due to the lack of outcrop of these fine-grained rocks. Thin beds of arenite outcrop within this topographically depressed zone which divides the quartzite outcrop of the southwestern study area into two units. The presence of such sandy beds shows that the intermediate mud facies is possibly composed of interbedded sands and mud. The inference that mud rocks are present is based upon the existence of an andalusite hornfels, forming sparse outcrops within this unit, on Waterpoortjie 281 (Figure 6) further to the north of the southwestern study area. The absence of this facies, in the other study areas, confirms that it is a locally developed facies restricted to the southwestern sector of the Vredefort Structure.

The tidal-dominated facies (consistently developed in the area of the Vredefort Structure) follows the intermediate mud facies and is characterized by brown to brownish-buff outcrops of quartzite. It is composed of arenites which vary from coarse to fine. Upward fining cycles are evident in this facies, but applies only to the southwestern study area. The presence of various amounts of mud within the sands of this facies is revealed by the development of some sericite (as seen under the microscope) and the physical appearance of thin mud drapes on the foresets of some cross-beds. Mud-draped reactivation surfaces and scoured surfaces, which cut accross cross-bedded structures, are not uncommon in this facies. In the other study areas these features are rare. Despite the presence of mud, some well-winnowed sands are present. The lower, but major, part of this facies is characterized by well-developed cross-bedded structures which show a bi-directional palaeocurrent pattern. The two dominant and opposing directions of palaeocurrents, which are towards and away from the core of the Vredefort Structure, are southeast and northwest (Figure 7) after undoing the overfolding.

Towards the upper part of the tidal-dominated facies some plane beds, but mostly medium-scaled planar cross-beds (set thicknesses varying between 20 cm and 50 cm) (Figure 5), are developed to the exclusion of trough cross-bedding. Although the foresets of these cross-beds show a dominant southwesterly inclination (after restoring the overfolding) opposite dipping planar cross-beds, with their forsets inclined towards the northeast, are also developed (Figure 9a). In this upper subfacies, consisting of planar cross-bedded sands, the foresets of some of the units are disturbed by convolute folds which show a statistical parallelism of their fold axes to the strike of the foresets of the planar cross-beds (Figure 9a).

The tidal-dominated facies is followed by the upper mud facies (consistent in the area of the Vredefort Structure) and the transition of sands to mud is abrupt. The contact between the sand and the mud facies is obscure due to the poor outcropping of the mudrocks which, in this study area, is an andalusite hornfels. Higher up the clays are replaced by finely laminated ironstones, but due to poor outcrop the character of the transition is not known. Two thin quartzite beds are contained in upper mud facies. The lower of the two shows faint parallel bedding whereas the stratigraphically higher quartzite is extremely white, fine grained, and structureless.

The northwestern study area (Commandonek 1185)

In the northwestern sector of the Vredefort Structure the Witwatersrand strata are overturned and dip steeply (80° southeast) towards the granite-gneiss core of the structure. This causes the upper quartzite succession of the Hospital Hill Subgroup, to outcrop spectacularly in the area. On the farm Commandonek 1185 (IQ) (Figure 6) this topographically conspicuous ridge, donned with white quartzite on its smoothly stripped dip slope, is breached by the Vaal River. At this point a low neck has been cut into the quartzite hill through which the river flows. The orthogonal crossing of the Witwatersrand strata by the Vaal River in this area is ascribed to superposed drainage (King, 1951).

Whereas the upper and lower mud facies are present in this study area, no distinct intermediate mud facies separates the orthoquartzite facies and the tidal-dominated facies. In the lower well-winnowed orthoquartzite facies, similar to the southwestern study area, cross-bedded troughs with a unidirectional palaeocurrent pattern are developed. The palaeocurrent direction, which is towards the granite gneiss core of the

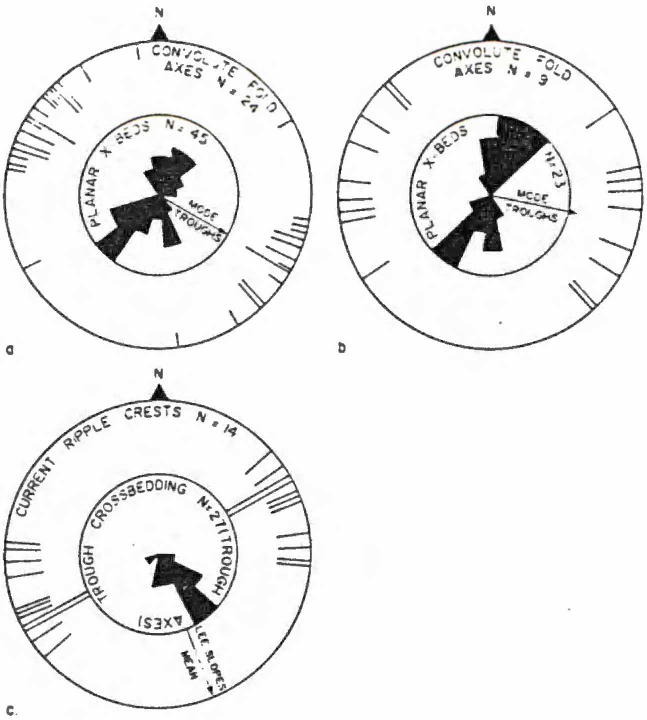

Figure 9 Diagrams comparing the orientation of sedimentary structures: a. Southwestern study area (planar cross-beds and convolute fold axes). b. Northwestern study area (planar cross-beds and convolute fold axes). c. Northern study area (trough cross-bedding and current ripple crests).

Vredefort Structure, is east-southeast when the steeply dipping beds are rotated to the horizontal (Figure 8b). This corresponds to the direction found for the southwestern study area (Figure 8a). Planar cross-beds, with an average set thickness of 30 cm, occasionally intervene with the trough cross-bedding in this facies. These cross-beds show bidirectional preferred modes which are at right angles to the direction obtained from the trough axes (Figure 9b).

In the upper tidal-dominated facies of this region bidirectional or herringbone trough cross-bedded structures are again developed, but the traces of foresets are rather faint and the trough axes are difficult to identify. Recording of palaeocurrent directions was therefore restricted to the dipslopes of the basal orthoquartzite facies where trustworthy data could be obtained from the casts of troughs.

Convolute folding is evident in some cross-beds of the upper tidal facies of the northwestern study area but its occurrence is limited to a more restricted area. Although the orientation of the axes of convolute folds show a greater degree of variance, the approximate northwesterly to southeasterly trend, after restoring the overfolding, is once again apparent (Figure 9b).

The northern study area (Brakfontein 476)

The northern study area, located on Brakfontein 476 (IQ) (Figure 6), comprises the steeply overturned (84° towards the core), topographically prominent ridge of upper Hospital Hill quartzite on the western side of the Parys-Lindequesdrift road. In this area the road passes through a faulted neck in the quartzites which strike northeast to southwest. Whereas the ridge of upper Hospital Hill quartzite to the west of the road (and fault) dips steeply, the displaced outcrop on the eastern side is composed of low interrupted ridges and the strata dip at lower (60°) angles towards the granite-gneiss core.

Because of the greater degree of disturbance by faulting, which affect the strata of the eastern outcrop, the recording of primary sedimentary structures was restricted to the western outcrop. In this study area it is again clear that the stratigraphic basal, light-coloured, and well-winnowed orthoquartzite facies exclusively contains sedimentary structures which originated from undirectional current flow. In addition to troughs, which again show up as casts on the overturned dip slopes of the basal facies of the arenitic succession of this area, current ripples are also abundantly developed. The ripples show slightly sinuous ripple crests and are markedly asymmetrical, the observer having to appreciate the fact that negatives are viewed on the overturned dip slopes. The ripples vary in wavelength from 3,5 to 14 cm and in amplitude from 0,5 to 2 cm. The mean values for their ratios of ripple index and ripple symmetry are 8.9 and 4.3 respectively, which places them well inside Tanner's (1966) field of current ripples. The mean direction of the lee slopes of the current ripples is towards the southeast and agrees approximately with the direction obtained from troughs (Figure 9c). The tidal-dominated facies of this study area appears to be more mature than that of the southwestern and northwestern study areas. No structures, for palaeocurrent data, were recorded from this facies because the reliability of the data obtained from recording structures on the dip slopes of the basal facies is greater than for the top parts of the outcrop.

The northeastern study area (Kameelkraal 82, Tweefontein 385, and Vlensburg 155)

In the northeastern sector of the Vredefort Structure the dip of the collar rocks varies from relatively steeply overturned (60°) through to steep the right-way-up (80°). From Kameelkraal 82 (IQ) and Tweefontein 385 (IQ) towards Vlensburg 155 (IQ) (Figure 6), the strata of the lower part of the Witwatersrand Supergroup are broken up by faulting, and in this direction the topography becomes increasingly subdued so that the once prominent quartzite ridges are here reduced to low hills. Both the upper and lower quartzitic formations of the Hospital Hill Subgroup are developed in this area.

Here the basal orthoquartzite facies, containing the unidirectional current pattern, appears to be less prominently developed. The casts of cross-bedded troughs are not as abundant on the overturned dip slopes as in the other study areas. The tidal-dominated facies, by contrast, is prominently developed and differs from its counterpart in the southwestern study area in the sense that the quartzites are well-winnowed and mature. On Vlensburg 155 (IQ) (Figure 6) the development of herringbone trough cross-bedding is particularly well displayed on the low and flat-topped outcrops of near-vertical strata which occur to the north of the new Johannesburg-Kroonstad highway which bypasses Parys on its southern side. In this area the attitude of trough axes vary from nearly horizontal to plunging at low angles to the northwest. Near longitudinal sections of troughs, showing cross-bedding in opposite directions, can be seen on the crest of this outcrop. Some of the steeper plunging troughs give the impression of transverse sectioning. A survey of apparent trough lengths shows a maximum value of 4 m. The maximum set thickness of cross-bedding or trough depth is 20 cm. The mean set thickness of cross-bedding in troughs, directed to the southeast (towards the core of the Vredefort Structure, overfolding restored) is 11,3 cm, whereas troughs directed to the northwest (away from the core, overfolding restored) is 9,8 cm. The palaeocurrent pattern for the northeastern study area, which is based on recordings of structures occurring on all three farms (Kameelkraal 82 IQ, Tweefontein 385 IQ, and Vlensburg 155 IQ) (Figure 6) and taken from different stratigraphic levels within the arenitic succession, is consistent with the general trend i.e., southeast when compared with the ebb directions of the other study areas (Figure 8d). The flood direction, for this area is directly opposite and towards the northwest (Figure 8d).

The palaeosetting of the area of the Vredefort Structure during upper Hospital Hill times

Leeder (1982) maintained that it is not possible to prove that an ancient facies was deposited in a certain environment. A number of suggestions with regard to the tectono-sedimentary setting of this early Witwatersrand environment, based on the characteristics of the sediments, are nevertheless made in the following paragraphs.

The presence of herringbone trough cross-bedding in the tidal-dominated facies of the upper Hospital Hill Quartzite of all the study areas point to an unequivocally marine environment of deposition for this arenitic succession. The depositional environment was, presumably, directly connected to an open, unrestricted ocean because tidal waves rapidly loose their efficiency if they have to traverse very wide shallow seas (Anderton, 1976). The relatively consistent northeasterly to southwesterly strike of the palaeoslope, indicated by the palaeocurrent data and the wide distribution of the major facies, indicate the existence of an open shelf type of depositional environment with a fairly consistent attitude. The textural and mineralogical maturity of the basal orthoquartzite facies point to a shallow marine environment, though the paucity of horizontal bedding and lack of indicators of exposure, such as mud cracks or mud clasts, outweighs deposition in the near-shore regime. This, however, is no guarantee that no near-shore conditions ever existed because the preservation potential of high-energy, near-shore deposits could be relatively low especially where transgression takes place under conditions of slow subsidence (Clifton *et al.*, 1971).

The presence of asymmetric current ripples, sets of interference ripples, and unidirectional cross-bedded troughs in the basal orthoquartzite facies point to a possible inner offshore palaeogeographical regime of deposition for this facies. Initially, only seaward flowing ebb currents predominated as indicated by the unidirectional palaeocurrent pattern. In the course of time, however, a transformation of the character of the areas under consideration was brought about and bi-directional tidal currents started to operate. In this facies the mud-draped reactivation surfaces, as well as mud-draped erosional features which are not uncommon in tidal sands (Johnson, 1978), could also indicate storm deposits which collected under conditions of abnormally high suspended sediment concentrations (Johnson, 1978). The water escape structures, such as the convolute structures which appear in the tidal-dominated facies of the southwestern and northwestern study areas, are regarded as uncommon in shallow marine sands (Anderton, 1976), and considered especially rare in their ancient counterparts (Lowe, 1975; Johnson, 1977). These structures are closely associated with other deformation structures such as buckled and overturned cross-beds and are generally ascribed to the effects of liquefaction usually caused by earthquake shock (Allen & Banks, 1972; Anderton, 1976), though storm-induced microseisms could also be invoked as a trigger mechanism (Johnson, 1977).

The fact that these structures have been observed in two of the four selected study areas on the Vredefort Structure and have also been reported from the upper arenaceous unit of the Brixton Formation in the Heidelberg area (Camden-Smith, 1980) gives the authors reason to think that they are not so rare in what appears to be relatively shallow marine sands of the study areas. The apparent influence that the foresets of the cross-bedding in the study areas had on the attitude of the folds which formed, seem to indicate that initial slumping on some foresets (possibly due to differential loading) could have induced liquefaction. This process, in turn, was responsible for the characteristic cuspy nature of the 'anticlines'. In Figure 4a the sharp pointed cusps are inverted as result of the overfolding of the strata in the Vredefort Structure.

The exclusive occurence of medium-scaled planar cross-bedding with a predominance of southeasterly inclined foresets (overfolding restored), which is a local subfacies of the tidal-dominated facies of the southwestern study area, is somewhat enigmatic. Its limited occurrence and exposure makes it difficult to assess. It could form part of a local subtidal channelling system in which the accretion of lateral sandbars to the southwest has been preserved as the dominant direction of accumulation due to the lateral migration of this system. The presence of smaller sets of planar crossbeds, which intervene in the trough cross-bedded facies of the northwestern study area, possibly point to some form of shallow channellized flow with accompanying lateral accretion of sandbars.

Very little can be said about the intermediate mudfacies of the upper quartzitic succession of the Hospital Hill Subgroup in the southwestern sector of the Vredefort Structure because of poor exposure. It is possibly constructed of interbedded sands and mud and could relate to a period of extreme storm conditions and rapid deposition. It certainly represents an interval which started abrubtly and ended abrubtly. The thin fine-grained quartzite beds, intercalated in the upper muddy sediments of the southwestern study area could represent sand patches which lie down-current along tidal current transport paths (Johnson, 1978).

In general, the sandy succession of the upper Hospital Hill quartzite might be viewed as representing an overall sedimentary cycle of transgression which followed an initial regression wherein deep-water conditions of deposition were transformed to total shallow near-shore conditions and back again to offshore deep-water conditions. The overall cycle of transgression was probably accompanied by minor fluctuations or oscillations of water depth. Relief on the early granite shell was probably much subdued compared with modern continental areas. Therefore, shelf areas with fairly uniform and relatively low angles of declivity occurred bordering shallow intercontinental and epicontinental seas (with an average depth of 0,5–2 km, which existed during the early Precambrian (Timofeyev *et al.*, 1986). Tectonic activity, therefore, could give rise to a rapid shift of the shoreline and the transformation of near-shore areas to offshore areas on the shelf.

Summary and conclusion

Directional data obtained from sedimentary structures in the upper quartzite member of the Hospital Hill Subgroup at four different localities in the area of the Vredefort Structure point to a fairly uniform palaeostrike for the entire area of the Structure during the early history of Witwatersrand sedimentation. This direction was approximately northeast to southwest with the palaeodeclivity in a general southeasterly direction. The evidence therefore indicates that no hub existed in the foundation, destined to become the centre of the Vredefort Structure, during the early part of the history of Witwatersrand sedimentation. This also means that the endogenetic rising of the floor in the area of the Vredefort Structure, if it did take place at a rate conformable to isostatic adjustment, may either be detected at a much higher stratigraphic level in the Witwatersrand succession or its incipience may even lie beyond the Witwatersrand Era.

In summary, therefore, the early Witwatersrand sea is pictured as one which was characterized by a relative straight coastline orientated more or less northeast to southwest. Transgressive movement, in particular, of the sea onto a broad shelf-like area gave rise to the rapid transformation of near-shore to offshore areas. The distal offshore areas were regimes subjected to conditions of chemical precipitation and occasional turbidite sedimentation (the andalusite hornfelses), whereas the near-shore sediments (the quartzites), due to fluctuating but progressive subsidence, were reworked and preserved in the inner offshore parts of the shelf.

Acknowledgements

This work was supported by the Bureau for Research, Potchefstroom University for C.H.E. and the South African Council for Scientific and Industrial Research. The authors wish to thank Professor Laurie Minter for his willingness to visit the study areas where his guidance in connection with the interpretation of the sedimentary structures was highly appreciated. Professor Minter is also thanked for his constructive criticism and advice towards improving the quality of this paper. A word of thanks is also due to Mrs. I. de Beer for the draughting of the diagrams, Alta van den Berg for the typing of the manuscript, and our colleague Marthie Coetzee for proof-reading of the manuscript.

References

Allen, J.R.L. & Banks, N.L. (1972). An interpretation and analysis of recumbent-folded deformed crossbedding. *Sedimentology*, **19**, 257–283.

Allsopp, H. L., Evans, I. B., Giusti, L., Hallbauer, D. K., Jones, M.Q.W. & Welke, H.J. (1986). U-Pb dating and isotopic characterization of carbonaceous components of Witwatersrand reefs. *Ext. Abstr. Geocongress 86*, Univ. Witwatersrand, Johannesburg, 85–88.

Anderton, R. (1976). Tidal-shelf sedimentation: an example from the Scottish Dalradian. *Sedimentology*, **23**, 429–458.

Bishopp, D.W. (1941). The geodynamics of the Vredefort Dome. *Trans. geol. Soc. S. Afr.*, **33**, 1–18.

Bisschoff, A.A. (1969). *The petrology of the igneous and metamorphic rocks in the Vredefort Dome and the adjoining parts of the Potchefstroom syncline.* D.Sc. thesis (unpubl.) Univ. Pretoria, 243pp.

Brock, B.B. & Pretorius, D.A. (1964). Rand basin sedimentation and tectonics. p.34 and 549–599. *In:* S.H. Haughton, Ed., *The Geology of Some Ore Deposits of Southern Africa, 1*, Geol. Soc. S. Afr., Johannesburg. 625pp.

Camden-Smith, P.M. (1980). *The sedimentology, geochemistry and diagenesis of West Rand Group sediments in the Heidelberg area, Transvaal.* M.Sc. thesis (unpubl.), Univ. Cape Town, 232pp.

Clifton, H.E., Hunter, R.E. & Phillips, R. L. (1971). Depositional structures and processes in the non-barred high-energy nearshore. *J. Sedim. Petrol.*, **41**, 651–670.

Dietz, R.S. (1961). Vredefort ring structure: meteorite impact scar? *J. Geol.*, **69**, 499–516.

Du Toit, A.L. (1954). *The Geology of South Africa.* Oliver & Boyd, Edinburgh, 3rd. Edition, 611pp.

Eriksson, K.A., Turner, B.R. & Vos, R.G. (1979). Evidence of tidal processes from the lower part of the Witwatersrand Supergroup, South Africa. *Inform. Circ. econ. Geol. Res. Unit*, **140**, Univ. Witwatersrand, Johannesburg, 9pp.

Hargraves, R.B. (1961). Shatter cones in the rocks of the Vredefort Ring. *Trans. geol. Soc. S. Afr.*, **64**, 147–153.

Johnson, H.D. (1977). Water escape structures in shallow marine sandstones. *Sedimentology*, **24**, 389–411.

---- (1978). Shallow siliciclastic seas. 207–257. *In:* H.G. Reading, Ed., *Sedimentary Environments and Facies.* Elsevier, New York, 557pp.

King, L.C. (1951). *South African Scenery.* Oliver & Boyd, Edinburgh, 2nd. Edition, 379pp.

Leeder, M. R. (1982). *Sedimentology, Process and Product.* Allen & Unwin, London, 344pp.

Lowe, D.R. (1975). Water escape structures in coarse-grained sediments. *Sedimentology*, **22**, 157–204.

Manton, W.I. (1965). The orientation and origin of shatter cones in the Vredefort Ring. *Ann. New York Acad. Sci.*, **123**, 1017–1049.

Maree, B.D. (1944). The Vredefort Structure as revealed by a gravimetric survey. *Trans. geol. Soc. S. Afr.*, **47**, 183–196.

Nicolaysen, L.O. (1972). North American cryptoexplosion structures: interpreted as diapirs which obtain release from strong lateral confinement. *Mem. geol. Soc. Amer.*, **132**, 605–620

Tanner, W.F. (1966). Ripple mark indices and their uses. *Sedimentology*, **9**, 89–104.

Tankard, A.J., Jackson, M.P.A., Eriksson, K.A., Hobday, D.K., Hunter, D.R. & Minter, W.E.L. (1982). *Crustal Evolution of Southern Africa, 3.8 Billion Years of Earth History*. Springer-Verlag, New York, 523pp.

Timofeyev, P.P., Kholodov, V.N. & Zverov, V.P. (1986). Evolution of the earth's water mass and sedimentation. *Int. Geol. Rev.*, **28**, 507–510.

Truswell, J.F. (1977). *An Introduction to the Historical Geology of South Africa*. Purnell, Cape Town, 167pp.

Watchorn, M.B. (1980). The stratigraphy and sedimentological development of the Witwatersrand Basin in the Klerksdorp area. *Inform. Circ. econ. Geol. Res. Unit*. Univ. Witwatersrand, Johannesburg, **148**, 9pp.

Willemse, J. (1937). On the Old Granite of the Vredefort region and some of its associated rocks. *Trans. geol. Soc. S. Afr.*, **40**, 43–119.

Winter, H. de la R. (1986). A cratonic-foreland model for Witwatersrand Basin-development in a continental, back-arc, plate-tectonic setting. Inform. circ. econ. Geol. Res. Unit, Univ. Witwatersrand, Johannesburg, **193**, 36pp.

ADDENDUM TO CHAPTER 2

The findings of subsequent research (see Chapter 4), with regard to the nature of the Vredefort Structure and the restoration of the strata to their original horizontal attitude, necessitate a reconsideration of the restored palaeocurrent directions presented in Chapter 2. In Chapter 4 the conclusion is reached that the restoration of strata by rotation about their tectonic strikes renders inaccurate results because the later northwesterly tilting of the major Structure, and additional tilting associated with faulting, are ignored by the simple rotational procedure.

The axis of tilt for the Vredefort Structure was determined statistically from tectonic dips recorded in the Central Rand Group, and the nature of further tilting of the strata of this Group by a major fault system (trending north-northeast on Buffelshoek 471), was inferred from stereographic projection of bedding poles of Central Rand strata (Chapter 4). The axis of the major structure (proposed to have originally been a vertical cylindrical diapir) has been found to verge 39^0 towards 136^0 (Chapter 4). The mentioned additional tilting of the northeastern sector of Central Rand Group strata, as result of the fault system, is described by a 20^0 clockwise rotation in relation to the northwestern sector (the observer facing west). The effect of this secondary tilting on the Hospital Hill Subgroup, however, is different from that on the Central Rand Group. The Hospital Hill Subgroup is only slightly affected by the major fault system of Buffelshoek 471. A fault system further east, however, shows a larger displacement for the Orange Grove Formation, compared to that for the Central Rand Group (see map of the Vredefort area, Nel, 1927).

No accurate data base for the present tectonic attitude of Hospital Hill Subgroup strata is available. For this reason the procedure for tectonic correction, proposed to restore the strata of the western sector of the Central Rand Group, was simplified and adopted for correcting Hospital Hill palaeocurrent data of the same sector (Appendix I). The procedure involves rotating the axis of the major structure vertical (51^0 towards 316^0) and the concomitant rotation of the recorded palaeocurrent data and bedding. Thereafter the bedding is rotated about their newly acquired strike axes to a horizontal attitude with the concomitant rotation of palaeocurrent data (see Chapter 4).

From the results (Appendix I) palaeocurrent vectors were calculated and compared to the modes (obtained by means of the "conventional" method of restoration) of palaeocurrent readings for the same study areas (Fig. 10). From figure 10 it is clear that although the proposed revised method of restoration of strata produces a slight change of palaeocurrent means for each study area, the changes are relatively minor and do not alter the conclusions of Chapter 2.

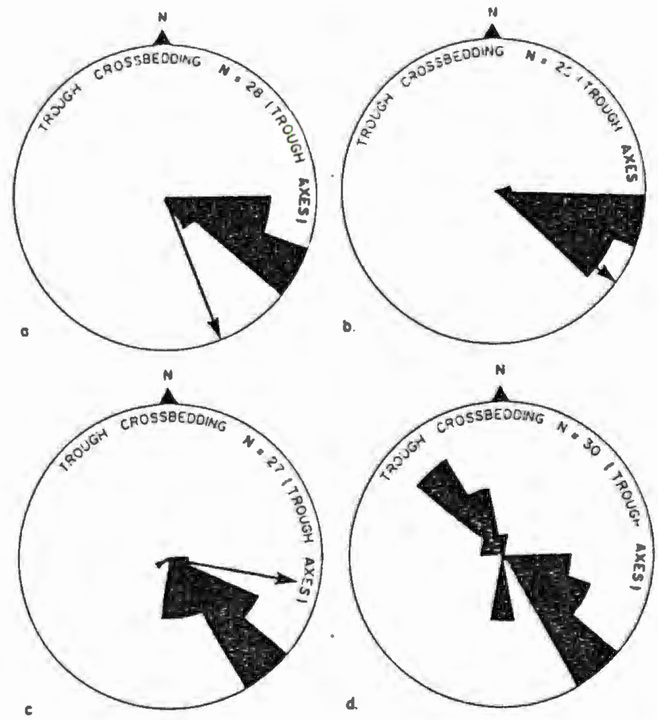

Fig. 10 Comparison of the modes of palaeocurrent rose diagrams (obtained by "conventional" technique of restoration) shown on Figure 8 of Chapter 3 with palaeocurrent vector means (arrows) calculated from the same raw data restored by means of the proposed procedure outlined in Chapter 4. a. Southwestern study area (basal facies only). b. Northwestern study area (basal facies only). c. Northern study area (basal facies only). d. Northeastern study area (composite of basal and tidal-dominated facies).

Reference

Nel, L.T. (1927). The geology of the country around Vredefort – An explanation of the geological map. *Spec. Publ. geol. Surv. S. Afr.*, **6**, 134pp.

CHAPTER 3

AN APPRAISAL OF THE SIGNIFICANCE OF SMALL-SCALE FOLD STRUCTURES IN THE CONTORTED BED OF THE AREA OF THE VREDEFORT STRUCTURE

An appraisal of the significance of small-scale fold structures in the contorted bed of the area of the Vredefort Structure

J.J. Mayer and H.M. Albat

Department of Geology, Potchefstroom University for CHE, Potchefstroom 2520, Republic of South Africa

Accepted 30 November 1990

The axial orientation of small-scale folds in the contorted bed, of the area of the Vredefort Structure, shows an approximate northwest–southeast mode if the updomed and overturned strata of the collar of this major structure are restored to their original horizontal attitude. If the assumption is correct that an epidiorite sill, presumably of Ventersdorp age, is transgressive with respect to the folding then the evidence points to an early episode, prior to the outpouring of Ventersdorp lavas, during which the Witwatersrand depository was subjected to a compressive event directed approximately northeast–southwest. The findings indicate a tectonic rather than a diagenetic or sedimentary origin for the folding of the contorted bed and point to the improbability that a granite-gneiss dome existed during the early history of Witwatersrand tectonics in the floor of the collar rocks.

Die asse van kleinskaalse plooie van die kronkellaag, in die gebied van die Vredefortstruktuur, vertoon 'n ongeveer noordwes–suidoostelike modus met betrekking tot hul oriëntasie indien die opgekoepelde en oorgeplooide strata van die kraag van die hoofstruktuur herstel word na hulle horisontale stand. Indien die veronderstelling korrek is dat 'n epidiorietplaat, waarskynlik van Ventersdorpouderdom, transgressief is met betrekking tot die plooiing dan dui die getuienis op 'n vroeë episode, voor die uitvloeiing van die Ventersdorplawas, toe die Witwatersrandafsetting onderworpe was aan kompressiewe kragte wat naasteby noordoos–suidwes opgerig was. Die bevindings toon aan dat die plooiing van die kronkellaag 'n tektoniese eerder as 'n diagenetiese of sedimentêre oorsprong gehad het en dui ook op die onwaarskynlikheid dat 'n graniet-gneiskoepel in die vloer van die kraaggesteentes, gedurende die geskiedenis van vroeë Witwatersrandtektoniek bestaan het.

Introduction

An investigation of the interrelationships and the structural geometry of all structural elements present in the rocks of the collar and hub of the Vredefort Structure forms the basis of a research programme followed by the authors. Basic research of this nature is viewed as being a fundamental step towards the unravelling of the history of the enigmatic Vredefort Structure (Figure 1). Albat (1988) has recently re-examined shatter cones and, on the grounds of shatter cone/bedding interrelationships, was able to confirm their age as being prior to the event of the overturning of the collar rocks (Hargraves, 1961; Manton, 1965).

The discovery in the collar rocks of a system of closely spaced megascopic planar fractures (Figure 7), geometrically and consequently genetically related to shatter cones, has provided the authors with an additional 'shock feature' to be used as a 'time marker' in Vredefort Structure history (Albat & Mayer, 1989). The employment of these features as a time marker is based on the premise that they originated, in a similar way to shatter cones, as a result of the passage of high-speed shock waves through the rocks (Shoemaker *et al.*, 1961; Schneider & Wagner, 1976; Roddy & Davis, 1977) and therefore represent an event which was geologically short-lived. Being omnipresent, more so than the shatter cones, the planar fractures are readily available to be used for the purpose of relating other elements to an event which was precursive to the overturning of the collar rocks.

Amongst the variety of other structural elements, such as cleavage, joints, faults, bedding-plane striations, quartz veins, etc., being investigated by the authors, the small-scale folding of the so-called contorted bed, near the base of the Witwatersrand succession (Figure 1), has also attracted the attention. Although these small-scale folds in banded iron-formations have traditionally been ascribed to slumping (Beukes, 1973), investigators of later years have shown them to either fit in with the regional structural pattern (De Beer, 1965; Mason, 1970; Myers *et al.*, 1987) or to be of tectonic origin (Fripp & Gay, 1972).

The objective of this paper, therefore, is to present the results of an investigation with respect to the geometry of the axial orientation of these small-scale folds in relation to the major structure and their structural significance in the domain of the Vredefort Structure.

Characteristics of the contorted bed in the Vredefort Mountain Land

The contorted bed of the Hospital Hill Subgroup, Witwatersrand Supergroup (Figure 1), forms part of a banded iron-formation which is interbedded with ferruginous and iron-rich shale, siltstone, and very fine-grained sandstone. It normally consists of alternating magnetite-rich and silica-rich mesobands, but micro- and macrobanding are also common primary sedimentary features of this formation (Beukes, 1973).

Although pod- and 'boudinage'-type structures (Figure 2), believed to be of a diagenetic origin (Pretorius, 1964; Beukes, 1973), have been observed in the strata containing the contortions, no small-scale turbidite-type structures or structures indicative of currents or agitated water have been noticed. No oölite or granular types of ironstone have been observed in sections where contortions appear. This, however, is no guarantee that these features may not exist in other parts of the banded iron-formation which were not investigated. This is because the complete succession of beds in the banded iron-formation, with a total thickness of at least 300m (Nel, 1927), is nowhere entirely exposed.

In the Vredefort Mountain Land the banded iron-formation, which contains the contortions, normally forms a

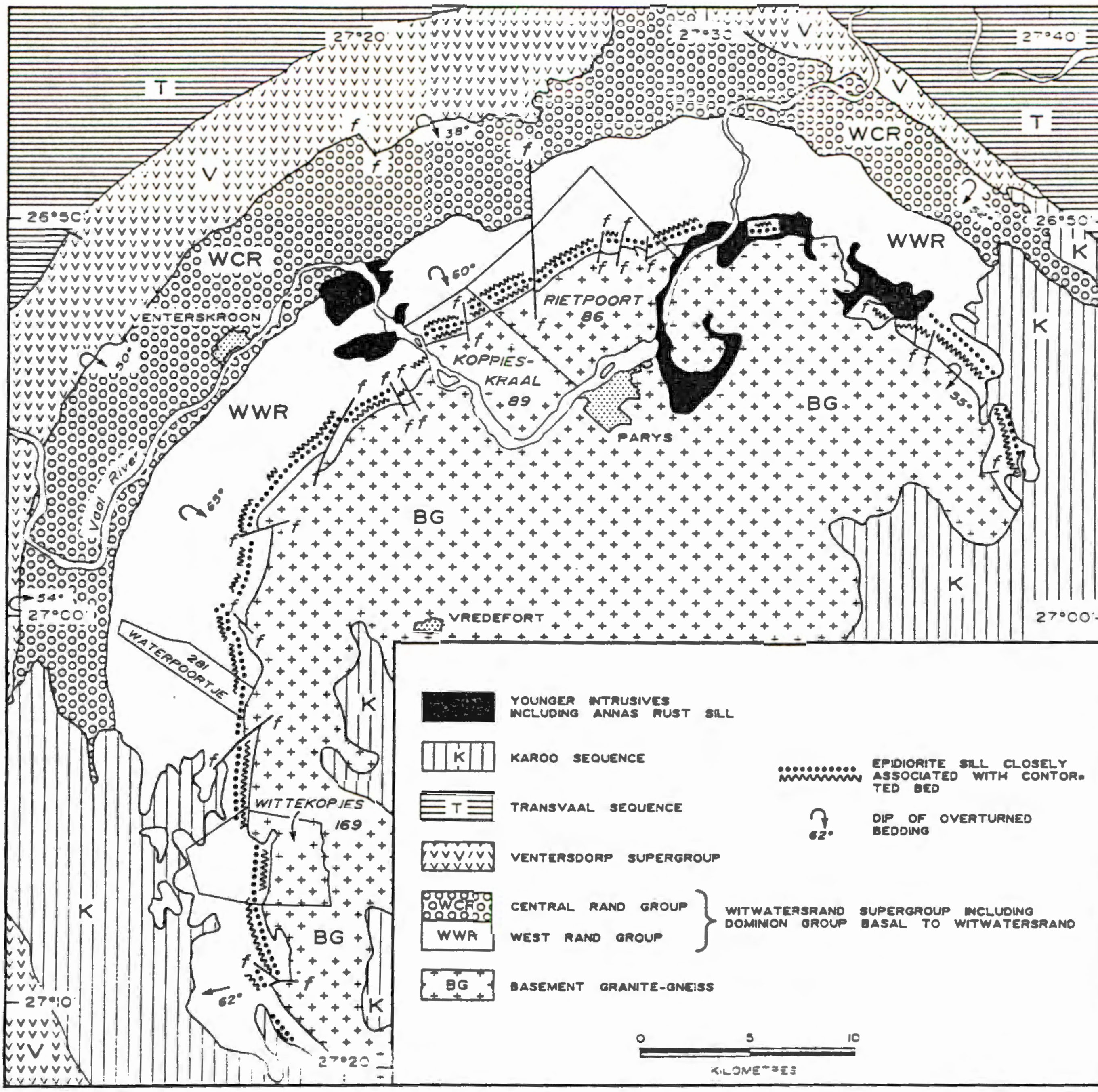

Figure 1 Map of the Vredefort Structure showing relationship of intrusive epidiorite sill to the contorted bed of the Hospital Subgroup.

topographically low ridge near the base of the up-dip scarp slope of the Orange Grove quartzite hill. The iron-formation is to a large extent overgrown with clumps of trees and bush and covered by ironstone rubble and rubble which gravitates down to it from weathering formations higher up on this slope. Strips of the banded iron-formation are therefore mostly exposed as more or less 'two-dimensional' outcrops in the Vredefort Mountain Land. Often the better exposed and more prominent outcrops are found where the banded iron-formation is generally contorted.

Stretches along these partly exposed outcrops of the banded iron-formation, in the order of a few tens of metres long and several metres wide, and containing highly contorted layering are very rare. It is more common to find rather long strike distances of practically unaffected banded iron-formation containing a few or just a single plication here and there. These small folds, which seldom affect more than a few centimetres in width of the formation at a time, may appear in zones located at more than one stratigraphic level in the banded iron-formation.

In the northwestern sector of the arc, formed by the collar rocks of the Vredefort Structure, there appear to be at least two of these zones. The stratigraphically higher of the two zones shows the more consistent development of folding and is characterized by a dominance of microbanding. The stratigraphically lower zone more typically contains mesobanding and shows less consistent folding. The two zones are in the order of 60m apart. On the farms

Figure 2 Small-scale fold showing 'pinching' structures in chert bands.

Koppieskraal 89 and Rietpoort 86 the two zones are split by an epidiorite sill of presumably Ventersdorp age (Figure 1). The epidiorite intrusion remains in close association with the contorted bed in the entire western sector of the Vredefort Structure. On no occasion, however, was it possible to see the direct relationship of the intrusion of epidiorite to the small-scale folding. The reason for this is the absence of good exposures. Although not conclusive it would appear that, judging from the fact that the zone containing the contortions in the banded iron-formation alternatively appears on either side of the intrusive sill in the western sector of the Vredefort Structure, the sill is transgressive with respect to the folding. The sill transgresses the contorted bed in the area of Waterpoortjie 281 and Wittekopjes 169 (Figure 1).

The amplitude of the small-scale folding can vary from microcrenulations to as much as 350mm and the intensity of folding from gentle to tightly folded structures (Figure 3). The microcrenulations often form a lineation, on bedding plane surfaces, which is parallel to the fold axes (Figure 4).

At some localities small fold structures are seen to have been ruptured giving rise to miniature thrust faults. Small reverse faults and brecciated zones are also encountered. Of the small-scale folds recorded the majority are of the open fold type (Hobbs *et al.*, 1976), showing an interlimb angle larger than 70° (Figure 3). Folds in the highly contorted horizons are mostly non-cylindrical, showing axes and axial planes which themselves are bent and curved. This is also typical of the folding of the highly contorted zones of the contorted bed elsewhere e.g. the Heidelberg-Balfour area (Myers *et al.*, 1987). Besides the small-scale folding, folds of larger amplitudes which are younger than the small-scale folding, have also affected the banded iron-formation of the Hospital Hill Subgroup. These folds are often associated with faults and were not included in the survey.

Recording of minor fold axes: field procedures and results

With the view to establishing the geometry of the small-scale folding in the contorted bed of the Vredefort Structure, a survey was carried out of the attitude of the axes of these folds in the banded iron-formation marker horizon. Because of the highly magnetic nature of the contorted bed a conventional magnetic compass could not be used for the recording of azimuths. Instead use was made of a sun compass as an alternative instrument with which to accomplish the task. Odling (1984), who studied the variation in the local magnetic declination near a magnetic body at Gamsberg, provided a description of the construction and use of such a compass. To enable her to take magnetic measurements simultaneously with sun compass measurements she attached a small magnetic compass to the aluminium base plate carrying the protractor, as well as a bubble, enabling the base plate to be maintained in a horizontal position. The rod casting the shadow on the protractor was brass and was detachable.

Because it was impossible to take magnetic readings on the contorted bed the sun compass, devised by the authors, did

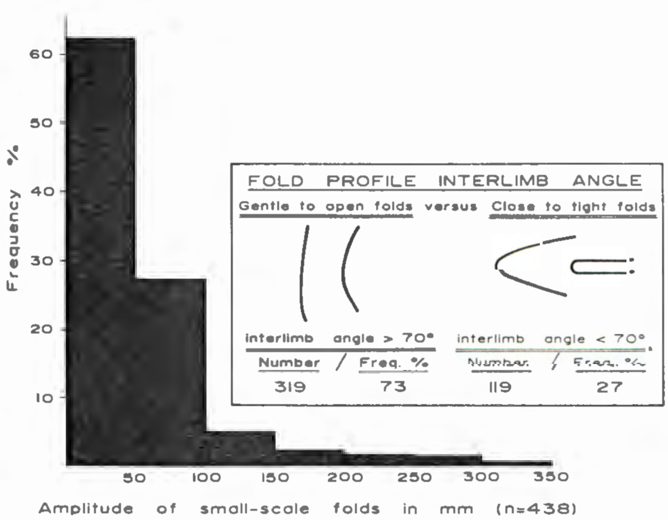

Figure 3 Distribution of amplitudes and fold-shape classification of recorded small-scale folds in the contorted bed of the area of the Vredefort Structure.

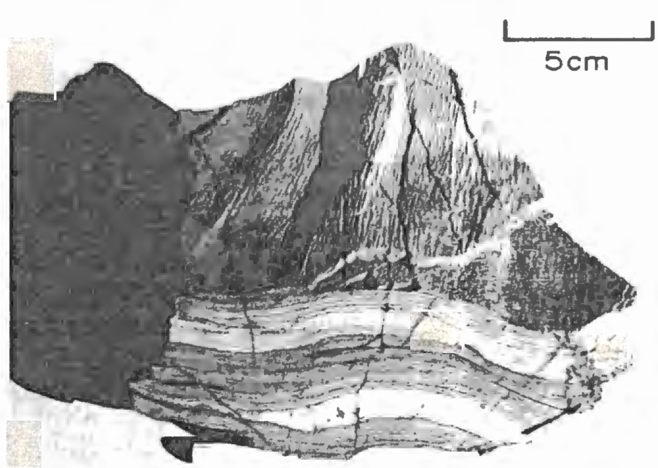

Figure 4 Microcrenulations on small-scale gentle fold. (Note that the lineation caused by the microcrenulations is approximately parallel to axis of small-scale fold).

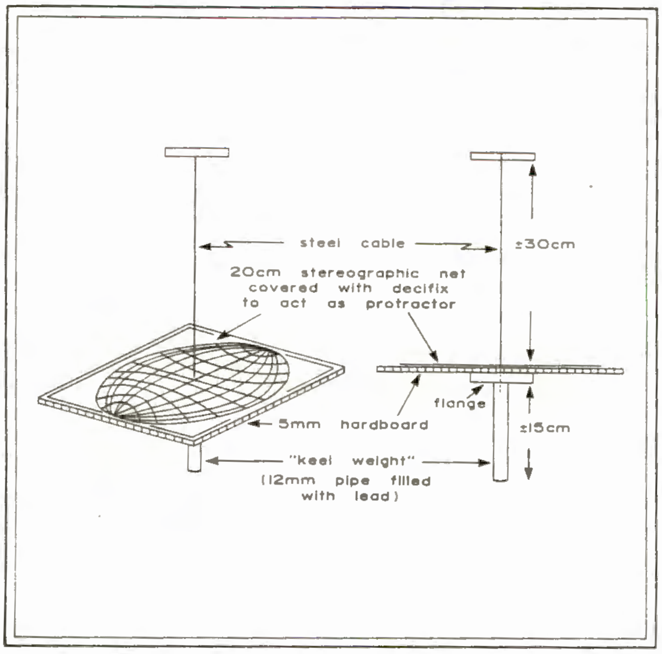

Figure 5 Construction of the sun compass used by the authors.

not specifically require non-ferrous materials. With the view to allowing gravity to automatically level the base plate, this was suspended from a steel cable which acted as a rod for the casting of a shadow. A longish 'keel weight', in the form of a 12mm pipe acting as a plumb-bob, was attached centrally underneath the base plate. Figure 5 illustrates the construction of this sun compass. Recordings were made by suspending the sun compass over a fold structure, aligning the north–south edge of the compass with the horizontal trace of the fold using the index finger on the free hand, and taking a reading of the sun angle. The plunge of each fold axis was taken with the aid of the clinometer on a Brunton compass.

Because of the stubbiness and two-dimensionality of the outcrops, the clumsiness of the sun compass, the problem of warped axial planes, and attempts to speed up the survey in general, no efforts were made to formally record the attitude of the axial planes of individual folds. Casual observations, however, made on the simpler folds conforming to types which may be described as plane folds, showed that the majority of these folds have axial planes which would dip in a roughly southwesterly direction for an 'unfolded' Vredefort Structure. There are, however, a smaller number of these folds which seem to show axial planes dipping to the northeast if the beds were to be rotated to their original horizontal attitude. In order to avoid a bias of readings as a result of zones of very intense folding, no more than ten recordings per metre strike section, along such zones, were taken.

Figure 6 Segments of shatter cones superimposed on small-scale folding (the folding has been traced on specimen to enhance its discernibility).

Figure 7 Megascopic planar shock fractures as manifested by their traces on bedding plane surface in the banded iron-formation.

From the outset there was no doubt that the small-scale folding predated the overturning of the collar rocks. This was evident from the fact that segments of shatter cone structures (Figure 6) as well as planar shock features (Figure 7) could be seen cutting the small folds. The results of the survey are therefore presented in terms of the 'unfolding' of the Vredefort Structure (Figure 8). The simple procedure of rotating the data around the present-day strike of the collar strata, to unravel the Vredefort Structure, has been shown to give satisfactory results (Albat, 1988; Mayer & Albat, 1988).

Conclusions

Despite a fair degree of dispersion, the results of the investigation showed that a consistent northwest–southeast to west–northwest-east–southeast mode for the orientation of axes of small-scale folds existed prior to the event of the overturning of the collar rocks (Figure 8). This implies a pre-Vredefort Structure age for the folding in the contorted bed, a

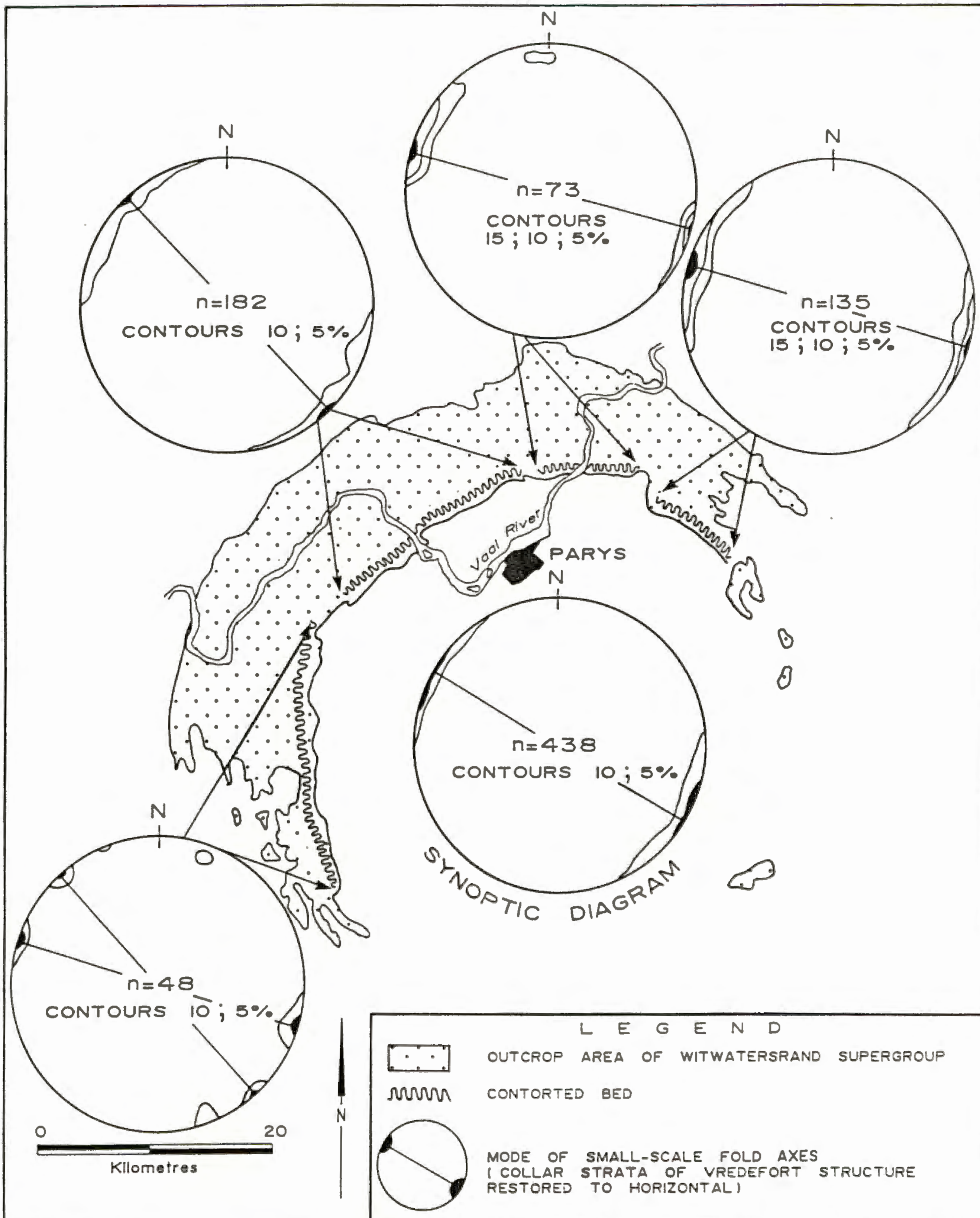

Figure 8 Equal area lower hemisphere projections, including synoptic diagram, of the orientation of the axes of small-scale fold structures in the contorted bed of the area of the Vredefort Structure along selected strike sections. (Note up-domed and overturned collar strata are restored to their horizontal attitude).

fact which is also confirmed by evidence from shatter cones and planar shock fractures which cut the small-scale folding. It is reasoned that, on the grounds of the transgressive nature of the epidiorite sill with respect to the zones containing the contortions in the western sector of the Vredefort Structure, the small-scale folding possibly also predates the outpouring of the Ventersdorp lava. These findings, therefore, point to an early episode of regional northeast–southwest compression in the structural history of the Witwatersrand depository. This agrees with the findings of Myers *et al.* (1987) for the Heidelberg-Balfour area.

Some additional conclusions, which can be drawn from the results of the present study, include the following:

1. The contorted bed of the Vredefort Mountain Land can best be explained in terms of a tectonic origin; and
2. it appears improbable that a pre-Vredefort Structure granite-gneiss dome, destined to become the hub of the Vredefort Structure, had been in existence during the early part of the tectonic history of the Witwatersrand rocks.

Three modes for the origin of the folding in the contorted bed have been advanced (Fripp & Gay, 1972). These include diagenetic causes, soft-sediment deformation due to slumping, and a tectonic origin. Hatch & Corstorphine (1904) argued that subsequent to the deposition of the banded iron-formation some chemical change was responsible for an increase in the mass of the rock so that it had to bend, crumple, and break as a result of the expansion. This appears to be a very attractive hypothesis to explain the crumpled characteristics of banded iron-formations all over the world. In opposition to this hypothesis, however, is the fact that in many studies the small-scale folds do seem to fit in with the regional tectonic pattern. Moreover, no process involving a volume increase in ironstone diagenesis is known. On the contrary, the occurrence of shrinkage cracks in these rocks rather points to a decrease in volume due to the dehydration of possibly gelatinous material (Blatt, 1982). The reason for the world-wide association of crumpled layering with most banded iron-formations is the fact that most Archaean formations occur in highly deformed supracrustal sequences (Gole & Klein, 1981).

A penecontemporaneous soft-sediment deformation origin, due to slumping, for the folding of the contorted bed in the area of the Vredefort Structure can be ruled out. The reason for this is that the pre-Vredefort Structure pattern, showing a northwesterly to southeasterly mode of orientation for the axes of small-scale folds in the contorted bed, is contradictory to a slump origin considering the fact that the palaeodeclivity for this area was approximately to the southeast in early Witwatersrand times (Mayer & Albat, 1988) and thus at right angles to the folding.

A tectonic origin, therefore, seems to best explain the contorted bed. There remains, however, the problem of explaining the relatively high degree of axial dispersion of the small-scale folds and the inconsistency of the dip of axial planes of these folds. In this respect the views of Myers *et al.* (1987) are fully endorsed; namely, that the answer possibly lies in the rheological properties of the banded iron-formation and that competency differences of the layers can give rise to differences in the vergence of the folding and dip of the axial planes.

Finally, it is reasoned that if a dome-like feature of some prominence existed in the basement rocks of the hub area of the Vredefort Structure, at the time of the small-scale folding, its presence would most likely have influenced the pattern of these folds. The consistent northwesterly to southeasterly mode of the small-scale fold axes in the collar banded iron-formation therefore seems to rather favour the absence of such a protuberance in the floor rocks during the early tectonic history of the area. Palaeocurrent evidence derived from the upper Hospital Hill quartzite formation (Mayer & Albat, 1988), indicates that it is highly unlikely that a domed-up floor existed during the early stages of Witwatersrand sedimentation.

Acknowledgments

This work was supported by the Bureau for Research, Potchefstroom University for C.H.E. The authors wish to thank Mrs. T. van der Walt for typing the manuscript and Mrs. I. de Beer for draughting the diagrams.

References

Albat, H.M. (1988). Shatter cone/bedding interrelationship in the Vredefort Structure: evidence for meteorite impact? *S. Afr. J. Geol.*, **91**, 106–113.

---- & Mayer, J.J. (1989). Megascopic planar shock fractures in the Vredefort Structure: a potential time marker? *Tectonophysics*, **162**, 265–276.

Beukes, N.J. (1973). Precambrian iron-formations of southern Africa. *Econ. Geol.*, **68**, 960–1004.

Blatt, H. (1982). *Sedimentary Petrology*. W.H. Freeman & Co., San Francisco, 564pp.

De Beer, J.H. (1965). *A detailed geological and soil map of the Johannesburg city area*. M.Sc. thesis (unpubl.), University of the Witwatersrand, Johannesburg.

Fripp, R.E.P. & Gay, N.C. (1972). Some structural aspects of the Hospital Hill Series on the north-central margin of the Witwatersrand Basin. *Trans. geol. Soc. S. Afr.*, **75**, 187–196.

Gole, M.J. & Klein, C. (1981). Banded iron-formations through much of Precambrian Time. *J. Geol.*, **89**, 169–183.

Hatch, F.H. & Corstorphine, G.S. (1904). The geology of the Bezuidenhout Valley and the district east of Johannesburg. *Trans. geol. Soc. S. Afr.*, **7**, 97–109.

Hargraves, R.B. (1961). Shatter cones in the rocks of the Vredefort Ring. *Trans. geol. Soc. S. Afr.*, **64**, 147–154.

Hobbs, B.E., Means, W.D. & Williams, P.F. (1976). *An outline of structural geology*. John Wiley & Sons Inc., New York, 571pp.

Manton, W.I. (1965). The orientation and origin of shatter cones in the Vredefort ring. *Ann. N.Y. Acad. Sci.*, **123**, 1017–1049.

Mason, R. (1970). *The geology of the country between Francistown and Madinare, Northern Botswana*. Ph.D. thesis (unpubl.), University of the Witwatersrand, Johannesburg.

Mayer, J.J. & Albat, H.M. (1988). The tectono-sedimentary setting of the area of the Vredefort Structure during deposition of the upper quartzite member of the Hospital Hill Subgroup. *S. Afr. J. Geol.*, **91**, 239–247.

Myers, M., Myers, R.E. & McCarthy, T.S. (1987). Re-examination of the Sugarbush Fault and associated structures. *S. Afr. J. Geol.*, **90**, 270–281.

Nel, L.T. (1927). The geology of the country around Vredefort. *Explan. geol. map, Geol. Surv. S. Afr.*, 134pp.

Odling, N.E. (1984). A statistical study of the variation in local magnetic declination near a magnetic body at Gamsberg, North-Western Cape. *Trans. geol. Soc. S. Afr.*, **87**, 79–85.

Pretorius, D.A. (1964). The geology of the South Rand goldfield. 219–282. *In*: S. H. Haughton (Ed.), *The Geology of Some Ore Deposits of Southern Africa*. 1. Geol. Soc. S. Afr., 625pp.

Roddy, D.J. & Davis, L.K. (1977). Shatter cones formed in large-scale experimental explosion craters, 715–750. *In*: D.J. Roddy, R.O. Pepin & R.B. Merril (Eds.), *Impact and Explosion Cratering*. Pergamon, New York.

Schneider, E. & Wagner, G.A. (1976). Shatter cones produced experimentally by impact in limestone targets. *Earth Planet. Sci. Lett.*, **32**, 40.

Shoemaker, E.M., Gault, D.E. & Lugn, R.V. (1961). Shatter cones formed by high speed impact in dolomite. *Prof. Pap. U.S. Geol. Surv.*, **424-D**, 365–368.

ADDENDUM TO CHAPTER 3

The findings of Chapter 3 are based upon the "conventional" technique of restoring strata to their original horizontal attitude by rotation about their tectonic strikes. In Chapter 4 (see also addendum to Chapter 2) it is indicated that this simple method of rotation produces results which may be incorrect because tilting of the proposed initial impact diapir (the Vredefort Structure), and subsequent additional tilting associated with faulting, are not taken into consideration. A proposed procedure which considers tilting (Chapter 4) was therefore applied to the data of Chapter 3 and the results compared with those of the conventional method.

As indicated in the addendum to Chapter 2, the effects of secondary tilting, as result of faulting, on the Hospital Hill Subgroup differ from those on the Central Rand Group, particularly for the northeastern sector of the collar. The overall character of the major structure, however, remains essentially the same for all parts of the collar strata. For this reason a simplified method of tectonic correction was adopted in which the axis of the major structure was rendered vertical, whereafter the strata were rotated about their strikes to their original horizontal attitude. Because of the unknown character of the tilting caused by major faults of the northern and northeastern sectors, with respect to the Contorted Bed, this procedure was not applied to these sectors of the collar.

Figure 9 compares the results of the "conventional" and the proposed new methods of tectonic correction, applied to the preferred orientation of small-scale fold axes of the Contorted Bed of the northwestern sector of the Vredefort collar. It can be seen that the preferred northwesterly to southeasterly palaeo-orientation of small-scale axes, obtained by application of the proposed new method, does not differ significantly from that produced by the conventional method. The main findings of Chapter 3 therefore remain valid.

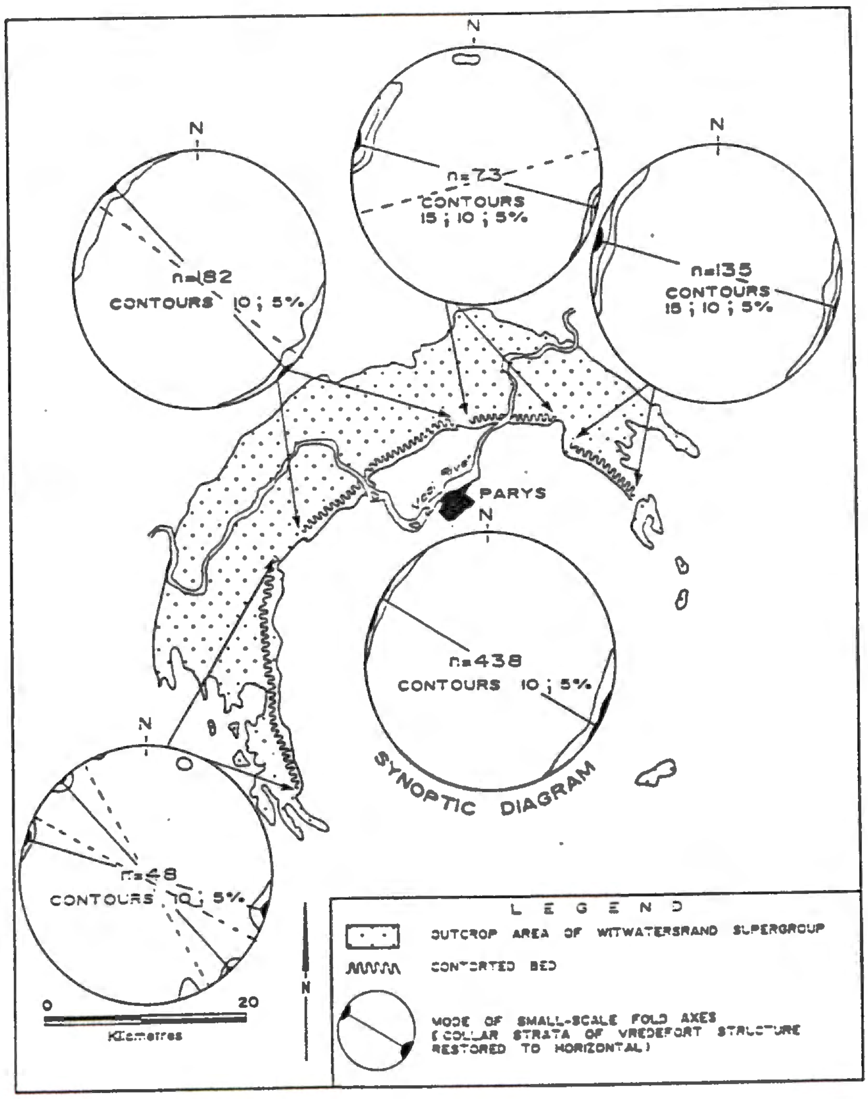

Fig. 9. Preferred palaeo-axial orientation of small-scale folds of the Contorted Bed (equal area lower hemisphere projections, collar strata horizontal). Broken lines represent preferred axial orientation obtained by reconstructing according to the "tectonic model" procedure proposed in Chapter 4, solid lines represent axes as in Fig. 8 Chapter 3.

CHAPTER 4

THE RECONSRTUCTION OF PALAEOCURRENT DISPERSAL PATTERNS FOR TURFFONTEIN STRATA IN THE VREDEFORT STRUCTURE IN RELATION TO A TECTONIC MODEL FOR THE AREA

S.Afr. J. Geol., 1992, 95

THE RECONSTRUCTION OF PALAEOCURRENT DISPERSAL PATTERNS FOR TURFFONTEIN STRATA IN THE VREDEFORT STRUCTURE IN RELATION TO A TECTONIC MODEL FOR THE AREA

J. J. Mayer and B.G. Els

Department of Geology, Potchefstroom University for CHE, Potchefstroom 2520, Republic of South Africa

Subdivision of the Turffontein Subgroup, in the Vredefort area, into five Formations viz. the Buffelskloof, Rooderand, Witkop, Leeufontein and Koedoesfontein Formations is tentatively introduced. The results of a reconstruction of palaeocurrent vectors for the Rooderand and Leeufontein Formations, using the conventional procedure of rotating the beds to the horizontal about their tectonic strikes, is presented. As these results appeared to be questionable it was realised that the method of tectonic correction of palaeocurrents in the area needed to be reconsidered in relation to the most probable model for the origin of the Structure. Models explaining the origin of the Vredefort Structure are discussed and one visualising the Structure as an impact-rebound diapir, which has subsequently been tilted, is proposed. An equal area projection of bedding poles of the Turffontein strata demonstrates that the tilted diapir has a near vertical axial plane and a structural axis plunging 39^0 on a bearing 136^0. Subsequent faulting of the northwestern sector of the collar caused additional tilting which may be corrected by a 20^0clockwise rotation about a horizontal axis striking N 17^0E. Processing of the palaeocurrent field data by stereographic rotational procedures, based upon the proposed model, produces a uniform palaeocurrent pattern of sub-parallel, basinward vectors for the Leeufontein Formation in the 075^0 to 178^0 azimuth quadrant. Palaeocurrent vectors of the Rooderand Formation are based upon a smaller data set and show a greater variance, with palaeocurrent vectors ranging from 084^0 to 248^0 azimuth. The possible effect of the diameter of the Vredefort collar having earlier been larger by 15 km is considered but, it is concluded that such an increase in diameter would not affect the regional palaeocurrent pattern significantly. Bipolar palaeocurrent

distributions along part of the strike of the Leeufontein Formation are considered evidence for shallow marine conditions during mid-Turffontein times. The dominance of unimodal palaeocurrent vectors for this Formation in the southwestern and northeastern sectors, however, is tentatively ascribed to possible subsequent fluvial reworking of the coastal facies.

Onderverdeling van die Turffonteinsubgroep in vyf Formasies nl. die Buffelskloof–, Rooderand–, Witkop–, Leeufontein– en Koedoesfonteinformasies word tentatief bekend gestel. Die resultate van 'n rekonstruksie van paleostroom-vektorrigtings vir die Rooderand– en Leeufonteinformasies, deur gebruik te maak van die konvensionele prosedure waarvolgens die lae na die horisontaal om hulle tektoniese strekkings geroteer word, word aangebied. Aangesien hierdie resultate bevraagteken is, is daar besef dat dit nodig was om die metode van tektoniese korreksie van paleostrome te hersien en in verband te bring met 'n bepaalde model vir die oorsprong van die Vredefortstruktuur. Modelle wat die oorsprong van die Vredefortstruktuur verklaar, word bespreek en een wat die Struktuur visualiseer as 'n impak-terugskok-diapier, wat wat daarna gekantel is, word voorgestel. 'n Gelyke-oppervlakte-projeksie van laagvlakpole van Turffonteinstrata demonstreer dat die Struktuur 'n bykans vertikale asvlak en 'n strukturele as besit wat 39^0 duik in 'n rigting 136^0. Latere verskuiwing van die noordoostelike sektor van die kraag het bykomstige kanteling veroorsaak wat deur 'n kloksgewyse rotasie van 20^0 om 'n horisontale as met strekking $N17^0O$ reggestel kan word. Verwerking van die veldgegewens deurmiddel van stereografiese rotasieprosedures, gebaseer op hierdie model, lewer 'n eenvormige paleostroompatroon van sub-paralelle komwaartse vektore vir die Leeufonteinformasie in die kwadrant 075^0–178^0asimut. Paleostroomvektore vir die Rooderandformasie is gebaseer op 'n kleiner databasis en toon 'n groter variansie met paleostroomvektore in die bereik 084^0–248^0 asimut. Die moontlike effek van 'n vyftien kilometer groter deursnee as tans, vir die Vredefortkraag, word bespreek, maar die gevolgtrekking word gemaak dat so 'n vergroting in deursnee nie enige betekenisvolle uitwerking op die paleostroompatroon sou hê nie. Bipolêre paleostroomverspreidings langs 'n noordwestelike gedeelte van die strekking van die Leeufonteinformasie word beskou as getuienis van marine toestande in middel-Turffontein tye. Die oorheersing van unimodale paleostroomvektore in hierdie Formasie, in die suidwestelike en noordoostelike sektore, word egter tentatief geïnterpreteer as moontlike latere fluviale herwerking van die kusfasies.

INTRODUCTION

Nel's (1927) geological map of the "Country around Vredefort" has, up to the present, served as the exclusive base map used by earth scientists involved in studies of various aspects of the renowned Vredefort Dome. The mapping of this unusual structure, which lies almost centrally within the preserved Witwatersrand Basin (Fig. 1), was accomplished by Nel within the short time span of two years.

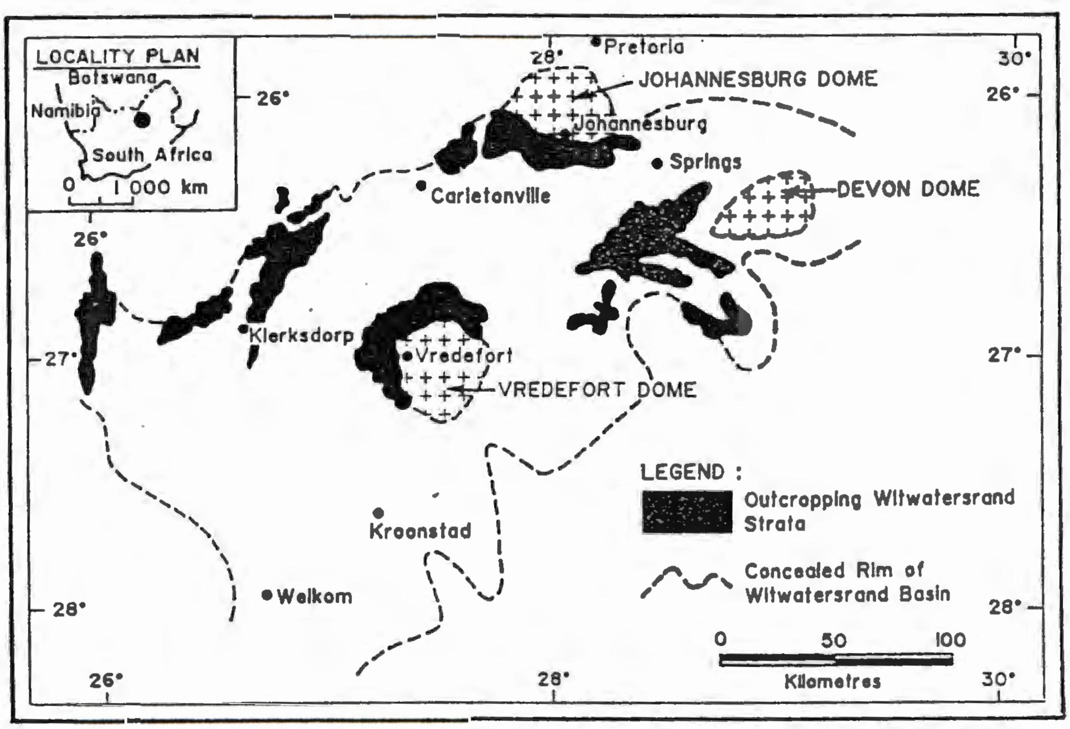

Figure 1. Simplified map showing outlines of the Witwatersrand Tectonic Basin and the Vredefort Structure.

The strata of the lower divisions of the Witwatersrand Supergroup were mapped by Nel in remarkable detail but the strata of the upper divisions (the Johannesburg and Turffontein Subgroups) which comprise predominantly quartzites, were passed over with practically no differentiation. With the view to revising Nel's map, a mapping project sponsored by the Geological Survey of South Africa was initiated in 1988. The part of this project which involved the mapping, in more detail, of the strata of the Central Rand Group was started in 1990. A reconnaissance investigation of the Turffontein Subgroup led to the identification of an 80 m thick unit of probable shallow marine origin (Els and Mayer, in press). This formation, for which the lithostratigraphic name "Leeufontein Quartzite Formation" is proposed, lies at a stratigraphic elevation in the order of 540 to 770 metres above the base of the Turffontein Subgroup (Fig. 2) and displays a collection of very striking sedimentary structures. Mapping of the Leeufontein Formation provided the opportunity to carry out simultaneous recording of palaeocurrent data. Because this Formation was traced along its entire arcuate strike a large number palaeo-flow indicators were recorded. A number of recordings were also carried out on sedimentary structures in a conglomeratic unit near the base of the Turffontein Subgroup for which the lithostratigraphic name "Rooderand Conglomerate Formation" is proposed. On account of the paucity of suitable palaeocurrent indicators in this Formation, and because study areas were spaced selectively along its outcrop in the Vredefort collar, the palaeocurrent data base for the Rooderand is much smaller than that of the Leeufontein Formation.

Palaeocurrent data recorded in the Vredefort Structure obviously require correction and any attempt to reconstruct palaeo-flow patterns necessitates that the long and complex deformational history for the area (Roering et al., 1990) be borne in mind. Apart from the "Vredefort Event" other events pre- and post-dating this major episode of diastrophism possibly also contributed towards rendering the area one of the most complexly strained parts of the Witwatersrand Tectonic Basin. It is therefore extremely important that the

Figure 2. Map showing the distribution of exposed Turffontein Subgroup Formations, in the Vredefort Structure, and palaeocurrent directions (vector-means) for the Rooderand and Leeufontein Formations. Palaeocurrent modal directions of the upper Hospital Hill quartzite shown, are after Mayer and Albat (1988).

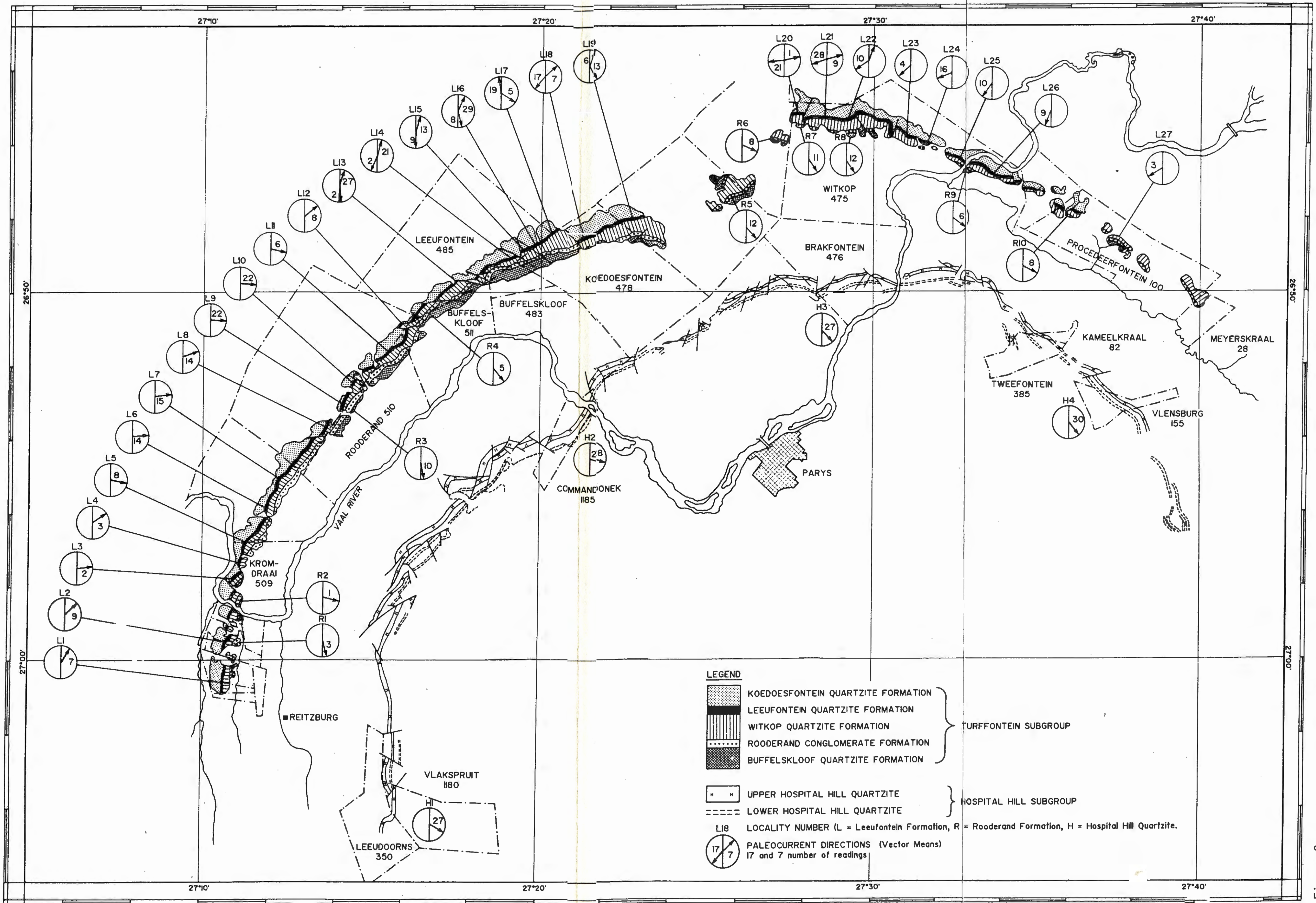
27°10'
27°20'
27°30'
27°40'
26°50'
27°00'
LEEUFONTEIN 485
KOEDOESFONTEIN 478
BUFFELSKLOOF 483
BUFFELS-KLOOF 511
WITKOP 475
BRAKFONTEIN 476
PROCEDEERFONTEIN 100
KAMEELKRAAL 82
MEYERSKRAAL 28
TWEEFONTEIN 385
VLENSBURG 155
PARYS
COMMANDONEK 1185
ROODERAND 510
VAAL RIVER
KROM-DRAAI 509
REITZBURG
VLAKSPRUIT 1180
LEEUDOORNS 350
LEGEND
KOEDOESFONTEIN QUARTZITE FORMATION
LEEUFONTEIN QUARTZITE FORMATION
WITKOP QUARTZITE FORMATION
ROODERAND CONGLOMERATE FORMATION
BUFFELSKLOOF QUARTZITE FORMATION
TURFFONTEIN SUBGROUP
UPPER HOSPITAL HILL QUARTZITE
LOWER HOSPITAL HILL QUARTZITE
HOSPITAL HILL SUBGROUP
L18 LOCALITY NUMBER (L = Leeufontein Formation, R = Rooderand Formation, H = Hospital Hill Quartzite.
PALEOCURRENT DIRECTIONS (Vector Means)
17 and 7 number of readings

Figure 2

reconstruction of palaeocurrent patterns for the Vredefort area be carried out in terms of a definite tectonic model which takes into account the total deformation suffered by the strata in the area as far as can be ascertained.

The objective of this paper is therefore threefold. The first aim is to tentatively introduce a lithostratigraphic subdivision for the Turffontein Subgroup in the Vredefort area (Fig. 2). Secondly, the authors wish to demonstrate that the conventional method of reconstruction of palaeocurrent vectors, effectuated by simply rotating the overturned beds to the horizontal about their present tectonic strikes, is open to question. A final aim of this paper is to propose a procedure for the reconstruction of palaeocurrent vectors in the Vredefort area, in terms of a definite tectonic model for the area, and to present the results of palaeocurrent data processed in terms of this procedure.

MODELS FOR THE ORIGIN OF THE VREDEFORT STRUCTURE: A DISCUSSION

From the literature it is clear that there are two views regarding the origin of the Vredefort Structure. Supporters of the extra-terrestrial hypothesis (Boon and Albritton, 1937, 1938; Daly, 1947; Dietz, 1961, 1963, 1968; Hargraves, 1961; Manton, 1965; Albat, 1988; Grieve et al., 1990; Martini, 1991) visualise the Vredefort Structure as an impact structure. Proponents of the terrestrial hypothesis (Hall and Molengraaff, 1925; Bailey, 1926; Nel, 1927; Maree, 1944; Brock, 1951; Du Toit 1954; Bucher, 1963; Brock and Pretorius, 1964; Bisschoff, 1969; Nicolaysen, 1972; Lilly, 1981; Simpson, 1981; Winter, 1987; Colliston, 1990), all link the genesis of the Vredefort Structure to tectonic and igneous processes. The main argument of the latter group is that the Vredefort Structure lies on a north-northeast striking lineament which includes the Great Dyke of Zimbabwe, the Bushveld Complex and the Trompsburg Complex (Bucher, 1963).

In considering the impact model the following points are relevant. Meteorites do not strike planetary surfaces exactly vertical and, according to Melosh (1989) the most probable angle of impact of a randomly incident projectile is 45^0. However, despite the obliquity of the impact, a circular crater would result if the impact angle were greater than 10^0 and a crudely hemispherical shock wave would propagate into the target (Melosh, 1989). In the case of the Vredefort Structure it is, therefore, most likely that an impact on the surface of the earth, at that time approximately 16 km above the present surface (the thickness of the volcanic and sedimentary pile covering the basement), would have resulted in the vertical updoming of the basement as a response to the rebound shock. If the strata were approximately horizontal at that time, it would be expected that their upturning would have been symmetrical around the circumference of the updomed basement. In the case of the Vredefort Structure overturned beds are found in the northwestern sector of the Structure but normal dipping beds most likely occur below the cover of Karoo strata to the southeast. This asymmetry of the Structure, regarding the dip of the beds, must therefore be explained. As the overturned strata cannot be ascribed to the angle of impact of the meteorite this phenomenon probably represents subsequent tilting of the structure to the northwest during a later phase of diastrophism. According to Roering (1990) gentle warping of the Witwatersrand Basin, in post-Transvaal times, is not unlikely. The absence of the Dwyka Formation in the Karoo rocks, overlying the Vredefort Structure, points to the probability that the southeastern portion of the Vredefort Structure, at least, was an elevated region at the inception of the Karoo sedimentation (De Villiers, 1989). The event of tilting had therefore probably preceded Karoo deposition.

Regarding the terrestrial models for the Vredefort Structure, some of the gravity-generated tectonic models such as Brock and Pretorius' (1964) diapiric dome model, for example, or a cryptoexplosion model (Nicolaysen, 1972) could in a similar way, as the impact model, have resulted in the upturning of the strata. Other tectonic models which presuppose an updoming of the basement, combined with a northwesterly thrust, imply the formation of a gigantic kind of thrust-generated fold to account for the apparent horseshoe-shaped deformation (as seen in plan) of the successions from Dominion Group lavas up to the Transvaal rocks in the Potchefstroom Synclinorium. Examples of these are Du Toit's (1954) or the proposed model by Colliston (1990).

In assessing the models outlined above consideration of a number of attributes of the impact model has inclined the authors towards accepting this as the ultimate model for explaining the Vredefort Structure. These attributes include the unique structural and mineralogical phenomena such as the shatter cones (Dietz, 1961; Hargraves, 1961; Manton, 1965; Albat, 1988; Albat and Mayer, 1990), the microscopic planar features in quartz (Lilly 1981; Grieve et al., 1990; the megascopic planar features (Albat and Mayer,1989) and the high pressure phases of silica, coesite and stishovite (Martini, 1991) which are associated with the Vredefort Structure and which are regarded as reliable geologic criterion for the recognition of impact structures (Melosh, 1989). Finally, when considering these phenomena in conjunction with the manifestations of brittle fracture and the practically complete circular periclinal folding of Witwatersrand, Ventersdorp and Transvaal rocks in the Vredefort Structure (McCarthy et al., 1990, their Fig. 2), the authors find it difficult to believe that the origin of this structure can be ascribed to normal orogeny.

THE RECONSTRUCTION OF PALAEOCURRENT VECTORS IN THE TURFFONTEIN SUBGROUP OF THE VREDEFORT AREA: THE CONVENTIONAL METHOD

Up to the present the technique generally used to restore the strata of the Vredefort area to their original horizontal attitude has been the simple stereographic rotation of the overturned beds to the horizontal about their present tectonic strikes (Manton 1965; Albat, 1988; Mayer and Albat 1988; Albat and Mayer, 1989; Holland et al., 1989; Mayer and Albat, 1990). Therefore, after having recorded some 500 palaeocurrent indicators (mostly overturned crossbedded troughs but also current ripples and planar crossbeds, Appendices

TABLE 1

Vector-means of restored palaeocurrent directions (conventional stereographic method). For locations see Figure 2.

	PALAEOCURRENT VECTOR-MEANS (STRATA HORIZONTAL)				TECTONIC ATTITUDE OF DEFORMED STRATA
Locality	Vect A	n	Vect B	n	Az/dip
L1	029	7			088/48
L2	046	9			95/47
L3	083	2			108/66
L4	057	3			113/51
L5	101	8			134/47
L6	086	14			113/53
L7	081	14			128/55
L8	072	14			119/56
L9	093	22			130/42
L10	099	22			140/40
L11	104	6			149/49
L12	050	8			110/50
L13	176	2	017	27	133/35
L14	211	2	021	21	153/47
L15	179	9	011	13	157/46
L16	173	8	027	29	148/40
L17	125	5	352	19	139/42
L18	219	17	052	7	170/29
L19	150	13	015	6	153/30

TABLE 1 (continued)

Vector-means of restored palaeocurrent directions (conventional stereographic method). For locations see Figure 2.

	PALAEOCURRENT VECTOR-MEANS (STRATA HORIZONTAL)				TECTONIC ATTITUDE OF DEFORMED STRATA
Locality	Vect A	n	Vect B	n	Az/dip
L20	263	21	080	1	202/50
L21	253	28	078	9	192/45
L22	237	10	014	1	197/51
L23	227	4			214/58
L24	245	16			208/49
L25	215	10			196/70
L26	200	9			200/43
L27	242	3			210/44
R1	171	3			134/34
R2	103	1			140/55
R3	177	10			124/45
R4	139	5			132/48
R5	130	12			171/32
R6	115	8			183/36
R7	148	11			188/44
R8	140	12			183/52
R9	103	6			210/75
R10	117	8			221/66

II to VI and XI) for the Leeufontein and Rooderand Formations the data were treated according to this standard procedure correcting each recording individually on a Wulff net. From the results vector means (Potter and Pettijohn, 1963) were calculated by computer (Table 1) for the palaeocurrent directions along selected strike segments (L1–L27 for the Leeufontein and R1 to R10 for the Rooderand Formations). Note that for Localities L13 to L22 the stereographically corrected data naturally fall into two distinct azimuth groups (Table 1) and were therefore treated as separate vectors of a bimodal distribution.

The palaeocurrent patterns which emerged from this simplistic method of reconstruction, for the different Formations, is shown by Figure 2. Note that the palaeocurrent modal directions, for the Hospital Hill quartzite, are after Mayer and Albat (1988). Because of the much larger data base for the Leeufontein Formation, and the continuous recording of data along its entire outcrop in the Vredefort collar, most of the attention was focused on the character of the palaeocurrent pattern for this Formation. Figure 2 shows a conspicuous systematic change in the A- or basinward directed vectors, from locality L1 to L20, for the Leeufontein Formation. Over this relatively short distance these vectors change through 180^{0}; palaeocurrent directions being to the southwest in the northeastern sector of the collar and towards the northeast in the southwestern sector of the collar. The validity of such a pattern seems questionable. The Witwatersrand depository is generally regarded as having been originally much larger than the size preserved within the present tectonic margins of the Witwatersrand Basin (Winter, 1987; McCarthy et al., 1990; Myers et al., 1990). It is therefore questionable whether such a drastic change of regional palaeocurrent pattern is normal for this part of the depository when the palaeocurrent dispersal patterns on the rim of the depository-relict show gradual regional changes (Fig. 3). For this reason it seemed logical to critically reconsider the conventional procedure of palaeocurrent reconstruction for the Vredefort area. It was realised that it was essential that a procedure for reconstruction be developed in terms of a specific tectonic model for the area.

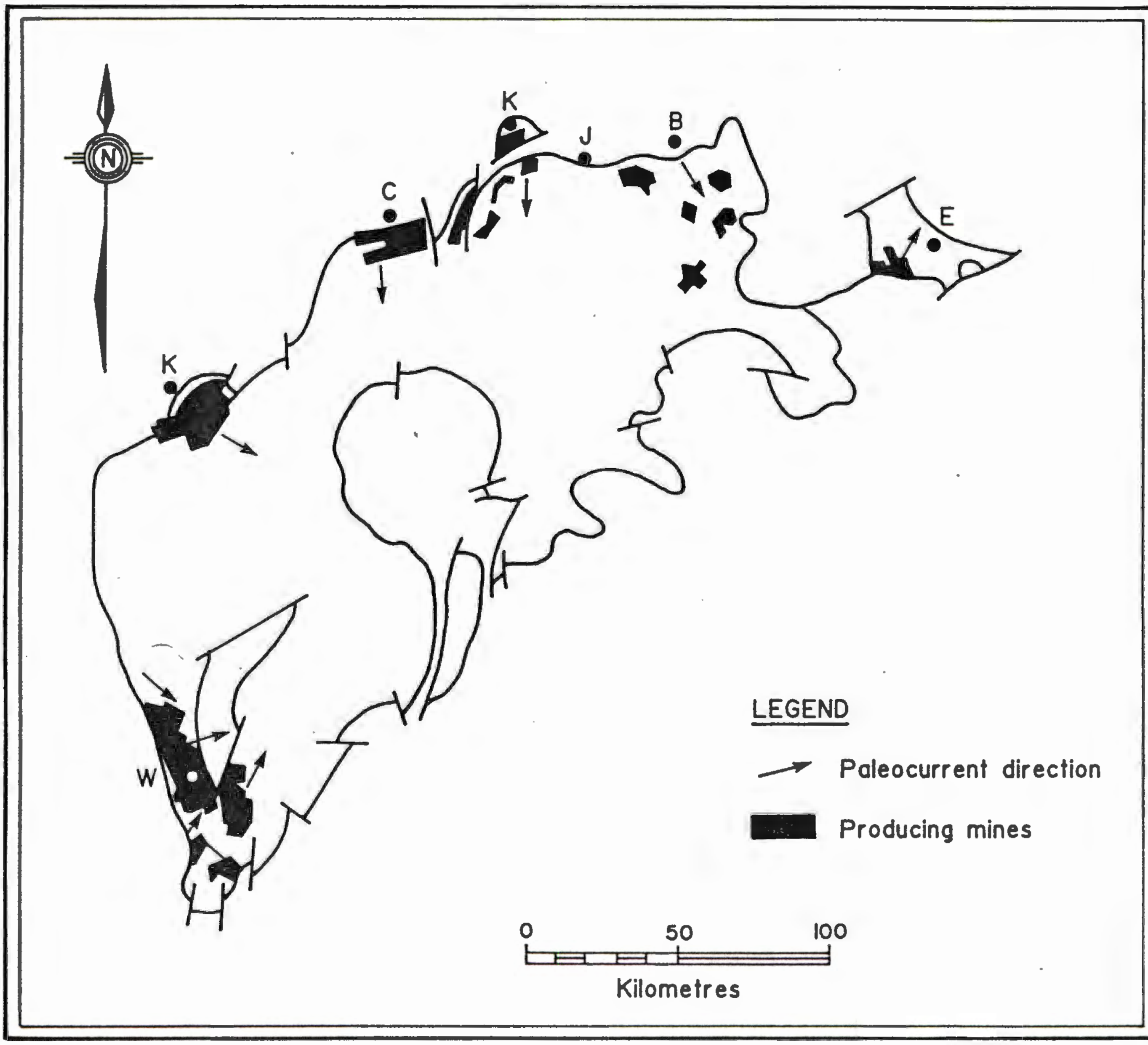

Figure 3. Composite of palaeocurrent directions for gold–bearing placers in the outer rim of the Witwatersrand Tectonic Basin (After Minter & Loen, 1991).

THE RECONSTRUCTION OF PALAEOCURRENT VECTORS IN THE TURFFONTEIN SUBGROUP OF THE VREDEFORT AREA: RATIONALE FOR A NEW METHOD

If the Vredefort Structure were an impact structure which resulted from the vertical rising of a plug of basement granite-gneiss one would normally expect the strata to be turned up steeply but not to be overturned in the way that they are at present in the northwestern arc of the collar. The authors therefore suggest that the overturning of these strata is due to the effect of a subsequent northwesterly tilting of the Structure. For this reason it would be invalid to attempt restoring the strata to their original horizontality by a simple rotation of the beds about their tectonic strikes. The obvious procedure to follow would be to first render the structure vertical and, thereafter, to rotate the beds horizontal about the arcuate tectonic strike of the now vertical strata.

In order to determine the axis of tilt of the Structure for the Turffontein strata an equal-area bedding pole projection of the present tectonic attitude of the bedding of the Leeufontein and the Rooderand Formations was employed. The data were available as result of the mapping of these Formations. Figure 4 represents the results of this projection and shows 352 poles to the bedding, contoured in terms of frequency of points per unit area. Three modes for the attitude of the Turffontein rocks in the Vredefort collar emerge from the projected data. These respectively represent, from the southwest to the northeast, strata striking approximately northsouth and northeast-southwest in the northwestern sector, and eastwest in the northeastern sector of the collar arc. It must be noted that the strata of the northeastern sector have been displaced towards the north in relation to those of the northwestern sector as result of major faulting. This is manifested by the gap, to the north of Parys, in Turffontein strata (See Fig. 2). It is possible to draw a large circle through the two modes of poles representing the preferred attitude of strata of the uninterrupted northwestern portion of the collar arc but the mode representing the bedding attitude of the northeastern sector does not quite lie on this large circle (Fig. 4). This is probably due to the effect of the additional tectonic tilting caused by the major faulting.

The outcropping part of the original Major Structure may therefore be visualised as an apparent plunging symmetrical "fold structure" with an axis verging 39^0 on a bearing of $136.^0$ It has a virtually vertical symmetry or axial plane which strikes 317^0 and dips 88^0 to the northeast (Fig. 4). To restore the effect of subsequent faulting the mode of poles representing the strata of the northeastern sector was rotated to its symmetrical position on the large circle assuming a perfect symmetrical configuration for the original structure. This represents a 20^0 clockwise rotation along a small circle with an axis positioned N17^0E (Fig. 4).

The field data were first prepared as follows before their subjection to procedures of stereographic rotation based on the tectonic model outlined above: Mean values for the azimuth and dip of the strata in each selected strike locality were calculated. In the cases of bimodal distributions the azimuths of trough axes, as measured on outcrop, for individual strike localities were treated as two separate groups and a vector-mean azimuth for each group was calculated (Table 2). Only trough crossbedding data were used and the odd anomalous datum, which appeared to fall outside of the range of azimuth values of any group was omitted.

The data (Table 2) were then manipulated on a Wulff-stereonet as follows: For the northwestern sector of the Structure (L1–L19 and R1–R5) the pole and large circle representing the attitude of the bedding for each strike locality were plotted. The vector-mean azimuth of the trough axes for each strike locality was plotted as a lineation on the trace representing the bedding for that particular locality. The axis and axial plane of the Major Structure were plotted. Next the axial plane was first rotated to the vertical (rotated 2^0 clockwise about its strike on a bearing 317^0, resulting in the concomitant

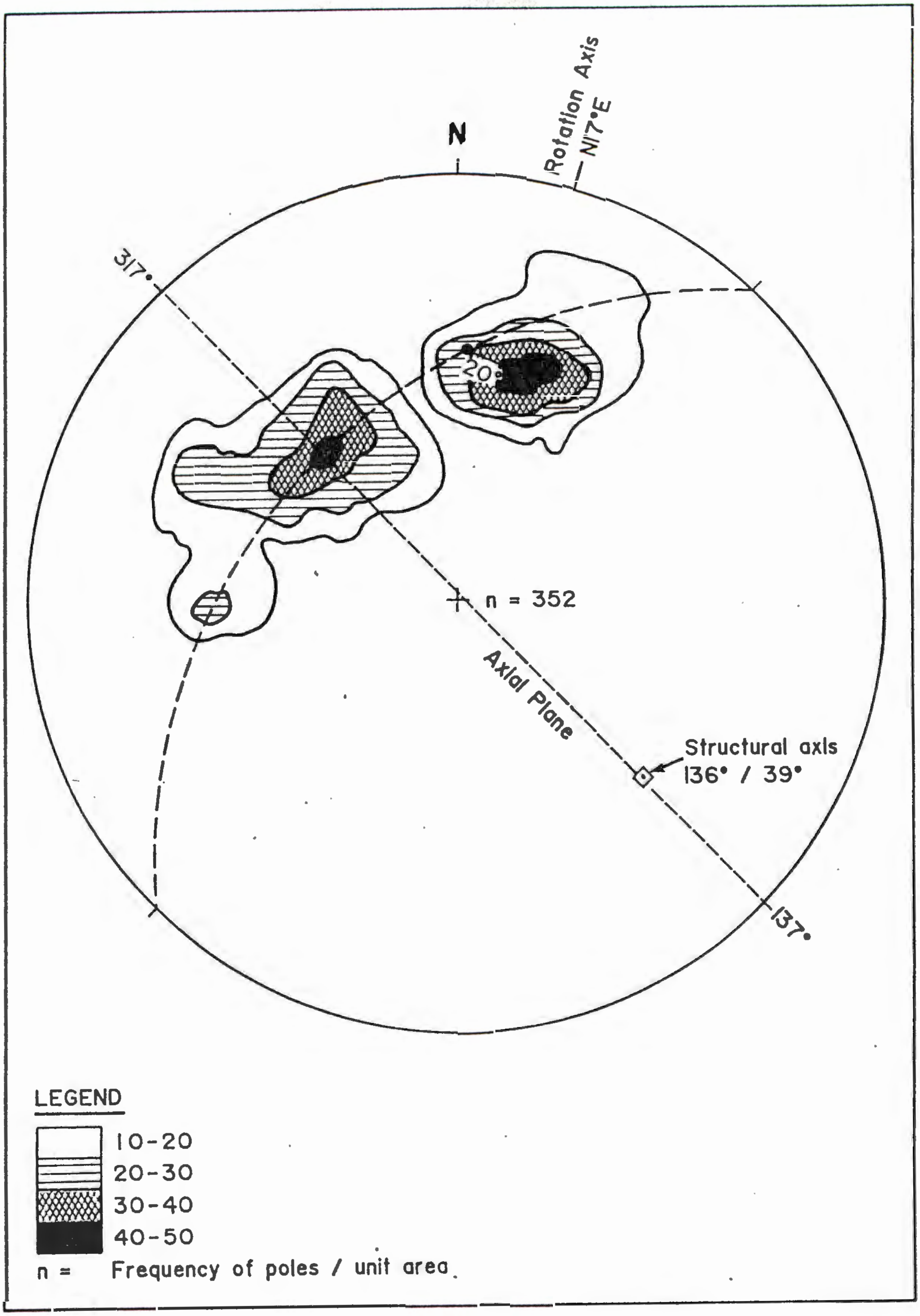

Figure 4. Contoured equal-area projection of poles to bedding of Turffontein Subgroup strata showing structural axis and axial plane of the tilted diapir.

TABLE 2

Unrestored palaeocurrent field data (vector means of trough axis azimuths recorded on outcrop)

Locality	TROUGH AXES VECTORS-MEANS IN DIRECTION OF FLOW (DATA AS RECORDED ON OVERTURNED STRATA)				TECTONIC ATTITUDE OF DEFORMED STRATA
	Vect A	n	Vect B	n	Az/dip
L1	338	7			088/48
L2	335	9			095/47
L3	328	2			108/66
L4	002	3			113/51
L5	358	7			134/47
L6	329	14			113/53
L7	353	13			125/55
L8	355	13			119/56
L9	353	22			130/42
L10	009	22			140/40
L11	024	6			149/49
L12	001	8			110/50
L13	023	1	67	25	133/35
L14	279	2	108	21	153/47
L15	310	8	113	13	157/46
L16	316	7	102	24	148/40
L17	320	5	102	19	139/42
L18	315	12	106	7	170/29
L19	329	13	113	6	153/30

TABLE 2 (continued)

Unrestored palaeocurrent field data (vector means of trough axis azimuths recorded on outcrop)

Locality	TROUGH AXES VECTORS—MEANS IN DIRECTION OF FLOW (DATA AS RECORDED ON OVERTURNED STRATA) Vect A	n	Vect B	n	TECTONIC ATTITUDE OF DEFORMED STRATA Az/dip
L20	310	21	146	1	202/50
L21	311	23	122	8	191/45
L22	326	10	210	1	197/51
L23	014	4			214/58
L24	339	13			208/49
L25	336	10			196/70
L26	016	7			200/41
L27	351	3			210/44
R1	272	3			134/34
R2	010	1			140/55
R3	242	10			124/45
R4	299	5			132/48
R5	036	12			171/32
R6	076	8			183/36
R7	059	11			188/44
R8	040	7			183/52
R9	132	4			210/75
R10	136	8			221/66

rotation of all plotted poles by 2^0, in the same sense, along small circles). The axis of the major Structure was thereafter rotated to the vertical, 51^0 (clockwise, looking northeast) about the now horizontal pole of the axial plane. All plotted poles were also rotated this angle, and in the same sense, along small circles. With the axis of the major Structure assuming a vertical attitude previously overturned strata should also be vertical if they were cylindrically folded. The stereographic plots revealed that, in the vast majority of cases, near vertical attitudes resulted from the latter rotation. The vertical strata were finally restored to their original horizontal attitude by clockwise rotation around the strike of the vertical bedding. The trough-axis lineations are rendered horizontal by this rotation and, having recorded the polarity of palaeoflow in the field, the azimuth of the restored palaeo-flow indicators was read. The data of the northeastern sector (L20–L27 and R6–R10) were treated in a similar fashion except for a preliminary 20^0clockwise rotation with respect to a horizontal axis striking N17^0E. Table 3 and Figure 5 show the results obtained by restoration of the palaeo-flow pattern through this new proposed method.

The regional palaeo-flow pattern of the Leeufontein Formation, resulting from this procedure (Fig. 5), is much more uniform in direction compared to the pattern for this Formation shown by Figure 2, obtained by the standard method of rotation of the beds around their tectonic strikes. Figure 5 shows that the direction of the A-series of vectors (basinward) vary from approximately east-southeast to south-southeast and their bipolar counterparts (B-series) have directions which vary from north-northeast to northwest (see L13 to L22, Fig. 5). The pattern for the Rooderand Formation exhibits greater variance but nevertheless shows palaeoflow directions which vary between approximately east and south-southwest.

It is clear on inspecting Nel's map that the exposed collar of the Vredefort Structure is not exactly circular in plan view. In fact it is polygonal comprising possibly six approximate

TABLE 3

Restored palaeocurrent vectors (stereographic rotation, based on proposed tectonic model, of data in Table 2 – See text)

	PALAEOCURRENT VECTORS (STRATA HORIZONTAL)				TECTONIC ATTITUDE OF DEFORMED STRATA
Locality	Vect A	n	Vect B	n	Az/dip
L1	075	7			088/48
L2	088	9			095/47
L3	112	2			108/66
L4	078	3			113/51
L5	103	7			134/47
L6	110	14			113/53
L7	100	13			125/55
L8	096	13			119/56
L9	100	22			130/42
L10	094	22			140/40
L11	092	6			149/49
L12	074	8			110/50
L13	119	1	016	25	133/35
L14	178	2	350	21	153/47
L15	154	8	348	13	157/46
L16	137	7	351	24	148/40
L17	132	5	347	19	139/42
L18	154	12	005	7	170/29
L19	132	13	349	6	153/30
L20	168	21	329	1	202/50
L21	161	23	351	8	191/45
L22	149	10	283	1	197/51
L23	125	4			214/58
L24	142	13			208/49
L25	142	10			196/70
L26	107	7			200/41
L27	130	3			210/44

TABLE 3 (continued)

Restored palaeocurrent vectors (stereographic rotation, based on proposed tectonic model, of data in Table 2 – See text)

Locality	PALAEOCURRENT VECTORS (STRATA HORIZONTAL) Vect A	n	Vect B	n	TECTONIC ATTITUDE OF DEFORMED STRATA Az/dip
R1	171	3			134/34
R2	100	1			140/55
R3	188	10			124/45
R4	143	5			132/48
R5	084	12			171/32
R6	217	8			183/36
R7	248	11			188/44
R8	091	7			183/52
R9	184	4			210/75
R10	244	8			221/66

Figure 5. Map showing palaeocurrent vector–means along the outcrops of the Rooderand and Leeufontein Formations. Reconstruction effectuated by means of rotational method based on a proposed tectonic model for the diastrophism of the Vredefort area (See text).

straight strike segments. To further simplify the regional palaeocurrent pattern the results of Figure 5 have been statistically reduced (Fig. 6) to portray the representative palaeoflow directions for the larger strike segments observable on the map.

Finally it must be pointed out that circumference of the Vredefort collar may originally have been somewhat larger than it is at present. It has been noted by Manton (1962) that the strike length of any of the collar units in the Vredefort Structure has been shortened by faulting. The effect of this is especially noticeable for some strike segments of the inner formations which show repeated duplication. Note for example the duplication of the Hospital Hill quartzites as result of faulting (Fig. 2). It is, of course, possible that some of the faults, which duplicate strata in the collar, could have originated during a pre-Vredefort phase of thrusting. A possible example of such a pre-Vredefort thrust fault is the strike fault which has duplicated the strata of the Jeppestown Subgroup and into which the alkali granite of the Schurwedraai pluton has intruded (Elsenbroek, 1991). However, most of the faults and folding, such as the fold structure in the Hospital Hill quartzite on the farm Leeudoorns 350 (Mayer and Albat, 1988), are associated with pseudotachylite and are presumably connected with the overturning of the collar strata. Lilly (1980) analysed the fault pattern in the Vredefort collar and came to the conclusion that a gross centripetal movement of the strata, along curved and concentric bounding faults, took place. This faulting therefore possibly reduced the circumference of the Vredefort collar.

If the circumference of the Vredefort collar has indeed been reduced it would mean that the regional palaeocurrent pattern as presented by Figure 6 may still require a measure of further correction. A rough calculation, based on a straightening of the folding and the elimination of the duplication of the Orange Grove Quartzite in the inner circumference of the collar of the Vredefort Structure, shows that it is not too implausible to hypothesise that the inner diameter of the Structure was larger, by as much as fifteen kilometres, compared to what it is today. In the reconstruction of the palaeocurrent pattern, shown on Figure 7, a model in which the inner diameter of the collar has been increased by

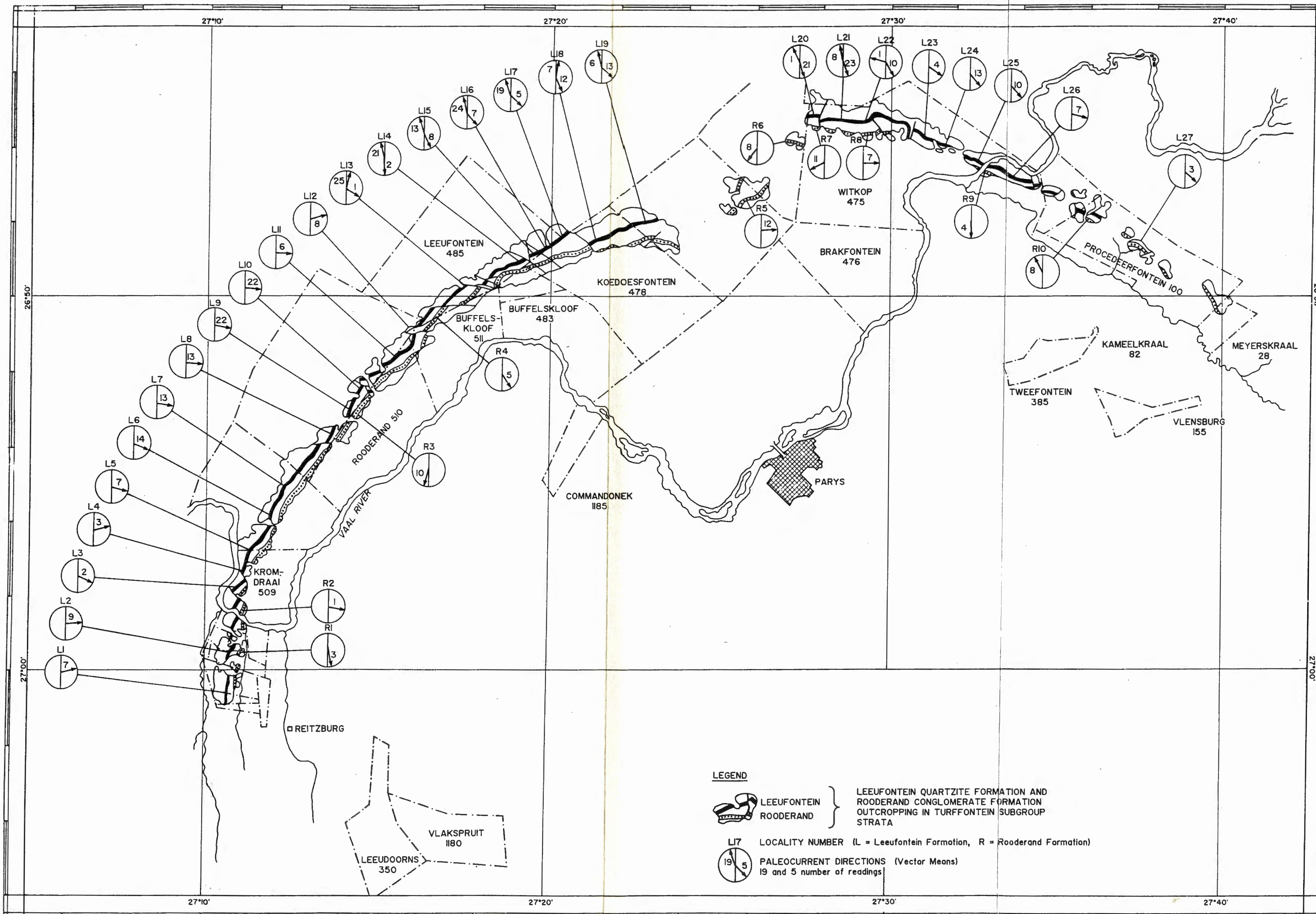
27°10'
27°20'
27°30'
27°40'
26°50'
27°00'
L1 L2 L3 L4 L5 L6 L7 L8 L9 L10 L11 L12 L13 L14 L15 L16 L17 L18 L19 L20 L21 L22 L23 L24 L25 L26 L27
R1 R2 R3 R4 R5 R6 R7 R8 R9 R10
LEEUFONTEIN 485
KOEDOESFONTEIN 478
BUFFELSKLOOF 483
BUFFELS-KLOOF 511
ROODERAND 510
VAAL RIVER
KROM-DRAAI 509
REITZBURG
VLAKSPRUIT 1180
LEEUDOORNS 350
COMMANDONEK 1185
PARYS
WITKOP 475
BRAKFONTEIN 476
PROCEDEERFONTEIN 100
KAMEELKRAAL 82
MEYERSKRAAL 28
TWEEFONTEIN 385
VLENSBURG 155
LEGEND
LEEUFONTEIN
ROODERAND
LEEUFONTEIN QUARTZITE FORMATION AND ROODERAND CONGLOMERATE FORMATION OUTCROPPING IN TURFFONTEIN SUBGROUP STRATA
L17 LOCALITY NUMBER (L = Leeufontein Formation, R = Rooderand Formation)
PALEOCURRENT DIRECTIONS (Vector Means)
19 and 5 number of readings

Figure 5

Figure 6. Map of simplified regional palaeocurrent trends for the Turffontein Subgroup in the Vredefort area. Palaeocurrent trends are averages of vector-means totals per strike segment of the Turffontein Subgroup. Strike segments for Hospital Hill quartzite are shown to demonstrate their slightly different disposition in relation to those of the Turffontein Subgroup

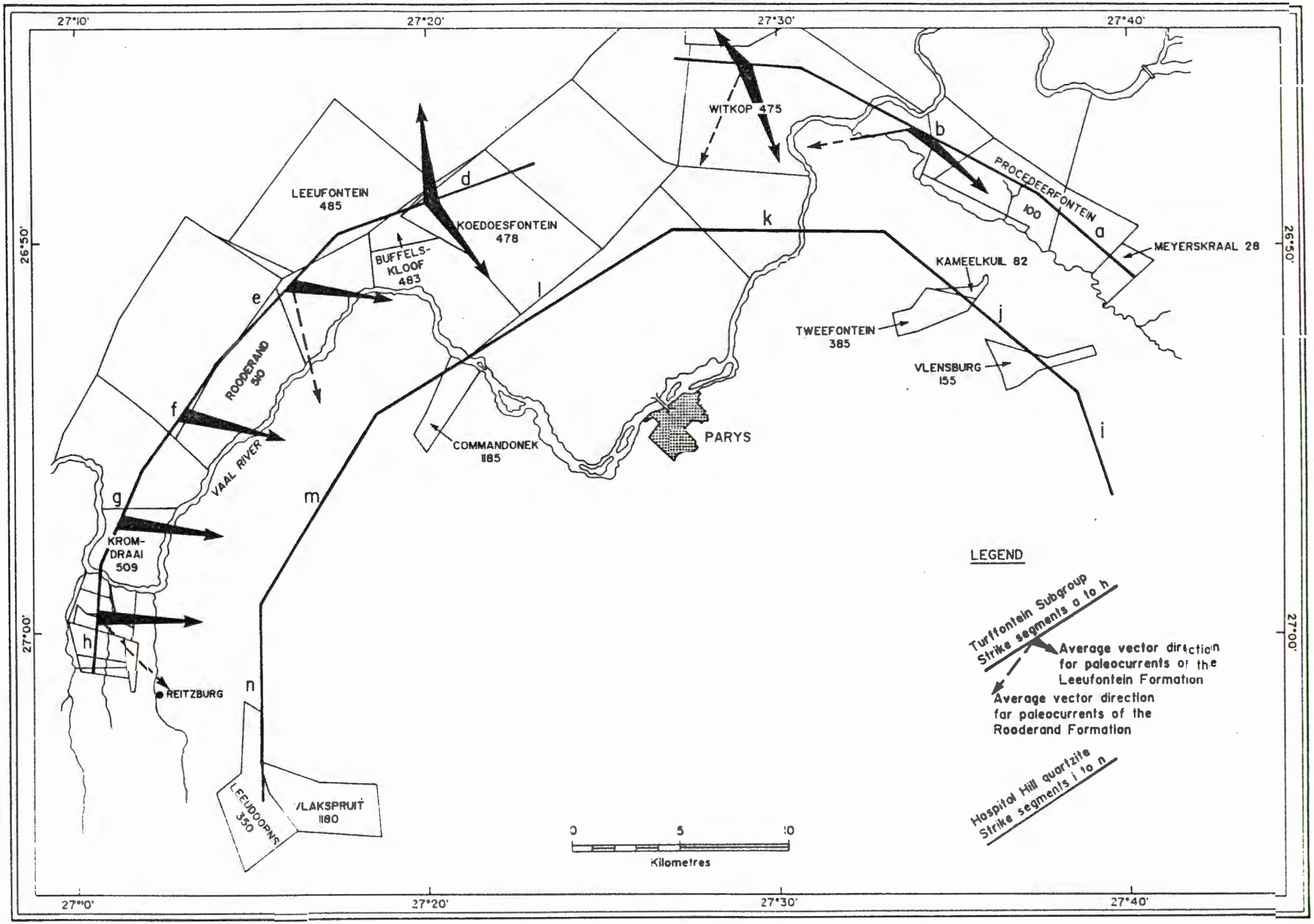

27°10'
27°20'
27°30'
27°40'
26°50'
27°00'
27°0'
WITKOP 475
LEEUFONTEIN 485
KOEDOESFONTEIN 478
BUFFELS-KLOOF 483
PROCEDEERFONTEIN 100
MEYERSKRAAL 28
KAMEELKUIL 82
TWEEFONTEIN 385
VLENSBURG 155
ROODERAND 510
COMMANDONEK 1185
PARYS
VAAL RIVER
KROM-DRAAI 509
REITZBURG
LEEUDOORNS 350
VLAKSPRUIT 1180
a
b
d
e
f
g
h
i
j
k
l
m
n
LEGEND
Turffontein Subgroup Strike segments a to h
Average vector direction for paleocurrents of the Leeufontein Formation
Average vector direction for paleocurrents of the Rooderand Formation
Hospital Hill quartzite Strike segments i to n
0
5
10
Kilometres

Figure 6

Figure 7. Map of the strike segments in the Vredefort Structure, identified for Turffontein Subgroup Formations and Hospital Hill quartzite, corrected for an apparent post-overturning radius of curvature reduction of the tilted Structure. Diameter enlargement is approximately 15 km. Palaeocurrent information as on Figure 6.

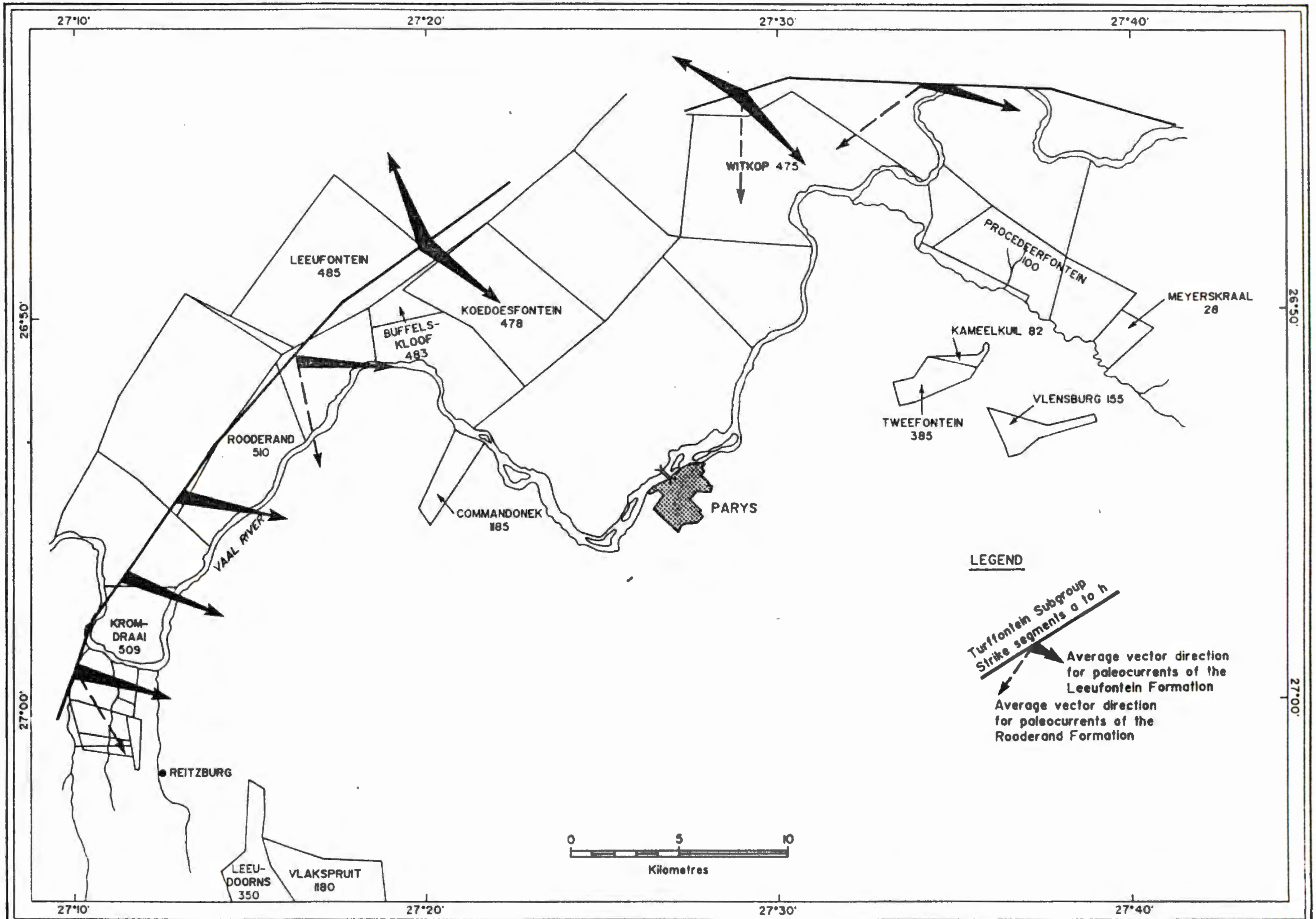

27°10'
27°20'
27°30'
27°40'
26°50'
27°00'
LEEUFONTEIN 485
KOEDOESFONTEIN 478
BUFFELS-KLOOF 483
WITKOP 475
PROCEDEERFONTEIN 100
MEYERSKRAAL 28
KAMEELKUIL 82
TWEEFONTEIN 385
VLENSBURG 155
ROODERAND 510
COMMANDONEK 1185
PARYS
VAAL RIVER
KROM-DRAAI 509
REITZBURG
LEEU-DOORNS 350
VLAKSPRUIT 1180
0
5
10
Kilometres
LEGEND
Turffontein Subgroup Strike segments a to h
Average vector direction for paleocurrents of the Leeufontein Formation
Average vector direction for paleocurrents of the Rooderand Formation

Figure 7

approximately 15 km has been adopted. A fifteen kilometre increase in the hub diameter of the Vredefort Structure, and a complementary decrease in the degree of curvature of the collar arc, does not significantly change the general character of the palaeo-flow pattern for the Turffontein strata. The pattern retains its easterly to southeasterly, for the Leeufontein, and southeasterly to southwesterly character for the Rooderand Formation.

INTERPRETATION OF THE PALAEOCURRENTS

The Leeufontein Quartzite Formation has been investigated in two detailed sedimentary profiles on the farms Witkop 475 and Leeufontein 485 area (Els & Mayer, in press – Chapter 5) where bipolar palaeocurrents are present (Fig. 5). These profiles revealed, besides polymodal palaeocurrent distributions, several additional characteristics considered typical of silisiclastic nearshore and beach deposits. These traits led to the conclusion that the Formation was deposited during successive transgressive and progradational episodes. Palaeocurrent modes pertaining to the two profiles were therefore interpreted in terms of the proposed beach and nearshore depositional environment. Figure 5, however, shows that palaeocurrent distributions of the Leeufontein Formation are apparently exclusively unimodal in the southwestern and the northeastern sectors of the Vredefort Structure; a trait very uncharacteristic of beach and nearshore depositional environment, but typical of fluvial deposition. Therefore, although the Formation in the southwestern and northeastern sectors of the Structure has not been investigated in detailed vertical profiles, it is tentatively suggested that coastal lithofacies, formed during the subsequent proposed transgression, have been reworked by fluvial processes during the subsequent progradation. In these regions the palaeocurrent vectors probably indicate the palaeoslope.

The Rooderand Conglomerate Formation has not been investigated by the authors in sufficient detail to justify an environmental interpretation. The Formation has, however, been studied by Holland et al. (1990) who termed it "the Kimberley Formation conglomerates" and cited several characteristics which point to a fluvial origin for this conglomeratic Formation. Palaeocurrent modes pertaining to the Formation therefore most likely indicate palaeoslope dip directions.

SUMMARY AND CONCLUSIONS

Mapping of the Turffontein strata provided the opportunity for palaeocurrent data to be recorded for two newly proposed stratigraphic units in this Subgroup of the Vredefort area; the Leeufontein Formation, for which a larger data base has been established, and the Rooderand Formation which yielded a much smaller one. Processing of the palaeocurrent data, to correct for the deformation of the strata, was initially carried out by means of the conventional rotation of the beds to their original horizontality about their present tectonic strikes. This produced a regional palaeocurrent pattern for the Leeufontein Formation which showed large directional variances over a comparative short distance. This raised doubt about the correcting technique applied and necessitated a reconsideration of the tectonic model used as a basis for tectonic correction. Consideration of the various proposed hypotheses for the origin of the Vredefort Structure lead the authors to accepting the impact model for this Structure on grounds of the salient features pointing to such an origin. Reasoning on the mechanism of this model lead the authors to conclude that the Vredefort Structure, if regarded as an impact-rebound diapiric structure, cannot be considered an upright structure but one that has undergone a measure of post-impact tilting. The nature of the tilted structure was assessed stereographically with the aid of an equal area projection using the available data base on the attitude of Turffontein strata. The projection shows that the structure closely conforms to a cylindrical fold-like structure with an axis verging 39^0 on a bearing 136^0. Although the northeastern part of the structure has been displaced by faulting it is concluded that it was originally symmetrical with an axial plane dipping 88^0 N48^0E. Assuming perfect symmetry for the Structure, before the faulting, a 20^0 clockwise rotation of the strata about an axis striking N17^0E is proposed to correct for the tilting associated with the faulting.

The palaeocurrent field data, condensed by calculation of vector-means of crossbed trough axes along short strike segments (strike localities L1-L20 and R1-R10),were subjected to stereographic manipulation in accordance with this model. The procedure adopted involves a sequence of stereographic rotations of the palaeocurrent data, first bringing the major Structure upright before rotating the strata to the horizontal about the tectonic strike of the vertical beds. Treatment of the data according to this procedure produces a more uniform palaeo-flow pattern for the Turffontein strata compared to the one obtained by the conventional method.

The following final conclusions may be drawn:

1. The highly deformed area of the Vredefort Structure, consisting of overturned vertical and right-way up, folded and faulted strata, requires treatment more sophisticated than the simple rotation of the beds about their tectonic strikes to effectuate palaeogeographic reconstruction.
2. The rotations proposed for restoring the deformation of the Turffontein strata in the Vredefort Structure may only be valid for these strata considering the somewhat different configuration of the collar segments (Fig. 6) and style of faulting of the inner formations of the collar (Fig. 2).
3. If the results obtained by the proposed new procedure of palaeogeographic reconstruction are valid, the uniformity and consistency of the pattern of palaeo-drainage vectors for the Leeufontein indicate that, if at all, the circumference of the Vredefort collar could not originally have been significantly larger than it is today.
4. The restoring of the palaeodrainage to a pattern of sub-parallel vectors by centripetal rotations about an arcuate axis also apparently negates the possibility that the Vredefort Structure represents a huge tectonic thrust fold.

5. The occurrence of bipolar palaeocurrent distributions and other features along a portion of the the northwestern arc of the present strike of the Leeufontein Formation may indicate shoreline conditions in this area in mid-Turffontein times. The dominance, however, of apparently exclusively unimodal palaeocurrent vectors for this Formation in the southwestern and the northeastern sectors of the collar may indicate subsequent fluvial reworking of the coastal lithofacies and therefore conform to the dip direction of the palaeoslope.

6. The general directional character of the palaeo-flow pattern for the dispersal currents of Turffontein sediments in the Vredefort area, between approximately east and south, is consistent with palaeocurrents for the the gold placers of the Johannesburg Subgroup of the Klerksdorp (Antrobus et al., 1986; Minter and Loen, 1991) and the Carletonville Gold Fields (Minter and Loen, 1991). This consistency indicates that a relatively uniform palaeoslope was maintained over a wide area and in time in the history of Witwatersrand sedimentation.

ACKNOWLEDGMENTS

This work was supported by the Bureau for Research, Potchefstroom University for C.H.E. and the Geological Survey of South Africa. The following students, who assisted with the fieldwork, are thanked: Herman Olivier, Jan Myburgh, Deon du Plessis, Fanie Yssel and Gerda Davids. A word of thanks is also due to former colleague Hans Albat for useful discussions and Mrs. I. van Rensburg for the draughting of the diagrams. Russel W Shone and the unknown referee are specially thanked for their constructive criticism which resulted in improving the quality of this paper tremendously.

REFERENCES

Albat, H.M. (1988). Shatter cone/bedding interrelationship in the Vredefort Structure: evidence for meteorite impact? *S. Afr. J. Geol.*, **91**, 106-113.

——— & Mayer, J.J. (1989). Megascopic planar shock fractures in the Vredefort Structure: a potential time marker? *Tectonophysics*, **162**, 265-276.

——— & Mayer, J.J. (1990). Shatter cones in Vredefort rocks – imagination or reality? *S. Afr. J. Geol.*, **93**, Note, 547-548.

Antrobus, E.S.A., Brink, W.J.C., Brink, M.C., Caulkin, J., Hutchison, R.I., Thomas, D.E., Van Graan, J.A., and Viljoen, J.J., (1986). The Klerksdorp Goldfield. In: C.R. Anhaeusser and S. Maske, Eds., *Mineral Deposits of Southern Africa.* Geol. Soc. S. Afr., Johannesburg, pp.549-598.

Bailey, E.B. (1926). Domes in Scotland and South Africa. *Geol. Mag.*, **43**, 481-494.

Bisschoff, A.A. (1969). *The petrology of the igneous and metamorphic rocks in the Vredefort Dome and adjoining parts of the Potchefstroom Syncline.* D.Sc. thesis (unpubl.) Univ. Pretoria, 243pp.

Boon, J.D., & Albritton, C.C. (1937). Meteorite scars in the ancient rocks. *Field Lab.*, **5**, 53-64.

——— (1938). Established and supposed examples of meteoritic craters. *Field Lab.*, **6**, 44-56.

Brock, B.B. (1951). The Vredefort Ring. *Trans. geol. Soc. S. Afr.*, **53**, 131-157.

Brock, B.B. & Pretorius, D.A.(1964). Rand basin sedimentation and tectonics, pp. 549-599. In: S.H. Haughton, Ed., *The Geology of some Ore Deposits of Southern Africa*, **1**, Geol. Soc. S.Afr., Johannesburg, 625pp.

Bucher, W.H. (1963). Cryptoexplosion structures caused from without or from within the Earth ('astroblemes' or 'geoblemes')? *Amer. J. Sci.*, **261**, 597-649.

Colliston, W.P. (1990). A model of compressional tectonics for the origin of the Vredefort Structure. *Tectonophysics*, **171**, 115-118.

Daly, R.A. (1947). The Vredefort ring-structure of South Africa. J. Geol., **55**, 125-145.

De Villiers, A.B. (1989) The fossil landscape of the Vredefort Dome. *Z. Geomorph. N.F.*, **33**, 93-101.

Dietz, R.S. (1961). Vredefort ring-structure – Meteorite impact scar? *J. Geol.*, 69, 499-516.

—— (1963). Astroblemes, ancient meteorite-impact structures on the Earth, 285–300. In: Middlehurst, B.M. & Kuiper, G.P., Eds., *The Moon, Meteorites and Comets*. Univ. Chicago press, Chicago.

—— (1968). Shatter cones in cryptoexplosion structures, 267-285. In: French, B.M. & Short, N.M., Eds., *Shock Metamorphism of Natural Materials*, Baltimore, M.D. Mono Book Corp.

Du Toit,A.L. (1954). *The Geology of South Africa*. Oliver and Boyd, Edinburgh, 3rd ed., 611pp.

Els, B.G. and Mayer, J.J. (1992, in press). Transgressive and progradational beach and nearshore facies in the late Archaean Turffontein Subgroup of the Witwatersrand Supergroup in the Vredefort area South Africa. *S. Afr. J. Geol* **95**.

Elsenbroek, J.H. (1991). *Die Struktuur en Petrologie van die Alkaligraniet in die Vredefortkoepel noordwes van Parys*. M.Sc. thesis (unpubl.) Univ. Potchefstroom for C.H.E., 105pp.

Grieve, R.A.F., Coderre, J.M., Robertson, P.B. & Alexopoulos, J. (1990). Microscopic planar deformation features in quartz of the Vredefort Structure: Anomalous but still suggestive of an impact origin. *Tectonophysics*, **171**, 185-200.

Hall, A.L. & Molengraaff, G.A.F. (1925). The Vredefort Mountain Land in southern Transvaal and northern Orange Free State. *Verh. K. Akad. Wet.*, 24, 1–183.

Hargraves, R.B. (1961). Shatter cones in the rocks of the Vredefort Ring. *Trans. geol. Soc. S. Afr.*, **64**, 147–154.

Holland, M.J., Stanistreet, I.G. & Mccarthy, T.S. (1990). Tectonic control on the deposition of the Turffontein Subgroup around the Vredefort Dome. *S. Afr. J. Geol.*, **93**, 158-168.

Lilly, P.A. (1980) Faulting mechanics in the collar rocks of the Vredefort ring structure. *Tectonophysics*, **67**, 45-60.

—— (1981) Shock metamorphism in the Vredefort collar: evidence for internal shock sources. *J. geophys. Res.*, **86**, 10689-10700.

Manton, W.I. (1965) The orientation and origin of shatter cones in the Vredefort Ring. In: *Geological Problems in Lunar Research.* Ann. New York Akad. Sci., **123**, 1017-1049.

Maree, B.D. (1944) The Vredefort Structure as revealed by a gravimetric survey. *Trans. geol. Soc. S. Afr.*, **47**, 183–196.

Martini, J.E.J. (1991). The nature, distribution and genesis of the coesite and stishovite associated with the pseudotachylite of the Vredefort Dome, South Africa. *Earth Planet. Sci. Lett.*, 103, **285**–300.

Mayer, J.J. & Albat, H.M. (1988). The tectono-sedimentary setting of the area of the Vredefort Structure during deposition of the upper quartzite member of the Hospital Hill Subgroup. *S. Afr. J. Geol.*, **91**, 239–247.

—— (1990). An appraisal of the significance of small-scale fold structures in the contorted bed of the area of the Vredefort Structure. *S. Afr. J. Geol.*, **93**, 311–317.

McCarthy, T.S., Stanistreet, I.G. & Robb, L.J. (1990). Geological studies related to the origin of the Witwatersrand Basin and its mineralization – an introduction and strategy for research and exploration. *S. Afr. J. Geol.*, **93**, 1-4.

Melosh, H.J. (1989). *Impact Cratering A Geologic Process.* Oxford University Press, New York, 245pp.

Minter, W.E.L. & Loen, J.S. (1991). Palaeocurrent dispersal patterns of Witwatersrand gold placers. *S. Afr. J. Geol.*, **94**, 70–85.

Myers, R.E., T.S. McCarthy and I.G. Stanistreet (1990). A tectono-sedimentary reconstruction of the development and evolution of the Witwatersrand Basin, with particular emphasis on the Central Rand Group. *S. Afr. J. Geol.*, **93**, 180–201.

Nel, L.T. (1927). The geology of the country around Vredefort – An explanation of the geological map. *Spec. Publ. geol. Surv. S. Afr.*, **6**, 134pp.

Nicolaysen, L.O. (1972). North American cryptoexplosion structures: interpreted as diapirs which obtain release from strong lateral confinement. *Mem. geol. Soc. Amer.*, 132, 605–620.

Potter, P.E. & Pettijohn, F.J. (1963). *Paleocurrents and basin analysis.* Springer-Verlag, Berlin, 296 pp.

Roering, C., Barton, J.M., Jr. and Winter, H de la R. (1990). The Vredefort Structure: a perspective with regard to new tectonic data form adjoining terrains. *Tectonophysics*, 171, 7–22.

Simpson, C. (1981). Occurrence and orientation of shatter cones in Pretoria Group quartzites in the collar of the Vredefort 'Dome': impact origin precluded. *J. geophys. Res.*, **86**, 10701–10706.

Tankard, A.J., Jackson, M.P.A., Eriksson, K.A., Hobday, D.K. Hunter, D.R. & Minter, W.E.L. (1982). *Crustal Evolution of Southern Africa, 3.8 Billion years of Earth History.* Springer-Verlag, New York, 523pp.

Winter, H. de la R. (1987). A cratonic foreland model for Witwatersrand Basin development in a continental back-arc, plate-tectonic setting. *S. Afr. J. Geol.*, **90**, 409–427.

CHAPTER 5

TRANSGRESSIVE AND PROGRADATIONAL BEACH AND NEAR-SHORE FACIES IN THE LATE ARCHAEAN TURFFONTEIN SUBGROUP OF THE WITWATERSRAND SUPERGROUP, VREDEFORT AREA, SOUTH AFRICA

S. Afr. J. Geol., 1992, 95

TRANSGRESSIVE AND PROGRADATIONAL BEACH AND NEARSHORE FACIES IN THE LATE ARCHAEAN TURFFONTEIN SUBGROUP OF THE WITWATERSRAND SUPERGROUP, VREDEFORT AREA, SOUTH AFRICA.

B.G. Els and J.J. Mayer

Department of Geology
Potchefstroom University for C.H.E.
Private Bag X6001
2550 Potchefstroom.
Republic of South Africa

ABSTRACT

The Vredefort Structure of South Africa is situated on the border of the Orange Free State and Transvaal provinces and occurs roughly near the centre of the oblong Witwatersrand basin, where the strata of the entire 7 000m thick Witwatersrand Supergroup crop out in an arcuate periclinal structure. Although no formal differentiation has previously been made for the Central Rand Group beyond the rank of Subgroup, the uppermost Turffontein Subgroup is tentatively subdivided into five Formations. This paper reports on a sedimentological and preliminary petrographic study of one of these proposed Formations, the Leeufontein Quartzite, and parts of the underlying and overlying Formations.

Palaeocurrent distributions in this Formation were determined at 27 localities along the outcrop in the Vredefort Structure, using trough cross-bed axes as palaeocurrent indicators. This revealed bi- and polymodal distributions in the central parts of the arcuate Structure, whereas in the western and eastern regions palaeocurrent distributions are unimodal, with modes towards the east and southeast, respectively.

The lithofacies of the Leeufontein Quartzite Formation and those of the uppermost and lowermost portions of the underlying and overlying Formations were studied in three detailed vertical profiles. These revealed that the Leeufontein Quartzite is most probably of shallow marine origin, but that the underlying and overlying successions represent deposition in fluvial environments. The Formation contains several lithofacies, typical of beach and nearshore depositional environments, which may have been deposited no farther offshore than the inner shelf zone.

It is proposed that the Leeufontein Quartzite Formation was deposited during successive transgressive and progradational episodes and that the deposits of these contrasting processes are partially preserved.

The findings of this study have important implications for the configuration of the Witwatersrand basin and for its stratigraphy. The probable presence of an ancient shoreline in the central regions of the preserved Witwatersrand basin suggests a basinal location on a continental margin. It follows that marine facies, absent in the northwestern sector of the preserved basin, would most probably occur in the southeastern parts. This may present regional correlation problems to those who are unaware of the facies transition in the Turffontein Subgroup of the Vredefort area.

UITTREKSEL

Die bekende Vredefort Struktuur van Suid-Afrika is op die grens tussen die provinsies van Transvaal en die Oranje-Vrystaat geleë en kom naby die middel van die bewaarde Witwatersrand-afsettingskom voor. In hierdie gebied dagsoom die 7 000 m dik Witwatersrand Supergroep in sy geheel in 'n boogvormige periklinale struktuur. Alhoewel daar geen formele onderverdeling van die Sentrale Rand Groep van die Vredefort-gebied bestaan nie, word die boonste Subgroep, die Turffontein, in vyf Formasies verdeel. Hierdie artikel is 'n verslag van 'n sedimentologiese en voorlopige petrografiese studie van een van hierdie Formasies, die Leeufontein Kwartsiet, asook van gedeeltes van die onderliggende en oorliggende Formasies.

Paleostroomverspreidings is op 27 lokaliteite langs die dagsoom van die Formasie met behulp van die asse van trogkruisgelaagheid bepaal. Hierdie ondersoek het getoon dat die verspreiding in die sentrale gedeelte van die Struktuur bi- en polimodaal is. In die westelike en oostelike gebiede is die verspreidings egter oorwegend unimodaal met modusse wat onderskeidelik na die ooste en suidooste gerig is.

Litofasies wat in die Leeufontein Kwartsiet Formasie voorkom, asook dié van die boonste en onderste gedeeltes van onderskeidelik die onderliggende en oorliggende Formasies, is in drie vertikale profiele bestudeer. Hulle toon dat die Formasie heelwaarskynlik van vlak marine oorsprong is, maar dat die onderliggende en oorliggende Formasies 'n fluviale oorsprong het. Die Leeufontein Kwartsiet Formasie bevat sekere litofasies wat as kenmerkend van die strand en bylandige afsettingsomgewings beskou word. Die sub-omgewings wat deur die litofasies verteenwoordig word, was nie verder van die kus geleë as as die binne-platsone nie.

Daar word voorgestel dat die Leeufontein Kwartsiet Formasie gedurende opeenvolgende transgressiewe en prograderende episodes afgesit is en dat die afsettings van albei hierdie teenstellende prosesse gedeeltelik in die gesteenterekord bewaar is.

Die bevindings van hierdie studie het belangrike implikasies vir die konfigurasie van die Witwatersrand-afsettingskom en vir die stratigrafie van die Supergroep. Die waarskynlike teenwoordigheid van 'n oer-strandlyn in die sentrale gedeeltes van die afsettingskom ten tye van afsetting van die Turffontein Subgroep, dui op 'n ligging van die kom op die rand van 'n kontinent. Hieruit kan die afleiding gemaak word dat marine fasies, wat nie in die Turffontein Subgroep van die noordwestelike gedeelte van die afsettingskom voorkom nie, waarskynlik in die suidoostelike gebiede gevind sal word. Dit mag regionale stratigrafiese korrelasies bemoeilik, tensy daar kennis geneem word van die fasieverandering in die Vredefort-gebied.

INTRODUCTION

The contrasting general lithologies of the argillaceous West Rand and arenaceous Central Rand Groups of the Late Archaean Witwatersrand Supergroup of South Africa are conspicuous, even to the casual observer and reader. It follows that the dominant depositional processes for these two Groups probably were very different. The West Rand Group contains several thick mudstone/siltstone units and a number of thick, very mature quartz arenites and it has been suggested that at least some of these units were deposited under marine conditions (Camden-Smith, 1980; Watchorn, 1981) or in a lacustrine environment (Vos, 1975). This contrasts with the arenaceous Central Rand Group, which seems to be predominantly fluvial in origin; a conclusion borne out by numerous studies, listed by Minter and Loen (1991), of the auriferous placers and their underlying and overlying beds. Bailey et al. (1990), however, argued the case for marginal marine sedimentation within the Central Rand Group of the Zandfontein Quartzite Formation in the Evander goldfield and Karpeta et al. (1991) suggested a similar origin for the basal portion of the Johannesburg Subgroup in the Heidelberg area. It is noteworthy that both these areas occur near the extreme eastern edge of the preserved Witwatersrand basin, as envisaged by Pretorius (1986).

The Turffontein is the upper Subgroup of the Central Rand Group and it contains a number of economic gold placers. Sedimentological studies of this Subgroup have therefore been directed mainly at the placers, with notable contributions by Armstrong (1968) and Tweedie (1986) on the Kimberley placer, Bailey et al. (1990) on the Zandfontein, Tucker and Viljoen (1986) on the Composite placer and Wheelock (1987) on the Elsburg No. 5. In addition, a sedimentological synthesis of the Eldorado Formation in the Welkom goldfield has been compiled by Kingsley (1987). With the exception of the paper by Bailey et al. (1990), no marine facies is described by the remaining authors listed.

During recent mapping of the Central Rand Group in the Vredefort area, a thin succession of very mature quartz arenites, termed the Leeufontein Quartzite Formation, captured the authors' interest. This led to a more detailed study which indicated that the sequence, which occurs between two fluvial successions, is most probably of shallow marine origin. Since marine facies are apparently absent in the Turffontein Subgroup of the Klerksdorp and Carletonville goldfields, the discovery of an ancient Turffontein shoreline in the Vredefort Structure has far-reaching implications for the stratigraphy of the Central Rand Group and for the configuration of the Witwatersrand basin.

GEOGRAPHIC SETTING

The well-known Vredefort Structure is situated on the border between the Transvaal and Orange Free State (O.F.S.) provinces of South Africa in the vicinity of Parys and Vredefort (Fig. 1). The Structure, the exposed part of which is often portrayed as semi-circular on large-scale maps, has a "diameter" of about 55 km and occurs roughly near the centre of the preserved oblong Witwatersrand basin, as depicted by Pretorius (1986). Within the inner parts of the arcuate structure the topographic relief is low, but on the rim local elevation differences up to 350 m occur (de Villiers, 1989).

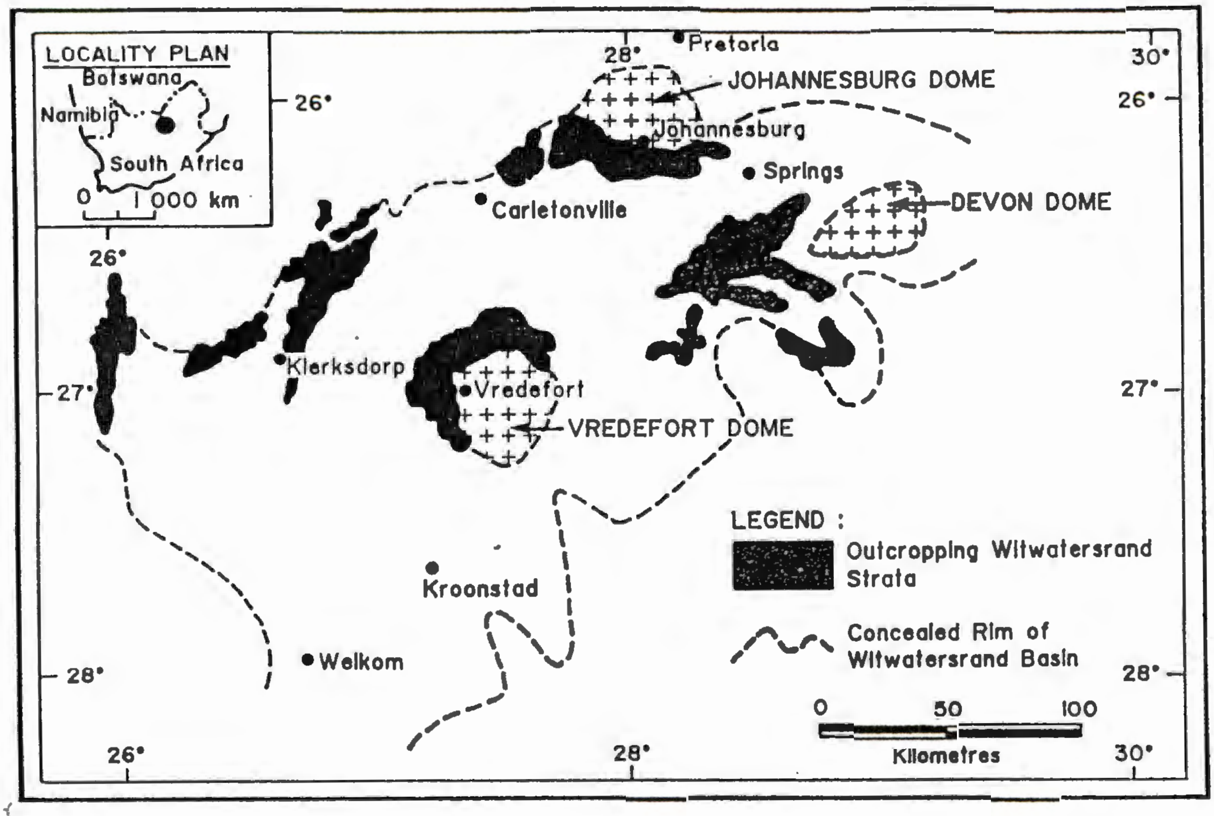

Figure 1: Map showing the locality of the Vredefort Structure within the preserved Witwatersrand basin.

STRUCTURE AND METAMORPHISM

The Vredefort Structure comprises a central granitic "hub" and an arcuate rim consisting of steeply-dipping sediments and volcanics of the Dominion Group, the Witwatersrand and Ventersdorp Supergroups and the Transvaal Sequence. With the exception of the south-western parts of the Structure, the beds constituting the rim are mostly overturned, dipping periclinally towards the "hub". The collar of the Vredefort Structure comprises a number of approximate straight-line segments, separated by inferred faults. Within each segment, tectonic strikes remain remarkably constant. The mean tectonic dip azimuths show a gradual increase for successive clockwise segments.

The Vredefort area abounds with intrusives of various ages and has been affected by thermal metamorphism, demonstrated by metamorphic facies variations within different regions of the structure (Bisschoff, 1969, 1982). Additional structural features include shatter cones (Albat, 1988) and planar shock fractures (Albat and Mayer, 1989).

In spite of their complex post-depositional history, the arenaceous rocks of the Vredefort Structure have generally remained remarkably undeformed and unaltered. Primary sedimentary structures are readily observed in these rocks and meaningful sedimentary petrographic investigations are possible.

STRATIGRAPHY AND GENERAL LITHOLOGY

Although the Vredefort area was first mapped more than 60 years ago by Nel (1927), stratigraphic differentiation of the Central Rand Group has not, until very recently, progressed beyond subdivision at the rank of subgroup. Following the initial phase of a systematic mapping programme of the Central Rand Group, Mayer and Els (1992, in press) proposed a lithostratigraphic subdivision of the Turffontein Subgroup (previously the Kimberley-Elsburg Series)(Fig. 2). Of the five proposed Formations, the Leeufontein Quartzite is the most conspicuous, notwithstanding the fact that it is only about 80 m thick. It consists of light grey to white, very mature quartz arenites, which form a prominent outcrop that can be traced throughout the Vredefort area, even on large-scale aerial photographs.

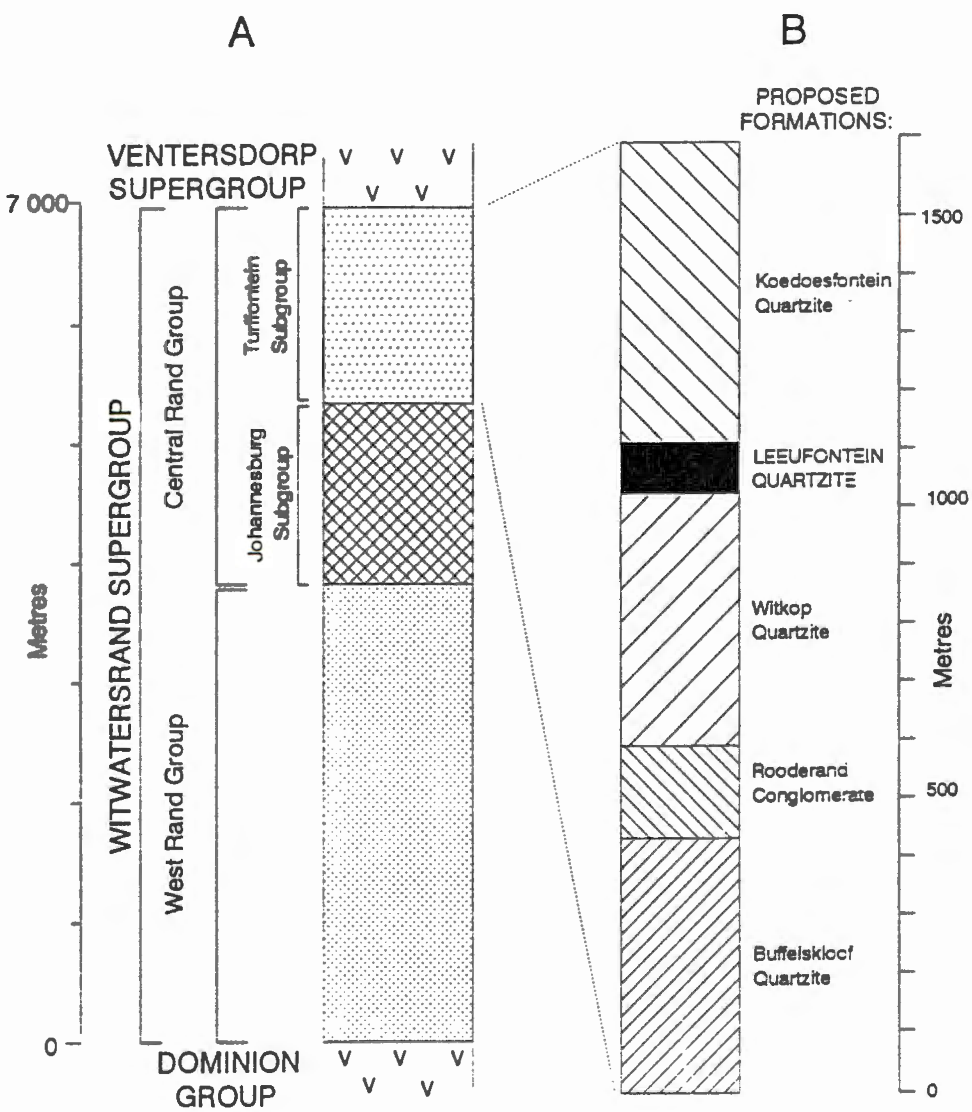

Figure 2: A: Simplified stratigraphic column showing the subdivision of the Witwatersrand Supergroup B: Proposed lithostratigraphic subdivision of the Turffontein Subgroup.

METHODS OF INVESTIGATION

(a) Regional palaeocurrent directions and distributions of the Leeufontein Quartzite Formation.

For this part of the investigation trough cross-bedding was used as the sole palaeocurrent indicator. These sedimentary structures are particularly prominent in the Formation and the steep tectonic dip of the beds afforded the opportunity to view complete (overturned) troughs. These splendid exposures were used to measure the plunge angles and directions of trough axes at 27 localities in the study area. For each reading, the dip direction of trough foresets was determined relative to the plunge direction of the trough axis.

Tectonic correction of palaeocurrents

The standard stereographic correction, for tectonic tilt, of palaeocurrents comprises simple rotation of the beds to horizontal about their tectonic strikes (Potter and Pettijohn, 1977). Mayer and Els (1992, in press), however, have shown that this procedure yields questionable results in the Vredefort area and suggested an alternative correction technique for this area, based upon a specific tectonic model for the diastrophism of the area. These authors consider the Vredefort Structure an initially-vertical, cylindrical impact-rebound diapir, which has subsequently been tilted. Viewed as such, the Structure has an axis which plunges 39° towards 136° and an axial plane dipping 88° towards 047°. Mayer and Els (op cit.) furthermore suggested that, due to a major fault zone which bisects the Structure, its eastern sector (Fig. 3) has undergone additional clockwise tilting of 20°, about an axis with direction 017° (clockwise as viewed down the rotation axis).

Applying this model, correction of the palaeocurrents of this study was carried out in successive steps to compensate, in reversed order, for sequential phases of diastrophism (Table 1):

(a) Rotation of the beds of the eastern sector of the Structure, to eliminate tilt associated with major faulting.
(b) Rotation of the axial plane of the Structure to vertical;
(c) Rotation of the axis of the Structure to vertical;
(d) Rotation of the beds to the horizontal, with correct stratigraphic polarity.

Preliminary step (a) of the sequence of stereogragphic rotations (Table 1) was applied to the palaeocurrent readings and related tectonic dips of the eastern sector only and subsequent steps (b) and (c) to those of both sectors. The bedding strikes obtained this way were finally used as axes to rotate the beds of both sectors to horizontal, with correct stratigraphic polarity (Step (d), Table 1).

From the corrected readings, compass roses were constructed to illustrate the regional palaeocurrent directions and distributions for the Formation (Fig. 3).

(b) Lithofacies, lithofacies successions and sedimentary structures in the Leeufontein Quartzite Formation, the uppermost part of the Witkop Quartzite Formation and the lowermost part of the Koedoesfontein Quartzite Formation (Fig 2).

These aspects were investigated by the compilation of three detailed sedimentological profiles, recorded along traverses perpendicular to the tectonic strike, at outcrops on the farms Witkop 475 and Leeufontein 485 (Fig. 3). On the former farm the entire Leeufontein Quartzite Formation is exposed in a single outcrop, as well as the uppermost and lowermost portions of the Witkop Quartzite and Koedoesfontein Quartzite Formations, respectively.

TABLE 1: Sequence of *clockwise stereographic rotations applied to palaeocurrent data to correct for tectonic tilt.

	EASTERN SECTOR		WESTERN SECTOR		
Sequence of rotations	Axis of rotation	Angle of rotation	Axis of rotation	Angle of rotation	EFFECT
a	017°	20°	---	---	Re-alignment of eastern sector
b	317°	2°	317°	2°	Axial plane of Structure rendered vertical
c	046°	51°	046°	51°	Axis of Structure rendered vertical
d	**Resultant strike	***Resultant dip angle	**Resultant strike	***Resultant dip angle	Strata rendered horizontal

* Clockwise as viewed along the rotation axes specified in columns 2 and 4.

** Strike of beds after rotations a - c have been carried out

***Rotation angle required to restore bedding to horizontal, with normal stratigraphic polarity

This situation made it possible to compile a continuous profile for the mentioned succession (Fig. 4 - data in Appendices V, VII, IX). On the farm Leeufontein 485 no complete exposure within a single outcrop was available for the Leeufontein Quartzite Formation. Sedimentological data were therefore recorded along two traverses, spaced about 200 m apart, to compile two profiles. The first of these (Fig. 5 - data in Appendices VI, VIII) shows the beds of the uppermost portion of the Witkop Quartzite Formation and of the lower 65 m of the Leeufontein Quartzite Formation. The second profile (Fig. 6) overlaps the first by about 8 m and includes the beds of the upper 20 m of the latter Formation and of the lowermost 12 m of the overlying Koedoesfontein Quartzite Formation.

For the demarcation of sedimentary units within the sedimentological profiles, maximum grain size, dominant internal structure, and textural maturity were chosen as distinguishing parameters. Mean maximum grain size was estimated by comparison with a scale of diagrammatic grain-size patterns. Palaeocurrent directions were recorded throughout the profiles using trough cross-bed axes, planar cross-bed foresets and the orientation of lee faces of current ripples as indicators. Tectonic tilting was stereographically corrected, as outlined before. The occurrence of deformational sedimentary structures was also recorded. Where possible, the orientations of fold axes of recumbent foresets were determined by measuring a number of dip angles and dip directions on a folded foreset. These measurements were then used to determine the present orientations of the fold axes (Ramsay and Huber, 1987), which were thereafter corrected for tectonic dip.

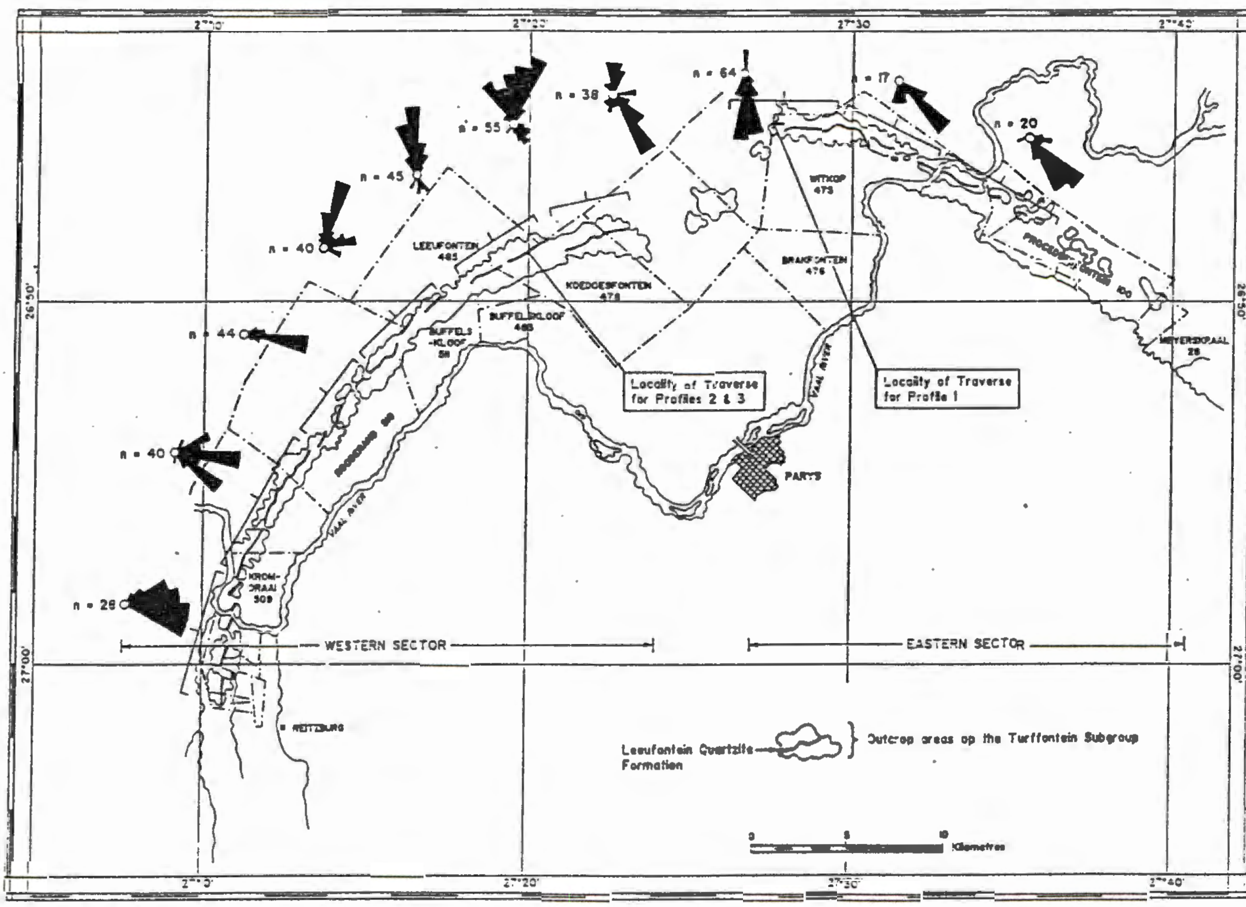

Figure 3: Map showing palaeocurrent distributions for the Leeufontein Quartzite Formation in the Vredefort Structure and localities mapped for the compilation of vertical profiles (Figs. 4, 5 and 6).

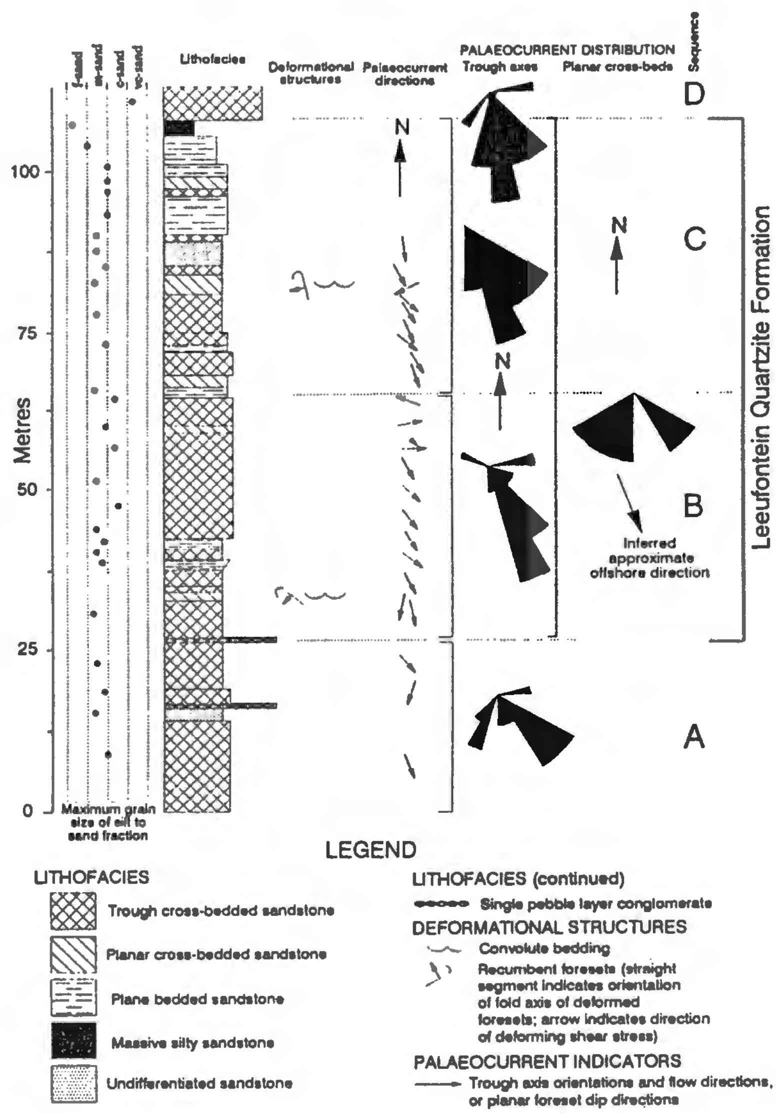

Figure 4: Sedimentological profile of the Leeufontein Quartzite Formation on the farm Witkop 475.

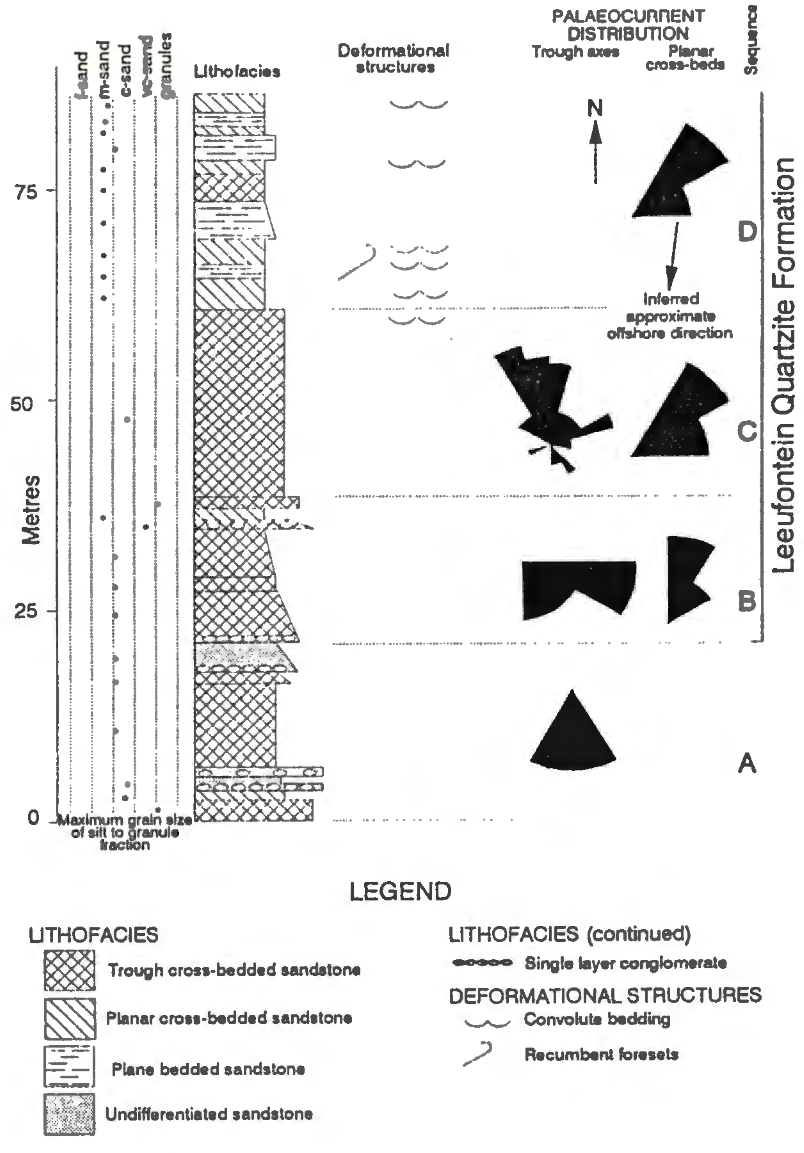

Figure 5: Sedimentological profile representing the lower part of the Leeufontein Quartzite Formation on the farm Leeufontein 485.

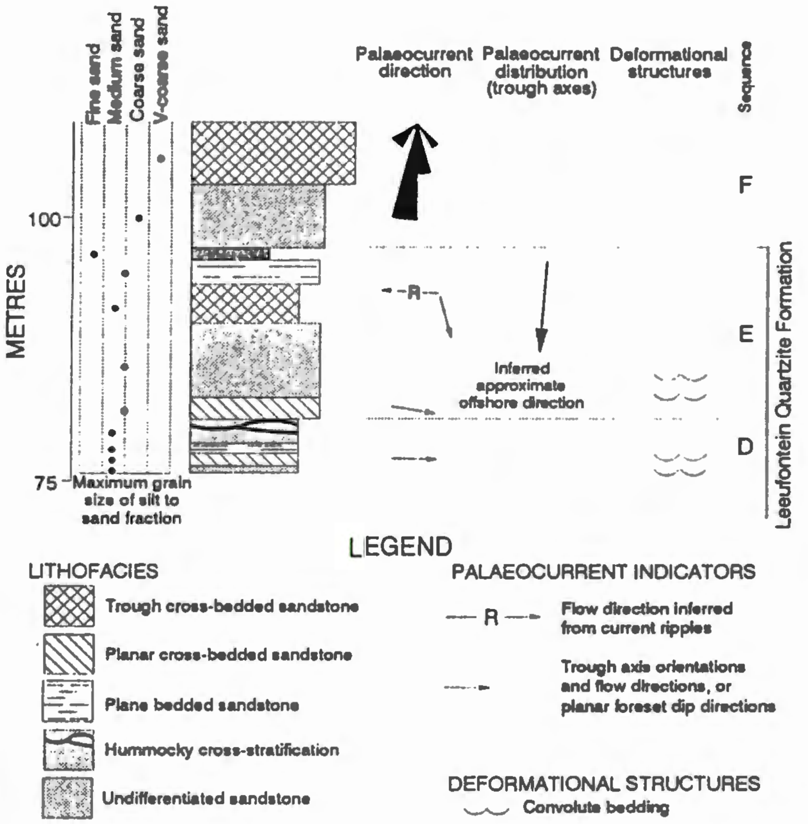

Figure 6: Sedimentological profile showing the upper portion of the Leeufontein Quartzite Formation on the farm Leeufontein 485.

(c) Preliminary petrographic investigation of the Leeufontein Quartzite- the uppermost part of the Witkop Quartzite- and the lowermost part of the Koedoesfontein Quartzite Formations.

Thin sections, representing three beds of the Leeufontein Quartzite Formation and one each of the Witkop Quartzite and the Koedoesfontein Quartzite Formations, were examined in order to obtain some quantitative comparison of the textural maturity of the arenites, as well as their grain-size parameters and grain roundness. Standard point-counting techniques, described by Galehouse (1971), were applied to the thin-sections, counting 300 points per bed. For the determination of grain-size parameters the apparent long dimensions of grains were measured, adopting a lower size limit of 30 μm to separate framework grains from matrix, as suggested by Pettijohn et al. (1973). From the grain-size measurements, statistics were calculated, using "Statgraphics" software (Table 2).

TABLE 2: Textural composition and grain-size parameters of beds of the Witkop Quartzite, Leeufontein Quartzite and Koedoesfontein Quartzite Formations

		Composition %			Grain size parameters (phi units)		
		Framework		Matrix			
Unit	Formation	Quartz	Chert		Mean	Sorting	Skewness
5	Koedoesfontein Quartzite	74,6	0,6	24,8	1,35	0,96	-0,08
4	Leeufontein Quartzite	50,8	-	49,2	2,35	0,64	-0,04
3	Leeufontein Quartzite	97,7	-	2,3	1,75	0,88	-0,15
2	Leeufontein Quartzite	95,7	0,6	3,7	1,83	0,63	0,75
1	Witkop Quartzite	81,2	1,0	17,8	1,34	0,97	0,18

RESULTS AND DESCRIPTIONS

Lateral variation of palaeocurrent directions and distributions of the Leeufontein Quartzite Formation (Fig. 3).

These aspects are illustrated on figure 3, which shows predominantly bi- and polymodal palaeocurrent distributions in the central parts of the arcuate series of outcrops (from the farm Leeufontein 485 to Witkop 475). In some instances the distributions of this area are bipolar (Selley, 1982, p. 244). Within this central region the orientations of palaeocurrent modes vary considerably, even within segments of constant tectonic strike.

Unimodal palaeocurrent distributions are dominant in the western sector of the study area, with modes towards the east. The eastern parts of the study area, too, are characterised by unimodal palaeocurrent distributions. In this region, mean directions are generally towards the southeast.

Succession on the farm Witkop 475 (Fig. 4).

The upper stratigraphic boundary of the Leeufontein Quartzite Formation in this profile is exceptionally clear, demarcated by an abrupt grain-size increase and a decrease in textural maturity. In contrast, its lower contact is gradational over a number of metres.

The basal 26 m of the recorded profile (Sequence A) (Fig. 4) is included in the Witkop Quartzite Formation, for reasons submitted later in this discussion. This part is dominated by brownish-grey, trough-cross-bedded arenites, pebbly in places. Some of these arenite units gradationally overlie single layers of pebbles (Facies Gl of Buck and Minter, 1985; facies Glag of Krapez, 1985), thus constituting fining-upward sedimentary cycles (Fig. 4). Maximum apparent long pebble dimensions are about 30 mm. Petrographic investigation of a single bed within this part of the profile showed that this is a medium-grained (Wentworth scale) quartz wacke with a textural maturity approaching that of a quartz arenite (Table 2), though the framework grains are poorly rounded (Fig. 7). The palaeocurrent distribution (Fig. 4), based upon eleven readings of trough cross-bed axes, has a directional variance (Miall, 1974; Long, 1978) of 1165 and shows a dominant mode towards the southeast.

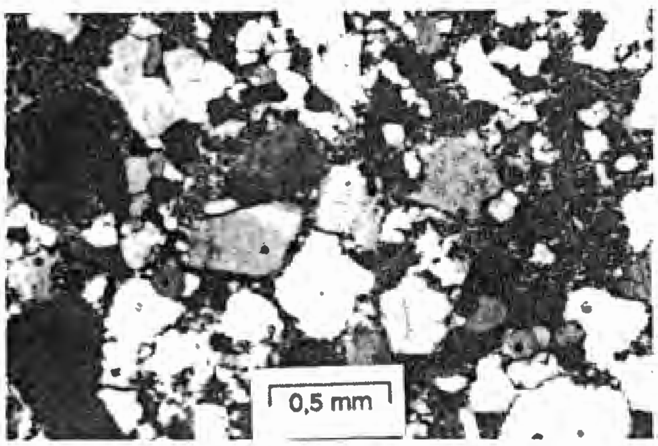

Figure 7: Photomicrograph, crossed nicols, of a quartz wacke of the Witkop Quartzite Formation. Note the poor roundness and sorting of the framework grains.

Sequence B of the profile is also dominated by light grey to white, trough cross-bedded arenites with grain sizes similar to those of Sequence A. The arenites, however, are visibly more mature and pebbles are absent. Transverse dimensions of the troughs vary from about 25 cm to 100 cm and the depth to width ratios from 0,10 to 0,13. Two thin, but conspicuous plane-bedded units (Facies Sh of Miall, 1977), occur within the lower half of this unit. Although subordinate in terms of thickness and frequency, planar cross-bedded sandstone (Facies Sp of Miall, 1977), with set thicknesses up to 50 cm, is not uncommon. The corrected foreset dip angles of these units vary from 21° to 32°. The palaeocurrent distribution for cross-bed trough axes is weakly polymodal, and the dominant mode is also towards the southeast. Convolute bedding (Fig. 8) and recumbent foresets (Fig. 9) are common deformational structures, occurring typically in mutual association, and are especially characteristic of planar cross-bedded sets. For two such sets it was possible to determine the orientations of the axes of the folded foresets at the top of the units and infer the directions of the deforming shear stresses. Figure 4 shows that the corrected fold axes are oriented roughly perpendicular to the dip directions of undeformed foresets near the bases of the units, while the inferred directions of the deforming shear stresses are approximately parallel to the dip directions of undeformed foresets.

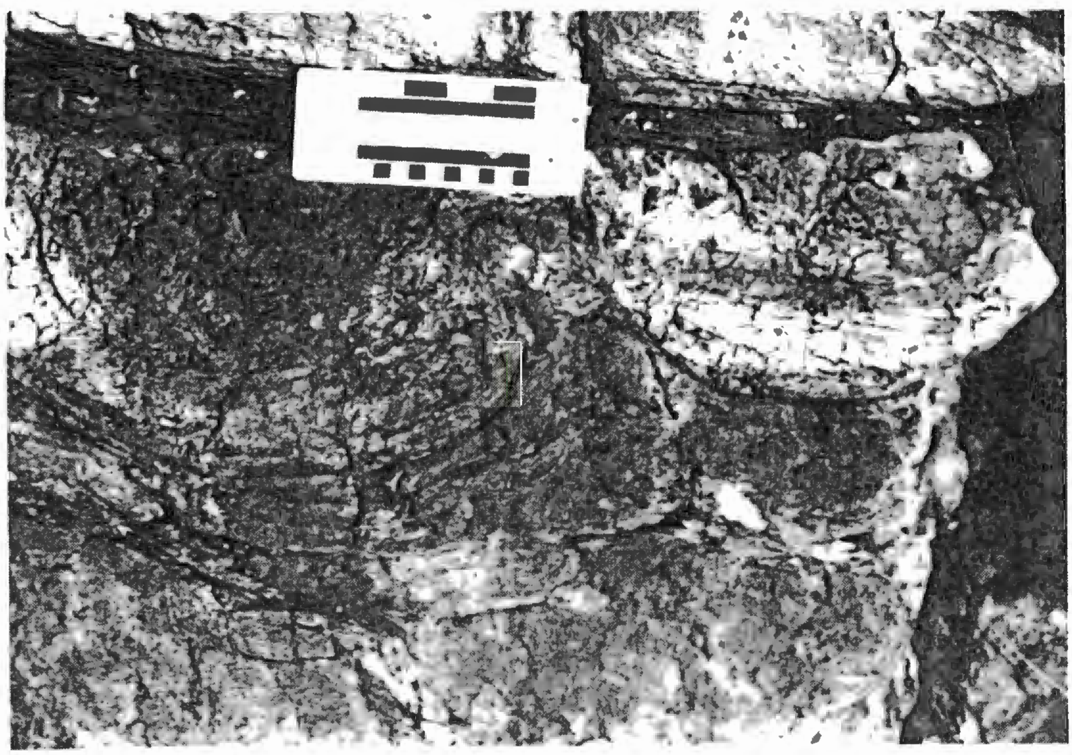

Figure 8: Example of convolute bedding in the Leeufontein Quartzite Formation. The photograph is orientated to show correct stratigraphic polarity

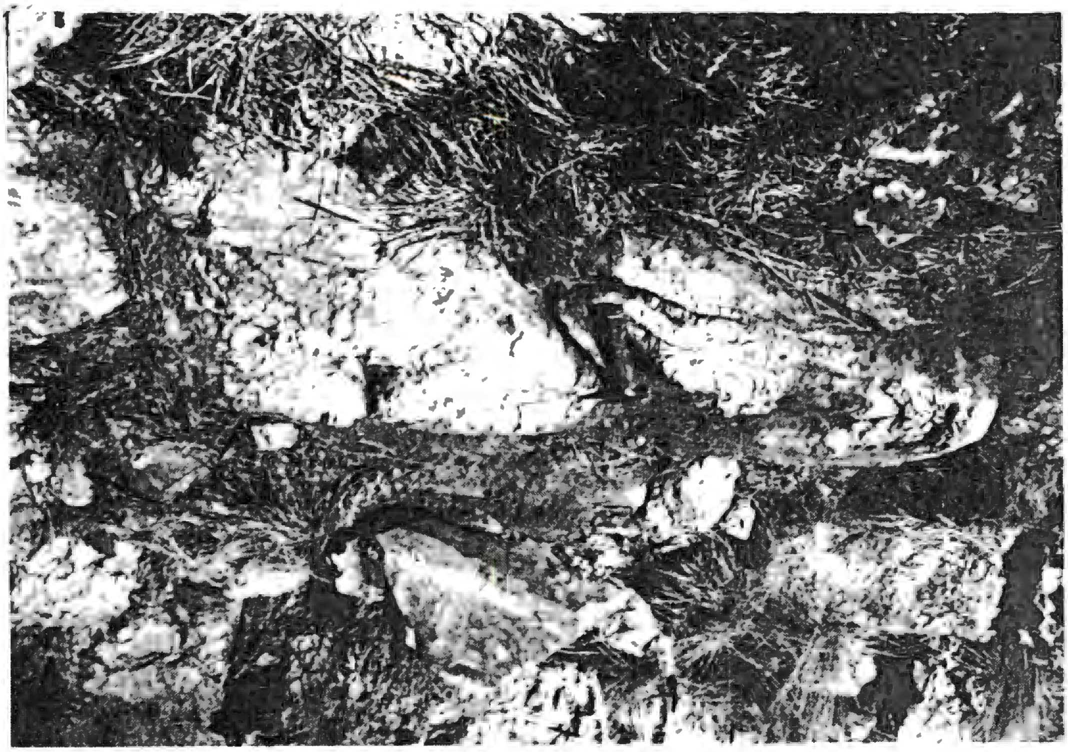

Figure 9: A: Photograph of recumbent foresets in the Leeufontein Quartzite. The photograph is orientated to show correct stratigraphic polarity Formation.

B: Diagrammatic representation of the salient features of the structure.

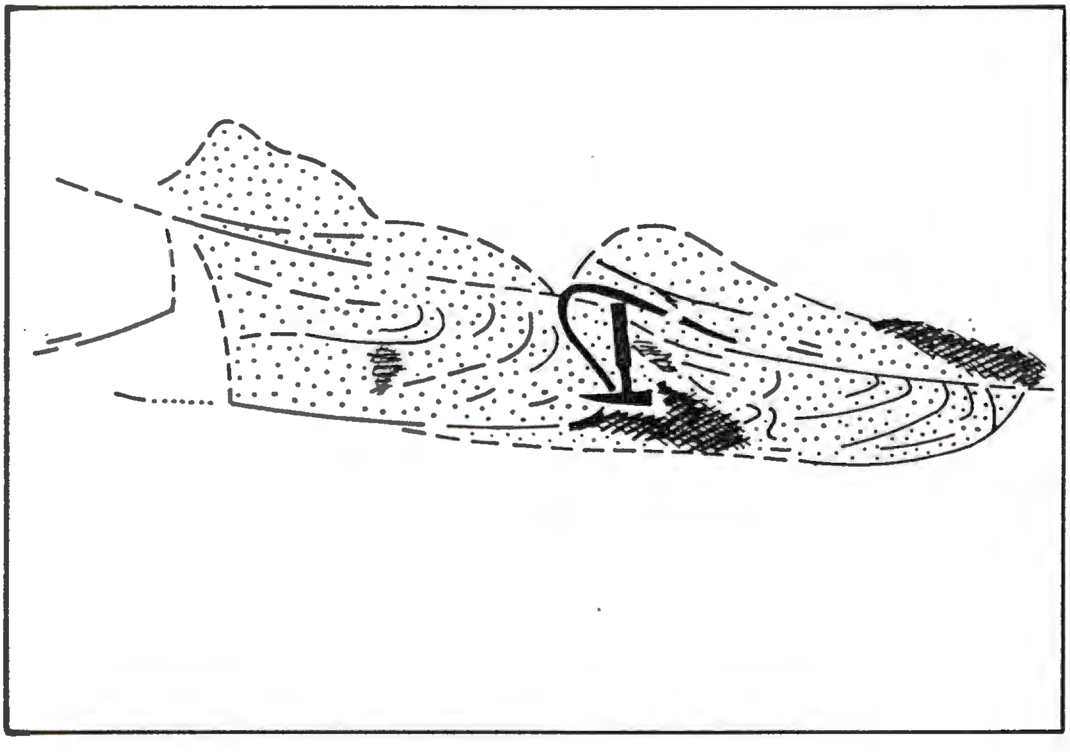

Sequence C is characterised by a light grey colour, similar to that of Sequence B, but the arenites have a somewhat smaller general grain-size. A smaller proportion of trough cross-bedded units occur in this sequence, but the dimensions and geometries of the cross-bed troughs are similar to those of Sequence B. The palaeocurrent distribution of cross-bed axes is unimodal towards the southeast (Fig. 4). Trough cross-bedding becomes progressively less common towards the top, giving way to plane bedded units and solitary planar cross-bedded sets with thicknesses up to 100 cm. Corrected foreset dip angles of the latter are about 25°. Plane bed units dominate near the top, where they are particularly well-laminated, consisting of supermature quartz arenite, showing one to two centimetre thick laminae (Fig. 10). The sequence is capped by a reddish, fine-grained, immature sandstone, apparently without internal structure.

A petrographic investigation of the sandstone at the top of Sequence C showed that the matrix content is almost 50% (Unit 4, Table 2). This is in striking contrast with the remaining beds of the sequence, two of which proved to contain only 3,7% and 2,3% matrix (Table 2). Despite the secondary effects of pressure solution, roundness of the framework grains of these two beds is noticeably higher than that of the remaining beds listed in Table 2 (Fig. 11). Soft sediment deformational structures, similar to those of Sequence B, seem to occur preferentially in planar cross-bed sets. The orientation of the axis of folded top foresets of one such set was again found to be normal to the dip direction of undeformed foresets, lower down in the set, with the direction of the inferred deforming shear stress approximately the same as that of the foreset dip direction (Fig. 4).

Figure 10: Parallel lamination, thought to have formed in a swash zone, in the upper part of the steeply-dipping Leeufontein Quartzite Formation on the farm Witkop 475. The stratigraphic top of the unit is on the right-hand side. (Centimetre and inch divisions on the scale-chart)

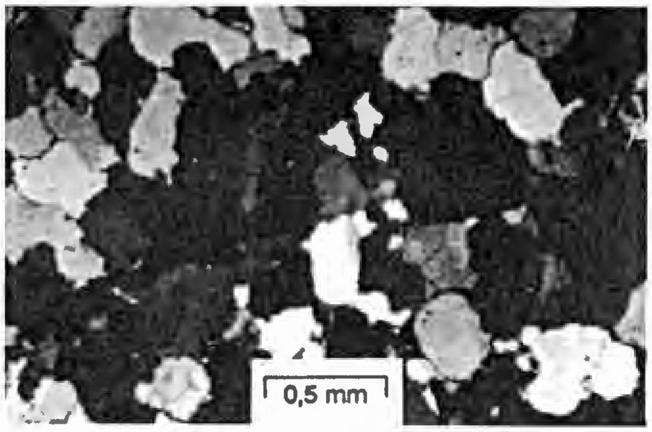

Figure 11: Photomicrograph, crossed nicols, of a very mature quartz arenite of the Leeufontein Quartzite Formation. Note the high roundness and good sorting of the framework grains, relative to those of the quartz wacke shown on figure 7.

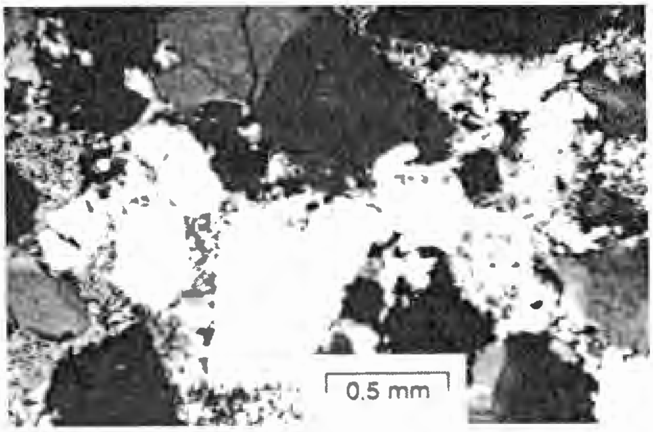

Figure 12: Photomicrograph, crossed nicols, of a quartz wacke of the Koedoesfontein Quartzite Formation. Note the poor roundness and sorting of the framework grains, and the high proportion of sericite matrix.

Sequence D (Fig. 4) probably belongs to the Koedoesfontein Quartzite Formation and is a homogeneous reddish-brown, coarse-grained, mainly trough cross-bedded succession of quartz wackes. The cross-bed troughs are, in contrast to those of Sequences B and C, up to several metres wide and have noticeably smaller depth to width ratios. Petrographic examination of one of the beds indicated that this is a quartz wacke with a matrix content of about 25% (Unit 5, Table 2). Roundness of the framework grains is visibly lower than that of the quartz arenites of Sequences B and C (Fig. 12). The palaeocurrent distribution for cross-bed trough axes shows a dominant mode towards the south and yielded a directional variance of 1153. No deformational sedimentary structures were found in this Sequence.

Succession on the farm Leeufontein 485

The basal 20m of the succession (Sequence A, fig. 5) is considered part of the Witkop Quartzite Formation. It comprises fining-upward sedimentary cycles consisting of single pebble layer conglomerates that are gradationally overlain by coarse-grained, moderately mature, trough cross-bedded quartz wackes. The conglomerates contain mainly quartz pebbles with apparent long dimensions up to 80mm. The palaeocurrent distribution, based upon a limited number of trough axis readings, shows a mode towards the south.

Sequence B (Fig. 5) is dominated by light grey, medium to coarse-grained, trough cross-bedded sandstones. These, however, are conspicuously texturally more mature than the sandstones of Sequence A. Single pebble layer conglomerates occur less frequently than in Sequence A. The palaeocurrent distribution for cross-bed trough axes reveals a dominant mode towards the east, while that of planar cross-bed foresets is towards the north-northeast.

The dominant lithofacies of Sequence C (Fig. 5) is light grey, mature, medium- to coarse-grained, trough cross-bedded quartz arenite. The general scale and geometry of the troughs are similar to those of Sequences B and C of figure 4. Solitary planar cross-bedded quartz arenite sets, with typical set thicknesses of less than 50 cm, are subordinate in terms of thickness and frequency. Corrected foreset dip angles of these sets vary from 21° to 33°. The palaeocurrent distribution for cross-bed trough axes is polymodal, with a dominant mode towards the north-northwest. The distribution for planar cross-bed foresets, however, shows a dominant mode towards the northeast. Convolute bedding occurs towards the top of the Sequence.

The upward transition to Sequence D (Fig. 5) is accompanied by an abrupt decrease in general grain-size, which remains fairly even throughout the Sequence above the transition. Texturally, the arenites remain remarkably mature throughout. Sequence D is characterised by parallel, often wavy, lamination and subordinate planar cross-bedded units with set thicknesses up to one metre. Corrected foreset dip angles of such sets vary from 16° to 35°. A single occurrence of undoubted hummocky cross-stratification was found at the top of this Sequence (Fig. 13). This structure bears a remarkable resemblance to that illustrated by Walker (1979, his Fig. 13) for the Fernie Formation, Alberta. As can be expected, suitable palaeocurrent indicators are rare within Sequence D. However, the distribution for planar cross-bed foresets reveals a mode towards the northeast. Deformational sedimentary structures, convolute bedding in particular, abound in Sequence D (Figs. 5 and 6). In addition, some large-scale sand volcanoes (Fig. 14) were found in the area where the second profile (Fig. 6) was recorded. Recumbent foresets are occasionally found at the tops of planar cross-bed sets.

Figure 13: A: Hummocky cross-stratification in the upper portion of the Leeufontein Quartzite Formation on the farm Leeufontein 485. The photograph is orientated to show correct stratigraphic polarity.

B: Diagrammatic representation of the salient features of the structure.

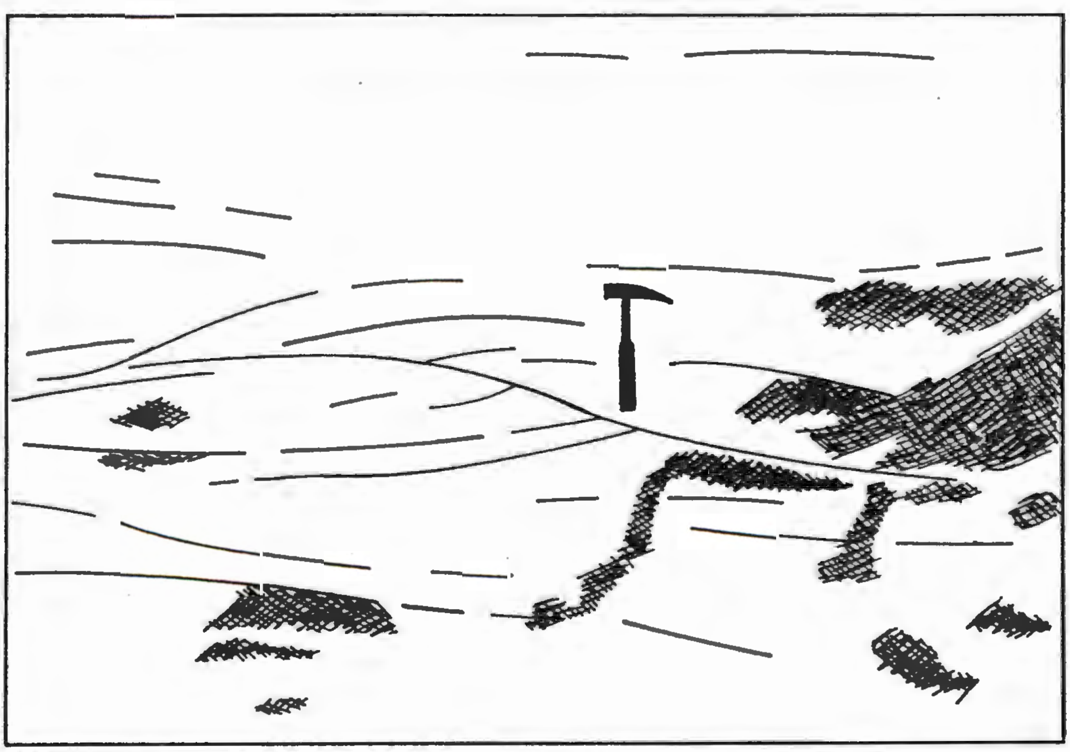

Figure 14: Example of a sand volcano in the Leeufontein Quartzite Formation. The photograph is orientated to show correct stratigraphic polarity.

The beds of Sequence E (Fig. 6) are poorly exposed, but an upward transition into this Sequence is indicated by an increase in general grain-size. Textural maturity is similar to that of Sequence D. A solitary planar cross-bed, which indicates an easterly palaeocurrent direction, occurs at the base of the Sequence. At the top, an arenaceous succession consisting of a trough cross-bedded and a plane-bedded unit is overlain by a reddish, fine-grained, immature sandstone. The latter is thought to be the correlative of the bed that occurs at the top of Sequence C on figure 4. Current ripples, indicating a west-southwesterly flow direction, occur near the top of the Sequence. Convolute bedding appears to be confined to the basal parts.

The lowermost 8 m of Sequence F is also poorly exposed, but nevertheless reveals a general upward increase in grain-size, accompanied by a decrease in textural maturity. The overlying beds comprise very coarse-grained, trough cross-bedded quartz wackes, with occasional small scattered pebbles. The palaeocurrent distribution of trough axes shows a mode towards the south-southwest and has a directional variance of 586. No deformational sedimentary structures were found. This Sequence is considered part of the Koėdoesfontein Quartzite Formation.

INTERPRETATION AND DISCUSSION

General sedimentological and palaeogeographical setting

The Leeufontein Quartzite Formation exhibits a number of characteristics that are typical of coastal depositional environments. The most significant of these traits are:

(a) poly- and bimodal palaeocurrent distributions (Davis, 1985);
(b) great textural maturity of the sandstones (Pettijohn et al., 1973);
(c) well-rounded sandstone framework grains (Pettijohn et al., 1973);
(d) the occurrence of typical shallow marine sedimentary structures such as hummocky cross-stratification (Walker, 1979) and wavy parallel lamination (Clifton et al., 1988).

Among the types of shoreline deposits, described by various authors (Davis, 1985b), only three bear sufficient resemblance to the Leeufontein Quartzite Formation to justify comparison. These are the deposits of (i) tidal inlets, (ii) estuaries and (iii) beach and nearshore environments. Of these, the first two are considered unlikely analogies for the Leeufontein Quartzite Formation, because of the complete lack of fine-grained units in the latter. Such mudstone/siltstone beds and laminae are characteristic of the profiles of estuaries and tidal inlets (Elliott, 1981; Boothroyd, 1985), occurring as either discrete beds or in flaser/lenticular bedding. Also, estuarine and tidal inlet sands generally do not exhibit the high degree of textural maturity that characterises modern beach and nearshore sands (Pettijohn et al., 1973) and the sandstones of the Leeufontein Quartzite Formation.

The Leeufontein Quartzite Formation is therefore thought to represent deposition in a littoral environment, probably the beach and nearshore areas. An interpretation, in terms of this proposed depositional environment, of various parts of the recorded vertical profiles, is submitted later in this discussion.

The underlying Witkop Quartzite and Koedoesfontein Quartzite Formations have not been studied in detail, except for their uppermost and lowermost beds, which are included in the recorded vertical profiles (Figs. 4, 5 and 6). These beds, however, are considered typical of their respective Formations and reveal several characteristics that are commonly associated with the fluvial depositional environment:

(a) repetitive fining-upward conglomerate-sandstone sedimentary cycles (Ethridge and Westcott, 1984; Nemec and Steel, 1984);

(b) textural immaturity of the sandstones (Andrews-Speed, 1986; Pettijohn et al., 1973);

(c) unidirectional palaeocurrents (Visher, 1972; Selley, 1982; Long, 1978, Pettijohn et al., 1973);

(d) low directional variances (Miall, 1974; Long, 1978);

(e) the dominance of large- and medium-scale trough and planar cross-beds (Long, 1978);

(f) poor roundness of sandstone framework grains (Pettijohn et al., 1973).

The Witkop Quartzite and Koedoesfontein Quartzite Formations are therefore thought to have been deposited in braided stream fluvial environments.

The hypothesis that the Leeufontein Quartzite Formation, which is most probably shallow marine in origin, is underlain and overlain by fluvial deposits, necessarily implies two opposing events during deposition of the Turffontein Subgroup of the Vredefort Area: an initial transgression, followed by a progradation. Applying Walther's Law, vertical profiles of the Leeufontein Quartzite Formation should theoretically contain both transgressive and progradational deposits. However, since transgressive sequences have a low preservation potential (Davis, 1985), the Leeufontein Quartzite Formation may be dominated by lithofacies deposited during the proposed progradation.

An important datum in the interpretation of ancient beach and nearshore lithofacies is the approximate offshore direction, relative to the shoreline. In the case of the Leeufontein Quartzite Formation, this direction can be inferred with reasonable confidence, because of the availability of sufficient palaeocurrent data for the Central Rand Group in the Klerksdorp and Carletonville goldfields, situated to the northwest and west of the study area. Minter and Loen (1991) have shown that, within these goldfields, the palaeocurrent distributions for the fluvial gold placers, located at various stratigraphic positions within the Central Rand Group, are unimodal, with modes towards the southeast to south. These modal directions are in agreement with those recorded in the fluvial Witkop and Koedoesfontein Formations during this study. Applying these data to the Leeufontein Quartzite Formation, an offshore direction towards the southeast to south is inferred (Figs. 4, 5 and 6).

Interpretation of the vertical profiles

A problem in the interpretation of the lithofacies and lithofacies associations of the Leeufontein Quartzite Formation is that of separating progradational and transgressive sequences, if both were preserved. A potentially useful tool to solve this problem, is the seaward decrease in grain-size commonly found within modern beach and nearshore environments (Davis, 1985; Kraft and Chrzastowdki, 1985). Applying this axiom to vertical profiles of the proposed transgressive-progradational succession of the Leeufontein Quartzite Formation, a transgressive sequence, if present, should be indicated by an upward decrease in grain-size and the progradational deposits by an upward grain-size increase.

Because of the complexity of the beach and nearshore depositional environment and because of its variability, interpretation of individual lithofacies of ancient shallow marine deposits is largely speculative. For this reason, interpretations of lithofacies will be confined mainly to those for which palaeoenvironments can be inferred confidently.

Profile for the succession on the farm Witkop 475 (Fig. 4)

Based upon the palaeocurrent modes of the underlying and overlying fluvial Witkop and Koedoesfontein Formations, the approximate offshore direction for this profile is roughly southeast.

In this profile, the Leeufontein Quartzite Formation does not exhibit an unambiguous upward grain-size increase or decrease, although grain-size appears to be somewhat finer at the base. The entire sequence is therefore thought to have been deposited during the proposed progradation. The bottom unit of the progradational sequence would therefore represent the most seaward sub-environment and the thin basal conglomerate probably demarcates the transgressive-regressive unconformity. The fact that sandstone, rather than silt/mudstone, overlies this unconformity, suggests that this sandstone was deposited no farther seawards than the nearshore-offshore boundary (Hunter et al., 1979; Clifton et al., 1988). The entire preserved sequence therefore probably belongs to one or more of the outer rough, outer planar, inner rough and inner planar facies of Clifton et al. (1971).

The plane-bedded units near the top of the sequence (Figs. 4 and 10) almost certainly represent the inner planar facies of the swash zone, because of the nature and scale of their stratification and because of their stratigraphic position. The development of such beach lamination is to a large extent controlled by the strength (volume and velocity) of the back-wash (Clifton, 1969). Among the factors that control the volume of back-washed water, is the porosity of the beach sand, which determines the degree of percolation, and therefore the volume of water lost into the sand (Davis, 1985). Porosity, in turn, is proportional to grain-size. Since the plane beds in question are medium-grained sandstones, they probably had low porosities shortly after deposition, which consequently lead to low water losses during back-wash and therefore strong back-wash currents. The fine grain-size of these plane beds, therefore, is probably the main reason for their relatively large thickness and consequent good preservation.

The origin of the additional, thinner plane beds towards the base and middle of the profile is uncertain, but some may represent the outer planar facies of Clifton et al. (1971).

The large thickness of predominantly seaward-dipping trough cross-beds of Sequence B (Fig. 4) is problematic to interpret. Such cosets may form in the inner rough facies as a result of infilling of elongated, seaward-migrating scour hollows (Clifton et al., 1971). Seaward-dipping trough cross-beds are also produced in rip currents (Hunter et al., 1979). It is doubted, however, if thicknesses in excess of 30 m of offshore-directed trough cross-beds can be produced by the mentioned processes only.

Considering its position within the vertical profile and its lithology, the fine-grained, immature quartz wacke at the top of Sequence C possibly represents deposition from suspension in the backshore sub-environment, which was probably flooded only during spring tides. Clifton et al. (1988) report similar "clayey sediment" in the backshore facies of the Merced Formation, San Franscisco.

Convolute bedding, such as that found at Witkop 475, may occur in a wide range of environmental settings (Collinson and Thompson, 1982; Selley, 1982) and according to these authors, indicates rapid deposition. The fact that the directions of the inferred shear stresses responsible for the overturning of planar cross-bed foresets are in the same directions as the dips of undeformed ones, suggests that these shear stresses have probably been the result of drag exerted by currents which, in this case flowed in the same direction as those from which the cross-bed set was deposited. This mode of origin of recumbent foresets has been proposed by Selley (1982) and Reineck and Singh (1980).

As mentioned before, authors on sedimentary structures are of the opinion that convolute bedding and recumbent foresets may occur in a variety of depositional environments. These structures, however, seem to be more abundant in texturally-mature sandstones (quartz arenites) of interpreted shoreline origins. Recently-reported examples of soft sediment deformation of such quartz arenites are the Upper Quartzite Member of the Hospital Hill Subgroup, Vredefort area (Mayer and Albat, 1988), the Cleremont Formation of the Waterberg Group (Callaghan et al., 1991), the Mozaan Group, Pongola Sequence (Beukes and Cairncross, 1991) and the Nigel placer, Johannesburg Subgroup (Karpeta et al., 1991).

Profiles on the farm Leeufontein 485 (Figs. 5 and 6)

The vertical profiles representing the Leeufontein Quartzite Formation at this locality are different, in a number of respects, from the Witkop 475 profile. Firstly, there appears to be a more conspicuous grouping of lithofacies. Secondly, grain-size variations within the profiles are more pronounced than those of figure 4 and, finally, palaeocurrent distributions are quite different.

Considering the palaeocurrent modes of the underlying and overlying fluvial Witkop and Koedoesfontein Formations, the approximate offshore direction is thought to have been south-southwest.

The Leeufontein Quartzite Formation, as depicted in the vertical profiles (Figs. 5 and 6), shows an initial upward decrease in grain-size, followed by an increase towards the top. Both transgressive and progradational deposits are therefore preserved at this locality. Applying the models developed by Davis (1985), Clifton et al. (1988) and Walker (1980), the hummocky cross-stratified unit shown on figure 6 represents the most seaward-situated subenvironment of all the lithofacies depicted on figures 5 and 6. The sequence underlying this unit therefore probably represents deposition during the proposed transgression, while the beds overlying it are considered progradational deposits.

The abrupt grain-size decrease at the base of Sequence D (Fig. 6) is typical of the vertical profiles of (longshore)-barred shoreline environments (Hunter et al., 1979). If a barred shoreline depositional environment is accepted, trough cross-beds of Sequences B and C that indicate flow normal to oblique to the inferred shoreline (Fig. 6) would probably represent deposition in longshore troughs, while offshore-directed ones may represent rip current deposits (Hunter et al., 1979). Onshore-orientated trough cross-beds within a barred shoreline environment, however, present an interpretational problem because of their paucity in the idealized vertical profile for this environment (Hunter et al., 1979). Planar cross-beds with foresets dipping steeply in the onshore direction may have been produced by landward-migrating ridge-runnel systems (Davis, 1985).

The fine-grained, predominantly plane-bedded units of Sequence D are similar to those described by Clifton et al. (1988) for their inner shelf and nearshore zones and are therefore thought to represent deposition in the nearshore-offshore (Hunter et al., 1979) transition zone.

Although the thin, plane-laminated unit near the top of the Formation (Fig. 6) lacks well-defined stratification, it may represent deposition in the swash zone. The fact that it is thin relative to the parallel-laminated unit occupying a similar stratigraphic position in the succession on the farm Witkop 475 (Fig. 4), is probably due to the coarse grain size of the former. This characteristic would have resulted in a porous beach, permitting rapid water percolation. As a consequence, back-wash currents were probably weak, thus precluding the formation of well-defined beach lamination. The thin, immature, fine-grained quartz wacke at the top of the Formation is thought to be the correlative of the lithologically-similar uppermost unit in the profile recorded on Witkop 475 (Fig. 4).

Preservation of transgressive and progradational shoreline deposits

As mentioned before, transgressive shoreline deposits have a low preservation potential, while their progradational counterparts are more likely to be preserved in the rock record. The presence and thickness of the lower, fining-upward part of the Formation on the farm Leeufontein 485 is therefore surprising and its final interpretation as a transgressive sequence was only reached after much deliberation and consideration of alternatives. A factor that should be considered, however, is the probable abundant sediment supply to pre-Devonian shorelines. Pre-Devonian rivers transported abundant bedload sediment, because of the lack of land vegetation (Schumm, 1968). Sediment supply to pre-Devonian shorelines was therefore greater than that laid down in post-Devonian times. If plentiful sediment supply was available during a eustatic sea level rise and/or subsidence of the depositional surface, the preservation of transgressive deposits during the Late Archaean seems a distinct possibility.

Possible cause(s) for the proposed transgression-progradation

Shifts in the position of a shoreline depend on a combination of three factors: (a) eustatic sea level change; (b) vertical movement of the land; (c) rate of sedimentation (Clifton et al., 1988). Since no detailed sea level curve is available for the Late Archaean, it is impossible to confidently separate the possible effect of eustatic sea level changes from the mentioned remaining factors.

The possibility of a more abundant sediment supply to pre-Devonian shorelines has been discussed. Although fluctuations in sediment supply undoubtedly occurred during this geological time period, it seems probable that sediment accumulation was greater, relative to post-Devonian times. It may therefore reasonably be assumed that sediment supply was not the major factor responsible for the proposed transgression.

In summary, it seems likely that vertical movement of the depositional surface and/or a eustatic sea level change was the dominant factor(s) causing the proposed transgression.

Implications for Witwatersrand stratigraphy and basin configuration

The recognition of the Leeufontein Quartzite Formation as a shallow marine deposit has an important implication for the configuration of the Witwatersrand basin during Central Rand times, namely the presence of a body of standing water of sufficient size to generate waves and related currents strong enough for the formation of typical marine facies.

Within the proposed palaeogeographical setting during deposition of the Leeufontein Quartzite Formation, the Formation separates two palaeoenvironments; a westerly to northerly-situated terrestrial region and an ocean, located in the south to east. An important implication of this hypothesis is the probable occurrence of additional marine facies, not present in outcrops of the Formation or in exposures farther to the west and north, in areas to the south and east of the Vredefort Structure. It has been suggested that no lithofacies of the Leeufontein Quartzite Formation represents a shoreline sub-environment that had been located farther offshore than the outer nearshore. It follows, however, that offshore (shelf) facies, probably siltstone/mudstone (Kraft and Chrzastowski, 1985), were most likely deposited towards the south or southeast of the Vredefort Structure. Such fine-grained beds are favourite marker beds utilised in Witwatersrand stratigraphy, for example the Booysens Shale Formation. Therefore, the possible occurrence of additional mudstone units within the Turffontein Subgroup in the area south and east of the Vredefort Structure may constitute a major correlation problem, should stratigraphers not be aware of the facies change across the Leeufontein Quartzite Formation.

CONCLUSIONS

The Leeufontein Quartzite Formation displays several characteristics typical of beach and nearshore deposits. Since it occurs between two fluvial sequences, it is thought to have been deposited during successive transgressive and progradational events. Deposits representing both these contrasting processes appear to have been preserved. Eustatic sea level rise and subsidence of the depositional surface are the two most likely possible causes for the initial transgression.

An implication of the findings of this study is the probable extension, during Central Rand times, of the Witwatersrand basin into a southern ocean.
Recognition of the Formation as shallow marine in origin has a significant stratigraphic implication for the stratigraphy of the Central Rand Group, because of the likely occurrence of fine-grained shelf facies, not present in the Klerksdorp and Carletonville goldfields and their surroundings, in the area to the south of the Vredefort Structure.

ACKNOWLEDGEMENTS

The Leeufontein Quartzite Formation was initially recognised as a possible shoreline deposit during a mapping programme carried out for the Geological Survey of South Africa, with the aim of compiling a new geological map for the Vredefort area. We wish to thank the G.S.S.A. for permission to publish the recorded information. Thanks are due to land owners of the area for their kind permission to investigate the succession on their properties. We thank the following students for assistance in the field and laboratory: Derrick Coetzee, Gerda Davids, Deon du Plessis, Jan Myburgh and Fanie Yssel. Dr. T.R. Mason and an anonymous referee offered constructive critisism, which substantially improved the paper.

REFERENCES

Albat, H.M. (1988). Shatter cone/bedding interrelationships in the Vredefort Structure: evidence for meteorite impact? S. Afr. J. Geol., 91, 106 - 113.

Albat, H.M. & Mayer, J.J. (1989). Megascopic planar shock fractures in the Vredefort Structure: a potential time marker? Tectonophysics, 162, 265 - 276.

Andrews-Speed, C.P. (1986). Gold-bearing fluvial and associated tidal marine sediments of Proterozoic age in the Mporokoso Basin, Northern Zambia: Sedim. Geol., 48, 193 - 222.

Armstrong, G.C. (1968). Sedimentological control of gold mineralisation in the Kimberley Reef of the East Rand Goldfield. University of the Witwatersrand. Inform. Circ. Econ. Geol. Res. Unit, Univ. Witwatersrand, Johannesburg, 47, 24 pp.

Bailey, A.C., Law, J.D.M., Cadle, A.B., & Phillips, G.N. (1990). The Zandfontein Quartzite Formation, a marine deposit in the Central Rand Group, Witwatersrand Supergroup. S. Afr. J. Geol., 93 (1), 135 - 146.

Beukes, N.J., & Cairncross, B. (1991). A lithostratigraphic-sedimentological reference profile for the Late Archaean Mozaan Group, Pongola Sequence: application to sequence stratigraphy and correlation with the Witwatersrand Supergroup. S. Afr. J. Geol., 94 (1), 44 - 69.

Bisschoff, A.A. (1969). The petrology of the igneous and metamorphic rocks in the Vredefort Dome and adjoining parts of the Potchefstroom Syncline. D.Sc. thesis (unpubl.), Univ. Pretoria, 243 pp.

--- (1982). Thermal metamorphism in the Vredefort Dome. Trans. Geol. Soc. S. Afr., 85, 43 - 57.

Boothroyd, J.C. (1985). Tidal inlets and tidal deltas, 445 - 532. In: Davis, R.A. (Jr.), Ed., Coastal sedimentary environments. Springer-Verlag, New York, 420 pp

Buck, S.G. & Minter, W.E.L. (1985). Placer formation by fluvial degradation of an alluvial fan sequence: the Proterozoic Carbon Leader placer, Witwatersrand Supergroup, South Africa. J. Geol. Soc. London, 142, 1 - 8.

Callaghan, C.C., Eriksson, P.G., & Snyman, C.P. (1991). The sedimentology of the Waterberg Group in the Transvaal, South Africa: an overview. J. Afr. Earth Sci., 13 (1), 121 - 139.

Camden-Smith, P.M. (1980). The sedimentology, geochemistry and diagenesis of West Rand Group sediments in the Heidelberg area, Transvaal. M.Sc. thesis (unpubl.), Univ. Cape Town, 232 pp.

Clifton, H.E. (1969). Beach lamination - nature and origin. Mar. Geol., 7, 552 - 559.

----, Hunter, R.E., & Phillips, R.L. (1971). Depositional structures and processes in the non-barred high-energy nearshore. J. Sedim. Petrol., 41, 651 - 670.

----, Hunter, R.E., & Gardner J.V. (1988). Analysis of eustatic, tectonic and sedimentologic influences on transgressive and regressive cycles in the Upper Cenozoic Merced Formation, San Fransisco, California, 109 - 128. In: Kleinsphen, K.L., & Paola, C., Eds, New Perspectives in Basin Analysis. Springer-Verlag, New York, 453 pp.

Collinson, J.D., & Thompson, D.B. (1982). Sedimentary Structures. George Allen & Urwin, London, 194 pp.

Davis, R.A. (Jr.) (1985). Beach and Nearshore zone, 379 - 444. In: Davis, R.A. (Jr.), Ed., Coastal sedimentary environments. Springer-Verlag, New York, 420 pp.

--- (Ed.) (1985b) Coastal Sedimentary Environments. Springer-Verlag, New York, 420 pp.

De Villiers, A.B. (1989). The fossil landscape of the Vredefort Dome. Z. Geomorph., 33 (1), 93 - 101.

Elliott, T. (1981). Clastic Shorelines, 143 - 177. In: Reading, H.G., Ed., Sedimentary Environments and Facies. Blackwell Scientific Publ., London, 569 pp.

Ethridge, F.G., & Westcott, W.A. (1984). Tectonic setting, recognition and hydrocarbon reservoir potential of fan-delta deposits, 217 - 235. In: Koster E.H., & Steel, R.J. (Eds.), Sedimentology of gravels and conglomerates. Can. Soc. Petrol. Geol. Mem. 10. 441 pp.

Galehouse, J.S. (1971). Point counting, 385 - 407. In: Carver, R.E., Ed. Procedures in Sedimentary Geology. Wiley-Interscience, New York, 653 pp.

Hunter, R.E., Clifton, H.E., & Phillips, R.L. (1979). Depositional processes, sedimentary structures, and predicted vertical sequences in barred nearshore systems, Southern Oregon coast. J. Sedim. Petrol., 49 (3), 711 - 726.

Karpeta, W.P., Gendall, I.R., & King, J.A. (1991). Evidence for marine marginal and submarine canyon sedimentation in the Central Rand Group: implications for the geometry of the Witwatersrand basin. 16 - 17. Abstract. Conference on Precambrian Sedimentary Basins of Southern Africa, Pretoria. Terra Abstracts ISSN 0954 4887.

Kingsley, C.S. (1987). Facies changes from fluvial conglomerate to braided sandstone of the early Proterozoic Eldorado Formation, Welkom Goldfield, South Africa, 359 - 370. In: Ethridge, F.G., Flores, R.M. & Harvey, M.D. (Eds.), Recent Developments in Fluvial Sedimentology, Soc. Econ. Paleont. Miner. Spec. Publ. 39, 389 pp.

Kraft, J.C., & Chrzastowski, M.J. (1985). Coastal stratigraphic sequences, 625 - 663. In: Davis, R.A. (Jr.), Ed., Coastal sedimentary environments. Springer-Verlag, New York, 420 pp.

Krapez, B. (1985). The Ventersdorp Contact Placer: a gold-pyrite placer of stream and debris-flow origins from the Archaean Witwatersrand Basin of South Africa. Sedimentology, 32, p. 223 - 234.

Long, D.G.F. (1978). Proterozoic stream deposits: some problems of recognition and interpretation of ancient sandy fluvial systems, 313 - 341. In: Miall, A.D., Ed., Fluvial Sedimentology. Mem. Can. Soc. Petrol. Geol., 5. 859 pp.

Mayer, J.J., & Albat, H.M. (1989). The tectono-sedimentary setting of the area of the Vredefort Structure during deposition of the upper quartzite member of the Hospital Hill Subgroup. S. Afr. J. Geol., 91 (2), 239 - 247.

----, & Els, B.G. (1992, in press). The reconstruction of palaeocurrent dispersal patterns for Turffontein strata in the Vredefort Structure in relation to a tectonic model for the area S. Afr. J. Geol., 95.

Miall, A.D. (1974). Paleocurrent analysis of alluvial sediments: a discussion of directional variance and vector magnitude. Jour. Sediment. Petrol., 44 (4), 174 - 185.

Miall, A.D. (1977). A review of the braided-river depositional environment. Earth Sci. Rev., 13, 1 - 62.

Minter, W.E.L. & Loen, J.S. (1991). Palaeocurrent Dispersal Patterns of Witwatersrand Gold Placers. S. Afr. J. Geol., 94 (1), 70 - 85.

Nel, L.T. (1927). The geology of the around Vredefort - an explanation of the geological map. Spec. Publ. Geol. Surv. S. Afr, 6, 134 pp.

Nemec, W., & Steel, R.J. (1984). Alluvial and coastal conglomerates: their significant features and some comments on gravelly mass-flow deposits, 1 - 31. In: Koster E.H., & Steel, R.J. (Eds.), Sedimentology of gravels and conglomerates. Can. Soc. Petrol. Geol. Mem. 10. 441 pp.

Pettijohn, F.J., Potter, P.E., & Siever, R. (1973). Sand and Sandstone. Springer-Verlag, New York, 618 pp.

Potter, P.E., & Pettijohn, F.J. (1977). Paleocurrents and Basin Analysis. Springer-Verlag, New York, 296 pp.

Pretorius, D.A. (1986). The Witwatersrand Basin: surface and subsurface geology and structure. Map (1:500 000), Geol. Soc. S. Afr.

Ramsay, G., & Huber, M.I. (1987). The technique of modern structural geology. Volume 2: Folds and Fractures. Academic Press, London, 700 pp.

Reineck, H.E., & Singh I.B. (1980). Depositional Sedimentary Environments. Springer-Verlag, New York, 549 pp.

Schumm, S.A. (1968). Speculations concerning paleohydrological controls of terrestrial sedimentation. Geol. Soc. Am. Bull., 79, 1573 - 1588.

Selley, R.C. (1982). An introduction to Sedimentology. Academic Press, London. 408 pp.

Tucker, R.F., & Viljoen, R.P. (1986). The geology of the West Rand Goldfield, with special reference to the Southern Limb, 649 - 688. In: Anhaeusser, C.R. & Maske, S., Eds., Mineral Deposits of Southern Africa, I. Geol. Soc. S. Afr., Johannesburg. 1022 pp.

Tweedie, E.B. (1986). The Evander Goldfield, 705 - 730. In: Anhaeusser, C.R. & Maske, S., Eds., Mineral Deposits of Southern Africa, I. Geol. Soc. S. Afr., 1020 pp.

Visher, G.S. (1972). Physical characteristics of fluvial deposits. In: Rigby, J.K. & Hamblin, W.K., Eds., Recognition of ancient sedimentary environments. Soc. Econ. Paleont. Miner. Spec. Publ. 16, 84 - 97.

Vos, R.G., 1975, An alluvial plain and lacustrine model for the Precambrian Witwatersrand deposits of South Africa: J. Sedim. Petrol., 45 (2), 480 - 493.

Walker R.G. (1979). Facies Models 7: Shallow marine Sands, 75 - 89. In: Walker, R.G., Ed., Facies Models. Geoscience Canada, 211 pp

Watchorn, M.B. (1981). The stratigraphy and sedimentology of the West Rand basin in the Western Transvaal. Ph.D. thesis (unpubl.), Univ. Witwatersrand, Johannesburg, 154 pp.

Wheelock, G. (1987). The sedimentology and mineralisation of the Archaean Elsburg No. 5 Reef on Vaal Reefs West gold mine, Transvaal, South Africa. M.Sc. thesis (unpubl.), Univ. Cincinnati (Ohio, U.S.A.), 104 pp.

CHAPTER 6

MEGASCOPIC PLANAR SHOCK FRACTURES IN THE VREDEFORT STRUCTURE: A POTENTIAL TIME MARKER ?

Tectonophysics, 162 (1989) 265–276
Elsevier Science Publishers B.V., Amsterdam – Printed in The Netherlands

Megascopic planar shock fractures in the Vredefort Structure: a potential time marker?

H.M. ALBAT and J.J. MAYER

Department of Geology, Potchefstroom University for C.H.E., Potchefstroom 2520 (Republic of South Africa)

(Received May 19, 1988; revised version accepted August 25, 1988)

Abstract

Albat, H.M. and Mayer, J.J., 1989. Megascopic planar shock fractures in the Vredefort Structure: a potential time marker? *Tectonophysics*, 162: 265–276.

Megascopic planar shock response fractures (densely spaced s-surfaces), hitherto ignored in the Vredefort Structure by geoscientists, reveal a systematic and symmetrical geometric pattern in the Vredefort "collar" rocks. The s-surfaces, where occurring as a conjugate system, display an intimate geometrical relationship to the shatter cones suggesting a common origin for these features. The master cone is enveloped by two sets of s-surfaces and occupies the obtuse angle of the conjugate system in such a manner that its axis bisects the angle between these surfaces and is approximately perpendicular to their line of intersection. The angle between the two sets of s-surfaces and their respective angular relationships to the bedding vary little around the structure. This is concluded from structural data recorded at 41 study areas spaced at regular intervals around the circumference of the Vredefort Structure. A pre-overturning age for the s-surfaces is postulated from their geometrical relationship to the shatter cones and their low variance angular relationship to bedding. We suggest that the occurrence of these planar shock fractures provides a potential geological time marker.

Introduction

The Vredefort Structure in South Africa comprises a central basement core of Archaean granitoids, gneisses and greenstone remnants surrounded by a "collar" of sedimentary–metasedimentary and volcanic–metavolcanic rocks belonging to the Dominion Group, Witwatersrand Supergroup, Ventersdorp Supergroup and Transvaal Sequence (Fig. 1). The granite–gneiss of the basement has been uplifted by some 25–30 km (Nicolaysen, 1987) and the collar rocks are overturned over much of the exposed part of the structure (Nel, 1927). A thin cover of horizontal Karoo strata conceals the southern and southeastern sectors of the structure (Fig. 1). The presence of strongly magnetic strata towards the base of the Witwatersrand Supergroup has made it possible, however, to establish the geometry of the concealed portion of the collar (Weiss, 1949). The extreme southern outcrops of Witwatersrand strata are the right-way-up and this appears to apply for the entire covered southern sector of the Vredefort Structure as confirmed by exploration drilling. The reader, not familiar with the local geology, is referred to publications by Hall and Molengraaff (1925), Nel (1927), Bisschoff (1969, 1972a, 1972b, 1973, 1982) and Nicolaysen (1987).

The existing literature on the Vredefort Structure is voluminous and is characterised by controversial issues relating to the chronologic sequence of events and the mode of origin of this enigmatic cryptoexplosion structure. Some geoscientists involved in Vredefort research have reached consensus that the genesis of the Vredefort Structure was intimately connected with a

0040-1951/89/$03.50

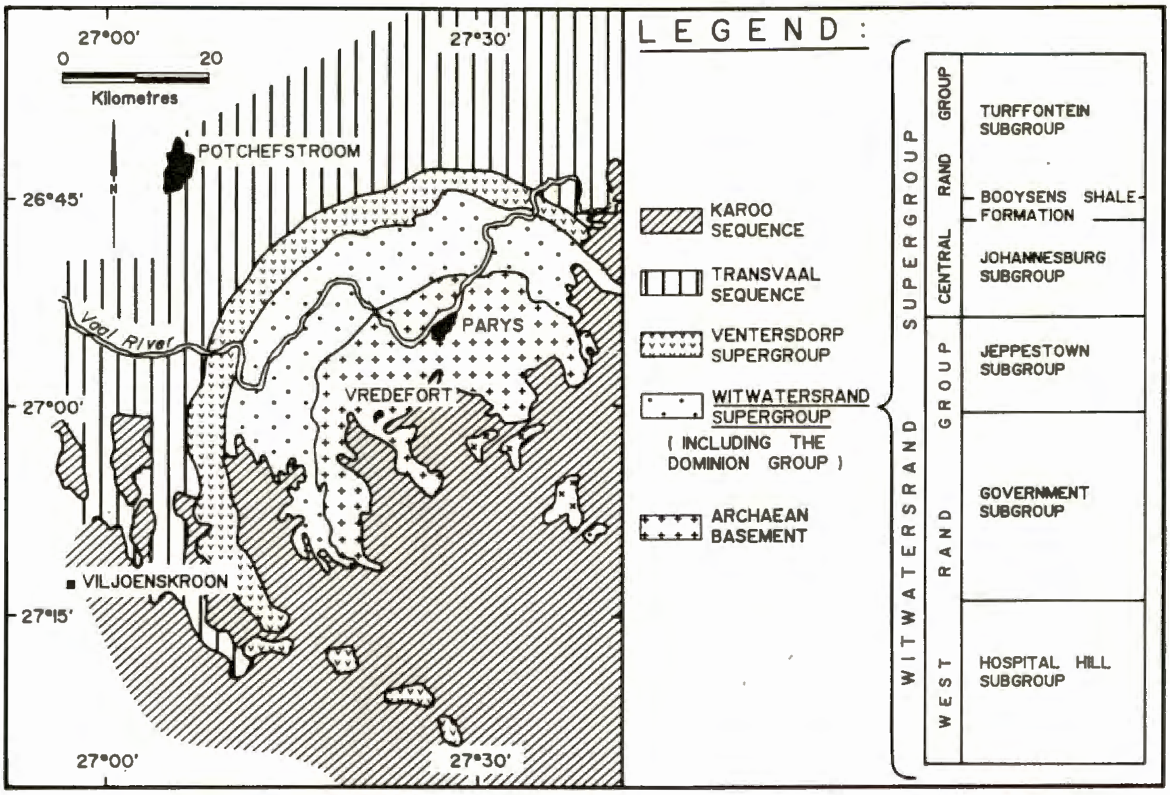

Fig. 1. Geological map of the Vredefort Structure, simplified after Bisschoff (1982).

catastrophic crater forming event accompanied by severe shock waves. The involvement of shock waves is inferred from the characteristic response features encountered. Amongst these are the shatter cones which are axially symmetric conical fracture surfaces radially striated from the apex (Dietz, 1959, 1961, 1963, 1968; Hargraves, 1961; Manton, 1962, 1965; Albat, 1988). Complete cones (Fig. 2) are extremely rare in the Vredefort Structure but partial cone segments are very common. It appears that the natural occurrence of shatter cones world-wide is confined to cryptoexplosion structures (Dietz, 1959; Milton, 1977). Experimental investigations (Shoemaker et al., 1961; Schneider and Wagner, 1976; Roddy and Davis, 1977) have revealed that shatter cones are a manifestation of the damage caused by the passage of shock waves through the rocks. It has been experimentally verified that the axes of the cones are arranged approximately normal to the advancing hemispherical shock front and that the cone apices point into the direction of the energy source (Milton, 1977; Roddy and Davis, 1977). Manton (1962, 1965) established that the apices of the shatter cones point towards the centre of the Vredefort Structure and upwards, focusing in a point proximal to the reconstructed paleosurface when the collar strata are restored to their original horizontal position. Such a symmetry is consistent with a superficial shock source as postulated by the impact hypothesis (Boon and Albritton, 1937, 1938;

Fig. 2. Photograph showing a complete shatter cone in metabasites from the Vredefort Structure.

Fig. 3. Traces of densely spaced s-surfaces in quartzite of the Hospital Hill Subgroup.

Daly, 1947; Dietz, 1961, 1963, 1968; Hargraves, 1961; Manton, 1962, 1965). Opponents to this hypothesis (Lilly, 1981, Simpson, 1981; Nicolaysen and Reimold, 1985), however, have questioned the presumption, crucial to the impact hypothesis, that shatter cone formation predated the overturning of the collar rocks. This controversy is addressed by Albat (1988) who furnishes additional evidence in support of the pre-overturning age of the shatter cones in the Vredefort Structure.

Apart from the shatter cones a variety of shock metamorphic microstructures have been described in quartz grains of the Witwatersrand quartzites (Carter, 1965; Lilly, 1979, 1981). Shock pressures of up to 150 kbar were estimated from these microstructures (Lilly, 1981). Such high pressures, well above the values encountered in the crust, call for extraordinary circumstances. The pressure estimates are in harmony with the reported presence of the high pressure silica polymorphs, coesite and stishovite, in pseudotachylite veins encountered in the Witwatersrand strata of the Vredefort collar (Martini, 1978). The violent nature of the disruption at Vredefort can also be deduced from the volume and widespread distribution of megabreccias, mylonite and pseudotachylite (Shand,

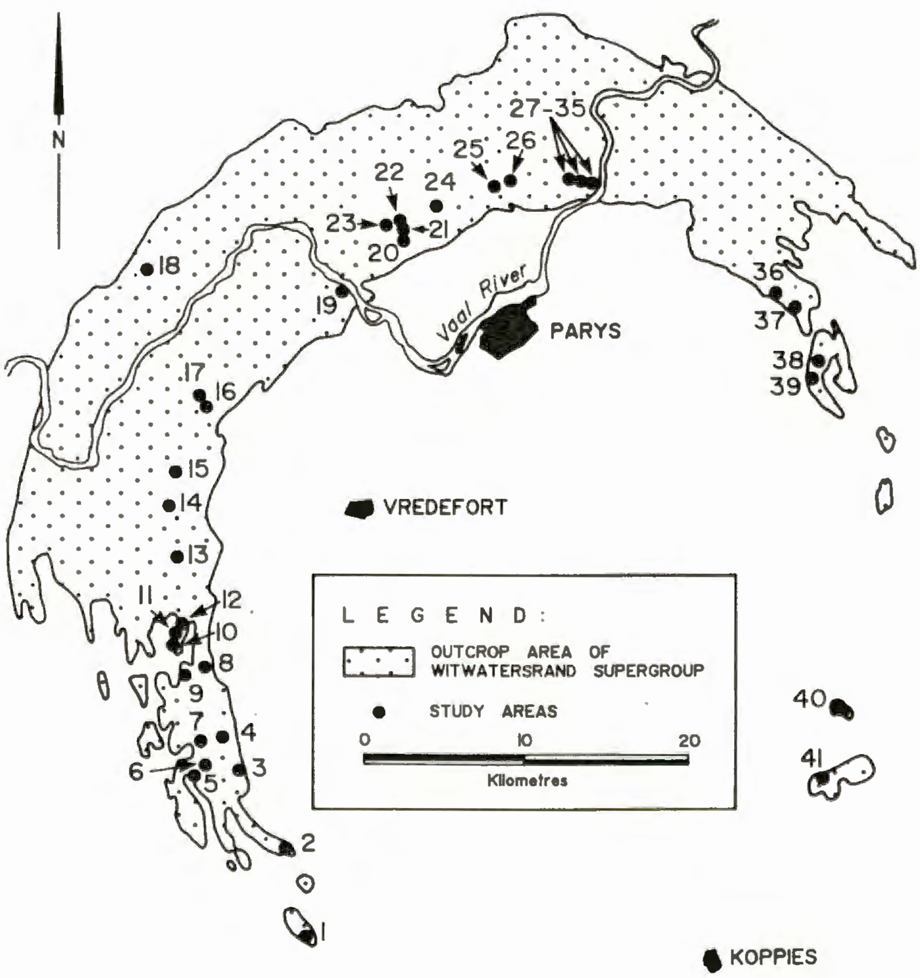

Fig. 4. Locality map of study areas (numbered 1 to 41) in relation to the outcrop of the Witwatersrand Supergroup.

1916; Willemse, 1937; Bisschoff, 1962; Wilshire, 1971; Schwarzman et al., 1983).

Megascopic planar fractures, which we consider to be shock response features, have hitherto been completely neglected in the Vredefort Structure. These features will be referred to as densely spaced s-surfaces in this paper. The development of the s-surfaces is ubiquitous in the quartzitic rock types of the Witwatersrand Supergroup where they are very conspicuous. They are rarely obvious in the argillaceous units (hornfelses) and in the banded iron formations. Their noticeability in the quartzites is due to the fact that these planar structures are manifested by an array of systematic, relatively straight but sometimes gently curved, discretely spaced hairline cracks which pervade most areas of the quartzite outcrop. The intervals between successive cracks are typically between 1 and 1.5 cm (Fig. 3), but spacings of a few millimetres have been observed. If a sample of the quartzite is sectioned with a diamond saw, it becomes obvious that the cracks are mere surface phenomena and that they close up to become faint welded lines (in section) deeper into the sample. Microscopic examination reveals that these faint lines, which represent the traces of the planar structures, contain fine-grained recrystallised quartz which contrasts against the medium- to coarse-grained nature of the host rocks. A single set or a conjugate system of s-surfaces pervades the rocks. It is not uncommon to observe distinct striations on the exposed planes of the s-surfaces. The densely spaced s-surfaces bear a striking resemblance to the "shatter cleavage" in the Carmichael sandstone, a photograph of which is contained in a paper by Milton (1977), and may suggest that similar planar fractures occur also in other cryptoexplosion structures.

The objective of this paper is to present the results of an essentially field-orientated research programme which is aimed in particular at establishing the geometry of the s-surfaces in the Vredefort Structure. The present study is confined to the strata of the Witwatersrand Supergroup exposed in the collar of the Vredefort Structure. Study areas are numbered 1 to 41 as indicated on the locality map (Fig. 4).

Geometric relationship between s-surfaces and shatter cones

Research by the present authors has revealed that the s-surfaces are intimately related to the shatter cones. This relationship is illustrated by way of an example established from field measurements recorded on the farm Rooderand (510) (study area 18, Fig. 4) in outcrops of quartzwacke belonging to the Turffontein Subgroup. Amongst the megascopic structural elements which are recorded are bedding planes, a slaty cleavage developed in units of less winnowed quartzwacke, joints, s-surfaces which form a conjugate system, and converging striations defining the shatter cone segments. Equal area, lower hemisphere projections representing the attitudes of these structures at study area 18 are shown in Fig. 5a, b. The slaty cleavage and the joints form the subject of a different paper, and therefore mention is made here only of the fact that the slaty cleavage is cut by, and therefore predates, the s-surfaces while the joints are demonstrably younger than the s-surfaces. In Fig. 5a the poles to the s-surfaces project as two clusters reflecting a conjugate system consisting of two sets here referred to as sets 1 and 2. A mean pole was computed for each set from the data and the corresponding planes to these poles, representing the mean s-surfaces, are shown as shaded great circle projections in Fig. 5c. The *in situ* shatter cone striations recorded at study area 18 (Fig. 5b) define a cone of best fit which is referred to as the master cone (Dietz, 1963; 1968; Milton, 1977; Roddy and Davis, 1977; Simpson, 1981). The master cone was computed using the statistical method outlined by Ramsay (1967, pp. 20–22) and its projection is shown graphically enhanced in Fig. 5c. From Fig. 5c it is apparent that the master cone is enveloped by the two sets of s-surfaces and occupies the obtuse angle of the conjugate system. Analysing the angular relationships between the cone and the s-surfaces (Fig. 5d) the following information is obtained: The axis of the master cone projects approximately perpendicularly to the intersection between the conjugate sets of s-surfaces (in this particular case the angle is seen to be 80°) and

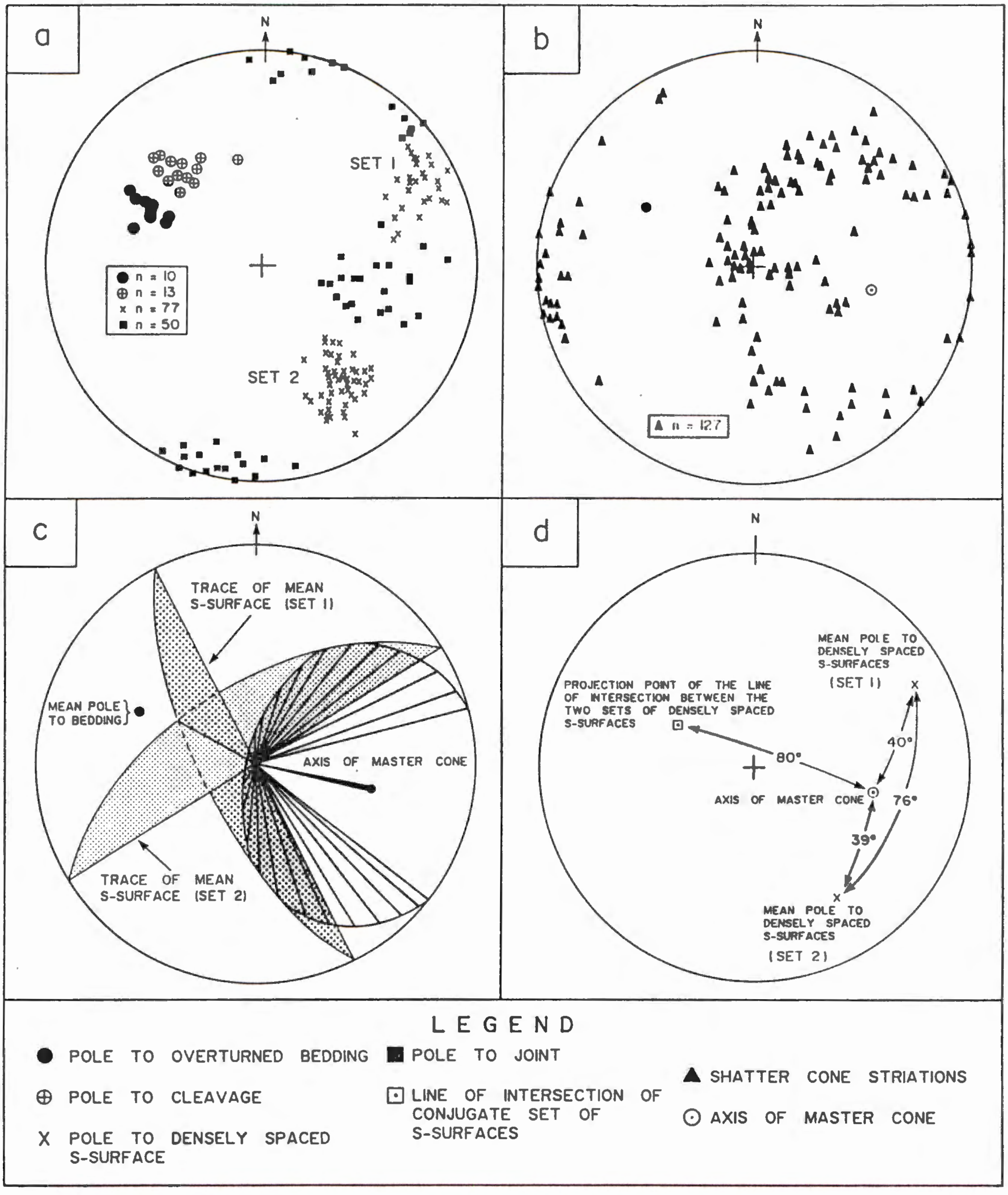

Fig. 5. Equal area, lower hemisphere projections of structural elements recorded at study area 18. *n*—number of individually measured structural elements. a. Poles to planar structures including bedding, cleavage, densely spaced s-surfaces and joints. b. Plunge of *in situ* shatter cone striations defining the axis of the master cone. c. Idealised geometrical relationship between the mean conjugate system of sets of s-surfaces and the master cone. d. Angular relationship between the axis of the master cone and the conjugate system of sets of s-surfaces.

approximately bisects the obtuse angle of 104° (Fig. 5d) between them.

Albat (1988) demonstrated that the mean apical angle of all master cones recorded in the Vredefort Structure is 100° with a small standard deviation for the entire population of 8°. If the geometrical relationships between the s-surfaces and the shatter cones (Fig. 5c and 5d) apply generally, the obtuse angle between the s-surfaces should remain constant and be approximately equal to the apical angle of the cones for all areas.

Geometric relationship between s-surfaces and bedding

The attitudes of bedding and s-surfaces were recorded at regular intervals along the entire exposed circumference of the Vredefort Structure. All study areas, with the exception of Rooderand (study area 18, Fig. 4), are located within the Government and Hospital Hill Subgroups. In each of the 41 study areas recordings were made on structurally homogeneous portions of the outcrop. A complete conjugate system of s-surfaces is identifiable in some of the study areas. Frequently, however, only one of the two sets is developed. The results of the survey are presented in Fig. 6 and Table 1. In Fig. 6 the bedding attitude for each study area is shown by a computed mean pole. The data representing the poles to the s-surfaces have been contoured and are used to establish their mode. From the lower hemisphere, equal area plots, shown in Fig. 6, we read and recorded the following parametric angles for each study area:

(a) angle u—the acute angle between the mean pole to bedding and the mode of the poles to the set 1 s-surfaces (s-set 1);

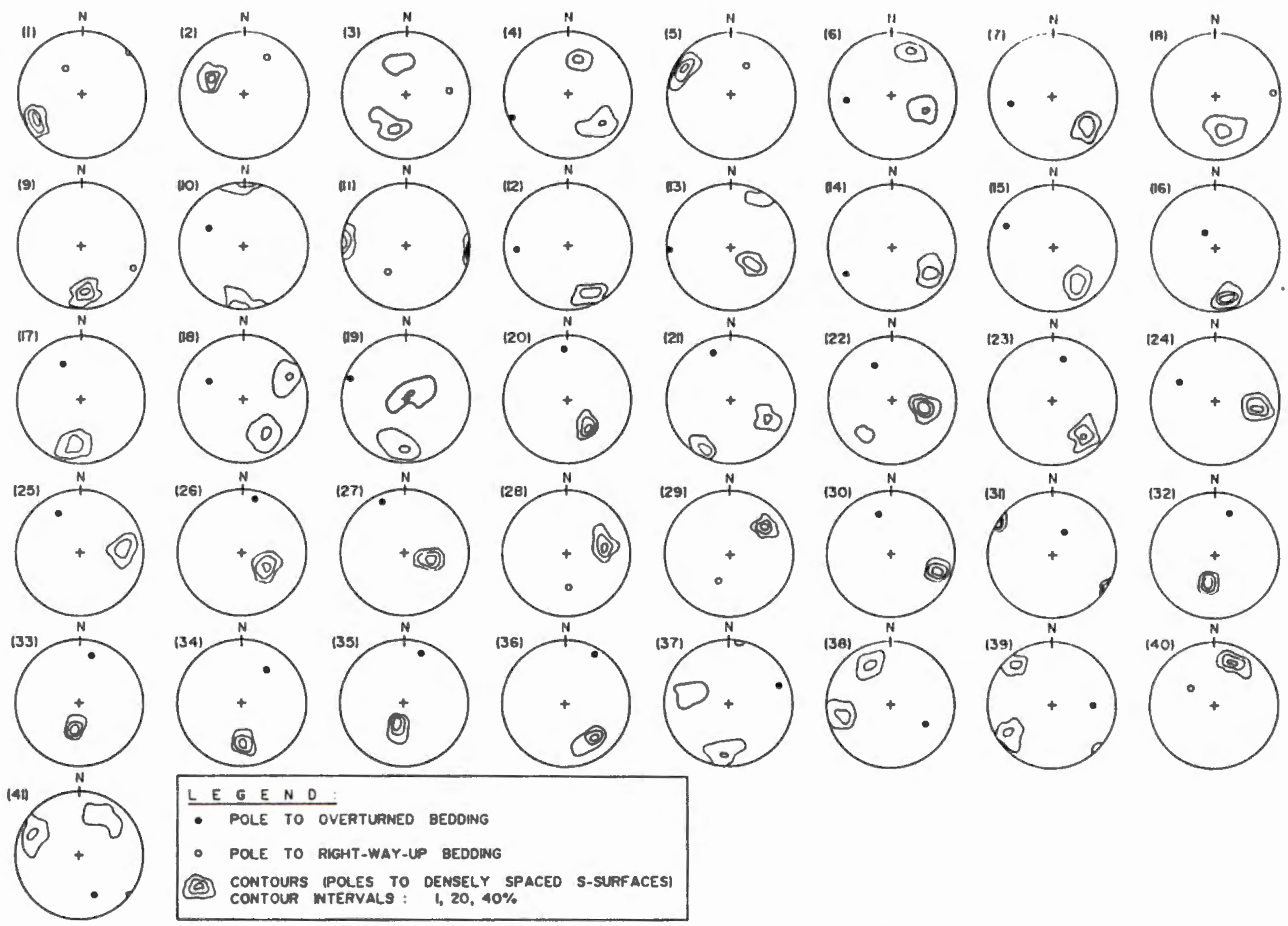

Fig. 6. Equal area, lower hemisphere projections of mean bedding pole and poles to s-surfaces (contoured) for study areas 1 to 41 (numerals in parentheses as in Fig. 4). The number of individual measurements represented in each projection is tabulated in Table 1.

TABLE 1

Structural data for study areas 1–41

Study area	nS_0	nS_1	nS_2	S_0	S_1	S_2	u (°)	v (°)	w (°)
1	5	20		62°/41°SE(R)	150°/70°NE		77		
2	8	20		117°/59°SW(R)	28°/46°SE		70		
3	5	8	19	171°/53°W(R)	76°/39°SE	105°/47°NE	69	82	84
4	3	21	23	157°/84°NE(O)	109°/49°SW	40°/60°NW	64	69	84
5	4	20		118°/48°SW(R)	35°/70°SE		73		
6	3	14	15	175°/57°E(O)	115°/69°S	20°/49°W	78	77	73
7	3		19	170°/54°E(O)		41°/60°NW		81	
8	2		23	175°/81°W(R)		75°/46°N		78	
9	3		21	23°/76°W(R)		87°/60°N		60	
10	3		31	25°/50°E(O)		95°/09°N		79	
11	3		24	125°/42°NE(R)		04°/74°E		66	
12	3		23	175°/67°E(O)		60°/75°NW		75	
13	6	6	18	176°/82°E(O)	120°/75°SW	38°/35°NW	61	72	82
14	1		20	149°/70°NE(O)		34°/64°NW		76	
15	1		20	26°/67°SE(O)		53°/56°NW		72	
16	1		20	58°/22°SE(O)		75°/70°N		88	
17	7		20	62°/50°SE(O)		96°/60°N		76	
18	10	27	50	25°/49°E(O)	153°/70°SW	58°/58°NW	78	78	76
19	6	25	25	22°/79°E(O)	145°/10°SW	91°/69°N	86	75	76
20	5	11		86°/67°S(O)	51°/50°NW		71		
21	13	8	10	72°/68°S(O)	24°/57°NW	115°/73°NE	71	57	81
22	18	26	4	68°/51°SE(O)	14°/46°W	131°/59°NE	85	90	85
23	21	17		105°/59°S(O)	48°/60°NW		80		
24	3	11		32°/50°SE(O)	10°/56°W		76		
25	5	15		62°/60°SE(O)	174°/59°W		90		
26	4	11		103°/76°S(O)	34°/36°NW		90		
27	6	15		67°/75°SE(O)	15°/36°W		82		
28	4	10		84°/44°N(R)	174°/50°W		63		
29	4	9		110°/38°N(R)	142°/59°SW		87		
30	6	14		76°/52°S(O)	21°/70°W		78		
31	4	10		122°/33°SW(O)	30°/83°SE		88		
32	4	10		110°/56°S(O)	99°/40°N		82		
33	4	10		104°/66°S(O)	104°/34°N		78		
34	4	10		126°/52°SW(O)	89°/55°N		80		
35	4	10		108°/74°S(O)	106°/27°N		78		
36	3	10		121°/78°SW(O)	51°/60°NW		79		
37	7	13	10	159°/72°SW(O)	93°/70°N	26°/40°SE	75	78	88
38	8	20	12	29°/53°NW(O)	165°/60°E	69°/59°SE	79	77	70
39	4	10	10	03°/52°W(O)	148°/68°NE	51°/70°SE	68	74	76
40	5	20		34°/35°SE(R)	113°/61°S		60		
41	6	20	13	71°/54°N(O)	24°/69°E	128°/60°SW	71	85	90

nS_0 = number of bedding planes recorded.
nS_1 = number of s-surfaces measured in s-set 1.
nS_2 = number of s-surfaces measured in s-set 2.
S_0 = mean strike and dip of bedding.
(R) = right-way-up strata.
(O) = overturned strata.
S_1 = strike and dip of mode of s-set 1.
S_2 = strike and dip of mode of s-set 2.
u = acute angle between mean bedding and mode of s-set 1.
v = acute angle between mean bedding and mode of s-set 2.
w = acute angle between the modes of the conjugate mean s-sets.

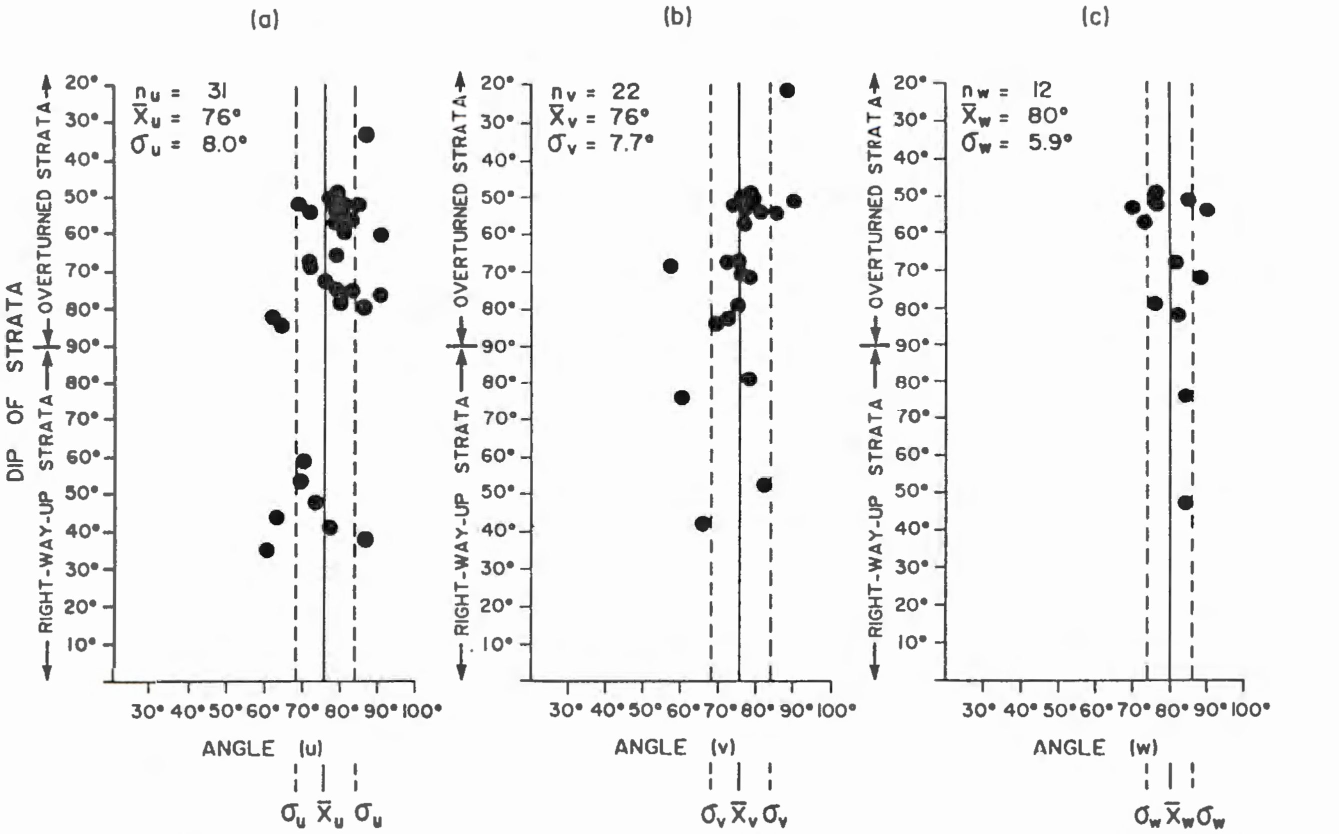

Fig. 7. Bedding dip versus angle u (a), angle v (b) and angle w (c) in study areas 1 to 41. n—number of individual measurements depicted in each graph, $\bar{x}$—their arithmetic mean and σ—one standard deviation.

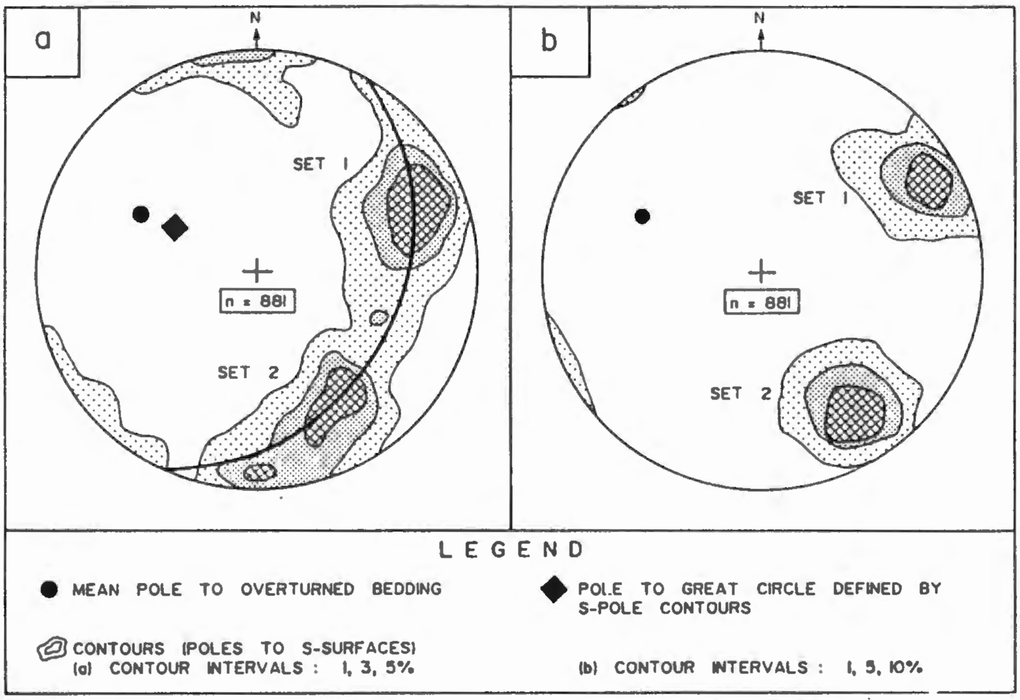

Fig. 8. Equal-area, lower-hemisphere projections of poles to the entire population of s-surfaces recorded at study areas 1 to 41 and rotated to a common reference orientation (see text). n—number of individual measurements. a. After rotations around a vertical and a strike axis. b. After an additional rotation around the mean pole to overturned bedding.

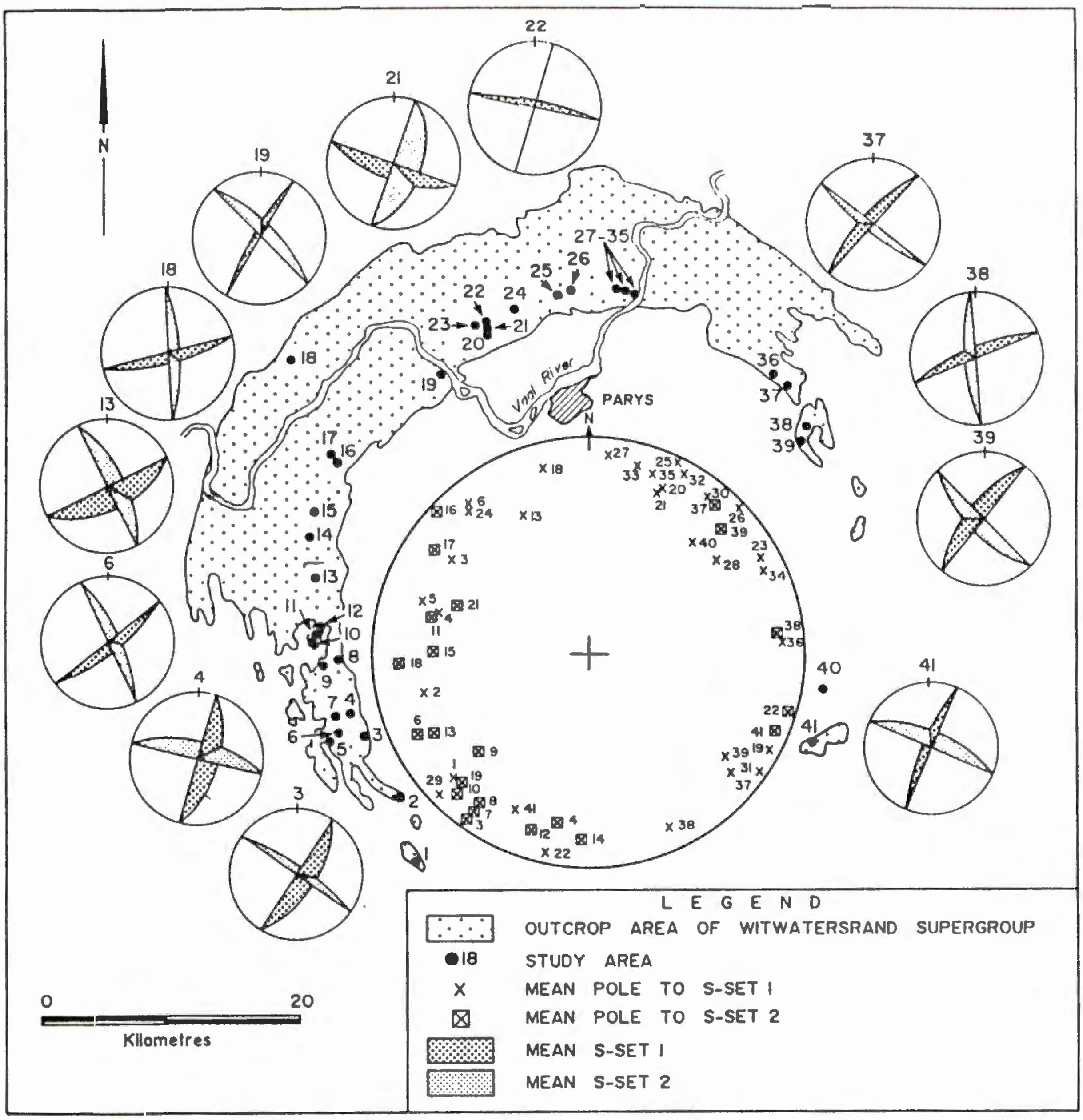

Fig. 9. Structural data (equal-area, lower-hemisphere projections) after restoration of bedding to horizontal by rotations around the local strike. The small projections show the conjugate sets of s-surfaces. The large projection synoptically shows mean s-surface poles. Numerals in the projections refer to study areas.

(b) angle v—the acute angle between the mean pole to bedding and the mode of poles to the set 2 s-surfaces (s-set 2);

(c) angle w—the acute angle between the modes of the poles of the two s-sets.

The magnitude of the angles referred to above, plotted against the present-day dip of the strata, is illustrated in Fig. 7. From Fig. 7a it is evident that u varies over a narrow range of approximately 30°. This variation, however, is clearly independent of the bedding dip. Similar results are evident for v (Fig. 7b). Angle u has a mean of 76° with a standard deviation $\sigma = 8.0°$ which is statistically indistinguishable from the mean of 76° (standard deviation $\sigma = 7.7°$) of angle v (Fig. 7). Angle w (Fig. 7c) is approximately constant at 80° (standard deviation $\sigma = 5.9°$).

For comparison of the geometrical relationships of structural elements, data from all localities were rotated so that they conform with those of study area 18 (Fig. 5), arbitrarily chosen as a reference. This involved firstly a rotation of the individual data sets about a vertical axis so as to align the local bedding strikes with that of area 18. Secondly, a further rotation about the bedding strike line produced coincidence of the bedding dips with that of the reference area. The results of the combined rotations are presented by the synoptic contoured diagram (Fig. 8a). It is evident that the rotated poles to the s-surfaces from all 41 study areas define a great circle girdle with its pole near the mean bedding pole (Fig. 8a). Using the mean bedding pole as a third rotational axis and rotating the s-surface poles independently for each study area to conform as close as possible to those of the reference area the distinctness of the s-surface pole clusters in Fig. 8a is enhanced (Fig. 8b).

Figure 9 presents the resulting geometry of the s-surfaces, for the entire Vredefort Structure, after the strata have been restored to the horizontal (rotation around bedding strike). The larger equal area projection in the centre of Fig. 9 illustrates the configuration of the modes of s-surface poles whereas the small projections show the conjugate sets derived from these modes for selected study areas around the collar. Figures 7, 8 and 9 demonstrate the systematic nature of the s-surfaces around the circumference of the Vredefort Structure.

Conclusions

A genetic link between s-surfaces and shatter cones is proposed from their geometric relationship established in study area 18 (Fig. 5). In the study areas where the conjugate system of s-surfaces exists, we have demonstrated that the obtuse angle between s-sets closely approximates 100° because its complementary angle *w* approaches a near constant value of 80° (Fig. 7c). It is proposed that this confirms the general validity of the geometric relationships outlined in Fig. 5c and d. If it is accepted, as proposed in the literature, that shatter cones are generated by severe shock it follows, by virtue of this established geometric relationship, that s-surfaces are likewise a product of shock waves. Albat (1988) has demonstrated that shatter cones predate the overturning of the collar rocks, therefore, s-surfaces are similarly viewed to be elements which preceded the folding.

The similarity of the three angles *u*, *v* and *w* around the Vredefort Structure (Figs. 7 and 8) has additional implications for the age of the s-surfaces relative to that of the overturning of the collar rocks. The low variance of these angles is remarkable considering that they were measured around the entire exposed perimeter of the Vredefort collar, probing the total spectrum of bedding attitude. If it were assumed that the s-surfaces had been generated after the collar rocks had already been overfolded, then the magnitude of the angles *u* and *v* would have to vary with the dip of the strata. On the contrary, if the s-surfaces formed before the collar rocks were overturned, the angles *u* and *v* would tend towards constancy provided the strata originally had a constant (more or less horizontal) attitude. Hence we propose that the s-surfaces preceded the folding.

If it is accepted that the s-surfaces predate the overfolding, either by virtue of their geometrical relationship to bedding outlined above or their suggested linkage to shatter cones, it is desirable to establish their initial geometry. This is illustrated in Fig. 9. Although our restoration of the bedding to the horizontal may be somewhat simplistic, restored poles to the sets are seen to plot close to the fundamental circle in Fig. 9, which implies that the s-surfaces had an initial steep dip. They are arranged systematically and fairly symmetrically around the centre of the Vredefort Structure. This is probably more easily appreciated from inspection of the small projections (Fig. 9). Most intersections of the conjugate sets plunge steeply towards the centre of the structure. This configuration is in harmony with the central high-level focusing of shatter cone axes outlined by Manton (1965).

It is conceivable that the states of stress resulting from severe pressure accompanying the shock waves, which affected the rocks, were geologically short-lived. Thus the resulting rock failure (shatter cones and s-surfaces) is likely to have occurred practically instantaneously. Accordingly we propose that the s-surfaces may in fact represent a marker of geological time. In this respect the s-surfaces are preferred to the synchronous shatter cones as their development appears to be more uniformly spread over the entire Vredefort Structure. Furthermore, if the same forces that generated the shatter cones and s-surfaces were also responsible for the formation of the Vredefort Structure as a whole then the s-surface marker may prove useful in establishing a sequence of events. As a consequence it may be argued that all geological phenomena that are cut by, and therefore predate the s-surfaces, are unrelated to the cryptoexplosion structure and are accordingly ascribed to pre-Vredefort history. In contrast all geological phenomena that are younger than the s-surfaces may either be related or may postdate the Vredefort Structure.

Acknowledgements

This project was supported by the Bureau for Research, Potchefstroom University for C.H.E. and the South African Council for Scientific and Industrial Research. The authors wish to thank mrs. I. de Beer for draughting the diagrams and mrs. T. van der Walt for typing the manuscript.

References

Albat, H.M., 1988. Shatter cone/bedding interrelationship in the Vredefort Structure: evidence for meteorite impact? S.Afr. J. Geol., 91: 106–113.

Bisschoff, A.A., 1962. The pseudotachylite of the Vredefort Dome. Trans. Geol. Soc. S. Afr., 65: 207–226.

Bisschoff, A.A., 1969. The petrology of the igneous and the metamorphic rocks in the Vredefort Dome and the adjoining parts of the Potchefstroom syncline. D.Sc. thesis, Univ. of Pretoria, Pretoria, 243 pp.

Bisschoff, A.A., 1972a. Tholeiitic intrusions in the Vredefort Dome. Trans. Geol. Soc. S. Afr., 75: 23–30.

Bisschoff, A.A., 1972b. The dioritic rocks of the Vredefort Dome. Trans. Geol. Soc. S. Afr., 75: 31–45.

Bisschoff, A.A., 1973. The petrology of some mafic and peralkaline intrusions in the Vredefort Dome, South Africa. Trans. Geol. Soc. S. Afr., 76: 28–49.

Bisschoff, A.A., 1982. Thermal metamorphism in the Vredefort Dome. Trans. Geol. Soc. S. Afr., 85: 43–57.

Boon, J.D. and Albritton, C.C., 1937. Meteorite scars in the ancient rocks. Field Lab., 5: 53–64.

Boon, J.D. and Albritton, C.C., 1938. Established and supposed examples of meteorite craters. Field Lab., 6: 44–56.

Carter, N.L., 1965. Basal quartz deformation lamellae—a criterion for recognition of impactites. Am. J. Sci., 263: 786–806.

Daly, R.A., 1947. The Vredefort ring structure of South Africa. J. Geol., 55: 125–145.

Dietz, R.S., 1959. Shatter cones in cryptoexplosion structures (meteorite impact?). J. Geol., 67: 496–505.

Dietz, R.S., 1961. Vredefort ring structure—Meteorite impact scar? J. Geol., 69: 499–516.

Dietz, R.S., 1963. Astroblemes, ancient meteorite-impact structures on the Earth. In: B.M. Middlehurst and G.P. Kuiper (Editors), The Moon, Meteorites and Comets. University of Chicago Press, Chicago, Ill., pp. 285–300.

Dietz, R.S., 1968. Shatter cones in cryptoexplosion structures. In: B.M. French and N.M. Short (Editors), Shock Metamorphism of Natural Materials. M.D. Mono Book Corp., Baltimore, Md., pp. 267–285.

Hall, A.L. and Molengraaff, G.A.F., 1925. The Vredefort Mountain Land in southern Transvaal and northern Orange Free State. Verh. K. Akad. Wet., 24: 1–183.

Hargraves, R.B., 1961. Shatter cones in the rocks of the Vredefort Ring. Trans. Geol. Soc. S. Afr., 64: 147–154.

Lilly, P.A., 1979. Coesite and stishovite in the Vredefort Dome, South Africa: a discussion. Nature, 277: 495.

Lilly, P.A., 1981. Shock metamorphism in the Vredefort collar: Evidence for internal shock sources. J. Geophys. Res., 86: 10689–10700.

Manton, W.I., 1962. The orientation and implication of shatter cones in the Vredefort Ring structure. M.Sc. thesis, Univ. Witwatersrand, Johannesburg, 167 pp. (unpubl.).

Manton, W.I., 1965. The orientation and origin of shatter cones in the Vredefort Ring. Ann. N.Y. Acad. Sci., 123: 1017–1049.

Martini, J.E.J., 1978. Coesite and stishovite in the Vredefort Dome, South Africa. Nature 272: 715–717.

Milton, D.J., 1977. Shatter cones—an outstanding problem in shock mechanics. In: D.J. Roddy, R.O. Pepin and R.B. Merrill (Editors), Impact and Explosion Cratering. Pergamon, New York, N.Y., pp. 703–714.

Nel, L.T., 1927. The geology of the country around Vredefort—an explanation of the geological map. Spec. Publ. Geol. Surv. S. Afr., 6: 134 pp.

Nicolaysen, L.O., 1987. The Vredefort Structure. In: Contributions to International Workshop on Cryptoexplosions and Catastrophes in the Geological Record, Parys, South Africa, Section N1.

Nicolaysen, L.O. and Reimold, W.U., 1985. Shock deformation, Shatter cones, and pseudotachylite at Vredefort: a review of major unsolved problems and current efforts to resolve them. Lunar Planet. Sci., 15: 618–619.

Ramsay, J.G., 1967. Folding and Fracturing of Rocks. McGraw-Hill, New York, N.Y., 568 pp.

Roddy, D.J. and Davis, L.K., 1977. Shatter cones formed in large-scale experimental explosion craters. In: D.J. Roddy, R.O. Pepin and R.B. Merrill (Editors), Impact and Explosion Cratering. Pergamon, New York, N.Y., pp. 715–750.

Schneider, E. and Wagner, G.A., 1976. Shatter cones produced experimentally by impact in limestone targets. Earth Planet Sci. Lett., 32: 40.

Schwarzman, E.C., Meyer, C.E. and Wilshire, H.G., 1983. Pseudotachylite from the Vredefort ring, South Africa, and the origins of some lunar breccias. Bull. Geol. Soc. Am., 94: 926–935.

Shand, J.S., 1916. The pseudotachylite of Parys (Orange Free State), and its relation to "trap-shotten gneiss" and "flinty crushrock". J. Geol. Soc. London, 72: 198–221.

Shoemaker, E.M., Gault, D.E. and Lugn, R.V., 1961. Shatter cones formed by high speed impact in dolomite. U.S. Geol. Surv., Prof. Pap., 424-D: 365–368.

Simpson, C., 1981. Occurrence and orientation of shatter cones in Pretoria Group quartzites in the collar of the Vredefort "Dome": Impact origin precluded. J. Geophys. Res., 86: 10701–10706.

Weiss, O., 1949. Aerial magnetic survey of the Vredefort Dome in the Union of South Africa. Min. Trans., 184: 433–438.

Willemse, J., 1937. On the old granite of the Vredefort region and some of its associated rocks. Trans. Geol. Soc. S. Afr., 40: 43–119.

Wilshire, H.G., 1971. Pseudotachylite from the Vredefort ring, South Africa. J. Geol., 79: 195–206.

CHAPTER 7

THE INTERRELATIONSHIPS OF STRUCTURAL ELEMENTS IN THE UPPER QUARTZITE MEMBER OF THE HOSPITAL HILL SUBGROUP IN THE SOUTHWESTERN PORTION OF THE VREDEFORT COLLAR

THE INTERRELATIONSHIPS OF SMALL-SCALE STRUCTURAL ELEMENTS IN THE UPPER QUARTZITE MEMBER OF THE HOSPITAL HILL SUBGROUP IN THE SOUTHWESTERN PORTION OF THE VREDEFORT COLLAR

Introduction

This chapter is based on a poster presented by H.M. Albat and J.J. Mayer at the *International Workshop on Cryptoexplosions and Catastrophes in the Geological Record, Parys, South Africa*, during 1987. The objective of this chapter, and that of the original poster, is to demonstrate the value of studying the interrelationships of small-scale structural elements, within the domain of a single outcrop or megascopic structure, in order to resolve the sequence of a number of events constituting part of the diastrophism in the area. In addition, the practical use of megascopic planar fractures (Chapter 6), to perform relative dating, is illustrated. These planar fractures, or s-surfaces, which are regarded as shock features allied to shatter cones (Albat and Mayer, 1989; Chapter 6), pervade almost all quartzite beds of the Witwatersrand succession of the Vredefort collar.

Shatter cones and pseudotachylite are regarded by most geoscientists as the respective manifestations of co-related successive events of relative short geological duration: a "shock", endogenous or exogenous, and the response to the shock, the upturning, or so-called overfolding, of the collar strata.

The relative dating of rocks and events by shatter cones and pseudotachylite

Although shatter cones were observed by Nel (1927), they were not given much attention at that time. Pseudotachylite, however, was observed and described by Shand (1916), and Hall and Molengraaff (1925) pointed out that pseudotachylite was found in all rocks of pre-Karoo age except the enstatite granophyre (bronzite granophyre, as presently known). Bisschoff (1969) pointed out that neither pseudotachylite nor shatter cones are present in the bronzite granophyre and that both the Annasrust intrusion (Waterberg or Karoo age?) and the Wonderfontein dyke (Pilanesberg age) are free of pseudotachylite. He further pointed out that shatter cone surfaces are in places covered by pseudotachylite and that slickenside surfaces are also present in inclusions in the pseudotachylite without cutting it. Pseudotachylite therefore postdates the shatter cones. Bisschoff (1971) found that the bronzite granophyre cuts through a coarse "pseudotachylite-cemented" breccia on Spitskop 1090 and is therefore younger than the pseudotachylite

Relative dating by small-scale structural elements

Figure 1 shows the study area which comprises an interesting fold structure (Fig. 2) of the

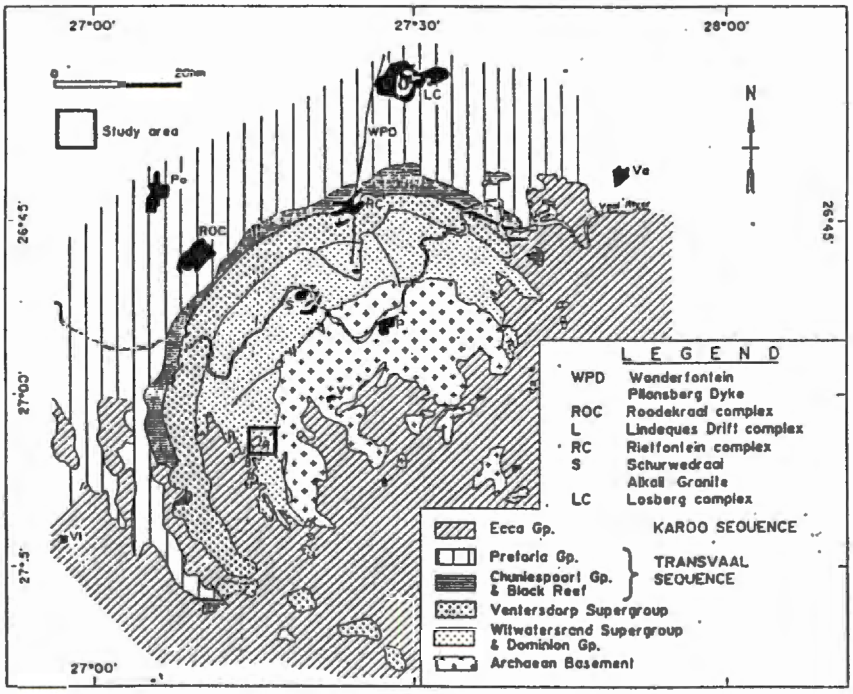

Fig. 1 Setting of the study area

upper quartzite member of the Hospital Subgroup in the southwestern sector of the Vredefort collar. The quartzite beds in this formation forms a low but prominent ridge configured in a z-like pattern in plan view. At the southern end of the structure the strata are terminated against a major fault (Fig. 2). From this point, in a northerly direction, the consecutive outcrop segments of the z-pattern are respectively presented by overturned easterly dipping strata (Domain a, Fig. 2), followed by right-way-up northerly dipping strata (Domain b, Fig. 2), followed by overturned easterly dipping strata (Domain c, Fig. 2). Within this fold structure the quartzite beds are pervaded by densely spaced s-surfaces, the traces of which show up well as result of weathering (Fig. 3). Other structural elements are bedding-plane slickenside-striae related to the relative slip on the bedding during the final stages of the folding (Ramsay and Huber, 1987), and widely spaced joints (Fig. 4). Veins of pseudotachylite (Fig. 5) are found in all the domains of the study area.

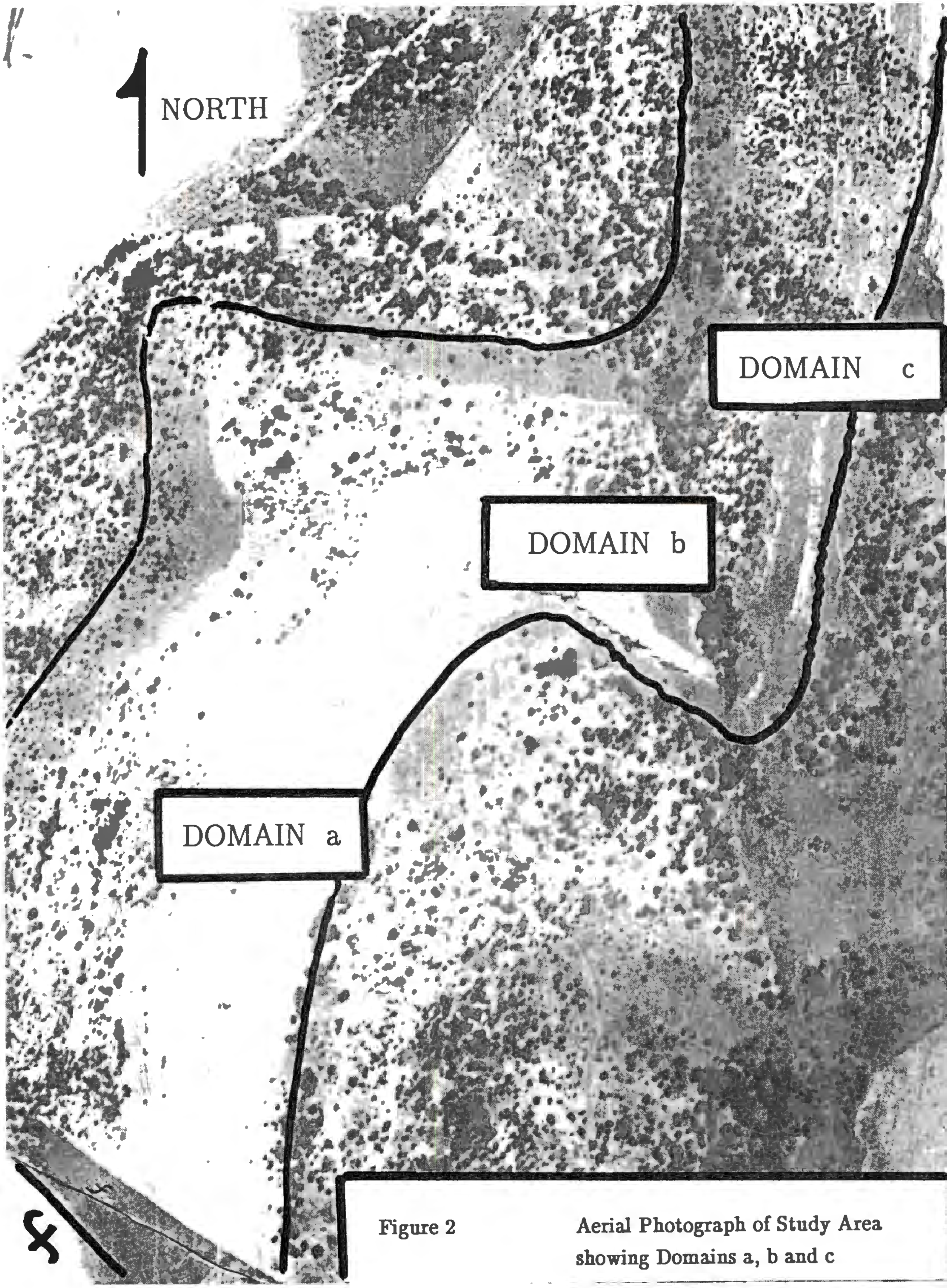

Figure 2 Aerial Photograph of Study Area showing Domains a, b and c

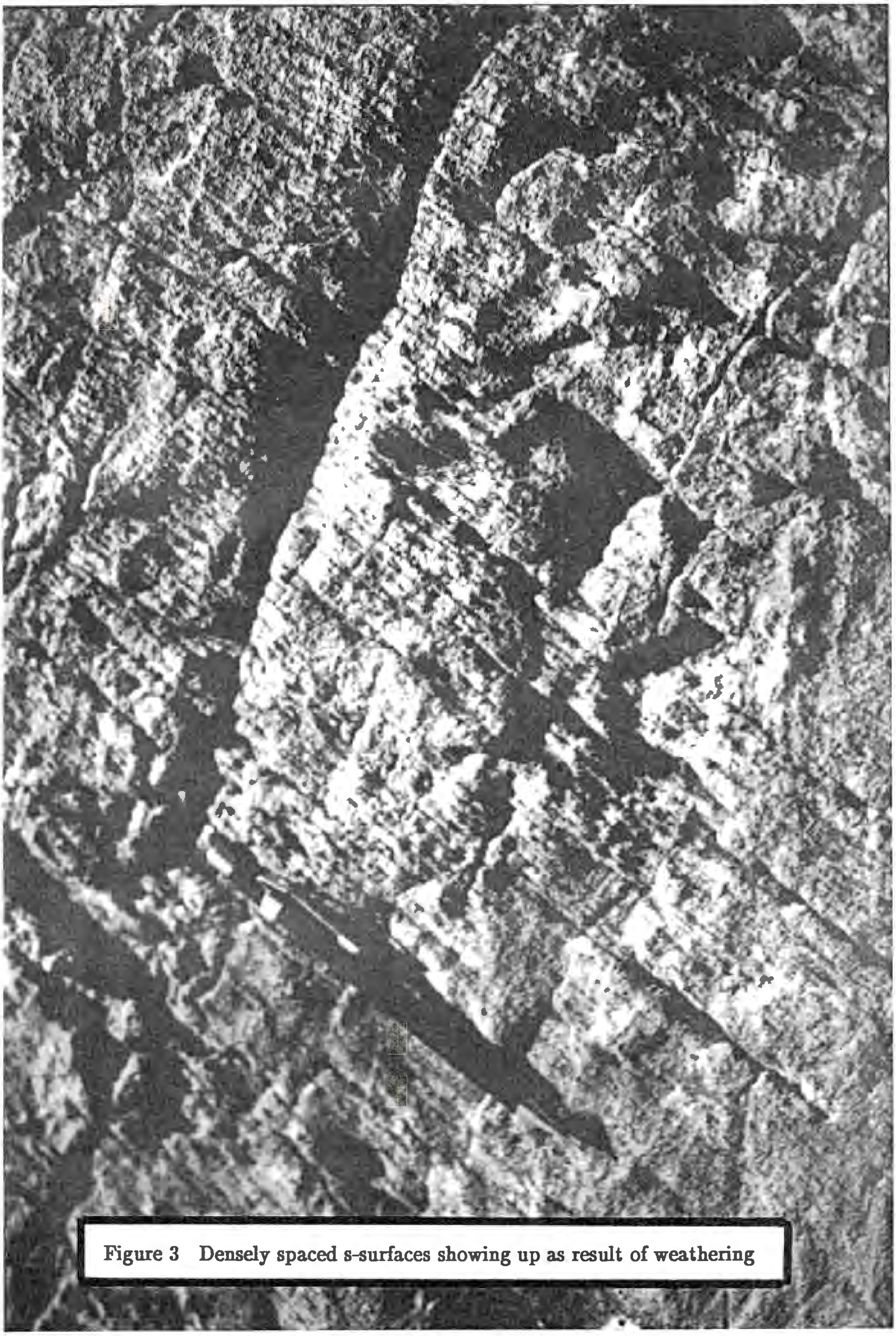

Figure 3 Densely spaced s-surfaces showing up as result of weathering

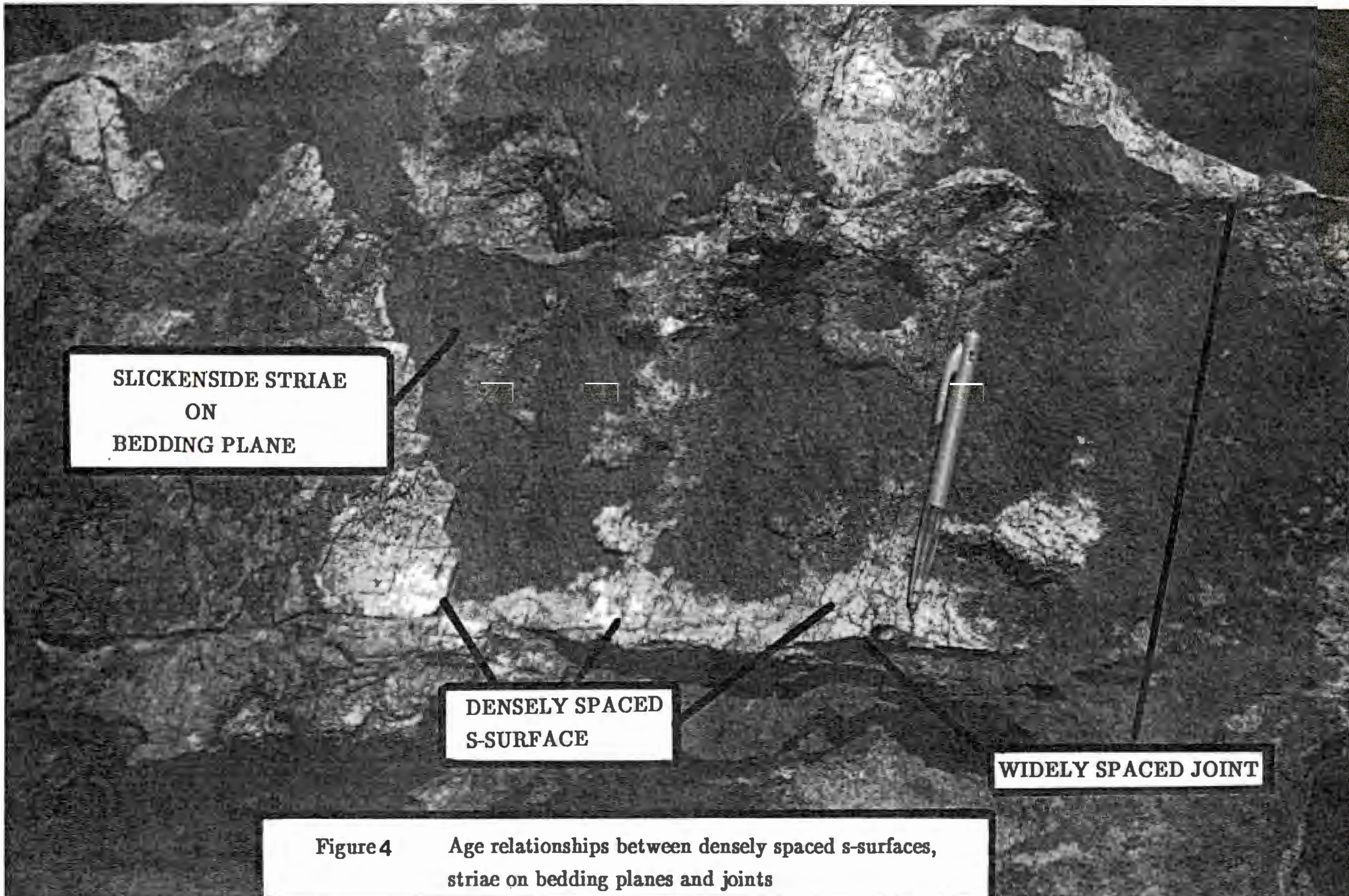

Figure 4 Age relationships between densely spaced s-surfaces, striae on bedding planes and joints

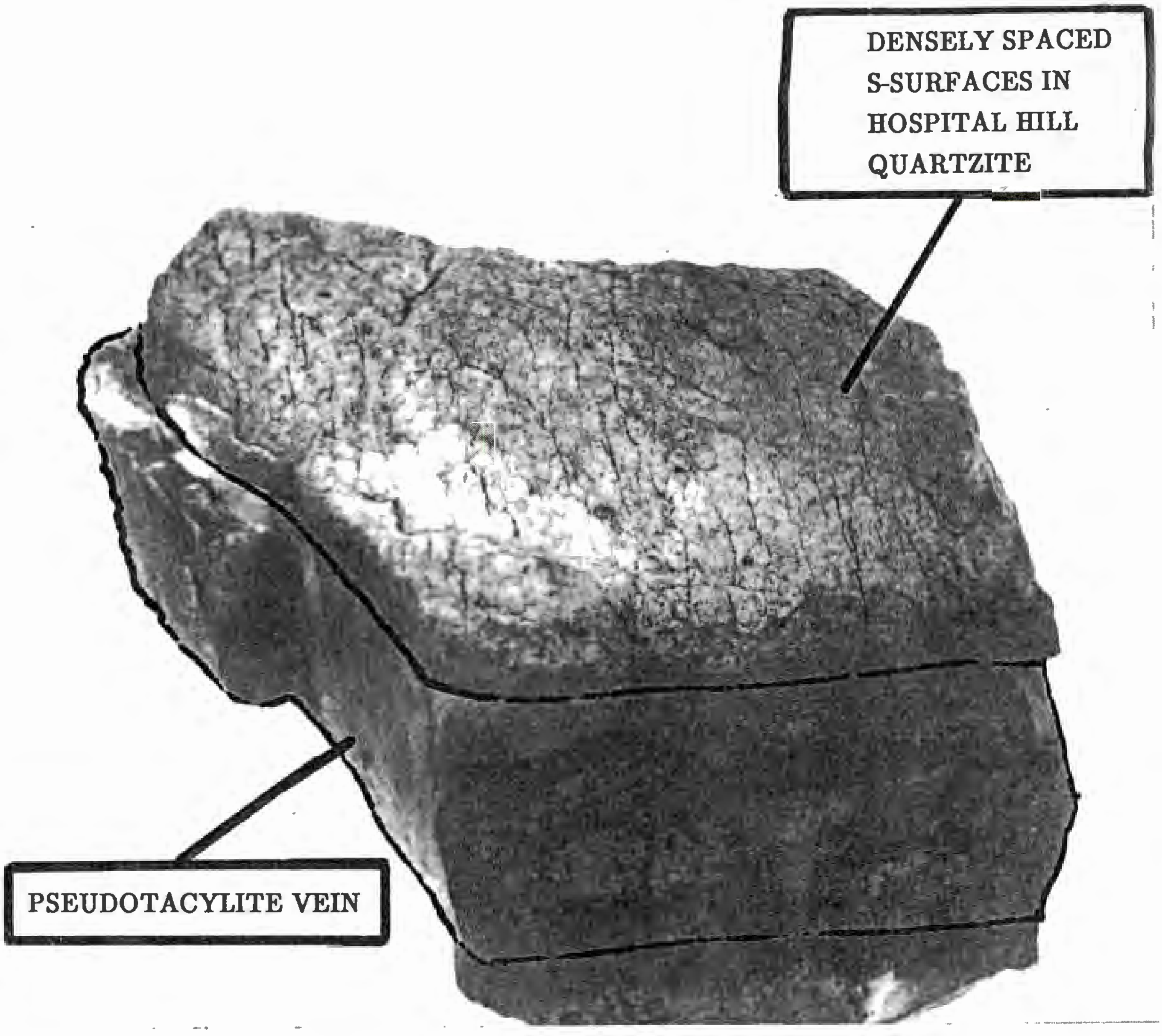

Figure 5 Age relationship between the densly spaced s-surfaces and a pseudotachylite vein

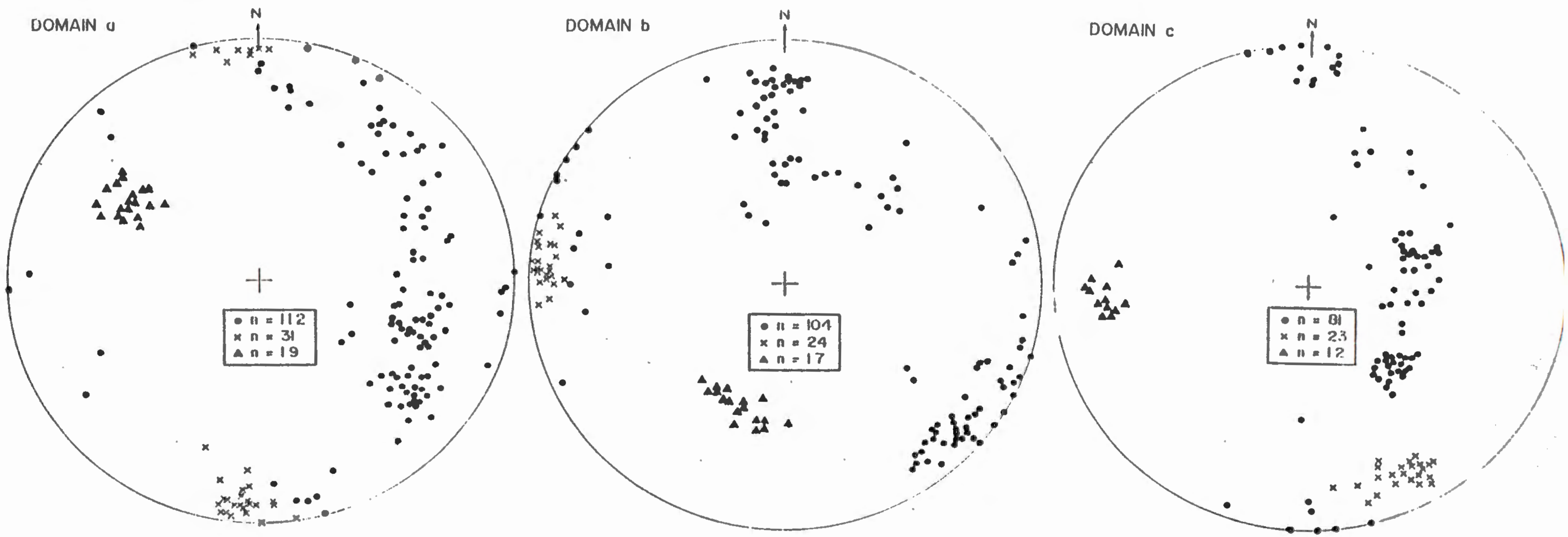

Fig.6 Equal area projections of planar structures in domains a, b and c.

● poles to joints
X poles to densely spaced s-surfaces
▲ poles to bedding planes

NOTE: — There is a marked change in attitude of the densely spaced s-surfaces in domains a, b and c.

Figure 6 a, b and c represent equal area projections of the poles of the various planar structures in the respective domains a, b and c.

Findings

Figure 4 presents convincing field evidence that the slickenside striae (presumably a record of the last movement during the process of folding) are younger than the densely spaced systematic s-surfaces and older than the less systematic widely spaced joints.

Figure 5 presents evidence for a younger age of the pseudotachylite relative to that of the densely spaced systematic s-surfaces. In the study area there is evidence that pseudotachylite, in turn, is cut by the widely spaced jointing (not illustrated).

Figure 6 shows that the general attitude of the densely spaced s-surfaces is markedly different for the three respective domains (Fig. 6, a, b, c). This suggests that the densely spaced systematic s-surfaces have been folded whereas the less systematic widely spaced joints have not. The densely spaced s-surfaces are therefore older than the folding (and presumably the overfolding) whereas the jointing postdates the folding. This also fits in with the relationships illustrated by Figure 4. From this study the sequence of events therefore is as follows: s-surfaces, folding, pseudotachylite, jointing.

Opposing ideas and opinions

Simpson (1981) believes that shatter cones are post-overfolding in age and Reimold (1990), regards them as the product of a number of intersecting joint sets generated by tectonic stresses over a time interval (see also Chapter 8).

Simpson (1981) claimed that she found evidence of shatter cones cutting a fault breccia associated with the down-faulting of previously overturned Pretoria Group quartzites. Such evidence repudiates the hypothesis that shatter cones formed on impact and pre-date the overturning of the collar rocks. The study area of Simpson (1981), in the northern region of the collar, was revisited by the author and co-author, Hans Albat. No evidence, however, for a post-overturning age for shatter cones could be found in this area. A point of criticism on Simpson's work is that her recorded data for shatter cones, in the study area of the northern region (locality 2), are very scant (only 29 and 10 data points). From these data points she obtains master cones showing apical angles varying from 88^0 to as excessive as 140^0. Albat (1988), who has constructed a fair number of master cones and has based his projections on an average of more than 110 data points per master cone, has convincingly shown that shatter cones have a statistically-constant apical angle close to 100^0 with a standard deviation of 7.5^0. Joints with random orientations, which contain parallel striations, are common in the Vredefort rocks. The majority of these joints presumably originated as result of the upfolding of the collar strata and by subsequent deformational events. It is possible that these, sometimes curved joint surfaces, may be mistaken for shatter cone segments especially where the striations have become faint on highly weathered surfaces.

The existence of shatter cones, as discrete, truly conically-shaped phenomena has been challenged by Nicolaysen and Reimold (1987) who believe that these structures are the manifestations of the intersections of multipli-striated joint sets. Reimold (1990), furthermore, believes that "shatter cones" were formed by orogenic stresses which extended over a relative long period of geological time. This viewpoint implies that features such as shatter cones are not usable as markers of geological "moments" of a very short duration.

The discovery of a magnificent specimen, representing a discreet and complete shatter cone from the Vredefort area (Albat and Mayer, 1990, Chapter 8), however, ought to be convincing evidence that shatter cones are real features indeed, and their absence in normal orogenic terrains indicates that they are probably not the product of an ordinary orogenic stress field.

Pseudotachylite, as indicated, is regarded as another "time marker" representative of the catastrophic event which resulted in the upfolding of the Vredefort collar strata. Rocks postdating this event, therefore, show no pseudotachylite development. Reimold *et al.* (1990a), however, propose six pseudotachylite events having occurred over a period of 1.16 (Ga) and Reimold *et al.* (1990b) claim a discovery of pseudotachylite and of shatter cone related fractures in the bronzite granophyre. The author and prof. A.A. Bisschoff visited one of the sites (Rensburgsdrift 432), mentioned by Reimold *et al.* (1990b), where the granophyre allegedly contains pseudotachylite. We were unable to find this "rare" occurrence of pseudotachylite, nor any convincing shatter cone related s-surfaces in this rock type. The host rocks to the granophyre dyke of this area, however, show unmistakable evidence of pseudotachylite development. On Spitskop 1090, adjoining Rensburgsdrift 432, the specific occurrence, where a granophyre dyke cuts across pseudotachylite (Bisschoff, 1971), and is chilled against the pseudotachylite (A.A. Bisschoff, personal communication), was revisited. Here it is very clear that the granophyre dyke postdates the pseudotachylite and that there must be a considerable time gap between the formation of the two rock types, considering the fact that the pseudotachylite was cold enough for the intruding granophyre to be chilled against it.

A question which may be asked is whether the solitary small vein of black material found by Reimold et al. (1990b), in the granophyre on Rensburgsdrift 432, is real pseudotachylite or an elongated inclusion of some dark rock type. If pseudotachylite is older then the granophyre the possibility of a xenolith of pseudotachylite in the granophyre is not excluded.

Conclusion

Megascopic shock fractures (systematic densely spaced s-surfaces) are almost omnipresent in the Vredefort rocks whereas shatter cone sectors are not found all that frequently. The s-surfaces may therefore be most useful to relatively date other structural elements or rocks when shatter cones are absent. On Rooderand 510, for example, the s-surfaces cut a foliation delineated by the development of "metamorphic" mica in some of the quartzite beds, which possibly were argillaceous sandstones originally. Ramsay (1963), speculated that this foliation, which is also developed in the Vredefort Siltstone Formation (correlative of the Booysens shale – see Chapter 9), is an axial plane foliation connected with the collar folding. From the evidence of the s-surfaces the observed foliation thus predates the Vredefort Event.

REFERENCES

Albat, H.M. (1988). Shatter cone/bedding interrelationship in the Vredefort Structure: evidence for meteorite impact? *S. Afr. J. Geol.*, **91**, 106-113.

Albat, H.M. & Mayer, J.J. (1989). Megascopic planar shock fractures in the Vredefort Structure: a potential time marker? *Tectonophysics*, **162**, 265-276.

Bisschoff, A.A. (1969). *The petrology of the igneous and metamorphic rocks in the Vredefort Dome and adjoining parts of the Potchefstroom Syncline.* D.Sc. thesis (unpubl.) Univ. Pretoria, 243pp.

Bisschoff, A.A. (1972). The dioritic rocks of the Vredefort dome. *Trans. geol. Soc. S. Afr.*,**75**, 31–45.

Hall, A.L. & Molengraaff, G.A.F. (1925). The Vredefort Mountain Land in southern Transvaal and northern Orange Free State. *Verh. K. Akad. Wet.*, 24, 1–183.

Nel, L.T. (1927). The geology of the country around Vredefort – An explanation of the geological map. *Spec. Publ. geol. Surv. S. Afr.*, **6**, 134pp.

Nicolaysen, L.O. and Reimold, W.U. (1978). Shatter cones revisited (working paper). *Contributions to International Workshop on Cryptoexplosions and Catastrophes in the Geological Record, Parys, South Africa, Section N2.*

Ramsay, J.G. (1961). Discussion on 'Shatter cones in the rocks of the Vredefort Ring'. *Trans. geol. Soc. S. Afr.*, **64**, 156–157.

Ramsay, J.G. & Huber, M.I.(1987). *The techniques of modern structural geology. Volume 2: Folds and Fractures.* Academic Press, Oxford, 462pp.

Reimold, W.U., Jessberger, E.K. and Stephan, T., Bayly, B. (1990a). ^{40}Ar–^{39}Ar dating of pseudotachylite from the Vredefort dome South Africa: a Progress report. *Tectonophysics*, **192**, 139–152.

Reimold, W.U., Horsch, H., and Durrheim, R.J. (1990b). The "Bronzite"-Granophyre from the Vredefort Structure – A detailed analytical study and reflections on the genesis of one of the Vredefort's enigmas. *Proceedings of the 20th Lunar and Planetary Science Conference*, pp. 433–450.

Shand, S.J. (1916). The pseudotachylyte of Parys (Orange Free State) and its relation to "trap-shotten gneiss" and "flinty chrush-rock". *Quart. J. geol. Soc. Lond.*, **72**, 198–221.

Simpson, C. (1981). Occurrence and orientation of shatter cones in Pretoria Group quartzites in the collar of the Vredefort 'Dome': impact origin precluded. *J. geophys. Res.*, **86**, 10701–10706.

CHAPTER 8

SHATTER CONES IN VREDEFORT ROCKS – IMAGINATION OR REALITY ?

S.Afr.J.Geol.,1990,93(3),547–548

Note / Nota

Shatter cones in Vredefort rocks - imagination or reality?

H.M. Albat and J.J. Mayer
Department of Geology, Potchefstroom University for C.H.E., Potchefstroom 2520, Republic of South Africa

Accepted 5 April 1990

The authors have recently discovered a perfect shatter cone representing a discrete and full-cone fracture surface. Photographic evidence of this structure is herewith presented with a view to convincing the critics of the reality of these structures. If the shatter cone is real then the concept of the statistical master cone must therefore also be valid.

Die outeurs het onlangs 'n perfekte splinterkeël wat die diskrete breekoppervlak van 'n volle keël verteenwoordig ontdek. Fotografiese getuienis van hierdie struktuur word hiermee aangebied met die oog daarop om diegene wat kritiek teen die realiteit van hierdie struktuur gelewer het te oortuig. Indien die splinterkeël 'n werklikheid is, moet die konsep van die statistiese meesterkeël dus ook geldig wees.

Shatter cones can be described as axially symmetric conical fracture surfaces which are radially striated from the apex (Dietz, 1959, 1961, 1963, 1968). The nature and geometry of these conical fractures in the rocks of the Vredefort Structure are well documented in the literature (Hargraves, 1961; Manton, 1965; Albat, 1988) and it was recently established that cones bear a geometrical relationship to certain megascopic planar fractures which are omnipresent in the Vredefort rocks (Albat & Mayer, 1989).

Field experience has taught the authors that a complete cone is very rarely observed in exposure. The rocks generally display a large population of variously disposed cone segments. If a large number of random measurements of striations on these curved surfaces is recorded in a structurally homogeneous terrain, and processed by means of projection techniques (equal area projection), it becomes obvious that the entire population of converging striae on cone segments defines a full cone (Figure 1). This conceptional cone has been referred to as the full shatter cone or statistical master cone (Manton, 1965; Simpson, 1981; Albat, 1988) which has two geometrical features, a cone axis and an apical angle of approximately 100°.

Some earth scientists, however, notably Nicolaysen & Reimold (1987), doubt the validity of the statistical master cone concept and also question whether the curved fracture surfaces are part of actual cone structures. These authors interpret the geometrical pattern of striae on projections as the result of the intersection of a large population of joint planes, referred to as multiple-striated joint sets.

It is our objective to convince fellow researchers that the curved fracture surfaces containing the convergent striations are in fact segments related to complete cones. If the projection pattern (Manton, 1962, 1965; Albat, 1988; see also Figure 1) fails to be convincing the alternative is to provide evidence in the form of specimens of complete cones from the Vredefort area. Figure 2 illustrates a complete shatter cone in metabasites. Critics, however, may still argue that the particular specimen represents a composite cone. In order to convince even the most critical minds the authors present, in Figures 3 and 4, photographs of a perfectly shaped shatter cone. Figures 3 and 4, respectively, represent the same specimen *in situ* and after it had been removed from its surroundings. It is hoped that this evidence will prove beyond doubt that complete shatter cones do in fact exist in the Vredefort rocks and that the geometrical concept of a statistical master cone is accordingly valid and meaningful.

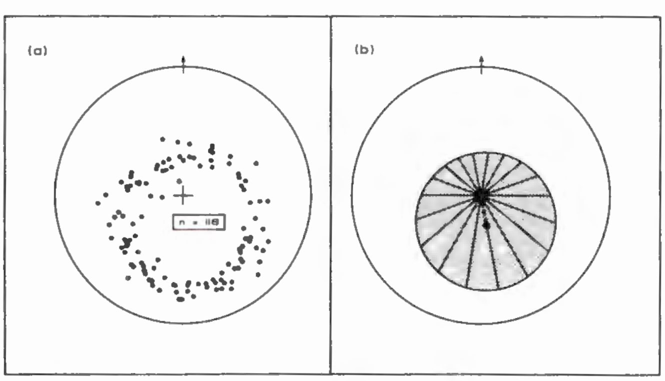

Figure 1 (a) Example of an equal area projection showing direction and plunge of striations on shatter cone segments for a structurally homogeneous area of Witwatersrand strata in the Vredefort Structure, **(b)** Equal area projection of statistical master cone based on data in 1(a). Heavy broken line represents cone axis.

Figure 2 A complete shatter cone in metabasites.

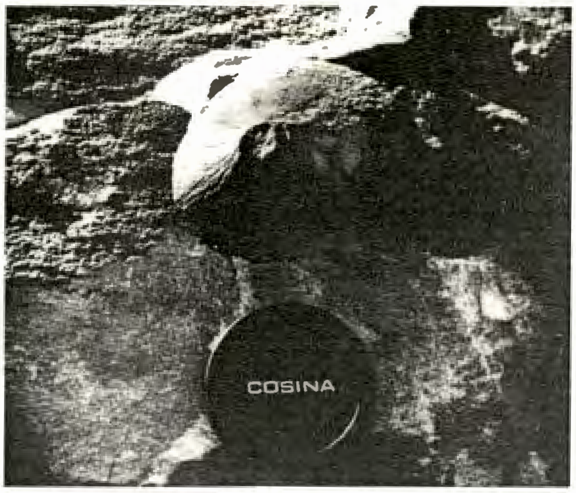

Figure 3 A perfect shatter cone *in situ* in Hospital Hill quartzites (north-eastern sector of the Vredefort Structure).

Figure 4 The shatter cone shown in Figure 3, after removal from its surroundings (scale in cm).

The specimen shown in Figure 2 is in the possession of A.A. Bisschoff whereas the specimen documented in Figure 4 has recently been discovered by the authors (in Hospital Hill quartzites from the north-eastern sector of the Vredefort Structure) and it is kept in the private collection of H.M. Albat. Researchers interested in seeing the specimen are welcome to make arrangements to inspect it.

References

Albat, H.M. (1988) Shatter cone/bedding interrelationship in the Vredefort Structure: evidence for meteorite impact? *S. Afr. J Geol.*, **91**, 106–113.

---- & Mayer, J.J. (1989). Megascopic planar shock fractures in the Vredefort Structure: a potential time marker? *Tectonophysics*, **162**, 265–276.

Dietz, R.S. (1959). Shatter cones in cryptoexplosion structures (meteorite impact?). *J. Geol.*, **67**, 496–505.

---- (1961). Vredefort ring structure - meteorite impact scar? *J. Geol.*, **69**, 499–516

---- (1963). Astroblemes, ancient meteorite impact structures on the Earth, 285–300. *In*: Middlehurst, B.M. & Kuiper, G.P. (Eds.), *The Moon, Meteorites and Comets*. Univ. Chicago Press, Chicago.

---- (1968). Shatter cones in cryptoexplosion structures, 267–285. *In*: French, B.M. & Short, N.M. (Eds.), *Shock Metamorphism of Natural Materials*. M.D. Mono Book Corp., Baltimore.

Hargraves, R.B. (1961). Shatter cones in the rocks of the Vredefort Ring. *Trans. geol. Soc. S. Afr.*, **64**, 147–154.

Manton, W.I. (1962). *The orientation and implication of shatter cones in the Vredefort Ring structure*. M.Sc. thesis (unpubl.), Univ. Witwatersrand, Johannesburg, 167 pp.

---- (1965). The orientation and origin of shatter cones in the Vredefort Ring. In: *Geological Problems in Lunar Research*. Ann. New York Akad. Sci., **123**, 1017–1049.

Nicolaysen, L.O. & Reimold, W.U. (1987). Shatter cones revisited (working paper). *Contributions to International Workshop on Cryptoexplosions and Catastrophes in the Geological Record, Parys, South Africa, Section N2.*

Simpson, C. (1981). Occurrence and orientation of shatter cones in Pretoria Group quartzites in the collar of the Vredefort 'Dome': impact origin precluded. *J. geophys. Res.*, **86**, 10701–10706.

CHAPTER 9

THE STRATIGRAPHY AND GEOLOGY OF THE CENTRAL RAND GROUP IN THE VREDEFORT AREA: AN EXPLANATION OF THE ACCOMPANYING GEOLOGICAL MAP (SCALE 1: 50 000)

THE STRATIGRAPHY AND GEOLOGY OF THE CENTRAL RAND GROUP IN THE VREDEFORT AREA: AN EXPLANATION OF THE ACCOMPANYING GEOLOGICAL MAP (SCALE 1: 50 000)

Introduction

The Central Rand Group of the Vredefort Structure forms two arcuate outcrop areas, northwest and northeast of Parys, separated by a zone of major faulting. These exposures of Central Rand strata in the Vredefort collar will be referred to as the western and eastern outcrop sectors respectively (Fig. 1). In the area, where it ~~where it~~ displaces the Central Rand strata, the system of major faults separating the two sectors is contained

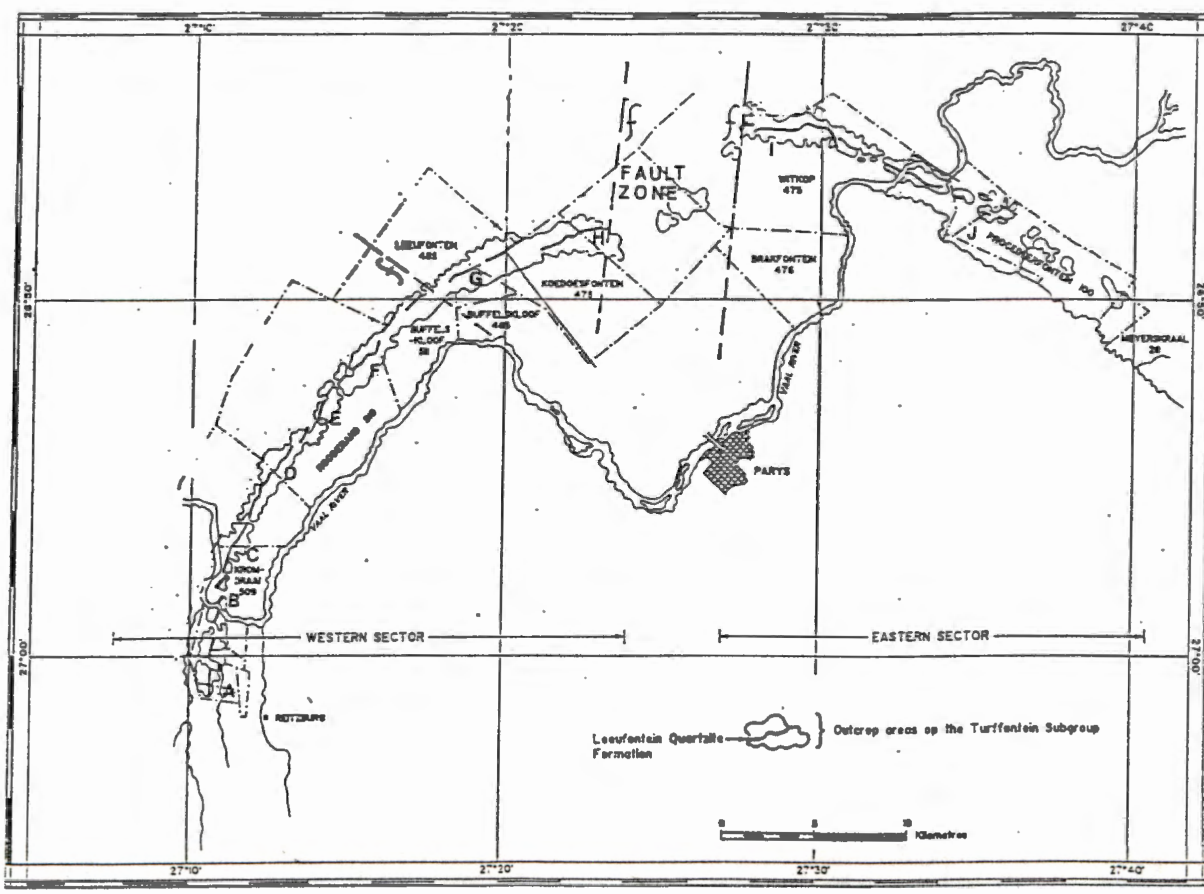

Fig. 1 Map showing major fault zone affecting Central Rand strata of Vredefort area. A to J are locations where pebble samples of Rooderand Formation were taken (For pebble data see Appendix XIII)

within a zone approximately 7 km wide. The fault system, which trends north-northeast, results in a total horizontal separation of 6,5 km along the fault zone between outcropping marker Formations in the Turffontein Subgroup of the two sectors. This major displacement is characterised by the progressive northward displacement (relative to the southwestern sector) of separate, large, more or less intact blocks of Central Rand strata in the fault zone. In the West Rand Group the horizontal separation of beds is small, but increases northwards moving through Central Rand Group into the Ventersdorp Supergroup. Further north, going up in the succession, the separation seems to diminish again to the extent that in the Pretoria Group of the Transvaal Sequence, the effect of the faulting is no longer visible. The fault system possibly postdates, but may perhaps be concurrent with, the upturning of the collar strata. Associated with the displacement is tectonic tilting which represents an anticlockwise rotation of the strata of the eastern sector with respect to those of the western sector; the observer facing east (refer to Chapter 4).

Numerous faults with much smaller horizontal separations (along their inferred trends) than that of the major system pervade the Central Rand strata of the two sectors. Most of these are dip faults with horizontal separations varying from a few metres to tens of metres. The largest of these occurs on the farm Koedoesfontein 478 and shows an apparent right lateral horizontal separation of marker beds in the Turffontein Subgroup of the order of 1km. The Johannesburg Subgroup is less affected by this fault. Its displacement, however, also decreases northwards (going up in the stratigraphy), so that the top contact of the Ventersdorp Supergroup, as shown on the map of Nel (1927), is not affected.

The strata of both outcrop sectors form important parts of the tract of country known as the Vredefort Mountain Land. To the south of Reitzburg, in the western sector, and to the southeast of the Vaal River towards Procedeerfontein 100, in the eastern sector, the Central Rand strata quickly lose topographic expression and level off to first become scattered inliers within the cover of younger deposits before they finally disappear under this cover further south. The cover comprises sandy soils which, in the Viljoenskroon area, are considered to be Tertiary aeolian deposits (Harmse, 1963), and Karoo sediments, which seldom crop out and, according to Nel (1927), belong to the "Coal Measures" (the middle portion of the Ecca Group). In the south Ecca sandstones are often found in boreholes and sometimes outcrop around pans. One such outcrop, for example, can be examined on the eastern side of the pan on the border between Mount Jackson 358 and De Put 289.

Although some Dwyka tillite is exposed in the bed of the Rhenoster River near Viljoenskroon, and tillite is known to occur in the Vierfontein area, no occurrences are known in the area where Witwatersrand rocks of the Vredefort Structure are overlain by

Karoo strata. However, scattered large, polished boulders, occasionally faceted, and accumulations of gravels comprising smaller clasts, some of which seem to be foreign to the area, have been noticed in the area where the Witwatersrand strata of the western sector start to disappear under the younger cover. Examples of such boulder and gravel occurrences are to be found on the farms Goedheid 886 and Hercules 800 in the western sector. Nel (1927), too, mentions similar occurrences on Morgenzon 799, Smaldeel 493 and other farms in the eastern arc. He expressed the opinion that these deposits might represent disintegrated till.

On the geological map of the Central Rand Group, presented in this thesis, Nel's (1927) limits for the Karoo cover have been adopted and are reproduced without any adjustment.

The stratigraphy and petrography of the Central Rand Group

On his geological map of the "Country around Vredefort" Nel (1927), following the subdivision of the Witwatersrand succession in the Johannesburg area, divided the Upper Witwatersrand strata (the Central Rand Group) of the Parys–Vredefort area into the Main Bird Series and the Kimberley Elsburg Series (presently known as the Johannesburg and Turffontein Subgroups). At that time he equated the single amygdaloidal lava formation, in the succession of the Vredefort area, with the Bird Amygdaloid of the Johannesburg succession. Later, when more data became available on the Witwatersrand succession in the Klerksdorp area, Nel et al. (1939) concluded that this volcanic formation could possibly be correlated with the Jeppestown amygdaloidal lava rather than with the Bird lava. The stratigraphic boundary between the Jeppestown and the Johannesburg Subgroups, in the Vredefort area, was therefore conceptually moved upward in the succession to the top of the uppermost persistent shale unit, formerly regarded by Nel (1927) to be the "Kimberley shale" (the Booysens Shale). With the stratigraphically highest persistent argillaceous formation in the succession being placed in the Jeppestown Subgroup, an "inconstant" shale horizon (Nel, 1927), further up in the sequence, came to be regarded as the equivalent of the Kimberley shale (or Booysens Shale).

On the geological map presented in this thesis the "inconstant shale" occurring approximately in the middle of the Central Rand Group, for which the name Vredefort Siltstone Formation is proposed, has likewise been accepted as a Formation dividing the Central Rand Group into the Johannesburg and Turffontein Subgroups. Outcrops of this Formation are limited to a single exposure of very fine-grained siltstone on Rooderand 510 in a cutting along the road from Potchefstroom to Venterskroon. Elsewhere a strike valley indicates its supposed presence. Except for the extreme eastern sector of the Vredefort collar, where it is absent, this valley serves as the petitioning feature which separates the two dominantly arenaceous Subgroups. It should be noted that in the area of Procedeerfontein 100, in the eastern sector, a section which covers about three quarters of the lower portion of the total Central Rand succession can be seen. In this exposure, along the banks of a southwestward-draining tributary of the Kromellenboog Spruit, no shale or siltstone is present, but an arenaceous succession, part of which comprises fine-grained immature quartzites, can be seen. Here the stratigraphic boundary between the two Subgroups has been placed at approximately at the top of the immature quartzite succession. The latter, which is regarded as a possible facies variation of the Vredefort Siltstone Formation, is overlain by a sequence of apparently more mature quartzites.

Formations of the Central Rand Subgroup in the Vredefort area

A lithostratigraphic subdivision of the Johannesburg Subgroup, into two Formations and the Turffontein Subgroup into five Formations, is proposed for the Vredefort area:

Subgroup	**Formation**	**Estimated max.thickness (metres)**
	Koedoesfontein Quartzite Formation	700
	Leeufontein Quartzite Formation	80
Turffontein	Witkop Quartzite Formation	330
Subgroup	Rooderand Conglomerate Formation	150
	Buffelskloof Quartzite Formation	440
Vredefort Siltstone Formation		70
	Nooitgedacht Quartzite Formation	840
Johannesburg		
Subgroup	Venterskroon Quartzite Formation	780

The Johannesburg Subgroup

The Johannesburg Subgroup comprises almost entirely arenaceous sediments with only sporadic occurrences of rudites. Its maximum thickness is estimated to be in the order of 1600 metres. The Jeppestown shale, at the base of this Subgroup, is exposed at only a few locations, notably in the vicinity of Reitzburg and Venterskroon in the western sector and on Procedeerfontein 100, in the eastern sector of the Vredefort collar. The upper contact of the Jeppestown shale (base of the Johannesburg Subgroup) is almost everywhere obscured by alluvium. On Procedeerfontein 100, there is an indication that the upper part of the so-called shale grades into siltstone which in turn is followed by a succession of coarse-grained, mature arenites with a thin basal conglomerate. This conglomerate possibly indicates an unconformity between the two Subgroups. In practice, however, the statigraphic boundary between the Jeppestown and Johannesburg Subgroups is normally inferred as lying close to the base of the hills comprising the more weathering-resistant Venterskroon Quartzite Formation.

The Venterskroon Quartzite Formation – This lowermost Formation of the Johannesburg Subgroup constitutes the ridges on the western, western and northern sides of a wide and prominent valley along the arcuate strike of less resistant strata near the top of the Jeppestown Subgroup. This specific valley is very noticeably followed by a stretch of the Vaal River in the Venterskroon area. The upper boundary between the Venterskroon Quartzite Formation and the overlying Nooitgedacht Formation is not entirely sharp. Differentiation of the two Formations has been based on a difference of topographic expression as revealed by stereoscopic studies of aerial photographs of the area. The Venterskroon Formation is generally highly weathering-resistant and its steeply dipping (overturned) strata give rise to prominent hills as, for example, in the vicinity of Venterskroon. In contrast, the overlying Nooitgedacht Formation is generally more weatherable and is topographically less prominent. Away from Venterskroon, towards Reitzburg, the topographic distinction between the two formations becomes more marked. In the vicinity of Reitzburg the Venterskroon Formation forms a single line of narrow quartzite hills. In the eastern sector of the collar arc, however, the topographic basis of distinction does not equally apply. Here the entire outcrop of the Johannesburg Subgroup forms low ground and the position of the boundary between the two formations is somewhat speculative.

In lithological terms the Venterskroon Formation can be described as a succession of light coloured, relatively mature arenites with a number of thin intercalated, texturally less mature, units. The latter are normally brown to red-stained on outcrop (sometimes fairly iron-rich) and weather more easily than their more mature counterparts. The grain size of the light coloured (often greenish) succession ranges from small pebbles to very fine sand. Occasionally thin clay-rich beds show up as result of their knotty texture, due to the development of metamorphic minerals.

Trough crossbedding (Fig. 2) and planar crossbeds are fairly abundant in the Venterskroon Formation. In the lower part of the succession lenticular small-pebble conglomerates, comprising mainly quartz clasts, can be traced for short strike lengths, as for example in the Venterskroon and Reitzburg areas. On the map, the locations of prominent conglomerate occurrences are indicated diagrammatically by single rows of small circles, following Nel, (1927). In all, the relatively immature character of the quartzites, their unimodal palaeocurrent distribution (Fig. 2), and the lenticular nature of the conglomerates point to a possible fluvial origin for the entire Formation.

Fig. 2 Rose diagram based on trough crossbedding showing palaeocurrent distribution for the Venterskroon Quartzite Formation (for data see Appendix XII)

The Nooitgedacht Quartzite Formation — As mentioned above, the Nooitgedacht Quartzite Formation is distinguished from the Venterskroon Quartzite Formation by quartzite beds which are generally somewhat more susceptible to weathering, giving rise to less prominent topography. The lower weathering resistance of the Nooitgedacht Formation may be ascribed to a possible high content of primary matrix. Aided by stereoscopic studies of aerial photographs of the area, a thin sequence of relatively weak strata, manifested as a narrow strike valley, has been chosen to demarcate the base of the Nooitgedacht Formation of the western sector of the collar. In the northeast this Formation outcrops poorly and its distinction is based solely on the relative position of its outcrops.

The Nooitgedacht Quartzite Formation contains mostly brown- to red-weathering quartzites. Although the strata are generally less resistant to weathering than those of the preceding Formation, some beds, composed of more resistant quartzite, do form conspicuous ridges. These probably comprise sandstones which, for some sedimentological reason, are texturally more mature. None of these ridges, however, is consistent enough to be used as a regional marker. This phenomenon possibly indicates that these units are lenticular in nature.

The arenite lithofacies in the Nooitgedacht Formation are highly variable and apparently constitute thin fining-upward sedimentary cycles. The presence of stacked fining-upward sedimentary cycles, the dominance of trough crossbeds with relatively wide transverse dimensions, and the development of lenticular conglomerates, possibly indicate a predominantly fluvial origin for the Nooitgedacht quartzites.

The upper boundary of the Nooitgedacht Formation, which is nowhere exposed, is taken within the partitioning valley which separates the two Sub Groups of the Central Rand Group.

The Turffontein Subgroup

Within the Turffontein Subgroup there are, similar to the Johannesburg Subgroup, no discrete argillaceous units and the entire succession is composed of arenaceous quartzites and occasional conglomerates. The arenites form prominent outcrops for the most part, except for the upper 300 to 400 metres of the 1700 metre thick succession, which comprises quartzites that are extremely weatherable. This upper sequence generally constitutes part of a pediment which forms the eastern, southeastern and southwestern slopes of a very wide valley, marking the contact between Witwatersrand and Ventersdorp rocks. The lower part of this pediment is covered by a thick blanket of sandy soil and bedrock is encountered only in boreholes or deep dongas.

The Buffelskloof Quartzite Formation – This Formation forms the basal unit of the Turffontein Subgroup in the Vredefort area. Its lower boundary is taken at the base of the stratigraphically higher side of the partitioning valley containing the Vredefort Siltstone Formation. Although some light coloured quartzite beds, which probably posses a relatively high degree of textural maturity, occur at intervals within the succession, the bulk of the Formation weathers to brown and buff colours due to the presence of fine clastic matrix with a variable content of iron oxides. Scattered pebbles occur throughout the Formation. Towards the top their frequency increases and lenticular thin conglomerates and layers of single pebbles are found. In total, the character of the succession point to it having been deposited under fluvial conditions. This tentative interpretation is again based on the presence of scattered pebbles, the lenticular nature of conglomerates and an estimated high clay matrix proportion indicated by the presence of plate silicates.

The upper boundary of the Buffelskloof Formation (the base of the overlying Rooderand Formation) is subjective, being placed at the base of the first conglomerate comprising more than one pebble layer. Because the individual conglomerate beds are lenticular and never persist for long strike lengths, the position of this stratigraphic boundary may vary up to several metres among different localities.

The Rooderand Conglomerate Formation – The Rooderand Conglomerate Formation comprises a succession of arenaceous and rudaceous sediments deposited during a period characterised by a marked increase in the supply of coarse clastic material to the basin. The thickness and frequency of the conglomerates, as well as the stratigraphic width of the conglomerate zone, are highly variable. As many as twenty (western sector) or as few as four to five (eastern sector) individual conglomerate beds may be contained in a zone, which varies in thickness from as little as 40 to over 150 metres. Individual conglomerates vary in thickness from a single layer of pebbles to beds up to 4 metres wide. The latter is rather the exception and conglomerate beds are in general less than a metre wide. Mean sizes of pebbles, which comprise mainly quartz varieties, are markedly larger in the western sector than in the eastern sector. The pebbles generally have coefficients of flatness and sphericty that exceed 45% and 0,65 respectively (Table 1 and Appendix XIII). According to Stratten (1974), such values indicate a fluvial environment in which the clasts were shaped.

Farm & No.	Symbol on Fig. 1	n	Pebble size mm	Pebble size phi	Pebble roundness	Pebble flatness	Pebble sphericity
Kleinfontein 1101	A	177	19.51	−4.23	0.76	58.10	0.76
Kromdraai S 509	B	251	19.60	−4.25	0.79	56.77	0.75
Kromdraai N 509	C	203	18.68	−4.16	0.80	57.25	0.75
Tygerfontein 488	D	406	19.77	−4.25	0.71	58.37	0.76
Rooderand S 510	E	399	21.65	−4.37	0.68	60.85	0.77
Rooderand N 488	F	418	23.72	−4.50	0.69	61.32	0.77
Leeufontein 485	G	517	17.94	−4.10	0.74	57.37	0.86
Buffelshoek 471	H	514	13.03	−3.68	0.64	58.01	0.77
Witkop 475	I	374	12.47	−3.62	0.64	57.93	0.76
Procedeerfontein 100	J	301	15.79	−3.95	0.79	59.93	0.77

Table 1 Table showing pebble size, –shape and -roundness parameters for the conglomerates of the Rooderand Conglomerate Formation (see Appendix XIII a to XIII j for data)

Towards the base of the Formation the interbedded quartzites show a number of thin layers with a knotty texture, due to the development of spherical aggregates of kyanite and andalusite (Bisschoff, 1969). This indicates a relatively high original clay content.

The lenticular nature of the conglomerate beds, their unimodal east to southwesterly palaeocurrent dispersal pattern (Chapter 4), pebble shape, and immaturity of the matrix sandstones and interbedded sandstones, undoubtedly indicate a fluvial, probably braided stream depositional environment for this Formation.

The upper boundary of the Rooderand Formation is taken, in the same way as the lower boundary, at the uppermost, prominent (thicker than one pebble layer) conglomerate.

The Witkop Quartzite Formation – As indicated in the foregoing section, the base of this Formation (the top of the Rooderand Formation) is placed on the upper contact of the uppermost prominent conglomerate bed in the sequence. Conglomerate beds, considered to be the uppermost prominent ones, may again occupy different stratigraphic levels at different localities. The position of the boundary between the Rooderand and Witkop Formations may therefore be slightly different in different areas.

Pebbles, and single pebble conglomerates, constituting the bases of fining-upward sedimentary cycles, occur throughout the Witkop sequence. The brown-weathering quartzites may contain as much as 18 percent matrix and the quartz grains of such beds are poorly sorted and poorly rounded (Table 2, Unit 1, and Fig. 7, Chapter 5). Analyses of trough crossbedding data of the Witkop Formation on the farms Leeuwfontein 485 and Witkop 475 (Chapter 5, Figs. 4 and 5, sequences A) show palaeocurrent distributions with strong single modes towards the south and southeast respectively. Overall, the entire sequence of the Witkop Formation exhibit most characteristics of sandy braided streams.

The Leeufontein Quartzite Formation – The transition from the Witkop Quartzite Formation to the Leeufontein Quartzite Formation is indicated by a visible upward colour change of the sediments and an absence of pebbles. From a particular stratigraphic level the brown coloured quartzites of the Witkop Formation give way to much lighter coloured strata, reflecting a markedly higher degree of textural maturity. Some quartzite beds in the Leeufontein Formation may exhibit a very high degree of textural maturity; as high as 98 percent quartz framework grains. The grains of such beds also show a high degree of roundness (See Unit 3, Table 2 and Fig. 11, Chapter 5).

A distinctive feature of the Leeufontein Formation, not normally well developed in any other Formation of the Central Rand strata, is the presence of plane-bedded units (Fig. 10, Chapter 5). Convolute bedding and recumbent foresets abound in the Leeufontein Formation and have been observed in practically all areas where this Formation has been mapped.

Both trough crossbedding and planar crossbeds are common primary sedimentary structures found in the Leeufontein Formation. Current and oscillation ripples, however, are also present. Going eastwards, along the outcrop of the eastern sector, the ripple structures seem to increase in frequency of occurrence, while trough crossbeds appear to decrease in transverse dimension from half a metre to as narrow as 10 to 15 cm, with amplitudes of less than 2 cm. Hummocky cross stratification was observed at one locality on the farm Leeuwfontein 485 (Fig. 13, Chapter 5). Palaeocurrent distribution patterns of trough crossbeds in the Leeufontein Formation show strong eastward-directed modes in the southwest but moving northeastwards along the arcuate outcrop they gradually become more southeasterly. The central outcrops of this Formation in the Vredefort collar, however, show bi- and polymodal palaeocurrent distributions with prominent modes directed towards the northwest and southeast (See Fig. 3, Chapter 4).

The top of the Leeufontein Formation is marked by a sharp and distinct break in the lithological characteristics of the quartzites, changing in colour from nearly white to reddish brown. In the eastern sector the Formation is capped by a very conspicuous fine-grained immature sandstone which, apparently due to its lack of internal structure, exhibits weathering characteristics typical of mudstone (see analysis of Unit 4, Table 2, Chapter 5). This relatively thin bed is traceable for some distance to the east of Witkop 475 in the eastern sector, whereafter it apparently disappears, along with the general deterioration of outcrops of Turffontein strata before these become completely covered by Karoo sediments. It is possible that this unique fine-grained unit may also be present in the western sector. However, in this region the upper contact of the Leeufontein Formation is most often obscured by a cover of scree which accumulates at the base of the topographical scarp, formed by the comparatively weathering-resistant overturned beds of latter Formation.

The occurrence of poly- and bimodal palaeocurrent distributions, the high degree of textural maturity and the occurrence of typical shallow marine sedimentary structures in the Leeufontein Formation point to a possible shallow marine origin for at least the central section of its entire arcuate outcrop of this Formation (refer to Chapter 5).

The Koedoesfontein Quartzite Formation – The Koedoesfontein Formation constitutes the uppermost lithostratigraphic unit of the Turffontein Subgroup and, as pointed out in the foregoing sections, its base is marked by a distinct break in the textural character of the quartzitic beds. Above the contact, the lower part of the Koedoesfontein Formation shows an abrupt upward increase in grain-size and a concomitant decrease in textural maturity (Unit 5, Table 2, Chapter 5). Occasional small, scattered pebbles are found and, higher up in the sequence, inconsistent conglomerate beds (as on Rooderand 510 – see geological map) may sporadically be developed.

The upper part of this Formation, as indicated earlier on, forms no outcrops. The contact between the Witwatersrand and Ventersdorp Supergroup is mostly covered by alluvium and is not directly observable. Nel *et al.* (1939), however, regard the contact to be more or less conformable. Only one occurrence of conglomerate, near the base of the lavas, is known from the western sector, i.e. on Scotts Valley 384 and Tweelingkop 388. In this area the Alberton Formation, at the base of the Ventersdorp Supergroup is also prominently developed.

Intrusive rocks

In terms of their outcrop areas, intrusive rocks constitute an insignificant part within the overall outcrop of the Central Rand Group. The most important of these intrusives are epidiorites associated with the outpouring of the Ventersdorp lavas. They generally form thin dykes but a sill of epidiorite may, for most part, be present in the strike valley separating the Johannesburg and Turffontein Subgroups. Normally no bedrock is exposed in this valley, but on Kromdraai 509 and Elandslaagte 28, just south of the Vaal River, in the western sector, there are indications that a sill is present (Nel, 1927). According to A.A. Bisschoff (personal communication) epidiorite has also been found in a borehole within this valley on Buffelskloof 511. He is of opinion that the sill has served as a reservoir, during Ventersdorp times, supplying magma to numerous narrow fissures (now thin epidiorite dykes) from which the Ventersdorp lava issued. These thin dykes appear mainly on the stratigraphic higher side of the valley i.e. in Turffontein strata and are abundantly developed on Rooderand 510, Leeuwfontein 485 and Koedoesfontein 478.

Very small exposures of alkali granite (indicated on the geological map) are found in a spruit and on the side of an isolated hill formed by Johannesburg Subgroup strata, east of the Potchefstroom-Parys road on Koedoesfontein 478. Other dyke-like intrusions (not differentiated on the map) of lamprophyric nature, forming part of a complex of mafic intrusions (Bisschoff, 1969), also occur in this vicinity, but outcrops are rather poor, and their age relationships remain obscure.

The youngest phase of igneous intrusion in the area is the so-called Wonderfontein dyke which is part of the "Pilanesberg dyke swarm". This persistent syenite dyke can be followed almost from its origin, the Pilanesberg ring complex, to where it reaches into the collar of Witwatersrand strata of the Vredefort Structure before apparently disappearing on Buffelshoek 471. Although it forms no prominent outcrops further south, it is possible that the dyke continues in this direction to at least the boundary between Buffelshoek 472 and Koedoesfontein 478. Here some odd small boulders of this dyke are found to the west of the Potchefstroom-Parys road, directly on the boundary between the mentioned farms. This may indicate its possible presence at this particular point.

References

Bisschoff, A.A. (1969). *The petrology of the igneous and metamorphic rocks in the Vredefort Dome and adjoining parts of the Potchefstroom Syncline.* D.Sc. thesis (unpubl.) Univ. Pretoria, 243pp.

Harmse, H.J. von M. (1963). *The sedimentary petrology of the aeolian sands in the north-western Orange Free State.* M.Sc. thesis (unpublished), Potchefstroom University for C.H.E., 101pp.

Nel, L.T. (1927). The geology of the country around Vredefort – An explanation of the geological map. *Spec. Publ. geol. Surv. S. Afr.*, **6**, 134pp.

Nel, L.T., Truter, F.C., Willemse, J. and Mellor, E.T. (1939). *The geology of the country around Potchefstroom and Klerksdorp.* Expl. Sheet 61 (Potchefstroom), geol. Surv. S. Afr., Dept. Min., Govt. Printer, Pretoria 156pp.

Stratten, T. (1974). Notes on the application of shape parameters to differentiate between beach and river deposits in Southern Africa. *Trans. geol. Soc. S. Afr.*, 77, 59–64.

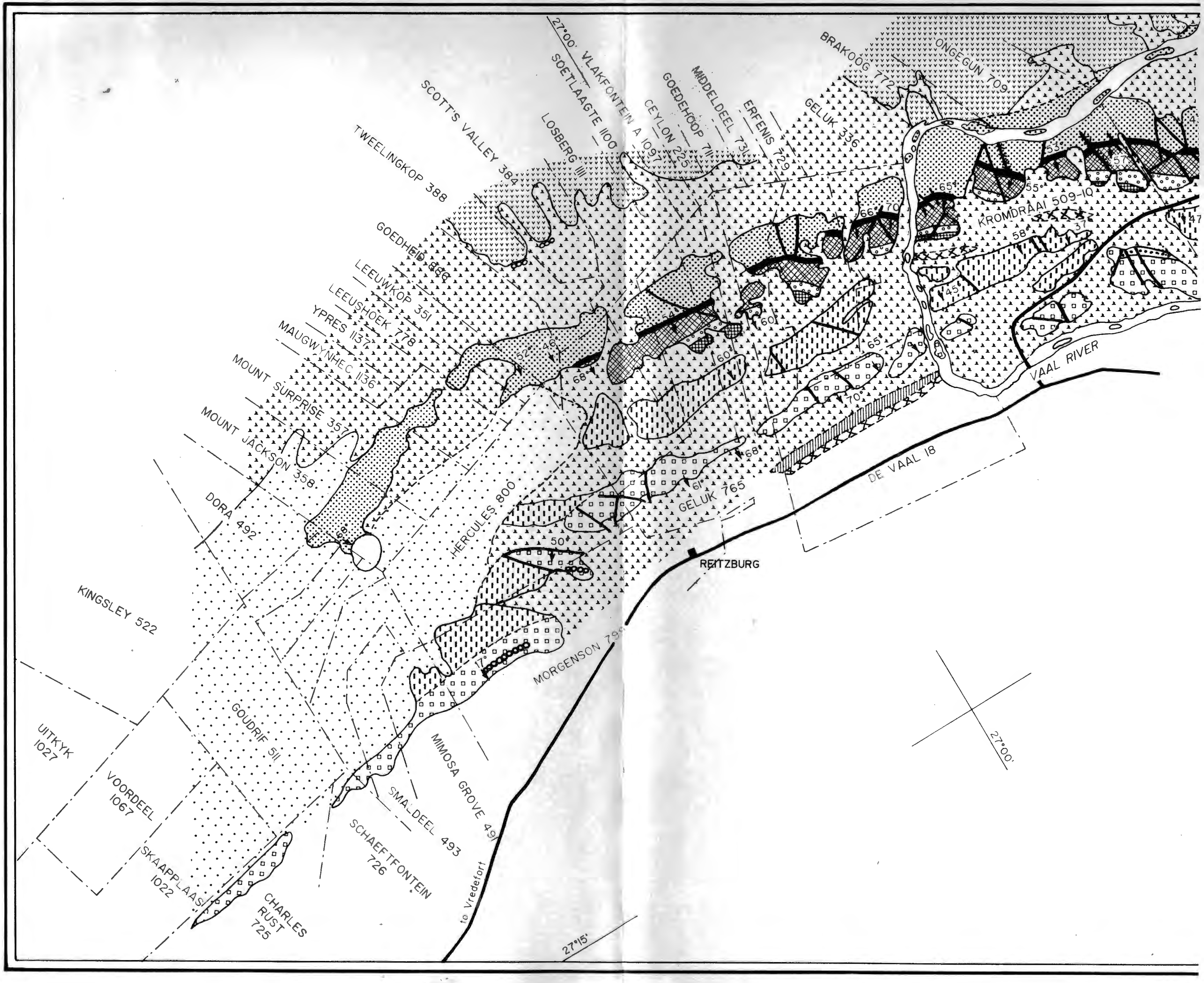

27°00'
VLAKFONTEIN A 1097
SOETLAAGTE 1100
SCOTT'S VALLEY 384
LOSBERG III
CEYLON 225
GOEDEHOOP 711
MIDDELDEEL 731
ERFENIS 729
GELUK 336
BRAKOOG 772
ONGEGUN 709
TWEELINGKOP 388
GOEDHEID 886
LEEUWKOP 351
LEEUSHOEK 778
YPRES 1137
MAUGWYNHEC 1136
MOUNT SURPRISE 357
MOUNT JACKSON 358
DORA 492
HERCULES 800
GELUK 765
KROMDRAAI 509-IQ
VAAL RIVER
DE VAAL 18
REITZBURG
KINGSLEY 522
MORGENSON 799
UITKYK 1027
VOORDEEL 1067
GOUDRIF 511
MIMOSA GROVE 491
SMALDEEL 493
SKAAPPLAAS 1022
SCHAEFTFONTEIN 726
CHARLES RUST 725
to Vredefort
27°15'
27°00'

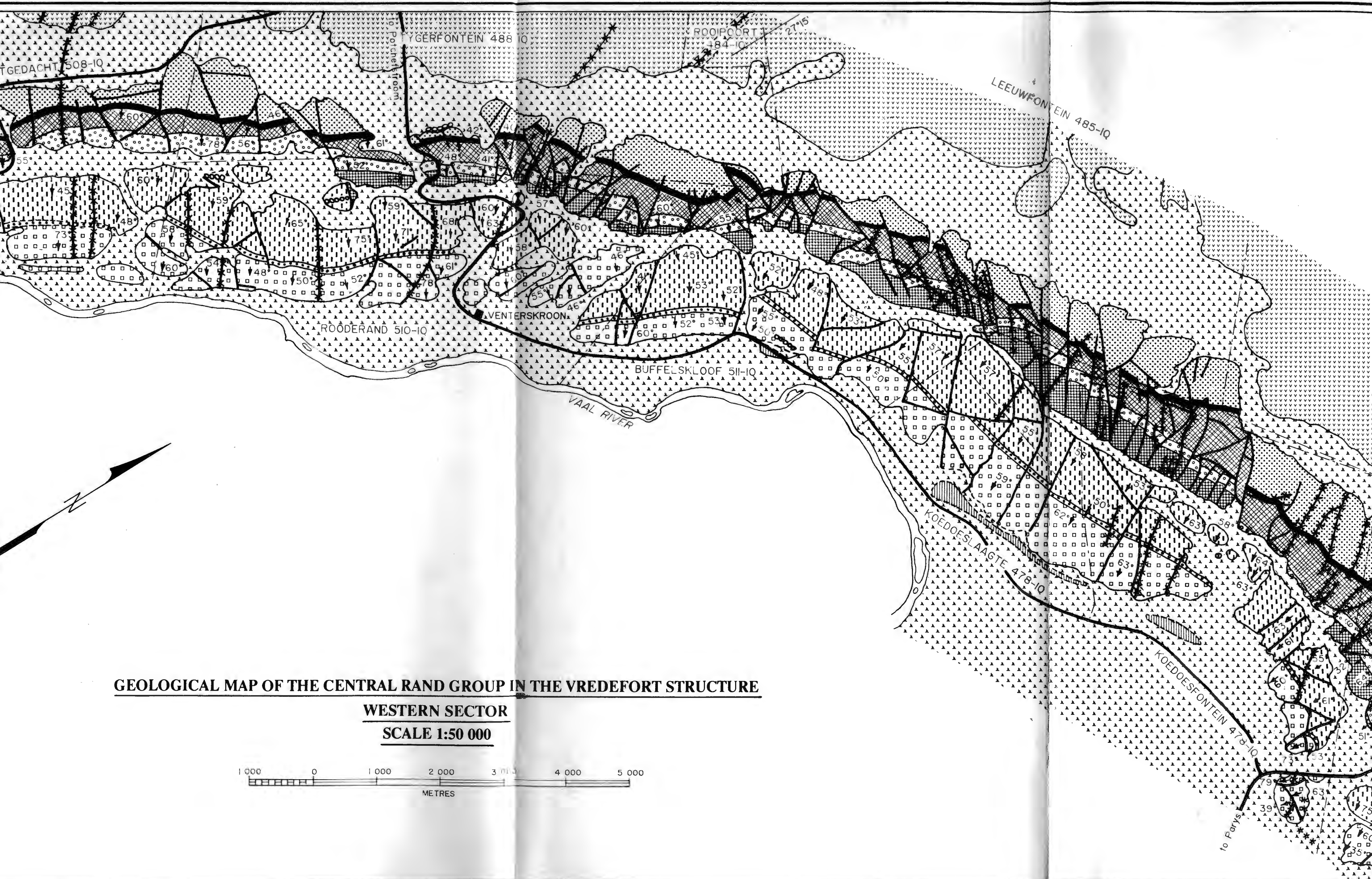

GEOLOGICAL MAP OF THE CENTRAL RAND GROUP IN THE VREDEFORT STRUCTURE

WESTERN SECTOR

SCALE 1:50 000

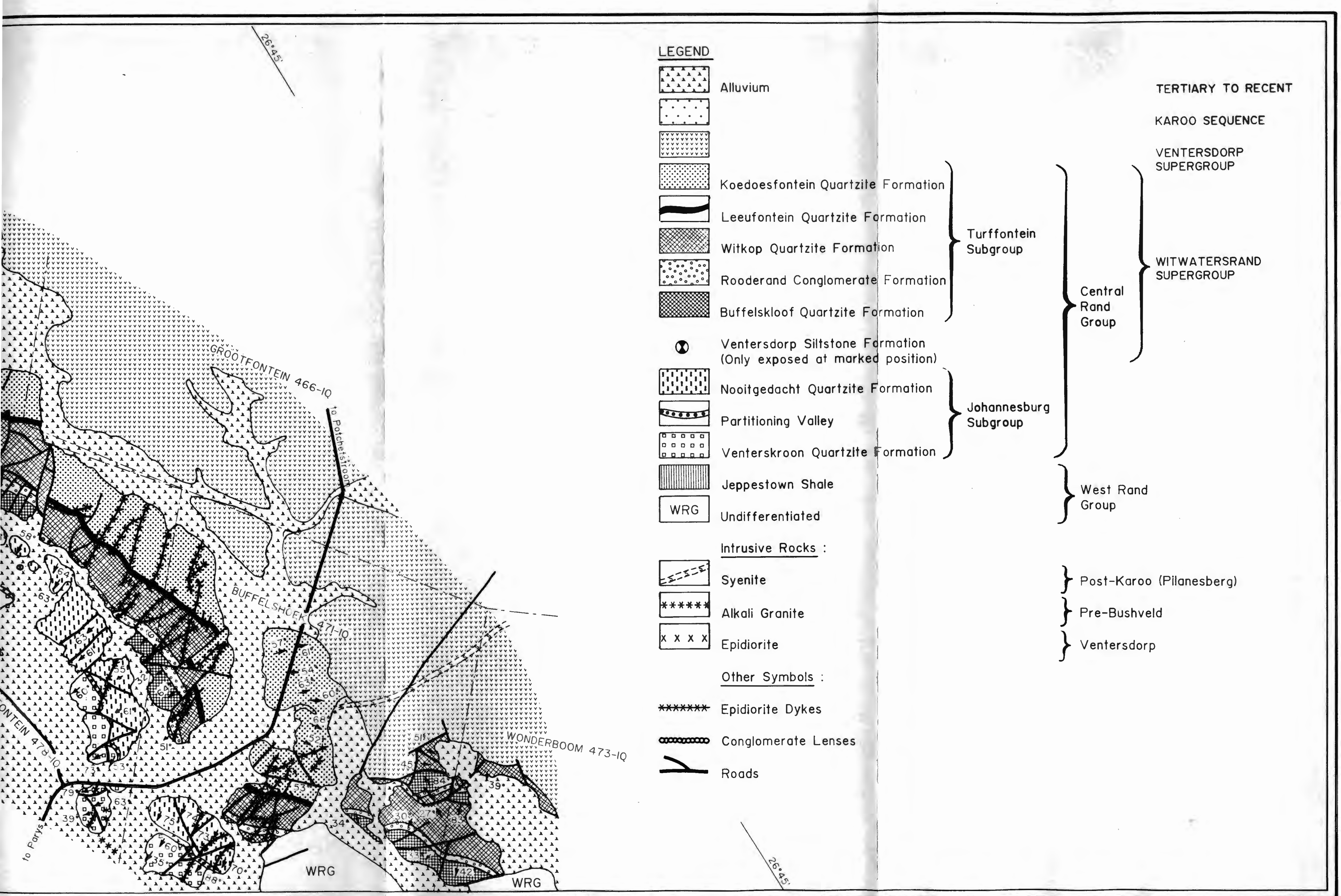

26°45'
GROOTFONTEIN 466-IQ
to Potchefstroom
BUFFELSHOEK 471-IQ
WONDERBOOM 473-IQ
to Parys
WRG
WRG
26°45'
LEGEND
Alluvium
TERTIARY TO RECENT
KAROO SEQUENCE
VENTERSDORP SUPERGROUP
Koedoesfontein Quartzite Formation
Leeufontein Quartzite Formation
Witkop Quartzite Formation
Rooderand Conglomerate Formation
Buffelskloof Quartzite Formation
Turffontein Subgroup
Ventersdorp Siltstone Formation (Only exposed at marked position)
Nooitgedacht Quartzite Formation
Partitioning Valley
Venterskroon Quartzite Formation
Johannesburg Subgroup
Central Rand Group
WITWATERSRAND SUPERGROUP
Jeppestown Shale
WRG
Undifferentiated
West Rand Group
Intrusive Rocks :
Syenite
Post-Karoo (Pilanesberg)
Alkali Granite
Pre-Bushveld
x x x x
Epidiorite
Ventersdorp
Other Symbols :
Epidiorite Dykes
Conglomerate Lenses
Roads

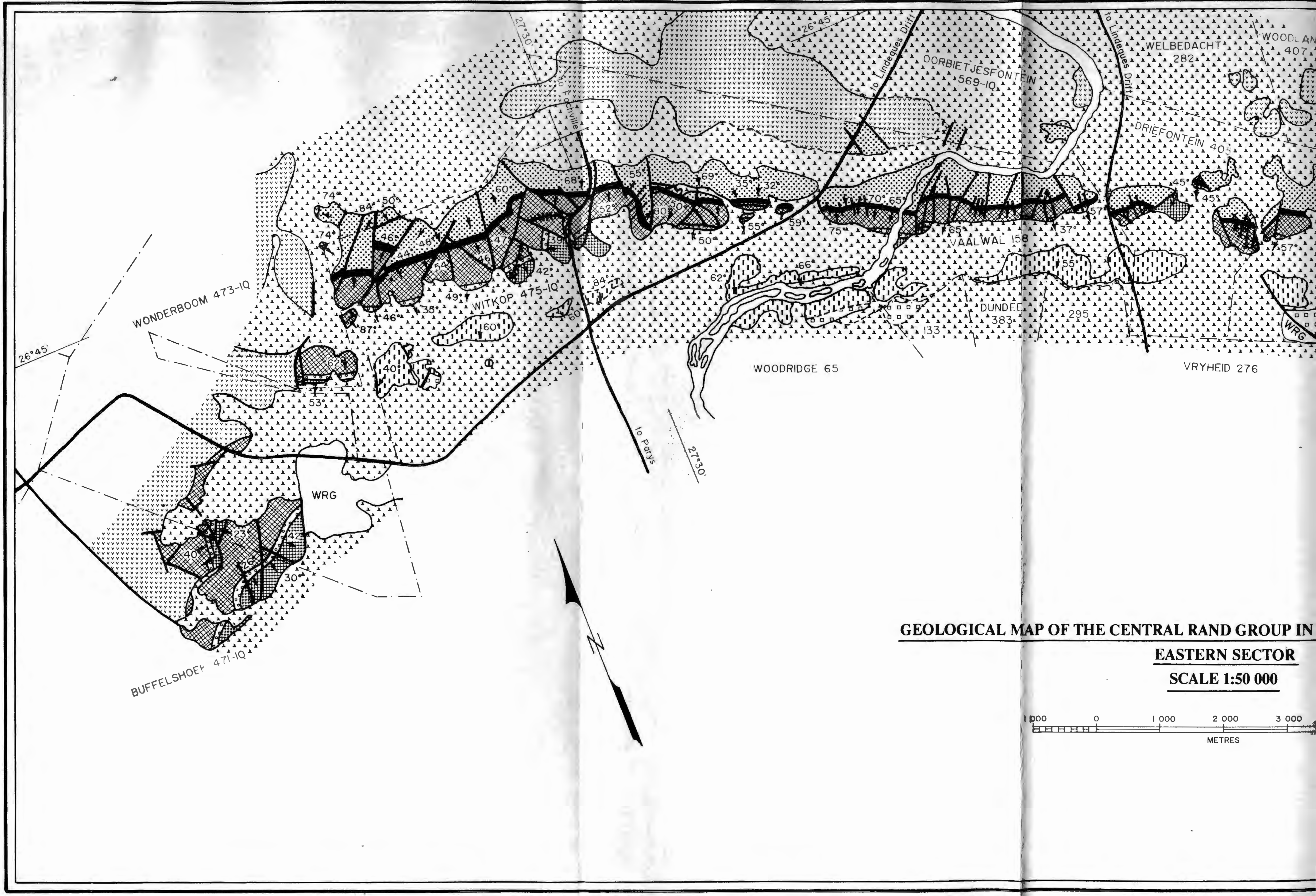

GEOLOGICAL MAP OF THE CENTRAL RAND GROUP IN

EASTERN SECTOR

SCALE 1:50 000

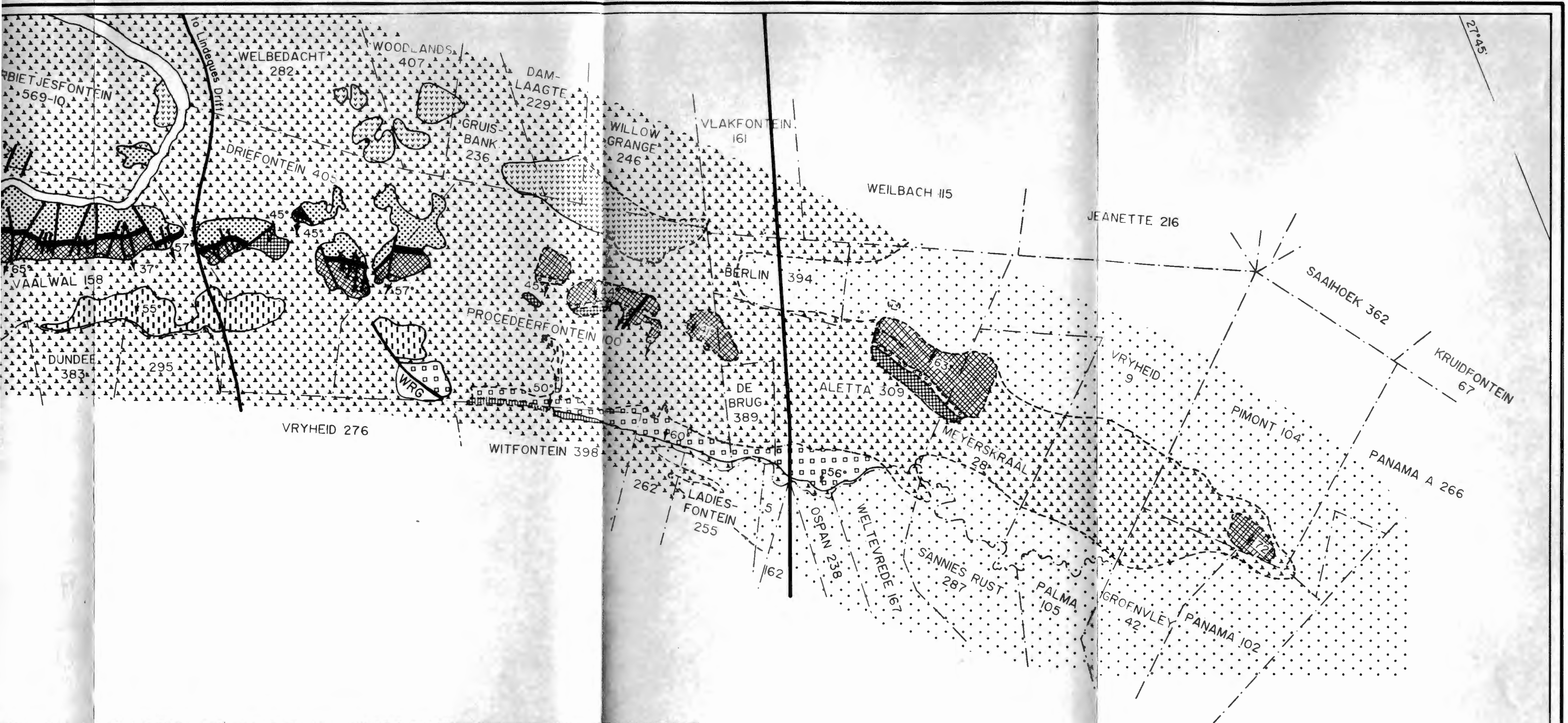

LOGICAL MAP OF THE CENTRAL RAND GROUP IN THE VREDEFORT STRUCTURE

EASTERN SECTOR

SCALE 1:50 000

1 000 0 1 000 2 000 3 000 4 000 5 000
METRES

CHAPTER 10

SUMMARY AND CONCLUSIONS

SUMMARY AND CONCLUSIONS

The papers comprising the body of this thesis, although apparently divergent, are strung together by a common objective. This is to contribute towards a better understanding of one of the most intriguing and fascinating geological enigmas in South Africa: the Vredefort Structure. The aspects addressed fall into the following categories: (i) reconstruction of scenarios of Witwatersrand sedimentation and tectonics with a view to unraveling the depositional history of this part of the Witwatersrand basin (ii) verification or invalidation of the apriori bases of some of the early endogenous hypotheses for the origin of the Vredefort Structure; (iii) the development of a tectonic model for the diastrophism of the Vredefort area; (iv) establishment and extension of a scheme for the relative dating of events, particularly with respect to the main event: the upfolding of the collar strata; and (v) mapping and stratigraphic subdivision of the hitherto undifferentiated Johannesburg and Turffontein Subgroups of the Witwatersrand Succession.

Sedimentological and structural evidence against a tectonically controlled diapiric origin for the Vredefort Structure

Some of the early endogenous hypotheses for the Vredefort Structure suggest that the basement granite of this Structure constituted an incipient dome in the area even before the commencement of sedimentation (Willemse, 1937; Brock and Pretorius, 1964). This "dome" was predestined to rise either isostatically due to the progressive sediment loading of the adjacent area or by virtue of an upthrusting pressure, caused by a hidden intrusive body below the granite hub (Hall and Molengraaff, 1925; Maree, 1944), or by a combination of the aforementioned processes (Bisschoff, 1969). The results of the palaeocurrent study of the upper Hospital Hill quartzite (Mayer and Albat, 1988, Chapter 2) negates the existence of any incipient dome for this area in primeval Witwatersrand times. This is also verified by the consistent axial pattern of small-scale fold structures in the Contorted Bed (Mayer and Albat, 1990, Chapter 3).

There is again no indication of doming towards the closing stages of Witwatersrand sedimentation, as verified by palaeocurrent patterns in Formations of the Turffontein Subgroup (Mayer and Els, in press, Chapter 4; Els and Mayer, in press, Chapter 5). It can therefore decisively be concluded that the Vredefort Structure does not represent a rudimentary dome which evolved at the slow rate associated with isostatic- or orogenic-related forces.

Witwatersrand palaeo-environments

The scenario revealed by palaeocurrent patterns during Hospital Hill times is that of an open shelf marine environment with a low gradient and consistent slope. The palaeo continental shelf was probably connected to the open ocean to the east-southeast, with a source area lying to the west-northwest. This area apparently remained a tectonically stable continental edge for the entire duration of Witwatersrand deposition. Throughout the early history of Witwatersrand sedimentation the depositional area was subjected to transgressions contraposed by regressions of the shoreline, giving rise to alternating deep and shallow-water deposits. Gradually the cumulative effect of tectonic cycles of uplift gained at the expense of tectonically quieter periods, characterised by transgression. The position of the fluctuating shoreline, therefore, migrated towards the east or southeast resulting in domination in the stratigraphic column of braided stream fluvial sequences after the close of the West Rand Period. Although the sporadic influx of gravels indicates steep gradients at the beginning of Johannesburg Subgroup times, the shoreline could not have been too distant. This is borne out by the presence of a thin sequence of shallow marine facies, probably deposited during successive transgressive and progradational episodes (Els and Mayer, in press, Chapter 5) during mid-Turffontein times. An implication of this finding is the probable occurrence of marine Turffontein facies, absent in the northwestern portion of the preserved Witwatersrand basin, in the southeastern regions.

Nature of the Vredefort Structure

The results of an initial reconstruction of palaeocurrent dispersal patterns for Turffontein strata (Mayer and Els, in press, Chapter 4) necessitated a critical reconsideration of the technique of reconstructing palaeocurrents or other palaeo-directional vectors for the Vredefort area predating the formation of the Vredefort Structure. The conventional technique involves the rotation of the so-called "over-folded" collar strata of the Vredefort Structure, about their present tectonic strikes, to the horizontal. Consideration of the likely tectonic model for the Vredefort Structure led to the realisation that the collar of the Vredefort Structure had probably never been folded over, but only folded to the vertical. If the concept that diapirism took place at a crustal depth of 13 to 16 km below the surface of the earth (thickness of the cover of Ventersdorp and Transvaal strata) is accepted, it would be impossible for such deeply buried strata to become overturned by the vertical "punching action" of a granite plug. The apparent overfolding of the northwestern part of the Vredefort Structure must therefore be ascribed to subsequent tilting to the northwest of the original diapir. This model is empirically supported by an equal area plot of a large number of bedding poles of Turffontein strata, which shows that the axis of the Structure verges at 39^0 towards 136^0. From this projection it is also inferred that major faulting of the rim of the original diapiric structure was responsible for additional tilting of the northeastern sector (Mayer and Els, in press, Chapter 4). It is proposed that tilting of the Structure, and the additional tilting of a sector of the rim by faulting, followed after the main event of diapirism of the Witwatersrand strata by the granite-gneiss core.

Origin of the Vredefort Structure and the relative dating of geological events

The bolide hypothesis is accepted in this thesis as the most feasible explanation for the Vredefort Structure. According to this hypothesis an impact on the surface of the earth was responsible for the diapiric uprising of the basement and the consequent upfolding of the collar strata of the Vredefort Structure. Shatter cones are viewed as the manifestation of the downward-transmitted shock wave resulting from an impact, and pseudotachylite as the product of the diastrophic rebound shock. By implication of the aforegoing hypothesis shatter cones, if superimposed thereupon, may be used to identify any rock type or structural element that predate the Vredefort Event. Shatter cones were recognised by Nel (1927), but their value as a possible indicator of a specific "moment" in geological time, was only realised when the attention was drawn to these structures by Dietz (1961) and Hargraves (1961), who pointed them out as possible indicators of impact shock. The Vredefort collar strata, in particular the quartzites, are pervaded by a system of densely spaced fracture surfaces which have been shown to be geometrically related to shatter cones (Albat and Mayer, 1988, Chapter 6). These fracture surfaces (or s-surfaces) can thus be regarded as shock structures which resulted, in the same way as shatter cones, from the passage of a shock wave through the strata at the moment of impact of an extra-terrestrial body on the surface of the earth. The s-surfaces may therefore serve as an "extension" of shatter cones, to be used as a potential time marker to relatively date various structures and structural elements such as joints and foliations in the absence of shatter cone sectors (Albat and Mayer, 1987, Chapter 7).

Central Rand geology and stratigraphy

Although more than 60 years have lapsed since publication of Nel's (1927) map of the "Country around Vredefort", this has remained the sole "official" map of the area in question. While this map shows magnificent details of the Hospital Hill, Government and Jeppestown Subgroups, little attention was paid to the stratigraphy of the economically-important Central Rand Group. Since publication of Nel's (1927) map, stratigraphic differentiation of this group has not progressed beyond the rank of subgroup. The lack of an acceptable stratigraphic column for the Central Rand Group and the want of a suitable accompanying map have had several serious negative implications for gold exploration companies and researchers of the Witwatersrand Supergroup.

In this thesis the first strides towards rectifying the mentioned deficiencies are taken. Firstly, a workable lithostratigraphical subdivision for the Central Rand Group is proposed. This proposed stratigraphic column is by no means seen as an ultimate and will (hopefully) be replaced by a chronostratigraphic subdivision, once the sedimentology of the Central Rand Group in the Vredefort area has been studied in sufficient detail, supposedly through the application of Sequence Stratigraphy. Meanwhile the proposed lithostratigraphic column could serve as an important communication tool among Witwatersrand researchers, while the lithological descriptions of the proposed Formations should provide useful guidance to newcomers to the Central Rand Group in the Vredefort Structure.

The map of the Vredefort Structure contained in this thesis, too, is not viewed as necessarily a final product, as future workers in the area may require more detailed versions of their particular areas of interest. The map would nevertheless serve as a guide to the most important outcrops in the area and may save many days of search and preliminary mapping.

REFERENCES

Albat, H.M. & Mayer, J.J. (1987). Interrelationships of structural elements in the upper quartzite member of the Hospital Hill Subgroup in the southwestern sector of the Vredefort Structure (poster presentation). *Contributions to International Workshop on Cryptoexplosions and Catastrophes in the Geological Record, Parys, South Africa.*

Albat, H.M. & Mayer, J.J. (1989). Megascopic planar shock fractures in the Vredefort Structure: a potential time marker? *Tectonophysics*, **162**, 265–276.

Albat, H.M. & Mayer, J.J. (1990). Shatter cones in Vredefort rocks – imagination or reality ? *S. Afr. J. Geol.*, **93**, 547-548.

Bisschoff, A.A. (1969). *The petrology of the igneous and metamorphic rocks in the Vredefort Dome and adjoining parts of the Potchefstroom Syncline.* D.Sc. thesis (unpubl.) Univ. Pretoria, 243pp.

Brock, B.B. and Pretorius, D.A. (1964). Rand basin sedimentation and tectonics, pp.549-599. In: S.H. Haughton, Ed., *The Geology of some Ore Deposits of Southern Africa*, **1**, Geol. Soc. S.Afr., Johannesburg, 625pp.

Dietz, R.S. (1961). Vredefort ring-structure – Meteorite impact scar? *J. Geol.*, **69**, 499–516.

Els, B.G. and Mayer, J.J. (1992, in press). Transgressive and progradational beach and nearshore facies in the late Archaean Turffontein Subgroup of the Witwatersrand Supergroup, Vredefort Area, South Africa. *S. Afr. J. Geol.*, **95**.

Hall, A.L. & Molengraaff, G.A.F. (1925). The Vredefort Mountain Land in southern Transvaal and northern Orange Free State. *Verh. K. Akad. Wet.*, **24**, 1–183.

Hargraves, R.B. (1961). Shatter cones in the rocks of the Vredefort Ring. *Trans. geol. Soc. S. Afr.*, **64**, 147–154.

Maree, B.D. (1944). The Vredefort Structure as revealed by a gravimetric survey. *Trans. geol. Soc. S. Afr.*, **47**, 183–196.

Mayer, J.J. & Albat, H.M. (1988). The tectono-sedimentary setting of the area of the Vredefort Structure during deposition of the upper quartzite member of the Hospital Hill Subgroup. *S. Afr. J. Geol.*, **91**, 239–247.

Mayer, J.J. & Albat, H.M. (1990). An appraisal of the significance of small-scale fold structures in the contorted bed of the area of the Vredefort Structure. *S. Afr. J. Geol.*, **93**, 311–317.

Mayer, J.J. & Els, B.G. (1992, in press). The reconstruction of palaeodispersal patterns for Turffontein strata in the Vredefort Structure in relation to a tectonic model for the area. *S. Afr. J. Geol.*, **95**.

Nel, L.T. (1927). The geology of the country around Vredefort – An explanation of the geological map. *Spec. Publ. geol. Surv. S. Afr.*, **6**, 134pp.

Willemse, J. (1937). On the Old granite of the Vredefort region and some of its associated rocks. *Trans. geol. S. Afr.*, **40**, 43–119.

APPENDICES

Appendix (I)

TROUGH CROSSBEDDING DATA UPPER HOSPITAL HILL QUARTZITE

* See Addendum Chapt. 2
u = direction of palaeo-flow on dipping strata is updip

LOCALITY	CROSSBEDDING TROUGH AXIS			STRATA TECTONIC DIP		*CORRECTED PAL. FLOW DIR.	
	Plunge Az	Plunge	Flow dir.	Dip	Dip Az	Az	Vector means
Leeuwdoorns 350 Southwestern study area	52	66	u	69	81	170	
	58	64	u	66	81	168	
	76	70	u	70	85	159	
	42	50	u	60	84	180	
	35	41	u	60	94	188	
	53	46	u	48	74	189	
	49	33	u	44	97	199	
	75	39	u	40	90	206	
	79	39	u	40	92	207	
	82	42	u	43	94	203	
	71	33	u	40	110	211	
	74	40	u	43	98	204	
	65	37	u	43	100	204	
	85	40	u	42	108	207	162
	35	22	u	42	99	198	
	130	58	u	58	122	142	
	112	48	u	50	132	159	
	238	35	u	40	92	107	
	235	32	u	41	98	109	
	239	36	u	40	89	106	
	225	34	u	44	90	100	
	225	35	u	44	89	100	
	230	33	u	40	88	104	
	225	34	u	48	97	205	
	238	39	u	50	105	106	
	230	38	u	52	103	106	
	239	33	u	55	122	84	

LOCALITY	CROSSBEDDING TROUGH AXIS			STRATA TECTONIC DIP		*CORRECTED PAL. FLOW DIR.	
	Plunge Az	Plunge	Flow dir.	Dip	Dip Az	Az	Vector means
Commandonek 1185 Northwestern study area	88	54	u	72	115	170	138
	292	72	u	72	102	127	
	95	72	u	72	105	152	
	64	67	u	72	105	162	
	305	80	u	80	118	133	
Brakfontein 476 Northern study area	124	68	u	72	162	133	105
	137	64	u	66	161	123	
	182	65	u	66	161	109	
	214	55	u	64	168	93	
	205	62	u	67	167	102	
	217	50	u	60	171	86	
	166	60	u	60	171	102	
	185	62	u	63	171	102	
	195	76	u	79	155	121	
	228	75	u	77	167	118	
	190	63	u	65	164	104	
	215	59	u	72	158	101	
	174	76	u	76	166	122	
	226	40	u	62	162	76	
	100	74	u	76	164	140	
	187	63	u	65	161	105	
	214	87	u	88	162	132	
	204	65	u	72	159	108	
	227	74	u	82	166	117	
	230	46	u	72	160	87	
	206	65	u	70	166	106	
	215	69	u	78	159	112	
	225	63	u	78	160	106	
	224	77	u	78	161	120	
	215	44	u	51	205	78	
	213	44	u	45	202	77	

Appendix (II)

TROUGH CROSSBEDDING DATA LEEUFONTEIN QUARTZITE FORMATION ROODERAND CONGLOMERATE FORMATION RECORDED IN NORTHWESTERN SECTOR

Legend: L= Leeufontein Formation R= Rooderand Formation
For Locality numbers See Chapt. 4 Fig. 2

Palaeocurrent vectors corrected according to conventional method [See Chapt. 4]
* Palaeocurrent vectors corrected according to tectonic model [See chapt. 4]
u= direction of palaeo-flow on dipping strata is up dip
d= direction of palaeo-flow on dipping strata is down dip

LOCALITY	CROSSBEDDING TROUGH AXIS			STRATA TECTONIC		PALAEOCURRENT VECTORS CORRECTED	
	Plunge dir.	Plunge	Flow dir.	Dip	Dip dir	#Az	*Az
L1	132	38	u	44	95	67	110
	128	38	u	46	88	57	108
	170	7	u	55	85	9	50
	172	3	u	54	84	10	44
	165	13	u	45	88	26	66
	160	21	u	48	90	33	75
	180	0	u	44	90	1	51
L2	160	27	u	47	98	47	85
	145	32	u	45	94	57	95
	157	35	u	51	101	58	91
	156	26	u	47	93	42	84
	162	17	u	44	91	28	73
	144	38	u	51	94	50	97
	135	43	u	51	94	53	107
	152	26	u	45	91	44	86
	182	9	u	45	101	38	60
L3	145	60	u	66	105	110	110
	150	59	u	65	110	86	111
L4	188	20	u	46	118	57	74
	170	36	u	55	110	63	88
	188	14	u	51	110	50	62
L5	190	40	u	48	150	122	104

LOCALITY	CROSSBEDDING TROUGH AXIS			STRATA TECTONIC		PALAEOCURRENT VECTORS CORRECTED	
	Plunge dir.	Plung	Flow dir.	Dip	Dip dir	#Az	*Az
	182	44	u	49	148	123	110
	199	43	u	55	150	111	101
	175	22	u	35	120	78	88
	170	34	u	46	121	80	96
	165	35	u	45	119	79	100
	165	40	u	48	125	94	105
L6	203	0	u	70	113	28	41
	203	0	u	70	113	28	41
	174	29	u	76	92	22	62
	71	57	u	59	95	95	145
	177	43	u	60	119	81	93
	150	46	u	48	130	119	121
	180	52	u	64	128	102	104
	160	60	u	64	128	110	118
	155	61	u	64	128	40	122
	57	24	u	37	110	144	186
	130	42	u	43	115	103	127
	133	35	u	37	110	90	121
	99	36	u	37	110	116	148
	144	38	u	38	136	126	128
L7	141	65	u	66	122	111	124
	203	17	u	55	125	54	65
	185	37	u	47	140	106	99
	172	42	u	56	120	83	97
	184	45	u	63	125	88	95
	172	43	u	54	124	87	100
	165	45	u	55	120	89	104
	195	21	u	56	120	58	68
	185	37	u	61	120	73	85
	180	36	u	52	125	82	92
	140	47	u	47	132	127	130
	154	52	u	57	119	90	112
	176	45	u	56	128	86	101
L8	195	25	u	56	123	68	74
	176	36	u	52	117	69	89
	160	49	u	56	120	93	108

LOCALITY	CROSSBEDDING TROUGH AXIS			STRATA TECTONIC		PALAEOCURRENT VECTORS CORRECTED	
	Plunge dir.	Plung	Flow dir.	Dip	Dip dir	#Az	*Az
	161	38	u	46	121	85	105
	188	17	u	56	110	62	63
	163	48	u	59	115	88	102
	200	14	u	55	120	42	60
	178	47	u	65	118	71	95
	190	35	u	54	130	82	89
	201	7	u	62	115	55	49
	192	33	u	63	121	54	79
	139	32	u	33	126	113	125
	125	57	u	58	111	103	126
L9	170	33	u	41	129	99	100
	176	29	u	40	128	85	94
	178	28	u	40	128	85	92
	180	27	u	40	128	83	90
	175	30	u	40	128	88	95
	174	34	u	44	128	91	97
	180	33	u	47	128	84	94
	173	33	u	43	128	89	98
	195	15	u	45	120	60	66
	143	41	u	42	131	122	126
	205	12	u	37	131	61	64
	165	32	u	37	131	102	106
	168	34	u	38	138	112	109
	175	32	u	38	138	107	104
	145	43	u	44	132	122	125
	130	44	u	44	132	132	137
	180	33	u	44	132	90	96
	175	35	u	44	132	97	99
	177	36	u	44	137	94	102
	165	33	u	40	125	90	103
	176	28	u	40	125	83	91
	190	20	u	40	125	61	76
L10	186	25	u	38	133	86	83
	197	12	u	35	125	70	68
	185	19	u	35	125	77	81
	200	23	u	40	140	89	80

LOCALITY	CROSSBEDDING TROUGH AXIS			STRATA TECTONIC		PALAEOCURRENT VECTORS CORRECTED	
	Plunge dir.	Plung	Flow dir.	Dip	Dip dir	#Az	*Az
	175	34	u	38	145	119	108
	198	26	u	47	135	90	81
	190	30	u	42	139	99	91
	197	28	u	40	147	101	89
	180	28	u	34	141	106	99
	185	35	u	43	143	109	100
	190	32	u	43	143	106	95
	183	36	u	47	135	92	97
	175	39	u	47	135	101	104
	193	29	u	40	145	104	92
	185	33	u	40	145	112	100
	174	36	u	40	145	120	109
	195	31	u	44	143	109	91
	203	21	u	44	137	80	76
	195	28	u	37	149	108	93
	183	25	u	34	138	106	94
	174	35	u	40	142	116	106
	207	15	u	36	138	77	72
L11	175	37	u	43	140	118	106
	213	32	u	54	150	90	85
	203	37	u	50	152	110	96
	225	20	u	48	154	98	71
	182	46	u	51	149	131	112
	226	16	u	51	149	78	65
L12	182	18	u	46	110	46	71
	183	28	u	55	115	58	78
	178	29	u	56	110	48	78
	175	35	u	57	112	53	85
	190	4	u	45	104	40	52
	185	16	u	48	110	48	67
	181	20	u	45	112	52	75
	175	24	u	45	112	54	82
L13 a	152	25	u	27	128	108	116
L13 b	65	16	d	35	130	7	17
	66	17	d	35	130	5	15
	73	21	d	35	130	1	8

LOCALITY	CROSSBEDDING TROUGH AXIS			STRATA TECTONIC		PALAEOCURRENT VECTORS CORRECTED	
	Plunge dir.	Plung	Flow dir.	Dip	Dip dir	#Az	*Az
	63	12	d	27	128	358	21
	56	9	d	22	122	7	25
	58	10	d	22	122	359	23
	58	11	d	45	137	24	29
	62	10	d	30	135	26	26
	50	0	d	32	143	51	46
	73	25	d	39	127	354	4
	64	24	d	42	125	358	9
	110	37	d	41	141	350	338
	74	19	d	41	141	29	15
	84	25	d	41	141	13	4
	79	18	d	31	137	4	9
	42	6	d	34	123	14	36
	67	21	d	34	123	354	8
	95	33	d	39	132	344	347
	50	6	d	39	132	29	36
	59	13	d	39	132	22	24
	81	27	d	39	132	3	359
	52	8	d	39	132	23	33
	71	11	d	36	145	35	24
	68	9	d	36	145	37	28
	71	11	d	36	145	30	24
L14 a	102	25	u	45	164	219	196
L14b	96	40	u	54	148	202	172
	100	24	d	45	164	39	8
	114	33	d	45	164	353	353
	99	23	d	45	164	25	10
	115	41	d	45	144	344	336
	120	42	d	45	144	340	333
	93	38	d	54	148	17	355
	114	49	d	54	148	359	337
	72	18	d	54	148	32	23
	75	17	d	44	146	27	19
	123	42	d	44	146	345	331
	100	33	d	47	153	16	356
	105	36	d	47	153	11	352

LOCALITY	CROSSBEDDING TROUGH AXIS			STRATA TECTONIC		PALAEOCURRENT VECTORS CORRECTED	
	Plunge dir.	Plung	Flow dir.	Dip	Dip dir	#Az	*Az
	125	45	d	49	155	0	336
	79	16	d	49	155	47	24
	101	34	d	49	155	18	356
	98	26	d	43	156	21	2
	139	42	d	43	156	350	324
	127	39	d	43	156	358	334
	141	46	d	47	157	349	324
	116	39	d	47	157	8	346
	104	33	d	47	157	18	356
L15 a	113	36	u	47	160	195	171
	109	34	u	47	160	199	174
	85	17	u	48	159	222	201
	125	39	u	44	158	186	159
	200	38	u	47	157	118	101
	137	45	u	47	157	171	147
	154	47	u	47	157	159	136
	136	42	u	44	157	173	149
	120	38	u	44	157	189	162
L15 b	76	8	d	44	158	48	32
	108	40	d	51	156	16	350
	114	43	d	51	156	6	345
	93	28	d	53	159	30	10
	109	40	d	53	159	22	352
	115	44	d	53	159	20	346
	112	42	d	53	159	18	349
	178	42	d	44	157	322	297
	136	42	d	44	157	354	329
	116	32	d	39	155	7	344
	94	21	d	39	155	30	7
	117	35	d	39	148	350	338
	117	35	d	39	148	353	338
L16 a	141	39	u	39	151	158	140
	133	38	u	39	151	166	147
	117	34	u	41	155	185	162
	150	41	u	41	155	159	135
	150	43	u	43	151	152	133

LOCALITY	CROSSBEDDING TROUGH AXIS			STRATA TECTONIC		PALAEOCURRENT VECTORS CORRECTED	
	Plunge dir.	Plung	Flow dir.	Dip	Dip dir	#Az	*Az
	51	2	u	39	139	215	221
	189	39	u	49	143	105	100
L16 b	89	11	d	31	161	34	17
	108	25	d	32	151	9	349
	101	22	d	32	151	14	357
	140	32	d	32	151	340	319
	93	23	d	39	151	24	4
	78	13	d	39	151	33	22
	72	14	d	41	145	22	23
	113	36	d	41	145	352	339
	75	17	d	41	145	31	18
	121	32	d	35	146	346	333
	137	35	d	35	146	333	320
	81	16	d	35	146	25	13
	138	42	d	43	151	342	322
	79	16	d	43	151	36	19
	135	42	d	43	151	345	325
	77	14	d	43	151	33	23
	56	1	d	41	145	51	43
	91	36	d	49	141	8	353
	73	23	d	49	141	21	14
	96	30	d	43	147	18	365
	62	5	d	43	147	47	38
	76	14	d	35	145	25	18
	82	18	d	35	145	21	11
	96	32	d	44	146	6	355
L17 a	154	44	u	45	139	128	123
	111	36	u	38	130	142	160
	99	34	u	38	130	153	170
	175	29	u	38	130	91	107
	157	35	u	38	130	110	114
L17 b	111	36	d	44	151	3	344
	73	11	d	44	151	38	28
	87	23	d	44	151	21	9
	118	43	d	45	139	334	330
	155	44	d	45	139	305	302

LOCALITY	CROSSBEDDING TROUGH AXIS			STRATA TECTONIC		PALAEOCURRENT VECTORS CORRECTED	
	Plunge dir.	Plung	Flow dir.	Dip	Dip dir	#Az	*Az
	70	20	d	45	139	16	16
	126	44	d	45	139	328	324
	105	40	d	45	139	346	340
	63	14	d	45	139	27	26
	138	45	d	45	139	318	315
	79	27	d	45	139	5	5
	80	27	d	45	139	14	4
	83	29	d	45	139	357	5
	155	44	d	45	139	305	302
	98	37	d	45	139	353	346
	88	30	d	41	137	357	356
	50	3	d	41	137	41	41
	118	39	d	41	137	334	329
	161	38	d	41	137	299	296
L18 a	103	15	d	41	175	66	17
	103	15	d	41	175	67	17
	98	11	d	41	175	70	23
	115	16	d	26	169	42	355
	115	18	d	28	167	30	354
	96	8	d	23	166	53	11
	113	14	d	23	166	36	353
L18 b	147	24	u	26	169	189	143
	166	26	u	26	169	172	126
	211	20	u	26	169	132	83
	213	19	u	26	169	128	83
	140	23	u	26	169	196	140
	185	27	u	28	167	150	109
	141	26	u	28	167	192	149
	110	13	u	23	166	218	176
	90	4	u	26	172	251	204
	85	2	u	28	172	258	210
	108	13	u	28	172	231	185
	109	14	u	28	172	232	183
L19 a	100	14	d	28	161	35	5
	132	26	d	28	155	354	330
	110	25	d	35	158	20	354

LOCALITY	CROSSBEDDING TROUGH AXIS			STRATA TECTONIC		PALAEOCURRENT VECTORS CORRECTED	
	Plunge dir.	Plung	Flow dir.	Dip	Dip dir	#Az	*Az
	92	17	d	34	155	33	9
	101	22	d	34	155	23	0
	143	33	d	34	155	346	320
L19 b	137	25	u	25	137	137	135
	122	24	u	25	137	152	149
	150	23	u	24	135	121	121
	130	24	u	24	135	139	140
	143	24	u	24	135	128	128
	162	28	u	28	161	160	125
	132	25	u	28	161	187	153
	179	27	u	28	161	145	110
	146	32	u	32	153	160	135
	154	32	u	32	153	152	128
	143	31	u	32	160	176	143
	135	31	u	33	156	174	148
	210	20	u	31	157	116	80
R1	94	29	u	35	131	166	168
	85	20	u	32	140	188	184
	98	31	u	35	130	159	164
R2	190	43	u	55	140	103	99
R3	55	24	u	49	122	178	193
	40	7	u	45	123	202	36
	60	19	u	44	129	192	198
	51	12	u	51	131	198	210
	56	16	u	35	122	183	200
	52	13	u	35	122	185	205
	51	14	u	48	128	186	207
	52	5	u	43	137	208	219
	80	42	u	45	105	118	147
	144	40	u	44	115	116	114
R4	115	57	u	60	141	154	149
	114	53	u	55	137	155	148
	120	50	u	50	125	129	138
	120	42	u	43	135	144	146
	128	34	u	34	121	114	131
R5	235	34	u	43	191	151	94

LOCALITY	CROSSBEDDING TROUGH AXIS			STRATA TECTONIC		PALAEOCURRENT VECTORS CORRECTED	
	Plunge dir.	Plung	Flow dir.	Dip	Dip dir	#Az	*Az
	231	32	u	38	193	156	92
	224	38	u	46	183	142	100
	180	33	u	34	165	153	116
	210	12	u	23	149	91	70
	218	17	u	26	168	122	87
	250	4	u	35	166	94	146
	215	25	u	35	166	125	85
	223	18	u	25	177	138	74
	187	24	u	24	184	180	112
	208	18	u	28	155	107	79
	215	14	u	26	155	96	70

Appendix (III)

TROUGH CROSSBEDDING DATA LEEUFONTEIN QUARTZITE FORMATION ROODERAND CONGLOMERATE FORMATION RECORDED IN NORTHWESTERN SECTOR

Legend: L= Leeufontein Formation R= Rooderand Formation
For locality numbers see Chapter 4, Fig. 2

Paleocurrent vectors corrected according to conventional method [See Chapt. 4]
* Paleocurrent vectors corrected according to tectonic model [See Chapt. 4]
u= direction of palaeo-flow on dipping strata is up dip
d= direction of palaeo-flow on dipping strata is down dip

LOCALITY	CROSSBEDDING TROUGH AXIS			STRATA TECTONIC		PALAEOCURRENT VECTORS CORRECTED	
	Plunge Az	Plung	Flow dir.	Dip	Dip Az	#Az	*Az
L20	137	26	u	52	205	259	166
	133	23	u	45	198	255	162
	129	17	u	44	201	263	170
	138	24	u	44	201	254	158
	140	25	u	44	201	251	157
	129	23	u	52	200	260	171
	129	23	u	52	200	266	171
	122	15	u	52	200	267	181
	138	28	u	49	201	252	160
	127	18	u	49	201	263	174
	123	16	u	51	200	262	180
	131	22	u	49	200	260	168
	116	7	u	49	200	277	190
	126	19	u	53	201	260	178
	123	15	u	53	201	272	182
	121	16	u	52	198	273	180
	127	23	u	52	198	264	172
	137	32	u	52	198	254	158
	137	28	u	50	201	255	161
	126	18	u	51	201	270	177

LOCALITY	CROSSBEDDING TROUGH AXIS			STRATA TECTONIC		PALAEOCURRENT FLOW DIR CORRECTED	
	Plunge Az	Plung	Flow dir.	Dip	Dip Az	#Az	*Az
	132	18	u	49	206	275	174
L20 b	146	34	d	58	211	80	342
L21	108	18	d	48	181	71	359
	133	20	d	50	205	88	349
	128	24	d	50	196	76	349
	121	19	d	48	193	80	353
	120	20	d	54	195	85	0
	106	10	d	45	186	80	7
	127	19	d	48	199	81	352
	133	20	d	48	204	87	349
L21 b	115	19	u	38	179	243	167
	132	32	u	43	179	222	149
	140	37	u	44	179	211	142
	123	28	u	42	177	226	157
	125	30	u	49	185	239	161
	122	22	u	40	183	238	163
	135	31	u	46	190	233	154
	128	22	u	38	186	240	157
	150	32	u	41	193	230	139
	135	29	u	45	192	238	154
	123	19	u	45	193	256	171
	123	16	u	43	195	256	172
	140	23	u	39	199	250	153
	125	18	u	44	195	258	170
	127	20	u	44	195	254	167
	133	24	u	44	195	250	161
	135	28	u	44	191	238	155
	145	34	u	44	191	230	143
	143	30	u	51	205	258	159
	126	14	u	43	200	269	175
	136	24	u	46	200	258	163
	125	18	u	48	198	255	174
	120	18	u	62	200	263	188
L22	140	35	u	52	197	243	154
	155	43	u	52	199	230	140

LOCALITY	CROSSBEDDING TROUGH AXIS			STRATA TECTONIC		PALAEOCURRENT FLOW DIR CORRECTED	
	Plunge Az	Plung	Flow dir.	Dip	Dip Az	#Az	*Az
	160	45	u	51	195	220	134
	155	32	u	42	200	236	140
	147	35	u	47	196	236	146
	125	23	u	55	198	254	175
	128	18	u	45	199	258	170
	125	25	u	54	195	251	174
	160	41	u	46	193	222	132
	165	50	u	55	199	224	134
L22 b	210	58	d	58	200	14	290
L23	214	52	u	52	214	214	108
	142	27	u	59	214	257	174
	200	54	u	55	215	224	109
	213	67	u	67	212	213	121
L24	126	9	u	49	208	280	185
	160	31	u	39	202	241	133
	116	4	u	44	210	296	194
	142	27	u	46	202	255	155
	183	59	u	62	211	231	130
	176	46	u	52	211	231	130
	178	47	u	52	211	238	129
	190	43	u	44	208	222	113
	182	46	u	51	215	241	126
	149	27	u	42	204	258	149
	138	30	u	59	208	257	170
	145	32	u	52	206	260	157
	182	49	u	52	206	221	126
L25	155	67	u	72	195	206	138
	186	69	u	69	195	198	126
	170	74	u	76	196	204	134
	145	57	u	68	196	223	148
	145	49	u	65	202	238	153
	133	44	u	67	199	246	163
	155	79	u	81	193	202	137
	157	81	u	83	196	207	137
	154	68	u	73	195	212	140

LOCALITY	CROSSBEDDING TROUGH AXIS			STRATA TECTONIC		PALAEOCURRENT FLOW DIR CORRECTED	
	Plunge Az	Plung	Flow dir.	Dip	Dip Az	#Az	*Az
	160	46	u	50	191	214	131
L26	175	39	u	44	208	232	124
	180	34	u	36	200	217	112
	250	36	u	45	206	170	248
	200	43	u	43	199	198	101
	166	36	u	43	204	233	131
	200	40	u	40	193	186	97
	209	34	u	35	191	176	84
L27	175	38	u	44	210	237	126
	168	33	u	47	211	246	138
	169	34	u	41	209	243	130
R6	257	9	u	34	180	110	210
	249	14	u	34	180	119	220
	251	14	u	33	183	118	220
	254	12	u	33	183	115	216
	258	10	u	33	183	113	211
	259	11	u	37	184	115	215
	261	10	u	37	184	109	212
	255	15	u	39	184	118	221
R7	228	37	u	46	185	151	77
	235	33	u	41	193	160	69
	233	34	u	41	193	164	71
	245	27	u	45	186	149	60
	250	24	u	45	186	138	54
	235	33	u	45	186	148	70
	258	17	u	45	186	131	45
	228	37	u	45	186	150	77
	237	32	u	45	186	148	68
	247	26	u	42	189	141	57
	237	31	u	42	189	151	67
R8	235	34	u	48	183	136	70
	250	31	u	50	190	146	63
	227	51	u	60	183	148	92
	225	48	u	55	185	154	90
	230	41	u	53	181	142	80

LOCALITY	CROSSBEDDING TROUGH AXIS			STRATA TECTONIC		PALAEOCURRENT FLOW DIR. CORRECTED	
	Plunge Az	Plung	Flow dir.	Dip	Dip Az	#Az	*Az
	225	41	u	47	188	153	82
	125	35	u	40	159	154	143
R9	130	42	d	80	211	94	180
	133	42	d	78	212	92	178
	129	21	d	77	214	97	200
	137	42	d	77	215	98	178
R10	125	0	d	76	215	110	42
	140	21	d	60	217	106	180
	129	3	d	70	220	111	216
	145	0	d	76	235	134	186
	170	44	d	66	235	104	228
	150	24	d	60	225	112	196
R10 b	300	10	u	54	217	138	144
	290	0	u	67	200	123	214

Appendix (IV)

PLANAR CROSSBEDDING ROODERAND CONGLOMERATE FORMATION NORTHEASTERN SECTOR

Legend: R= Rooderand Formation
For location numbers see Chapter 4, Fig. 2
 # conventional method of palaeo-reconstruction
* proposed method of palaeo-reconstruction based on tectonic model [See Chapter 4]

LOCATION	PLANAR CROSS-BEDS FORESETS		STRATA TECTONIC DIP		# CORRECTED PAL. FLOW DIR		* CORRECTED PAL. FLOW DIR.		
	Az.	Dip	Az.	Dip	Dip	Dir	Dip	Dir	Vector means
R8	213	74	184	52	–	126	34	61	
	211	71	184	52	–	125	31	57	
	204	63	188	49	–	138	19	63	
	204	66	182	55	–	113	22	6	
	205	63	184	57	–	106	20	43	55
R9	229	71	196	62	–	114	31	42	
	232	73	196	62	–	120	34	43	43

Appendix (V)

PLANAR CROSSBEDDING (PROFILE WITKOP 475) NORTHEASTERN SECTOR

For profile see Chapter 5, Fig. 4
* proposed method of palaeo-reconstruction based on tectonic model [See Chapter 4]

LITHOFACIES	PLANAR CROSS-BEDS FORESETS		STRATA TECTONIC DIP		* CORRECTED PAL. FLOW DIR.		
	Az.	Dip	Az.	Dip	Dip	Dir	Vector means
	164	53	197	53	26	210	
	160	45	197	53	27	233	
	166	45	197	53	23	228	
B/C	164	46	197	53	25	228	228
	184	72	195	46	28	133	
	187	60	195	46	16	135	134
	167	76	200	63	32	196	196

Appendix (VI)

PLANAR CROSSBEDDING LEEUFONTEIN QUARTZITE FORMATION (PROFILE LEEUFONTEIN 485) NORTHWESTERN SECTOR

For profile see Chapter 5, Fig. 5
* proposed method of palaeo-reconstruction based on tectonic model

LITHOFACIES	PLANAR CROSS-BEDS FORESETS		STRATA TECTONIC DIP		* CORRECTED PAL. FLOW DIR.		
	Az.	Dip	Az.	Dip	Dip	Dir	Vector means
Fig 5 B	177	31	152	40	17	002	
	183	30	152	40	20	003	
	177	32	152	40	16	007	4
	180	37	145	45	24	014	
	189	23	145	45	30	343	
	187	34	145	45	28	005	1
	190	51	147	47	32	040	
	189	51	147	47	31	037	
	193	55	147	47	36	043	40
Fig 5 C	181	43	147	51	26	018	
	173	58	145	40	28	076	
	175	57	145	40	24	078	
	177	57	145	40	28	072	75
Fig. 5 D	188	41	148	46	28	021	
	169	47	148	46	16	40	
	180	43	148	46	24	23	
	174	43	148	46	19	26	
	170	58	148	46	21	69	
	177	45	148	46	21	32	
	169	47	148	46	17	39	
	174	54	148	46	22	56	
	165	50	148	46	14	58	40
	180	60	147	45	30	62	
	186	73	147	45	42	73	
	184	63	147	45	34	62	66
	173	58	150	48	23	61	
	169	48	150	48	16	40	
	162	56	150	48	14	74	58
fig. 6 (not shown)	154	59	133	44	22	78	
	146	65	133	44	24	106	
	155	65	133	44	28	88	
	153	58	133	44	22	79	91
	152	63	141	46	19	107	
	159	64	141	46	23	92	100

LITHOFACIES	PLANAR CROSS-BEDS FORESETS		STRATA TECTONIC DIP		* CORRECTED PAL. FLOW DIR.		
	Az.	Dip	Az.	Dip	Dip	Dir	Vector means
Fig. 5 C	185	40	140	34	27	39	
	183	62	140	34	41	69	58
	165	45	140	34	18	69	
	170	44	145	39	16	51	
	180	49	145	39	26	54	
	175	50	145	39	24	60	56
	183	33	144	39	23	15	
	181	35	144	39	24	19	
	176	45	144	39	21	52	26
	170	53	142	36	26	72	
	172	56	142	36	30	76	
	183	62	142	36	41	68	
	183	44	142	36	28	45	65

Appendix (VII)

TROUGH CROSSBEDDING LEEUFONTEIN QUARTZITE FORMATION (PROFILE WITKOP 475) NORTHEASTERN SECTOR

for Profile see Chapter 5 Fig. 4
* palaeo–current vectors corrected according to proposed tectonic model [see chapt. 4]
u = direction of palaeo–flow on dipping strata is updip

LITHOFACIES	TROUGH AXIS			STRATA TECTONIC DIP		*CORRECTED PAL FLOW DIR.
	Az	Dip	Flow dir.	Az	Dip	PAL. DIR.
Fig 4 C	12	125	u	40	200	173
	36	140	u	50	192	150
	44	149	u	49	183	136
	48	132	u	58	178	148
	45	160	u	50	194	133
	40	150	u	44	178	131
	31	127	u	44	178	153
	28	123	u	53	189	167
	41	135	u	58	192	156
	49	163	u	52	190	129
	43	135	u	54	182	148
	33	122	u	54	184	163
Fig 4 D	36	141	u	49	192	149
	35	150	u	47	199	186
	47	238	u	54	199	86
	26	125	u	53	193	169
	39	130	u	55	185	156
	36	142	u	59	206	163
	16	270	u	49	194	221
	3	104	u	45	191	194
	35	137	u	49	189	151
	32	126	u	59	194	169
	41	142	u	52	190	146

LITHOFACIES	TROUGH AXIS			STRATA TECTONIC DIP		*CORRECTED PAL FLOW DIR.
	Az	Dip	Flow dir.	Az	Dip	PAL. DIR.
Fig 4 A	38	150	u	46	191	139
	51	167	u	53	190	126
	43	226	u	48	193	85
	13	271	u	43	195	214
Fig 4 B	63	225	d	65	204	290
	42	239	u	49	201	79
	48	233	u	54	197	89
	32	134	u	48	190	154
	33	135	u	48	189	154
	30	134	u	42	185	150
	37	154	u	42	188	133
	41	145	u	51	190	143
	36	134	u	53	191	155
	44	147	u	53	191	143
	49	177	u	50	189	118
	45	155	u	51	190	135
	27	128	u	44	186	157
	47	153	u	52	187	135
	27	125	u	45	185	161
	25	122	u	50	189	168
Fig 4 A	40	163	u	44	192	128
	36	141	u	48	190	147
	1	106	u	51	195	200
	25	127	u	49	193	166
	28	135	u	49	197	160
	42	156	u	46	187	131
	11	93	u	54	191	205
	39	143	u	50	190	145

TROUGH CROSSBEDDING LEEUFONTEIN QUARTZITE FORMATION (PROFILE LEEUFONTEIN 485) NORTHWESTERN SECTOR

Legend: L= Leeufontein Formation R= Rooderand Formation
For Profile See Chapt. 5 Fig. 5 and 6
* Palaeocurrent vectors corrected according to tectonic model [See chapt. 4]
u= direction of palaeo–flow on dipping strata is up dip
d= direction of palaeo–flow on dipping strata is down dip

LITHOFACIES	TROUGH AXIS			STRATA TECTONIC DIP		* CORRECTED PAL. FLOW DIR.
	Az	Dip	Flow dir.	Az	Dip	Dir.
Fig 5 A	97	17	u	47	170	199
	90	31	u	42	138	174
Fig 5 B	123	44	u	45	135	144
	170	34	u	38	140	109
	200	33	u	47	147	92
	104	38	u	47	147	167
Fig 5 C	85	22	d	49	154	15
	63	1	d	40	152	41
	65	0	d	45	155	45
	124	38	d	42	155	337
	164	47	u	48	153	127
	95	17	d	41	164	14
	124	35	d	38	152	335
	75	6	d	36	156	30
	105	27	d	46	165	4
	91	18	d	37	156	11
	160	51	u	51	163	135
	95	23	d	41	155	6
	89	17	d	39	157	14
	201	36	u	46	155	98
	222	8	u	45	140	55
	208	13	u	41	133	64
	210	16	u	40	140	68

LITHOFACIES	TROUGH AXIS			STRATA TECTONIC DIP		* CORRECTED PAL. FLOW DIR.
	Az	Dip	Flow dir.	Az	Dip	Dir.
Fig 5 C (continued)	123	38	d	40	146	331
	154	40	d	40	146	307
	94	33	d	42	138	350
	96	40	u	46	132	163
	100	39	d	46	138	344
	93	28	d	42	146	359
	97	31	d	41	143	352
	78	17	d	48	152	21
	145	44	d	44	148	315
	106	36	d	44	148	346
	136	45	d	46	154	325
	191	29	u	43	138	89
	124	41	u	42	135	140
	221	16	d	49	145	245
	236	18	u	45	165	68
	221	21	u	44	155	74
	105	30	u	42	156	175
	97	26	d	39	150	359
	119	32	d	35	145	336
	114	31	d	35	145	340
	104	34	d	43	148	348
	155	48	d	48	155	313
	115	38	d	43	148	339
data not shown on fig 6	92	35	u	42	130	165
	102	39	u	44	134	149
	110	46	u	52	146	149
	76	24	u	52	146	195
Fig 6 F	97	37	u	47	143	170
	89	31	u	43	138	175
	84	24	u	47	149	191
	74	28	u	48	135	186
	223	2	d	48	135	226
	84	22	u	32	133	181
	115	33	u	37	144	149
	82	28	u	46	141	184
	58	2	d	41	146	222

Appendix IX
Data: recumbant forsets crossbedding, Leeufontein Formation (Fig. 4, Chapter 5)

Lithofacies	Strata overturned						Strata horiz.
	Overturned crossbedding		Normal bedding		Fold axis		Fold axis
	Dip	Azimuth of dip	Dip	Azimuth of dip	Plunge	Az. of plunge	Strike
Fig. 4 B	87 76 66	257 235 207	63	200	62	172	133
Fig. 4 C	28 38 26	161 70 150	49 46	191 188	24	126	166

Appendix (X)

CURRENT RIPPLES (LEEUFONTEIN QUARTZITE FORMATION)

Legend: L5crc= Leeufontein Formation Locality 5 current ripple crest. Locality No. shown on Fig. 2, Chapter 4.
Paleocurrents corrected according to conventional method [See Chpt. 4]
* Paleocurrents corrected according to proposed tectonic model [See Chpt. 4]

LOCATION	CURRENT RIPPLE CREST		PAL. FLOW DIR. ON OUTCROP	INVERTED BEDDING		# CORRECTED PAL. FLOW DIR.	* CORRECTED PAL. FLOW DIR.
	Az	Plunge		Az	Dip		
L5crc	62	13	Az 350	140	50	123	117
L21crc	256	20	Az 166	198	38	54	316
	152	36	Az 242	184	44	299	45
	249	24	Az 339	188	39	223	142
	168	34	Az 258	188	39	294	31
L24crc	128	17	up dip	203	37	226	256
	120	0	up dip	210	44	210	282
	278	33	up dip	209	61	248	155
L26crc	114	0	up dip	204	44	204	104
	95	0	up dip	185	57	186	119

Appendix (XI)

TROUGH CROSSBEDDING DATA VENTERSKROON QUARTZITE FORMATION

* Palaeo–reconstruction according to proposed tectonic model [See Chapt. 4]
u = direction of palaeo–flow on dipping strata is updip

LOCALITY	CROSSBEDDING TROUGH AXIS			STRATA TECTONIC DIP		*CORRECTED PAL FLOW DIR.
	Punge Az	Plunge	Flow dir.	Dip	Dip Az	Az
	149	48	u	65	208	184
Rooderand	165	57	u	62	201	162
510	170	56	u	60	200	159
	165	43	u	47	196	153
	150	30	u	42	200	168
	161	29	u	45	218	176
	175	43	u	50	213	160
	145	24	u	50	213	191

Appendix (XII) (a)

PEBBLE DATA ROODERAND CONGLOMERATE FORMATION KLEINFONTEIN 1101

A-axis	B-axis	C-axis	Roundness	Flatness	Sphericity	OP-index	b/a	c/b	B-axis phi	c/a	a-b/a-c
61.6	52.2	37.0	0.7	60.06	0.75	0.60	0.85	0.71	-5.71	0.60	0.38
56.7	45.7	24.9	0.8	43.92	0.62	0.75	0.81	0.54	-5.51	0.44	0.35
41.9	38.3	24.2	0.7	57.76	0.71	0.30	0.91	0.63	-5.26	0.58	0.20
40.3	37.3	26.9	0.6	66.75	0.78	0.28	0.93	0.72	-5.22	0.67	0.22
41.5	31.6	17.5	0.8	42.17	0.62	0.93	0.76	0.55	-4.98	0.42	0.41
34.0	30.9	17.6	0.7	51.76	0.67	0.31	0.91	0.57	-4.95	0.52	0.19
45.7	30.8	27.5	0.8	60.18	0.81	1.31	0.67	0.89	-4.94	0.60	0.82
34.6	28.2	21.3	0.9	61.56	0.77	0.72	0.82	0.76	-4.82	0.62	0.48
33.6	27.7	26.3	0.7	78.27	0.91	0.95	0.82	0.95	-4.79	0.78	0.81
33.0	27.5	16.0	0.8	48.48	0.66	0.61	0.83	0.58	-4.78	0.48	0.32
39.8	27.4	22.3	0.9	56.03	0.77	1.21	0.69	0.81	-4.78	0.56	0.71
31.6	27.4	23.0	0.9	72.78	0.85	0.59	0.87	0.84	-4.78	0.73	0.49
29.2	26.2	20.0	0.7	68.49	0.81	0.40	0.90	0.76	-4.71	0.68	0.33
27.0	26.0	14.8	0.8	54.81	0.68	0.07	0.96	0.57	-4.70	0.55	0.08
27.8	25.2	15.0	0.7	53.96	0.68	0.30	0.91	0.60	-4.66	0.54	0.20
30.6	25.2	19.9	0.6	65.03	0.80	0.70	0.82	0.79	-4.66	0.65	0.50
31.0	25.1	20.5	0.9	66.13	0.81	0.78	0.81	0.82	-4.65	0.66	0.56
31.5	25.0	18.7	0.7	59.37	0.76	0.79	0.79	0.75	-4.64	0.59	0.51
27.0	25.0	17.1	0	63.33	0.76	0.24	0.93	0.68	-4.64	0.63	0.20
32.6	24.6	17.2	0.7	52.76	0.72	0.92	0.75	0.70	-4.62	0.53	0.52
38.4	24.5	18.0	0.5	46.88	0.70	1.40	0.64	0.73	-4.61	0.47	0.68
42.5	24.4	23.5	0.7	55.29	0.81	1.68	0.57	0.96	-4.61	0.55	0.95
27.7	24.3	15.5	0.8	55.96	0.71	0.42	0.88	0.64	-4.60	0.56	0.28
25.0	24.2	17.0	0.7	68.00	0.78	0.06	0.97	0.70	-4.60	0.68	0.10
26.4	24.0	13.6	0.8	51.52	0.66	0.29	0.91	0.57	-4.58	0.52	0.19
27.1	24.0	16.3	0.7	60.15	0.74	0.40	0.89	0.68	-4.58	0.60	0.29
35.6	24.0	17.0	0.7	47.75	0.70	1.25	0.67	0.71	-4.58	0.48	0.62
28.1	24.0	18.8	0.8	66.90	0.81	0.58	0.85	0.78	-4.58	0.67	0.44
40.7	24.0	20.5	0.8	50.37	0.75	1.59	0.59	0.85	-4.58	0.50	0.83
25.9	23.7	14.0	0.8	54.05	0.68	0.26	0.92	0.59	-4.57	0.54	0.18
26.5	23.5	15.1	0.8	56.98	0.72	0.38	0.89	0.64	-4.55	0.57	0.26
27.9	23.5	15.5	0.9	55.56	0.72	0.57	0.84	0.66	-4.55	0.56	0.35
25.0	23.4	11.6	0.8	46.40	0.61	0.18	0.94	0.50	-4.55	0.46	0.12
33.7	23.4	16.0	0.8	47.48	0.69	1.17	0.69	0.68	-4.55	0.47	0.58
28.8	23.4	15.7	0.9	54.51	0.72	0.69	0.81	0.67	-4.55	0.55	0.41
31.2	23.3	21.4	0.7	68.59	0.86	1.10	0.75	0.92	-4.54	0.69	0.81
24.5	23.3	18.0	0.7	73.47	0.83	0.15	0.95	0.77	-4.54	0.73	0.18

A−axis	B−axis	C−axis	Roundness	Flatness	Sphericity	OP−index	b/a	c/b	B−axis phi	c/a	a−b/a−c
25.2	23.3	17.8	0.9	70.63	0.81	0.27	0.92	0.76	−4.54	0.71	0.26
30.8	23.3	18.2	0.8	59.09	0.77	0.94	0.76	0.78	−4.54	0.59	0.60
25.8	23.2	14.0	0.7	54.26	0.69	0.33	0.90	0.60	−4.54	0.54	0.22
38.1	23.2	14.5	0.7	38.06	0.62	1.60	0.61	0.63	−4.54	0.38	0.63
29.4	23.1	17.1	0.7	58.16	0.76	0.81	0.79	0.74	−4.53	0.58	0.51
33.0	23.0	16.5	0.9	50.00	0.71	1.15	0.70	0.72	−4.52	0.50	0.61
28.5	23.0	17.0	0.7	59.65	0.76	0.73	0.81	0.74	−4.52	0.60	0.48
28.8	22.9	18.3	0.7	63.54	0.80	0.81	0.80	0.80	−4.52	0.64	0.56
29.2	22.9	15.4	0.8	52.74	0.71	0.80	0.78	0.67	−4.52	0.53	0.46
33.0	22.6	16.6	0.7	50.30	0.72	1.20	0.68	0.73	−4.50	0.50	0.63
25.7	22.5	15.3	0.9	59.53	0.74	0.44	0.88	0.68	−4.49	0.60	0.31
34.4	22.3	16.0	0.7	46.51	0.69	1.36	0.65	0.72	−4.48	0.47	0.66
30.0	22.2	19.6	0.8	65.33	0.83	1.07	0.74	0.88	−4.47	0.65	0.75
27.6	21.6	18.0	0.8	65.22	0.82	0.88	0.78	0.83	−4.43	0.65	0.62
22.0	21.5	11.0	0.8	50.00	0.63	0.00	0.98	0.51	−4.43	0.50	0.05
27.1	21.5	12.5	0.7	46.13	0.64	0.76	0.79	0.58	−4.43	0.46	0.38
30.4	21.5	19.4	0.7	63.82	0.83	1.20	0.71	0.90	−4.43	0.64	0.81
23.1	21.5	15.9	0.8	68.83	0.80	0.22	0.93	0.74	−4.43	0.69	0.22
32.4	21.3	18.4	0.8	56.79	0.79	1.33	0.66	0.86	−4.41	0.57	0.79
25.3	21.2	15.3	0.9	60.47	0.76	0.60	0.84	0.72	−4.41	0.60	0.41
24.0	21.2	15.7	0.7	65.42	0.79	0.42	0.88	0.74	−4.41	0.65	0.34
22.9	21.2	17.0	0.7	74.24	0.84	0.27	0.93	0.80	−4.41	0.74	0.29
26.0	21.2	12.5	0.7	48.08	0.66	0.66	0.82	0.59	−4.41	0.48	0.36
22.6	21.2	13.9	0.9	61.50	0.74	0.17	0.94	0.66	−4.41	0.62	0.16
28.0	21.2	18.6	0.9	66.43	0.84	1.01	0.76	0.88	−4.41	0.66	0.72
24.9	21.2	11.9	0.7	47.79	0.64	0.52	0.85	0.56	−4.41	0.48	0.28
22.0	21.1	11.0	0.7	50.00	0.64	0.07	0.96	0.52	−4.40	0.50	0.08
27.0	21.1	18.3	0.7	67.78	0.84	0.92	0.78	0.87	−4.40	0.68	0.68
21.0	21.0	11.9	0.7	56.67	0.68	−0.10	1.00	0.57	−4.39	0.57	0.00
26.7	20.8	19.1	0.9	71.54	0.87	0.99	0.78	0.92	−4.38	0.72	0.78
29.5	20.6	16.3	0.7	55.25	0.76	1.15	0.70	0.79	−4.36	0.55	0.67
28.7	20.5	14.9	0.8	51.92	0.72	1.07	0.71	0.73	−4.36	0.52	0.59
28.1	20.5	18.1	0.8	64.41	0.83	1.10	0.73	0.88	−4.36	0.64	0.76
22.2	20.4	18.0	0.8	81.08	0.89	0.38	0.92	0.88	−4.35	0.81	0.43
23.7	20.3	14.1	0.8	59.49	0.74	0.51	0.86	0.69	−4.34	0.59	0.35
25.6	20.3	15.7	0.7	61.33	0.78	0.79	0.79	0.77	−4.34	0.61	0.54
21.2	20.3	11.1	0.8	52.36	0.66	0.08	0.96	0.55	−4.34	0.52	0.09
25.0	20.2	13.4	0.7	53.60	0.71	0.69	0.81	0.66	−4.34	0.54	0.41
23.3	20.2	13.3	0.8	57.08	0.72	0.46	0.87	0.66	−4.34	0.57	0.31
29.4	20.1	14.2	0.8	48.30	0.70	1.20	0.68	0.71	−4.33	0.48	0.61
26.9	20.0	14.9	0.8	55.39	0.74	0.96	0.74	0.75	−4.32	0.55	0.58
26.7	20.0	11.6	0.7	43.45	0.63	0.95	0.75	0.58	−4.32	0.43	0.44

A-axis	B-axis	C-axis	Roundness	Flatness	Sphericity	OP-index	b/a	c/b	B-axis phi	c/a	a-b/a-c
23.7	20.0	14.0	0.8	59.07	0.75	0.56	0.84	0.70	-4.32	0.59	0.38
29.3	20.0	16.5	0.7	56.31	0.77	1.22	0.68	0.83	-4.32	0.56	0.73
25.9	19.8	16.7	0.7	64.48	0.82	0.94	0.76	0.84	-4.31	0.64	0.66
27.8	19.5	17.9	0.7	64.39	0.84	1.22	0.70	0.92	-4.29	0.64	0.84
23.0	19.5	12.3	0.7	53.48	0.70	0.52	0.85	0.63	-4.29	0.53	0.33
24.3	19.4	13.9	0.9	57.20	0.74	0.74	0.80	0.72	-4.28	0.57	0.47
25.5	19.1	15.0	0.8	58.82	0.77	0.96	0.75	0.79	-4.26	0.59	0.61
26.3	19.1	17.2	0.6	65.40	0.84	1.13	0.73	0.90	-4.26	0.65	0.79
24.2	19.0	13.8	0.7	57.02	0.75	0.79	0.79	0.73	-4.25	0.57	0.50
24.9	19.0	13.4	0.7	53.82	0.72	0.87	0.76	0.71	-4.25	0.54	0.51
21.7	18.6	13.7	0.7	63.13	0.77	0.51	0.86	0.74	-4.22	0.63	0.39
21.3	18.2	13.7	0.7	64.32	0.79	0.53	0.85	0.75	-4.19	0.64	0.41
21.2	18.2	12.3	0.8	58.02	0.73	0.48	0.86	0.68	-4.19	0.58	0.34
27.0	18.0	11.1	0.8	41.11	0.63	1.30	0.67	0.62	-4.17	0.41	0.57
23.4	18.0	14.5	0.7	61.97	0.79	0.89	0.77	0.81	-4.17	0.62	0.61
28.6	18.0	15.0	0.8	52.45	0.76	1.42	0.63	0.83	-4.17	0.52	0.78
29.5	18.0	15.2	0.8	51.53	0.76	1.49	0.61	0.84	-4.17	0.52	0.80
21.0	18.0	10.3	0.7	49.05	0.65	0.48	0.86	0.57	-4.17	0.49	0.25
22.1	17.9	12.0	0.8	54.30	0.71	0.67	0.81	0.67	-4.16	0.54	0.42
25.0	17.9	11.8	0.8	47.20	0.68	1.06	0.72	0.66	-4.16	0.47	0.54
21.5	17.9	11.8	0.9	54.88	0.71	0.58	0.83	0.66	-4.16	0.55	0.37
26.9	17.8	12.5	0.6	46.47	0.69	1.29	0.66	0.70	-4.15	0.46	0.63
25.5	17.8	13.2	0.7	51.76	0.73	1.13	0.70	0.74	-4.15	0.52	0.63
27.0	17.8	15.4	0.9	57.04	0.79	1.31	0.66	0.87	-4.15	0.57	0.79
26.5	17.5	13.5	0.8	50.94	0.73	1.28	0.66	0.77	-4.13	0.51	0.69
28.1	17.3	13.0	0.8	46.26	0.70	1.47	0.62	0.75	-4.11	0.46	0.72
25.4	17.3	14.7	0.7	57.87	0.79	1.23	0.68	0.85	-4.11	0.58	0.76
22.4	17.3	15.2	0.7	67.86	0.84	0.94	0.77	0.88	-4.11	0.68	0.71
24.1	17.2	15.4	0.8	63.90	0.83	1.15	0.71	0.90	-4.10	0.64	0.79
22.2	17.1	12.5	0.8	56.31	0.74	0.84	0.77	0.73	-4.10	0.56	0.53
21.7	17.1	13.1	0.8	60.37	0.77	0.79	0.79	0.77	-4.10	0.60	0.53
25.0	17.1	16.0	0.8	64.00	0.84	1.28	0.68	0.94	-4.10	0.64	0.88
30.0	17.1	14.2	0.7	47.33	0.73	1.66	0.57	0.83	-4.10	0.47	0.82
22.6	17.0	15.5	0.8	68.58	0.86	1.05	0.75	0.91	-4.09	0.69	0.79
25.3	17.0	11.9	0.6	47.04	0.69	1.24	0.67	0.70	-4.09	0.47	0.62
18.9	17.0	12.1	0.8	64.02	0.77	0.32	0.90	0.71	-4.09	0.64	0.28
23.6	17.0	14.5	0.8	61.44	0.81	1.09	0.72	0.85	-4.09	0.61	0.73
19.4	16.9	14.2	0.8	73.20	0.85	0.53	0.87	0.84	-4.08	0.73	0.48
24.1	16.9	13.9	0.9	57.68	0.78	1.14	0.70	0.82	-4.08	0.58	0.71
17.9	16.7	10.9	0.7	60.89	0.74	0.16	0.93	0.65	-4.06	0.61	0.17
22.4	16.5	9.2	0.7	41.07	0.61	1.00	0.74	0.56	-4.04	0.41	0.45
18.3	16.4	11.5	0.9	62.84	0.76	0.33	0.90	0.70	-4.04	0.63	0.28

A−axis	B−axis	C−axis	Roundness	Flatness	Sphericity	OP−index	b/a	c/b	B−axis phi	c/a	a−b/a−c
19.8	16.3	11.9	0.7	60.10	0.76	0.63	0.82	0.73	−4.03	0.60	0.44
28.0	16.3	14.3	0.7	51.07	0.77	1.60	0.58	0.88	−4.03	0.51	0.85
20.9	16.3	13.5	0.7	64.59	0.81	0.86	0.78	0.83	−4.03	0.65	0.62
21.1	16.0	14.1	0.8	66.82	0.84	0.98	0.76	0.88	−4.00	0.67	0.73
21.6	15.9	11.6	0.7	53.70	0.73	0.97	0.74	0.73	−3.99	0.54	0.57
23.9	15.7	14.5	0.8	60.67	0.82	1.35	0.66	0.92	−3.97	0.61	0.87
27.5	15.7	10.5	0.8	38.18	0.63	1.74	0.57	0.67	−3.97	0.38	0.69
18.2	15.6	10.2	0.7	56.04	0.72	0.47	0.86	0.65	−3.96	0.56	0.33
17.1	15.5	13.5	0.7	78.95	0.88	0.39	0.91	0.87	−3.95	0.79	0.44
17.9	15.4	14.9	0.8	83.24	0.93	0.80	0.86	0.97	−3.94	0.83	0.83
21.0	15.4	12.1	0.8	57.62	0.77	0.99	0.73	0.79	−3.94	0.58	0.63
22.8	15.3	12.5	0.7	54.82	0.77	1.24	0.67	0.82	−3.94	0.55	0.73
22.1	15.3	12.6	0.7	57.01	0.78	1.16	0.69	0.82	−3.94	0.57	0.72
17.3	15.2	12.0	0.9	69.36	0.82	0.44	0.88	0.79	−3.93	0.69	0.40
22.3	15.2	12.0	0.7	53.81	0.75	1.19	0.68	0.79	−3.93	0.54	0.69
20.0	15.2	12.6	0.7	63.00	0.81	0.92	0.76	0.83	−3.93	0.63	0.65
24.3	15.2	14.5	0.8	59.67	0.83	1.47	0.63	0.95	−3.93	0.60	0.93
16.7	15.1	7.5	0.7	44.91	0.61	0.27	0.90	0.50	−3.92	0.45	0.17
20.2	15.0	12.3	0.8	60.89	0.79	0.98	0.74	0.82	−3.91	0.61	0.66
21.3	15.0	10.6	0.8	49.77	0.71	1.09	0.70	0.71	−3.91	0.50	0.59
20.7	14.7	9.2	0.9	44.44	0.65	1.08	0.71	0.63	−3.88	0.44	0.52
17.1	14.7	10.0	0.7	58.48	0.74	0.46	0.86	0.68	−3.88	0.58	0.34
19.3	14.6	12.7	0.7	65.80	0.83	0.97	0.76	0.87	−3.87	0.66	0.71
17.4	14.6	9.5	0.8	54.60	0.71	0.53	0.84	0.65	−3.87	0.55	0.35
19.6	14.4	10.7	0.9	54.59	0.74	0.97	0.73	0.74	−3.85	0.55	0.58
15.2	14.4	8.9	0.9	58.55	0.71	0.08	0.95	0.62	−3.85	0.59	0.13
25.0	14.3	10.2	0.7	40.80	0.66	1.69	0.57	0.71	−3.84	0.41	0.72
19.0	14.1	12.9	0.7	67.89	0.85	1.06	0.74	0.91	−3.82	0.68	0.80
21.5	14.0	9.0	0.7	41.86	0.65	1.34	0.65	0.64	−3.81	0.42	0.60
22.1	13.9	11.1	0.6	50.23	0.74	1.39	0.63	0.80	−3.80	0.50	0.75
22.2	13.9	12.1	0.7	54.50	0.78	1.42	0.63	0.87	−3.80	0.55	0.82
18.0	13.9	12.3	0.8	68.33	0.85	0.92	0.77	0.88	−3.80	0.68	0.72
15.0	13.5	9.6	0.9	64.00	0.77	0.29	0.90	0.71	−3.75	0.64	0.28
17.1	13.5	10.0	0.8	58.48	0.76	0.75	0.79	0.74	−3.75	0.58	0.51
17.2	13.5	10.2	0.9	59.30	0.77	0.77	0.78	0.76	−3.75	0.59	0.53
17.6	13.4	9.0	0.8	51.14	0.70	0.84	0.76	0.67	−3.74	0.51	0.49
16.1	13.3	8.5	0.8	52.80	0.70	0.57	0.83	0.64	−3.73	0.53	0.37
16.0	13.2	11.8	0.7	73.75	0.87	0.74	0.83	0.89	−3.72	0.74	0.67
17.0	13.1	7.3	0.9	42.94	0.62	0.82	0.77	0.56	−3.71	0.43	0.40
15.6	13.1	11.5	0.9	73.72	0.86	0.66	0.84	0.88	−3.71	0.74	0.61
14.1	13.0	9.2	0.7	65.25	0.77	0.19	0.92	0.71	−3.70	0.65	0.22
14.5	13.0	10.5	0.8	72.41	0.84	0.35	0.90	0.81	−3.70	0.72	0.38

A-axis	B-axis	C-axis	Roundness	Flatness	Sphericity	OP-index	b/a	c/b	B-axis phi	c/a	a-b/a-c
21.5	13.0	11.0	0.8	51.16	0.76	1.49	0.60	0.85	-3.70	0.51	0.81
18.2	12.6	11.9	0.7	65.38	0.85	1.24	0.69	0.94	-3.66	0.65	0.89
21.9	12.5	11.0	0.7	50.23	0.76	1.63	0.57	0.88	-3.64	0.50	0.86
13.0	12.5	9.5	0.7	73.08	0.82	0.00	0.96	0.76	-3.64	0.73	0.14
16.7	12.3	10.8	0.9	64.67	0.83	1.02	0.74	0.88	-3.62	0.65	0.75
16.5	12.1	11.5	0.8	69.70	0.87	1.12	0.73	0.95	-3.60	0.70	0.88
20.0	12.0	8.9	0.8	44.50	0.69	1.52	0.60	0.74	-3.58	0.45	0.72
13.9	11.2	9.9	0.8	71.22	0.86	0.77	0.81	0.88	-3.49	0.71	0.68
18.7	10.9	9.5	0.7	50.80	0.76	1.56	0.58	0.87	-3.45	0.51	0.85
13.4	10.7	9.1	0.9	67.91	0.83	0.75	0.80	0.85	-3.42	0.68	0.63
15.9	10.5	8.3	0.9	52.20	0.74	1.24	0.66	0.79	-3.39	0.52	0.71
13.1	10.5	8.5	0.9	64.89	0.81	0.70	0.80	0.81	-3.39	0.65	0.57
14.2	10.2	10.0	0.7	70.42	0.88	1.18	0.72	0.98	-3.35	0.70	0.95

Appendix (XII) (b)

PEBBLE DATA ROODERAND CONGLOMERATE FORMATION KROMDRAAI 509 S

A−axis	B−axis	C−axis	Roundness	Flatness	Sphericity	OP−index	b/a	c/b	B−axis phi	c/a	a−b/a−c
24.0	17.3	15.1	0.7	62.92	0.82	1.11	0.72	0.87	−4.11	0.63	0.75
30.1	22.3	15.5	0.8	51.50	0.71	0.97	0.74	0.70	−4.48	0.51	0.53
15.6	13.2	11.2	0.7	71.79	0.85	0.60	0.85	0.85	−3.72	0.72	0.55
22.3	18.1	14.9	0.9	66.82	0.82	0.75	0.81	0.82	−4.18	0.67	0.57
54.3	33.4	29.5	0.7	54.33	0.78	1.51	0.62	0.88	−5.06	0.54	0.84
29.0	22.6	14.1	0.7	48.62	0.67	0.81	0.78	0.62	−4.50	0.49	0.43
31.2	22.5	11.8	0.7	37.82	0.58	1.12	0.72	0.52	−4.49	0.38	0.45
24.6	22.7	12.9	0.9	52.44	0.67	0.23	0.92	0.57	−4.50	0.52	0.16
22.9	19.3	15.8	0.9	69.00	0.83	0.63	0.84	0.82	−4.27	0.69	0.51
36.5	27.8	18.3	0.7	50.14	0.69	0.90	0.76	0.66	−4.80	0.50	0.48
19.4	14.8	10.8	0.9	55.67	0.74	0.86	0.76	0.73	−3.89	0.56	0.53
37.5	29.2	24.3	0.9	64.80	0.81	0.91	0.78	0.83	−4.87	0.65	0.63
32.2	23.3	16.4	0.8	50.93	0.71	1.04	0.72	0.70	−4.54	0.51	0.56
23.9	17.9	13.0	0.9	54.39	0.73	0.93	0.75	0.73	−4.16	0.54	0.55
24.9	17.0	12.6	0.9	50.60	0.72	1.19	0.68	0.74	−4.09	0.51	0.64
21.5	15.6	10.7	0.9	49.77	0.70	1.00	0.73	0.69	−3.96	0.50	0.55
20.0	14.9	12.3	0.8	61.50	0.80	0.97	0.75	0.83	−3.90	0.62	0.66
21.0	15.5	10.2	0.9	48.57	0.68	0.95	0.74	0.66	−3.95	0.49	0.51
27.0	21.0	16.2	0.7	60.00	0.77	0.85	0.78	0.77	−4.39	0.60	0.56
24.0	23.1	13.8	0.7	57.50	0.70	0.07	0.96	0.60	−4.53	0.58	0.09
25.0	19.5	15.3	0.8	61.20	0.78	0.84	0.78	0.78	−4.29	0.61	0.57
19.3	17.9	10.7	0.8	55.44	0.69	0.19	0.93	0.60	−4.16	0.55	0.16
27.2	24.5	17.9	0.8	65.81	0.78	0.36	0.90	0.73	−4.61	0.66	0.29
21.4	16.0	12.2	0.8	57.01	0.76	0.93	0.75	0.76	−4.00	0.57	0.59
21.0	16.5	12.8	0.9	60.95	0.78	0.80	0.79	0.78	−4.04	0.61	0.55
30.0	20.8	13.8	0.9	46.00	0.67	1.17	0.69	0.66	−4.38	0.46	0.57
19.0	17.1	11.0	0.9	57.89	0.72	0.30	0.90	0.64	−4.10	0.58	0.24
14.8	13.7	11.3	0.8	76.35	0.86	0.22	0.93	0.82	−3.78	0.76	0.31
17.0	13.2	8.9	0.8	52.35	0.71	0.78	0.78	0.67	−3.72	0.52	0.47
15.3	10.0	8.9	0.7	58.17	0.80	1.29	0.65	0.89	−3.32	0.58	0.83
34.7	26.5	23.0	0.8	66.28	0.83	0.99	0.76	0.87	−4.73	0.66	0.70
20.9	15.2	13.9	0.8	66.51	0.85	1.12	0.73	0.91	−3.93	0.67	0.81
19.1	17.6	11.9	0.8	62.30	0.75	0.22	0.92	0.68	−4.14	0.62	0.21
20.9	16.4	9.5	0.8	45.45	0.64	0.77	0.78	0.58	−4.04	0.45	0.39
24.3	17.0	15.2	0.7	62.55	0.82	1.19	0.70	0.89	−4.09	0.63	0.80
30.2	22.4	15.3	0.8	50.66	0.70	0.97	0.74	0.68	−4.49	0.51	0.52
15.8	13.5	11.4	0.7	72.15	0.85	0.57	0.85	0.84	−3.75	0.72	0.52

A-axis	B-axis	C-axis	Roundness	Flatness	Sphericity	OP-index	b/a	c/b	B-axis phi	c/a	a-b/a-c
22.5	18.3	14.7	0.9	65.33	0.81	0.73	0.81	0.80	-4.19	0.65	0.54
54.6	33.3	29.4	0.7	53.85	0.78	1.53	0.61	0.88	-5.06	0.54	0.85
29.6	22.7	14.3	0.7	48.31	0.67	0.87	0.77	0.63	-4.50	0.48	0.45
31.3	22.4	11.7	0.7	37.38	0.58	1.15	0.72	0.52	-4.49	0.37	0.45
24.4	22.5	12.8	0.9	52.46	0.67	0.23	0.92	0.57	-4.49	0.52	0.16
22.6	19.4	15.4	0.9	68.14	0.81	0.55	0.86	0.79	-4.28	0.68	0.44
36.2	27.6	18.6	0.7	51.38	0.70	0.90	0.76	0.67	-4.79	0.51	0.49
19.6	14.3	10.6	0.9	54.08	0.74	0.99	0.73	0.74	-3.84	0.54	0.59
37.3	29.3	24.4	0.9	65.42	0.82	0.89	0.79	0.83	-4.87	0.65	0.62
32.1	23.4	16.2	0.8	50.47	0.70	1.02	0.73	0.69	-4.55	0.50	0.55
23.7	17.8	13.1	0.9	55.27	0.74	0.92	0.75	0.74	-4.15	0.55	0.56
24.6	17.1	12.5	0.9	50.81	0.72	1.14	0.70	0.73	-4.10	0.51	0.62
21.3	15.3	10.5	0.9	49.30	0.70	1.03	0.72	0.69	-3.94	0.49	0.56
20.3	14.3	12.5	0.8	61.58	0.81	1.15	0.70	0.87	-3.84	0.62	0.77
21.1	15.3	10.4	0.9	49.29	0.69	1.00	0.73	0.68	-3.94	0.49	0.54
27.3	21.3	16.1	0.7	58.97	0.76	0.83	0.78	0.76	-4.41	0.59	0.54
24.0	23.4	13.7	0.7	57.08	0.69	0.02	0.98	0.59	-4.55	0.57	0.06
25.3	19.3	15.2	0.8	60.08	0.78	0.91	0.76	0.79	-4.27	0.60	0.59
18.6	17.6	10.7	0.8	57.53	0.70	0.11	0.95	0.61	-4.14	0.58	0.13
27.3	24.3	17.6	0.8	64.47	0.78	0.40	0.89	0.72	-4.60	0.64	0.31
21.6	16.3	12.5	0.8	57.87	0.76	0.91	0.75	0.77	-4.03	0.58	0.58
21.3	16.4	12.3	0.9	57.75	0.76	0.85	0.77	0.75	-4.04	0.58	0.54
30.1	20.4	13.8	0.9	45.85	0.68	1.23	0.68	0.68	-4.35	0.46	0.60
19.0	17.2	11.2	0.9	58.95	0.73	0.28	0.91	0.65	-4.10	0.59	0.23
14.6	13.4	11.3	0.8	77.40	0.87	0.27	0.92	0.84	-3.74	0.77	0.36
17.2	13.3	8.9	0.8	51.74	0.70	0.79	0.77	0.67	-3.73	0.52	0.47
15.2	10.0	8.5	0.7	55.92	0.78	1.25	0.66	0.85	-3.32	0.56	0.78
34.3	26.5	23.1	0.8	67.35	0.84	0.97	0.77	0.87	-4.73	0.67	0.70
20.8	15.3	13.9	0.8	66.83	0.85	1.08	0.74	0.91	-3.94	0.67	0.80
19.3	17.2	11.9	0.8	61.66	0.75	0.35	0.89	0.69	-4.10	0.62	0.28
20.9	16.3	9.6	0.8	45.93	0.65	0.79	0.78	0.59	-4.03	0.46	0.41
27.6	22.0	20.3	0.7	73.55	0.88	0.95	0.80	0.92	-4.46	0.74	0.77
27.2	20.3	11.3	0.8	41.54	0.61	0.97	0.75	0.56	-4.34	0.42	0.43
25.0	22.2	14.3	0.8	57.20	0.72	0.38	0.89	0.64	-4.47	0.57	0.26
21.9	19.1	16.2	0.7	73.97	0.86	0.55	0.87	0.85	-4.26	0.74	0.49
31.2	20.1	10.9	0.9	34.94	0.57	1.49	0.64	0.54	-4.33	0.35	0.55
21.3	14.3	13.6	0.9	63.85	0.85	1.32	0.67	0.95	-3.84	0.64	0.91
29.0	22.6	17.5	0.8	60.34	0.78	0.85	0.78	0.77	-4.50	0.60	0.56
23.1	13.8	12.4	0.8	53.68	0.78	1.53	0.60	0.90	-3.79	0.54	0.87
26.3	18.4	17.1	0.7	65.02	0.85	1.24	0.70	0.93	-4.20	0.65	0.86
19.6	15.3	13.2	0.9	67.35	0.83	0.88	0.78	0.86	-3.94	0.67	0.67
17.0	13.2	11.4	0.7	67.06	0.83	0.88	0.78	0.86	-3.72	0.67	0.68

A-axis	B-axis	C-axis	Roundness	Flatness	Sphericity	OP-index	b/a	c/b	B-axis phi	c/a	a-b/a-c
17.2	15.3	11.3	0.7	65.70	0.79	0.36	0.89	0.74	-3.94	0.66	0.32
16.3	12.4	11.3	0.9	69.33	0.86	0.98	0.76	0.91	-3.63	0.69	0.78
21.3	18.4	12.0	0.8	56.34	0.72	0.46	0.86	0.65	-4.20	0.56	0.31
18.3	13.4	9.0	0.7	49.18	0.69	0.96	0.73	0.67	-3.74	0.49	0.53
32.1	27.6	18.8	0.7	58.57	0.74	0.51	0.86	0.68	-4.79	0.59	0.34
38.1	20.3	19.1	0.9	50.13	0.78	1.82	0.53	0.94	-4.34	0.50	0.94
39.4	31.2	20.8	0.9	52.79	0.71	0.78	0.79	0.67	-4.96	0.53	0.44
42.5	29.3	20.4	0.9	48.00	0.69	1.20	0.69	0.70	-4.87	0.48	0.60
34.8	28.1	15.3	0.9	43.97	0.62	0.72	0.81	0.54	-4.81	0.44	0.34
31.0	25.3	14.3	0.7	46.13	0.64	0.68	0.82	0.57	-4.66	0.46	0.34
35.5	29.3	21.4	0.7	60.28	0.76	0.67	0.83	0.73	-4.87	0.60	0.44
33.5	17.3	13.4	0.8	40.00	0.68	1.95	0.52	0.77	-4.11	0.40	0.81
34.2	28.3	20.7	0.7	60.53	0.76	0.66	0.83	0.73	-4.82	0.61	0.44
24.1	23.5	17.5	0.7	72.61	0.81	0.02	0.98	0.74	-4.55	0.73	0.09
25.3	20.4	12.7	0.7	50.20	0.68	0.70	0.81	0.62	-4.35	0.50	0.39
31.2	20.3	15.8	0.7	50.64	0.73	1.33	0.65	0.78	-4.34	0.51	0.71
23.7	18.2	14.3	0.8	60.34	0.78	0.88	0.77	0.79	-4.19	0.60	0.59
18.3	16.3	13.2	0.8	72.13	0.84	0.41	0.89	0.81	-4.03	0.72	0.39
24.1	14.2	10.1	0.7	41.91	0.67	1.60	0.59	0.71	-3.83	0.42	0.71
20.1	14.3	12.3	0.7	61.19	0.81	1.11	0.71	0.86	-3.84	0.61	0.74
24.0	17.5	15.2	0.7	63.33	0.82	1.08	0.73	0.87	-4.13	0.63	0.74
30.1	22.5	15.2	0.8	50.50	0.70	0.94	0.75	0.68	-4.49	0.50	0.51
15.2	13.4	11.2	0.7	73.68	0.85	0.44	0.88	0.84	-3.74	0.74	0.45
22.4	18.5	14.9	0.9	66.52	0.81	0.68	0.83	0.81	-4.21	0.67	0.52
54.2	33.3	29.5	0.7	54.43	0.78	1.52	0.61	0.89	-5.06	0.54	0.85
29.3	22.4	14.1	0.7	48.12	0.67	0.87	0.76	0.63	-4.49	0.48	0.45
31.2	22.3	11.4	0.7	36.54	0.57	1.16	0.71	0.51	-4.48	0.37	0.45
23.1	22.1	12.4	0.9	53.68	0.67	0.09	0.96	0.56	-4.47	0.54	0.09
22.2	19.2	15.8	0.9	71.17	0.84	0.55	0.86	0.82	-4.26	0.71	0.47
36.3	27.1	18.3	0.7	50.41	0.70	0.96	0.75	0.68	-4.76	0.50	0.51
19.4	14.3	10.5	0.9	54.12	0.74	0.95	0.74	0.73	-3.84	0.54	0.57
37.5	29.4	24.5	0.9	65.33	0.82	0.89	0.78	0.83	-4.88	0.65	0.62
32.2	23.6	15.4	0.8	47.83	0.68	1.01	0.73	0.65	-4.56	0.48	0.51
23.4	17.9	13.4	0.9	57.26	0.75	0.87	0.76	0.75	-4.16	0.57	0.55
24.5	17.5	12.6	0.9	51.43	0.72	1.06	0.71	0.72	-4.13	0.51	0.59
21.6	15.4	10.7	0.9	49.54	0.70	1.06	0.71	0.69	-3.94	0.50	0.57
20.3	14.2	12.3	0.8	60.59	0.81	1.16	0.70	0.87	-3.83	0.61	0.76
21.4	15.3	10.2	0.9	47.66	0.68	1.05	0.71	0.67	-3.94	0.48	0.54
27.6	21.6	16.2	0.7	58.70	0.76	0.82	0.78	0.75	-4.43	0.59	0.53
24.0	23.3	13.4	0.7	55.83	0.68	0.03	0.97	0.58	-4.54	0.56	0.07
25.0	19.4	15.8	0.8	63.20	0.80	0.88	0.78	0.81	-4.28	0.63	0.61
19.4	17.6	10.7	0.8	55.15	0.69	0.27	0.91	0.61	-4.14	0.55	0.21

A-axis	B-axis	C-axis	Roundness	Flatness	Sphericity	OP-index	b/a	c/b	B-axis phi	c/a	a-b/a-c
27.6	24.1	17.9	0.8	64.86	0.78	0.48	0.87	0.74	-4.59	0.65	0.36
21.4	16.3	12.4	0.8	57.94	0.76	0.88	0.76	0.76	-4.03	0.58	0.57
21.0	16.3	12.4	0.9	59.05	0.77	0.83	0.78	0.76	-4.03	0.59	0.55
30.2	20.4	13.8	0.9	45.70	0.68	1.24	0.68	0.68	-4.35	0.46	0.60
19.6	17.3	11.0	0.9	56.12	0.71	0.37	0.88	0.64	-4.11	0.56	0.27
14.3	13.5	11.3	0.8	79.02	0.87	0.13	0.94	0.84	-3.75	0.79	0.27
17.0	13.4	8.4	0.8	49.41	0.68	0.73	0.79	0.63	-3.74	0.49	0.42
15.3	10.5	8.5	0.7	55.56	0.77	1.14	0.69	0.81	-3.39	0.56	0.71
34.2	26.3	23.0	0.8	67.25	0.84	0.98	0.77	0.87	-4.72	0.67	0.71
20.6	15.4	13.9	0.8	67.48	0.85	1.04	0.75	0.90	-3.94	0.67	0.78
19.3	17.4	11.9	0.8	61.66	0.75	0.31	0.90	0.68	-4.12	0.62	0.26
20.3	16.5	9.5	0.8	46.80	0.65	0.65	0.81	0.58	-4.04	0.47	0.35
24.6	17.4	15.1	0.7	61.38	0.81	1.15	0.71	0.87	-4.12	0.61	0.76
30.3	22.5	15.5	0.8	51.16	0.71	0.96	0.74	0.69	-4.49	0.51	0.53
15.6	13.1	11.3	0.7	72.44	0.85	0.64	0.84	0.86	-3.71	0.72	0.58
22.3	18.4	14.6	0.9	65.47	0.80	0.67	0.83	0.79	-4.20	0.65	0.51
54.3	33.3	29.6	0.7	54.51	0.79	1.52	0.61	0.89	-5.06	0.55	0.85
29.0	22.4	14.3	0.7	49.31	0.68	0.84	0.77	0.64	-4.49	0.49	0.45
31.8	22.4	11.8	0.7	37.11	0.58	1.20	0.70	0.53	-4.49	0.37	0.47
24.3	22.4	12.9	0.9	53.09	0.67	0.23	0.92	0.58	-4.49	0.53	0.17
22.9	19.4	15.2	0.9	66.38	0.80	0.59	0.85	0.78	-4.28	0.66	0.45
36.5	27.6	18.4	0.7	50.41	0.70	0.92	0.76	0.67	-4.79	0.50	0.49
19.2	14.6	10.8	0.9	56.25	0.75	0.87	0.76	0.74	-3.87	0.56	0.55
37.1	29.6	24.3	0.9	65.50	0.81	0.83	0.80	0.82	-4.89	0.65	0.59
32.0	23.1	16.4	0.8	51.25	0.71	1.05	0.72	0.71	-4.53	0.51	0.57
23.0	17.0	13.0	0.9	56.52	0.76	0.97	0.74	0.76	-4.09	0.57	0.60
24.9	17.6	12.3	0.9	49.40	0.70	1.09	0.71	0.70	-4.14	0.49	0.58
21.5	15.0	10.0	0.9	46.51	0.68	1.12	0.70	0.67	-3.91	0.47	0.57
20.0	14.6	12.0	0.8	60.00	0.79	1.02	0.73	0.82	-3.87	0.60	0.68
21.0	15.9	10.3	0.9	49.05	0.68	0.88	0.76	0.65	-3.99	0.49	0.48
27.0	21.5	16.0	0.7	59.26	0.76	0.77	0.80	0.74	-4.43	0.59	0.50
24.0	23.5	13.7	0.7	57.08	0.69	0.00	0.98	0.58	-4.55	0.57	0.05
25.3	19.4	15.3	0.8	60.47	0.78	0.89	0.77	0.79	-4.28	0.60	0.59
19.6	19.1	10.7	0.8	54.59	0.67	0.00	0.97	0.56	-4.26	0.55	0.06
27.0	24.0	17.9	0.8	66.30	0.79	0.41	0.89	0.75	-4.58	0.66	0.33
21.2	16.6	12.2	0.8	57.55	0.75	0.79	0.78	0.73	-4.05	0.58	0.51
21.0	16.3	12.0	0.9	57.14	0.75	0.82	0.78	0.74	-4.03	0.57	0.52
30.0	20.0	13.2	0.9	44.00	0.66	1.29	0.67	0.66	-4.32	0.44	0.60
19.8	17.0	11.0	0.9	55.56	0.71	0.47	0.86	0.65	-4.09	0.56	0.32
14.0	13.5	11.3	0.8	80.71	0.88	0.00	0.96	0.84	-3.75	0.81	0.19
17.5	13.5	8.9	0.8	50.86	0.69	0.80	0.77	0.66	-3.75	0.51	0.47
15.6	10.3	8.9	0.7	57.05	0.79	1.26	0.66	0.86	-3.36	0.57	0.79

A-axis	B-axis	C-axis	Roundness	Flatness	Sphericity	OP-index	b/a	c/b	B-axis phi	c/a	a-b/a-c
34.7	26.0	23.5	0.8	67.72	0.85	1.08	0.75	0.90	-4.70	0.68	0.78
20.9	15.3	13.0	0.8	62.20	0.81	1.04	0.73	0.85	-3.94	0.62	0.71
19.3	17.0	11.9	0.8	61.66	0.76	0.39	0.88	0.70	-4.09	0.62	0.31
20.6	16.0	9.5	0.8	46.12	0.65	0.80	0.78	0.59	-4.00	0.46	0.41
27.4	22.3	20.0	0.7	72.99	0.87	0.85	0.81	0.90	-4.48	0.73	0.69
27.1	20.5	11.0	0.8	40.59	0.60	0.93	0.76	0.54	-4.36	0.41	0.41
25.0	22.0	14.3	0.8	57.20	0.72	0.41	0.88	0.65	-4.46	0.57	0.28
21.9	19.4	16.4	0.7	74.89	0.86	0.49	0.89	0.85	-4.28	0.75	0.45
31.1	20.1	10.0	0.9	32.15	0.54	1.55	0.65	0.50	-4.33	0.32	0.52
21.2	14.0	13.2	0.9	62.26	0.84	1.35	0.66	0.94	-3.81	0.62	0.90
29.8	22.5	17.2	0.8	57.72	0.76	0.94	0.76	0.76	-4.49	0.58	0.58
23.6	13.8	12.6	0.8	53.39	0.79	1.58	0.58	0.91	-3.79	0.53	0.89
26.4	18.0	17.0	0.7	64.39	0.85	1.31	0.68	0.94	-4.17	0.64	0.89
19.4	14.9	13.5	0.9	69.59	0.86	0.97	0.77	0.91	-3.90	0.70	0.76
17.0	13.0	12.8	0.7	75.29	0.91	1.11	0.76	0.98	-3.70	0.75	0.95
17.2	15.4	11.5	0.7	66.86	0.79	0.34	0.90	0.75	-3.94	0.67	0.32
16.2	12.4	11.3	0.9	69.75	0.86	0.97	0.77	0.91	-3.63	0.70	0.78
21.3	18.4	12.0	0.8	56.34	0.72	0.46	0.86	0.65	-4.20	0.56	0.31
18.3	13.4	9.0	0.7	49.18	0.69	0.96	0.73	0.67	-3.74	0.49	0.53
32.0	27.1	18.8	0.7	58.75	0.74	0.57	0.85	0.69	-4.76	0.59	0.37
38.4	19.3	17.0	0.9	44.27	0.73	1.96	0.50	0.88	-4.27	0.44	0.89
39.5	32.5	20.0	0.9	50.63	0.68	0.66	0.82	0.62	-5.02	0.51	0.36
42.3	29.0	20.7	0.9	48.94	0.70	1.21	0.69	0.71	-4.86	0.49	0.62
34.6	28.0	15.7	0.9	45.38	0.63	0.71	0.81	0.56	-4.81	0.45	0.35
31.0	25.0	14.6	0.7	47.10	0.65	0.71	0.81	0.58	-4.64	0.47	0.37
35.5	30.0	21.0	0.7	59.15	0.75	0.58	0.85	0.70	-4.91	0.59	0.38
33.5	18.0	12.0	0.8	35.82	0.62	1.95	0.54	0.67	-4.17	0.36	0.72
34.4	28.3	20.3	0.7	59.01	0.75	0.67	0.82	0.72	-4.82	0.59	0.43
24.5	23.3	17.2	0.7	70.20	0.80	0.14	0.95	0.74	-4.54	0.70	0.16
25.5	20.2	12.0	0.7	47.06	0.65	0.76	0.79	0.59	-4.34	0.47	0.39
31.2	21.0	15.8	0.7	50.64	0.72	1.24	0.67	0.75	-4.39	0.51	0.66
23.7	18.3	15.2	0.8	64.14	0.81	0.90	0.77	0.83	-4.19	0.64	0.64
18.3	16.3	13.2	0.8	72.13	0.84	0.41	0.89	0.81	-4.03	0.72	0.39
25.1	14.2	10.1	0.7	40.24	0.66	1.72	0.57	0.71	-3.83	0.40	0.73
20.0	15.2	12.3	0.7	61.50	0.79	0.91	0.76	0.81	-3.93	0.62	0.62
20.0	16.3	14.2	0.8	71.00	0.85	0.78	0.82	0.87	-4.03	0.71	0.64
20.5	16.9	12.5	0.7	60.98	0.77	0.64	0.82	0.74	-4.08	0.61	0.45
19.7	16.1	12.3	0.8	62.44	0.78	0.67	0.82	0.76	-4.01	0.62	0.49
15.5	11.3	10.0	0.8	64.52	0.83	1.04	0.73	0.88	-3.50	0.65	0.76
16.5	11.0	10.0	0.7	60.61	0.82	1.27	0.67	0.91	-3.46	0.61	0.85
38.3	28.3	16.9	0.8	44.13	0.64	1.01	0.74	0.60	-4.82	0.44	0.47
32.8	21.3	16.1	0.8	49.09	0.72	1.34	0.65	0.76	-4.41	0.49	0.69

A-axis	B-axis	C-axis	Roundness	Flatness	Sphericity	OP-index	b/a	c/b	B-axis phi	c/a	a-b/a-c
25.2	18.3	10.0	0.9	39.68	0.60	1.06	0.73	0.55	−4.19	0.40	0.45
32.1	21.0	16.0	0.9	49.84	0.72	1.32	0.65	0.76	−4.39	0.50	0.69
30.0	19.3	17.2	0.7	57.33	0.80	1.39	0.64	0.89	−4.27	0.57	0.84
24.0	20.3	12.3	0.7	51.25	0.68	0.53	0.85	0.61	−4.34	0.51	0.32
21.0	20.0	13.2	0.9	62.86	0.75	0.10	0.95	0.66	−4.32	0.63	0.13
40.3	32.4	23.2	0.9	57.57	0.74	0.75	0.80	0.72	−5.02	0.58	0.46
26.5	21.5	16.7	0.7	63.02	0.79	0.73	0.81	0.78	−4.43	0.63	0.51
28.0	20.3	16.3	0.8	58.21	0.78	1.06	0.73	0.80	−4.34	0.58	0.66
46.8	26.5	21.3	0.8	45.51	0.72	1.71	0.57	0.80	−4.73	0.46	0.80
24.0	19.0	10.0	0.7	41.67	0.60	0.77	0.79	0.53	−4.25	0.42	0.36
29.7	19.2	16.5	0.9	55.56	0.78	1.36	0.65	0.86	−4.26	0.56	0.80
22.3	21.4	15.0	0.8	67.26	0.78	0.08	0.96	0.70	−4.42	0.67	0.12
22.3	16.3	9.1	0.7	40.81	0.61	1.02	0.73	0.56	−4.03	0.41	0.45
22.2	13.1	11.3	0.8	50.90	0.76	1.55	0.59	0.86	−3.71	0.51	0.83
29.6	20.0	19.2	0.7	64.86	0.85	1.35	0.68	0.96	−4.32	0.65	0.92
24.2	19.3	15.3	0.7	63.22	0.79	0.78	0.80	0.79	−4.27	0.63	0.55
25.3	18.5	12.0	0.9	47.43	0.68	1.00	0.73	0.65	−4.21	0.47	0.51
28.1	24.1	14.5	0.7	51.60	0.68	0.50	0.86	0.60	−4.59	0.52	0.29
19.6	15.3	11.0	0.8	56.12	0.74	0.79	0.78	0.72	−3.94	0.56	0.50
22.0	19.4	12.5	0.8	56.82	0.72	0.39	0.88	0.64	−4.28	0.57	0.27
18.5	14.2	11.5	0.7	62.16	0.80	0.87	0.77	0.81	−3.83	0.62	0.61
35.3	28.0	13.4	0.8	37.96	0.57	0.82	0.79	0.48	−4.81	0.38	0.33
16.9	13.6	10.2	0.7	60.36	0.77	0.69	0.80	0.75	−3.77	0.60	0.49
29.4	26.3	25.1	0.7	85.37	0.93	0.71	0.89	0.95	−4.72	0.85	0.72
24.0	20.0	15.2	0.8	63.33	0.78	0.63	0.83	0.76	−4.32	0.63	0.45
21.3	19.4	13.5	0.7	63.38	0.76	0.28	0.91	0.70	−4.28	0.63	0.24
39.4	32.0	23.2	0.8	58.88	0.75	0.72	0.81	0.73	−5.00	0.59	0.46
26.3	21.5	16.3	0.8	61.98	0.78	0.69	0.82	0.76	−4.43	0.62	0.48
28.2	19.4	15.0	0.7	53.19	0.74	1.18	0.69	0.77	−4.28	0.53	0.67
46.0	26.3	21.6	0.8	46.96	0.73	1.68	0.57	0.82	−4.72	0.47	0.81
24.5	18.3	10.8	0.8	44.08	0.64	0.94	0.75	0.59	−4.19	0.44	0.45
29.8	18.0	16.4	0.9	55.03	0.79	1.53	0.60	0.91	−4.17	0.55	0.88
22.5	21.6	15.6	0.8	69.33	0.79	0.08	0.96	0.72	−4.43	0.69	0.13
22.6	16.9	9.5	0.7	42.04	0.62	0.94	0.75	0.56	−4.08	0.42	0.44
22.9	13.2	11.0	0.8	48.03	0.74	1.61	0.58	0.83	−3.72	0.48	0.82
29.6	20.4	19.6	0.7	66.22	0.86	1.31	0.69	0.96	−4.35	0.66	0.92
24.2	20.3	15.2	0.7	62.81	0.78	0.60	0.84	0.75	−4.34	0.63	0.43
25.1	18.3	12.0	0.9	47.81	0.68	1.01	0.73	0.66	−4.19	0.48	0.52
28.6	23.4	14.0	0.7	48.95	0.66	0.66	0.82	0.60	−4.55	0.49	0.36
19.6	15.9	10.3	0.8	52.55	0.70	0.65	0.81	0.65	−3.99	0.53	0.40
22.9	19.4	12.6	0.8	55.02	0.71	0.53	0.85	0.65	−4.28	0.55	0.34
18.5	13.9	11.5	0.7	62.16	0.80	0.94	0.75	0.83	−3.80	0.62	0.66

A−axis	B−axis	C−axis	Roundness	Flatness	Sphericity	OP−index	b/a	c/b	B−axis phi	c/a	a−b/a−c
35.0	27.0	13.5	0.8	38.57	0.58	0.90	0.77	0.50	−4.75	0.39	0.37
16.2	13.1	10.2	0.7	62.96	0.79	0.69	0.81	0.78	−3.71	0.63	0.52
52.3	26.9	25.0	0.7	47.80	0.76	1.91	0.51	0.93	−4.75	0.48	0.93

Appendix (XII) (c)

PEBBLE DATA ROODERAND CONGLOMERATE FORMATION KROMDRAAI 509 N

A–axis	B–axis	C–axis	Roundness	Flatness	Sphericity	OP–index	b/a	c/b	B–axis phi	c/a	a–b/a–c
28.8	13.2	10.5	0.8	36.46	0.66	2.26	0.46	0.80	−3.72	0.36	0.85
19.0	11.8	7.7	0.9	40.53	0.64	1.46	0.62	0.65	−3.56	0.41	0.64
18.2	13.6	8.7	0.8	47.80	0.67	0.90	0.75	0.64	−3.77	0.48	0.48
16.8	11.9	7.8	0.8	46.43	0.67	1.05	0.71	0.66	−3.57	0.46	0.54
17.8	14.4	14.0	0.9	78.65	0.91	0.97	0.81	0.97	−3.85	0.79	0.89
16.4	13.1	11.0	0.8	67.07	0.83	0.77	0.80	0.84	−3.71	0.67	0.61
28.8	21.3	18.5	0.8	64.24	0.82	1.06	0.74	0.87	−4.41	0.64	0.73
16.0	12.0	7.7	0.8	48.13	0.68	0.88	0.75	0.64	−3.58	0.48	0.48
15.3	12.7	9.6	0.9	62.75	0.78	0.59	0.83	0.76	−3.67	0.63	0.46
23.8	18.9	7.9	0.8	33.19	0.52	0.83	0.79	0.42	−4.24	0.33	0.31
20.9	16.2	9.9	0.9	47.37	0.66	0.81	0.76	0.61	−4.02	0.47	0.43
18.7	15.2	11.7	0.8	62.57	0.78	0.68	0.81	0.77	−3.93	0.63	0.50
20.0	17.2	12.9	0.9	64.50	0.79	0.50	0.86	0.75	−4.10	0.65	0.39
19.6	17.5	9.8	0.7	50.00	0.65	0.33	0.89	0.56	−4.13	0.50	0.21
25.0	24.3	14.4	0.8	57.60	0.70	0.03	0.97	0.59	−4.60	0.58	0.07
18.3	11.9	10.2	0.8	55.74	0.78	1.31	0.65	0.86	−3.57	0.56	0.79
16.0	12.0	10.0	0.7	62.50	0.80	0.93	0.75	0.83	−3.58	0.63	0.67
15.8	12.1	7.7	0.9	48.73	0.68	0.81	0.77	0.64	−3.60	0.49	0.46
15.0	11.9	8.3	0.8	55.33	0.73	0.70	0.79	0.70	−3.57	0.55	0.46
15.0	9.6	7.1	0.8	47.33	0.70	1.31	0.64	0.74	−3.26	0.47	0.68
14.1	11.8	9.1	0.7	64.54	0.79	0.56	0.84	0.77	−3.56	0.65	0.46
15.0	11.9	7.4	0.8	49.33	0.67	0.69	0.79	0.62	−3.57	0.49	0.41
13.9	10.8	7.3	0.8	52.52	0.71	0.75	0.78	0.68	−3.43	0.53	0.47
15.9	10.9	9.0	0.8	56.60	0.78	1.15	0.69	0.83	−3.45	0.57	0.72
16.0	14.9	13.2	0.8	82.50	0.90	0.26	0.93	0.89	−3.90	0.83	0.39
17.0	11.2	7.0	0.8	41.18	0.64	1.29	0.66	0.63	−3.49	0.41	0.58
14.1	9.8	7.9	0.8	56.03	0.77	1.09	0.70	0.81	−3.29	0.56	0.69
18.4	12.3	9.1	0.7	49.46	0.72	1.22	0.67	0.74	−3.62	0.49	0.66
13.2	10.0	8.7	0.8	65.91	0.83	0.91	0.76	0.87	−3.32	0.66	0.71
15.0	12.9	10.8	0.9	72.00	0.84	0.53	0.86	0.84	−3.69	0.72	0.50
15.0	11.1	9.2	0.7	61.33	0.80	0.96	0.74	0.83	−3.47	0.61	0.67
15.0	10.2	9.3	0.8	62.00	0.83	1.22	0.68	0.91	−3.35	0.62	0.84
12.1	9.0	7.3	0.8	60.33	0.79	0.90	0.74	0.81	−3.17	0.60	0.65
13.5	9.7	6.9	0.8	51.11	0.71	0.98	0.72	0.71	−3.28	0.51	0.58
11.1	10.1	7.4	0.9	66.67	0.79	0.20	0.91	0.73	−3.34	0.67	0.27
25.0	19.7	12.8	0.7	51.20	0.69	0.77	0.79	0.65	−4.30	0.51	0.43
34.9	31.8	21.0	0.9	60.17	0.74	0.31	0.91	0.66	−4.99	0.60	0.22

A-axis	B-axis	C-axis	Roundness	Flatness	Sphericity	OP-index	b/a	c/b	B-axis phi	c/a	a-b/a-c
32.1	27.3	19.0	0.8	59.19	0.74	0.55	0.85	0.70	-4.77	0.59	0.37
28.4	19.0	17.2	0.8	60.56	0.82	1.31	0.67	0.91	-4.25	0.61	0.84
29.8	24.1	18.2	0.7	61.07	0.77	0.73	0.81	0.76	-4.59	0.61	0.49
32.8	28.9	21.0	0.8	64.02	0.77	0.45	0.88	0.73	-4.85	0.64	0.33
28.2	21.8	13.9	0.8	49.29	0.68	0.84	0.77	0.64	-4.45	0.49	0.45
21.0	18.4	12.1	0.9	57.62	0.72	0.41	0.88	0.66	-4.20	0.58	0.29
28.2	18.9	13.6	0.8	48.23	0.70	1.25	0.67	0.72	-4.24	0.48	0.64
24.6	19.1	15.5	0.8	63.01	0.80	0.87	0.78	0.81	-4.26	0.63	0.60
20.1	17.4	14.2	0.7	70.65	0.83	0.53	0.87	0.82	-4.12	0.71	0.46
17.3	16.5	13.9	0.9	80.35	0.88	0.11	0.95	0.84	-4.04	0.80	0.24
18.0	14.6	12.7	0.8	70.56	0.85	0.78	0.81	0.87	-3.87	0.71	0.64
15.6	13.5	10.9	0.8	69.87	0.83	0.49	0.87	0.81	-3.75	0.70	0.45
22.1	18.4	14.5	0.9	65.61	0.80	0.64	0.83	0.79	-4.20	0.66	0.49
23.1	22.0	12.1	0.9	52.38	0.66	0.10	0.95	0.55	-4.46	0.52	0.10
21.1	16.8	14.4	0.8	68.25	0.84	0.83	0.80	0.86	-4.07	0.68	0.64
22.0	20.1	18.0	0.9	81.82	0.90	0.43	0.91	0.90	-4.33	0.82	0.47
22.0	16.9	11.2	0.8	50.91	0.70	0.84	0.77	0.66	-4.08	0.51	0.47
19.8	16.9	10.0	0.8	50.51	0.67	0.48	0.85	0.59	-4.08	0.51	0.30
20.9	15.0	11.8	0.8	56.46	0.76	1.05	0.72	0.79	-3.91	0.56	0.65
28.6	16.3	15.1	0.8	52.80	0.79	1.66	0.57	0.93	-4.03	0.53	0.91
30.0	20.5	16.1	0.8	53.67	0.75	1.21	0.68	0.79	-4.36	0.54	0.68
17.1	14.0	11.9	0.9	69.59	0.84	0.72	0.82	0.85	-3.81	0.70	0.60
18.0	14.0	12.3	0.8	68.33	0.84	0.90	0.78	0.88	-3.81	0.68	0.70
18.7	14.7	10.0	0.7	53.48	0.71	0.75	0.79	0.68	-3.88	0.53	0.46
16.6	15.1	12.3	0.8	74.10	0.85	0.31	0.91	0.81	-3.92	0.74	0.35
16.0	14.1	11.9	0.7	74.38	0.86	0.46	0.88	0.84	-3.82	0.74	0.46
23.1	16.4	14.1	0.7	61.04	0.81	1.13	0.71	0.86	-4.04	0.61	0.74
28.2	23.1	16.7	0.9	59.22	0.75	0.68	0.82	0.72	-4.53	0.59	0.44
22.0	17.1	13.1	0.7	59.55	0.77	0.83	0.78	0.77	-4.10	0.60	0.55
22.9	16.2	13.4	0.8	58.52	0.79	1.12	0.71	0.83	-4.02	0.59	0.71
27.0	18.5	14.6	0.7	54.07	0.75	1.19	0.69	0.79	-4.21	0.54	0.69
29.7	21.8	15.3	0.8	51.52	0.71	1.00	0.73	0.70	-4.45	0.52	0.55
32.9	24.4	17.9	0.7	54.41	0.74	0.98	0.74	0.73	-4.61	0.54	0.57
55.1	32.2	19.8	0.7	35.93	0.60	1.77	0.58	0.61	-5.01	0.36	0.65
34.6	28.9	16.9	0.9	48.84	0.66	0.60	0.84	0.58	-4.85	0.49	0.32
32.2	22.3	19.0	0.8	59.01	0.80	1.21	0.69	0.85	-4.48	0.59	0.75
35.0	27.7	19.1	0.9	54.57	0.72	0.78	0.79	0.69	-4.79	0.55	0.46
31.2	24.8	19.2	0.7	61.54	0.78	0.80	0.79	0.77	-4.63	0.62	0.53
32.2	25.2	19.7	0.8	61.18	0.78	0.85	0.78	0.78	-4.66	0.61	0.56
37.8	34.0	17.4	0.7	46.03	0.62	0.35	0.90	0.51	-5.09	0.46	0.19
25.2	16.3	13.2	0.9	52.38	0.75	1.34	0.65	0.81	-4.03	0.52	0.74
28.5	16.5	13.0	0.8	45.61	0.71	1.63	0.58	0.79	-4.04	0.46	0.77

A-axis	B-axis	C-axis	Roundness	Flatness	Sphericity	OP-index	b/a	c/b	B-axis phi	c/a	a-b/a-c
44.5	31.7	21.7	0.9	48.76	0.69	1.11	0.71	0.68	-4.99	0.49	0.56
22.8	16.8	9.9	0.8	43.42	0.63	0.98	0.74	0.59	-4.07	0.43	0.47
34.8	25.0	17.6	0.9	50.57	0.71	1.07	0.72	0.70	-4.64	0.51	0.57
37.8	25.9	15.2	0.8	40.21	0.62	1.25	0.69	0.59	-4.69	0.40	0.53
37.1	24.3	22.4	0.7	60.38	0.82	1.39	0.65	0.92	-4.60	0.60	0.87
21.0	16.4	11.1	0.7	52.86	0.71	0.78	0.78	0.68	-4.04	0.53	0.46
20.7	15.8	13.6	0.8	65.70	0.83	0.94	0.76	0.86	-3.98	0.66	0.69
23.6	17.2	13.1	0.7	55.51	0.75	1.01	0.73	0.76	-4.10	0.56	0.61
27.9	19.5	15.5	0.8	55.56	0.76	1.15	0.70	0.79	-4.29	0.56	0.68
28.5	25.3	12.6	0.9	44.21	0.60	0.38	0.89	0.50	-4.66	0.44	0.20
15.0	12.7	11.3	0.8	75.33	0.88	0.65	0.85	0.89	-3.67	0.75	0.62
16.8	15.8	11.7	0.7	69.64	0.80	0.14	0.94	0.74	-3.98	0.70	0.20
18.8	17.4	12.9	0.7	68.62	0.80	0.22	0.93	0.74	-4.12	0.69	0.24
20.8	19.6	13.8	0.9	66.35	0.78	0.15	0.94	0.70	-4.29	0.66	0.17
19.9	12.7	10.7	0.8	53.77	0.77	1.35	0.64	0.84	-3.67	0.54	0.78
17.9	12.8	9.2	0.7	51.40	0.72	1.03	0.72	0.72	-3.68	0.51	0.59
19.5	14.4	11.3	0.7	57.95	0.77	0.97	0.74	0.78	-3.85	0.58	0.62
18.8	14.6	11.7	0.8	62.23	0.79	0.84	0.78	0.80	-3.87	0.62	0.59
18.0	13.7	11.9	0.7	66.11	0.83	0.94	0.76	0.87	-3.78	0.66	0.70
26.4	20.0	17.2	0.8	65.15	0.82	0.98	0.76	0.86	-4.32	0.65	0.70
23.8	19.5	11.0	0.7	46.22	0.64	0.64	0.82	0.56	-4.29	0.46	0.34
34.5	25.6	21.4	0.7	62.03	0.80	1.03	0.74	0.84	-4.68	0.62	0.68
19.7	12.8	11.0	0.8	55.84	0.78	1.32	0.65	0.86	-3.68	0.56	0.79
36.5	24.3	14.4	0.9	39.45	0.62	1.34	0.67	0.59	-4.60	0.39	0.55
36.4	22.7	15.2	0.8	41.76	0.65	1.49	0.62	0.67	-4.50	0.42	0.65
36.3	25.1	23.3	0.7	64.19	0.84	1.28	0.69	0.93	-4.65	0.64	0.86
36.9	29.9	20.6	0.7	55.83	0.73	0.71	0.81	0.69	-4.90	0.56	0.43
22.3	16.5	9.2	0.9	41.26	0.61	0.98	0.74	0.56	-4.04	0.41	0.44
30.0	23.0	15.5	0.7	51.67	0.70	0.87	0.77	0.67	-4.52	0.52	0.48
26.0	20.2	13.5	0.8	51.92	0.70	0.82	0.78	0.67	-4.34	0.52	0.46
43.1	31.0	15.3	0.9	35.50	0.56	1.18	0.72	0.49	-4.95	0.35	0.44
44.4	28.5	25.0	0.9	56.31	0.79	1.41	0.64	0.88	-4.83	0.56	0.82
27.1	20.1	10.8	0.7	39.85	0.60	1.00	0.74	0.54	-4.33	0.40	0.43
30.0	18.0	12.0	0.7	40.00	0.64	1.60	0.60	0.67	-4.17	0.40	0.67
24.4	18.5	16.9	0.9	69.26	0.86	1.04	0.76	0.91	-4.21	0.69	0.79
29.7	19.0	16.0	0.8	53.87	0.77	1.38	0.64	0.84	-4.25	0.54	0.78
28.0	20.0	16.0	0.8	57.14	0.77	1.09	0.71	0.80	-4.32	0.57	0.67
58.0	32.9	24.3	0.7	41.90	0.68	1.74	0.57	0.74	-5.04	0.42	0.74
25.5	17.0	12.0	0.8	47.06	0.69	1.26	0.67	0.71	-4.09	0.47	0.63
21.0	18.3	12.2	0.7	58.10	0.73	0.43	0.87	0.67	-4.19	0.58	0.31
34.0	25.6	19.5	0.8	57.35	0.76	0.95	0.75	0.76	-4.68	0.57	0.58
19.5	17.6	9.8	0.8	50.26	0.65	0.29	0.90	0.56	-4.14	0.50	0.20

A-axis	B-axis	C-axis	Roundness	Flatness	Sphericity	OP-index	b/a	c/b	B-axis phi	c/a	a-b/a-c
21.8	13.5	9.5	0.7	43.58	0.67	1.46	0.62	0.70	-3.75	0.44	0.67
18.3	18.0	13.3	0.9	72.68	0.81	-0.06	0.98	0.74	-4.17	0.73	0.06
19.5	15.9	12.7	0.7	65.13	0.80	0.70	0.82	0.80	-3.99	0.65	0.53
25.5	17.6	10.0	0.8	39.22	0.61	1.22	0.69	0.57	-4.14	0.39	0.51
16.4	12.7	10.3	0.7	62.80	0.80	0.84	0.77	0.81	-3.67	0.63	0.61
20.4	15.0	12.4	0.7	60.78	0.80	1.01	0.74	0.83	-3.91	0.61	0.68
22.0	14.6	14.0	0.9	63.64	0.85	1.36	0.66	0.96	-3.87	0.64	0.93
15.0	12.0	10.0	0.8	66.67	0.82	0.75	0.80	0.83	-3.58	0.67	0.60
11.7	9.0	6.5	0.7	55.56	0.74	0.76	0.77	0.72	-3.17	0.56	0.52
28.0	21.1	18.6	0.9	66.43	0.84	1.02	0.75	0.88	-4.40	0.66	0.73
27.9	24.0	17.8	0.8	63.80	0.78	0.53	0.86	0.74	-4.58	0.64	0.39
31.5	26.1	18.0	0.9	57.14	0.73	0.64	0.83	0.69	-4.71	0.57	0.40
22.7	21.1	13.4	0.7	59.03	0.72	0.20	0.93	0.64	-4.40	0.59	0.17
33.0	15.0	12.4	0.8	37.58	0.68	2.26	0.45	0.83	-3.91	0.38	0.87
26.9	20.1	15.2	0.8	56.51	0.75	0.95	0.75	0.76	-4.33	0.57	0.58
22.5	15.2	13.0	0.9	57.78	0.79	1.24	0.68	0.86	-3.93	0.58	0.77
20.2	15.0	8.9	0.9	44.06	0.64	0.94	0.74	0.59	-3.91	0.44	0.46
30.4	19.0	17.1	0.8	56.25	0.80	1.46	0.63	0.90	-4.25	0.56	0.86
22.9	14.2	12.0	0.7	52.40	0.76	1.44	0.62	0.85	-3.83	0.52	0.80
22.3	18.1	14.9	0.8	66.82	0.82	0.75	0.81	0.82	-4.18	0.67	0.57
54.3	33.4	29.5	0.7	54.33	0.78	1.51	0.62	0.88	-5.06	0.54	0.84
29.0	22.6	14.1	0.9	48.62	0.67	0.81	0.78	0.62	-4.50	0.49	0.43
31.2	22.5	11.8	0.7	37.82	0.58	1.12	0.72	0.52	-4.49	0.38	0.45
22.7	22.0	12.9	0.7	56.83	0.69	0.04	0.97	0.59	-4.46	0.57	0.07
22.9	19.3	15.8	0.7	69.00	0.83	0.63	0.84	0.82	-4.27	0.69	0.51
36.5	27.8	18.3	0.9	50.14	0.69	0.90	0.76	0.66	-4.80	0.50	0.48
19.4	14.8	10.8	0.9	55.67	0.74	0.86	0.76	0.73	-3.89	0.56	0.53
31.5	29.2	24.1	0.7	76.51	0.86	0.32	0.93	0.83	-4.87	0.77	0.31
32.2	23.3	16.4	0.9	50.93	0.71	1.04	0.72	0.70	-4.54	0.51	0.56
23.9	17.9	13.0	0.9	54.39	0.73	0.93	0.75	0.73	-4.16	0.54	0.55
24.9	17.0	12.6	0.8	50.60	0.72	1.19	0.68	0.74	-4.09	0.51	0.64
21.5	15.6	10.7	0.9	49.77	0.70	1.00	0.73	0.69	-3.96	0.50	0.55
20.0	14.9	12.3	0.9	61.50	0.80	0.97	0.75	0.83	-3.90	0.62	0.66
21.0	15.5	10.2	0.9	48.57	0.68	0.95	0.74	0.66	-3.95	0.49	0.51
27.0	21.0	16.2	0.8	60.00	0.77	0.85	0.78	0.77	-4.39	0.60	0.56
24.0	23.1	13.8	0.9	57.50	0.70	0.07	0.96	0.60	-4.53	0.58	0.09
25.0	19.5	15.3	0.7	61.20	0.78	0.84	0.78	0.78	-4.29	0.61	0.57
19.3	17.9	10.7	0.7	55.44	0.69	0.19	0.93	0.60	-4.16	0.55	0.16
27.2	24.5	17.9	0.8	65.81	0.78	0.36	0.90	0.73	-4.61	0.66	0.29
21.4	16.0	12.2	0.8	57.01	0.76	0.93	0.75	0.76	-4.00	0.57	0.59
21.0	16.5	12.8	0.8	60.95	0.78	0.80	0.79	0.78	-4.04	0.61	0.55
30.0	20.8	18.2	0.8	60.67	0.81	1.22	0.69	0.88	-4.38	0.61	0.78

A−axis	B−axis	C−axis	Roundness	Flatness	Sphericity	OP−index	b/a	c/b	B−axis phi	c/a	a−b/a−c
19.0	17.1	13.8	0.9	72.63	0.84	0.37	0.90	0.81	−4.10	0.73	0.37
14.8	13.7	11.0	0.9	74.32	0.84	0.21	0.93	0.80	−3.78	0.74	0.29
17.0	13.2	11.3	0.9	66.47	0.83	0.87	0.78	0.86	−3.72	0.66	0.67
15.3	10.0	8.9	0.8	58.17	0.80	1.29	0.65	0.89	−3.32	0.58	0.83
34.7	26.5	23.0	0.8	66.28	0.83	0.99	0.76	0.87	−4.73	0.66	0.70
20.9	15.2	13.2	0.7	63.16	0.82	1.07	0.73	0.87	−3.93	0.63	0.74
19.1	17.6	11.9	0.8	62.30	0.75	0.22	0.92	0.68	−4.14	0.62	0.21
20.9	16.4	9.5	0.8	45.45	0.64	0.77	0.78	0.58	−4.04	0.45	0.39
26.1	24.6	18.1	0.7	69.35	0.80	0.18	0.94	0.74	−4.62	0.69	0.19
28.9	20.6	16.8	0.8	58.13	0.78	1.11	0.71	0.82	−4.36	0.58	0.69
23.4	18.9	13.7	0.7	58.55	0.75	0.70	0.81	0.72	−4.24	0.59	0.46
26.5	22.6	16.0	0.8	60.38	0.75	0.54	0.85	0.71	−4.50	0.60	0.37
31.0	26.1	24.6	0.7	79.35	0.91	0.87	0.84	0.94	−4.71	0.79	0.77
16.8	11.8	9.3	0.8	55.36	0.76	1.08	0.70	0.79	−3.56	0.55	0.67
16.8	15.2	12.8	0.8	76.19	0.86	0.36	0.90	0.84	−3.93	0.76	0.40
23.1	19.0	14.8	0.8	64.07	0.79	0.68	0.82	0.78	−4.25	0.64	0.49
19.6	17.2	12.8	0.8	65.31	0.79	0.43	0.88	0.74	−4.10	0.65	0.35
33.8	31.9	18.5	0.8	54.73	0.68	0.17	0.94	0.58	−5.00	0.55	0.12
20.6	18.4	12.5	0.8	60.68	0.74	0.35	0.89	0.68	−4.20	0.61	0.27
38.0	26.7	22.2	0.7	58.42	0.79	1.17	0.70	0.83	−4.74	0.58	0.72
34.9	27.9	20.9	0.9	59.89	0.77	0.78	0.80	0.75	−4.80	0.60	0.50
23.6	19.0	14.5	0.8	61.44	0.78	0.73	0.81	0.76	−4.25	0.61	0.51
20.8	17.2	12.7	0.9	61.06	0.77	0.63	0.83	0.74	−4.10	0.61	0.44
40.9	25.0	17.1	0.7	41.81	0.66	1.55	0.61	0.68	−4.64	0.42	0.67
18.2	16.8	8.8	0.8	48.35	0.63	0.20	0.92	0.52	−4.07	0.48	0.15
28.5	22.8	16.6	0.7	58.25	0.75	0.75	0.80	0.73	−4.51	0.58	0.48
24.8	20.8	16.9	0.9	68.15	0.82	0.65	0.84	0.81	−4.38	0.68	0.51
29.8	20.6	13.0	0.8	43.62	0.65	1.19	0.69	0.63	−4.36	0.44	0.55
25.4	22.9	12.1	0.9	47.64	0.63	0.32	0.90	0.53	−4.52	0.48	0.19
24.5	18.1	14.9	0.9	60.82	0.79	1.01	0.74	0.82	−4.18	0.61	0.67
24.6	18.2	11.9	0.8	48.37	0.68	0.96	0.74	0.65	−4.19	0.48	0.50
33.8	21.5	15.4	0.9	45.56	0.69	1.41	0.64	0.72	−4.43	0.46	0.67
33.9	24.9	18.1	0.7	53.39	0.73	1.01	0.73	0.73	−4.64	0.53	0.57
21.0	18.8	13.0	0.8	61.90	0.75	0.34	0.90	0.69	−4.23	0.62	0.27
27.9	21.1	15.3	0.9	54.84	0.74	0.91	0.76	0.73	−4.40	0.55	0.54
26.8	22.9	17.3	0.8	64.55	0.79	0.55	0.85	0.76	−4.52	0.65	0.41
24	17.2	16.8	0.9	70.00	0.88	1.25	0.72	0.98	−4.10	0.70	0.94
30.2	22.3	15.5	0.8	51.32	0.71	0.98	0.74	0.70	−4.48	0.51	0.54
15.6	13.2	11.2	0.7	71.79	0.85	0.60	0.85	0.85	−3.72	0.72	0.55

Appendix (XII)(d)

PEBBLE DATA ROODERAND CONGLOMERATE FORMATION TYGERFONTEIN 488

A-axis	B-axis	C-axis	Roundness	Flatness	Sphericity	OP-index	b/a	c/b	B-axis phi	c/a	a-b/a-c
73.7	47.8	26.2	0.9	35.55	0.58	1.50	0.65	0.55	-5.58	0.36	0.55
44.8	40.0	23.5	0.6	52.46	0.68	0.38	0.89	0.59	-5.32	0.52	0.23
40.1	39.3	33.3	0.8	83.04	0.89	0.05	0.98	0.85	-5.30	0.83	0.12
40.7	38.2	27.2	0.8	66.83	0.78	0.22	0.94	0.71	-5.26	0.67	0.19
49.1	36.6	29.8	0.6	60.69	0.79	1.02	0.75	0.81	-5.19	0.61	0.65
39.1	35.4	15.3	0.7	39.13	0.55	0.34	0.91	0.43	-5.15	0.39	0.16
48.2	33.3	27.8	0.8	57.68	0.78	1.22	0.69	0.83	-5.06	0.58	0.73
34.9	33.1	11.2	0.9	32.09	0.48	0.17	0.95	0.34	-5.05	0.32	0.08
34.3	32.6	29.1	0.9	84.84	0.91	0.27	0.95	0.89	-5.03	0.85	0.33
39.3	31.7	23.0	0.8	58.52	0.75	0.74	0.81	0.73	-4.99	0.59	0.47
33.2	31.3	22.0	0.6	66.27	0.78	0.19	0.94	0.70	-4.97	0.66	0.17
46.0	31.0	20.3	0.7	44.13	0.66	1.28	0.67	0.65	-4.95	0.44	0.58
42.3	30.8	23.9	0.8	56.50	0.76	1.06	0.73	0.78	-4.94	0.57	0.62
37.5	30.2	24.5	0.6	65.33	0.81	0.80	0.81	0.81	-4.92	0.65	0.56
35.9	30.1	9.3	0.6	25.91	0.43	0.77	0.84	0.31	-4.91	0.26	0.22
38.0	30.1	25.1	0.9	66.05	0.82	0.87	0.79	0.83	-4.91	0.66	0.61
30.9	30.0	24.8	0.6	80.26	0.87	0.08	0.97	0.83	-4.91	0.80	0.15
41.9	29.8	17.2	0.5	41.05	0.62	1.14	0.71	0.58	-4.90	0.41	0.49
35.3	29.4	16.6	0.7	47.03	0.64	0.61	0.83	0.56	-4.88	0.47	0.32
33.8	29.4	23.1	0.8	68.34	0.81	0.53	0.87	0.79	-4.88	0.68	0.41
35.0	29.4	16.3	0.7	46.57	0.64	0.59	0.84	0.55	-4.88	0.47	0.30
39.6	29.4	22.2	0.6	56.06	0.75	0.99	0.74	0.76	-4.88	0.56	0.59
36.4	29.3	24.5	0.6	67.31	0.83	0.82	0.80	0.84	-4.87	0.67	0.60
48.2	29.2	24.1	0.7	50.00	0.74	1.54	0.61	0.83	-4.87	0.50	0.79
38.3	28.6	16.8	0.7	43.86	0.64	0.98	0.75	0.59	-4.84	0.44	0.45
40.1	28.4	14.1	0.8	35.16	0.56	1.23	0.71	0.50	-4.83	0.35	0.45
33.0	28.2	15.6	0.6	47.27	0.64	0.52	0.85	0.55	-4.82	0.47	0.28
29.7	28.0	24.2	0.7	81.48	0.89	0.27	0.94	0.86	-4.81	0.81	0.31
36.7	28.0	24.3	0.6	66.21	0.83	1.00	0.76	0.87	-4.81	0.66	0.70
35.8	27.9	23.6	0.7	65.92	0.82	0.92	0.78	0.85	-4.80	0.66	0.65
35.0	27.9	24.9	0.6	71.14	0.86	0.92	0.80	0.89	-4.80	0.71	0.70
31.3	27.9	23.3	0.7	74.44	0.85	0.49	0.89	0.84	-4.80	0.74	0.43
33.1	27.5	27.1	0.8	81.87	0.93	1.04	0.83	0.99	-4.78	0.82	0.93
37.0	27.4	22.4	0.6	60.54	0.79	1.03	0.74	0.82	-4.78	0.61	0.66
35.6	27.2	18.3	0.8	51.40	0.70	0.89	0.76	0.67	-4.77	0.51	0.49
31.2	27.1	17.2	0.8	55.13	0.70	0.47	0.87	0.63	-4.76	0.55	0.29
31.2	27.1	20.7	0.7	66.35	0.80	0.52	0.87	0.76	-4.76	0.66	0.39

A-axis	B-axis	C-axis	Roundness	Flatness	Sphericity	OP-index	b/a	c/b	B-axis phi	c/a	a-b/a-c
31.5	27.0	17.5	0.8	55.56	0.71	0.51	0.86	0.65	-4.75	0.56	0.32
33.2	27.0	24.0	0.9	72.29	0.86	0.86	0.81	0.89	-4.75	0.72	0.67
44.5	27.0	17.8	0.6	40.00	0.64	1.59	0.61	0.66	-4.75	0.40	0.66
30.1	26.8	17.1	0.6	56.81	0.71	0.38	0.89	0.64	-4.74	0.57	0.25
28.9	26.7	21.5	0.6	74.39	0.84	0.31	0.92	0.81	-4.74	0.74	0.30
31.8	26.6	16.3	0.9	51.26	0.68	0.59	0.84	0.61	-4.73	0.51	0.34
42.1	26.6	25.0	0.7	59.38	0.82	1.48	0.63	0.94	-4.73	0.59	0.91
40.1	26.5	24.0	0.6	59.85	0.82	1.36	0.66	0.91	-4.73	0.60	0.84
29.6	26.5	16.3	0.9	55.07	0.70	0.35	0.90	0.62	-4.73	0.55	0.23
37.3	26.3	17.4	0.5	46.65	0.68	1.13	0.71	0.66	-4.72	0.47	0.55
27.2	26.2	16.9	0.8	62.13	0.74	0.08	0.96	0.65	-4.71	0.62	0.10
33.0	26.1	25.4	0.7	76.97	0.91	1.09	0.79	0.97	-4.71	0.77	0.91
27.3	26.1	13.9	0.6	50.92	0.65	0.10	0.96	0.53	-4.71	0.51	0.09
27.1	26.1	20.1	0.8	74.17	0.83	0.10	0.96	0.77	-4.71	0.74	0.14
30.4	26.0	17.9	0.7	58.88	0.74	0.53	0.86	0.69	-4.70	0.59	0.35
32.6	26.0	19.1	0.6	58.59	0.76	0.77	0.80	0.73	-4.70	0.59	0.49
27.3	26.0	11.3	0.8	41.39	0.56	0.12	0.95	0.43	-4.70	0.41	0.08
30.3	25.9	19.0	0.9	62.71	0.77	0.55	0.85	0.73	-4.69	0.63	0.39
33.2	25.7	16.0	0.6	48.19	0.67	0.84	0.77	0.62	-4.68	0.48	0.44
33.8	25.6	18.9	0.8	55.92	0.74	0.92	0.76	0.74	-4.68	0.56	0.55
31.7	25.5	17.9	0.7	56.47	0.73	0.73	0.80	0.70	-4.67	0.56	0.45
28.1	25.2	17.6	0.8	62.63	0.76	0.36	0.90	0.70	-4.66	0.63	0.28
36.1	25.2	16.2	0.5	44.88	0.66	1.16	0.70	0.64	-4.66	0.45	0.55
37.1	25.1	20.0	0.9	53.91	0.75	1.25	0.68	0.80	-4.65	0.54	0.70
31.9	25.1	19.5	0.8	61.13	0.78	0.83	0.79	0.78	-4.65	0.61	0.55
50.1	25.1	19.8	0.8	39.52	0.68	2.05	0.50	0.79	-4.65	0.40	0.83
26.8	25.1	20.7	0.7	77.24	0.86	0.25	0.94	0.82	-4.65	0.77	0.28
28.0	25.1	13.9	0.7	49.64	0.65	0.34	0.90	0.55	-4.65	0.50	0.21
31.9	25.1	23.0	0.6	72.10	0.87	0.98	0.79	0.92	-4.65	0.72	0.76
32.3	25.0	18.9	0.8	58.51	0.76	0.87	0.77	0.76	-4.64	0.59	0.54
28.6	25.0	10.6	0.7	37.06	0.54	0.46	0.87	0.42	-4.64	0.37	0.20
28.5	25.0	24.7	0.7	86.67	0.95	0.91	0.88	0.99	-4.64	0.87	0.92
27.3	25.0	18.2	0.5	66.67	0.79	0.30	0.92	0.73	-4.64	0.67	0.25
37.1	24.7	13.8	0.7	37.20	0.59	1.37	0.67	0.56	-4.63	0.37	0.53
33.9	24.7	19.9	0.8	58.70	0.78	1.06	0.73	0.81	-4.63	0.59	0.66
29.3	24.7	14.0	0.6	47.78	0.65	0.56	0.84	0.57	-4.63	0.48	0.30
28.4	24.6	17.6	0.8	61.97	0.76	0.49	0.87	0.72	-4.62	0.62	0.35
29.4	24.6	13.3	0.8	45.24	0.63	0.59	0.84	0.54	-4.62	0.45	0.30
36.0	24.5	18.8	0.7	52.22	0.74	1.22	0.68	0.77	-4.61	0.52	0.67
25.0	24.5	15.0	0.6	60.00	0.72	0.00	0.98	0.61	-4.61	0.60	0.05
27.3	24.4	13.4	0.8	49.08	0.65	0.35	0.89	0.55	-4.61	0.49	0.21
28.5	24.3	14.6	0.7	51.23	0.68	0.52	0.85	0.60	-4.60	0.51	0.30

A−axis	B−axis	C−axis	Roundness	Flatness	Sphericity	OP−index	b/a	c/b	B−axis phi	c/a	a−b/a−c
46.0	24.3	20.2	0.6	43.91	0.71	1.87	0.53	0.83	−4.60	0.44	0.84
25.3	24.2	17.2	0.7	67.98	0.78	0.11	0.96	0.71	−4.60	0.68	0.14
25.4	24.1	10.6	0.7	41.73	0.57	0.13	0.95	0.44	−4.59	0.42	0.09
37.0	24.1	23.2	0.9	62.70	0.85	1.43	0.65	0.96	−4.59	0.63	0.93
28.0	24.0	18.4	0.6	65.71	0.80	0.55	0.86	0.77	−4.58	0.66	0.42
42.0	24.0	23.0	0.6	54.76	0.81	1.68	0.57	0.96	−4.58	0.55	0.95
46.6	23.9	20.2	0.8	43.35	0.72	1.94	0.51	0.85	−4.58	0.43	0.86
31.1	23.9	15.0	0.8	48.23	0.67	0.86	0.77	0.63	−4.58	0.48	0.45
28.1	23.9	18.0	0.8	64.06	0.78	0.57	0.85	0.75	−4.58	0.64	0.42
28.9	23.9	13.0	0.9	44.98	0.63	0.63	0.83	0.54	−4.58	0.45	0.31
40.1	23.9	22.6	0.9	56.36	0.81	1.59	0.60	0.95	−4.58	0.56	0.93
34.7	23.9	19.0	0.7	54.76	0.76	1.20	0.69	0.79	−4.58	0.55	0.69
29.2	23.8	14.7	0.8	50.34	0.68	0.67	0.82	0.62	−4.57	0.50	0.37
37.3	23.8	13.7	0.7	36.73	0.60	1.50	0.64	0.58	−4.57	0.37	0.57
40.0	23.7	21.2	0.7	53.00	0.78	1.59	0.59	0.89	−4.57	0.53	0.87
28.3	23.7	12.2	0.7	43.11	0.61	0.59	0.84	0.51	−4.57	0.43	0.29
27.7	23.6	16.7	0.8	60.29	0.75	0.54	0.85	0.71	−4.56	0.60	0.37
25.9	23.6	15.1	0.7	58.30	0.72	0.29	0.91	0.64	−4.56	0.58	0.21
32.5	23.6	13.2	0.8	40.62	0.61	1.07	0.73	0.56	−4.56	0.41	0.46
27.6	23.6	22.8	0.6	82.61	0.93	0.88	0.86	0.97	−4.56	0.83	0.83
32.3	23.5	21.4	0.7	66.25	0.84	1.15	0.73	0.91	−4.55	0.66	0.81
23.9	23.4	17.4	0.7	72.80	0.82	0.00	0.98	0.74	−4.55	0.73	0.08
33.6	23.4	19.7	0.6	58.63	0.79	1.19	0.70	0.84	−4.55	0.59	0.73
29.6	23.3	17.2	0.6	58.11	0.75	0.80	0.79	0.74	−4.54	0.58	0.51
28.9	23.2	16.0	0.7	55.36	0.73	0.73	0.80	0.69	−4.54	0.55	0.44
29.1	23.2	14.3	0.8	49.14	0.67	0.74	0.80	0.62	−4.54	0.49	0.40
27.4	23.1	12.8	0.8	46.72	0.64	0.56	0.84	0.55	−4.53	0.47	0.29
27.3	23.1	21.0	0.6	76.92	0.89	0.76	0.85	0.91	−4.53	0.77	0.67
28.1	23.0	18.5	0.7	65.84	0.81	0.73	0.82	0.80	−4.52	0.66	0.53
39.2	23.0	8.7	0.6	22.19	0.44	2.32	0.59	0.38	−4.52	0.22	0.53
35.6	22.9	15.8	0.6	44.38	0.67	1.39	0.64	0.69	−4.52	0.44	0.64
23.9	22.9	14.1	0.9	59.00	0.71	0.09	0.96	0.62	−4.52	0.59	0.10
27.5	22.8	14.3	0.5	52.00	0.69	0.61	0.83	0.63	−4.51	0.52	0.36
33.0	22.6	9.7	0.6	29.39	0.50	1.45	0.68	0.43	−4.50	0.29	0.45
27.2	22.6	16.2	0.6	59.56	0.75	0.63	0.83	0.72	−4.50	0.60	0.42
24.3	22.5	13.7	0.6	56.38	0.70	0.22	0.93	0.61	−4.49	0.56	0.17
32.0	22.5	21.9	0.6	68.44	0.87	1.30	0.70	0.97	−4.49	0.68	0.94
24.2	22.4	11.1	0.7	45.87	0.61	0.22	0.93	0.50	−4.49	0.46	0.14
23.5	22.3	13.6	0.7	57.87	0.71	0.12	0.95	0.61	−4.48	0.58	0.12
28.6	22.3	14.8	0.8	51.75	0.70	0.81	0.78	0.66	−4.48	0.52	0.46
31.1	22.2	18.1	0.7	58.20	0.78	1.11	0.71	0.82	−4.47	0.58	0.68
28.6	22.2	14.9	0.8	52.10	0.70	0.83	0.78	0.67	−4.47	0.52	0.47

A-axis	B-axis	C-axis	Roundness	Flatness	Sphericity	OP-index	b/a	c/b	B-axis phi	c/a	a-b/a-c
36.2	22.2	16.6	0.6	45.86	0.70	1.50	0.61	0.75	-4.47	0.46	0.71
29.4	22.2	13.0	0.7	44.22	0.64	0.92	0.76	0.59	-4.47	0.44	0.44
24.3	22.2	22.1	0.8	90.95	0.97	0.80	0.91	1.00	-4.47	0.91	0.95
28.1	22.1	19.5	0.7	69.40	0.85	0.92	0.79	0.88	-4.47	0.69	0.70
34.1	22.1	16.7	0.8	48.97	0.72	1.35	0.65	0.76	-4.47	0.49	0.69
28.5	22.0	20.6	0.7	72.28	0.88	1.05	0.77	0.94	-4.46	0.72	0.82
26.9	22.0	11.9	0.8	44.24	0.62	0.66	0.82	0.54	-4.46	0.44	0.33
23.9	22.0	17.1	0.8	71.55	0.82	0.29	0.92	0.78	-4.46	0.72	0.28
34.1	21.9	16.5	0.7	48.39	0.71	1.37	0.64	0.75	-4.45	0.48	0.69
23.1	21.8	11.9	0.6	51.52	0.66	0.14	0.94	0.55	-4.45	0.52	0.12
34.7	21.7	15.8	0.8	45.53	0.69	1.45	0.63	0.73	-4.44	0.46	0.69
29.3	21.6	16.5	0.6	56.31	0.75	1.00	0.74	0.76	-4.43	0.56	0.60
25.0	21.6	17.3	0.6	69.20	0.82	0.54	0.86	0.80	-4.43	0.69	0.44
25.1	21.6	17.3	0.6	68.92	0.82	0.56	0.86	0.80	-4.43	0.69	0.45
22.9	21.6	16.3	0.5	71.18	0.81	0.17	0.94	0.75	-4.43	0.71	0.20
39.4	21.6	13.7	0.6	34.77	0.60	1.94	0.55	0.63	-4.43	0.35	0.69
25.2	21.5	14.1	0.7	55.95	0.72	0.52	0.85	0.66	-4.43	0.56	0.33
25.8	21.5	18.5	0.7	71.71	0.85	0.73	0.83	0.86	-4.43	0.72	0.59
23.2	21.5	13.4	0.6	57.76	0.71	0.21	0.93	0.62	-4.43	0.58	0.17
27.3	21.4	19.8	0.8	72.53	0.88	0.99	0.78	0.93	-4.42	0.73	0.79
25.5	21.4	11.4	0.8	44.71	0.62	0.57	0.84	0.53	-4.42	0.45	0.29
23.8	21.3	11.2	0.7	47.06	0.63	0.34	0.89	0.53	-4.41	0.47	0.20
27.7	21.3	18.1	0.7	65.34	0.82	0.94	0.77	0.85	-4.41	0.65	0.67
32.0	21.2	19.5	0.9	60.94	0.82	1.35	0.66	0.92	-4.41	0.61	0.86
25.4	21.1	20.8	0.7	81.89	0.93	1.01	0.83	0.99	-4.40	0.82	0.93
28.3	21.1	15.4	0.6	54.42	0.74	0.95	0.75	0.73	-4.40	0.54	0.56
26.4	21.1	18.0	0.7	68.18	0.83	0.84	0.80	0.85	-4.40	0.68	0.63
24.1	21.0	14.7	0.5	61.00	0.75	0.45	0.87	0.70	-4.39	0.61	0.33
25.3	21.0	9.8	0.7	38.74	0.57	0.63	0.83	0.47	-4.39	0.39	0.28
34.0	21.0	19.1	0.7	56.18	0.80	1.49	0.62	0.91	-4.39	0.56	0.87
23.6	21.0	17.2	0.8	72.88	0.84	0.45	0.89	0.82	-4.39	0.73	0.41
26.6	21.0	13.9	0.8	52.26	0.70	0.77	0.79	0.66	-4.39	0.52	0.44
36.1	21.0	20.7	0.8	57.34	0.83	1.65	0.58	0.99	-4.39	0.57	0.98
21.0	20.9	13.8	0.7	65.71	0.76	-0.08	1.00	0.66	-4.39	0.66	0.01
22.0	20.9	19.4	0.9	88.18	0.94	0.26	0.95	0.93	-4.39	0.88	0.42
22.5	20.9	14.5	0.8	64.44	0.76	0.21	0.93	0.69	-4.39	0.64	0.20
24.1	20.9	12.0	0.6	49.79	0.66	0.45	0.87	0.57	-4.39	0.50	0.26
26.1	20.9	12.1	0.7	46.36	0.65	0.72	0.80	0.58	-4.39	0.46	0.37
27.0	20.8	12.0	0.6	44.44	0.64	0.86	0.77	0.58	-4.38	0.44	0.41
33.2	20.8	19.7	0.7	59.34	0.83	1.49	0.63	0.95	-4.38	0.59	0.92
22.4	20.7	11.6	0.7	51.79	0.66	0.21	0.92	0.56	-4.37	0.52	0.16
27.4	20.6	14.9	0.7	54.38	0.73	0.93	0.75	0.72	-4.36	0.54	0.54

A−axis	B−axis	C−axis	Roundness	Flatness	Sphericity	OP−index	b/a	c/b	B−axis phi	c/a	a−b/a−c
22.1	20.6	16.3	0.6	73.76	0.84	0.23	0.93	0.79	−4.36	0.74	0.26
24.3	20.5	17.0	0.6	69.96	0.83	0.65	0.84	0.83	−4.36	0.70	0.52
33.5	20.5	16.8	0.6	50.15	0.74	1.49	0.61	0.82	−4.36	0.50	0.78
28.1	20.4	10.1	0.7	35.94	0.56	1.11	0.73	0.50	−4.35	0.36	0.43
22.9	20.3	11.0	0.8	48.03	0.64	0.37	0.89	0.54	−4.34	0.48	0.22
32.1	20.2	13.7	0.6	42.68	0.66	1.45	0.63	0.68	−4.34	0.43	0.65
25.6	20.2	16.0	0.8	62.50	0.79	0.82	0.79	0.79	−4.34	0.63	0.56
28.8	20.2	18.3	0.7	63.54	0.83	1.21	0.70	0.91	−4.34	0.64	0.82
29.0	20.2	10.6	0.9	36.55	0.58	1.23	0.70	0.52	−4.34	0.37	0.48
26.1	20.1	9.1	0.7	34.87	0.54	0.93	0.77	0.45	−4.33	0.35	0.35
31.8	20.1	15.4	0.8	48.43	0.72	1.41	0.63	0.77	−4.33	0.48	0.71
21.1	20.1	17.3	0.9	81.99	0.89	0.16	0.95	0.86	−4.33	0.82	0.26
25.5	20.0	18.1	0.7	70.98	0.86	0.95	0.78	0.91	−4.32	0.71	0.74
27.1	20.0	16.6	0.7	61.25	0.80	1.03	0.74	0.83	−4.32	0.61	0.68
24.8	20.0	17.3	0.6	69.76	0.85	0.82	0.81	0.87	−4.32	0.70	0.64
40.7	20.0	14.7	0.7	36.12	0.64	2.15	0.49	0.74	−4.32	0.36	0.80
31.6	20.0	14.7	0.6	46.52	0.70	1.41	0.63	0.74	−4.32	0.47	0.69
22.7	19.9	14.5	0.7	63.88	0.77	0.44	0.88	0.73	−4.31	0.64	0.34
21.5	19.9	14.1	0.7	65.58	0.77	0.23	0.93	0.71	−4.31	0.66	0.22
31.3	19.9	15.9	0.8	50.80	0.74	1.39	0.64	0.80	−4.31	0.51	0.74
20.1	19.8	13.0	0.9	64.68	0.75	−0.04	0.99	0.66	−4.31	0.65	0.04
35.0	19.8	16.4	0.5	46.86	0.73	1.69	0.57	0.83	−4.31	0.47	0.82
26.2	19.8	16.3	0.5	62.21	0.80	0.96	0.76	0.82	−4.31	0.62	0.65
24.1	19.7	16.1	0.8	66.80	0.82	0.73	0.82	0.82	−4.30	0.67	0.55
26.2	19.7	17.2	0.8	65.65	0.83	1.02	0.75	0.87	−4.30	0.66	0.72
32.8	19.7	14.1	0.8	42.99	0.68	1.57	0.60	0.72	−4.30	0.43	0.70
25.6	19.6	14.3	0.6	55.86	0.74	0.87	0.77	0.73	−4.29	0.56	0.53
25.6	19.5	13.0	0.6	50.78	0.70	0.88	0.76	0.67	−4.29	0.51	0.48
23.1	19.5	17.3	0.6	74.89	0.87	0.71	0.84	0.89	−4.29	0.75	0.62
32.2	19.5	16.3	0.6	50.62	0.75	1.52	0.61	0.84	−4.29	0.51	0.80
20.0	19.4	14.1	0.7	70.50	0.80	0.03	0.97	0.73	−4.28	0.71	0.11
23.2	19.3	15.4	0.8	66.38	0.81	0.66	0.83	0.80	−4.27	0.66	0.50
23.5	19.3	13.0	0.8	55.32	0.72	0.64	0.82	0.67	−4.27	0.55	0.40
27.5	19.2	18.1	0.6	65.82	0.85	1.26	0.70	0.94	−4.26	0.66	0.88
19.4	19.2	10.5	0.9	54.12	0.67	−0.06	0.99	0.55	−4.26	0.54	0.02
27.0	19.1	12.1	0.9	44.81	0.66	1.11	0.71	0.63	−4.26	0.45	0.53
38.1	19.1	18.6	0.8	48.82	0.78	1.94	0.50	0.97	−4.26	0.49	0.97
21.4	19.0	13.6	0.6	63.55	0.77	0.38	0.89	0.72	−4.25	0.64	0.31
24.8	19.0	18.1	0.8	72.98	0.89	1.08	0.77	0.95	−4.25	0.73	0.87
20.7	19.0	11.3	0.8	54.59	0.69	0.23	0.92	0.59	−4.25	0.55	0.18
23.5	19.0	13.7	0.6	58.30	0.75	0.70	0.81	0.72	−4.25	0.58	0.46
32.1	19.0	12.5	0.8	38.94	0.64	1.65	0.59	0.66	−4.25	0.39	0.67

A-axis	B-axis	C-axis	Roundness	Flatness	Sphericity	OP-index	b/a	c/b	B-axis phi	c/a	a-b/a-c
26.7	19.0	12.3	0.9	46.07	0.67	1.09	0.71	0.65	-4.25	0.46	0.53
23.0	19.0	18.1	0.5	78.70	0.91	0.91	0.83	0.95	-4.25	0.79	0.82
22.0	18.9	11.8	0.7	53.64	0.69	0.48	0.86	0.62	-4.24	0.54	0.30
30.7	18.8	14.8	0.7	48.21	0.72	1.49	0.61	0.79	-4.23	0.48	0.75
24.3	18.7	17.4	0.6	71.60	0.87	1.03	0.77	0.93	-4.22	0.72	0.81
22.5	18.7	15.0	0.7	66.67	0.81	0.66	0.83	0.80	-4.22	0.67	0.51
25.3	18.6	13.2	0.8	52.17	0.72	0.98	0.74	0.71	-4.22	0.52	0.55
28.7	18.6	15.5	0.7	54.01	0.77	1.35	0.65	0.83	-4.22	0.54	0.77
20.1	18.6	12.4	0.6	61.69	0.74	0.21	0.93	0.67	-4.22	0.62	0.19
23.1	18.5	14.4	0.9	62.34	0.79	0.76	0.80	0.78	-4.21	0.62	0.53
31.8	18.5	16.0	0.6	50.31	0.76	1.61	0.58	0.86	-4.21	0.50	0.84
27.1	18.5	11.7	0.6	43.17	0.65	1.22	0.68	0.63	-4.21	0.43	0.56
27.2	18.4	11.4	0.8	41.91	0.64	1.25	0.68	0.62	-4.20	0.42	0.56
26.0	18.3	14.8	0.5	56.92	0.77	1.13	0.70	0.81	-4.19	0.57	0.69
27.1	18.3	12.0	0.7	44.28	0.66	1.24	0.68	0.66	-4.19	0.44	0.58
31.0	18.3	16.4	0.6	52.90	0.78	1.58	0.59	0.90	-4.19	0.53	0.87
20.7	18.3	12.3	0.8	59.42	0.74	0.38	0.88	0.67	-4.19	0.59	0.29
27.3	18.2	12.5	0.9	45.79	0.68	1.27	0.67	0.69	-4.19	0.46	0.61
28.3	18.2	12.5	0.6	44.17	0.67	1.38	0.64	0.69	-4.19	0.44	0.64
19.6	18.2	10.2	0.5	52.04	0.66	0.18	0.93	0.56	-4.19	0.52	0.15
18.6	18.2	14.5	0.8	77.96	0.85	-0.03	0.98	0.80	-4.19	0.78	0.10
28.1	18.2	14.7	0.7	52.31	0.75	1.34	0.65	0.81	-4.19	0.52	0.74
25.0	18.2	16.5	0.8	66.00	0.84	1.12	0.73	0.91	-4.19	0.66	0.80
22.0	18.0	17.5	0.8	79.55	0.92	0.98	0.82	0.97	-4.17	0.80	0.89
19.5	18.0	14.1	0.7	72.31	0.83	0.26	0.92	0.78	-4.17	0.72	0.28
21.9	18.0	15.9	0.7	72.60	0.86	0.78	0.82	0.88	-4.17	0.73	0.65
22.2	18.0	14.9	0.8	67.12	0.82	0.76	0.81	0.83	-4.17	0.67	0.58
23.7	18.0	16.3	0.7	68.78	0.85	1.02	0.76	0.91	-4.17	0.69	0.77
21.2	17.9	14.2	0.6	66.98	0.81	0.60	0.84	0.79	-4.16	0.67	0.47
26.6	17.9	14.9	0.8	56.02	0.78	1.25	0.67	0.83	-4.16	0.56	0.74
28.1	17.8	14.7	0.8	52.31	0.76	1.40	0.63	0.83	-4.15	0.52	0.77
23.3	17.8	14.0	0.6	60.09	0.78	0.89	0.76	0.79	-4.15	0.60	0.59
20.6	17.8	15.1	0.6	73.30	0.85	0.57	0.86	0.85	-4.15	0.73	0.51
20.1	17.7	12.0	0.9	59.70	0.74	0.39	0.88	0.68	-4.15	0.60	0.30
19.4	17.6	11.6	0.6	59.79	0.73	0.28	0.91	0.66	-4.14	0.60	0.23
22.0	17.6	12.3	0.9	55.91	0.73	0.72	0.80	0.70	-4.14	0.56	0.45
28.2	17.6	14.5	0.6	51.42	0.75	1.43	0.62	0.82	-4.14	0.51	0.77
21.1	17.5	11.0	0.7	52.13	0.69	0.59	0.83	0.63	-4.13	0.52	0.36
26.2	17.5	13.2	0.6	50.38	0.72	1.25	0.67	0.75	-4.13	0.50	0.67
23.3	17.5	11.7	0.7	50.21	0.70	0.91	0.75	0.67	-4.13	0.50	0.50
23.1	17.5	12.0	0.7	51.95	0.71	0.88	0.76	0.69	-4.13	0.52	0.50
25.8	17.5	13.0	0.7	50.39	0.72	1.21	0.68	0.74	-4.13	0.50	0.65

A-axis	B-axis	C-axis	Roundness	Flatness	Sphericity	OP-index	b/a	c/b	B-axis phi	c/a	a-b/a-c
20.7	17.5	12.2	0.7	58.94	0.74	0.54	0.85	0.70	-4.13	0.59	0.38
25.0	17.5	14.1	0.5	56.40	0.77	1.14	0.70	0.81	-4.13	0.56	0.69
20.8	17.4	12.4	0.5	59.62	0.75	0.58	0.84	0.71	-4.12	0.60	0.40
18.8	17.3	9.3	0.8	49.47	0.64	0.21	0.92	0.54	-4.11	0.49	0.16
18.8	17.3	13.3	0.8	70.74	0.82	0.26	0.92	0.77	-4.11	0.71	0.27
19.1	17.3	10.6	0.7	55.50	0.70	0.28	0.91	0.61	-4.11	0.55	0.21
18.9	17.3	9.6	0.6	50.79	0.66	0.23	0.92	0.55	-4.11	0.51	0.17
24.8	17.3	16.9	0.8	68.15	0.87	1.30	0.70	0.98	-4.11	0.68	0.95
26.3	17.3	14.4	0.8	54.75	0.77	1.30	0.66	0.83	-4.11	0.55	0.76
19.0	17.2	13.8	0.8	72.63	0.84	0.34	0.91	0.80	-4.10	0.73	0.35
34.7	17.2	16.6	0.7	47.84	0.77	1.96	0.50	0.97	-4.10	0.48	0.97
33.1	17.2	17.2	0.6	51.96	0.80	1.86	0.52	1.00	-4.10	0.52	1.00
21.0	17.2	15.5	0.7	73.81	0.87	0.81	0.82	0.90	-4.10	0.74	0.69
22.4	17.2	13.1	0.6	58.48	0.76	0.86	0.77	0.76	-4.10	0.58	0.56
29.0	17.2	16.3	0.6	56.21	0.81	1.58	0.59	0.95	-4.10	0.56	0.93
21.0	17.1	9.9	0.7	47.14	0.65	0.65	0.81	0.58	-4.10	0.47	0.35
21.3	17.1	11.4	0.7	53.52	0.71	0.70	0.80	0.67	-4.10	0.54	0.42
28.2	17.1	17.0	0.5	60.28	0.84	1.57	0.61	0.99	-4.10	0.60	0.99
20.9	17.1	12.9	0.6	61.72	0.78	0.67	0.82	0.75	-4.10	0.62	0.47
19.3	17.1	10.6	0.8	54.92	0.70	0.36	0.89	0.62	-4.10	0.55	0.25
27.2	17.1	10.9	0.8	40.07	0.63	1.47	0.63	0.64	-4.10	0.40	0.62
18.5	17.0	12.1	0.8	65.41	0.78	0.24	0.92	0.71	-4.09	0.65	0.23
20.4	17.0	16.3	0.8	79.90	0.92	0.89	0.83	0.96	-4.09	0.80	0.83
23.9	17.0	15.0	0.7	62.76	0.82	1.15	0.71	0.88	-4.09	0.63	0.78
19.0	17.0	12.9	0.8	67.89	0.80	0.36	0.89	0.76	-4.09	0.68	0.33
23.3	17.0	11.3	0.8	48.50	0.69	1.00	0.73	0.66	-4.09	0.48	0.53
23.3	16.9	13.5	0.9	57.94	0.77	1.04	0.73	0.80	-4.08	0.58	0.65
18.7	16.9	10.3	0.9	55.08	0.69	0.28	0.90	0.61	-4.08	0.55	0.21
21.0	16.8	11.3	0.6	53.81	0.71	0.71	0.80	0.67	-4.07	0.54	0.43
21.0	16.8	9.9	0.6	47.14	0.65	0.71	0.80	0.59	-4.07	0.47	0.38
24.0	16.7	12.1	0.7	50.42	0.71	1.13	0.70	0.72	-4.06	0.50	0.61
18.3	16.7	9.8	0.8	53.55	0.68	0.24	0.91	0.59	-4.06	0.54	0.19
30.4	16.5	11.8	0.9	38.82	0.65	1.86	0.54	0.72	-4.04	0.39	0.75
20.3	16.5	13.2	0.6	65.02	0.80	0.71	0.81	0.80	-4.04	0.65	0.54
19.6	16.5	13.2	0.7	67.35	0.81	0.60	0.84	0.80	-4.04	0.67	0.48
21.9	16.5	13.2	0.5	60.27	0.78	0.93	0.75	0.80	-4.04	0.60	0.62
22.0	16.4	13.4	0.7	60.91	0.79	0.97	0.75	0.82	-4.04	0.61	0.65
22.4	16.3	13.1	0.6	58.48	0.78	1.03	0.73	0.80	-4.03	0.58	0.66
18.8	16.3	12.0	0.9	63.83	0.78	0.46	0.87	0.74	-4.03	0.64	0.37
18.5	16.2	15.3	0.7	82.70	0.92	0.68	0.88	0.94	-4.02	0.83	0.72
23.4	16.1	11.1	0.7	47.44	0.69	1.17	0.69	0.69	-4.01	0.47	0.59
16.2	16.1	10.2	0.6	62.96	0.74	-0.11	0.99	0.63	-4.01	0.63	0.02

A-axis	B-axis	C-axis	Roundness	Flatness	Sphericity	OP-index	b/a	c/b	B-axis phi	c/a	a-b/a-c
20.3	16.0	11.6	0.7	57.14	0.75	0.76	0.79	0.73	-4.00	0.57	0.49
19.5	16.0	15.0	0.6	76.92	0.90	0.87	0.82	0.94	-4.00	0.77	0.78
17.1	16.0	10.2	0.7	59.65	0.72	0.15	0.94	0.64	-4.00	0.60	0.16
16.5	15.9	11.1	0.6	67.27	0.78	0.03	0.96	0.70	-3.99	0.67	0.11
16.4	15.9	13.5	0.6	82.32	0.89	0.00	0.97	0.85	-3.99	0.82	0.17
23.5	15.7	10.4	0.7	44.26	0.66	1.26	0.67	0.66	-3.97	0.44	0.60
21.2	15.6	10.0	0.8	47.17	0.67	0.97	0.74	0.64	-3.96	0.47	0.50
19.0	15.6	11.7	0.8	61.58	0.77	0.65	0.82	0.75	-3.96	0.62	0.47
20.1	15.6	10.8	0.8	53.73	0.72	0.80	0.78	0.69	-3.96	0.54	0.48
20.3	15.6	12.0	0.6	59.11	0.77	0.86	0.77	0.77	-3.96	0.59	0.57
20.0	15.5	12.0	0.7	60.00	0.77	0.83	0.78	0.77	-3.95	0.60	0.56
17.3	15.5	12.3	0.8	71.10	0.83	0.37	0.90	0.79	-3.95	0.71	0.36
19.2	15.5	9.9	0.5	51.56	0.69	0.67	0.81	0.64	-3.95	0.52	0.40
22.0	15.4	12.5	0.7	56.82	0.77	1.13	0.70	0.81	-3.94	0.57	0.69
28.6	15.3	12.3	0.6	43.01	0.70	1.83	0.53	0.80	-3.94	0.43	0.82
17.1	15.3	13.5	0.6	78.95	0.89	0.46	0.89	0.88	-3.94	0.79	0.50
17.2	15.3	14.9	0.9	86.63	0.94	0.70	0.89	0.97	-3.94	0.87	0.83
26.0	15.3	14.0	0.7	53.85	0.79	1.58	0.59	0.92	-3.94	0.54	0.89
19.1	15.2	10.2	0.7	53.40	0.71	0.72	0.80	0.67	-3.93	0.53	0.44
19.6	15.2	9.7	0.6	49.49	0.68	0.80	0.78	0.64	-3.93	0.49	0.44
19.3	15.2	12.1	0.7	62.69	0.79	0.80	0.79	0.80	-3.93	0.63	0.57
17.9	15.2	9.9	0.6	55.31	0.71	0.50	0.85	0.65	-3.93	0.55	0.34
19.6	15.2	8.5	0.6	43.37	0.62	0.81	0.78	0.56	-3.93	0.43	0.40
16.0	15.2	11.9	0.8	74.38	0.84	0.10	0.95	0.78	-3.93	0.74	0.20
18.1	15.2	15.1	0.6	83.43	0.94	0.96	0.84	0.99	-3.93	0.83	0.97
17.2	15.1	12.2	0.8	70.93	0.83	0.45	0.88	0.81	-3.92	0.71	0.42
22.3	15.0	13.5	0.6	60.54	0.82	1.28	0.67	0.90	-3.91	0.61	0.83
23.3	15.0	10.3	0.6	44.21	0.67	1.36	0.64	0.69	-3.91	0.44	0.64
18.5	15.0	9.9	0.7	53.51	0.71	0.65	0.81	0.66	-3.91	0.54	0.41
15.6	15.0	14.1	0.7	90.38	0.95	0.07	0.96	0.94	-3.91	0.90	0.40
18.2	15.0	9.1	0.7	50.00	0.67	0.59	0.82	0.61	-3.91	0.50	0.35
21.4	15.0	12.2	0.6	57.01	0.77	1.12	0.70	0.81	-3.91	0.57	0.70
26.1	15.0	12.1	0.8	46.36	0.72	1.63	0.57	0.81	-3.91	0.46	0.79
15.1	14.9	9.7	0.7	64.24	0.75	-0.09	0.99	0.65	-3.90	0.64	0.04
15.3	14.9	13.6	0.6	88.89	0.93	-0.07	0.97	0.91	-3.90	0.89	0.24
18.4	14.9	11.3	0.7	61.41	0.78	0.69	0.81	0.76	-3.90	0.61	0.49
18.9	14.9	12.0	0.7	63.49	0.80	0.80	0.79	0.81	-3.90	0.63	0.58
20.4	14.8	14.7	0.8	72.06	0.89	1.24	0.73	0.99	-3.89	0.72	0.98
16.3	14.8	14.0	0.6	85.89	0.93	0.51	0.91	0.95	-3.89	0.86	0.65
23.6	14.7	10.1	0.8	42.80	0.66	1.45	0.62	0.69	-3.88	0.43	0.66
20.3	14.7	10.9	0.8	53.69	0.74	1.01	0.72	0.74	-3.88	0.54	0.60
14.9	14.6	14.1	0.8	94.63	0.97	-0.26	0.98	0.97	-3.87	0.95	0.38

A-axis	B-axis	C-axis	Roundness	Flatness	Sphericity	OP-index	b/a	c/b	B-axis phi	c/a	a-b/a-c
20.2	14.6	9.7	0.6	48.02	0.68	1.01	0.72	0.66	-3.87	0.48	0.53
17.1	14.6	11.2	0.7	65.50	0.79	0.52	0.85	0.77	-3.87	0.65	0.42
18.2	14.6	9.1	0.7	50.00	0.68	0.68	0.80	0.62	-3.87	0.50	0.40
19.0	14.5	11.4	0.8	60.00	0.78	0.88	0.76	0.79	-3.86	0.60	0.59
21.2	14.5	12.0	0.8	56.60	0.78	1.19	0.68	0.83	-3.86	0.57	0.73
19.6	14.3	12.0	0.9	61.22	0.80	1.03	0.73	0.84	-3.84	0.61	0.70
20.4	14.3	12.5	0.6	61.27	0.81	1.16	0.70	0.87	-3.84	0.61	0.77
25.0	14.2	13.6	0.7	54.40	0.80	1.66	0.57	0.96	-3.83	0.54	0.95
18.0	14.2	14.2	0.5	78.89	0.92	1.10	0.79	1.00	-3.83	0.79	1.00
21.4	14.2	12.2	0.8	57.01	0.79	1.28	0.66	0.86	-3.83	0.57	0.78
17.3	14.2	11.8	0.7	68.21	0.83	0.69	0.82	0.83	-3.83	0.68	0.56
16.1	14.2	8.9	0.9	55.28	0.70	0.35	0.88	0.63	-3.83	0.55	0.26
18.5	14.2	10.0	0.6	54.05	0.72	0.83	0.77	0.70	-3.83	0.54	0.51
18.0	14.2	11.6	0.7	64.44	0.81	0.80	0.79	0.82	-3.83	0.64	0.59
17.5	14.1	12.1	0.5	69.14	0.84	0.78	0.81	0.86	-3.82	0.69	0.63
19.1	14.1	10.2	0.8	53.40	0.73	0.95	0.74	0.72	-3.82	0.53	0.56
19.0	14.1	13.7	0.7	72.11	0.89	1.15	0.74	0.97	-3.82	0.72	0.92
17.0	14.1	11.2	0.6	65.88	0.81	0.63	0.83	0.79	-3.82	0.66	0.50
21.1	14.1	12.0	0.9	56.87	0.79	1.26	0.67	0.85	-3.82	0.57	0.77
19.9	14.1	6.8	0.8	34.17	0.55	1.18	0.71	0.48	-3.82	0.34	0.44
18.1	14.1	10.8	0.7	59.67	0.77	0.80	0.78	0.77	-3.82	0.60	0.55
25.0	14.1	11.9	0.8	47.60	0.74	1.67	0.56	0.84	-3.82	0.48	0.83
19.9	14.1	11.2	0.5	56.28	0.76	1.08	0.71	0.79	-3.82	0.56	0.67
19.6	14.0	12.0	0.6	61.22	0.81	1.10	0.71	0.86	-3.81	0.61	0.74
16.3	14.0	9.3	0.6	57.06	0.72	0.45	0.86	0.66	-3.81	0.57	0.33
17.0	14.0	9.8	0.9	57.65	0.74	0.60	0.82	0.70	-3.81	0.58	0.42
17.4	13.9	13.1	0.6	75.29	0.89	0.93	0.80	0.94	-3.80	0.75	0.81
18.9	13.9	11.5	0.8	60.85	0.80	1.00	0.74	0.83	-3.80	0.61	0.68
23.9	13.8	13.0	0.6	54.39	0.80	1.62	0.58	0.94	-3.79	0.54	0.93
18.8	13.7	13.6	0.7	72.34	0.90	1.22	0.73	0.99	-3.78	0.72	0.98
17.9	13.7	12.6	0.6	70.39	0.87	0.99	0.77	0.92	-3.78	0.70	0.79
16.9	13.7	11.0	0.8	65.09	0.81	0.70	0.81	0.80	-3.78	0.65	0.54
21.8	13.7	12.9	0.7	59.17	0.82	1.44	0.63	0.94	-3.78	0.59	0.91
16.5	13.6	11.4	0.5	69.09	0.83	0.68	0.82	0.84	-3.77	0.69	0.57
13.7	13.5	11.4	0.7	83.21	0.89	-0.16	0.99	0.84	-3.75	0.83	0.09
16.1	13.5	10.2	0.9	63.35	0.78	0.56	0.84	0.76	-3.75	0.63	0.44
15.9	13.5	10.0	0.9	62.89	0.78	0.51	0.85	0.74	-3.75	0.63	0.41
17.0	13.5	11.2	0.8	65.88	0.82	0.79	0.79	0.83	-3.75	0.66	0.60
19.5	13.4	12.0	0.9	61.54	0.82	1.21	0.69	0.90	-3.74	0.62	0.81
22.5	13.4	10.4	0.5	46.22	0.71	1.54	0.60	0.78	-3.74	0.46	0.75
21.4	13.4	13.2	0.8	61.68	0.85	1.48	0.63	0.99	-3.74	0.62	0.98
24.1	13.3	10.3	0.7	42.74	0.69	1.75	0.55	0.77	-3.73	0.43	0.78

A-axis	B-axis	C-axis	Roundness	Flatness	Sphericity	OP-index	b/a	c/b	B-axis phi	c/a	a-b/a-c
16.0	13.3	11.2	0.6	70.00	0.84	0.65	0.83	0.84	-3.73	0.70	0.56
17.2	13.3	12.5	0.8	72.67	0.88	1.00	0.77	0.94	-3.73	0.73	0.83
17.0	13.2	9.8	0.7	57.65	0.75	0.80	0.78	0.74	-3.72	0.58	0.53
16.0	13.1	8.7	0.7	54.38	0.71	0.60	0.82	0.66	-3.71	0.54	0.40
25.0	13.1	9.8	0.6	39.20	0.66	1.91	0.52	0.75	-3.71	0.39	0.78
16.1	13.1	12.4	0.6	77.02	0.90	0.88	0.81	0.95	-3.71	0.77	0.81
24.8	13.0	12.5	0.7	50.40	0.79	1.82	0.52	0.96	-3.70	0.50	0.96
16.8	13.0	11.5	0.5	68.45	0.85	0.91	0.77	0.88	-3.70	0.68	0.72
21.8	13.0	12.0	0.5	55.05	0.80	1.54	0.60	0.92	-3.70	0.55	0.90
13.9	13.0	8.1	0.8	58.27	0.71	0.12	0.94	0.62	-3.70	0.58	0.16
16.0	12.9	9.9	0.8	61.88	0.78	0.69	0.81	0.77	-3.69	0.62	0.51
15.7	12.8	9.9	0.7	63.06	0.79	0.66	0.82	0.77	-3.68	0.63	0.50
17.2	12.6	9.5	0.8	55.23	0.75	0.96	0.73	0.75	-3.66	0.55	0.60
16.0	12.5	9.9	0.7	61.88	0.79	0.79	0.78	0.79	-3.64	0.62	0.57
15.0	12.3	11.0	0.7	73.33	0.87	0.75	0.82	0.89	-3.62	0.73	0.67
22.1	12.3	11.3	0.7	51.13	0.78	1.68	0.56	0.92	-3.62	0.51	0.91
12.5	12.2	9.6	0.7	76.80	0.85	-0.09	0.98	0.79	-3.61	0.77	0.10
17.5	12.1	10.3	0.9	58.86	0.79	1.16	0.69	0.85	-3.60	0.59	0.75
18.7	12.1	12.0	0.7	64.17	0.86	1.42	0.65	0.99	-3.60	0.64	0.99
18.1	12.1	11.0	0.5	60.77	0.82	1.27	0.67	0.91	-3.60	0.61	0.85
14.1	12.0	10.1	0.7	71.63	0.84	0.56	0.85	0.84	-3.58	0.72	0.52
16.2	12.0	8.9	0.7	54.94	0.74	0.92	0.74	0.74	-3.58	0.55	0.58
17.3	11.6	7.5	0.9	43.35	0.65	1.22	0.67	0.65	-3.54	0.43	0.58
18.3	11.0	10.1	0.8	55.19	0.80	1.50	0.60	0.92	-3.46	0.55	0.89
14.1	11.0	10.8	0.7	76.60	0.91	1.03	0.78	0.98	-3.46	0.77	0.94
12.2	10.6	8.1	0.7	66.39	0.80	0.40	0.87	0.76	-3.41	0.66	0.39
13.4	10.2	7.0	0.5	52.24	0.71	0.81	0.76	0.69	-3.35	0.52	0.50
12.3	10.0	8.6	0.7	69.92	0.84	0.70	0.81	0.86	-3.32	0.70	0.62
17.7	9.9	5.9	0.9	33.33	0.58	1.86	0.56	0.60	-3.31	0.33	0.66
14.3	9.9	9.0	0.5	62.94	0.83	1.17	0.69	0.91	-3.31	0.63	0.83
12.3	8.9	7.5	0.8	60.98	0.80	0.99	0.72	0.84	-3.15	0.61	0.71
7.8	4.1	1.1	0.5	14.10	0.34	3.39	0.53	0.27	-2.04	0.14	0.55

Appendix (XII)(e)

PEBBLE DATA ROODERAND CONGLOMERATE FORMATION ROODERAND 510 S

A-axis	B-axis	C-axis	Roundness	Flatness	Sphericity	OP-index	b/a	c/b	B-axis phi	c/a	a-b/a-c
53.0	46.9	28.0	0.6	52.83	0.68	0.42	0.88	0.60	-5.55	0.53	0.24
55.5	44.7	33.5	0.7	60.36	0.77	0.78	0.81	0.75	-5.48	0.60	0.49
55.0	43.7	34.3	0.6	62.36	0.79	0.84	0.79	0.78	-5.45	0.62	0.55
39.9	37.9	23.7	0.8	59.40	0.72	0.16	0.95	0.63	-5.24	0.59	0.12
52.2	39.7	34.5	0.7	66.09	0.83	1.03	0.76	0.87	-5.31	0.66	0.71
62.9	38.5	23.1	0.7	36.72	0.60	1.64	0.61	0.60	-5.27	0.37	0.61
38.0	37.6	22.4	0.7	58.95	0.71	-0.01	0.99	0.60	-5.23	0.59	0.03
46.5	36.9	20.7	0.7	44.52	0.63	0.79	0.79	0.56	-5.21	0.45	0.37
39.6	36.4	24.2	0.8	61.11	0.74	0.29	0.92	0.66	-5.19	0.61	0.21
43.3	36.2	35.5	0.7	81.99	0.93	1.03	0.84	0.98	-5.18	0.82	0.91
40.0	36.1	30.0	0.8	75.00	0.85	0.45	0.90	0.83	-5.17	0.75	0.39
41.0	36.0	24.5	0.7	59.76	0.74	0.46	0.88	0.68	-5.17	0.60	0.30
41.8	36.0	35.0	0.8	83.73	0.93	0.93	0.86	0.97	-5.17	0.84	0.85
44.4	35.5	25.9	0.5	58.33	0.75	0.78	0.80	0.73	-5.15	0.58	0.48
41.4	35.5	24.5	0.7	59.18	0.74	0.54	0.86	0.69	-5.15	0.59	0.35
43.1	35.3	21.2	0.7	49.19	0.67	0.68	0.82	0.60	-5.14	0.49	0.36
50.2	35.0	21.2	0.7	42.23	0.63	1.20	0.70	0.61	-5.13	0.42	0.52
40.1	34.5	18.5	0.6	46.13	0.63	0.51	0.86	0.54	-5.11	0.46	0.26
45.9	34.5	28.6	0.9	62.31	0.80	1.01	0.75	0.83	-5.11	0.62	0.66
61.3	34.5	32.0	0.7	52.20	0.79	1.72	0.56	0.93	-5.11	0.52	0.91
49.1	34.5	21.7	0.6	44.20	0.65	1.16	0.70	0.63	-5.11	0.44	0.53
36.5	34.3	19.7	0.7	53.97	0.68	0.19	0.94	0.57	-5.10	0.54	0.13
43.2	34.1	26.9	0.6	62.27	0.79	0.85	0.79	0.79	-5.09	0.62	0.56
41.6	34.0	26.3	0.7	63.22	0.79	0.73	0.82	0.77	-5.09	0.63	0.50
36.9	33.9	24.3	0.6	65.85	0.78	0.30	0.92	0.72	-5.08	0.66	0.24
36.9	33.7	22.5	0.5	60.98	0.74	0.31	0.91	0.67	-5.07	0.61	0.22
41.1	33.6	21.5	0.9	52.31	0.69	0.68	0.82	0.64	-5.07	0.52	0.38
34.7	33.4	23.7	0.8	68.30	0.79	0.11	0.96	0.71	-5.06	0.68	0.12
43.9	33.2	14.9	0.5	33.94	0.53	1.04	0.76	0.45	-5.05	0.34	0.37
39.6	33.0	15.6	0.8	39.39	0.57	0.65	0.83	0.47	-5.04	0.39	0.28
50.4	32.4	31.6	0.7	62.70	0.85	1.48	0.64	0.98	-5.02	0.63	0.96
33.7	32.3	18.7	0.6	55.49	0.68	0.11	0.96	0.58	-5.01	0.55	0.09
44.4	32.2	28.3	0.6	63.74	0.82	1.14	0.73	0.88	-5.01	0.64	0.76
42.4	32.2	22.5	0.6	53.07	0.72	0.92	0.76	0.70	-5.01	0.53	0.51
36.3	32.0	17.6	0.5	48.48	0.64	0.42	0.88	0.55	-5.00	0.48	0.23
39.0	31.9	21.3	0.9	54.62	0.71	0.68	0.82	0.67	-5.00	0.55	0.40
36.1	31.9	16.3	0.8	45.15	0.61	0.41	0.88	0.51	-5.00	0.45	0.21

A-axis	B-axis	C-axis	Roundness	Flatness	Sphericity	OP-index	b/a	c/b	B-axis phi	c/a	a-b/a-c
32.5	31.9	14.8	0.7	45.54	0.60	0.01	0.98	0.46	-5.00	0.46	0.03
40.0	31.7	25.7	0.6	64.25	0.80	0.85	0.79	0.81	-4.99	0.64	0.58
41.4	31.6	18.5	0.8	44.69	0.64	0.91	0.76	0.59	-4.98	0.45	0.43
35.9	31.3	23.0	0.6	64.07	0.78	0.50	0.87	0.73	-4.97	0.64	0.36
36.5	31.2	26.7	0.6	73.15	0.86	0.67	0.85	0.86	-4.96	0.73	0.54
32.5	31.0	21.2	0.7	65.23	0.76	0.14	0.95	0.68	-4.95	0.65	0.13
31.5	30.9	28.2	0.8	89.52	0.93	0.03	0.98	0.91	-4.95	0.90	0.18
40.3	30.9	26.6	0.6	66.00	0.83	0.98	0.77	0.86	-4.95	0.66	0.69
33.8	30.7	25.6	0.9	75.74	0.86	0.42	0.91	0.83	-4.94	0.76	0.38
35.0	30.7	21.4	0.6	61.14	0.75	0.46	0.88	0.70	-4.94	0.61	0.32
37.3	30.6	27.0	0.6	72.39	0.86	0.83	0.82	0.88	-4.94	0.72	0.65
33.5	30.6	20.7	0.7	61.79	0.75	0.30	0.91	0.68	-4.94	0.62	0.23
40.9	30.5	22.8	0.7	55.75	0.75	0.98	0.75	0.75	-4.93	0.56	0.57
46.0	30.2	28.0	0.6	60.87	0.83	1.40	0.66	0.93	-4.92	0.61	0.88
39.5	30.1	20.5	0.7	51.90	0.71	0.90	0.76	0.68	-4.91	0.52	0.49
40.0	30.0	23.2	0.8	58.00	0.77	0.97	0.75	0.77	-4.91	0.58	0.60
39.9	29.6	19.0	0.7	47.62	0.67	0.98	0.74	0.64	-4.89	0.48	0.49
34.6	29.6	25.3	0.6	73.12	0.85	0.66	0.86	0.85	-4.89	0.73	0.54
44.1	29.6	20.9	0.6	47.39	0.69	1.27	0.67	0.71	-4.89	0.47	0.62
31.4	29.6	21.5	0.7	68.47	0.79	0.19	0.94	0.73	-4.89	0.68	0.18
36.3	29.5	19.1	0.9	52.62	0.70	0.70	0.81	0.65	-4.88	0.53	0.40
32.0	29.4	27.2	0.7	85.00	0.92	0.51	0.92	0.93	-4.88	0.85	0.54
33.0	29.3	23.4	0.6	70.91	0.83	0.47	0.89	0.80	-4.87	0.71	0.39
33.1	29.3	26.9	0.6	81.27	0.91	0.65	0.89	0.92	-4.87	0.81	0.61
38.3	29.2	18.4	0.7	48.04	0.67	0.90	0.76	0.63	-4.87	0.48	0.46
29.8	29.2	11.8	0.7	39.60	0.54	0.01	0.98	0.40	-4.87	0.40	0.03
34.8	29.1	21.1	0.7	60.63	0.76	0.63	0.84	0.73	-4.86	0.61	0.42
33.9	28.9	15.8	0.7	46.61	0.63	0.53	0.85	0.55	-4.85	0.47	0.28
35.2	28.9	17.5	0.6	49.72	0.67	0.66	0.82	0.61	-4.85	0.50	0.36
39.5	28.6	16.4	0.5	41.52	0.62	1.08	0.72	0.57	-4.84	0.42	0.47
31.8	28.4	18.2	0.7	57.23	0.72	0.37	0.89	0.64	-4.83	0.57	0.25
37.9	28.4	24.8	0.6	65.44	0.83	1.05	0.75	0.87	-4.83	0.65	0.73
41.3	28.3	23.3	0.8	56.42	0.77	1.23	0.69	0.82	-4.82	0.56	0.72
28.3	28.1	24.1	0.9	85.16	0.90	-0.08	0.99	0.86	-4.81	0.85	0.05
31.9	28.2	20.7	0.5	64.89	0.78	0.44	0.88	0.73	-4.82	0.65	0.33
35.0	28.0	21.2	0.8	60.57	0.77	0.78	0.80	0.76	-4.81	0.61	0.51
29.9	27.9	20.1	0.8	67.22	0.79	0.23	0.93	0.72	-4.80	0.67	0.20
34.1	27.8	16.2	0.7	47.51	0.65	0.68	0.82	0.58	-4.80	0.48	0.35
29.9	27.8	19.3	0.8	64.55	0.77	0.23	0.93	0.69	-4.80	0.65	0.20
34.8	27.7	17.8	0.7	51.15	0.69	0.76	0.80	0.64	-4.79	0.51	0.42
30.3	27.7	19.0	0.7	62.71	0.75	0.30	0.91	0.69	-4.79	0.63	0.23
32.2	27.5	14.5	0.7	45.03	0.62	0.53	0.85	0.53	-4.78	0.45	0.27

A-axis	B-axis	C-axis	Roundness	Flatness	Sphericity	OP-index	b/a	c/b	B-axis phi	c/a	a-b/a-c
35.7	27.5	23.5	0.6	65.83	0.83	0.96	0.77	0.85	-4.78	0.66	0.67
31.6	27.5	24.8	0.6	78.48	0.89	0.67	0.87	0.90	-4.78	0.78	0.60
29.5	27.4	13.3	0.8	45.08	0.60	0.22	0.93	0.49	-4.78	0.45	0.13
57.3	27.3	19.7	0.8	34.38	0.63	2.28	0.48	0.72	-4.77	0.34	0.80
33.2	27.3	18.0	0.5	54.22	0.71	0.66	0.82	0.66	-4.77	0.54	0.39
32.6	27.0	20.3	0.6	62.27	0.78	0.67	0.83	0.75	-4.75	0.62	0.46
28.1	27.0	18.8	0.8	66.90	0.78	0.10	0.96	0.70	-4.75	0.67	0.12
34.2	27.0	22.2	0.8	64.91	0.81	0.86	0.79	0.82	-4.75	0.65	0.60
35.0	27.0	21.9	0.6	62.57	0.80	0.91	0.77	0.81	-4.75	0.63	0.61
35.2	26.9	23.6	0.7	67.05	0.84	1.00	0.76	0.88	-4.75	0.67	0.72
41.8	26.8	13.1	0.8	31.34	0.54	1.61	0.64	0.49	-4.74	0.31	0.52
31.3	26.7	15.6	0.6	49.84	0.66	0.52	0.85	0.58	-4.74	0.50	0.29
36.8	26.6	22.5	0.7	61.14	0.80	1.11	0.72	0.85	-4.73	0.61	0.71
34.3	26.2	19.6	0.7	57.14	0.75	0.90	0.76	0.75	-4.71	0.57	0.55
31.8	26.1	19.1	0.8	60.06	0.76	0.68	0.82	0.73	-4.71	0.60	0.45
30.9	25.8	17.4	0.7	56.31	0.72	0.61	0.83	0.67	-4.69	0.56	0.38
46.1	25.7	23.7	0.8	51.41	0.78	1.73	0.56	0.92	-4.68	0.51	0.91
43.0	25.7	24.0	0.7	55.81	0.80	1.58	0.60	0.93	-4.68	0.56	0.91
28.0	25.6	16.2	0.6	57.86	0.72	0.28	0.91	0.63	-4.68	0.58	0.20
28.5	25.5	19.7	0.8	69.12	0.81	0.41	0.89	0.77	-4.67	0.69	0.34
28.4	25.4	21.6	0.7	76.06	0.86	0.48	0.89	0.85	-4.67	0.76	0.44
37.8	25.4	16.5	0.7	43.65	0.66	1.28	0.67	0.65	-4.67	0.44	0.58
34.7	25.3	18.2	0.6	52.45	0.72	1.03	0.73	0.72	-4.66	0.52	0.57
35.6	25.2	19.1	0.6	53.65	0.74	1.12	0.71	0.76	-4.66	0.54	0.63
31.5	25.2	11.5	0.6	36.51	0.55	0.79	0.80	0.46	-4.66	0.37	0.32
26.4	25.1	18.5	0.8	70.08	0.80	0.14	0.95	0.74	-4.65	0.70	0.16
27.1	25.1	16.3	0.6	60.15	0.73	0.23	0.93	0.65	-4.65	0.60	0.19
34.7	25.1	21.5	0.7	61.96	0.81	1.11	0.72	0.86	-4.65	0.62	0.73
34.5	25.0	17.4	0.7	50.43	0.71	1.04	0.72	0.70	-4.64	0.50	0.56
25.0	23.9	15.0	0.7	60.00	0.72	0.10	0.96	0.63	-4.58	0.60	0.11
38.0	25.0	18.8	0.6	49.47	0.72	1.32	0.66	0.75	-4.64	0.49	0.68
26.4	25.0	23.3	0.5	88.26	0.94	0.33	0.95	0.93	-4.64	0.88	0.45
33.4	24.9	21.1	0.7	63.17	0.81	1.03	0.75	0.85	-4.64	0.63	0.69
24.8	24.4	14.1	0.6	56.85	0.69	-0.02	0.98	0.58	-4.61	0.57	0.04
30.0	24.8	19.4	0.7	64.67	0.80	0.69	0.83	0.78	-4.63	0.65	0.49
26.3	24.6	15.7	0.7	59.70	0.72	0.19	0.94	0.64	-4.62	0.60	0.16
28.8	24.6	20.0	0.6	69.44	0.83	0.61	0.85	0.81	-4.62	0.69	0.48
34.2	24.6	21.3	0.6	62.28	0.81	1.13	0.72	0.87	-4.62	0.62	0.74
28.8	24.3	19.8	0.7	68.75	0.82	0.65	0.84	0.81	-4.60	0.69	0.50
34.3	24.2	22.1	0.8	64.43	0.84	1.22	0.71	0.91	-4.60	0.64	0.83
25.0	24.1	23.0	0.8	92.00	0.96	0.22	0.96	0.95	-4.59	0.92	0.45
31.8	24.1	17.2	0.7	54.09	0.73	0.91	0.76	0.71	-4.59	0.54	0.53

A-axis	B-axis	C-axis	Roundness	Flatness	Sphericity	OP-index	b/a	c/b	B-axis phi	c/a	a-b/a-c
28.4	24.0	12.4	0.6	43.66	0.61	0.56	0.85	0.52	-4.58	0.44	0.28
30.6	24.0	17.7	0.7	57.84	0.75	0.82	0.78	0.74	-4.58	0.58	0.51
42.1	23.9	12.3	0.7	29.22	0.53	2.03	0.57	0.51	-4.58	0.29	0.61
31.9	23.9	22.2	0.7	69.59	0.86	1.11	0.75	0.93	-4.58	0.70	0.82
26.1	23.8	17.1	0.8	65.52	0.78	0.31	0.91	0.72	-4.57	0.66	0.26
24.3	23.7	16.2	0.8	66.67	0.77	0.02	0.98	0.68	-4.57	0.67	0.07
24.1	23.6	18.0	0.8	74.69	0.83	0.00	0.98	0.76	-4.56	0.75	0.08
34.7	23.5	19.6	0.9	56.48	0.78	1.25	0.68	0.83	-4.55	0.56	0.74
29.1	23.5	23.4	0.7	80.41	0.93	1.11	0.81	1.00	-4.55	0.80	0.98
24.2	23.5	15.2	0.6	62.81	0.74	0.04	0.97	0.65	-4.55	0.63	0.08
28.5	23.5	19.6	0.8	68.77	0.83	0.74	0.82	0.83	-4.55	0.69	0.56
28.5	23.4	22.3	0.6	78.25	0.91	0.95	0.82	0.95	-4.55	0.78	0.82
29.2	23.3	18.6	0.7	63.70	0.80	0.80	0.80	0.80	-4.54	0.64	0.56
29.6	23.3	17.3	0.7	58.45	0.76	0.81	0.79	0.74	-4.54	0.58	0.51
28.6	23.2	16.4	0.8	57.34	0.74	0.70	0.81	0.71	-4.54	0.57	0.44
27.0	23.2	17.0	0.9	62.96	0.77	0.52	0.86	0.73	-4.54	0.63	0.38
36.7	23.2	19.9	0.7	54.22	0.77	1.43	0.63	0.86	-4.54	0.54	0.80
29.5	23.1	20.5	0.8	69.49	0.85	0.94	0.78	0.89	-4.53	0.69	0.71
31.7	23.0	14.2	0.9	44.79	0.65	1.05	0.73	0.62	-4.52	0.45	0.50
24.7	23.0	16.3	0.5	65.99	0.78	0.22	0.93	0.71	-4.52	0.66	0.20
30.7	23.0	14.9	0.7	48.53	0.68	0.94	0.75	0.65	-4.52	0.49	0.49
29.5	23.0	19.0	0.7	64.41	0.81	0.89	0.78	0.83	-4.52	0.64	0.62
26.9	22.7	16.9	0.6	62.83	0.78	0.59	0.84	0.74	-4.50	0.63	0.42
32.0	22.7	16.0	0.7	50.00	0.71	1.10	0.71	0.70	-4.50	0.50	0.58
32.7	22.7	15.6	0.6	47.71	0.69	1.16	0.69	0.69	-4.50	0.48	0.58
30.0	22.7	16.0	0.7	53.33	0.72	0.91	0.76	0.70	-4.50	0.53	0.52
24.3	22.6	15.6	0.8	64.20	0.76	0.21	0.93	0.69	-4.50	0.64	0.20
26.1	22.6	19.2	0.6	73.56	0.85	0.59	0.87	0.85	-4.50	0.74	0.51
25.4	22.5	17.0	0.6	66.93	0.80	0.43	0.89	0.76	-4.49	0.67	0.35
27.5	22.5	15.3	0.6	55.64	0.72	0.66	0.82	0.68	-4.49	0.56	0.41
28.0	22.5	18.3	0.8	65.36	0.81	0.79	0.80	0.81	-4.49	0.65	0.57
23.4	22.5	12.0	0.4	51.28	0.65	0.07	0.96	0.53	-4.49	0.51	0.08
26.5	22.4	19.2	0.6	72.45	0.85	0.68	0.85	0.86	-4.49	0.72	0.56
27.0	22.4	15.6	0.6	57.78	0.74	0.62	0.83	0.70	-4.49	0.58	0.40
24.3	22.3	15.0	0.7	61.73	0.75	0.26	0.92	0.67	-4.48	0.62	0.22
31.0	22.3	13.0	0.4	41.94	0.63	1.09	0.72	0.58	-4.48	0.42	0.48
26.2	22.3	14.9	0.5	56.87	0.72	0.53	0.85	0.67	-4.48	0.57	0.35
27.6	22.3	17.8	0.8	64.49	0.80	0.76	0.81	0.80	-4.48	0.64	0.54
25.7	22.3	15.0	0.6	58.37	0.73	0.46	0.87	0.67	-4.48	0.58	0.32
38.8	22.3	15.4	0.7	39.69	0.65	1.72	0.57	0.69	-4.48	0.40	0.71
24.8	22.2	13.8	0.8	55.65	0.70	0.34	0.90	0.62	-4.47	0.56	0.24
26.9	22.2	19.4	0.6	72.12	0.86	0.78	0.83	0.87	-4.47	0.72	0.63

A-axis	B-axis	C-axis	Roundness	Flatness	Sphericity	OP-index	b/a	c/b	B-axis phi	c/a	a-b/a-c
28.1	22.1	15.7	0.6	55.87	0.73	0.79	0.79	0.71	-4.47	0.56	0.48
30.1	22.1	17.8	0.9	59.14	0.78	1.03	0.73	0.81	-4.47	0.59	0.65
25.0	22.1	17.9	0.7	71.60	0.83	0.47	0.88	0.81	-4.47	0.72	0.41
29.4	22.1	21.5	0.6	73.13	0.89	1.18	0.75	0.97	-4.47	0.73	0.92
27.4	22.0	18.1	0.6	66.06	0.82	0.80	0.80	0.82	-4.46	0.66	0.58
26.1	22.0	15.0	0.6	57.47	0.73	0.56	0.84	0.68	-4.46	0.57	0.37
27.0	22.0	15.2	0.6	56.30	0.73	0.68	0.81	0.69	-4.46	0.56	0.42
28.0	22.0	15.5	0.6	55.36	0.73	0.79	0.79	0.70	-4.46	0.55	0.48
24.6	22.0	13.2	0.6	53.66	0.69	0.34	0.89	0.60	-4.46	0.54	0.23
25.6	22.0	19.9	0.7	77.73	0.89	0.70	0.86	0.90	-4.46	0.78	0.63
44.4	22.8	21.9	0.7	49.32	0.78	1.90	0.51	0.96	-4.51	0.49	0.96
27.1	21.9	13.0	0.7	47.97	0.66	0.69	0.81	0.59	-4.45	0.48	0.37
31.8	21.8	19.6	0.6	61.64	0.82	1.26	0.69	0.90	-4.45	0.62	0.82
26.0	21.8	12.1	0.6	46.54	0.64	0.57	0.84	0.56	-4.45	0.47	0.30
26.7	21.8	15.9	0.8	59.55	0.76	0.68	0.82	0.73	-4.45	0.60	0.45
29.6	21.8	13.1	0.7	44.26	0.64	1.00	0.74	0.60	-4.45	0.44	0.47
27.0	21.7	13.2	0.8	48.89	0.67	0.71	0.80	0.61	-4.44	0.49	0.38
28.0	21.7	19.0	0.7	67.86	0.84	0.95	0.78	0.88	-4.44	0.68	0.70
28.2	21.7	16.2	0.6	57.45	0.75	0.87	0.77	0.75	-4.44	0.57	0.54
27.9	21.6	16.7	0.8	59.86	0.77	0.87	0.77	0.77	-4.43	0.60	0.56
26.3	21.6	16.9	0.6	64.26	0.80	0.70	0.82	0.78	-4.43	0.64	0.50
25.0	21.5	19.6	0.8	78.40	0.89	0.71	0.86	0.91	-4.43	0.78	0.65
25.6	21.5	14.8	0.8	57.81	0.74	0.58	0.84	0.69	-4.43	0.58	0.38
28.2	21.5	15.1	0.6	53.55	0.72	0.88	0.76	0.70	-4.43	0.54	0.51
22.2	21.5	17.8	0.8	80.18	0.87	0.06	0.97	0.83	-4.43	0.80	0.16
35.1	21.4	15.5	0.5	44.16	0.68	1.53	0.61	0.72	-4.42	0.44	0.70
26.0	21.4	18.7	0.6	71.92	0.86	0.78	0.82	0.87	-4.42	0.72	0.63
25.1	21.3	17.3	0.7	68.92	0.82	0.61	0.85	0.81	-4.41	0.69	0.49
23.5	21.3	16.4	0.8	69.79	0.81	0.34	0.91	0.77	-4.41	0.70	0.31
28.1	21.1	12.3	0.6	43.77	0.63	0.94	0.75	0.58	-4.40	0.44	0.44
24.3	21.0	12.3	0.8	50.62	0.67	0.46	0.86	0.59	-4.39	0.51	0.28
21.9	21.0	16.3	0.6	74.43	0.83	0.10	0.96	0.78	-4.39	0.74	0.16
28.0	21.0	12.6	0.6	45.00	0.65	0.94	0.75	0.60	-4.39	0.45	0.45
28.6	21.0	16.9	0.5	59.09	0.78	1.03	0.73	0.80	-4.39	0.59	0.65
24.8	21.0	14.1	0.9	56.85	0.73	0.54	0.85	0.67	-4.39	0.57	0.36
31.0	21.0	16.6	0.7	53.55	0.75	1.23	0.68	0.79	-4.39	0.54	0.69
27.3	21.0	15.4	0.7	56.41	0.75	0.86	0.77	0.73	-4.39	0.56	0.53
27.8	21.0	16.9	0.8	60.79	0.79	0.95	0.76	0.80	-4.39	0.61	0.62
22.4	20.9	16.5	0.7	73.66	0.83	0.23	0.93	0.79	-4.39	0.74	0.25
23.0	20.8	19.3	0.9	83.91	0.92	0.55	0.90	0.93	-4.38	0.84	0.59
24.0	20.7	14.0	0.5	58.33	0.73	0.48	0.86	0.68	-4.37	0.58	0.33
27.3	20.7	13.3	0.8	48.72	0.68	0.89	0.76	0.64	-4.37	0.49	0.47

A-axis	B-axis	C-axis	Roundness	Flatness	Sphericity	OP-index	b/a	c/b	B-axis phi	c/a	a-b/a-c
28.0	20.6	15.1	0.7	53.93	0.73	0.99	0.74	0.73	-4.36	0.54	0.57
22.9	20.6	18.4	0.6	80.35	0.90	0.50	0.90	0.89	-4.36	0.80	0.51
22.0	20.6	13.5	0.7	61.36	0.74	0.17	0.94	0.66	-4.36	0.61	0.16
23.5	20.6	14.8	0.6	62.98	0.77	0.44	0.88	0.72	-4.36	0.63	0.33
21.6	20.5	17.9	0.8	82.87	0.90	0.20	0.95	0.87	-4.36	0.83	0.30
24.8	20.5	9.3	0.7	37.50	0.55	0.65	0.83	0.45	-4.36	0.38	0.28
24.9	20.4	14.8	0.8	59.44	0.76	0.67	0.82	0.73	-4.35	0.59	0.45
25.6	20.4	14.1	0.7	55.08	0.72	0.74	0.80	0.69	-4.35	0.55	0.45
27.0	20.4	13.9	0.6	51.48	0.71	0.90	0.76	0.68	-4.35	0.51	0.50
27.8	20.3	19.3	0.7	69.42	0.87	1.19	0.73	0.95	-4.34	0.69	0.88
37.5	20.2	16.7	0.7	44.53	0.72	1.81	0.54	0.83	-4.34	0.45	0.83
25.6	20.2	15.1	0.7	58.98	0.76	0.79	0.79	0.75	-4.34	0.59	0.51
24.4	20.1	12.2	0.7	50.00	0.67	0.62	0.82	0.61	-4.33	0.50	0.35
25.1	20.1	14.0	0.8	55.78	0.73	0.73	0.80	0.70	-4.33	0.56	0.45
21.1	20.1	18.1	0.7	85.78	0.92	0.19	0.95	0.90	-4.33	0.86	0.33
43.4	20.0	18.3	0.6	42.17	0.73	2.16	0.46	0.92	-4.32	0.42	0.93
28.0	20.0	17.3	0.8	61.79	0.81	1.13	0.71	0.87	-4.32	0.62	0.75
21.6	20.0	15.9	0.8	73.61	0.84	0.26	0.93	0.80	-4.32	0.74	0.28
26.0	20.0	14.4	0.7	55.38	0.74	0.86	0.77	0.72	-4.32	0.55	0.52
25.8	19.9	13.9	0.7	53.88	0.72	0.84	0.77	0.70	-4.31	0.54	0.50
31.3	19.8	15.1	0.5	48.24	0.72	1.41	0.63	0.76	-4.31	0.48	0.71
33.9	19.6	14.9	0.9	43.95	0.69	1.65	0.58	0.76	-4.29	0.44	0.75
20.1	19.6	13.8	0.6	68.66	0.78	0.00	0.98	0.70	-4.29	0.69	0.08
27.6	19.5	13.9	0.8	50.36	0.71	1.10	0.71	0.71	-4.29	0.50	0.59
22.8	19.4	15.0	0.6	65.79	0.80	0.57	0.85	0.77	-4.28	0.66	0.44
24.7	19.3	13.7	0.5	55.47	0.73	0.80	0.78	0.71	-4.27	0.55	0.49
24.1	19.3	18.6	0.7	77.18	0.91	1.01	0.80	0.96	-4.27	0.77	0.87
25.0	19.3	15.7	0.6	62.80	0.80	0.89	0.77	0.81	-4.27	0.63	0.61
21.6	19.3	13.5	0.6	62.50	0.76	0.36	0.89	0.70	-4.27	0.63	0.28
23.2	19.3	16.8	0.7	72.41	0.86	0.73	0.83	0.87	-4.27	0.72	0.61
24.7	19.2	13.1	0.6	53.04	0.71	0.81	0.78	0.68	-4.26	0.53	0.47
25.3	19.2	13.6	0.9	53.75	0.72	0.89	0.76	0.71	-4.26	0.54	0.52
20.1	19.1	17.3	0.9	86.07	0.92	0.21	0.95	0.91	-4.26	0.86	0.36
25.0	19.0	14.5	0.5	58.00	0.76	0.90	0.76	0.76	-4.25	0.58	0.57
25.0	19.0	16.7	0.6	66.80	0.84	0.99	0.76	0.88	-4.25	0.67	0.72
24.0	19.0	13.7	0.6	57.08	0.74	0.77	0.79	0.72	-4.25	0.57	0.49
32.0	19.0	11.8	0.7	36.88	0.61	1.68	0.59	0.62	-4.25	0.37	0.64
21.1	19.0	13.1	0.9	62.09	0.75	0.32	0.90	0.69	-4.25	0.62	0.26
21.4	19.0	13.2	0.7	61.68	0.75	0.38	0.89	0.69	-4.25	0.62	0.29
21.0	19.0	16.4	0.6	78.10	0.88	0.42	0.90	0.86	-4.25	0.78	0.43
21.9	18.8	17.3	0.8	79.00	0.90	0.72	0.86	0.92	-4.23	0.79	0.67
27.7	18.8	17.0	0.7	61.37	0.82	1.28	0.68	0.90	-4.23	0.61	0.83

A-axis	B-axis	C-axis	Roundness	Flatness	Sphericity	OP-index	b/a	c/b	B-axis phi	c/a	a-b/a-c
24.3	18.8	11.4	0.5	46.91	0.66	0.83	0.77	0.61	-4.23	0.47	0.43
26.2	18.7	15.4	0.4	58.78	0.79	1.10	0.71	0.82	-4.22	0.59	0.69
24.6	18.7	14.7	0.6	59.76	0.78	0.91	0.76	0.79	-4.22	0.60	0.60
20.0	18.7	11.9	0.6	59.50	0.72	0.17	0.94	0.64	-4.22	0.60	0.16
25.3	18.7	15.6	0.8	61.66	0.80	1.02	0.74	0.83	-4.22	0.62	0.68
28.0	18.6	16.0	0.6	57.14	0.79	1.30	0.66	0.86	-4.22	0.57	0.78
22.7	18.6	16.9	0.5	74.45	0.88	0.83	0.82	0.91	-4.22	0.74	0.71
28.6	18.6	17.4	0.7	60.84	0.83	1.39	0.65	0.94	-4.22	0.61	0.89
23.6	18.6	15.4	0.6	65.25	0.81	0.84	0.79	0.83	-4.22	0.65	0.61
24.6	18.5	12.6	0.6	51.22	0.70	0.91	0.75	0.68	-4.21	0.51	0.51
21.1	18.4	10.8	0.8	51.18	0.67	0.42	0.87	0.59	-4.20	0.51	0.26
23.5	18.4	14.4	0.6	61.28	0.78	0.82	0.78	0.78	-4.20	0.61	0.56
21.9	18.4	13.0	0.6	59.36	0.75	0.57	0.84	0.71	-4.20	0.59	0.39
22.5	18.3	11.7	0.7	52.00	0.69	0.66	0.81	0.64	-4.19	0.52	0.39
25.5	18.3	13.6	0.6	53.33	0.73	1.06	0.72	0.74	-4.19	0.53	0.61
27.3	18.2	16.9	0.6	61.90	0.83	1.34	0.67	0.93	-4.19	0.62	0.88
21.6	18.2	14.6	0.8	67.59	0.82	0.61	0.84	0.80	-4.19	0.68	0.49
26.4	18.2	15.0	0.6	56.82	0.78	1.19	0.69	0.82	-4.19	0.57	0.72
33.0	18.0	15.2	0.6	46.06	0.73	1.77	0.55	0.84	-4.17	0.46	0.84
22.2	18.0	11.5	0.8	51.80	0.69	0.67	0.81	0.64	-4.17	0.52	0.39
25.0	17.9	13.1	0.7	52.40	0.73	1.06	0.72	0.73	-4.16	0.52	0.60
20.3	17.9	14.6	0.6	71.92	0.84	0.46	0.88	0.82	-4.16	0.72	0.42
21.1	17.9	15.1	0.7	71.56	0.85	0.63	0.85	0.84	-4.16	0.72	0.53
21.0	17.8	11.5	0.7	54.76	0.71	0.52	0.85	0.65	-4.15	0.55	0.34
21.9	17.7	14.1	0.8	64.38	0.80	0.74	0.81	0.80	-4.15	0.64	0.54
23.7	17.7	15.2	0.6	64.14	0.82	1.01	0.75	0.86	-4.15	0.64	0.71
18.4	17.7	16.3	0.5	88.59	0.93	0.11	0.96	0.92	-4.15	0.89	0.33
21.2	17.6	12.0	0.6	56.60	0.73	0.60	0.83	0.68	-4.14	0.57	0.39
21.1	17.6	14.9	0.8	70.62	0.84	0.69	0.83	0.85	-4.14	0.71	0.56
25.8	17.6	14.7	0.7	56.98	0.78	1.22	0.68	0.84	-4.14	0.57	0.74
19.0	17.5	12.8	0.9	67.37	0.79	0.24	0.92	0.73	-4.13	0.67	0.24
23.1	17.5	13.8	0.6	59.74	0.78	0.92	0.76	0.79	-4.13	0.60	0.60
21.3	17.5	12.8	0.6	60.09	0.76	0.65	0.82	0.73	-4.13	0.60	0.45
19.5	17.4	15.7	0.8	80.51	0.90	0.52	0.89	0.90	-4.12	0.81	0.55
27.4	17.3	12.4	0.6	45.26	0.69	1.41	0.63	0.72	-4.11	0.45	0.67
25.8	17.3	13.7	0.8	53.10	0.75	1.25	0.67	0.79	-4.11	0.53	0.70
23.6	17.2	14.9	0.7	63.14	0.82	1.07	0.73	0.87	-4.10	0.63	0.74
21.2	17.1	11.2	0.7	52.83	0.70	0.68	0.81	0.65	-4.10	0.53	0.41
23.3	17.1	14.1	0.7	60.52	0.79	1.02	0.73	0.82	-4.10	0.61	0.67
18.0	17.0	14.2	0.7	78.89	0.87	0.17	0.94	0.84	-4.09	0.79	0.26
23.7	17.0	14.6	0.7	61.60	0.81	1.11	0.72	0.86	-4.09	0.62	0.74
21.7	17.0	14.6	0.7	67.28	0.83	0.88	0.78	0.86	-4.09	0.67	0.66

A-axis	B-axis	C-axis	Roundness	Flatness	Sphericity	OP-index	b/a	c/b	B-axis phi	c/a	a-b/a-c
28.4	17.0	14.0	0.6	49.30	0.74	1.54	0.60	0.82	-4.09	0.49	0.79
23.3	17.0	11.4	0.6	48.93	0.69	1.00	0.73	0.67	-4.09	0.49	0.53
25.3	17.0	14.9	0.6	58.89	0.80	1.27	0.67	0.88	-4.09	0.59	0.80
21.8	16.9	12.8	0.5	58.72	0.76	0.83	0.78	0.76	-4.08	0.59	0.54
21.7	16.9	13.7	0.8	63.13	0.80	0.85	0.78	0.81	-4.08	0.63	0.60
24.1	16.9	16.8	0.7	69.71	0.88	1.32	0.70	0.99	-4.08	0.70	0.99
23.5	16.9	14.1	0.9	60.00	0.79	1.08	0.72	0.83	-4.08	0.60	0.70
20.0	16.9	10.0	0.5	50.00	0.67	0.52	0.85	0.59	-4.08	0.50	0.31
19.5	16.8	13.6	0.7	69.74	0.83	0.53	0.86	0.81	-4.07	0.70	0.46
25.2	16.8	10.7	0.7	42.46	0.65	1.28	0.67	0.64	-4.07	0.42	0.58
23.0	16.8	13.0	0.7	56.52	0.76	1.01	0.73	0.77	-4.07	0.57	0.62
22.3	16.7	12.2	0.6	54.71	0.74	0.92	0.75	0.73	-4.06	0.55	0.55
21.0	16.6	14.2	0.7	67.62	0.83	0.85	0.79	0.86	-4.05	0.68	0.65
26.6	16.5	14.0	0.7	52.63	0.76	1.45	0.62	0.85	-4.04	0.53	0.80
23.5	16.5	11.0	0.7	46.81	0.68	1.11	0.70	0.67	-4.04	0.47	0.56
19.0	16.3	12.4	0.7	65.26	0.79	0.51	0.86	0.76	-4.03	0.65	0.41
17.0	16.0	8.0	0.8	47.06	0.62	0.12	0.94	0.50	-4.00	0.47	0.11
19.0	16.0	14.0	0.8	73.68	0.86	0.68	0.84	0.88	-4.00	0.74	0.60
19.6	15.9	14.1	0.7	71.94	0.86	0.81	0.81	0.89	-3.99	0.72	0.67
18.8	15.9	13.7	0.7	72.87	0.86	0.65	0.85	0.86	-3.99	0.73	0.57
19.9	15.8	11.3	0.8	56.78	0.74	0.74	0.79	0.72	-3.98	0.57	0.48
18.9	15.7	13.9	0.7	73.54	0.87	0.73	0.83	0.89	-3.97	0.74	0.64
19.2	15.6	10.0	0.6	52.08	0.69	0.65	0.81	0.64	-3.96	0.52	0.39
21.6	15.6	14.9	0.5	68.98	0.87	1.19	0.72	0.96	-3.96	0.69	0.90
17.1	15.6	13.9	0.6	81.29	0.90	0.38	0.91	0.89	-3.96	0.81	0.47
22.0	15.6	14.0	0.6	63.64	0.83	1.16	0.71	0.90	-3.96	0.64	0.80
16.9	15.6	10.8	0.6	63.91	0.76	0.21	0.92	0.69	-3.96	0.64	0.21
18.9	15.6	12.5	0.8	66.14	0.81	0.66	0.83	0.80	-3.96	0.66	0.52
17.8	15.5	11.1	0.8	62.36	0.76	0.43	0.87	0.72	-3.95	0.62	0.34
19.1	15.4	13.1	0.7	68.59	0.84	0.78	0.81	0.85	-3.94	0.69	0.62
19.3	15.4	12.1	0.7	62.69	0.79	0.75	0.80	0.79	-3.94	0.63	0.54
17.1	15.3	12.6	0.7	73.68	0.85	0.39	0.89	0.82	-3.94	0.74	0.40
16.3	15.2	11.1	0.8	68.10	0.79	0.17	0.93	0.73	-3.93	0.68	0.21
22.1	15.2	15.0	0.6	67.87	0.87	1.33	0.69	0.99	-3.93	0.68	0.97
21.1	15.2	11.5	0.6	54.50	0.74	1.03	0.72	0.76	-3.93	0.55	0.61
17.3	15.2	11.9	0.6	68.79	0.81	0.43	0.88	0.78	-3.93	0.69	0.39
21.8	15.1	11.1	0.6	50.92	0.72	1.14	0.69	0.74	-3.92	0.51	0.63
20.1	15.1	13.3	0.7	66.17	0.84	1.00	0.75	0.88	-3.92	0.66	0.74
24.1	15.0	12.6	0.8	52.28	0.76	1.43	0.62	0.84	-3.91	0.52	0.79
28.2	15.0	11.3	0.6	40.07	0.67	1.88	0.53	0.75	-3.91	0.40	0.78
18.4	15.0	11.3	0.5	61.41	0.77	0.67	0.82	0.75	-3.91	0.61	0.48
19.1	14.9	13.2	0.5	69.11	0.85	0.91	0.78	0.89	-3.90	0.69	0.71

A-axis	B-axis	C-axis	Roundness	Flatness	Sphericity	OP-index	b/a	c/b	B-axis phi	c/a	a-b/a-c
16.9	14.8	11.2	0.5	66.27	0.79	0.42	0.88	0.76	-3.89	0.66	0.37
15.1	14.7	11.8	0.6	78.15	0.86	-0.04	0.97	0.80	-3.88	0.78	0.12
21.0	14.6	12.7	0.6	60.48	0.81	1.18	0.70	0.87	-3.87	0.60	0.77
18.1	14.6	13.3	0.8	73.48	0.87	0.85	0.81	0.91	-3.87	0.73	0.73
16.4	14.6	12.1	0.7	73.78	0.85	0.41	0.89	0.83	-3.87	0.74	0.42
19.7	14.5	12.0	0.7	60.91	0.80	1.00	0.74	0.83	-3.86	0.61	0.68
16.0	14.4	8.5	0.6	53.13	0.68	0.28	0.90	0.59	-3.85	0.53	0.21
27.0	14.3	12.6	0.6	46.67	0.74	1.82	0.53	0.88	-3.84	0.47	0.88
18.2	14.3	11.2	0.8	61.54	0.78	0.79	0.79	0.78	-3.84	0.62	0.56
16.2	14.3	11.4	0.7	70.37	0.82	0.41	0.88	0.80	-3.84	0.70	0.40
23.6	14.3	11.3	0.6	47.88	0.72	1.49	0.61	0.79	-3.84	0.48	0.76
15.5	14.3	12.4	0.6	80.00	0.89	0.28	0.92	0.87	-3.84	0.80	0.39
22.6	14.2	10.8	0.8	47.79	0.71	1.40	0.63	0.76	-3.83	0.48	0.71
16.1	14.2	11.1	0.7	68.94	0.81	0.41	0.88	0.78	-3.83	0.69	0.38
16.3	14.2	12.2	0.6	74.85	0.86	0.52	0.87	0.86	-3.83	0.75	0.51
15.3	14.2	13.4	0.8	87.58	0.94	0.36	0.93	0.94	-3.83	0.88	0.58
19.4	14.1	11.1	0.5	57.22	0.77	1.01	0.73	0.79	-3.82	0.57	0.64
19.0	14.0	12.5	0.8	65.79	0.84	1.05	0.74	0.89	-3.81	0.66	0.77
19.3	13.9	13.2	0.6	68.39	0.87	1.17	0.72	0.95	-3.80	0.68	0.89
18.0	13.9	11.0	0.6	61.11	0.78	0.84	0.77	0.79	-3.80	0.61	0.59
18.0	13.9	10.0	0.6	55.56	0.74	0.81	0.77	0.72	-3.80	0.56	0.51
15.3	13.8	10.5	0.9	68.63	0.81	0.30	0.90	0.76	-3.79	0.69	0.31
14.3	13.8	13.5	0.8	94.41	0.97	0.00	0.97	0.98	-3.79	0.94	0.62
18.1	13.8	11.2	0.5	61.88	0.79	0.89	0.76	0.81	-3.79	0.62	0.62
15.4	13.8	11.1	0.6	72.08	0.83	0.35	0.90	0.80	-3.79	0.72	0.37
14.8	13.7	10.9	0.9	73.65	0.84	0.21	0.93	0.80	-3.78	0.74	0.28
22.3	13.7	11.0	0.6	49.33	0.73	1.45	0.61	0.80	-3.78	0.49	0.76
21.3	13.6	10.9	0.8	51.17	0.74	1.35	0.64	0.80	-3.77	0.51	0.74
17.5	13.4	11.2	0.6	64.00	0.81	0.89	0.77	0.84	-3.74	0.64	0.65
17.1	13.4	9.3	0.5	54.39	0.72	0.75	0.78	0.69	-3.74	0.54	0.47
16.4	13.4	12.5	0.6	76.22	0.89	0.84	0.82	0.93	-3.74	0.76	0.77
17.1	13.3	12.5	0.7	73.10	0.88	0.98	0.78	0.94	-3.73	0.73	0.83
16.2	13.3	6.8	0.5	41.98	0.60	0.61	0.82	0.51	-3.73	0.42	0.31
18.9	13.2	12.9	0.7	68.25	0.87	1.27	0.70	0.98	-3.72	0.68	0.95
17.1	13.2	8.1	0.5	47.37	0.66	0.80	0.77	0.61	-3.72	0.47	0.43
15.3	13.2	11.1	0.6	72.55	0.85	0.53	0.86	0.84	-3.72	0.73	0.50
16.4	13.2	11.2	0.6	68.29	0.83	0.76	0.80	0.85	-3.72	0.68	0.62
23.2	13.2	12.1	0.5	52.16	0.78	1.64	0.57	0.92	-3.72	0.52	0.90
15.4	13.1	11.2	0.6	72.73	0.85	0.59	0.85	0.85	-3.71	0.73	0.55
18.2	13.1	12.6	0.7	69.23	0.87	1.19	0.72	0.96	-3.71	0.69	0.91
16.8	13.0	11.8	0.6	70.24	0.86	0.94	0.77	0.91	-3.70	0.70	0.76
18.1	12.9	10.0	0.6	55.25	0.75	1.05	0.71	0.78	-3.69	0.55	0.64

A-axis	B-axis	C-axis	Roundness	Flatness	Sphericity	OP-index	b/a	c/b	B-axis phi	c/a	a-b/a-c
18.2	12.9	10.1	0.7	55.49	0.76	1.07	0.71	0.78	-3.69	0.55	0.65
17.9	12.8	11.1	0.6	62.01	0.81	1.09	0.72	0.87	-3.68	0.62	0.75
17.2	12.8	10.0	0.6	58.14	0.77	0.93	0.74	0.78	-3.68	0.58	0.61
16.8	12.7	10.5	0.6	62.50	0.80	0.91	0.76	0.83	-3.67	0.63	0.65
15.5	12.6	11.1	0.8	71.61	0.86	0.76	0.81	0.88	-3.66	0.72	0.66
15.4	12.4	9.9	0.6	64.29	0.80	0.71	0.81	0.80	-3.63	0.64	0.55
17.2	12.4	10.1	0.7	58.72	0.78	1.03	0.72	0.81	-3.63	0.59	0.68
19.2	12.4	10.2	0.7	53.13	0.76	1.32	0.65	0.82	-3.63	0.53	0.76
15.1	12.3	10.6	0.6	70.20	0.85	0.73	0.81	0.86	-3.62	0.70	0.62
16.6	12.1	10.5	0.7	63.25	0.82	1.04	0.73	0.87	-3.60	0.63	0.74
12.3	11.9	11.7	0.9	95.12	0.98	-0.18	0.97	0.98	-3.57	0.95	0.67
12.9	11.9	7.7	0.9	59.69	0.73	0.16	0.92	0.65	-3.57	0.60	0.19
14.1	11.9	9.5	0.6	67.38	0.81	0.55	0.84	0.80	-3.57	0.67	0.48
15.6	11.6	8.5	0.6	54.49	0.74	0.90	0.74	0.73	-3.54	0.54	0.56
13.6	11.6	8.8	0.7	64.71	0.79	0.48	0.85	0.76	-3.54	0.65	0.42
14.3	11.5	10.5	0.7	73.43	0.88	0.82	0.80	0.91	-3.52	0.73	0.74
14.9	11.4	11.1	0.6	74.50	0.90	1.06	0.77	0.97	-3.51	0.74	0.92
12.6	11.4	9.1	0.6	72.22	0.83	0.28	0.90	0.80	-3.51	0.72	0.34
13.5	10.7	10.5	0.6	77.78	0.91	0.99	0.79	0.98	-3.42	0.78	0.93
10.8	9.8	7.8	0.8	72.22	0.83	0.23	0.91	0.80	-3.29	0.72	0.33
15.6	9.6	8.7	0.7	55.77	0.80	1.43	0.62	0.91	-3.26	0.56	0.87
17.1	9.2	6.4	0.7	37.43	0.64	1.85	0.54	0.70	-3.20	0.37	0.74
14.3	8.6	8.1	0.6	56.64	0.81	1.48	0.60	0.94	-3.10	0.57	0.92
9.8	8.5	8.3	0.9	84.69	0.94	0.63	0.87	0.98	-3.09	0.85	0.87
16.2	8.3	7.9	0.5	48.77	0.77	1.83	0.51	0.95	-3.05	0.49	0.95

Appendix (XII) (f)

PEBBLE DATA ROODERAND CONGLOMERATE FORMATION ROODERAND 510 N

A-axis	B-axis	C-axis	Roundness	Flatness	Sphericity	OP-index	b/a	c/b	B-axis phi	c/a	a-b/a-c
64.8	52.1	39.7	0.7	61.27	0.78	0.79	0.80	0.76	0.79	0.76	0.79
59.2	44.1	29.5	0.6	49.83	0.69	0.99	0.74	0.67	0.99	0.67	0.99
49.6	44.0	23.2	0.6	46.77	0.63	0.41	0.89	0.53	0.41	0.53	0.41
46.7	43.2	31.2	0.8	66.81	0.78	0.29	0.93	0.72	0.29	0.72	0.29
56.4	42.2	24.9	0.6	44.15	0.64	0.99	0.75	0.59	0.99	0.59	0.99
65.2	41.3	28.1	0.6	43.10	0.66	1.46	0.63	0.68	1.46	0.68	1.46
50.5	41.0	28.4	0.6	56.24	0.73	0.72	0.81	0.69	0.72	0.69	0.72
42.0	40.0	25.2	0.7	60.00	0.72	0.15	0.95	0.63	0.15	0.63	0.15
44.3	40.0	29.0	0.9	65.46	0.78	0.38	0.90	0.73	0.38	0.73	0.38
47.8	39.2	35.1	0.5	73.43	0.87	0.87	0.82	0.90	0.87	0.90	0.87
41.2	38.6	33.1	0.5	80.34	0.88	0.32	0.94	0.86	0.32	0.86	0.32
45.5	38.5	23.5	0.6	51.65	0.68	0.57	0.85	0.61	0.57	0.61	0.57
58.3	38.4	25.3	0.6	43.40	0.66	1.35	0.66	0.66	1.35	0.66	1.35
49.1	38.4	26.8	0.6	54.58	0.72	0.84	0.78	0.70	0.84	0.70	0.84
41.3	38.3	33.2	0.6	80.39	0.89	0.38	0.93	0.87	0.38	0.87	0.38
52.6	38.3	28.6	0.7	54.37	0.74	1.06	0.73	0.75	1.06	0.75	1.06
49.0	38.2	22.9	0.8	46.73	0.65	0.84	0.78	0.60	0.84	0.60	0.84
44.8	38.1	30.7	0.8	68.53	0.82	0.64	0.85	0.81	0.64	0.81	0.64
41.7	38.1	30.2	0.7	72.42	0.83	0.37	0.91	0.79	0.37	0.79	0.37
41.9	38.0	16.0	0.8	38.19	0.54	0.34	0.91	0.42	0.34	0.42	0.34
44.0	38.0	21.3	0.7	48.41	0.65	0.50	0.86	0.56	0.50	0.56	0.50
45.6	37.8	25.3	0.6	55.48	0.72	0.65	0.83	0.67	0.65	0.67	0.65
53.3	37.2	32.3	0.6	60.60	0.81	1.23	0.70	0.87	1.23	0.87	1.23
44.3	36.1	32.9	0.7	74.27	0.88	0.91	0.81	0.91	0.91	0.91	0.91
38.7	35.6	28.3	0.6	73.13	0.83	0.34	0.92	0.79	0.34	0.79	0.34
47.2	35.5	30.2	0.7	63.98	0.82	1.03	0.75	0.85	1.03	0.85	1.03
45.3	35.0	28.3	0.6	62.47	0.80	0.92	0.77	0.81	0.92	0.81	0.92
50.9	35.0	20.9	0.6	41.06	0.63	1.25	0.69	0.60	1.25	0.60	1.25
42.7	34.9	29.4	0.6	68.85	0.83	0.80	0.82	0.84	0.80	0.84	0.80
40.3	34.4	20.7	0.6	51.36	0.68	0.54	0.85	0.60	0.54	0.60	0.54
39.4	34.2	16.7	0.6	42.39	0.59	0.49	0.87	0.49	0.49	0.49	0.49
49.1	34.2	31.0	0.8	63.14	0.83	1.26	0.70	0.91	1.26	0.91	1.26
42.6	34.0	23.3	0.7	54.69	0.72	0.77	0.80	0.69	0.77	0.69	0.77
43.8	33.9	21.3	0.7	48.63	0.67	0.86	0.77	0.63	0.86	0.63	0.86
41.1	33.6	21.5	0.9	52.31	0.69	0.68	0.82	0.64	0.68	0.64	0.68
39.0	33.4	23.6	0.6	60.51	0.75	0.55	0.86	0.71	0.55	0.71	0.55
48.6	33.3	20.0	0.6	41.15	0.63	1.26	0.69	0.60	1.26	0.60	1.26

A–axis	B–axis	C–axis	Roundness	Flatness	Sphericity	OP–index	b/a	c/b	B–axis phi	c/a	a–b/a–c
48.6	33.3	20.0	0.6	41.15	0.63	1.26	0.69	0.60	1.26	0.60	1.26
54.6	33.3	22.1	0.7	40.48	0.65	1.58	0.61	0.66	1.58	0.66	1.58
40.2	33.2	26.4	0.6	65.67	0.81	0.72	0.83	0.80	0.72	0.80	0.72
38.3	33.2	28.9	0.7	75.46	0.87	0.65	0.87	0.87	0.65	0.87	0.65
51.2	33.1	24.2	0.6	47.27	0.70	1.38	0.65	0.73	1.38	0.73	1.38
36.3	33.0	25.0	0.9	68.87	0.81	0.36	0.91	0.76	0.36	0.76	0.36
45.5	33.0	28.0	0.8	61.54	0.81	1.11	0.73	0.85	1.11	0.85	1.11
44.1	32.9	27.9	0.9	63.27	0.81	1.04	0.75	0.85	1.04	0.85	1.04
42.4	32.9	21.0	0.6	49.53	0.68	0.85	0.78	0.64	0.85	0.64	0.85
43.4	32.6	31.4	0.6	72.35	0.89	1.19	0.75	0.96	1.19	0.96	1.19
34.5	32.2	18.9	0.8	54.78	0.69	0.21	0.93	0.59	0.21	0.59	0.21
46.2	32.2	20.4	0.7	44.16	0.65	1.19	0.70	0.63	1.19	0.63	1.19
37.2	32.1	27.8	0.8	74.73	0.86	0.65	0.86	0.87	0.65	0.87	0.65
36.2	31.9	20.2	0.9	55.80	0.71	0.43	0.88	0.63	0.43	0.63	0.43
44.1	31.8	25.0	0.7	56.69	0.76	1.09	0.72	0.79	1.09	0.79	1.09
34.8	31.7	26.1	0.6	75.00	0.85	0.40	0.91	0.82	0.40	0.82	0.40
40.9	31.6	23.7	0.6	57.95	0.76	0.88	0.77	0.75	0.88	0.75	0.88
35.0	31.5	19.9	0.8	56.86	0.71	0.35	0.90	0.63	0.35	0.63	0.35
33.8	31.5	23.9	0.6	70.71	0.81	0.26	0.93	0.76	0.26	0.76	0.26
39.3	31.4	26.5	0.6	67.43	0.83	0.86	0.80	0.84	0.86	0.84	0.86
35.5	31.4	28.3	0.8	79.72	0.90	0.63	0.88	0.90	0.63	0.90	0.63
62.3	31.4	25.3	0.6	40.61	0.69	2.02	0.50	0.81	2.02	0.81	2.02
37.4	31.4	17.5	0.7	46.79	0.64	0.59	0.84	0.56	0.59	0.56	0.59
37.4	31.4	24.2	0.6	64.71	0.79	0.64	0.84	0.77	0.64	0.77	0.64
42.3	31.3	20.1	0.6	47.40	0.67	1.00	0.74	0.64	1.00	0.64	1.00
39.3	31.3	29.4	0.6	74.81	0.89	1.01	0.80	0.94	1.01	0.94	1.01
33.2	31.3	20.6	0.6	62.05	0.74	0.18	0.94	0.66	0.18	0.66	0.18
34.2	31.2	28.7	0.7	83.92	0.92	0.54	0.91	0.92	0.54	0.92	0.54
36.4	31.2	19.9	0.8	54.67	0.70	0.52	0.86	0.64	0.52	0.64	0.52
39.4	31.2	21.6	0.6	54.82	0.72	0.79	0.79	0.69	0.79	0.69	0.79
35.2	31.1	24.6	0.7	69.89	0.82	0.49	0.88	0.79	0.49	0.79	0.49
33.4	31.0	26.3	0.8	78.74	0.87	0.34	0.93	0.85	0.34	0.85	0.34
32.4	30.9	26.2	0.6	80.86	0.88	0.20	0.95	0.85	0.20	0.85	0.20
34.9	30.8	14.7	0.7	42.12	0.59	0.42	0.88	0.48	0.42	0.48	0.42
42.3	30.7	22.2	0.7	52.48	0.72	1.05	0.73	0.72	1.05	0.72	1.05
38.1	30.4	22.1	0.7	58.01	0.75	0.78	0.80	0.73	0.78	0.73	0.78
36.0	30.3	22.6	0.8	62.78	0.78	0.62	0.84	0.75	0.62	0.75	0.62
35.1	30.2	27.4	0.7	78.06	0.89	0.73	0.86	0.91	0.73	0.91	0.73
32.4	30.1	26.6	0.7	82.10	0.90	0.38	0.93	0.88	0.38	0.88	0.38
32.3	30.1	25.4	0.6	78.64	0.87	0.31	0.93	0.84	0.31	0.84	0.31
37.4	30.1	25.9	0.6	69.25	0.84	0.85	0.80	0.86	0.85	0.86	0.85
40.2	30.1	26.2	0.6	65.17	0.83	1.05	0.75	0.87	1.05	0.87	1.05

A-axis	B-axis	C-axis	Roundness	Flatness	Sphericity	OP-index	b/a	c/b	B-axis phi	c/a	a-b/a-c
41.0	30.0	23.0	0.8	56.10	0.75	1.04	0.73	0.77	1.04	0.77	1.04
34.8	29.9	26.1	0.6	75.00	0.87	0.67	0.86	0.87	0.67	0.87	0.67
35.0	29.8	20.2	0.6	57.71	0.73	0.55	0.85	0.68	0.55	0.68	0.55
42.4	29.7	28.1	0.6	66.27	0.86	1.29	0.70	0.95	1.29	0.95	1.29
34.1	29.6	25.1	0.6	73.61	0.85	0.60	0.87	0.85	0.60	0.85	0.60
37.1	29.6	24.1	0.7	64.96	0.81	0.83	0.80	0.81	0.83	0.81	0.83
41.0	29.5	24.0	0.8	58.54	0.78	1.11	0.72	0.81	1.11	0.81	1.11
43.4	29.3	24.1	0.7	55.53	0.77	1.27	0.68	0.82	1.27	0.82	1.27
34.3	29.3	19.7	0.6	57.43	0.73	0.54	0.85	0.67	0.54	0.67	0.54
33.8	29.2	23.5	0.6	69.53	0.82	0.57	0.86	0.80	0.57	0.80	0.57
30.8	29.2	17.2	0.7	55.84	0.69	0.14	0.95	0.59	0.14	0.59	0.14
30.2	29.2	22.3	0.7	73.84	0.83	0.09	0.97	0.76	0.09	0.76	0.09
31.0	29.2	21.0	0.6	67.74	0.79	0.19	0.94	0.72	0.19	0.72	0.19
32.7	29.2	16.4	0.7	50.15	0.66	0.37	0.89	0.56	0.37	0.56	0.37
36.0	29.0	26.1	0.8	72.50	0.87	0.91	0.81	0.90	0.91	0.90	0.91
36.2	29.0	19.1	0.7	52.76	0.70	0.74	0.80	0.66	0.74	0.66	0.74
39.3	29.0	23.3	0.7	59.29	0.78	1.03	0.74	0.80	1.03	0.80	1.03
45.0	29.0	19.1	0.7	42.44	0.65	1.41	0.64	0.66	1.41	0.66	1.41
33.5	28.8	22.3	0.9	66.57	0.80	0.56	0.86	0.77	0.56	0.77	0.56
41.4	28.7	28.0	0.7	67.63	0.87	1.35	0.69	0.98	1.35	0.98	1.35
30.4	28.7	16.2	0.6	53.29	0.67	0.16	0.94	0.56	0.16	0.56	0.16
33.3	28.6	23.5	0.7	70.57	0.83	0.61	0.86	0.82	0.61	0.82	0.61
33.4	28.6	22.1	0.8	66.17	0.80	0.58	0.86	0.77	0.58	0.77	0.58
36.1	28.6	22.3	0.6	61.77	0.78	0.82	0.79	0.78	0.82	0.78	0.82
31.4	28.6	22.3	0.5	71.02	0.82	0.36	0.91	0.78	0.36	0.78	0.36
36.5	28.3	23.6	0.7	64.66	0.81	0.92	0.78	0.83	0.92	0.83	0.92
31.4	28.3	17.4	0.6	55.41	0.70	0.34	0.90	0.61	0.34	0.61	0.34
41.0	28.3	24.5	0.5	59.76	0.80	1.24	0.69	0.87	1.24	0.87	1.24
32.3	28.3	17.4	0.5	53.87	0.69	0.44	0.88	0.61	0.44	0.61	0.44
32.8	28.3	21.8	0.6	66.46	0.80	0.55	0.86	0.77	0.55	0.77	0.55
30.0	28.3	14.3	0.6	47.67	0.62	0.16	0.94	0.51	0.16	0.51	0.16
31.1	28.2	25.6	0.7	82.32	0.91	0.53	0.91	0.91	0.53	0.91	0.53
49.4	28.2	22.0	0.7	44.53	0.70	1.70	0.57	0.78	1.70	0.78	1.70
28.3	28.1	24.1	0.9	85.16	0.90	−0.08	0.99	0.86	−0.08	0.86	−0.08
32.3	28.1	20.7	0.6	64.09	0.78	0.50	0.87	0.74	0.50	0.74	0.50
35.6	28.1	18.2	0.7	51.12	0.69	0.79	0.79	0.65	0.79	0.65	0.79
34.0	28.1	21.8	0.6	64.12	0.79	0.69	0.83	0.78	0.69	0.78	0.69
35.6	28.1	18.2	0.7	51.12	0.69	0.79	0.79	0.65	0.79	0.65	0.79
35.0	28.1	19.5	0.5	55.71	0.73	0.74	0.80	0.69	0.74	0.69	0.74
43.7	27.9	15.7	0.6	35.93	0.59	1.52	0.64	0.56	1.52	0.56	1.52
31.8	27.9	16.0	0.9	50.31	0.66	0.43	0.88	0.57	0.43	0.57	0.43
31.0	27.9	20.0	0.9	64.52	0.77	0.37	0.90	0.72	0.37	0.72	0.37

A-axis	B-axis	C-axis	Roundness	Flatness	Sphericity	OP-index	b/a	c/b	B-axis phi	c/a	a-b/a-c
34.1	27.8	19.1	0.6	56.01	0.73	0.69	0.82	0.69	0.69	0.69	0.69
40.5	27.7	21.0	0.6	51.85	0.73	1.22	0.68	0.76	1.22	0.76	1.22
38.1	27.7	21.0	0.7	55.12	0.75	1.05	0.73	0.76	1.05	0.76	1.05
32.1	27.6	20.4	0.7	63.55	0.78	0.54	0.86	0.74	0.54	0.74	0.54
35.7	27.6	21.2	0.8	59.38	0.77	0.88	0.77	0.77	0.88	0.77	0.88
36.0	27.6	25.4	0.6	70.56	0.87	1.06	0.77	0.92	1.06	0.92	1.06
36.7	27.6	19.5	0.6	53.13	0.72	0.94	0.75	0.71	0.94	0.71	0.94
36.1	27.4	16.2	0.7	44.88	0.64	0.92	0.76	0.59	0.92	0.59	0.92
33.5	27.4	17.3	0.7	51.64	0.69	0.67	0.82	0.63	0.67	0.63	0.67
31.2	27.4	19.0	0.8	60.90	0.75	0.44	0.88	0.69	0.44	0.69	0.44
34.2	27.3	25.3	0.6	73.98	0.88	0.97	0.80	0.93	0.97	0.93	0.97
32.9	27.1	16.5	0.6	50.15	0.67	0.64	0.82	0.61	0.64	0.61	0.64
45.7	27.0	22.4	0.8	49.02	0.74	1.59	0.59	0.83	1.59	0.83	1.59
39.9	26.8	19.6	0.8	49.12	0.71	1.26	0.67	0.73	1.26	0.73	1.26
31.6	26.8	21.8	0.8	68.99	0.82	0.64	0.85	0.81	0.64	0.81	0.64
38.1	26.8	26.3	0.8	69.03	0.88	1.33	0.70	0.98	1.33	0.98	1.33
40.3	26.7	17.8	0.6	44.17	0.67	1.32	0.66	0.67	1.32	0.67	1.32
34.5	26.6	21.0	0.7	60.87	0.78	0.90	0.77	0.79	0.90	0.79	0.90
32.4	26.4	22.0	0.7	67.90	0.83	0.78	0.81	0.83	0.78	0.83	0.78
27.4	26.4	15.8	0.6	57.66	0.70	0.07	0.96	0.60	0.07	0.60	0.07
33.6	26.4	23.6	0.8	70.24	0.86	0.95	0.79	0.89	0.95	0.89	0.95
32.4	26.4	22.5	0.7	69.44	0.84	0.80	0.81	0.85	0.80	0.85	0.80
30.2	26.4	23.4	0.5	77.48	0.88	0.63	0.87	0.89	0.63	0.89	0.63
30.6	26.4	24.1	0.7	78.76	0.90	0.72	0.86	0.91	0.72	0.91	0.72
45.2	26.3	20.4	0.6	45.13	0.70	1.64	0.58	0.78	1.64	0.78	1.64
28.2	26.3	16.1	0.6	57.09	0.70	0.20	0.93	0.61	0.20	0.61	0.20
40.9	26.3	24.7	0.8	60.39	0.83	1.44	0.64	0.94	1.44	0.94	1.44
38.8	26.2	18.2	0.9	46.91	0.69	1.25	0.68	0.69	1.25	0.69	1.25
30.6	26.2	22.4	0.7	73.20	0.86	0.65	0.86	0.85	0.65	0.85	0.65
30.2	26.2	20.0	0.8	66.23	0.80	0.52	0.87	0.76	0.52	0.76	0.52
30.6	26.2	22.4	0.8	73.20	0.86	0.65	0.86	0.85	0.65	0.85	0.65
26.8	26.2	14.0	0.9	52.24	0.65	0.01	0.98	0.53	0.01	0.53	0.01
38.9	26.2	23.7	0.9	60.93	0.82	1.32	0.67	0.90	1.32	0.90	1.32
34.3	26.2	22.4	0.7	65.31	0.82	0.98	0.76	0.85	0.98	0.85	0.98
28.4	26.1	16.2	0.8	57.04	0.71	0.26	0.92	0.62	0.26	0.62	0.26
31.1	25.9	19.0	0.8	61.09	0.77	0.64	0.83	0.73	0.64	0.73	0.64
30.0	25.9	18.5	0.8	61.67	0.76	0.51	0.86	0.71	0.51	0.71	0.51
32.5	25.8	15.9	0.6	48.92	0.67	0.76	0.79	0.62	0.76	0.62	0.76
34.1	25.8	17.3	0.6	50.73	0.70	0.92	0.76	0.67	0.92	0.67	0.92
27.2	25.7	15.8	0.6	58.09	0.71	0.15	0.94	0.61	0.15	0.61	0.15
28.3	25.7	12.2	0.8	43.11	0.59	0.30	0.91	0.47	0.30	0.47	0.30
31.2	25.5	21.4	0.8	68.59	0.83	0.77	0.82	0.84	0.77	0.84	0.77

A-axis	B-axis	C-axis	Roundness	Flatness	Sphericity	OP-index	b/a	c/b	B-axis phi	c/a	a-b/a-c
33.8	25.5	17.0	0.7	50.30	0.69	0.92	0.75	0.67	0.92	0.67	0.92
28.3	25.4	16.0	0.6	56.54	0.71	0.35	0.90	0.63	0.35	0.63	0.35
30.8	25.4	21.0	0.6	68.18	0.83	0.73	0.82	0.83	0.73	0.83	0.73
35.9	25.3	15.0	0.8	41.78	0.63	1.16	0.70	0.59	1.16	0.59	1.16
29.1	25.2	17.2	0.7	59.11	0.74	0.48	0.87	0.68	0.48	0.68	0.48
32.5	25.2	19.8	0.7	60.92	0.78	0.88	0.78	0.79	0.88	0.79	0.88
29.7	25.0	20.8	0.7	70.03	0.84	0.67	0.84	0.83	0.67	0.83	0.67
31.8	25.0	20.7	0.7	65.09	0.81	0.87	0.79	0.83	0.87	0.83	0.87
28.3	25.0	15.5	0.6	54.77	0.70	0.40	0.88	0.62	0.40	0.62	0.40
37.1	25.0	21.7	0.8	58.49	0.80	1.29	0.67	0.87	1.29	0.87	1.29
25.3	24.8	15.8	0.6	62.45	0.74	0.00	0.98	0.64	0.00	0.64	0.00
32.6	24.7	19.1	0.6	58.59	0.77	0.94	0.76	0.77	0.94	0.77	0.94
32.0	24.7	18.8	0.7	58.75	0.76	0.88	0.77	0.76	0.88	0.76	0.88
37.0	24.5	16.0	0.7	43.24	0.66	1.32	0.66	0.65	1.32	0.65	1.32
36.0	24.5	22.0	0.8	61.11	0.82	1.29	0.68	0.90	1.29	0.90	1.29
27.0	24.3	18.7	0.6	69.26	0.81	0.38	0.90	0.77	0.38	0.77	0.38
29.2	24.3	22.1	0.8	75.68	0.88	0.82	0.83	0.91	0.82	0.91	0.82
32.5	24.3	22.8	0.8	70.15	0.87	1.13	0.75	0.94	1.13	0.94	1.13
32.5	24.3	15.6	0.7	48.00	0.68	0.95	0.75	0.64	0.95	0.64	0.95
29.9	24.2	16.3	0.8	54.52	0.72	0.70	0.81	0.67	0.70	0.67	0.70
34.3	24.2	20.0	0.8	58.31	0.78	1.15	0.71	0.83	1.15	0.83	1.15
33.9	24.2	17.3	0.5	51.03	0.71	1.09	0.71	0.71	1.09	0.71	1.09
32.3	24.2	20.0	0.8	61.92	0.80	1.00	0.75	0.83	1.00	0.83	1.00
26.0	24.2	20.0	0.8	76.92	0.86	0.28	0.93	0.83	0.28	0.83	0.28
31.4	24.1	17.8	0.6	56.69	0.75	0.88	0.77	0.74	0.88	0.74	0.88
27.8	24.1	20.6	0.6	74.10	0.86	0.60	0.87	0.85	0.60	0.85	0.60
26.4	24.1	15.2	0.8	57.58	0.71	0.28	0.91	0.63	0.28	0.63	0.28
38.7	24.0	16.9	0.8	43.67	0.67	1.49	0.62	0.70	1.49	0.70	1.49
27.4	24.0	16.4	0.7	59.85	0.74	0.44	0.88	0.68	0.44	0.68	0.44
36.7	24.0	17.0	0.7	46.32	0.69	1.34	0.65	0.71	1.34	0.71	1.34
30.0	24.0	18.2	0.6	60.67	0.77	0.77	0.80	0.76	0.77	0.76	0.77
33.9	24.0	21.7	0.7	64.01	0.83	1.20	0.71	0.90	1.20	0.90	1.20
31.0	23.9	19.3	0.8	62.26	0.80	0.91	0.77	0.81	0.91	0.81	0.91
28.3	23.9	21.1	0.9	74.56	0.87	0.73	0.84	0.88	0.73	0.88	0.73
37.3	23.9	16.9	0.7	45.31	0.68	1.40	0.64	0.71	1.40	0.71	1.40
27.1	23.8	15.0	0.8	55.35	0.70	0.42	0.88	0.63	0.42	0.63	0.42
30.5	23.6	20.1	0.6	65.90	0.82	0.93	0.77	0.85	0.93	0.85	0.93
36.3	23.5	18.0	0.6	49.59	0.72	1.36	0.65	0.77	1.36	0.77	1.36
29.3	23.5	21.0	0.6	71.67	0.86	0.89	0.80	0.89	0.89	0.89	0.89
25.3	23.5	15.6	0.6	61.66	0.74	0.22	0.93	0.66	0.22	0.66	0.22
29.7	23.5	14.6	0.6	49.16	0.67	0.77	0.79	0.62	0.77	0.62	0.77
30.8	23.4	20.6	0.6	66.88	0.84	1.01	0.76	0.88	1.01	0.88	1.01

A–axis	B–axis	C–axis	Roundness	Flatness	Sphericity	OP–index	b/a	c/b	B–axis phi	c/a	a–b/a–c
26.9	23.4	16.0	0.8	59.48	0.74	0.46	0.87	0.68	0.46	0.68	0.46
25.2	23.3	20.3	0.8	80.56	0.89	0.35	0.92	0.87	0.35	0.87	0.35
30.3	23.2	13.3	0.7	43.89	0.63	0.88	0.77	0.57	0.88	0.57	0.88
28.0	23.1	16.2	0.8	57.86	0.74	0.64	0.83	0.70	0.64	0.70	0.64
26.1	23.1	17.4	0.7	66.67	0.79	0.43	0.89	0.75	0.43	0.75	0.43
31.8	23.1	13.1	0.8	41.19	0.62	1.06	0.73	0.57	1.06	0.57	1.06
25.3	22.9	16.1	0.7	63.64	0.76	0.32	0.91	0.70	0.32	0.70	0.32
28.0	22.9	13.4	0.8	47.86	0.65	0.66	0.82	0.59	0.66	0.59	0.66
25.6	22.8	14.8	0.9	57.81	0.72	0.37	0.89	0.65	0.37	0.65	0.37
30.8	22.7	20.6	0.8	66.88	0.85	1.11	0.74	0.91	1.11	0.91	1.11
30.1	22.5	18.5	0.8	61.46	0.80	1.00	0.75	0.82	1.00	0.82	1.00
26.2	22.4	20.3	0.7	77.48	0.89	0.72	0.85	0.91	0.72	0.91	0.72
29.3	22.4	18.7	0.8	63.82	0.81	0.95	0.76	0.83	0.95	0.83	0.95
24.9	22.4	18.3	0.6	73.49	0.84	0.41	0.90	0.82	0.41	0.82	0.41
30.8	22.3	13.7	0.7	44.48	0.65	1.05	0.72	0.61	1.05	0.61	1.05
29.9	22.3	14.6	0.6	48.83	0.68	0.95	0.75	0.65	0.95	0.65	0.95
26.2	22.3	14.9	0.5	56.87	0.72	0.53	0.85	0.67	0.53	0.67	0.53
25.1	22.3	16.3	0.6	64.94	0.78	0.40	0.89	0.73	0.40	0.73	0.40
28.9	22.2	15.7	0.7	54.33	0.73	0.86	0.77	0.71	0.86	0.71	0.86
32.2	22.2	20.1	0.7	62.42	0.83	1.26	0.69	0.91	1.26	0.91	1.26
29.7	22.2	13.8	0.8	46.46	0.66	0.95	0.75	0.62	0.95	0.62	0.95
24.4	22.2	18.4	0.7	75.41	0.85	0.38	0.91	0.83	0.38	0.83	0.38
23.0	22.1	13.3	0.8	57.83	0.70	0.07	0.96	0.60	0.07	0.60	0.07
24.1	22.1	13.1	0.8	54.36	0.69	0.25	0.92	0.59	0.25	0.59	0.25
27.4	22.1	21.8	0.6	79.56	0.92	1.08	0.81	0.99	1.08	0.99	1.08
32.2	22.0	13.7	0.6	42.55	0.64	1.23	0.68	0.62	1.23	0.62	1.23
30.2	22.0	16.0	0.7	52.98	0.73	1.02	0.73	0.73	1.02	0.73	1.02
23.6	22.0	13.6	0.7	57.63	0.71	0.19	0.93	0.62	0.19	0.62	0.19
22.8	21.9	11.3	0.8	49.56	0.63	0.07	0.96	0.52	0.07	0.52	0.07
24.9	21.9	19.9	0.8	79.92	0.90	0.63	0.88	0.91	0.63	0.91	0.63
32.7	21.8	15.1	0.6	46.18	0.68	1.28	0.67	0.69	1.28	0.69	1.28
23.9	21.8	16.1	0.7	67.36	0.79	0.30	0.91	0.74	0.30	0.74	0.30
23.4	21.8	17.3	0.6	73.93	0.84	0.24	0.93	0.79	0.24	0.79	0.24
27.0	21.8	13.5	0.7	50.00	0.68	0.70	0.81	0.62	0.70	0.62	0.70
24.8	21.7	18.0	0.6	72.58	0.84	0.53	0.88	0.83	0.53	0.83	0.53
28.5	21.7	13.8	0.6	48.42	0.68	0.89	0.76	0.64	0.89	0.64	0.89
24.4	21.7	12.6	0.6	51.64	0.67	0.36	0.89	0.58	0.36	0.58	0.36
33.2	21.5	19.4	0.7	58.43	0.81	1.39	0.65	0.90	1.39	0.90	1.39
29.5	21.5	15.2	0.7	51.53	0.71	1.02	0.73	0.71	1.02	0.71	1.02
29.8	21.3	14.3	0.8	47.99	0.69	1.08	0.71	0.67	1.08	0.67	1.08
26.3	21.3	12.4	0.6	47.15	0.65	0.69	0.81	0.58	0.69	0.58	0.69
23.4	21.3	13.4	0.6	57.26	0.71	0.28	0.91	0.63	0.28	0.63	0.28

A–axis	B–axis	C–axis	Roundness	Flatness	Sphericity	OP–index	b/a	c/b	B–axis phi	c/a	a–b/a–c
27.8	21.2	14.0	0.8	50.36	0.69	0.88	0.76	0.66	0.88	0.66	0.88
25.1	21.2	19.6	0.7	78.09	0.90	0.79	0.84	0.92	0.79	0.92	0.79
31.4	21.2	20.3	0.7	64.65	0.85	1.35	0.68	0.96	1.35	0.96	1.35
24.1	21.1	15.1	0.7	62.66	0.77	0.44	0.88	0.72	0.44	0.72	0.44
32.4	21.1	16.9	0.7	52.16	0.75	1.34	0.65	0.80	1.34	0.80	1.34
23.2	21.1	16.3	0.6	70.26	0.82	0.33	0.91	0.77	0.33	0.77	0.33
24.6	21.0	17.9	0.7	72.76	0.85	0.64	0.85	0.85	0.64	0.85	0.64
28.5	21.0	14.2	0.8	49.82	0.70	0.98	0.74	0.68	0.98	0.68	0.98
24.3	21.0	13.2	0.8	54.32	0.70	0.46	0.86	0.63	0.46	0.63	0.46
28.0	21.0	17.2	0.6	61.43	0.80	0.98	0.75	0.82	0.98	0.82	0.98
24.5	21.0	15.2	0.8	62.04	0.77	0.52	0.86	0.72	0.52	0.72	0.52
25.2	20.9	16.3	0.6	64.68	0.80	0.66	0.83	0.78	0.66	0.78	0.66
31.3	20.9	17.6	0.7	56.23	0.78	1.29	0.67	0.84	1.29	0.84	1.29
32.3	20.9	19.8	0.6	61.30	0.83	1.42	0.65	0.95	1.42	0.95	1.42
27.0	20.8	19.8	0.7	73.33	0.89	1.08	0.77	0.95	1.08	0.95	1.08
24.6	20.8	14.3	0.7	58.13	0.74	0.55	0.85	0.69	0.55	0.69	0.55
25.9	20.8	15.3	0.6	59.07	0.76	0.73	0.80	0.74	0.73	0.74	0.73
26.4	20.7	16.1	0.6	60.98	0.78	0.83	0.78	0.78	0.83	0.78	0.83
21.8	20.7	16.8	0.6	77.06	0.86	0.16	0.95	0.81	0.16	0.81	0.16
46.7	20.6	15.0	0.5	32.12	0.62	2.51	0.44	0.73	2.51	0.73	2.51
22.9	20.6	18.4	0.6	80.35	0.90	0.50	0.90	0.89	0.50	0.89	0.50
23.0	20.6	13.9	0.7	60.43	0.74	0.35	0.90	0.67	0.35	0.67	0.35
22.1	20.5	12.7	0.6	57.47	0.71	0.20	0.93	0.62	0.20	0.62	0.20
25.6	20.4	14.1	0.7	55.08	0.72	0.74	0.80	0.69	0.74	0.69	0.74
28.8	20.3	16.1	0.9	55.90	0.76	1.13	0.70	0.79	1.13	0.79	1.13
22.2	20.3	11.6	0.6	52.25	0.67	0.25	0.91	0.57	0.25	0.57	0.25
21.1	20.3	19.7	0.8	93.36	0.97	0.23	0.96	0.97	0.23	0.97	0.23
22.3	20.3	18.7	0.8	83.86	0.92	0.50	0.91	0.92	0.50	0.92	0.50
29.3	20.3	15.4	0.8	52.56	0.74	1.16	0.69	0.76	1.16	0.76	1.16
28.9	20.2	13.6	0.6	47.06	0.68	1.14	0.70	0.67	1.14	0.67	1.14
22.3	20.1	18.3	0.7	82.06	0.91	0.52	0.90	0.91	0.52	0.91	0.52
26.1	20.1	17.7	0.7	67.82	0.84	0.97	0.77	0.88	0.97	0.88	0.97
25.3	20.0	11.4	0.6	45.06	0.64	0.77	0.79	0.57	0.77	0.57	0.77
23.0	19.9	14.2	0.7	61.74	0.76	0.48	0.87	0.71	0.48	0.71	0.48
24.4	19.9	16.1	0.5	65.98	0.81	0.73	0.82	0.81	0.73	0.81	0.73
23.0	19.9	17.1	0.8	74.35	0.86	0.59	0.87	0.86	0.59	0.86	0.59
31.9	19.8	14.8	0.8	46.39	0.70	1.46	0.62	0.75	1.46	0.75	1.46
29.8	19.7	19.0	0.7	63.76	0.85	1.39	0.66	0.96	1.39	0.96	1.39
33.5	19.5	15.4	0.7	45.97	0.71	1.62	0.58	0.79	1.62	0.79	1.62
24.9	19.4	13.0	0.8	52.21	0.70	0.80	0.78	0.67	0.80	0.67	0.80
28.3	19.4	8.3	0.7	29.33	0.50	1.43	0.69	0.43	1.43	0.43	1.43
24.7	19.3	13.7	0.5	55.47	0.73	0.80	0.78	0.71	0.80	0.71	0.80

A−axis	B−axis	C−axis	Roundness	Flatness	Sphericity	OP−index	b/a	c/b	B−axis phi	c/a	a−b/a−c
22.1	19.3	14.3	0.7	64.71	0.78	0.46	0.87	0.74	0.46	0.74	0.46
20.1	19.3	16.4	0.7	81.59	0.89	0.10	0.96	0.85	0.10	0.85	0.10
28.2	19.3	14.9	0.6	52.84	0.74	1.20	0.68	0.77	1.20	0.77	1.20
23.0	19.2	15.0	0.7	65.22	0.80	0.63	0.83	0.78	0.63	0.78	0.63
23.2	19.2	13.1	0.6	56.47	0.73	0.61	0.83	0.68	0.61	0.68	0.61
29.8	19.2	12.2	0.6	40.94	0.64	1.40	0.64	0.64	1.40	0.64	1.40
20.7	19.1	11.0	0.7	53.14	0.67	0.21	0.92	0.58	0.21	0.58	0.21
24.6	19.1	14.2	0.7	57.72	0.75	0.83	0.78	0.74	0.83	0.74	0.83
24.2	19.0	13.1	0.7	54.13	0.72	0.78	0.79	0.69	0.78	0.69	0.78
27.2	19.0	12.7	0.8	46.69	0.68	1.14	0.70	0.67	1.14	0.67	1.14
20.4	18.9	14.2	0.8	69.61	0.81	0.23	0.93	0.75	0.23	0.75	0.23
19.1	18.7	18.5	0.7	96.86	0.99	−0.17	0.98	0.99	−0.17	0.99	−0.17
20.4	18.7	14.3	0.9	70.10	0.81	0.28	0.92	0.76	0.28	0.76	0.28
25.3	18.7	15.6	0.8	61.66	0.80	1.02	0.74	0.83	1.02	0.83	1.02
23.1	18.7	12.4	0.6	53.68	0.71	0.68	0.81	0.66	0.68	0.66	0.68
24.3	18.6	16.3	0.6	67.08	0.84	0.97	0.77	0.88	0.97	0.88	0.97
28.3	18.4	13.6	0.6	48.06	0.71	1.33	0.65	0.74	1.33	0.74	1.33
21.3	18.3	16.2	0.6	76.06	0.88	0.64	0.86	0.89	0.64	0.89	0.64
21.7	18.3	16.7	0.7	76.96	0.89	0.75	0.84	0.91	0.75	0.91	0.75
22.4	18.3	14.9	0.5	66.52	0.82	0.72	0.82	0.81	0.72	0.81	0.72
25.4	18.3	17.1	0.8	67.32	0.86	1.18	0.72	0.93	1.18	0.93	1.18
21.3	18.3	16.2	0.7	76.06	0.88	0.64	0.86	0.89	0.64	0.89	0.64
20.7	18.3	16.4	0.7	79.23	0.89	0.56	0.88	0.90	0.56	0.90	0.56
19.9	18.2	11.0	0.8	55.28	0.69	0.24	0.91	0.60	0.24	0.60	0.24
20.8	18.2	12.5	0.8	60.10	0.74	0.42	0.88	0.69	0.42	0.69	0.42
23.4	18.1	15.6	0.7	66.67	0.83	0.92	0.77	0.86	0.92	0.86	0.92
22.3	18.1	16.4	0.6	73.54	0.87	0.85	0.81	0.91	0.85	0.91	0.85
24.0	18.1	14.2	0.8	59.17	0.77	0.93	0.75	0.78	0.93	0.78	0.93
21.1	18.0	14.0	0.7	66.35	0.80	0.55	0.85	0.78	0.55	0.78	0.55
21.0	18.0	12.1	0.8	57.62	0.73	0.49	0.86	0.67	0.49	0.67	0.49
20.2	18.0	13.6	0.6	67.33	0.80	0.38	0.89	0.76	0.38	0.76	0.38
19.2	18.0	14.7	0.5	76.56	0.86	0.20	0.94	0.82	0.20	0.82	0.20
22.6	17.9	13.7	0.7	60.62	0.77	0.78	0.79	0.77	0.78	0.77	0.78
25.7	17.9	14.2	0.7	55.25	0.76	1.15	0.70	0.79	1.15	0.79	1.15
23.9	17.8	17.3	0.6	72.38	0.89	1.17	0.74	0.97	1.17	0.97	1.17
19.2	17.8	13.1	0.7	68.23	0.79	0.22	0.93	0.74	0.22	0.74	0.22
27.2	17.8	16.0	0.8	58.82	0.81	1.35	0.65	0.90	1.35	0.90	1.35
25.8	17.8	17.5	0.6	67.83	0.87	1.33	0.69	0.98	1.33	0.98	1.33
23.9	17.7	14.9	0.8	62.34	0.81	1.02	0.74	0.84	1.02	0.84	1.02
24.1	17.7	14.9	0.8	61.83	0.80	1.04	0.73	0.84	1.04	0.84	1.04
20.5	17.6	13.1	0.5	63.90	0.78	0.51	0.86	0.74	0.51	0.74	0.51
18.6	17.5	12.4	0.8	66.67	0.78	0.15	0.94	0.71	0.15	0.71	0.15

A−axis	B−axis	C−axis	Roundness	Flatness	Sphericity	OP−index	b/a	c/b	B−axis phi	c/a	a−b/a−c
22.2	17.5	13.4	0.7	60.36	0.77	0.79	0.79	0.77	0.79	0.77	0.79
23.1	17.5	13.8	0.6	59.74	0.78	0.92	0.76	0.79	0.92	0.79	0.92
23.5	17.4	14.6	0.6	62.13	0.80	1.01	0.74	0.84	1.01	0.84	1.01
21.3	17.4	14.3	0.8	67.14	0.82	0.72	0.82	0.82	0.72	0.82	0.72
25.3	17.4	15.8	0.6	62.45	0.83	1.25	0.69	0.91	1.25	0.91	1.25
24.4	17.3	16.1	0.7	65.98	0.85	1.21	0.71	0.93	1.21	0.93	1.21
22.2	17.2	12.7	0.6	57.21	0.75	0.83	0.77	0.74	0.83	0.74	0.83
19.0	17.2	11.9	0.6	62.63	0.76	0.29	0.91	0.69	0.29	0.69	0.29
29.6	17.2	14.8	0.8	50.00	0.75	1.61	0.58	0.86	1.61	0.86	1.61
19.9	17.1	15.8	0.8	79.40	0.90	0.71	0.86	0.92	0.71	0.92	0.71
24.3	17.1	12.0	0.6	49.38	0.70	1.10	0.70	0.70	1.10	0.70	1.10
20.8	17.1	15.0	0.7	72.12	0.86	0.77	0.82	0.88	0.77	0.88	0.77
17.9	17.0	11.2	0.8	62.57	0.74	0.10	0.95	0.66	0.10	0.66	0.10
26.1	16.9	14.3	0.8	54.79	0.77	1.35	0.65	0.85	1.35	0.85	1.35
17.6	16.8	8.7	0.8	49.43	0.63	0.07	0.95	0.52	0.07	0.52	0.07
22.4	16.6	14.1	0.6	62.95	0.81	1.01	0.74	0.85	1.01	0.85	1.01
24.3	16.6	14.9	0.8	61.32	0.82	1.25	0.68	0.90	1.25	0.90	1.25
20.4	16.5	11.0	0.8	53.92	0.71	0.67	0.81	0.67	0.67	0.67	0.67
20.8	16.5	13.3	0.6	63.94	0.80	0.79	0.79	0.81	0.79	0.81	0.79
22.1	16.4	13.9	0.9	62.90	0.81	1.01	0.74	0.85	1.01	0.85	1.01
20.1	16.4	15.1	0.6	75.12	0.88	0.85	0.82	0.92	0.85	0.92	0.85
17.8	16.4	11.8	0.6	66.29	0.78	0.23	0.92	0.72	0.23	0.72	0.23
20.3	16.4	14.8	0.7	72.91	0.87	0.85	0.81	0.90	0.85	0.90	0.85
22.0	16.3	14.6	0.7	66.36	0.84	1.06	0.74	0.90	1.06	0.90	1.06
23.1	16.3	11.4	0.8	49.35	0.70	1.09	0.71	0.70	1.09	0.70	1.09
20.5	16.3	14.3	0.6	69.76	0.85	0.86	0.80	0.88	0.86	0.88	0.86
20.3	16.3	15.1	0.5	74.38	0.88	0.90	0.80	0.93	0.90	0.93	0.90
27.4	16.3	13.8	0.7	50.36	0.75	1.55	0.59	0.85	1.55	0.85	1.55
19.1	16.2	10.0	0.8	52.36	0.69	0.50	0.85	0.62	0.50	0.62	0.50
19.0	16.1	12.0	0.7	63.16	0.78	0.54	0.85	0.75	0.54	0.75	0.54
17.7	16.0	13.9	0.6	78.53	0.88	0.40	0.90	0.87	0.40	0.87	0.40
17.4	15.8	11.4	0.6	65.52	0.78	0.28	0.91	0.72	0.28	0.72	0.28
18.9	15.6	12.5	0.8	66.14	0.81	0.66	0.83	0.80	0.66	0.80	0.66
20.6	15.5	10.4	0.7	50.49	0.70	0.89	0.75	0.67	0.89	0.67	0.89
16.8	15.5	12.9	0.6	76.79	0.86	0.27	0.92	0.83	0.27	0.83	0.27
23.1	15.4	11.6	0.6	50.22	0.72	1.25	0.67	0.75	1.25	0.75	1.25
19.1	15.4	13.1	0.7	68.59	0.84	0.78	0.81	0.85	0.78	0.85	0.78
16.8	15.3	10.5	0.6	62.50	0.75	0.25	0.91	0.69	0.25	0.69	0.25
29.3	15.3	12.4	0.6	42.32	0.70	1.89	0.52	0.81	1.89	0.81	1.89
18.1	15.3	13.2	0.6	72.93	0.86	0.64	0.85	0.86	0.64	0.86	0.64
17.4	15.3	13.8	0.5	79.31	0.89	0.56	0.88	0.90	0.56	0.90	0.56
21.7	15.1	11.1	0.6	51.15	0.72	1.13	0.70	0.74	1.13	0.74	1.13

A-axis	B-axis	C-axis	Roundness	Flatness	Sphericity	OP-index	b/a	c/b	B-axis phi	c/a	a-b/a-c
17.1	15.0	10.1	0.6	59.06	0.74	0.39	0.88	0.67	0.39	0.67	0.39
16.4	14.9	11.3	0.7	68.90	0.81	0.28	0.91	0.76	0.28	0.76	0.28
19.2	14.9	13.0	0.7	67.71	0.84	0.91	0.78	0.87	0.91	0.87	0.91
19.6	14.8	12.2	0.9	62.24	0.80	0.93	0.76	0.82	0.93	0.82	0.93
18.0	14.8	13.2	0.9	73.33	0.87	0.77	0.82	0.89	0.77	0.89	0.77
17.3	14.6	11.4	0.7	65.90	0.80	0.57	0.84	0.78	0.57	0.78	0.57
15.8	14.3	11.6	0.8	73.42	0.84	0.32	0.91	0.81	0.32	0.81	0.32
18.6	14.3	11.7	0.6	62.90	0.80	0.88	0.77	0.82	0.88	0.82	0.88
16.1	14.3	10.8	0.7	67.08	0.80	0.37	0.89	0.76	0.37	0.76	0.37
18.9	14.3	11.2	0.6	59.26	0.77	0.90	0.76	0.78	0.90	0.78	0.90
16.2	14.2	13.9	0.5	85.80	0.94	0.76	0.88	0.98	0.76	0.98	0.76
16.8	14.2	9.8	0.9	58.33	0.74	0.51	0.85	0.69	0.51	0.69	0.51
17.9	14.2	10.7	0.9	59.78	0.77	0.74	0.79	0.75	0.74	0.75	0.74
20.2	14.1	12.2	0.8	60.40	0.81	1.16	0.70	0.87	1.16	0.87	1.16
15.5	14.1	11.6	0.9	74.84	0.85	0.31	0.91	0.82	0.31	0.82	0.31
21.0	14.0	13.2	0.6	62.86	0.84	1.33	0.67	0.94	1.33	0.94	1.33
17.7	13.8	10.0	0.6	56.50	0.74	0.78	0.78	0.72	0.78	0.72	0.78
21.0	13.7	13.5	0.6	64.29	0.86	1.41	0.65	0.99	1.41	0.99	1.41
21.7	13.7	10.7	0.7	49.31	0.73	1.38	0.63	0.78	1.38	0.78	1.38
14.1	13.5	10.3	0.6	73.05	0.82	0.04	0.96	0.76	0.04	0.76	0.04
16.2	13.4	11.8	0.8	72.84	0.86	0.72	0.83	0.88	0.72	0.88	0.72
17.1	13.4	9.3	0.5	54.39	0.72	0.75	0.78	0.69	0.75	0.69	0.75
17.1	13.2	10.4	0.8	60.82	0.78	0.83	0.77	0.79	0.83	0.79	0.83
15.4	13.2	10.1	0.6	65.58	0.79	0.49	0.86	0.77	0.49	0.77	0.49
18.1	12.9	10.0	0.6	55.25	0.75	1.05	0.71	0.78	1.05	0.78	1.05
18.2	12.9	10.1	0.7	55.49	0.76	1.07	0.71	0.78	1.07	0.78	1.07
14.3	12.7	11.0	0.8	76.92	0.87	0.43	0.89	0.87	0.43	0.87	0.43
14.8	12.6	10.3	0.7	69.59	0.83	0.54	0.85	0.82	0.54	0.82	0.54
15.0	12.4	9.9	0.8	66.00	0.81	0.62	0.83	0.80	0.62	0.80	0.62
17.3	12.4	11.1	0.7	64.16	0.83	1.11	0.72	0.90	1.11	0.90	1.11
14.6	12.3	9.0	0.7	61.64	0.77	0.52	0.84	0.73	0.52	0.73	0.52
14.9	12.3	9.8	0.6	65.77	0.81	0.63	0.83	0.80	0.63	0.80	0.63
14.3	12.3	10.9	0.8	76.22	0.88	0.58	0.86	0.89	0.58	0.89	0.58
17.4	12.2	11.3	0.7	64.94	0.84	1.19	0.70	0.93	1.19	0.93	1.19
13.9	12.1	11.0	0.8	79.14	0.90	0.57	0.87	0.91	0.57	0.91	0.57
16.4	12.1	11.0	0.6	67.07	0.85	1.05	0.74	0.91	1.05	0.91	1.05
13.3	12.1	10.9	0.8	81.95	0.90	0.36	0.91	0.90	0.36	0.90	0.36
17.6	11.9	11.8	0.7	67.05	0.87	1.34	0.68	0.99	1.34	0.99	1.34
16.3	11.7	11.4	0.6	69.94	0.88	1.20	0.72	0.97	1.20	0.97	1.20
13.6	11.6	8.8	0.7	64.71	0.79	0.48	0.85	0.76	0.48	0.76	0.48
16.2	11.6	10.2	0.7	62.96	0.82	1.09	0.72	0.88	1.09	0.88	1.09
14.3	11.1	9.9	0.7	69.23	0.85	0.89	0.78	0.89	0.89	0.89	0.89

A-axis	B-axis	C-axis	Roundness	Flatness	Sphericity	OP-index	b/a	c/b	B-axis phi	c/a	a-b/a-c
10.8	9.8	7.8	0.8	72.22	0.83	0.23	0.91	0.80	0.23	0.80	0.23
15.6	9.6	8.7	0.7	55.77	0.80	1.43	0.62	0.91	1.43	0.91	1.43
15.8	9.2	8.5	0.6	53.80	0.79	1.55	0.58	0.92	1.55	0.92	1.55

Appendix (XII)(g)

PEBBLE DATA ROODERAND CONGLOMERATE FORMATION LEEUFONTEIN 485

A−axis	B−axis	C−axis	Roundness	Flatness	Sphericity	OP−index	b/a	c/b	B−axis phi	c/a	a−b/a−c
64.1	62.8	37.9	0.8	59.13	0.71	0.05	0.98	0.60	−5.97	0.59	0.05
62.7	41.9	39.8	0.7	63.48	0.84	1.40	0.67	0.95	−5.39	0.63	0.91
42.9	36.2	20.1	0.9	46.85	0.64	0.58	0.84	0.56	−5.18	0.47	0.29
43.5	34.6	25.7	0.7	59.08	0.76	0.80	0.80	0.74	−5.11	0.59	0.50
43.2	34.5	23.3	0.8	53.94	0.71	0.76	0.80	0.68	−5.11	0.54	0.44
56.9	32.0	25.7	0.7	45.17	0.71	1.73	0.56	0.80	−5.00	0.45	0.80
42.0	31.1	23.9	0.6	56.90	0.76	1.01	0.74	0.77	−4.96	0.57	0.60
38.8	30.0	22.7	0.9	58.51	0.76	0.88	0.77	0.76	−4.91	0.59	0.55
42.1	30.0	18.8	0.8	44.66	0.65	1.11	0.71	0.63	−4.91	0.45	0.52
32.8	29.9	21.4	0.7	65.24	0.78	0.32	0.91	0.72	−4.90	0.65	0.25
43.9	29.8	25.1	0.7	57.18	0.78	1.27	0.68	0.84	−4.90	0.57	0.75
41.5	29.8	22.0	0.9	53.01	0.73	1.08	0.72	0.74	−4.90	0.53	0.60
30.9	29.7	18.6	0.8	60.19	0.72	0.09	0.96	0.63	−4.89	0.60	0.10
37.2	29.6	18.7	0.8	50.27	0.68	0.76	0.80	0.63	−4.89	0.50	0.41
44.2	29.1	21.7	0.7	49.10	0.72	1.32	0.66	0.75	−4.86	0.49	0.67
33.0	28.9	27.0	0.8	81.82	0.91	0.73	0.88	0.93	−4.85	0.82	0.68
33.9	28.8	24.5	0.9	72.27	0.85	0.68	0.85	0.85	−4.85	0.72	0.54
51.0	28.8	24.2	0.7	47.45	0.74	1.71	0.56	0.84	−4.85	0.47	0.83
31.0	28.7	18.3	0.7	59.03	0.72	0.24	0.93	0.64	−4.84	0.59	0.18
32.5	28.5	18.8	0.7	57.85	0.73	0.44	0.88	0.66	−4.83	0.58	0.29
39.4	28.5	25.1	0.8	63.71	0.82	1.14	0.72	0.88	−4.83	0.64	0.76
30.1	28.2	15.1	0.7	50.17	0.65	0.19	0.94	0.54	−4.82	0.50	0.13
30.0	28.1	20.1	0.7	67.00	0.78	0.21	0.94	0.72	−4.81	0.67	0.19
34.9	28.1	24.0	0.7	68.77	0.84	0.84	0.81	0.85	−4.81	0.69	0.62
36.9	28.0	18.9	0.8	51.22	0.70	0.91	0.76	0.68	−4.81	0.51	0.49
37.1	28.0	18.3	0.6	49.33	0.69	0.93	0.75	0.65	−4.81	0.49	0.48
50.0	27.9	20.8	0.7	41.60	0.68	1.78	0.56	0.75	−4.80	0.42	0.76
32.0	27.8	19.1	0.8	59.69	0.74	0.48	0.87	0.69	−4.80	0.60	0.33
34.6	27.8	25.0	0.8	72.25	0.87	0.91	0.80	0.90	−4.80	0.72	0.71
52.3	27.4	23.5	0.8	44.93	0.73	1.89	0.52	0.86	−4.78	0.45	0.86
34.1	27.2	16.2	0.8	47.51	0.66	0.75	0.80	0.60	−4.77	0.48	0.39
39.7	27.2	22.5	0.9	56.68	0.78	1.23	0.69	0.83	−4.77	0.57	0.73
34.2	27.0	18.9	0.7	55.26	0.73	0.79	0.79	0.70	−4.75	0.55	0.47
38.5	27.0	21.8	0.7	56.62	0.77	1.16	0.70	0.81	−4.75	0.57	0.69
35.9	26.9	18.0	0.9	50.14	0.69	0.95	0.75	0.67	−4.75	0.50	0.50
36.1	26.5	20.0	0.7	55.40	0.75	1.02	0.73	0.75	−4.73	0.55	0.60
33.1	26.4	20.2	0.7	61.03	0.78	0.79	0.80	0.77	−4.72	0.61	0.52

A−axis	B−axis	C−axis	Roundness	Flatness	Sphericity	OP−index	b/a	c/b	B−axis phi	c/a	a−b/a−c
32.8	26.3	20.0	0.8	60.98	0.77	0.77	0.80	0.76	−4.72	0.61	0.51
34.0	26.2	15.1	0.8	44.41	0.63	0.87	0.77	0.58	−4.71	0.44	0.41
30.9	26.0	17.9	0.7	57.93	0.74	0.58	0.84	0.69	−4.70	0.58	0.38
31.7	25.8	20.0	0.6	63.09	0.79	0.73	0.81	0.78	−4.69	0.63	0.50
33.1	25.7	15.3	0.8	46.22	0.65	0.84	0.78	0.60	−4.68	0.46	0.42
31.8	25.7	16.1	0.7	50.63	0.68	0.70	0.81	0.63	−4.68	0.51	0.39
29.0	25.6	15.1	0.9	52.07	0.67	0.40	0.88	0.59	−4.68	0.52	0.24
27.5	25.5	22.0	0.8	80.00	0.88	0.34	0.93	0.86	−4.67	0.80	0.36
26.0	25.4	15.2	0.6	58.46	0.70	0.02	0.98	0.60	−4.67	0.58	0.06
29.0	25.3	22.1	0.8	76.21	0.87	0.61	0.87	0.87	−4.66	0.76	0.54
34.4	25.2	19.8	0.9	57.56	0.77	1.04	0.73	0.79	−4.66	0.58	0.63
33.0	25.1	19.5	0.8	59.09	0.77	0.93	0.76	0.78	−4.65	0.59	0.59
42.5	24.8	18.1	0.7	42.59	0.68	1.66	0.58	0.73	−4.63	0.43	0.73
33.1	24.6	21.0	0.5	63.44	0.82	1.04	0.74	0.85	−4.62	0.63	0.70
33.1	24.4	15.6	0.7	47.13	0.67	0.99	0.74	0.64	−4.61	0.47	0.50
27.6	24.3	16.5	0.7	59.78	0.74	0.42	0.88	0.68	−4.60	0.60	0.30
31.9	24.2	18.1	0.8	56.74	0.75	0.92	0.76	0.75	−4.60	0.57	0.56
37.1	24.2	22.8	0.8	61.46	0.83	1.41	0.65	0.94	−4.60	0.61	0.90
28.5	24.1	15.5	0.9	54.39	0.70	0.55	0.85	0.64	−4.59	0.54	0.34
33.7	24.1	19.9	0.7	59.05	0.79	1.12	0.72	0.83	−4.59	0.59	0.70
31.0	24.1	20.9	0.9	67.42	0.84	0.94	0.78	0.87	−4.59	0.67	0.68
36.7	24.0	12.1	0.9	32.97	0.55	1.50	0.65	0.50	−4.58	0.33	0.52
27.9	24.0	20.7	0.5	74.19	0.86	0.64	0.86	0.86	−4.58	0.74	0.54
24.5	23.9	19.6	0.9	80.00	0.87	0.03	0.98	0.82	−4.58	0.80	0.12
32.0	23.9	21.9	0.7	68.44	0.86	1.10	0.75	0.92	−4.58	0.68	0.80
28.1	23.7	16.0	0.7	56.94	0.73	0.57	0.84	0.68	−4.57	0.57	0.36
32.3	23.5	14.7	0.9	45.51	0.66	1.04	0.73	0.63	−4.55	0.46	0.50
26.3	23.5	14.0	0.7	53.23	0.68	0.35	0.89	0.60	−4.55	0.53	0.23
29.8	23.4	18.0	0.8	60.40	0.77	0.83	0.79	0.77	−4.55	0.60	0.54
26.6	23.3	15.9	0.8	59.77	0.74	0.44	0.88	0.68	−4.54	0.60	0.31
28.9	23.1	16.7	0.6	57.79	0.75	0.75	0.80	0.72	−4.53	0.58	0.48
30.0	23.1	18.9	0.8	63.00	0.80	0.92	0.77	0.82	−4.53	0.63	0.62
24.1	23.1	14.5	0.6	60.17	0.72	0.09	0.96	0.63	−4.53	0.60	0.10
25.6	23.1	16.9	0.7	66.02	0.78	0.35	0.90	0.73	−4.53	0.66	0.29
30.9	23.1	16.1	0.8	52.10	0.71	0.95	0.75	0.70	−4.53	0.52	0.53
25.8	23.0	18.9	0.8	73.26	0.84	0.46	0.89	0.82	−4.52	0.73	0.41
26.5	23.0	20.6	0.9	77.74	0.89	0.65	0.87	0.90	−4.52	0.78	0.59
28.1	22.9	15.5	0.7	55.16	0.72	0.68	0.81	0.68	−4.52	0.55	0.41
27.5	22.9	20.6	0.7	74.91	0.88	0.79	0.83	0.90	−4.52	0.75	0.67
30.2	22.9	17.5	0.8	57.95	0.76	0.92	0.76	0.76	−4.52	0.58	0.57
25.5	22.9	18.9	0.8	74.12	0.85	0.43	0.90	0.83	−4.52	0.74	0.39
32.9	22.8	15.7	0.9	47.72	0.69	1.17	0.69	0.69	−4.51	0.48	0.59

A−axis	B−axis	C−axis	Roundness	Flatness	Sphericity	OP−index	b/a	c/b	B−axis phi	c/a	a−b/a−c
27.0	22.7	17.9	0.7	66.30	0.81	0.63	0.84	0.79	−4.50	0.66	0.47
28.9	22.7	18.1	0.6	62.63	0.79	0.84	0.79	0.80	−4.50	0.63	0.57
24.2	22.6	14.3	0.9	59.09	0.72	0.19	0.93	0.63	−4.50	0.59	0.16
30.4	22.5	16.8	0.9	55.26	0.74	0.98	0.74	0.75	−4.49	0.55	0.58
29.4	22.5	17.2	0.7	58.50	0.76	0.90	0.77	0.76	−4.49	0.59	0.57
32.1	22.4	13.1	0.7	40.81	0.62	1.19	0.70	0.58	−4.49	0.41	0.51
28.1	22.4	18.0	0.8	64.06	0.80	0.80	0.80	0.80	−4.49	0.64	0.56
31.1	22.4	16.7	0.6	53.70	0.74	1.06	0.72	0.75	−4.49	0.54	0.60
29.7	22.3	19.9	0.8	67.00	0.84	1.05	0.75	0.89	−4.48	0.67	0.76
33.5	22.3	19.1	0.7	57.01	0.79	1.30	0.67	0.86	−4.48	0.57	0.78
26.8	22.3	17.9	0.7	66.79	0.81	0.67	0.83	0.80	−4.48	0.67	0.51
31.5	22.3	19.0	0.9	60.32	0.80	1.15	0.71	0.85	−4.48	0.60	0.74
27.9	22.3	14.6	0.8	52.33	0.70	0.73	0.80	0.65	−4.48	0.52	0.42
25.0	22.3	18.1	0.8	72.40	0.84	0.44	0.89	0.81	−4.48	0.72	0.39
29.0	22.2	16.3	0.7	56.21	0.74	0.88	0.77	0.73	−4.47	0.56	0.54
27.3	22.1	15.2	0.7	55.68	0.73	0.70	0.81	0.69	−4.47	0.56	0.43
23.9	22.1	12.7	0.8	53.14	0.67	0.22	0.92	0.57	−4.47	0.53	0.16
26.2	22.1	11.9	0.9	45.42	0.63	0.55	0.84	0.54	−4.47	0.45	0.29
24.9	22.1	15.9	0.5	63.86	0.77	0.40	0.89	0.72	−4.47	0.64	0.31
24.0	22.1	12.5	0.8	52.08	0.67	0.23	0.92	0.57	−4.47	0.52	0.17
33.7	22.0	16.1	0.8	47.77	0.70	1.33	0.65	0.73	−4.46	0.48	0.66
41.9	22.0	16.3	0.8	38.90	0.66	1.95	0.53	0.74	−4.46	0.39	0.78
29.4	22.0	15.7	0.7	53.40	0.73	0.94	0.75	0.71	−4.46	0.53	0.54
24.5	22.0	10.9	0.7	44.49	0.60	0.33	0.90	0.50	−4.46	0.44	0.18
28.5	22.0	18.9	0.8	66.32	0.83	0.94	0.77	0.86	−4.46	0.66	0.68
34.2	22.0	14.1	0.7	41.23	0.64	1.41	0.64	0.64	−4.46	0.41	0.61
25.1	22.0	19.1	0.7	76.10	0.87	0.57	0.88	0.87	−4.46	0.76	0.52
35.0	21.9	16.0	0.7	45.71	0.69	1.45	0.63	0.73	−4.45	0.46	0.69
35.0	21.9	15.4	0.9	44.00	0.68	1.46	0.63	0.70	−4.45	0.44	0.67
26.0	21.9	17.6	0.7	67.69	0.82	0.63	0.84	0.80	−4.45	0.68	0.49
24.0	21.8	17.0	0.9	70.83	0.82	0.34	0.91	0.78	−4.45	0.71	0.31
36.5	21.8	16.0	0.7	43.84	0.69	1.58	0.60	0.73	−4.45	0.44	0.72
25.1	21.8	14.9	0.7	59.36	0.74	0.46	0.87	0.68	−4.45	0.59	0.32
35.3	21.8	19.9	0.6	56.37	0.80	1.50	0.62	0.91	−4.45	0.56	0.88
28.4	21.8	14.0	0.8	49.30	0.68	0.86	0.77	0.64	−4.45	0.49	0.46
23.9	21.7	15.1	0.9	63.18	0.76	0.31	0.91	0.70	−4.44	0.63	0.25
28.9	21.7	16.5	0.7	57.09	0.76	0.95	0.75	0.76	−4.44	0.57	0.58
26.9	21.5	16.1	0.9	59.85	0.77	0.76	0.80	0.75	−4.43	0.60	0.50
28.0	21.5	15.2	0.8	54.29	0.73	0.86	0.77	0.71	−4.43	0.54	0.51
25.8	21.4	14.7	0.7	56.98	0.73	0.62	0.83	0.69	−4.42	0.57	0.40
24.7	21.4	16.8	0.6	68.02	0.81	0.52	0.87	0.79	−4.42	0.68	0.42
26.9	21.3	14.1	0.7	52.42	0.70	0.76	0.79	0.66	−4.41	0.52	0.44

A−axis	B−axis	C−axis	Roundness	Flatness	Sphericity	OP−index	b/a	c/b	B−axis phi	c/a	a−b/a−c
24.5	21.2	15.0	0.9	61.22	0.76	0.48	0.87	0.71	−4.41	0.61	0.35
29.7	21.2	15.4	0.7	51.85	0.72	1.08	0.71	0.73	−4.41	0.52	0.59
27.5	21.1	13.4	0.9	48.73	0.68	0.86	0.77	0.64	−4.40	0.49	0.45
27.2	21.1	15.1	0.9	55.51	0.74	0.83	0.78	0.72	−4.40	0.56	0.50
22.6	21.1	13.8	0.6	61.06	0.74	0.19	0.93	0.65	−4.40	0.61	0.17
26.4	21.0	18.1	0.7	68.56	0.84	0.86	0.80	0.86	−4.39	0.69	0.65
23.6	21.0	11.9	0.9	50.42	0.66	0.36	0.89	0.57	−4.39	0.50	0.22
23.8	21.0	13.1	0.7	55.04	0.70	0.39	0.88	0.62	−4.39	0.55	0.26
23.1	21.0	12.5	0.6	54.11	0.69	0.28	0.91	0.60	−4.39	0.54	0.20
35.4	20.9	14.1	0.7	39.83	0.65	1.65	0.59	0.67	−4.39	0.40	0.68
31.0	20.8	19.9	0.8	64.19	0.85	1.36	0.67	0.96	−4.38	0.64	0.92
25.7	20.8	19.0	0.5	73.93	0.88	0.89	0.81	0.91	−4.38	0.74	0.73
25.0	20.7	17.8	0.6	71.20	0.85	0.74	0.83	0.86	−4.37	0.71	0.60
23.4	20.7	12.9	0.6	55.13	0.70	0.38	0.88	0.62	−4.37	0.55	0.26
34.6	20.7	15.1	0.8	43.64	0.68	1.57	0.60	0.73	−4.37	0.44	0.71
25.0	20.7	15.2	0.7	60.80	0.76	0.64	0.83	0.73	−4.37	0.61	0.44
21.3	20.5	14.3	0.7	67.14	0.78	0.06	0.96	0.70	−4.36	0.67	0.11
22.4	20.5	10.3	0.6	45.98	0.61	0.25	0.92	0.50	−4.36	0.46	0.16
24.2	20.5	18.7	0.8	77.27	0.89	0.75	0.85	0.91	−4.36	0.77	0.67
23.2	20.5	16.3	0.6	70.26	0.82	0.45	0.88	0.80	−4.36	0.70	0.39
22.3	20.5	15.4	0.8	69.06	0.80	0.27	0.92	0.75	−4.36	0.69	0.26
25.8	20.4	17.5	0.7	67.83	0.83	0.87	0.79	0.86	−4.35	0.68	0.65
26.9	20.4	14.3	0.8	53.16	0.72	0.90	0.76	0.70	−4.35	0.53	0.52
25.4	20.3	15.5	0.6	61.02	0.78	0.76	0.80	0.76	−4.34	0.61	0.52
24.9	20.3	13.2	0.7	53.01	0.70	0.66	0.82	0.65	−4.34	0.53	0.39
22.5	20.3	14.6	0.8	64.89	0.78	0.33	0.90	0.72	−4.34	0.65	0.28
30.0	20.2	14.0	0.6	46.67	0.69	1.25	0.67	0.69	−4.34	0.47	0.61
36.8	20.2	18.9	0.8	51.36	0.78	1.75	0.55	0.94	−4.34	0.51	0.93
25.5	20.1	13.9	0.7	54.51	0.72	0.77	0.79	0.69	−4.33	0.55	0.47
30.5	20.1	18.3	0.8	60.00	0.82	1.35	0.66	0.91	−4.33	0.60	0.85
25.0	20.1	16.4	0.9	65.60	0.81	0.78	0.80	0.82	−4.33	0.66	0.57
26.6	20.1	15.0	0.8	56.39	0.75	0.92	0.76	0.75	−4.33	0.56	0.56
32.4	20.1	14.7	0.9	45.37	0.69	1.47	0.62	0.73	−4.33	0.45	0.69
26.9	20.1	16.4	0.7	60.97	0.79	0.98	0.75	0.82	−4.33	0.61	0.65
24.5	20.1	12.5	0.6	51.02	0.68	0.64	0.82	0.62	−4.33	0.51	0.37
23.7	20.1	11.8	0.6	49.79	0.66	0.52	0.85	0.59	−4.33	0.50	0.30
24.6	20.1	16.0	0.9	65.04	0.80	0.72	0.82	0.80	−4.33	0.65	0.52
27.1	20.0	15.5	0.8	57.20	0.76	0.99	0.74	0.78	−4.32	0.57	0.61
29.3	20.0	13.6	0.9	46.42	0.68	1.21	0.68	0.68	−4.32	0.46	0.59
23.4	20.0	15.2	0.7	64.96	0.79	0.54	0.85	0.76	−4.32	0.65	0.41
28.8	20.0	10.9	0.7	37.85	0.59	1.23	0.69	0.55	−4.32	0.38	0.49
27.8	20.0	17.1	0.7	61.51	0.81	1.11	0.72	0.86	−4.32	0.62	0.73

A−axis	B−axis	C−axis	Roundness	Flatness	Sphericity	OP−index	b/a	c/b	B−axis phi	c/a	a−b/a−c
27.2	20.0	17.1	0.8	62.87	0.81	1.06	0.74	0.86	−4.32	0.63	0.71
23.7	20.0	14.5	0.7	61.18	0.76	0.57	0.84	0.73	−4.32	0.61	0.40
26.1	20.0	15.5	0.8	59.39	0.77	0.89	0.77	0.78	−4.32	0.59	0.58
24.3	20.0	12.9	0.6	53.09	0.70	0.63	0.82	0.65	−4.32	0.53	0.38
27.9	20.0	19.1	0.7	68.46	0.87	1.23	0.72	0.96	−4.32	0.68	0.90
24.6	20.0	18.9	0.6	76.83	0.90	0.94	0.81	0.95	−4.32	0.77	0.81
23.5	19.9	16.4	0.7	69.79	0.83	0.63	0.85	0.82	−4.31	0.70	0.51
22.0	19.9	12.2	0.8	55.45	0.70	0.29	0.90	0.61	−4.31	0.55	0.21
24.1	19.8	13.5	0.7	56.02	0.73	0.64	0.82	0.68	−4.31	0.56	0.41
23.1	19.8	14.5	0.9	62.77	0.77	0.52	0.86	0.73	−4.31	0.63	0.38
25.3	19.8	17.2	0.8	67.98	0.84	0.91	0.78	0.87	−4.31	0.68	0.68
24.0	19.8	17.1	0.7	71.25	0.85	0.75	0.83	0.86	−4.31	0.71	0.61
22.0	19.8	12.5	0.7	56.82	0.71	0.31	0.90	0.63	−4.31	0.57	0.23
24.6	19.8	13.2	0.8	53.66	0.71	0.70	0.80	0.67	−4.31	0.54	0.42
22.9	19.8	15.2	0.8	66.38	0.80	0.51	0.86	0.77	−4.31	0.66	0.40
29.2	19.8	14.5	0.7	49.66	0.71	1.22	0.68	0.73	−4.31	0.50	0.64
27.1	19.7	13.5	0.8	49.82	0.70	1.02	0.73	0.69	−4.30	0.50	0.54
28.0	19.5	12.1	0.8	43.21	0.64	1.16	0.70	0.62	−4.29	0.43	0.53
26.0	19.5	14.9	0.7	57.31	0.76	0.94	0.75	0.76	−4.29	0.57	0.59
21.2	19.5	16.7	0.8	78.77	0.88	0.34	0.92	0.86	−4.29	0.79	0.38
24.0	19.5	15.1	0.7	62.92	0.79	0.71	0.81	0.77	−4.29	0.63	0.51
26.1	19.5	14.3	0.7	54.79	0.74	0.94	0.75	0.73	−4.29	0.55	0.56
25.0	19.4	13.9	0.6	55.60	0.74	0.83	0.78	0.72	−4.28	0.56	0.50
20.1	19.3	14.4	0.8	71.64	0.81	0.07	0.96	0.75	−4.27	0.72	0.14
24.9	19.3	15.8	0.6	63.45	0.80	0.88	0.78	0.82	−4.27	0.63	0.62
22.0	19.2	12.3	0.7	55.91	0.71	0.42	0.87	0.64	−4.26	0.56	0.29
27.1	19.2	17.4	0.8	64.21	0.83	1.19	0.71	0.91	−4.26	0.64	0.81
23.2	19.1	13.4	0.9	57.76	0.74	0.64	0.82	0.70	−4.26	0.58	0.42
25.8	19.1	15.6	0.8	60.47	0.79	1.01	0.74	0.82	−4.26	0.60	0.66
22.0	19.1	12.6	0.6	57.27	0.72	0.45	0.87	0.66	−4.26	0.57	0.31
29.6	19.1	10.9	0.8	36.82	0.59	1.45	0.65	0.57	−4.26	0.37	0.56
24.3	19.1	12.1	0.9	49.79	0.68	0.77	0.79	0.63	−4.26	0.50	0.43
28.6	19.1	16.7	0.8	58.39	0.80	1.30	0.67	0.87	−4.26	0.58	0.80
25.2	19.1	11.8	0.6	46.83	0.66	0.89	0.76	0.62	−4.26	0.47	0.46
22.9	19.1	10.9	0.8	47.60	0.65	0.58	0.83	0.57	−4.26	0.48	0.32
20.6	19.1	16.2	0.8	78.64	0.87	0.29	0.93	0.85	−4.26	0.79	0.34
32.0	19.1	14.3	0.7	44.69	0.69	1.57	0.60	0.75	−4.26	0.45	0.73
26.9	19.0	16.3	0.7	60.59	0.80	1.15	0.71	0.86	−4.25	0.61	0.75
22.1	19.0	17.4	0.9	78.73	0.90	0.70	0.86	0.92	−4.25	0.79	0.66
30.2	19.0	17.3	0.9	57.28	0.80	1.45	0.63	0.91	−4.25	0.57	0.87
26.3	19.0	18.7	0.8	71.10	0.89	1.26	0.72	0.98	−4.25	0.71	0.96
25.9	19.0	13.1	0.7	50.58	0.70	0.99	0.73	0.69	−4.25	0.51	0.54

A-axis	B-axis	C-axis	Roundness	Flatness	Sphericity	OP-index	b/a	c/b	B-axis phi	c/a	a-b/a-c
23.9	19.0	14.8	0.6	61.92	0.78	0.78	0.79	0.78	-4.25	0.62	0.54
27.0	19.0	15.9	0.8	58.89	0.79	1.15	0.70	0.84	-4.25	0.59	0.72
24.1	19.0	13.7	0.7	56.85	0.74	0.78	0.79	0.72	-4.25	0.57	0.49
23.4	19.0	11.8	0.7	50.43	0.68	0.67	0.81	0.62	-4.25	0.50	0.38
30.2	18.9	11.1	0.8	36.75	0.60	1.54	0.63	0.59	-4.24	0.37	0.59
20.2	18.9	17.1	0.6	84.65	0.91	0.30	0.94	0.90	-4.24	0.85	0.42
22.4	18.9	12.9	0.9	57.59	0.73	0.55	0.84	0.68	-4.24	0.58	0.37
21.1	18.9	15.3	0.8	72.51	0.84	0.40	0.90	0.81	-4.24	0.73	0.38
26.2	18.8	13.0	0.7	49.62	0.70	1.05	0.72	0.69	-4.23	0.50	0.56
27.5	18.8	15.3	0.8	55.64	0.77	1.21	0.68	0.81	-4.23	0.56	0.71
23.6	18.8	10.0	0.7	42.37	0.61	0.75	0.80	0.53	-4.23	0.42	0.35
28.1	18.8	14.3	0.7	50.89	0.73	1.25	0.67	0.76	-4.23	0.51	0.67
22.0	18.8	10.2	0.6	46.36	0.63	0.49	0.85	0.54	-4.23	0.46	0.27
22.1	18.8	13.1	0.7	59.28	0.74	0.52	0.85	0.70	-4.23	0.59	0.37
30.9	18.7	16.2	0.8	52.43	0.77	1.52	0.61	0.87	-4.22	0.52	0.83
25.1	18.7	13.2	0.8	52.59	0.72	0.94	0.75	0.71	-4.22	0.53	0.54
22.4	18.6	10.6	0.7	47.32	0.65	0.59	0.83	0.57	-4.22	0.47	0.32
21.9	18.5	10.6	0.8	48.40	0.65	0.53	0.84	0.57	-4.21	0.48	0.30
32.3	18.5	13.2	0.7	40.87	0.66	1.70	0.57	0.71	-4.21	0.41	0.72
19.9	18.4	11.3	0.7	56.78	0.70	0.20	0.92	0.61	-4.20	0.57	0.17
32.5	18.4	14.9	0.8	45.85	0.72	1.69	0.57	0.81	-4.20	0.46	0.80
26.2	18.4	10.6	0.8	40.46	0.62	1.16	0.70	0.58	-4.20	0.40	0.50
24.9	18.3	13.9	0.7	55.82	0.75	0.99	0.73	0.76	-4.19	0.56	0.60
26.0	18.2	16.1	0.6	61.92	0.82	1.19	0.70	0.88	-4.19	0.62	0.79
25.1	18.2	14.7	0.7	58.57	0.78	1.05	0.73	0.81	-4.19	0.59	0.66
24.1	18.2	12.1	0.8	50.21	0.69	0.90	0.76	0.66	-4.19	0.50	0.49
23.0	18.1	15.7	0.7	68.26	0.84	0.88	0.79	0.87	-4.18	0.68	0.67
24.4	18.1	16.6	0.8	68.03	0.85	1.09	0.74	0.92	-4.18	0.68	0.81
23.0	18.1	14.7	0.9	63.91	0.80	0.83	0.79	0.81	-4.18	0.64	0.59
22.0	18.1	12.2	0.7	55.45	0.72	0.63	0.82	0.67	-4.18	0.55	0.40
21.2	18.1	12.0	0.7	56.60	0.72	0.50	0.85	0.66	-4.18	0.57	0.34
28.4	18.1	10.9	0.7	38.38	0.61	1.46	0.64	0.60	-4.18	0.38	0.59
21.0	18.1	13.6	0.8	64.76	0.79	0.50	0.86	0.75	-4.18	0.65	0.39
21.2	18.1	10.9	0.8	51.42	0.68	0.49	0.85	0.60	-4.18	0.51	0.30
23.0	18.1	12.1	0.7	52.61	0.71	0.77	0.79	0.67	-4.18	0.53	0.45
22.1	18.0	14.9	0.8	67.42	0.82	0.74	0.81	0.83	-4.17	0.67	0.57
23.4	18.0	11.5	0.7	49.15	0.68	0.84	0.77	0.64	-4.17	0.49	0.45
25.7	18.0	16.3	0.7	63.42	0.83	1.21	0.70	0.91	-4.17	0.63	0.82
20.8	18.0	14.7	0.7	70.67	0.83	0.53	0.87	0.82	-4.17	0.71	0.46
23.1	18.0	10.8	0.8	46.75	0.65	0.80	0.78	0.60	-4.17	0.47	0.41
20.9	18.0	11.3	0.9	54.07	0.70	0.46	0.86	0.63	-4.17	0.54	0.30
22.7	18.0	13.1	0.8	57.71	0.75	0.76	0.79	0.73	-4.17	0.58	0.49

A-axis	B-axis	C-axis	Roundness	Flatness	Sphericity	OP-index	b/a	c/b	B-axis phi	c/a	a-b/a-c
26.2	18.0	15.9	0.7	60.69	0.81	1.23	0.69	0.88	-4.17	0.61	0.80
23.0	18.0	14.8	0.9	64.35	0.81	0.85	0.78	0.82	-4.17	0.64	0.61
35.0	17.9	16.0	0.8	45.71	0.74	1.91	0.51	0.89	-4.16	0.46	0.90
20.7	17.9	14.8	0.8	71.50	0.84	0.55	0.86	0.83	-4.16	0.71	0.47
20.0	17.9	12.8	0.8	64.00	0.77	0.35	0.90	0.72	-4.16	0.64	0.29
27.0	17.9	13.8	0.9	51.11	0.73	1.27	0.66	0.77	-4.16	0.51	0.69
23.0	17.9	14.2	0.6	61.74	0.79	0.85	0.78	0.79	-4.16	0.62	0.58
18.9	17.9	9.9	0.6	52.38	0.66	0.11	0.95	0.55	-4.16	0.52	0.11
19.0	17.8	11.7	0.7	61.58	0.74	0.16	0.94	0.66	-4.15	0.62	0.16
22.0	17.8	9.0	0.7	40.91	0.59	0.70	0.81	0.51	-4.15	0.41	0.32
28.7	17.8	15.3	0.9	53.31	0.77	1.46	0.62	0.86	-4.15	0.53	0.81
22.4	17.8	10.1	0.9	45.09	0.63	0.74	0.79	0.57	-4.15	0.45	0.37
23.4	17.8	10.5	0.5	44.87	0.64	0.88	0.76	0.59	-4.15	0.45	0.43
21.8	17.6	15.1	0.5	69.27	0.84	0.80	0.81	0.86	-4.14	0.69	0.63
26.0	17.6	14.2	0.7	54.62	0.76	1.23	0.68	0.81	-4.14	0.55	0.71
19.3	17.5	12.3	0.7	63.73	0.77	0.29	0.91	0.70	-4.13	0.64	0.26
22.3	17.5	14.9	0.7	66.82	0.83	0.87	0.78	0.85	-4.13	0.67	0.65
19.3	17.5	11.6	0.7	60.10	0.74	0.28	0.91	0.66	-4.13	0.60	0.23
25.9	17.5	12.9	0.7	49.81	0.72	1.22	0.68	0.74	-4.13	0.50	0.65
20.3	17.4	13.4	0.8	66.01	0.80	0.53	0.86	0.77	-4.12	0.66	0.42
22.3	17.4	11.0	0.7	49.33	0.68	0.79	0.78	0.63	-4.12	0.49	0.43
22.6	17.3	13.5	0.8	59.73	0.78	0.88	0.77	0.78	-4.11	0.60	0.58
18.0	17.3	11.7	0.5	65.00	0.76	0.05	0.96	0.68	-4.11	0.65	0.11
23.4	17.3	13.5	0.7	57.69	0.77	0.98	0.74	0.78	-4.11	0.58	0.62
19.2	17.3	15.7	0.6	81.77	0.91	0.49	0.90	0.91	-4.11	0.82	0.54
24.0	17.3	15.1	0.7	62.92	0.82	1.11	0.72	0.87	-4.11	0.63	0.75
29.5	17.2	13.8	0.8	46.78	0.72	1.61	0.58	0.80	-4.10	0.47	0.78
22.4	17.2	11.2	0.8	50.00	0.69	0.84	0.77	0.65	-4.10	0.50	0.46
19.4	17.2	12.6	0.6	64.95	0.78	0.38	0.89	0.73	-4.10	0.65	0.32
18.9	17.1	12.9	0.6	68.25	0.80	0.32	0.90	0.75	-4.10	0.68	0.30
22.3	17.1	13.4	0.5	60.09	0.78	0.88	0.77	0.78	-4.10	0.60	0.58
23.5	17.1	8.7	0.7	37.02	0.57	1.08	0.73	0.51	-4.10	0.37	0.43
19.5	17.1	13.3	0.7	68.21	0.81	0.45	0.88	0.78	-4.10	0.68	0.39
25.0	17.1	11.9	0.9	47.60	0.69	1.19	0.68	0.70	-4.10	0.48	0.60
22.9	17.1	13.0	0.7	56.77	0.76	0.94	0.75	0.76	-4.10	0.57	0.59
21.0	17.1	9.4	0.7	44.76	0.63	0.65	0.81	0.55	-4.10	0.45	0.34
19.4	17.0	12.5	0.7	64.43	0.78	0.43	0.88	0.74	-4.09	0.64	0.35
23.7	17.0	9.9	0.7	41.77	0.62	1.08	0.72	0.58	-4.09	0.42	0.49
20.5	17.0	13.8	0.9	67.32	0.82	0.67	0.83	0.81	-4.09	0.67	0.52
21.3	17.0	10.8	0.7	50.70	0.69	0.71	0.80	0.64	-4.09	0.51	0.41
28.1	17.0	12.8	0.8	45.55	0.70	1.52	0.60	0.75	-4.09	0.46	0.73
20.9	17.0	15.7	0.8	75.12	0.89	0.87	0.81	0.92	-4.09	0.75	0.75

A-axis	B-axis	C-axis	Roundness	Flatness	Sphericity	OP-index	b/a	c/b	B-axis phi	c/a	a-b/a-c
18.9	16.9	11.1	0.7	58.73	0.73	0.33	0.89	0.66	-4.08	0.59	0.26
20.4	16.9	15.1	0.5	74.02	0.87	0.76	0.83	0.89	-4.08	0.74	0.66
24.6	16.9	12.7	0.7	51.63	0.73	1.17	0.69	0.75	-4.08	0.52	0.65
18.3	16.9	10.0	0.7	54.64	0.69	0.20	0.92	0.59	-4.08	0.55	0.17
22.1	16.9	11.2	0.8	50.68	0.70	0.85	0.76	0.66	-4.08	0.51	0.48
22.1	16.9	12.5	0.8	56.56	0.75	0.87	0.76	0.74	-4.08	0.57	0.54
17.9	16.8	12.1	0.6	67.60	0.79	0.15	0.94	0.72	-4.07	0.68	0.19
21.2	16.7	15.1	0.8	71.23	0.86	0.92	0.79	0.90	-4.06	0.71	0.74
19.4	16.7	11.2	0.7	57.73	0.73	0.46	0.86	0.67	-4.06	0.58	0.33
30.1	16.7	11.0	0.8	36.54	0.62	1.85	0.55	0.66	-4.06	0.37	0.70
19.3	16.6	12.0	0.7	62.18	0.77	0.48	0.86	0.72	-4.05	0.62	0.37
25.1	16.6	14.3	0.8	56.97	0.79	1.30	0.66	0.86	-4.05	0.57	0.79
24.1	16.5	11.3	0.8	46.89	0.68	1.18	0.68	0.68	-4.04	0.47	0.59
18.1	16.5	11.2	0.7	61.88	0.75	0.26	0.91	0.68	-4.04	0.62	0.23
23.8	16.5	14.7	0.8	61.76	0.82	1.21	0.69	0.89	-4.04	0.62	0.80
19.1	16.5	8.6	0.9	45.03	0.62	0.44	0.86	0.52	-4.04	0.45	0.25
19.9	16.5	12.8	0.7	64.32	0.79	0.64	0.83	0.78	-4.04	0.64	0.48
22.3	16.4	13.1	0.6	58.74	0.78	1.00	0.74	0.80	-4.04	0.59	0.64
20.9	16.3	12.0	0.9	57.42	0.75	0.80	0.78	0.74	-4.03	0.57	0.52
18.4	16.3	11.9	0.8	64.67	0.78	0.38	0.89	0.73	-4.03	0.65	0.32
21.8	16.3	9.9	0.7	45.41	0.65	0.93	0.75	0.61	-4.03	0.45	0.46
20.5	16.3	12.9	0.8	62.93	0.79	0.77	0.80	0.79	-4.03	0.63	0.55
22.5	16.2	12.6	0.7	56.00	0.76	1.05	0.72	0.78	-4.02	0.56	0.64
27.5	16.2	10.1	0.7	36.73	0.61	1.69	0.59	0.62	-4.02	0.37	0.65
19.0	16.2	12.0	0.6	63.16	0.78	0.52	0.85	0.74	-4.02	0.63	0.40
22.2	16.2	10.9	0.8	49.10	0.69	0.99	0.73	0.67	-4.02	0.49	0.53
21.3	16.1	14.3	0.7	67.14	0.84	1.00	0.76	0.89	-4.01	0.67	0.74
17.9	16.1	12.5	0.7	69.83	0.82	0.34	0.90	0.78	-4.01	0.70	0.33
21.7	16.1	14.9	0.8	68.66	0.86	1.09	0.74	0.93	-4.01	0.69	0.82
18.2	16.1	13.9	0.7	76.37	0.87	0.49	0.88	0.86	-4.01	0.76	0.49
21.7	16.1	13.6	0.7	62.67	0.81	1.00	0.74	0.84	-4.01	0.63	0.69
21.5	16.1	13.5	0.6	62.79	0.81	0.98	0.75	0.84	-4.01	0.63	0.67
19.5	16.1	11.9	0.8	61.03	0.77	0.63	0.83	0.74	-4.01	0.61	0.45
19.9	16.0	11.9	0.7	59.80	0.76	0.71	0.80	0.74	-4.00	0.60	0.49
18.3	16.0	9.9	0.8	54.10	0.69	0.40	0.87	0.62	-4.00	0.54	0.27
18.6	16.0	10.5	0.7	56.45	0.72	0.46	0.86	0.66	-4.00	0.56	0.32
18.1	16.0	11.9	0.7	65.75	0.79	0.39	0.88	0.74	-4.00	0.66	0.34
23.1	16.0	12.9	0.8	55.84	0.77	1.16	0.69	0.81	-4.00	0.56	0.70
29.6	16.0	14.1	0.7	47.64	0.75	1.77	0.54	0.88	-4.00	0.48	0.88
19.1	16.0	15.7	0.8	82.20	0.93	0.93	0.84	0.98	-4.00	0.82	0.91
23.1	16.0	9.9	0.8	42.86	0.64	1.17	0.69	0.62	-4.00	0.43	0.54
18.5	15.9	10.2	0.7	55.14	0.71	0.46	0.86	0.64	-3.99	0.55	0.31

A-axis	B-axis	C-axis	Roundness	Flatness	Sphericity	OP-index	b/a	c/b	B-axis phi	c/a	a-b/a-c
17.8	15.9	5.6	0.6	31.46	0.48	0.36	0.89	0.35	-3.99	0.31	0.16
19.5	15.9	13.3	0.9	68.21	0.83	0.73	0.82	0.84	-3.99	0.68	0.58
23.2	15.9	14.2	0.8	61.21	0.82	1.23	0.69	0.89	-3.99	0.61	0.81
21.0	15.9	9.9	0.8	47.14	0.66	0.88	0.76	0.62	-3.99	0.47	0.46
21.7	15.8	13.0	0.7	59.91	0.79	1.04	0.73	0.82	-3.98	0.60	0.68
16.5	15.8	11.2	0.9	67.88	0.78	0.06	0.96	0.71	-3.98	0.68	0.13
17.9	15.8	10.1	0.7	56.42	0.71	0.36	0.88	0.64	-3.98	0.56	0.27
17.1	15.7	10.8	0.8	63.16	0.76	0.23	0.92	0.69	-3.97	0.63	0.22
18.1	15.7	11.5	0.7	63.54	0.77	0.45	0.87	0.73	-3.97	0.64	0.36
20.8	15.7	14.1	0.8	67.79	0.85	1.01	0.75	0.90	-3.97	0.68	0.76
18.3	15.6	13.0	0.9	71.04	0.84	0.58	0.85	0.83	-3.96	0.71	0.51
24.7	15.6	14.0	0.9	56.68	0.80	1.42	0.63	0.90	-3.96	0.57	0.85
22.5	15.6	14.1	0.7	62.67	0.83	1.22	0.69	0.90	-3.96	0.63	0.82
20.0	15.6	12.1	0.7	60.50	0.78	0.82	0.78	0.78	-3.96	0.61	0.56
25.0	15.5	13.2	0.9	52.80	0.77	1.44	0.62	0.85	-3.95	0.53	0.81
16.1	15.5	11.0	0.6	68.32	0.79	0.03	0.96	0.71	-3.95	0.68	0.12
22.2	15.5	11.1	0.7	50.00	0.71	1.12	0.70	0.72	-3.95	0.50	0.60
19.8	15.5	13.9	0.7	70.20	0.86	0.92	0.78	0.90	-3.95	0.70	0.73
23.0	15.5	11.0	0.8	47.83	0.70	1.22	0.67	0.71	-3.95	0.48	0.63
20.2	15.5	11.1	0.9	54.95	0.73	0.84	0.77	0.72	-3.95	0.55	0.52
20.0	15.3	7.9	0.6	39.50	0.59	0.88	0.77	0.52	-3.94	0.40	0.39
26.1	15.3	13.9	0.7	53.26	0.79	1.59	0.59	0.91	-3.94	0.53	0.89
19.5	15.2	11.7	0.8	60.00	0.77	0.81	0.78	0.77	-3.93	0.60	0.55
16.5	15.2	14.1	0.8	85.45	0.93	0.39	0.92	0.93	-3.93	0.85	0.54
23.4	15.2	13.1	0.8	55.98	0.78	1.34	0.65	0.86	-3.93	0.56	0.80
19.1	15.2	10.7	0.8	56.02	0.73	0.72	0.80	0.70	-3.93	0.56	0.46
27.3	15.1	13.5	0.8	49.45	0.76	1.71	0.55	0.89	-3.92	0.49	0.88
16.3	15.1	11.6	0.7	71.17	0.82	0.21	0.93	0.77	-3.92	0.71	0.26
19.8	15.1	9.5	0.6	47.98	0.67	0.85	0.76	0.63	-3.92	0.48	0.46
21.5	15.1	11.0	0.7	51.16	0.72	1.10	0.70	0.73	-3.92	0.51	0.61
23.4	15.0	12.9	0.9	55.13	0.78	1.36	0.64	0.86	-3.91	0.55	0.80
20.6	15.0	13.3	0.8	64.56	0.83	1.08	0.73	0.89	-3.91	0.65	0.77
22.1	15.0	10.9	0.7	49.32	0.71	1.19	0.68	0.73	-3.91	0.49	0.63
26.0	14.9	12.1	0.7	46.54	0.72	1.64	0.57	0.81	-3.90	0.47	0.80
21.3	14.9	8.9	0.7	41.78	0.63	1.14	0.70	0.60	-3.90	0.42	0.52
23.8	14.9	11.4	0.7	47.90	0.72	1.41	0.63	0.77	-3.90	0.48	0.72
17.0	14.9	11.9	0.8	70.00	0.82	0.45	0.88	0.80	-3.90	0.70	0.41
17.7	14.9	10.4	0.7	58.76	0.74	0.54	0.84	0.70	-3.90	0.59	0.38
21.1	14.9	12.3	0.7	58.29	0.78	1.11	0.71	0.83	-3.90	0.58	0.70
22.9	14.9	10.0	0.7	43.67	0.66	1.33	0.65	0.67	-3.90	0.44	0.62
19.8	14.9	11.3	0.8	57.07	0.76	0.91	0.75	0.76	-3.90	0.57	0.58
19.5	14.8	11.8	0.8	60.51	0.78	0.90	0.76	0.80	-3.89	0.61	0.61

A-axis	B-axis	C-axis	Roundness	Flatness	Sphericity	OP-index	b/a	c/b	B-axis phi	c/a	a-b/a-c
16.1	14.8	11.3	0.7	70.19	0.81	0.24	0.92	0.76	-3.89	0.70	0.27
19.1	14.7	10.3	0.7	53.93	0.72	0.82	0.77	0.70	-3.88	0.54	0.50
26.0	14.6	12.1	0.7	46.54	0.73	1.68	0.56	0.83	-3.87	0.47	0.82
20.5	14.6	10.6	0.7	51.71	0.72	1.05	0.71	0.73	-3.87	0.52	0.60
18.9	14.5	13.2	0.8	69.84	0.86	0.98	0.77	0.91	-3.86	0.70	0.77
24.7	14.5	8.6	0.7	34.82	0.59	1.73	0.59	0.59	-3.86	0.35	0.63
17.8	14.5	11.9	0.6	66.85	0.82	0.71	0.81	0.82	-3.86	0.67	0.56
21.1	14.3	12.9	0.7	61.14	0.82	1.26	0.68	0.90	-3.84	0.61	0.83
16.4	14.3	10.0	0.8	60.98	0.75	0.41	0.87	0.70	-3.84	0.61	0.33
19.8	14.3	11.9	0.8	60.10	0.79	1.05	0.72	0.83	-3.84	0.60	0.70
19.0	14.3	11.2	0.7	58.95	0.77	0.91	0.75	0.78	-3.84	0.59	0.60
18.5	14.1	11.0	0.6	59.46	0.77	0.87	0.76	0.78	-3.82	0.59	0.59
16.9	14.1	13.4	0.9	79.29	0.91	0.83	0.83	0.95	-3.82	0.79	0.80
15.0	14.1	6.3	0.6	42.00	0.57	0.11	0.94	0.45	-3.82	0.42	0.10
15.5	14.1	11.3	0.6	72.90	0.84	0.29	0.91	0.80	-3.82	0.73	0.33
16.9	14.0	11.1	0.8	65.68	0.80	0.63	0.83	0.79	-3.81	0.66	0.50
15.9	14.0	10.2	0.7	64.15	0.78	0.38	0.88	0.73	-3.81	0.64	0.33
19.6	14.0	11.9	0.8	60.71	0.80	1.09	0.71	0.85	-3.81	0.61	0.73
15.0	13.9	10.6	0.9	70.67	0.81	0.19	0.93	0.76	-3.80	0.71	0.25
16.8	13.9	10.2	0.9	60.71	0.76	0.60	0.83	0.73	-3.80	0.61	0.44
24.7	13.9	10.6	0.8	42.91	0.69	1.70	0.56	0.76	-3.80	0.43	0.77
19.3	13.9	11.1	0.7	57.51	0.77	1.04	0.72	0.80	-3.80	0.58	0.66
17.9	13.9	11.0	0.7	61.45	0.79	0.83	0.78	0.79	-3.80	0.61	0.58
21.0	13.9	11.5	0.8	54.76	0.77	1.27	0.66	0.83	-3.80	0.55	0.75
17.3	13.9	9.0	0.6	52.02	0.70	0.67	0.80	0.65	-3.80	0.52	0.41
18.9	13.8	10.0	0.7	52.91	0.73	0.98	0.73	0.72	-3.79	0.53	0.57
16.1	13.8	10.1	0.8	62.73	0.77	0.48	0.86	0.73	-3.79	0.63	0.38
15.0	13.8	11.0	0.9	73.33	0.84	0.24	0.92	0.80	-3.79	0.73	0.30
20.0	13.7	10.1	0.9	50.50	0.72	1.16	0.69	0.74	-3.78	0.51	0.64
18.6	13.6	12.9	0.7	69.35	0.87	1.14	0.73	0.95	-3.77	0.69	0.88
23.5	13.5	9.7	0.9	41.28	0.67	1.67	0.57	0.72	-3.75	0.41	0.72
17.0	13.5	11.9	0.6	70.00	0.85	0.84	0.79	0.88	-3.75	0.70	0.69
15.0	13.4	12.1	0.8	80.67	0.90	0.47	0.89	0.90	-3.74	0.81	0.55
19.6	13.4	11.0	0.9	56.12	0.77	1.18	0.68	0.82	-3.74	0.56	0.72
14.5	13.3	10.0	0.9	68.97	0.80	0.23	0.92	0.75	-3.73	0.69	0.27
17.0	13.3	9.9	0.7	58.24	0.76	0.77	0.78	0.74	-3.73	0.58	0.52
17.8	13.2	8.5	0.6	47.75	0.67	0.92	0.74	0.64	-3.72	0.48	0.49
17.0	13.2	9.7	0.8	57.06	0.75	0.79	0.78	0.73	-3.72	0.57	0.52
16.0	13.2	8.9	0.8	55.63	0.72	0.58	0.83	0.67	-3.72	0.56	0.39
15.9	13.1	10.6	0.8	66.67	0.81	0.65	0.82	0.81	-3.71	0.67	0.53
15.5	13.1	12.2	0.7	78.71	0.90	0.73	0.85	0.93	-3.71	0.79	0.73
18.5	13.1	11.2	0.8	60.54	0.80	1.11	0.71	0.85	-3.71	0.61	0.74

A-axis	B-axis	C-axis	Roundness	Flatness	Sphericity	OP-index	b/a	c/b	B-axis phi	c/a	a-b/a-c
23.5	13.1	10.0	0.6	42.55	0.69	1.72	0.56	0.76	-3.71	0.43	0.77
23.0	13.1	11.5	0.8	50.00	0.76	1.63	0.57	0.88	-3.71	0.50	0.86
15.9	13.1	8.2	0.7	51.57	0.69	0.58	0.82	0.63	-3.71	0.52	0.36
14.8	13.0	9.5	0.7	64.19	0.78	0.38	0.88	0.73	-3.70	0.64	0.34
16.8	13.0	8.8	0.7	52.38	0.71	0.79	0.77	0.68	-3.70	0.52	0.48
15.9	13.0	10.0	0.7	62.89	0.79	0.65	0.82	0.77	-3.70	0.63	0.49
18.8	13.0	9.1	0.6	48.40	0.70	1.13	0.69	0.70	-3.70	0.48	0.60
14.5	13.0	9.0	0.8	62.07	0.75	0.29	0.90	0.69	-3.70	0.62	0.27
15.5	13.0	8.9	0.8	57.42	0.73	0.53	0.84	0.68	-3.70	0.57	0.38
16.5	13.0	10.4	0.8	63.03	0.80	0.78	0.79	0.80	-3.70	0.63	0.57
19.5	12.9	8.7	0.6	44.62	0.67	1.27	0.66	0.67	-3.69	0.45	0.61
20.4	12.9	10.1	0.7	49.51	0.73	1.37	0.63	0.78	-3.69	0.50	0.73
15.0	12.9	10.2	0.9	68.00	0.81	0.49	0.86	0.79	-3.69	0.68	0.44
16.9	12.9	10.0	0.7	59.17	0.77	0.86	0.76	0.78	-3.69	0.59	0.58
15.5	12.9	9.5	0.7	61.29	0.77	0.57	0.83	0.74	-3.69	0.61	0.43
14.5	12.8	6.8	0.7	46.90	0.63	0.33	0.88	0.53	-3.68	0.47	0.22
14.1	12.8	7.0	0.7	49.65	0.65	0.23	0.91	0.55	-3.68	0.50	0.18
14.3	12.7	6.2	0.7	43.36	0.60	0.31	0.89	0.49	-3.67	0.43	0.20
21.0	12.6	10.0	0.7	47.62	0.72	1.51	0.60	0.79	-3.66	0.48	0.76
14.0	12.6	10.0	0.7	71.43	0.83	0.32	0.90	0.79	-3.66	0.71	0.35
14.9	12.5	8.7	0.8	58.39	0.74	0.52	0.84	0.70	-3.64	0.58	0.39
17.0	12.3	8.6	0.7	50.59	0.71	0.99	0.72	0.70	-3.62	0.51	0.56
14.9	12.3	8.4	0.7	56.38	0.73	0.57	0.83	0.68	-3.62	0.56	0.40
19.1	12.3	9.8	0.7	51.31	0.74	1.32	0.64	0.80	-3.62	0.51	0.73
15.1	12.2	8.1	0.6	53.64	0.71	0.64	0.81	0.66	-3.61	0.54	0.41
17.4	12.2	11.0	0.6	63.22	0.83	1.16	0.70	0.90	-3.61	0.63	0.81
16.1	12.2	8.1	0.8	50.31	0.69	0.84	0.76	0.66	-3.61	0.50	0.49
17.4	12.1	9.9	0.6	56.90	0.78	1.12	0.70	0.82	-3.60	0.57	0.71
20.9	12.1	11.4	0.8	54.55	0.80	1.60	0.58	0.94	-3.60	0.55	0.93
14.9	12.1	10.8	0.6	72.48	0.86	0.77	0.81	0.89	-3.60	0.72	0.68
16.0	12.1	9.5	0.6	59.38	0.78	0.88	0.76	0.79	-3.60	0.59	0.60
18.2	12.1	9.0	0.8	49.45	0.72	1.23	0.66	0.74	-3.60	0.49	0.66
14.2	12.1	10.0	0.7	70.42	0.83	0.54	0.85	0.83	-3.60	0.70	0.50
13.2	12.1	9.0	0.8	68.18	0.80	0.21	0.92	0.74	-3.60	0.68	0.26
16.3	12.1	9.1	0.8	55.83	0.75	0.92	0.74	0.75	-3.60	0.56	0.58
15.8	12.0	7.9	0.7	50.00	0.69	0.84	0.76	0.66	-3.58	0.50	0.48
17.9	12.0	9.7	0.7	54.19	0.76	1.22	0.67	0.81	-3.58	0.54	0.72
13.9	12.0	9.2	0.9	66.19	0.80	0.45	0.86	0.77	-3.58	0.66	0.40
15.9	12.0	10.2	0.8	64.15	0.82	0.93	0.75	0.85	-3.58	0.64	0.68
19.1	12.0	8.3	0.7	43.46	0.67	1.41	0.63	0.69	-3.58	0.43	0.66
15.8	12.0	10.5	0.7	66.46	0.83	0.94	0.76	0.88	-3.58	0.66	0.72
16.5	12.0	7.1	0.7	43.03	0.63	0.99	0.73	0.59	-3.58	0.43	0.48

A-axis	B-axis	C-axis	Roundness	Flatness	Sphericity	OP-index	b/a	c/b	B-axis phi	c/a	a-b/a-c
18.0	11.8	9.2	0.9	51.11	0.74	1.27	0.66	0.78	-3.56	0.51	0.70
15.0	11.8	9.5	0.7	63.33	0.80	0.78	0.79	0.81	-3.56	0.63	0.58
12.0	11.8	8.9	0.8	74.17	0.82	-0.13	0.98	0.75	-3.56	0.74	0.06
12.4	11.6	7.9	0.7	63.71	0.76	0.10	0.94	0.68	-3.54	0.64	0.18
15.9	11.5	9.9	0.8	62.26	0.81	1.04	0.72	0.86	-3.52	0.62	0.73
18.5	11.4	8.9	0.7	48.11	0.72	1.43	0.62	0.78	-3.51	0.48	0.74
18.5	11.3	9.0	0.8	48.65	0.73	1.45	0.61	0.80	-3.50	0.49	0.76
14.0	11.2	8.1	0.6	57.86	0.75	0.67	0.80	0.72	-3.49	0.58	0.47
18.7	11.1	10.3	0.9	55.08	0.80	1.53	0.59	0.93	-3.47	0.55	0.90
17.0	11.1	9.8	0.8	57.65	0.80	1.30	0.65	0.88	-3.47	0.58	0.82
16.0	11.1	8.9	0.7	55.63	0.76	1.11	0.69	0.80	-3.47	0.56	0.69
14.1	11.0	9.9	0.7	70.21	0.86	0.88	0.78	0.90	-3.46	0.70	0.74
13.5	11.0	8.2	0.7	60.74	0.77	0.62	0.81	0.75	-3.46	0.61	0.47
16.0	10.9	8.0	0.8	50.00	0.72	1.15	0.68	0.73	-3.45	0.50	0.64
13.9	10.8	7.0	0.8	50.36	0.69	0.75	0.78	0.65	-3.43	0.50	0.45
15.5	10.7	8.5	0.7	54.84	0.76	1.12	0.69	0.79	-3.42	0.55	0.69
15.8	10.7	7.5	0.7	47.47	0.69	1.17	0.68	0.70	-3.42	0.47	0.61
16.2	10.5	7.9	0.7	48.77	0.72	1.28	0.65	0.75	-3.39	0.49	0.69
17.8	10.5	8.4	0.7	47.19	0.72	1.53	0.59	0.80	-3.39	0.47	0.78
17.7	10.5	7.0	0.7	39.55	0.64	1.58	0.59	0.67	-3.39	0.40	0.67
14.7	10.4	8.4	0.7	57.14	0.77	1.06	0.71	0.81	-3.38	0.57	0.68
15.0	10.3	3.8	0.7	25.33	0.45	1.48	0.69	0.37	-3.36	0.25	0.42
13.0	10.3	8.1	0.7	62.31	0.79	0.72	0.79	0.79	-3.36	0.62	0.55
12.0	10.2	7.0	0.7	58.33	0.74	0.45	0.85	0.69	-3.35	0.58	0.36
16.3	10.2	8.9	0.7	54.60	0.78	1.39	0.63	0.87	-3.35	0.55	0.82
13.2	10.1	6.2	0.7	46.97	0.66	0.79	0.77	0.61	-3.34	0.47	0.44
11.5	10.0	7.1	0.7	61.74	0.76	0.37	0.87	0.71	-3.32	0.62	0.34
13.6	10.0	7.7	0.7	56.62	0.76	0.93	0.74	0.77	-3.32	0.57	0.61
13.2	10.0	6.5	0.7	49.24	0.68	0.82	0.76	0.65	-3.32	0.49	0.48
15.2	10.0	6.5	0.8	42.76	0.65	1.26	0.66	0.65	-3.32	0.43	0.60
12.7	10.0	7.9	0.7	62.20	0.79	0.74	0.79	0.79	-3.32	0.62	0.56
11.8	9.9	8.0	0.7	67.80	0.82	0.54	0.84	0.81	-3.31	0.68	0.50
15.4	9.9	7.8	0.7	50.65	0.74	1.30	0.64	0.79	-3.31	0.51	0.72
16.3	9.8	8.2	0.7	50.31	0.75	1.47	0.60	0.84	-3.29	0.50	0.80
12.5	9.8	7.6	0.8	60.80	0.78	0.74	0.78	0.78	-3.29	0.61	0.55
11.5	9.4	6.9	0.7	60.00	0.76	0.58	0.82	0.73	-3.23	0.60	0.46
13.0	9.2	7.4	0.6	56.92	0.77	1.04	0.71	0.80	-3.20	0.57	0.68
12.5	9.1	8.3	0.8	66.40	0.85	1.04	0.73	0.91	-3.19	0.66	0.81
11.9	8.9	5.1	0.6	42.86	0.63	0.86	0.75	0.57	-3.15	0.43	0.44
14.7	8.9	7.3	0.8	49.66	0.74	1.44	0.61	0.82	-3.15	0.50	0.78
11.3	8.9	6.0	0.7	53.10	0.71	0.68	0.79	0.67	-3.15	0.53	0.45
11.8	8.9	5.3	0.7	44.92	0.64	0.82	0.75	0.60	-3.15	0.45	0.45

A-axis	B-axis	C-axis	Roundness	Flatness	Sphericity	OP-index	b/a	c/b	B-axis phi	c/a	a-b/a-c
12.0	8.8	6.0	0.7	50.00	0.70	0.90	0.73	0.68	-3.14	0.50	0.53
13.2	8.7	5.9	0.6	44.70	0.67	1.23	0.66	0.68	-3.12	0.45	0.62
11.3	8.5	5.2	0.7	46.02	0.66	0.82	0.75	0.61	-3.09	0.46	0.46
12.0	8.5	6.3	0.8	52.50	0.73	1.00	0.71	0.74	-3.09	0.53	0.61
13.8	8.3	7.5	0.6	54.35	0.79	1.46	0.60	0.90	-3.05	0.54	0.87
11.0	8.2	6.1	0.7	55.45	0.74	0.85	0.75	0.74	-3.04	0.55	0.57
10.6	8.1	6.3	0.7	59.43	0.77	0.78	0.76	0.78	-3.02	0.59	0.58
12.1	8.0	6.8	0.7	56.20	0.78	1.21	0.66	0.85	-3.00	0.56	0.77
9.7	8.0	5.7	0.7	58.76	0.75	0.51	0.82	0.71	-3.00	0.59	0.43
9.5	7.8	6.3	0.6	66.32	0.81	0.57	0.82	0.81	-2.96	0.66	0.53
13.9	7.7	6.5	0.7	46.76	0.73	1.65	0.55	0.84	-2.94	0.47	0.84
13.4	7.4	5.6	0.7	41.79	0.68	1.69	0.55	0.76	-2.89	0.42	0.77
10.0	7.2	6.1	0.6	61.00	0.80	0.97	0.72	0.85	-2.85	0.61	0.72
10.0	6.9	4.5	0.7	45.00	0.66	1.05	0.69	0.65	-2.79	0.45	0.56
8.3	6.8	4.9	0.7	59.04	0.75	0.50	0.82	0.72	-2.77	0.59	0.44
9.1	6.7	5.2	0.6	57.14	0.76	0.85	0.74	0.78	-2.74	0.57	0.62
7.5	5.9	4.8	0.6	64.00	0.80	0.64	0.79	0.81	-2.56	0.64	0.59

Appendix (XII)(h)

PEBBLE DATA ROODERAND CONGLOMERATE FORMATION BUFFELSHOEK 471

A–axis	B–axis	C–axis	Roundness	Flatness	Sphericity	OP–index	b/a	c/b	B–axis phi	c/a	a–b/a–c
24.0	22.6	18.2	0.7	75.83	0.85	0.20	0.94	0.81	−4.50	0.76	0.24
30.0	20.1	15.7	0.8	52.33	0.74	1.26	0.67	0.78	−4.33	0.52	0.69
32.0	20.0	16.7	0.6	52.03	0.76	1.44	0.63	0.83	−4.32	0.52	0.78
26.1	19.4	14.6	0.9	55.94	0.75	0.96	0.74	0.75	−4.28	0.56	0.58
20.6	19.4	14.0	0.6	67.96	0.79	0.16	0.94	0.72	−4.28	0.68	0.18
25.3	19.2	13.5	0.6	53.36	0.72	0.89	0.76	0.70	−4.26	0.53	0.52
24.8	19.2	11.8	0.6	47.58	0.66	0.82	0.77	0.61	−4.26	0.48	0.43
22.5	19.2	14.5	0.7	64.44	0.79	0.54	0.85	0.76	−4.26	0.64	0.41
22.4	19.1	14.3	0.5	63.84	0.78	0.54	0.85	0.75	−4.26	0.64	0.41
21.5	19.0	14.0	0.7	65.12	0.78	0.41	0.88	0.74	−4.25	0.65	0.33
18.8	18.6	11.4	0.6	60.64	0.72	−0.07	0.99	0.61	−4.22	0.61	0.03
25.7	18.4	15.0	0.7	58.37	0.78	1.09	0.72	0.82	−4.20	0.58	0.68
22.0	18.3	12.2	0.5	55.45	0.72	0.59	0.83	0.67	−4.19	0.55	0.38
27.0	18.3	13.7	0.5	50.74	0.72	1.22	0.68	0.75	−4.19	0.51	0.65
23.7	18.3	15.0	0.4	63.29	0.80	0.89	0.77	0.82	−4.19	0.63	0.62
24.0	18.2	14.7	0.6	61.25	0.79	0.93	0.76	0.81	−4.19	0.61	0.62
23.5	18.1	18.1	0.5	76.97	0.92	1.17	0.77	1.00	−4.18	0.77	0.99
23.8	18.0	12.9	0.7	54.20	0.73	0.90	0.76	0.72	−4.17	0.54	0.53
21.5	18.0	11.4	0.6	53.02	0.70	0.56	0.84	0.63	−4.17	0.53	0.35
22.8	18.0	17.0	0.7	74.56	0.89	0.99	0.79	0.94	−4.17	0.75	0.83
21.0	17.8	10.3	0.6	49.05	0.66	0.51	0.85	0.58	−4.15	0.49	0.30
21.0	17.7	11.0	0.4	52.38	0.69	0.53	0.84	0.62	−4.15	0.52	0.33
24.3	17.6	12.0	0.6	49.38	0.70	1.02	0.72	0.68	−4.14	0.49	0.54
26.0	17.5	14.3	0.5	55.00	0.77	1.24	0.67	0.82	−4.13	0.55	0.73
21.3	17.4	9.3	0.8	43.66	0.62	0.65	0.82	0.53	−4.12	0.44	0.33
19.7	17.3	12.2	0.5	61.93	0.76	0.41	0.88	0.71	−4.11	0.62	0.32
24.5	17.3	12.2	0.5	49.80	0.71	1.09	0.71	0.71	−4.11	0.50	0.59
22.8	17.3	14.0	0.8	61.40	0.79	0.93	0.76	0.81	−4.11	0.61	0.63
18.1	17.2	12.1	0.5	66.85	0.78	0.10	0.95	0.70	−4.10	0.67	0.15
21.1	17.2	13.5	0.6	63.98	0.79	0.70	0.82	0.78	−4.10	0.64	0.51
23.4	17.2	11.2	0.8	47.86	0.68	0.98	0.74	0.65	−4.10	0.48	0.51
18.2	17.2	10.9	0.7	59.89	0.72	0.11	0.95	0.63	−4.10	0.60	0.14
29.9	17.0	14.2	0.6	47.49	0.73	1.66	0.57	0.84	−4.09	0.47	0.82
23.0	16.9	14.9	0.6	64.78	0.83	1.07	0.73	0.88	−4.08	0.65	0.75
20.3	16.9	14.0	0.6	68.97	0.83	0.67	0.83	0.83	−4.08	0.69	0.54
25.3	16.5	16.0	0.5	63.24	0.85	1.41	0.65	0.97	−4.04	0.63	0.95

A-axis	B-axis	C-axis	Roundness	Flatness	Sphericity	OP-index	b/a	c/b	B-axis phi	c/a	a-b/a-c
25.0	16.5	16.1	0.6	64.40	0.86	1.40	0.66	0.98	-4.04	0.64	0.96
25.0	16.5	14.8	0.7	59.20	0.81	1.32	0.66	0.90	-4.04	0.59	0.83
24.4	16.3	13.5	0.6	55.33	0.77	1.26	0.67	0.83	-4.03	0.55	0.74
25.6	16.3	11.8	0.6	46.09	0.69	1.38	0.64	0.72	-4.03	0.46	0.67
23.3	16.3	10.0	0.5	42.92	0.64	1.14	0.70	0.61	-4.03	0.43	0.53
20.5	16.3	13.7	0.7	66.83	0.83	0.81	0.80	0.84	-4.03	0.67	0.62
19.4	16.3	8.3	0.4	42.78	0.60	0.55	0.84	0.51	-4.03	0.43	0.28
21.0	16.2	11.4	0.6	54.29	0.73	0.83	0.77	0.70	-4.02	0.54	0.50
21.1	16.2	14.6	0.6	69.19	0.85	0.98	0.77	0.90	-4.02	0.69	0.75
26.1	16.2	11.2	0.6	42.91	0.67	1.47	0.62	0.69	-4.02	0.43	0.66
21.7	16.2	11.2	0.9	51.61	0.71	0.92	0.75	0.69	-4.02	0.52	0.52
22.2	16.1	13.3	0.7	59.91	0.79	1.05	0.73	0.83	-4.01	0.60	0.69
17.0	16.1	11.2	0.5	65.88	0.77	0.10	0.95	0.70	-4.01	0.66	0.16
21.0	16.0	13.3	0.6	63.33	0.81	0.92	0.76	0.83	-4.00	0.63	0.65
32.0	16.0	14.2	0.5	44.38	0.73	1.96	0.50	0.89	-4.00	0.44	0.90
19.7	16.0	12.5	0.6	63.45	0.79	0.70	0.81	0.78	-4.00	0.63	0.51
25.0	16.0	13.0	0.6	52.00	0.75	1.36	0.64	0.81	-4.00	0.52	0.75
16.6	16.0	12.9	0.6	77.71	0.86	0.03	0.96	0.81	-4.00	0.78	0.16
21.3	16.0	13.7	0.8	64.32	0.82	0.98	0.75	0.86	-4.00	0.64	0.70
20.0	16.0	12.2	0.7	61.00	0.77	0.74	0.80	0.76	-4.00	0.61	0.51
21.1	16.0	11.8	0.6	55.92	0.74	0.88	0.76	0.74	-4.00	0.56	0.55
24.2	15.9	13.2	0.6	54.55	0.77	1.30	0.66	0.83	-3.99	0.55	0.75
17.6	15.9	12.5	0.6	71.02	0.82	0.33	0.90	0.79	-3.99	0.71	0.33
17.5	15.9	11.0	0.7	63.04	0.76	0.26	0.91	0.69	-3.99	0.63	0.24
22.2	15.9	12.2	0.6	54.95	0.75	1.06	0.72	0.77	-3.99	0.55	0.63
21.9	15.9	10.3	0.6	47.03	0.67	1.01	0.73	0.65	-3.99	0.47	0.52
20.0	15.9	12.7	0.6	63.50	0.80	0.78	0.80	0.80	-3.99	0.64	0.56
27.0	15.8	10.3	0.5	38.15	0.63	1.68	0.59	0.65	-3.98	0.38	0.67
16.8	15.7	10.9	0.7	64.88	0.77	0.16	0.93	0.69	-3.97	0.65	0.19
17.0	15.7	10.4	0.7	61.18	0.74	0.20	0.92	0.66	-3.97	0.61	0.20
16.6	15.7	10.8	0.7	65.06	0.76	0.11	0.95	0.69	-3.97	0.65	0.16
19.1	15.6	11.5	0.6	60.21	0.76	0.66	0.82	0.74	-3.96	0.60	0.46
25.8	15.6	12.3	0.6	47.67	0.72	1.51	0.60	0.79	-3.96	0.48	0.76
17.0	15.6	10.5	0.7	61.76	0.75	0.22	0.92	0.67	-3.96	0.62	0.22
24.5	15.6	11.4	0.6	46.53	0.70	1.38	0.64	0.73	-3.96	0.47	0.68
21.5	15.6	13.1	0.6	60.93	0.80	1.06	0.73	0.84	-3.96	0.61	0.70
19.2	15.5	9.8	0.8	51.04	0.69	0.67	0.81	0.63	-3.95	0.51	0.39
21.3	15.5	12.0	0.7	56.34	0.76	1.01	0.73	0.77	-3.95	0.56	0.62
19.0	15.5	15.0	0.6	78.95	0.91	0.95	0.82	0.97	-3.95	0.79	0.88
19.0	15.5	7.5	0.6	39.47	0.58	0.66	0.82	0.48	-3.95	0.39	0.30
18.7	15.5	11.1	0.6	59.36	0.75	0.60	0.83	0.72	-3.95	0.59	0.42
24.4	15.4	12.4	0.8	50.82	0.74	1.39	0.63	0.81	-3.94	0.51	0.75

A-axis	B-axis	C-axis	Roundness	Flatness	Sphericity	OP-index	b/a	c/b	B-axis phi	c/a	a-b/a-c
19.5	15.3	11.2	0.5	57.44	0.75	0.78	0.78	0.73	-3.94	0.57	0.51
22.0	15.3	15.3	0.9	69.55	0.89	1.33	0.70	1.00	-3.94	0.70	1.00
29.7	15.3	11.4	0.7	38.38	0.66	1.98	0.52	0.75	-3.94	0.38	0.79
15.5	15.3	12.9	0.9	83.23	0.89	-0.14	0.99	0.84	-3.94	0.83	0.08
20.0	15.3	14.9	0.7	74.50	0.90	1.11	0.77	0.97	-3.94	0.75	0.92
18.0	15.3	13.4	0.6	74.44	0.87	0.64	0.85	0.88	-3.94	0.74	0.59
20.7	15.2	12.0	0.5	57.97	0.77	0.99	0.73	0.79	-3.93	0.58	0.63
22.5	15.2	10.0	0.6	44.44	0.66	1.22	0.68	0.66	-3.93	0.44	0.58
18.6	15.2	10.2	0.6	54.84	0.72	0.63	0.82	0.67	-3.93	0.55	0.40
23.0	15.2	11.0	0.6	47.83	0.70	1.27	0.66	0.72	-3.93	0.48	0.65
22.0	15.2	13.4	0.7	60.91	0.81	1.20	0.69	0.88	-3.93	0.61	0.79
23.5	15.2	13.5	0.6	57.45	0.80	1.36	0.65	0.89	-3.93	0.57	0.83
22.7	15.2	11.2	0.6	49.34	0.71	1.23	0.67	0.74	-3.93	0.49	0.65
18.5	15.2	11.2	0.7	60.54	0.76	0.63	0.82	0.74	-3.93	0.61	0.45
18.3	15.1	12.9	0.6	70.49	0.84	0.71	0.83	0.85	-3.92	0.70	0.59
17.6	15.0	13.5	0.6	76.70	0.88	0.67	0.85	0.90	-3.91	0.77	0.63
18.0	15.0	10.6	0.7	58.89	0.75	0.57	0.83	0.71	-3.91	0.59	0.41
17.4	15.0	11.3	0.6	64.94	0.79	0.48	0.86	0.75	-3.91	0.65	0.39
18.9	15.0	10.3	0.6	54.50	0.72	0.73	0.79	0.69	-3.91	0.54	0.45
19.8	15.0	12.7	0.8	64.14	0.82	0.94	0.76	0.85	-3.91	0.64	0.68
19.0	15.0	10.0	0.7	52.63	0.71	0.74	0.79	0.67	-3.91	0.53	0.44
21.0	15.0	10.9	0.6	51.90	0.72	1.05	0.71	0.73	-3.91	0.52	0.59
18.0	15.0	10.0	0.6	55.56	0.72	0.56	0.83	0.67	-3.91	0.56	0.38
16.0	15.0	13.0	0.8	81.25	0.89	0.21	0.94	0.87	-3.91	0.81	0.33
17.0	15.0	9.7	0.6	57.06	0.72	0.36	0.88	0.65	-3.91	0.57	0.27
20.6	14.9	13.0	0.7	63.11	0.82	1.08	0.72	0.87	-3.90	0.63	0.75
17.0	14.9	9.0	0.7	52.94	0.68	0.38	0.88	0.60	-3.90	0.53	0.26
19.3	14.9	12.2	0.6	63.21	0.80	0.87	0.77	0.82	-3.90	0.63	0.62
18.6	14.9	11.3	0.6	60.75	0.77	0.72	0.80	0.76	-3.90	0.61	0.51
17.5	14.9	8.5	0.7	48.57	0.65	0.48	0.85	0.57	-3.90	0.49	0.29
15.5	14.9	9.9	0.4	63.87	0.75	0.03	0.96	0.66	-3.90	0.64	0.11
17.0	14.9	11.6	0.7	68.24	0.81	0.43	0.88	0.78	-3.90	0.68	0.39
22.0	14.8	9.2	0.6	41.82	0.64	1.25	0.67	0.62	-3.89	0.42	0.56
22.9	14.8	13.3	0.5	58.08	0.81	1.36	0.65	0.90	-3.89	0.58	0.84
16.6	14.8	10.9	0.5	65.66	0.78	0.35	0.89	0.74	-3.89	0.66	0.32
21.0	14.8	14.0	0.6	66.67	0.86	1.22	0.70	0.95	-3.89	0.67	0.89
19.4	14.8	12.9	0.7	66.49	0.83	0.95	0.76	0.87	-3.89	0.66	0.71
20.5	14.7	9.5	0.6	46.34	0.67	1.04	0.72	0.65	-3.88	0.46	0.53
21.1	14.7	13.6	0.6	64.45	0.84	1.22	0.70	0.93	-3.88	0.64	0.85
19.3	14.7	9.8	0.6	50.78	0.70	0.85	0.76	0.67	-3.88	0.51	0.48
16.4	14.7	9.9	0.7	60.37	0.74	0.31	0.90	0.67	-3.88	0.60	0.26
19.2	14.7	9.8	0.5	51.04	0.70	0.83	0.77	0.67	-3.88	0.51	0.48

A−axis	B−axis	C−axis	Roundness	Flatness	Sphericity	OP−index	b/a	c/b	B−axis phi	c/a	a−b/a−c
21.9	14.7	13.0	0.7	59.36	0.81	1.27	0.67	0.88	−3.88	0.59	0.81
20.9	14.7	13.0	0.6	62.20	0.82	1.16	0.70	0.88	−3.88	0.62	0.78
16.7	14.7	7.0	0.6	41.92	0.58	0.37	0.88	0.48	−3.88	0.42	0.21
17.0	14.7	10.2	0.6	60.00	0.75	0.44	0.86	0.69	−3.88	0.60	0.34
22.9	14.7	11.7	0.7	51.09	0.74	1.35	0.64	0.80	−3.88	0.51	0.73
23.6	14.6	11.5	0.7	48.73	0.73	1.44	0.62	0.79	−3.87	0.49	0.74
22.0	14.6	10.4	0.6	47.27	0.70	1.26	0.66	0.71	−3.87	0.47	0.64
20.0	14.6	9.4	0.6	47.00	0.67	0.98	0.73	0.64	−3.87	0.47	0.51
18.0	14.6	13.4	0.7	74.44	0.88	0.85	0.81	0.92	−3.87	0.74	0.74
16.6	14.6	11.0	0.7	66.27	0.79	0.40	0.88	0.75	−3.87	0.66	0.36
20.0	14.6	12.2	0.6	61.00	0.80	1.03	0.73	0.84	−3.87	0.61	0.69
16.3	14.5	10.9	0.5	66.87	0.80	0.36	0.89	0.75	−3.86	0.67	0.33
21.4	14.5	13.0	0.7	60.75	0.82	1.25	0.68	0.90	−3.86	0.61	0.82
19.9	14.5	11.3	0.7	56.78	0.76	1.00	0.73	0.78	−3.86	0.57	0.63
19.3	14.5	10.1	0.7	52.33	0.71	0.89	0.75	0.70	−3.86	0.52	0.52
24.5	14.5	12.3	0.7	50.20	0.75	1.55	0.59	0.85	−3.86	0.50	0.82
18.0	14.5	6.2	0.6	34.44	0.53	0.74	0.81	0.43	−3.86	0.34	0.30
17.9	14.5	10.3	0.7	57.54	0.74	0.66	0.81	0.71	−3.86	0.58	0.45
17.0	14.5	8.8	0.5	51.76	0.68	0.47	0.85	0.61	−3.86	0.52	0.30
23.4	14.4	11.2	0.5	47.86	0.72	1.46	0.62	0.78	−3.85	0.48	0.74
20.1	14.4	8.8	0.6	43.78	0.64	1.05	0.72	0.61	−3.85	0.44	0.50
17.3	14.4	11.8	0.5	68.21	0.82	0.64	0.83	0.82	−3.85	0.68	0.53
16.6	14.4	10.5	0.5	63.25	0.77	0.44	0.87	0.73	−3.85	0.63	0.36
17.4	14.4	7.3	0.7	41.95	0.60	0.59	0.83	0.51	−3.85	0.42	0.30
16.1	14.4	8.5	0.7	52.80	0.68	0.30	0.89	0.59	−3.85	0.53	0.22
24.0	14.4	12.0	0.8	50.00	0.75	1.52	0.60	0.83	−3.85	0.50	0.80
16.6	14.4	8.3	0.6	50.00	0.66	0.41	0.87	0.58	−3.85	0.50	0.27
27.6	14.4	11.6	0.5	42.03	0.70	1.89	0.52	0.81	−3.85	0.42	0.83
18.8	14.4	12.0	0.5	63.83	0.81	0.90	0.77	0.83	−3.85	0.64	0.65
19.4	14.4	10.9	0.7	56.19	0.75	0.94	0.74	0.76	−3.85	0.56	0.59
15.7	14.3	11.3	0.6	71.97	0.83	0.28	0.91	0.79	−3.84	0.72	0.32
20.5	14.3	10.9	0.6	53.17	0.74	1.12	0.70	0.76	−3.84	0.53	0.65
18.0	14.3	13.0	0.7	72.22	0.87	0.89	0.79	0.91	−3.84	0.72	0.74
23.6	14.3	11.1	0.6	47.03	0.71	1.50	0.61	0.78	−3.84	0.47	0.74
20.6	14.3	10.5	0.7	50.97	0.72	1.13	0.69	0.73	−3.84	0.51	0.62
20.9	14.3	9.3	0.6	44.50	0.66	1.18	0.68	0.65	−3.84	0.44	0.57
18.0	14.3	8.0	0.4	44.44	0.63	0.72	0.79	0.56	−3.84	0.44	0.37
20.0	14.3	11.1	0.7	55.50	0.76	1.05	0.72	0.78	−3.84	0.56	0.64
15.4	14.2	9.7	0.8	62.99	0.75	0.19	0.92	0.68	−3.83	0.63	0.21
17.9	14.2	8.9	0.6	49.72	0.68	0.72	0.79	0.63	−3.83	0.50	0.41
21.0	14.2	11.2	0.7	53.33	0.75	1.21	0.68	0.79	−3.83	0.53	0.69
24.6	14.2	12.3	0.7	50.00	0.76	1.61	0.58	0.87	−3.83	0.50	0.85

A-axis	B-axis	C-axis	Roundness	Flatness	Sphericity	OP-index	b/a	c/b	B-axis phi	c/a	a-b/a-c
15.1	14.0	8.8	0.5	58.28	0.72	0.16	0.93	0.63	-3.81	0.58	0.17
19.2	14.0	9.6	0.7	50.00	0.70	0.98	0.73	0.69	-3.81	0.50	0.54
20.9	14.0	9.8	0.6	46.89	0.69	1.23	0.67	0.70	-3.81	0.47	0.62
19.7	14.0	13.8	0.6	70.05	0.88	1.26	0.71	0.99	-3.81	0.70	0.97
17.5	14.0	12.2	0.4	69.71	0.85	0.81	0.80	0.87	-3.81	0.70	0.66
19.2	14.0	7.9	0.7	41.15	0.61	1.01	0.73	0.56	-3.81	0.41	0.46
19.0	14.0	10.5	0.5	55.26	0.75	0.96	0.74	0.75	-3.81	0.55	0.59
14.4	14.0	10.3	0.7	71.53	0.81	-0.03	0.97	0.74	-3.81	0.72	0.10
17.6	13.9	11.6	0.7	65.91	0.82	0.81	0.79	0.83	-3.80	0.66	0.62
17.3	13.9	10.0	0.6	57.80	0.75	0.69	0.80	0.72	-3.80	0.58	0.47
22.4	13.9	12.7	0.5	56.70	0.80	1.45	0.62	0.91	-3.80	0.57	0.88
15.0	13.9	10.0	0.4	66.67	0.78	0.18	0.93	0.72	-3.80	0.67	0.22
16.8	13.8	9.1	0.4	54.17	0.71	0.60	0.82	0.66	-3.79	0.54	0.39
22.2	13.8	11.7	0.7	52.70	0.76	1.43	0.62	0.85	-3.79	0.53	0.80
21.0	13.8	8.5	0.7	40.48	0.63	1.32	0.66	0.62	-3.79	0.40	0.58
17.9	13.8	10.0	0.4	55.87	0.74	0.82	0.77	0.72	-3.79	0.56	0.52
18.2	13.8	12.5	0.5	68.68	0.85	1.00	0.76	0.91	-3.79	0.69	0.77
14.9	13.8	11.5	0.7	77.18	0.86	0.23	0.93	0.83	-3.79	0.77	0.32
18.9	13.8	9.9	0.7	52.38	0.72	0.98	0.73	0.72	-3.79	0.52	0.57
21.5	13.8	8.5	0.6	39.53	0.62	1.40	0.64	0.62	-3.79	0.40	0.59
14.6	13.7	10.5	0.5	71.92	0.82	0.14	0.94	0.77	-3.78	0.72	0.22
19.3	13.7	8.6	0.6	44.56	0.65	1.07	0.71	0.63	-3.78	0.45	0.52
18.0	13.7	12.0	0.7	66.67	0.84	0.95	0.76	0.88	-3.78	0.67	0.72
20.0	13.7	9.0	0.7	45.00	0.67	1.17	0.69	0.66	-3.78	0.45	0.57
19.0	13.7	10.5	0.6	55.26	0.75	1.02	0.72	0.77	-3.78	0.55	0.62
17.6	13.7	10.9	0.8	61.93	0.79	0.82	0.78	0.80	-3.78	0.62	0.58
19.7	13.6	10.4	0.7	52.79	0.74	1.14	0.69	0.76	-3.77	0.53	0.66
18.7	13.6	11.3	0.8	60.43	0.79	1.03	0.73	0.83	-3.77	0.60	0.69
17.0	13.6	7.7	0.5	45.29	0.64	0.69	0.80	0.57	-3.77	0.45	0.37
18.4	13.6	12.0	0.7	65.22	0.83	1.03	0.74	0.88	-3.77	0.65	0.75
17.5	13.6	9.6	0.6	54.86	0.73	0.78	0.78	0.71	-3.77	0.55	0.49
17.8	13.6	10.6	0.6	59.55	0.77	0.86	0.76	0.78	-3.77	0.60	0.58
20.4	13.5	12.2	0.6	59.80	0.81	1.31	0.66	0.90	-3.75	0.60	0.84
19.4	13.5	12.7	0.7	65.46	0.85	1.23	0.70	0.94	-3.75	0.65	0.88
14.2	13.5	11.8	0.6	83.10	0.90	0.10	0.95	0.87	-3.75	0.83	0.29
14.5	13.5	9.3	0.7	64.14	0.76	0.15	0.93	0.69	-3.75	0.64	0.19
21.4	13.5	8.0	0.6	37.38	0.61	1.48	0.63	0.59	-3.75	0.37	0.59
17.6	13.5	11.1	0.5	63.07	0.80	0.89	0.76	0.83	-3.75	0.63	0.64
15.1	13.4	8.3	0.7	54.97	0.70	0.32	0.89	0.62	-3.74	0.55	0.25
16.9	13.4	10.2	0.7	60.36	0.77	0.74	0.79	0.76	-3.74	0.60	0.52
15.3	13.4	10.0	0.5	65.36	0.79	0.40	0.88	0.75	-3.74	0.65	0.36
17.2	13.4	12.2	0.6	70.93	0.86	0.93	0.78	0.91	-3.74	0.71	0.76

A−axis	B−axis	C−axis	Roundness	Flatness	Sphericity	OP−index	b/a	c/b	B−axis phi	c/a	a−b/a−c
17.5	13.4	10.0	0.6	57.14	0.75	0.84	0.77	0.75	−3.74	0.57	0.55
16.0	13.4	9.5	0.6	59.38	0.75	0.54	0.84	0.71	−3.74	0.59	0.40
14.7	13.3	13.0	0.5	88.44	0.95	0.60	0.90	0.98	−3.73	0.88	0.82
20.0	13.3	13.0	0.6	65.00	0.86	1.36	0.67	0.98	−3.73	0.65	0.96
18.0	13.3	9.6	0.6	53.33	0.73	0.94	0.74	0.72	−3.73	0.53	0.56
16.7	13.3	8.7	0.6	52.10	0.70	0.70	0.80	0.65	−3.73	0.52	0.42
16.5	13.3	12.8	0.6	77.58	0.91	0.94	0.81	0.96	−3.73	0.78	0.86
17.8	13.3	10.8	0.8	60.67	0.79	0.94	0.75	0.81	−3.73	0.61	0.64
17.7	13.3	11.8	0.6	66.67	0.84	0.99	0.75	0.89	−3.73	0.67	0.75
19.3	13.3	8.3	0.6	43.01	0.65	1.16	0.69	0.62	−3.73	0.43	0.55
20.5	13.3	9.0	0.6	43.90	0.67	1.33	0.65	0.68	−3.73	0.44	0.63
17.2	13.3	9.6	0.6	55.81	0.74	0.80	0.77	0.72	−3.73	0.56	0.51
21.1	13.3	13.1	0.6	62.09	0.85	1.47	0.63	0.98	−3.73	0.62	0.98
17.2	13.3	9.6	0.7	55.81	0.74	0.80	0.77	0.72	−3.73	0.56	0.51
15.4	13.3	7.8	0.7	50.65	0.67	0.42	0.86	0.59	−3.73	0.51	0.28
15.1	13.3	9.9	0.8	65.56	0.79	0.38	0.88	0.74	−3.73	0.66	0.35
15.0	13.3	9.7	0.6	64.67	0.78	0.35	0.89	0.73	−3.73	0.65	0.32
27.0	13.2	10.9	0.7	40.37	0.69	2.05	0.49	0.83	−3.72	0.40	0.86
15.0	13.2	11.6	0.6	77.33	0.88	0.49	0.88	0.88	−3.72	0.77	0.53
20.2	13.2	7.4	0.6	36.63	0.59	1.39	0.65	0.56	−3.72	0.37	0.55
17.9	13.2	10.0	0.7	55.87	0.75	0.95	0.74	0.76	−3.72	0.56	0.59
16.4	13.2	11.0	0.6	67.07	0.82	0.75	0.80	0.83	−3.72	0.67	0.59
14.4	13.2	11.4	0.5	78.82	0.88	0.29	0.92	0.86	−3.72	0.79	0.39
16.1	13.2	11.5	0.7	71.43	0.85	0.73	0.82	0.87	−3.72	0.71	0.63
18.0	13.2	10.5	0.5	58.33	0.77	0.98	0.73	0.80	−3.72	0.58	0.64
16.3	13.2	8.5	0.6	52.15	0.70	0.64	0.81	0.64	−3.72	0.52	0.40
20.1	13.1	10.3	0.6	51.24	0.74	1.29	0.65	0.79	−3.71	0.51	0.71
19.6	13.0	9.5	0.6	48.47	0.71	1.25	0.66	0.73	−3.70	0.48	0.65
13.9	13.0	8.0	0.6	57.55	0.71	0.12	0.94	0.62	−3.70	0.58	0.15
25.4	13.0	12.2	0.6	48.03	0.77	1.88	0.51	0.94	−3.70	0.48	0.94
17.0	13.0	10.6	0.7	62.35	0.80	0.88	0.76	0.82	−3.70	0.62	0.63
20.2	13.0	9.9	0.7	49.01	0.72	1.33	0.64	0.76	−3.70	0.49	0.70
21.0	13.0	10.3	0.6	49.16	0.73	1.42	0.62	0.79	−3.70	0.49	0.75
17.0	13.0	11.3	0.6	66.47	0.83	0.92	0.76	0.87	−3.70	0.66	0.70
14.7	13.0	9.6	0.7	65.31	0.78	0.36	0.88	0.74	−3.70	0.65	0.33
16.0	13.0	10.9	0.7	68.13	0.83	0.72	0.81	0.84	−3.70	0.68	0.59
13.4	13.0	8.3	0.6	61.94	0.73	−0.03	0.97	0.64	−3.70	0.62	0.08
16.9	13.0	9.9	0.7	58.58	0.76	0.83	0.77	0.76	−3.70	0.59	0.56
16.4	13.0	12.8	0.6	78.05	0.92	1.03	0.79	0.98	−3.70	0.78	0.94
20.7	13.0	11.6	0.8	56.04	0.79	1.41	0.63	0.89	−3.70	0.56	0.85
17.8	13.0	7.2	0.6	40.45	0.61	1.00	0.73	0.55	−3.70	0.40	0.45
18.5	13.0	8.0	0.6	43.24	0.64	1.10	0.70	0.62	−3.70	0.43	0.52

A-axis	B-axis	C-axis	Roundness	Flatness	Sphericity	OP-index	b/a	c/b	B-axis phi	c/a	a-b/a-c
15.9	13.0	11.5	0.7	72.33	0.86	0.75	0.82	0.88	-3.70	0.72	0.66
18.0	13.0	9.4	0.6	52.22	0.72	1.00	0.72	0.72	-3.70	0.52	0.58
16.5	13.0	9.3	0.6	56.36	0.74	0.74	0.79	0.72	-3.70	0.56	0.49
13.1	13.0	8.0	0.6	61.30	0.72	-0.15	1.00	0.62	-3.70	0.61	0.01
16.1	13.0	12.0	0.6	74.53	0.88	0.85	0.81	0.92	-3.70	0.75	0.76
17.0	13.0	10.0	0.6	58.82	0.77	0.85	0.76	0.77	-3.70	0.59	0.57
13.8	12.9	9.6	0.7	69.57	0.80	0.14	0.93	0.74	-3.69	0.70	0.21
14.9	12.9	8.3	0.5	55.70	0.71	0.41	0.87	0.64	-3.69	0.56	0.30
15.5	12.9	8.3	0.6	53.55	0.70	0.54	0.83	0.64	-3.69	0.54	0.36
19.4	12.9	8.8	0.5	45.36	0.68	1.25	0.66	0.68	-3.69	0.45	0.61
14.5	12.9	8.3	0.6	57.24	0.72	0.31	0.89	0.64	-3.69	0.57	0.26
18.0	12.9	10.0	0.6	55.56	0.76	1.04	0.72	0.78	-3.69	0.56	0.64
18.3	12.9	9.5	0.7	51.91	0.73	1.07	0.70	0.74	-3.69	0.52	0.61
16.2	12.9	9.3	0.6	57.41	0.75	0.71	0.80	0.72	-3.69	0.57	0.48
15.7	12.9	10.8	0.9	68.79	0.83	0.68	0.82	0.84	-3.69	0.69	0.57
17.0	12.8	8.5	0.6	50.00	0.69	0.87	0.75	0.66	-3.68	0.50	0.49
20.2	12.8	10.9	0.7	53.96	0.77	1.37	0.63	0.85	-3.68	0.54	0.80
13.7	12.8	9.8	0.6	71.53	0.82	0.14	0.93	0.77	-3.68	0.72	0.23
15.0	12.8	12.5	0.6	83.33	0.93	0.82	0.85	0.98	-3.68	0.83	0.88
17.6	12.7	10.3	0.6	58.52	0.78	1.03	0.72	0.81	-3.67	0.59	0.67
15.5	12.7	7.8	0.5	50.32	0.68	0.59	0.82	0.61	-3.67	0.50	0.36
19.6	12.7	11.0	0.6	56.12	0.79	1.33	0.65	0.87	-3.67	0.56	0.80
16.5	12.7	8.8	0.7	53.33	0.72	0.80	0.77	0.69	-3.67	0.53	0.49
15.5	12.7	9.9	0.6	63.87	0.79	0.64	0.82	0.78	-3.67	0.64	0.50
15.0	12.7	12.0	0.7	80.00	0.91	0.75	0.85	0.94	-3.67	0.80	0.77
15.1	12.6	11.2	0.7	74.17	0.87	0.69	0.83	0.89	-3.66	0.74	0.64
17.6	12.6	9.4	0.6	53.41	0.74	1.03	0.72	0.75	-3.66	0.53	0.61
17.8	12.6	10.9	0.7	61.24	0.81	1.11	0.71	0.87	-3.66	0.61	0.75
15.2	12.6	9.5	0.6	62.50	0.78	0.59	0.83	0.75	-3.66	0.63	0.46
14.6	12.6	9.2	0.7	63.01	0.77	0.44	0.86	0.73	-3.66	0.63	0.37
18.8	12.5	8.9	0.7	47.34	0.70	1.24	0.66	0.71	-3.64	0.47	0.64
17.2	12.5	9.5	0.8	55.23	0.75	0.99	0.73	0.76	-3.64	0.55	0.61
18.3	12.5	9.5	0.7	51.91	0.73	1.16	0.68	0.76	-3.64	0.52	0.66
16.1	12.5	10.1	0.8	62.73	0.80	0.82	0.78	0.81	-3.64	0.63	0.60
16.8	12.5	11.3	0.7	67.26	0.85	1.03	0.74	0.90	-3.64	0.67	0.78
15.8	12.5	10.3	0.6	65.19	0.81	0.78	0.79	0.82	-3.64	0.65	0.60
18.0	12.5	10.0	0.5	55.56	0.76	1.13	0.69	0.80	-3.64	0.56	0.69
14.0	12.5	10.5	0.7	75.00	0.86	0.38	0.89	0.84	-3.64	0.75	0.43
15.0	12.5	9.3	0.6	62.00	0.77	0.57	0.83	0.74	-3.64	0.62	0.44
17.6	12.5	10.0	0.6	56.82	0.77	1.07	0.71	0.80	-3.64	0.57	0.67
17.0	12.5	9.4	0.6	55.29	0.75	0.95	0.74	0.75	-3.64	0.55	0.59
15.5	12.5	8.9	0.6	57.42	0.74	0.66	0.81	0.71	-3.64	0.57	0.45

A-axis	B-axis	C-axis	Roundness	Flatness	Sphericity	OP-index	b/a	c/b	B-axis phi	c/a	a-b/a-c
21.7	12.4	10.9	0.8	50.23	0.76	1.62	0.57	0.88	−3.63	0.50	0.86
14.8	12.4	8.7	0.6	58.78	0.74	0.53	0.84	0.70	−3.63	0.59	0.39
19.0	12.4	11.6	0.6	61.05	0.83	1.35	0.65	0.94	−3.63	0.61	0.89
22.5	12.4	10.9	0.6	48.44	0.75	1.71	0.55	0.88	−3.63	0.48	0.87
20.9	12.4	8.5	0.8	40.67	0.65	1.59	0.59	0.69	−3.63	0.41	0.69
14.2	12.4	9.5	0.8	66.90	0.80	0.41	0.87	0.77	−3.63	0.67	0.38
20.0	12.4	10.0	0.7	50.00	0.74	1.42	0.62	0.81	−3.63	0.50	0.76
16.6	12.4	7.8	0.6	46.99	0.67	0.89	0.75	0.63	−3.63	0.47	0.48
19.9	12.3	11.9	0.6	59.80	0.83	1.48	0.62	0.97	−3.62	0.60	0.95
17.5	12.3	11.0	0.6	62.86	0.83	1.15	0.70	0.89	−3.62	0.63	0.80
15.6	12.3	9.8	0.5	62.82	0.79	0.77	0.79	0.80	−3.62	0.63	0.57
16.4	12.3	5.4	0.6	33.03	0.53	0.98	0.75	0.44	−3.62	0.33	0.37
16.9	12.3	8.2	0.6	48.52	0.69	0.97	0.73	0.67	−3.62	0.49	0.53
17.6	12.3	9.9	0.6	56.25	0.77	1.11	0.70	0.80	−3.62	0.56	0.69
17.9	12.3	9.4	0.7	52.51	0.74	1.14	0.69	0.76	−3.62	0.53	0.66
17.5	12.3	9.0	0.8	51.43	0.72	1.08	0.70	0.73	−3.62	0.51	0.61
18.0	12.3	10.9	0.6	60.56	0.81	1.21	0.68	0.89	−3.62	0.61	0.80
17.2	12.3	8.2	0.5	47.67	0.68	1.03	0.72	0.67	−3.62	0.48	0.54
16.5	12.3	7.3	0.6	44.24	0.64	0.91	0.75	0.59	−3.62	0.44	0.46
22.3	12.3	11.0	0.5	49.33	0.76	1.70	0.55	0.89	−3.62	0.49	0.88
14.2	12.3	9.2	0.7	64.79	0.79	0.43	0.87	0.75	−3.62	0.65	0.38
19.5	12.2	10.9	0.7	55.90	0.79	1.41	0.63	0.89	−3.61	0.56	0.85
13.3	12.2	8.3	0.9	62.41	0.75	0.19	0.92	0.68	−3.61	0.62	0.22
15.0	12.2	9.3	0.6	62.00	0.78	0.65	0.81	0.76	−3.61	0.62	0.49
16.4	12.2	8.4	0.6	51.22	0.71	0.90	0.74	0.69	−3.61	0.51	0.53
15.4	12.2	9.5	0.6	61.69	0.78	0.74	0.79	0.78	−3.61	0.62	0.54
14.4	12.2	7.9	0.7	54.86	0.71	0.48	0.85	0.65	−3.61	0.55	0.34
14.8	12.2	7.4	0.7	50.00	0.67	0.57	0.82	0.61	−3.61	0.50	0.35
19.2	12.2	10.0	0.8	52.08	0.75	1.36	0.64	0.82	−3.61	0.52	0.76
13.4	12.2	9.6	0.7	71.64	0.83	0.26	0.91	0.79	−3.61	0.72	0.32
13.0	12.0	8.8	0.7	67.69	0.79	0.18	0.92	0.73	−3.58	0.68	0.24
18.0	12.0	8.7	0.6	48.33	0.71	1.22	0.67	0.73	−3.58	0.48	0.65
17.2	12.0	10.0	0.8	58.14	0.79	1.12	0.70	0.83	−3.58	0.58	0.72
21.4	12.0	11.4	0.6	53.27	0.80	1.67	0.56	0.95	−3.58	0.53	0.94
19.0	12.0	11.9	0.6	62.63	0.85	1.46	0.63	0.99	−3.58	0.63	0.99
12.3	12.0	8.7	0.6	70.73	0.80	−0.08	0.98	0.73	−3.58	0.71	0.08
15.4	12.0	8.9	0.6	57.79	0.75	0.77	0.78	0.74	−3.58	0.58	0.52
13.8	12.0	11.1	0.5	80.43	0.91	0.60	0.87	0.93	−3.58	0.80	0.67
15.0	12.0	8.6	0.6	57.33	0.74	0.68	0.80	0.72	−3.58	0.57	0.47
15.4	12.0	5.1	0.6	33.12	0.52	0.85	0.78	0.43	−3.58	0.33	0.33
14.3	12.0	10.5	0.6	73.43	0.86	0.65	0.84	0.88	−3.58	0.73	0.61
13.3	12.0	9.9	0.6	74.44	0.85	0.32	0.90	0.83	−3.58	0.74	0.38

A−axis	B−axis	C−axis	Roundness	Flatness	Sphericity	OP−index	b/a	c/b	B−axis phi	c/a	a−b/a−c
14.9	12.0	9.6	0.7	64.43	0.80	0.70	0.81	0.80	−3.58	0.64	0.55
21.4	12.0	10.2	0.7	47.66	0.74	1.67	0.56	0.85	−3.58	0.48	0.84
19.6	12.0	11.9	0.5	60.71	0.84	1.52	0.61	0.99	−3.58	0.61	0.99
15.3	12.0	8.6	0.6	56.21	0.74	0.74	0.78	0.72	−3.58	0.56	0.49
14.4	12.0	9.3	0.7	64.58	0.79	0.58	0.83	0.78	−3.58	0.65	0.47
14.1	11.9	6.3	0.6	44.68	0.62	0.49	0.84	0.53	−3.57	0.45	0.28
20.5	11.9	10.2	0.5	49.76	0.75	1.58	0.58	0.86	−3.57	0.50	0.83
17.2	11.9	8.3	0.6	48.26	0.70	1.12	0.69	0.70	−3.57	0.48	0.60
14.0	11.9	8.0	0.6	57.14	0.73	0.47	0.85	0.67	−3.57	0.57	0.35
15.5	11.9	9.2	0.6	59.35	0.77	0.83	0.77	0.77	−3.57	0.59	0.57
12.6	11.9	7.8	0.5	61.90	0.74	0.07	0.94	0.66	−3.57	0.62	0.15
14.4	11.9	9.3	0.6	64.58	0.80	0.61	0.83	0.78	−3.57	0.65	0.49
15.0	11.9	9.9	0.6	66.00	0.82	0.77	0.79	0.83	−3.57	0.66	0.61
23.6	11.9	11.6	0.7	49.15	0.78	1.90	0.50	0.97	−3.57	0.49	0.98
12.9	11.9	8.9	0.9	68.99	0.80	0.18	0.92	0.75	−3.57	0.69	0.25
19.0	11.9	10.9	0.7	57.37	0.81	1.42	0.63	0.92	−3.57	0.57	0.88
22.0	11.9	8.5	0.7	38.64	0.65	1.84	0.54	0.71	−3.57	0.39	0.75
22.3	11.9	10.9	0.8	48.88	0.77	1.78	0.53	0.92	−3.57	0.49	0.91
14.8	11.9	6.3	0.7	42.57	0.61	0.66	0.80	0.53	−3.57	0.43	0.34
14.5	11.8	7.2	0.6	49.66	0.67	0.61	0.81	0.61	−3.56	0.50	0.37
15.0	11.8	8.3	0.6	55.33	0.73	0.73	0.79	0.70	−3.56	0.55	0.48
18.4	11.8	10.9	0.7	59.24	0.82	1.37	0.64	0.92	−3.56	0.59	0.88
15.2	11.8	10.0	0.6	65.79	0.82	0.85	0.78	0.85	−3.56	0.66	0.65
15.4	11.8	10.0	0.6	64.94	0.82	0.88	0.77	0.85	−3.56	0.65	0.67
15.9	11.8	10.9	0.5	68.55	0.86	1.05	0.74	0.92	−3.56	0.69	0.82
13.9	11.8	8.2	0.6	58.99	0.74	0.48	0.85	0.69	−3.56	0.59	0.37
12.6	11.7	11.0	0.6	87.30	0.94	0.29	0.93	0.94	−3.55	0.87	0.56
29.8	11.7	9.3	0.6	31.21	0.63	2.76	0.39	0.80	−3.54	0.31	0.89
15.5	11.6	10.5	0.6	67.74	0.85	1.00	0.75	0.91	−3.54	0.68	0.78
12.3	11.6	9.2	0.7	74.80	0.84	0.09	0.94	0.79	−3.54	0.75	0.23
16.6	11.6	9.0	0.7	54.22	0.75	1.09	0.70	0.78	−3.54	0.54	0.66
16.2	11.6	7.9	0.7	48.77	0.69	1.01	0.72	0.68	−3.54	0.49	0.55
16.6	11.6	10.9	0.7	65.66	0.85	1.20	0.70	0.94	−3.54	0.66	0.88
16.2	11.6	7.4	0.6	45.68	0.66	1.02	0.72	0.64	−3.54	0.46	0.52
15.0	11.6	7.3	0.6	48.67	0.67	0.77	0.77	0.63	−3.54	0.49	0.44
13.1	11.5	10.4	0.8	79.39	0.90	0.51	0.88	0.90	−3.52	0.79	0.59
17.3	11.5	8.2	0.6	47.40	0.70	1.23	0.66	0.71	−3.52	0.47	0.64
15.4	11.5	7.8	0.6	50.65	0.70	0.88	0.75	0.68	−3.52	0.51	0.51
19.0	11.5	8.0	0.7	42.11	0.66	1.51	0.61	0.70	−3.52	0.42	0.68
15.2	11.5	11.1	0.6	73.03	0.89	1.07	0.76	0.97	−3.52	0.73	0.90
15.1	11.5	10.0	0.7	66.23	0.83	0.92	0.76	0.87	−3.52	0.66	0.71
15.3	11.5	9.8	0.5	64.05	0.82	0.94	0.75	0.85	−3.52	0.64	0.69

A−axis	B−axis	C−axis	Roundness	Flatness	Sphericity	OP−index	b/a	c/b	B−axis phi	c/a	a−b/a−c
12.2	11.5	9.7	0.6	79.51	0.88	0.10	0.94	0.84	−3.52	0.80	0.28
22.2	11.5	10.1	0.7	45.50	0.74	1.85	0.52	0.88	−3.52	0.45	0.88
14.6	11.5	9.4	0.6	64.38	0.81	0.78	0.79	0.82	−3.52	0.64	0.60
15.5	11.5	9.4	0.8	60.65	0.79	0.96	0.74	0.82	−3.52	0.61	0.66
14.3	11.4	9.0	0.6	62.94	0.79	0.72	0.80	0.79	−3.51	0.63	0.55
12.2	11.4	9.0	0.7	73.77	0.84	0.13	0.93	0.79	−3.51	0.74	0.25
12.5	11.4	8.3	0.7	66.40	0.78	0.22	0.91	0.73	−3.51	0.66	0.26
15.3	11.4	8.9	0.7	58.17	0.77	0.91	0.75	0.78	−3.51	0.58	0.61
11.6	11.4	10.9	0.6	93.97	0.96	−0.46	0.98	0.96	−3.51	0.94	0.29
15.2	11.4	10.9	0.6	71.71	0.88	1.07	0.75	0.96	−3.51	0.72	0.88
15.0	11.3	7.0	0.7	46.67	0.66	0.86	0.75	0.62	−3.50	0.47	0.46
15.0	11.3	9.3	0.7	62.00	0.80	0.91	0.75	0.82	−3.50	0.62	0.65
15.0	11.3	8.3	0.7	55.33	0.74	0.86	0.75	0.73	−3.50	0.55	0.55
16.6	11.3	6.8	0.6	40.96	0.63	1.20	0.68	0.60	−3.50	0.41	0.54
16.4	11.3	8.8	0.7	53.66	0.75	1.13	0.69	0.78	−3.50	0.54	0.67
14.4	11.3	8.5	0.5	59.03	0.76	0.75	0.78	0.75	−3.50	0.59	0.53
15.9	11.3	10.7	0.7	67.30	0.86	1.17	0.71	0.95	−3.50	0.67	0.88
17.4	11.2	10.9	0.6	62.64	0.85	1.40	0.64	0.97	−3.49	0.63	0.95
15.8	11.2	9.8	0.7	62.03	0.82	1.10	0.71	0.88	−3.49	0.62	0.77
12.3	11.2	7.0	0.6	56.91	0.71	0.20	0.91	0.63	−3.49	0.57	0.21
13.3	11.2	7.4	0.7	55.64	0.72	0.49	0.84	0.66	−3.49	0.56	0.36
15.1	11.2	8.9	0.7	58.94	0.78	0.93	0.74	0.79	−3.49	0.59	0.63
14.1	11.2	8.0	0.6	56.74	0.74	0.69	0.79	0.71	−3.49	0.57	0.48
15.8	11.2	8.2	0.4	51.90	0.72	1.04	0.71	0.73	−3.49	0.52	0.61
20.2	11.2	9.6	0.7	47.52	0.74	1.69	0.55	0.86	−3.49	0.48	0.85
16.6	11.2	7.6	0.5	45.78	0.68	1.19	0.67	0.68	−3.49	0.46	0.60
14.4	11.2	9.6	0.6	66.67	0.83	0.84	0.78	0.86	−3.49	0.67	0.67
17.1	11.2	10.1	0.4	59.06	0.81	1.31	0.65	0.90	−3.49	0.59	0.84
15.2	11.2	8.3	0.6	54.61	0.74	0.93	0.74	0.74	−3.49	0.55	0.58
15.2	11.2	8.0	0.5	52.63	0.72	0.92	0.74	0.71	−3.49	0.53	0.56
14.9	11.2	10.5	0.6	70.47	0.87	1.03	0.75	0.94	−3.49	0.70	0.84
15.4	11.1	8.3	0.6	53.90	0.74	0.99	0.72	0.75	−3.47	0.54	0.61
11.2	11.1	8.3	0.7	74.11	0.82	−0.19	0.99	0.75	−3.47	0.74	0.03
12.2	11.1	9.8	0.6	80.33	0.89	0.31	0.91	0.88	−3.47	0.80	0.46
18.4	11.1	8.0	0.4	43.21	0.68	1.51	0.60	0.72	−3.47	0.43	0.70
12.9	11.0	8.8	0.7	68.22	0.82	0.50	0.85	0.80	−3.46	0.68	0.46
14.2	11.0	8.5	0.7	59.86	0.77	0.79	0.77	0.77	−3.46	0.60	0.56
14.3	11.0	8.5	0.6	59.44	0.77	0.81	0.77	0.77	−3.46	0.59	0.57
26.1	11.0	9.3	0.6	35.63	0.67	2.44	0.42	0.85	−3.46	0.36	0.90
17.7	11.0	10.6	0.5	59.89	0.83	1.46	0.62	0.96	−3.46	0.60	0.94
16.9	11.0	10.2	0.5	60.36	0.82	1.34	0.65	0.93	−3.46	0.60	0.88
11.6	11.0	11.0	0.6	94.83	0.98	0.18	0.95	1.00	−3.46	0.95	1.00

A−axis	B−axis	C−axis	Roundness	Flatness	Sphericity	OP−index	b/a	c/b	B−axis phi	c/a	a−b/a−c
18.0	11.0	9.5	0.6	52.78	0.77	1.45	0.61	0.86	−3.46	0.53	0.82
15.0	11.0	8.9	0.6	59.33	0.78	0.97	0.73	0.81	−3.46	0.59	0.66
15.8	11.0	9.7	0.8	61.39	0.82	1.15	0.70	0.88	−3.46	0.61	0.79
16.2	11.0	7.0	0.6	43.21	0.65	1.18	0.68	0.64	−3.46	0.43	0.57
20.3	11.0	10.9	0.6	53.69	0.81	1.74	0.54	0.99	−3.46	0.54	0.99
14.1	10.9	9.5	0.6	67.38	0.84	0.87	0.77	0.87	−3.45	0.67	0.70
15.2	10.9	9.9	0.7	65.13	0.84	1.10	0.72	0.91	−3.45	0.65	0.81
11.9	10.9	8.0	0.7	67.23	0.79	0.19	0.92	0.73	−3.45	0.67	0.26
22.0	10.9	10.0	0.5	45.45	0.75	1.94	0.50	0.92	−3.45	0.45	0.93
20.5	10.9	9.7	0.6	47.32	0.75	1.78	0.53	0.89	−3.45	0.47	0.89
15.3	10.9	10.5	0.7	68.63	0.87	1.18	0.71	0.96	−3.45	0.69	0.92
15.0	10.9	8.5	0.6	56.67	0.76	0.98	0.73	0.78	−3.45	0.57	0.63
15.4	10.9	9.6	0.5	62.34	0.82	1.11	0.71	0.88	−3.45	0.62	0.78
12.8	10.9	10.8	0.5	84.38	0.94	0.83	0.85	0.99	−3.45	0.84	0.95
17.8	10.8	9.0	0.6	50.56	0.75	1.46	0.61	0.83	−3.43	0.51	0.80
13.1	10.8	8.2	0.7	62.60	0.78	0.59	0.82	0.76	−3.43	0.63	0.47
17.6	10.8	8.0	0.6	45.45	0.70	1.44	0.61	0.74	−3.43	0.45	0.71
15.8	10.7	8.2	0.7	51.90	0.74	1.17	0.68	0.77	−3.42	0.52	0.67
20.5	10.7	8.3	0.6	40.49	0.68	1.88	0.52	0.78	−3.42	0.40	0.80
15.3	10.6	9.3	0.7	60.78	0.81	1.15	0.69	0.88	−3.41	0.61	0.78
13.5	10.5	8.0	0.7	59.26	0.77	0.77	0.78	0.76	−3.39	0.59	0.55
15.5	10.5	7.3	0.5	47.10	0.69	1.17	0.68	0.70	−3.39	0.47	0.61
14.9	10.5	9.0	0.7	60.40	0.80	1.09	0.70	0.86	−3.39	0.60	0.75
12.0	10.5	8.9	0.7	74.17	0.86	0.43	0.88	0.85	−3.39	0.74	0.48
11.0	10.5	8.2	0.7	74.55	0.83	0.00	0.95	0.78	−3.39	0.75	0.18
14.9	10.5	8.5	0.6	57.05	0.77	1.07	0.70	0.81	−3.39	0.57	0.69
15.2	10.5	9.2	0.7	60.53	0.81	1.16	0.69	0.88	−3.39	0.61	0.78
12.2	10.4	6.6	0.6	54.10	0.70	0.43	0.85	0.63	−3.38	0.54	0.32
17.3	10.4	10.0	0.8	57.80	0.82	1.52	0.60	0.96	−3.38	0.58	0.95
15.9	10.3	9.5	0.8	59.75	0.82	1.33	0.65	0.92	−3.36	0.60	0.88
14.4	10.3	9.8	0.6	68.06	0.87	1.15	0.72	0.95	−3.36	0.68	0.89
19.1	10.3	9.9	0.6	51.83	0.79	1.74	0.54	0.96	−3.36	0.52	0.96
18.2	10.3	9.0	0.7	49.45	0.76	1.63	0.57	0.87	−3.36	0.49	0.86
12.3	10.2	9.6	0.8	78.05	0.90	0.76	0.83	0.94	−3.35	0.78	0.78
14.3	10.2	7.0	0.6	48.95	0.70	1.01	0.71	0.69	−3.35	0.49	0.56
16.7	10.2	9.9	0.7	59.28	0.83	1.49	0.61	0.97	−3.35	0.59	0.96
12.2	10.2	9.4	0.7	77.05	0.89	0.70	0.84	0.92	−3.35	0.77	0.71
12.2	10.2	9.9	0.6	95.08	1.03	2.63	0.84	1.14	−3.35	0.95	3.33
11.6	10.1	7.2	0.5	62.07	0.76	0.37	0.87	0.71	−3.34	0.62	0.34
16.9	10.0	8.2	0.5	48.52	0.74	1.52	0.59	0.82	−3.32	0.49	0.79
13.9	10.0	8.2	0.8	58.99	0.79	1.01	0.72	0.82	−3.32	0.59	0.68
13.0	10.0	7.5	0.6	57.69	0.76	0.79	0.77	0.75	−3.32	0.58	0.55

A-axis	B-axis	C-axis	Roundness	Flatness	Sphericity	OP-index	b/a	c/b	B-axis phi	c/a	a-b/a-c
11.0	10.0	8.2	0.6	74.55	0.85	0.24	0.91	0.82	−3.32	0.75	0.36
13.6	10.0	9.6	0.7	70.59	0.88	1.10	0.74	0.96	−3.32	0.71	0.90
15.0	10.0	7.7	0.8	51.33	0.73	1.20	0.67	0.77	−3.32	0.51	0.68
16.6	10.0	9.0	0.7	54.22	0.79	1.48	0.60	0.90	−3.32	0.54	0.87
15.9	10.0	6.5	0.8	40.88	0.64	1.41	0.63	0.65	−3.32	0.41	0.63
12.2	10.0	7.3	0.7	59.84	0.76	0.58	0.82	0.73	−3.32	0.60	0.45
12.0	10.0	9.8	0.7	81.67	0.93	0.83	0.83	0.98	−3.32	0.82	0.91
14.8	10.0	8.9	0.7	60.14	0.81	1.21	0.68	0.89	−3.32	0.60	0.81
17.3	10.0	7.9	0.7	45.66	0.71	1.58	0.58	0.79	−3.32	0.46	0.78
13.2	10.0	9.8	0.7	74.24	0.90	1.07	0.76	0.98	−3.32	0.74	0.94
13.5	9.9	8.2	0.7	60.74	0.80	0.96	0.73	0.83	−3.31	0.61	0.68
15.0	9.9	8.5	0.8	56.67	0.79	1.25	0.66	0.86	−3.31	0.57	0.78
12.1	9.9	8.3	0.7	68.60	0.83	0.65	0.82	0.84	−3.31	0.69	0.58
16.7	9.9	9.1	0.7	54.49	0.79	1.52	0.59	0.92	−3.31	0.54	0.89
20.2	9.9	8.7	0.5	43.07	0.72	1.98	0.49	0.88	−3.31	0.43	0.90
17.2	9.9	8.8	0.8	51.16	0.77	1.58	0.58	0.89	−3.31	0.51	0.87
16.2	9.9	7.6	0.7	46.91	0.71	1.44	0.61	0.77	−3.31	0.47	0.73
17.2	9.9	7.3	0.7	42.44	0.68	1.62	0.58	0.74	−3.31	0.42	0.74
19.2	9.9	7.3	0.7	38.02	0.65	1.94	0.52	0.74	−3.31	0.38	0.78
15.1	9.9	8.7	0.7	57.62	0.80	1.27	0.66	0.88	−3.31	0.58	0.81
13.0	9.8	7.3	0.7	56.15	0.75	0.84	0.75	0.74	−3.29	0.56	0.56
17.3	9.8	8.4	0.6	48.55	0.75	1.62	0.57	0.86	−3.29	0.49	0.84
16.0	9.8	8.8	0.5	55.00	0.79	1.44	0.61	0.90	−3.29	0.55	0.86
18.5	9.8	7.2	0.6	38.92	0.66	1.86	0.53	0.73	−3.29	0.39	0.77
16.4	9.8	7.3	0.6	44.51	0.69	1.51	0.60	0.74	−3.29	0.45	0.73
11.7	9.8	7.3	0.7	62.39	0.77	0.51	0.84	0.74	−3.29	0.62	0.43
13.0	9.7	8.2	0.7	63.08	0.81	0.92	0.75	0.85	−3.28	0.63	0.69
13.8	9.7	6.7	0.5	48.55	0.69	1.04	0.70	0.69	−3.28	0.49	0.58
15.0	9.7	6.9	0.7	46.00	0.69	1.29	0.65	0.71	−3.28	0.46	0.65
15.3	9.7	8.3	0.7	54.10	0.77	1.35	0.63	0.85	−3.27	0.54	0.80
15.2	9.6	8.4	0.7	55.26	0.78	1.36	0.63	0.88	−3.26	0.55	0.82
13.2	9.6	9.0	0.7	68.18	0.86	1.08	0.73	0.94	−3.26	0.68	0.86
16.3	9.6	7.3	0.6	44.79	0.70	1.54	0.59	0.76	−3.26	0.45	0.74
13.0	9.5	6.9	0.7	53.08	0.73	0.93	0.73	0.73	−3.25	0.53	0.57
14.2	9.4	7.1	0.7	50.00	0.72	1.21	0.66	0.76	−3.23	0.50	0.68
19.3	9.4	8.3	0.7	43.01	0.72	1.99	0.49	0.88	−3.23	0.43	0.90
15.0	9.4	8.3	0.5	55.33	0.79	1.38	0.63	0.88	−3.23	0.55	0.84
13.0	9.4	7.9	0.7	60.77	0.80	1.00	0.72	0.84	−3.23	0.61	0.71
18.0	9.4	6.3	0.7	35.00	0.62	1.98	0.52	0.67	−3.23	0.35	0.74
14.4	9.3	7.2	0.6	50.00	0.73	1.28	0.65	0.77	−3.22	0.50	0.71
12.9	9.2	6.8	0.6	52.71	0.73	1.00	0.71	0.74	−3.20	0.53	0.61
13.1	9.2	8.9	0.8	67.94	0.87	1.19	0.70	0.97	−3.20	0.68	0.93

A-axis	B-axis	C-axis	Roundness	Flatness	Sphericity	OP-index	b/a	c/b	B-axis phi	c/a	a-b/a-c
18.3	9.1	5.9	0.5	32.24	0.59	2.18	0.50	0.65	-3.19	0.32	0.74
13.3	9.1	7.2	0.7	54.14	0.75	1.12	0.68	0.79	-3.19	0.54	0.69
14.9	9.0	6.4	0.6	42.62	0.67	1.48	0.60	0.71	-3.17	0.43	0.69
11.5	9.0	7.9	0.7	68.70	0.84	0.81	0.78	0.88	-3.17	0.69	0.69
10.2	8.9	7.9	0.7	77.45	0.88	0.45	0.87	0.89	-3.15	0.77	0.57
12.0	8.9	6.9	0.7	57.50	0.76	0.89	0.74	0.78	-3.15	0.58	0.61
10.0	8.9	7.9	0.8	79.00	0.89	0.36	0.89	0.89	-3.15	0.79	0.52
13.9	8.8	4.9	0.6	35.25	0.58	1.45	0.63	0.56	-3.14	0.35	0.57
11.1	8.7	7.4	0.5	66.67	0.83	0.77	0.78	0.85	-3.12	0.67	0.65
15.8	8.3	6.8	0.6	43.04	0.71	1.81	0.53	0.82	-3.05	0.43	0.83
12.2	8.3	5.4	0.7	44.26	0.66	1.13	0.68	0.65	-3.05	0.44	0.57
10.2	8.3	7.9	0.8	77.45	0.90	0.79	0.81	0.95	-3.05	0.77	0.83
13.2	8.0	7.2	0.6	54.55	0.79	1.44	0.61	0.90	-3.00	0.55	0.87
9.0	7.7	7.6	0.7	83.89	0.94	0.70	0.85	0.99	-2.94	0.84	0.93
11.4	7.5	7.0	0.8	61.40	0.83	1.26	0.66	0.93	-2.91	0.61	0.89

Appendix (XII) (i)

PEBBLE DATA ROODERAND CONGLOMERATE FORMATION WITKOP 475

A-axis	B-axis	C-axis	Roundness	Flatness	Sphericity	OP-index	b/a	c/b	B-axis phi	c/a	a-b/a-c
37.3	16.2	11.2	0.6	30.03	0.59	2.63	0.43	0.69	-4.02	0.30	0.81
14.9	10.2	7.2	0.7	48.32	0.70	1.13	0.68	0.71	-3.35	0.48	0.61
19.5	14.1	11.6	0.7	59.49	0.79	1.04	0.72	0.82	-3.82	0.59	0.68
21.2	14.0	11.8	0.7	55.66	0.78	1.28	0.66	0.84	-3.81	0.56	0.77
20.3	13.2	7.1	0.7	34.98	0.57	1.43	0.65	0.54	-3.72	0.35	0.54
15.7	11.8	7.4	0.7	47.13	0.67	0.87	0.75	0.63	-3.56	0.47	0.47
16.6	8.9	8.3	0.6	50.00	0.78	1.73	0.54	0.93	-3.15	0.50	0.93
14.3	12.5	12.3	0.6	86.01	0.95	0.76	0.87	0.98	-3.64	0.86	0.90
12.1	10.7	9.6	0.6	79.34	0.89	0.45	0.88	0.90	-3.42	0.79	0.56
19.6	14.6	12.5	0.6	63.78	0.82	0.99	0.74	0.86	-3.87	0.64	0.70
18.7	11.1	9.4	0.7	50.27	0.75	1.52	0.59	0.85	-3.47	0.50	0.82
9.6	8.3	6.7	0.7	69.79	0.83	0.40	0.86	0.81	-3.05	0.70	0.45
14.5	10.8	8.6	0.7	59.31	0.78	0.91	0.74	0.80	-3.43	0.59	0.63
19.8	12.7	12.6	0.8	63.64	0.86	1.44	0.64	0.99	-3.67	0.64	0.99
17.5	11.6	11.2	0.8	64.00	0.85	1.34	0.66	0.97	-3.54	0.64	0.94
25.2	17.3	13.1	0.6	51.98	0.73	1.18	0.69	0.76	-4.11	0.52	0.65
26.4	16.2	14.4	0.6	54.55	0.79	1.48	0.61	0.89	-4.02	0.55	0.85
17.6	12.1	9.0	0.5	51.14	0.72	1.14	0.69	0.74	-3.60	0.51	0.64
13.3	12.5	8.2	0.6	61.65	0.74	0.10	0.94	0.66	-3.64	0.62	0.16
20.5	13.8	12.2	0.7	59.51	0.81	1.26	0.67	0.88	-3.79	0.60	0.81
20.6	13.4	8.8	0.5	42.72	0.65	1.33	0.65	0.66	-3.74	0.43	0.61
12.1	10.0	7.6	0.8	62.81	0.78	0.57	0.83	0.76	-3.32	0.63	0.47
13.5	9.6	9.1	0.7	67.41	0.86	1.15	0.71	0.95	-3.26	0.67	0.89
16.2	13.9	8.2	0.5	50.62	0.67	0.44	0.86	0.59	-3.80	0.51	0.29
16.8	13.8	10.3	0.7	61.31	0.77	0.63	0.82	0.75	-3.79	0.61	0.46
18.0	11.4	10.1	0.5	56.11	0.79	1.38	0.63	0.89	-3.51	0.56	0.84
15.8	10.8	10.8	0.7	68.35	0.88	1.32	0.68	1.00	-3.43	0.68	1.00
14.6	12.4	8.6	0.6	58.90	0.74	0.48	0.85	0.69	-3.63	0.59	0.37
13.9	11.7	10.5	0.8	75.54	0.88	0.66	0.84	0.90	-3.55	0.76	0.65
12.9	12.4	7.2	0.6	55.81	0.69	0.00	0.96	0.58	-3.63	0.56	0.09
20.5	11.6	10.3	0.6	50.24	0.76	1.64	0.57	0.89	-3.54	0.50	0.87
16.4	14.3	10.4	0.6	63.41	0.77	0.42	0.87	0.73	-3.84	0.63	0.35
17.6	10.9	7.5	0.6	42.61	0.66	1.44	0.62	0.69	-3.45	0.43	0.66
21.1	12.1	7.4	0.5	35.07	0.60	1.77	0.57	0.61	-3.60	0.35	0.66
14.8	10.1	7.1	0.7	47.97	0.70	1.14	0.68	0.70	-3.34	0.48	0.61
17.6	14.2	7.0	0.5	39.77	0.58	0.69	0.81	0.49	-3.83	0.40	0.32
15.7	10.4	8.2	0.7	52.23	0.74	1.23	0.66	0.79	-3.38	0.52	0.71

A-axis	B-axis	C-axis	Roundness	Flatness	Sphericity	OP-index	b/a	c/b	B-axis phi	c/a	a-b/a-c
17.5	12.3	10.9	0.7	62.29	0.82	1.14	0.70	0.89	-3.62	0.62	0.79
16.7	10.6	9.9	0.7	59.28	0.82	1.39	0.63	0.93	-3.41	0.59	0.90
12.9	7.2	6.6	0.8	51.16	0.78	1.61	0.56	0.92	-2.85	0.51	0.90
13.7	10.1	9.4	0.7	68.61	0.86	1.05	0.74	0.93	-3.34	0.69	0.84
17.0	13.3	8.8	0.7	51.76	0.70	0.75	0.78	0.66	-3.73	0.52	0.45
15.5	14.8	11.2	0.6	72.26	0.82	0.06	0.95	0.76	-3.89	0.72	0.16
14.5	13.0	11.0	0.7	75.86	0.86	0.38	0.90	0.85	-3.70	0.76	0.43
11.7	9.4	8.2	0.7	70.09	0.85	0.73	0.80	0.87	-3.23	0.70	0.66
16.4	11.0	9.3	0.7	56.71	0.78	1.22	0.67	0.85	-3.46	0.57	0.76
15.3	10.7	9.2	0.8	60.13	0.80	1.12	0.70	0.86	-3.42	0.60	0.75
17.2	14.3	10.0	0.6	58.14	0.74	0.57	0.83	0.70	-3.84	0.58	0.40
13.7	11.3	7.3	0.7	53.28	0.70	0.56	0.82	0.65	-3.50	0.53	0.37
20.5	11.0	9.9	0.7	48.29	0.76	1.76	0.54	0.90	-3.46	0.48	0.90
14.0	11.6	7.8	0.7	55.71	0.72	0.55	0.83	0.67	-3.54	0.56	0.39
18.2	11.3	8.5	0.7	46.70	0.71	1.41	0.62	0.75	-3.50	0.47	0.71
15.4	12.6	11.0	0.8	71.43	0.85	0.73	0.82	0.87	-3.66	0.71	0.64
19.7	14.3	10.2	0.5	51.78	0.72	1.00	0.73	0.71	-3.84	0.52	0.57
17.0	11.7	9.8	0.5	57.65	0.78	1.16	0.69	0.84	-3.55	0.58	0.74
12.6	12.3	9.2	0.7	73.02	0.82	-0.08	0.98	0.75	-3.62	0.73	0.09
17.7	14.6	10.8	0.7	61.02	0.77	0.62	0.82	0.74	-3.87	0.61	0.45
18.4	11.9	8.3	0.7	45.11	0.68	1.32	0.65	0.70	-3.57	0.45	0.64
11.3	9.7	9.0	0.5	79.65	0.90	0.60	0.86	0.93	-3.28	0.80	0.70
10.3	10.0	8.2	0.8	79.61	0.87	-0.12	0.97	0.82	-3.32	0.80	0.14
14.7	12.6	8.4	0.8	57.14	0.72	0.44	0.86	0.67	-3.66	0.57	0.33
19.4	14.5	9.7	0.6	50.00	0.69	0.91	0.75	0.67	-3.86	0.50	0.51
14.5	13.0	10.3	0.7	71.03	0.83	0.34	0.90	0.79	-3.70	0.71	0.36
17.3	10.7	8.0	0.5	46.24	0.70	1.42	0.62	0.75	-3.42	0.46	0.71
16.3	11.1	9.3	0.7	57.06	0.78	1.18	0.68	0.84	-3.47	0.57	0.74
15.6	10.3	7.0	0.6	44.87	0.67	1.24	0.66	0.68	-3.36	0.45	0.62
17.3	13.7	8.8	0.7	50.87	0.69	0.72	0.79	0.64	-3.78	0.51	0.42
16.4	14.8	11.3	0.6	68.90	0.81	0.31	0.90	0.76	-3.89	0.69	0.31
20.5	14.9	11.0	0.7	53.66	0.73	1.00	0.73	0.74	-3.90	0.54	0.59
13.7	10.0	9.2	0.6	67.15	0.85	1.06	0.73	0.92	-3.32	0.67	0.82
13.2	11.0	8.6	0.8	65.15	0.80	0.57	0.83	0.78	-3.46	0.65	0.48
26.3	15.6	11.3	0.7	42.97	0.68	1.58	0.59	0.72	-3.96	0.43	0.71
20.4	19.0	14.5	0.8	71.08	0.82	0.21	0.93	0.76	-4.25	0.71	0.24
21.3	14.8	10.5	0.6	49.30	0.70	1.13	0.69	0.71	-3.89	0.49	0.60
13.2	10.3	7.8	0.8	59.09	0.76	0.75	0.78	0.76	-3.36	0.59	0.54
13.2	9.1	6.3	0.5	47.73	0.69	1.09	0.69	0.69	-3.19	0.48	0.59
17.2	10.8	10.0	0.7	58.14	0.81	1.41	0.63	0.93	-3.43	0.58	0.89
12.5	11.0	8.4	0.7	67.20	0.80	0.36	0.88	0.76	-3.46	0.67	0.37
14.4	13.0	9.3	0.6	64.58	0.77	0.27	0.90	0.72	-3.70	0.65	0.27

A−axis	B−axis	C−axis	Roundness	Flatness	Sphericity	OP−index	b/a	c/b	B−axis phi	c/a	a−b/a−c
22.6	14.6	7.8	0.5	34.51	0.57	1.47	0.65	0.53	−3.87	0.35	0.54
15.7	12.4	11.0	0.6	70.06	0.85	0.85	0.79	0.89	−3.63	0.70	0.70
15.3	12.3	8.5	0.6	55.56	0.73	0.66	0.80	0.69	−3.62	0.56	0.44
17.8	12.0	8.0	0.6	44.94	0.67	1.20	0.67	0.67	−3.58	0.45	0.59
23.7	17.7	12.6	0.7	53.16	0.72	0.93	0.75	0.71	−4.15	0.53	0.54
13.6	13.0	8.5	0.8	62.50	0.74	0.03	0.96	0.65	−3.70	0.63	0.12
12.4	9.2	7.0	0.7	56.45	0.75	0.89	0.74	0.76	−3.20	0.56	0.59
21.0	13.3	8.1	0.7	38.57	0.62	1.45	0.63	0.61	−3.73	0.39	0.60
17.5	13.1	11.0	0.7	62.86	0.81	0.95	0.75	0.84	−3.71	0.63	0.68
18.4	13.0	8.7	0.6	47.28	0.68	1.07	0.71	0.67	−3.70	0.47	0.56
27.7	14.5	12.4	0.6	44.77	0.73	1.85	0.52	0.86	−3.86	0.45	0.86
24.0	15.7	11.7	0.5	48.75	0.71	1.30	0.65	0.75	−3.97	0.49	0.67
25.0	18.6	14.3	0.6	57.20	0.76	0.96	0.74	0.77	−4.22	0.57	0.60
23.6	14.0	12.5	0.6	52.97	0.78	1.55	0.59	0.89	−3.81	0.53	0.86
27.3	18.5	15.3	0.6	56.04	0.77	1.23	0.68	0.83	−4.21	0.56	0.73
13.2	10.0	7.1	0.6	53.79	0.73	0.82	0.76	0.71	−3.32	0.54	0.52
20.5	13.1	10.0	0.7	48.78	0.72	1.35	0.64	0.76	−3.71	0.49	0.70
12.0	11.0	10.1	0.6	84.17	0.92	0.31	0.92	0.92	−3.46	0.84	0.53
20.4	14.3	11.2	0.5	54.90	0.75	1.11	0.70	0.78	−3.84	0.55	0.66
14.4	11.7	9.0	0.7	62.50	0.78	0.65	0.81	0.77	−3.55	0.63	0.50
19.7	12.9	9.5	0.7	48.22	0.71	1.28	0.65	0.74	−3.69	0.48	0.67
18.3	14.6	8.3	0.6	45.36	0.64	0.71	0.80	0.57	−3.87	0.45	0.37
16.0	13.3	9.4	0.6	58.75	0.75	0.57	0.83	0.71	−3.73	0.59	0.41
17.7	16.0	10.8	0.4	61.02	0.74	0.29	0.90	0.68	−4.00	0.61	0.25
19.3	13.8	12.1	0.7	62.69	0.82	1.11	0.72	0.88	−3.79	0.63	0.76
17.5	14.4	10.0	0.5	57.14	0.73	0.61	0.82	0.69	−3.85	0.57	0.41
16.5	10.2	9.2	0.6	55.76	0.80	1.42	0.62	0.90	−3.35	0.56	0.86
22.3	17.2	14.5	0.5	65.02	0.82	0.91	0.77	0.84	−4.10	0.65	0.65
14.0	13.1	7.3	0.6	52.14	0.66	0.11	0.94	0.56	−3.71	0.52	0.13
23.3	22.0	10.5	0.6	45.06	0.60	0.14	0.94	0.48	−4.46	0.45	0.10
22.4	17.7	11.0	0.6	49.11	0.67	0.75	0.79	0.62	−4.15	0.49	0.41
16.5	11.6	10.2	0.7	61.82	0.82	1.13	0.70	0.88	−3.54	0.62	0.78
11.4	10.1	8.3	0.8	72.81	0.84	0.35	0.89	0.82	−3.34	0.73	0.42
12.3	10.0	6.4	0.5	52.03	0.69	0.59	0.81	0.64	−3.32	0.52	0.39
27.3	15.6	12.4	0.5	45.42	0.71	1.65	0.57	0.79	−3.96	0.45	0.79
15.0	12.8	10.2	0.6	68.00	0.82	0.52	0.85	0.80	−3.68	0.68	0.46
23.4	16.3	12.5	0.5	53.42	0.74	1.13	0.70	0.77	−4.03	0.53	0.65
27.1	17.4	13.4	0.5	49.45	0.72	1.36	0.64	0.77	−4.12	0.49	0.71
23.2	16.6	12.2	0.5	52.59	0.73	1.05	0.72	0.73	−4.05	0.53	0.60
16.0	13.5	9.5	0.8	59.38	0.75	0.52	0.84	0.70	−3.75	0.59	0.38
16.7	12.1	8.0	0.7	47.90	0.68	0.98	0.72	0.66	−3.60	0.48	0.53
14.8	12.0	8.7	0.6	58.78	0.75	0.64	0.81	0.73	−3.58	0.59	0.46

A-axis	B-axis	C-axis	Roundness	Flatness	Sphericity	OP-index	b/a	c/b	B-axis phi	c/a	a-b/a-c
20.2	12.4	10.2	0.8	50.50	0.75	1.45	0.61	0.82	-3.63	0.50	0.78
22.1	15.5	11.0	0.7	49.77	0.71	1.10	0.70	0.71	-3.95	0.50	0.59
16.8	14.1	11.6	0.4	69.05	0.83	0.61	0.84	0.82	-3.82	0.69	0.52
14.5	10.6	8.6	0.6	59.31	0.78	0.97	0.73	0.81	-3.41	0.59	0.66
13.9	12.4	8.0	0.6	57.55	0.72	0.29	0.89	0.65	-3.63	0.58	0.25
17.0	14.0	10.7	0.6	62.94	0.78	0.63	0.82	0.76	-3.81	0.63	0.48
17.1	12.1	9.3	0.5	54.39	0.75	1.06	0.71	0.77	-3.60	0.54	0.64
15.3	11.6	8.1	0.6	52.94	0.72	0.84	0.76	0.70	-3.54	0.53	0.51
18.5	17.0	15.3	0.6	82.70	0.91	0.38	0.92	0.90	-4.09	0.83	0.47
24.0	18.3	13.3	0.5	55.42	0.74	0.88	0.76	0.73	-4.19	0.55	0.53
17.1	15.4	10.8	0.5	63.16	0.76	0.30	0.90	0.70	-3.94	0.63	0.27
19.1	16.8	12.6	0.7	65.97	0.79	0.42	0.88	0.75	-4.07	0.66	0.35
25.4	16.8	12.3	0.7	48.43	0.71	1.28	0.66	0.73	-4.07	0.48	0.66
17.3	13.4	11.0	0.7	63.58	0.81	0.85	0.77	0.82	-3.74	0.64	0.62
14.6	8.0	7.0	0.6	47.95	0.75	1.67	0.55	0.88	-3.00	0.48	0.87
14.9	13.4	8.4	0.5	56.38	0.71	0.27	0.90	0.63	-3.74	0.56	0.23
21.2	19.2	13.3	0.6	62.74	0.76	0.30	0.91	0.69	-4.26	0.63	0.25
20.1	16.3	13.1	0.5	65.17	0.81	0.72	0.81	0.80	-4.03	0.65	0.54
26.0	14.7	11.5	0.7	44.23	0.70	1.68	0.57	0.78	-3.88	0.44	0.78
17.7	15.0	8.1	0.5	45.76	0.63	0.50	0.85	0.54	-3.91	0.46	0.28
14.6	12.4	10.5	0.6	71.92	0.85	0.58	0.85	0.85	-3.63	0.72	0.54
15.3	12.7	11.0	0.6	71.90	0.85	0.68	0.83	0.87	-3.67	0.72	0.60
18.3	12.5	11.1	0.7	60.66	0.81	1.21	0.68	0.89	-3.64	0.61	0.81
16.1	11.7	8.7	0.5	54.04	0.74	0.98	0.73	0.74	-3.55	0.54	0.59
14.8	12.3	7.9	0.5	53.38	0.70	0.54	0.83	0.64	-3.62	0.53	0.36
16.5	12.2	7.6	0.6	46.06	0.66	0.93	0.74	0.62	-3.61	0.46	0.48
11.0	8.1	6.5	0.7	59.09	0.78	0.90	0.74	0.80	-3.02	0.59	0.64
16.5	12.3	9.7	0.7	58.79	0.77	0.93	0.75	0.79	-3.62	0.59	0.62
13.3	10.7	9.0	0.8	67.67	0.83	0.72	0.80	0.84	-3.42	0.68	0.60
17.3	12.8	10.0	0.6	57.80	0.77	0.95	0.74	0.78	-3.68	0.58	0.62
19.2	13.9	13.0	0.6	67.71	0.86	1.14	0.72	0.94	-3.80	0.68	0.85
17.8	12.1	10.5	0.7	58.99	0.80	1.21	0.68	0.87	-3.60	0.59	0.78
15.2	12.3	11.7	0.6	76.97	0.90	0.89	0.81	0.95	-3.62	0.77	0.83
19.7	13.0	11.3	0.5	57.36	0.79	1.29	0.66	0.87	-3.70	0.57	0.80
15.0	12.2	8.1	0.5	54.00	0.71	0.62	0.81	0.66	-3.61	0.54	0.41
18.2	14.4	10.3	0.5	56.59	0.74	0.74	0.79	0.72	-3.85	0.57	0.48
17.6	12.8	8.8	0.6	50.00	0.70	0.98	0.73	0.69	-3.68	0.50	0.55
15.8	12.0	6.7	0.6	42.41	0.62	0.86	0.76	0.56	-3.58	0.42	0.42
14.3	10.4	9.2	0.7	64.34	0.83	1.04	0.73	0.88	-3.38	0.64	0.76
18.2	12.2	10.6	0.6	58.24	0.80	1.24	0.67	0.87	-3.61	0.58	0.79
10.4	9.5	6.1	0.8	58.65	0.72	0.16	0.91	0.64	-3.25	0.59	0.21
13.5	10.6	9.0	0.6	66.67	0.83	0.80	0.79	0.85	-3.41	0.67	0.64

A−axis	B−axis	C−axis	Roundness	Flatness	Sphericity	OP−index	b/a	c/b	B−axis phi	c/a	a−b/a−c
16.6	14.7	12.2	0.5	73.49	0.85	0.43	0.89	0.83	−3.88	0.73	0.43
21.2	14.7	12.0	0.6	56.60	0.77	1.15	0.69	0.82	−3.88	0.57	0.71
12.9	12.5	7.8	0.5	60.47	0.72	−0.03	0.97	0.62	−3.64	0.60	0.08
11.6	7.4	7.0	0.7	60.34	0.83	1.33	0.64	0.95	−2.89	0.60	0.91
17.1	14.1	8.3	0.6	48.54	0.66	0.59	0.82	0.59	−3.82	0.49	0.34
17.0	13.0	10.9	0.6	64.12	0.81	0.89	0.76	0.84	−3.70	0.64	0.66
19.0	14.2	9.4	0.6	49.47	0.69	0.91	0.75	0.66	−3.83	0.49	0.50
17.3	13.0	11.2	0.6	64.74	0.82	0.96	0.75	0.86	−3.70	0.65	0.70
16.2	12.3	11.1	0.7	68.52	0.85	0.97	0.76	0.90	−3.62	0.69	0.76
16.2	14.9	11.1	0.6	68.52	0.80	0.23	0.92	0.74	−3.90	0.69	0.25
20.4	13.0	12.0	0.6	58.82	0.82	1.40	0.64	0.92	−3.70	0.59	0.88
15.6	10.0	10.0	0.5	64.10	0.86	1.42	0.64	1.00	−3.32	0.64	1.00
15.8	13.1	7.0	0.6	44.30	0.62	0.56	0.83	0.53	−3.71	0.44	0.31
15.0	10.3	8.3	0.5	55.33	0.76	1.13	0.69	0.81	−3.36	0.55	0.70
17.1	12.9	10.9	0.6	63.74	0.81	0.94	0.75	0.84	−3.69	0.64	0.68
16.3	13.7	10.8	0.6	66.26	0.81	0.58	0.84	0.79	−3.78	0.66	0.47
17.5	11.0	10.7	0.6	61.14	0.84	1.44	0.63	0.97	−3.46	0.61	0.96
16.7	13.2	11.5	0.6	68.86	0.84	0.84	0.79	0.87	−3.72	0.69	0.67
11.9	10.1	8.2	0.6	68.91	0.82	0.51	0.85	0.81	−3.34	0.69	0.49
13.0	10.4	7.1	0.6	54.62	0.72	0.65	0.80	0.68	−3.38	0.55	0.44
15.2	13.4	11.4	0.5	75.00	0.86	0.46	0.88	0.85	−3.74	0.75	0.47
13.1	11.9	11.4	0.5	87.02	0.94	0.47	0.91	0.96	−3.57	0.87	0.71
12.3	8.3	7.2	0.6	58.54	0.80	1.17	0.67	0.87	−3.05	0.59	0.78
15.4	11.2	7.1	0.7	46.10	0.66	0.97	0.73	0.63	−3.49	0.46	0.51
13.5	10.5	10.3	0.6	76.30	0.91	1.02	0.78	0.98	−3.39	0.76	0.94
16.7	14.6	12.6	0.5	75.45	0.87	0.52	0.87	0.86	−3.87	0.75	0.51
13.8	11.8	8.0	0.7	57.97	0.73	0.45	0.86	0.68	−3.56	0.58	0.34
14.9	13.8	10.0	0.5	67.11	0.79	0.18	0.93	0.72	−3.79	0.67	0.22
23.0	19.1	11.2	0.6	48.70	0.66	0.59	0.83	0.59	−4.26	0.49	0.33
13.8	12.5	8.0	0.7	57.97	0.72	0.24	0.91	0.64	−3.64	0.58	0.22
17.1	13.5	8.2	0.6	47.95	0.66	0.73	0.79	0.61	−3.75	0.48	0.40
16.8	11.0	9.3	0.5	55.36	0.78	1.28	0.65	0.85	−3.46	0.55	0.77
13.7	10.3	9.1	0.8	66.42	0.84	0.95	0.75	0.88	−3.36	0.66	0.74
17.6	10.2	9.1	0.5	51.70	0.77	1.57	0.58	0.89	−3.35	0.52	0.87
23.3	13.3	11.0	0.7	47.21	0.73	1.64	0.57	0.83	−3.73	0.47	0.81
12.2	10.0	8.5	0.8	69.67	0.84	0.66	0.82	0.85	−3.32	0.70	0.59
17.8	13.5	10.3	0.6	57.87	0.76	0.88	0.76	0.76	−3.75	0.58	0.57
14.5	12.8	8.5	0.7	58.62	0.73	0.34	0.88	0.66	−3.68	0.59	0.28
12.6	11.6	9.0	0.7	71.43	0.82	0.19	0.92	0.78	−3.54	0.71	0.28
20.2	16.6	10.3	0.5	50.99	0.68	0.61	0.82	0.62	−4.05	0.51	0.36
15.0	12.0	8.8	0.5	58.67	0.75	0.69	0.80	0.73	−3.58	0.59	0.48
18.0	12.5	10.1	0.7	56.11	0.77	1.13	0.69	0.81	−3.64	0.56	0.70

A−axis	B−axis	C−axis	Roundness	Flatness	Sphericity	OP−index	b/a	c/b	B−axis phi	c/a	a−b/a−c
13.6	10.8	9.1	0.6	66.91	0.83	0.76	0.79	0.84	−3.43	0.67	0.62
21.2	13.9	9.5	0.7	44.81	0.67	1.30	0.66	0.68	−3.80	0.45	0.62
15.8	12.5	9.0	0.7	56.96	0.74	0.72	0.79	0.72	−3.64	0.57	0.49
11.8	10.6	9.1	0.7	77.12	0.87	0.34	0.90	0.86	−3.41	0.77	0.44
15.4	11.6	10.1	0.6	65.58	0.83	0.95	0.75	0.87	−3.54	0.66	0.72
15.5	11.0	9.7	0.8	62.58	0.82	1.10	0.71	0.88	−3.46	0.63	0.78
18.0	13.7	10.6	0.6	58.89	0.77	0.87	0.76	0.77	−3.78	0.59	0.58
13.7	10.3	8.8	0.7	64.23	0.82	0.92	0.75	0.85	−3.36	0.64	0.69
15.8	13.2	6.9	0.6	43.67	0.61	0.54	0.84	0.52	−3.72	0.44	0.29
16.9	12.1	8.4	0.7	49.70	0.70	1.02	0.72	0.69	−3.60	0.50	0.56
13.9	10.5	10.0	0.6	71.94	0.88	1.03	0.76	0.95	−3.39	0.72	0.87
19.1	15.5	7.8	0.6	40.84	0.59	0.67	0.81	0.50	−3.95	0.41	0.32
16.0	13.6	10.3	0.6	64.38	0.79	0.52	0.85	0.76	−3.77	0.64	0.42
14.0	11.7	8.5	0.7	60.71	0.76	0.54	0.84	0.73	−3.55	0.61	0.42
15.9	13.6	9.5	0.7	59.75	0.75	0.47	0.86	0.70	−3.77	0.60	0.36
15.3	11.3	10.0	0.6	65.36	0.83	1.01	0.74	0.88	−3.50	0.65	0.75
14.1	9.0	8.1	0.8	57.45	0.80	1.33	0.64	0.90	−3.17	0.57	0.85
18.3	13.6	10.5	0.5	57.38	0.76	0.94	0.74	0.77	−3.77	0.57	0.60
18.5	15.3	8.7	0.4	47.03	0.64	0.59	0.83	0.57	−3.94	0.47	0.33
21.6	14.2	10.1	0.6	46.76	0.69	1.28	0.66	0.71	−3.83	0.47	0.64
20.7	16.4	11.7	0.5	56.52	0.74	0.75	0.79	0.71	−4.04	0.57	0.48
17.0	13.8	6.8	0.6	40.00	0.58	0.66	0.81	0.49	−3.79	0.40	0.31
17.5	10.1	9.0	0.6	51.43	0.77	1.58	0.58	0.89	−3.34	0.51	0.87
19.5	17.8	12.4	0.5	63.59	0.76	0.27	0.91	0.70	−4.15	0.64	0.24
12.3	10.5	9.8	0.8	79.67	0.91	0.65	0.85	0.93	−3.39	0.80	0.72
17.7	15.3	10.8	0.7	61.02	0.76	0.45	0.86	0.71	−3.94	0.61	0.35
10.8	6.2	5.3	0.8	49.07	0.75	1.52	0.57	0.85	−2.63	0.49	0.84
15.8	11.1	9.4	0.7	59.49	0.80	1.10	0.70	0.85	−3.47	0.59	0.73
15.1	10.1	7.1	0.7	47.02	0.69	1.20	0.67	0.70	−3.34	0.47	0.63
18.2	14.8	12.6	0.6	69.23	0.84	0.75	0.81	0.85	−3.89	0.69	0.61
20.7	13.8	11.3	0.7	54.59	0.76	1.25	0.67	0.82	−3.79	0.55	0.73
21.3	13.0	8.5	0.7	39.91	0.64	1.53	0.61	0.65	−3.70	0.40	0.65
15.6	13.3	10.0	0.5	64.10	0.78	0.50	0.85	0.75	−3.73	0.64	0.41
12.8	11.2	8.0	0.6	62.50	0.76	0.37	0.88	0.71	−3.49	0.63	0.33
14.5	10.6	7.1	0.6	48.97	0.69	0.94	0.73	0.67	−3.41	0.49	0.53
17.3	12.5	10.3	0.7	59.54	0.79	1.03	0.72	0.82	−3.64	0.60	0.69
13.0	8.1	7.0	0.7	53.85	0.77	1.36	0.62	0.86	−3.02	0.54	0.82
13.9	8.0	7.9	0.7	56.83	0.82	1.58	0.58	0.99	−3.00	0.57	0.98
17.8	12.7	7.0	0.6	39.33	0.60	1.08	0.71	0.55	−3.67	0.39	0.47
17.2	12.3	9.1	0.8	52.91	0.73	1.03	0.72	0.74	−3.62	0.53	0.60
21.2	14.2	10.5	0.7	49.53	0.72	1.23	0.67	0.74	−3.83	0.50	0.65
16.8	13.8	11.3	0.8	67.26	0.82	0.68	0.82	0.82	−3.79	0.67	0.55

A-axis	B-axis	C-axis	Roundness	Flatness	Sphericity	OP-index	b/a	c/b	B-axis phi	c/a	a-b/a-c
13.4	10.0	7.1	0.6	52.99	0.72	0.87	0.75	0.71	-3.32	0.53	0.54
17.5	12.1	9.8	0.7	56.00	0.77	1.14	0.69	0.81	-3.60	0.56	0.70
16.0	13.6	8.6	0.6	53.75	0.70	0.48	0.85	0.63	-3.77	0.54	0.32
15.8	10.5	8.3	0.6	52.53	0.75	1.22	0.66	0.79	-3.39	0.53	0.71
16.1	12.7	7.5	0.6	46.58	0.65	0.72	0.79	0.59	-3.67	0.47	0.40
21.4	16.4	13.9	0.6	64.95	0.82	0.92	0.77	0.85	-4.04	0.65	0.67
17.3	11.0	9.1	0.9	52.60	0.76	1.34	0.64	0.83	-3.46	0.53	0.77
22.0	12.2	9.4	0.7	42.73	0.69	1.73	0.55	0.77	-3.61	0.43	0.78
18.5	12.4	8.1	0.7	43.78	0.66	1.23	0.67	0.65	-3.63	0.44	0.59
17.6	13.1	11.0	0.7	62.50	0.81	0.97	0.74	0.84	-3.71	0.63	0.68
23.0	13.5	11.8	0.6	51.30	0.77	1.57	0.59	0.87	-3.75	0.51	0.85
19.3	10.3	10.3	0.6	53.37	0.81	1.77	0.53	1.00	-3.36	0.53	1.00
27.8	12.9	12.7	0.6	45.68	0.77	2.09	0.46	0.98	-3.69	0.46	0.99
19.6	14.7	9.4	0.6	47.96	0.67	0.90	0.75	0.64	-3.88	0.48	0.48
21.9	17.2	14.2	0.7	64.84	0.81	0.84	0.79	0.83	-4.10	0.65	0.61
23.6	16.6	11.0	0.7	46.61	0.68	1.11	0.70	0.66	-4.05	0.47	0.56
22.7	14.4	13.1	0.6	57.71	0.81	1.41	0.63	0.91	-3.85	0.58	0.86
19.0	16.6	11.4	0.7	60.00	0.74	0.42	0.87	0.69	-4.05	0.60	0.32
12.6	9.9	8.7	0.8	69.05	0.85	0.82	0.79	0.88	-3.31	0.69	0.69
15.5	14.0	9.9	0.7	63.87	0.77	0.28	0.90	0.71	-3.81	0.64	0.27
21.7	14.9	8.6	0.6	39.63	0.61	1.21	0.69	0.58	-3.90	0.40	0.52
27.8	14.9	11.7	0.7	42.09	0.69	1.83	0.54	0.79	-3.90	0.42	0.80
22.7	13.9	11.0	0.6	48.46	0.73	1.46	0.61	0.79	-3.80	0.48	0.75
19.5	16.4	13.3	0.7	68.21	0.82	0.61	0.84	0.81	-4.04	0.68	0.50
23.9	18.8	12.0	0.6	50.21	0.68	0.77	0.79	0.64	-4.23	0.50	0.43
25.0	12.5	12.3	0.7	49.20	0.79	1.92	0.50	0.98	-3.64	0.49	0.98
22.9	14.0	12.6	0.6	55.02	0.79	1.48	0.61	0.90	-3.81	0.55	0.86
26.8	16.2	11.9	0.7	44.40	0.69	1.53	0.60	0.73	-4.02	0.44	0.71
24.0	14.9	11.3	0.6	47.08	0.71	1.44	0.62	0.76	-3.90	0.47	0.72
19.8	11.0	9.2	0.7	46.46	0.73	1.69	0.56	0.84	-3.46	0.46	0.83
17.0	9.0	8.8	0.7	51.76	0.80	1.77	0.53	0.98	-3.17	0.52	0.98
19.0	11.4	7.9	0.6	41.58	0.66	1.54	0.60	0.69	-3.51	0.42	0.68
16.4	11.7	9.0	0.8	54.88	0.75	1.03	0.71	0.77	-3.55	0.55	0.64
16.9	10.9	5.7	0.5	33.73	0.56	1.46	0.64	0.52	-3.45	0.34	0.54
19.2	12.3	10.9	0.7	56.77	0.80	1.36	0.64	0.89	-3.62	0.57	0.83
20.0	13.7	11.4	0.7	57.00	0.78	1.18	0.69	0.83	-3.78	0.57	0.73
20.2	11.7	6.5	0.6	32.18	0.56	1.81	0.58	0.56	-3.55	0.32	0.62
13.0	11.0	8.7	0.7	66.92	0.81	0.52	0.85	0.79	-3.46	0.67	0.47
22.4	17.0	13.2	0.6	58.93	0.77	0.90	0.76	0.78	-4.09	0.59	0.59
20.0	11.6	10.0	0.7	50.00	0.76	1.58	0.58	0.86	-3.54	0.50	0.84
23.0	15.3	10.0	0.5	43.48	0.66	1.27	0.67	0.65	-3.94	0.43	0.59
21.7	15.4	10.5	0.5	48.39	0.69	1.07	0.71	0.68	-3.94	0.48	0.56

A-axis	B-axis	C-axis	Roundness	Flatness	Sphericity	OP-index	b/a	c/b	B-axis phi	c/a	a-b/a-c
18.0	13.0	7.2	0.6	40.00	0.61	1.04	0.72	0.55	−3.70	0.40	0.46
19.4	14.6	7.7	0.5	39.69	0.59	0.93	0.75	0.53	−3.87	0.40	0.41
19.3	13.9	12.5	0.7	64.77	0.84	1.11	0.72	0.90	−3.80	0.65	0.79
22.0	12.9	12.0	0.6	54.55	0.80	1.58	0.59	0.93	−3.69	0.55	0.91
20.0	10.9	8.9	0.7	44.50	0.71	1.74	0.55	0.82	−3.45	0.45	0.82
16.6	10.9	10.0	0.7	60.24	0.82	1.31	0.66	0.92	−3.45	0.60	0.86
17.8	11.9	9.4	0.8	52.81	0.75	1.22	0.67	0.79	−3.57	0.53	0.70
14.0	10.9	8.0	0.8	57.14	0.75	0.76	0.78	0.73	−3.45	0.57	0.52
17.3	10.2	8.0	0.7	46.24	0.71	1.53	0.59	0.78	−3.35	0.46	0.76
14.9	10.9	9.7	0.6	65.10	0.83	1.03	0.73	0.89	−3.45	0.65	0.77
14.9	11.9	7.5	0.7	50.34	0.68	0.67	0.80	0.63	−3.57	0.50	0.41
18.5	15.6	11.5	0.6	62.16	0.77	0.55	0.84	0.74	−3.96	0.62	0.41
16.6	12.0	10.0	0.8	60.24	0.79	1.03	0.72	0.83	−3.58	0.60	0.70
15.9	11.0	8.0	0.7	50.31	0.72	1.11	0.69	0.73	−3.46	0.50	0.62
14.5	10.0	7.4	0.6	51.03	0.72	1.10	0.69	0.74	−3.32	0.51	0.63
17.0	9.0	8.7	0.8	51.18	0.79	1.77	0.53	0.97	−3.17	0.51	0.96
21.1	12.0	9.8	0.7	46.45	0.72	1.64	0.57	0.82	−3.58	0.46	0.81
20.4	15.3	11.4	0.6	55.88	0.75	0.91	0.75	0.75	−3.94	0.56	0.57
13.0	9.9	9.0	0.7	69.23	0.86	0.94	0.76	0.91	−3.31	0.69	0.78
16.0	10.9	10.0	0.6	62.50	0.83	1.23	0.68	0.92	−3.45	0.63	0.85
13.3	10.7	9.8	0.7	73.68	0.88	0.81	0.80	0.92	−3.42	0.74	0.74
19.9	10.5	10.0	0.6	50.25	0.78	1.79	0.53	0.95	−3.39	0.50	0.95
14.9	11.7	11.5	0.7	77.18	0.91	1.03	0.79	0.98	−3.55	0.77	0.94
11.7	10.2	8.2	0.7	70.09	0.83	0.41	0.87	0.80	−3.35	0.70	0.43
15.7	12.0	8.7	0.7	55.41	0.74	0.82	0.76	0.73	−3.58	0.55	0.53
16.8	13.7	11.7	0.7	69.64	0.84	0.73	0.82	0.85	−3.78	0.70	0.61
15.4	11.2	9.4	0.7	61.04	0.80	1.01	0.73	0.84	−3.49	0.61	0.70
12.8	10.8	7.4	0.7	57.81	0.73	0.48	0.84	0.69	−3.43	0.58	0.37
15.6	10.0	6.0	0.6	38.46	0.61	1.38	0.64	0.60	−3.32	0.38	0.58
16.9	11.5	10.2	0.5	60.36	0.81	1.21	0.68	0.89	−3.52	0.60	0.81
14.6	11.0	8.4	0.7	57.53	0.76	0.87	0.75	0.76	−3.46	0.58	0.58
17.5	12.4	9.0	0.7	51.43	0.72	1.05	0.71	0.73	−3.63	0.51	0.60
19.0	14.7	9.4	0.6	49.47	0.68	0.80	0.77	0.64	−3.88	0.49	0.45
14.0	9.8	7.6	0.6	54.29	0.75	1.06	0.70	0.78	−3.29	0.54	0.66
15.2	9.4	8.3	0.6	54.61	0.78	1.41	0.62	0.88	−3.23	0.55	0.84
15.9	11.5	8.6	0.6	54.09	0.74	0.99	0.72	0.75	−3.52	0.54	0.60
15.0	11.6	8.3	0.6	55.33	0.73	0.78	0.77	0.72	−3.54	0.55	0.51
15.0	12.7	9.9	0.6	66.00	0.80	0.53	0.85	0.78	−3.67	0.66	0.45
11.0	10.7	9.3	0.7	84.55	0.90	−0.14	0.97	0.87	−3.42	0.85	0.18
12.8	11.4	7.4	0.6	57.81	0.72	0.29	0.89	0.65	−3.51	0.58	0.26
13.0	11.3	7.9	0.7	60.77	0.75	0.39	0.87	0.70	−3.50	0.61	0.33
13.7	12.3	9.6	0.6	70.07	0.82	0.31	0.90	0.78	−3.62	0.70	0.34

A−axis	B−axis	C−axis	Roundness	Flatness	Sphericity	OP−index	b/a	c/b	B−axis phi	c/a	a−b/a−c
16.4	10.7	9.4	0.6	57.32	0.80	1.30	0.65	0.88	−3.42	0.57	0.81
16.4	13.5	11.7	0.6	71.34	0.85	0.72	0.82	0.87	−3.75	0.71	0.62
16.4	11.2	7.5	0.6	45.73	0.67	1.15	0.68	0.67	−3.49	0.46	0.58
15.4	10.6	8.4	0.6	54.55	0.76	1.13	0.69	0.79	−3.41	0.55	0.69
17.2	10.5	8.2	0.6	47.67	0.72	1.44	0.61	0.78	−3.39	0.48	0.74
16.8	15.0	11.2	0.6	66.67	0.79	0.35	0.89	0.75	−3.91	0.67	0.32
14.9	10.6	8.6	0.6	57.72	0.78	1.05	0.71	0.81	−3.41	0.58	0.68
17.8	14.2	9.9	0.7	55.62	0.73	0.71	0.80	0.70	−3.83	0.56	0.46
15.0	11.5	9.2	0.6	61.33	0.79	0.84	0.77	0.80	−3.52	0.61	0.60
9.0	8.3	5.9	0.8	65.56	0.78	0.10	0.92	0.71	−3.05	0.66	0.23
8.4	7.7	5.0	0.7	59.52	0.73	0.10	0.92	0.65	−2.94	0.60	0.21
13.2	9.9	6.0	0.6	45.45	0.65	0.86	0.75	0.61	−3.31	0.45	0.46
17.0	11.4	6.6	0.6	38.82	0.61	1.26	0.67	0.58	−3.51	0.39	0.54
13.5	12.5	7.3	0.7	54.07	0.68	0.15	0.93	0.58	−3.64	0.54	0.16
13.7	12.0	9.3	0.8	67.88	0.81	0.40	0.88	0.78	−3.58	0.68	0.39
17.4	14.4	12.6	0.6	72.41	0.86	0.72	0.83	0.88	−3.85	0.72	0.62
15.6	14.4	11.5	0.6	73.72	0.84	0.23	0.92	0.80	−3.85	0.74	0.29
15.3	11.3	7.0	0.6	45.75	0.66	0.92	0.74	0.62	−3.50	0.46	0.48
13.9	9.6	7.8	0.7	56.12	0.77	1.11	0.69	0.81	−3.26	0.56	0.70
11.6	11.5	8.3	0.8	71.55	0.80	−0.17	0.99	0.72	−3.52	0.72	0.03
12.9	9.6	7.9	0.7	61.24	0.80	0.91	0.74	0.82	−3.26	0.61	0.66
12.7	10.0	8.1	0.7	63.78	0.80	0.75	0.79	0.81	−3.32	0.64	0.59
13.2	9.0	4.2	0.5	31.82	0.53	1.29	0.68	0.47	−3.17	0.32	0.47
14.8	10.9	9.4	0.6	63.51	0.82	0.99	0.74	0.86	−3.45	0.64	0.72
11.0	8.3	5.3	0.7	48.18	0.68	0.80	0.75	0.64	−3.05	0.48	0.47
11.8	9.0	7.7	0.6	65.25	0.82	0.86	0.76	0.86	−3.17	0.65	0.68
17.5	15.4	12.2	0.6	69.71	0.82	0.43	0.88	0.79	−3.94	0.70	0.40
15.5	11.4	9.3	0.7	60.00	0.79	0.97	0.74	0.82	−3.51	0.60	0.66
15.8	13.0	10.0	0.7	63.29	0.79	0.63	0.82	0.77	−3.70	0.63	0.48
17.4	12.7	10.2	0.5	58.62	0.78	1.00	0.73	0.80	−3.67	0.59	0.65
16.3	12.0	7.8	0.5	47.85	0.68	0.93	0.74	0.65	−3.58	0.48	0.51
14.6	11.7	9.0	0.5	61.64	0.78	0.70	0.80	0.77	−3.55	0.62	0.52
9.6	7.9	7.0	0.7	72.92	0.86	0.63	0.82	0.89	−2.98	0.73	0.65
13.7	10.9	10.0	0.8	72.99	0.87	0.85	0.80	0.92	−3.45	0.73	0.76
13.9	10.7	8.0	0.8	57.55	0.75	0.80	0.77	0.75	−3.42	0.58	0.54
11.3	8.2	6.9	0.5	61.06	0.80	0.97	0.73	0.84	−3.04	0.61	0.70
12.4	8.0	7.2	0.7	58.06	0.81	1.29	0.65	0.90	−3.00	0.58	0.85
12.0	8.5	6.0	0.7	50.00	0.71	1.00	0.71	0.71	−3.09	0.50	0.58
13.9	10.5	8.6	0.6	61.87	0.80	0.88	0.76	0.82	−3.39	0.62	0.64
12.2	9.5	7.5	0.7	61.48	0.79	0.76	0.78	0.79	−3.25	0.61	0.57
11.4	10.0	8.5	0.6	74.56	0.86	0.42	0.88	0.85	−3.32	0.75	0.48
12.3	10.7	7.2	0.6	58.54	0.73	0.37	0.87	0.67	−3.42	0.59	0.31

Appendix (XII)(j)

PEBBLE DATA ROODERAND CONGLOMERATE FORMATION PROCEDEERFONTEIN 100

A-axis	B-axis	C-axis	Roundness	Flatness	Sphericity	OP-index	b/a	c/b	B-axis phi	c/a	a-b/a-c
43.9	30.2	19.7	0.5	44.87	0.66	1.22	0.69	0.65	-4.92	0.45	0.57
36.9	29.7	21.4	0.5	57.99	0.75	0.75	0.80	0.72	-4.89	0.58	0.46
31.5	28.1	19.4	0.9	61.59	0.75	0.39	0.89	0.69	-4.81	0.62	0.28
37.2	26.2	22.0	0.5	59.14	0.79	1.17	0.70	0.84	-4.71	0.59	0.72
41.6	26.1	20.9	0.8	50.24	0.74	1.44	0.63	0.80	-4.71	0.50	0.75
31.0	25.0	19.3	0.7	62.26	0.78	0.76	0.81	0.77	-4.64	0.62	0.51
30.0	23.7	14.3	0.9	47.67	0.66	0.78	0.79	0.60	-4.57	0.48	0.40
37.0	22.8	17.0	0.8	45.95	0.70	1.49	0.62	0.75	-4.51	0.46	0.71
25.7	22.1	14.0	0.8	54.47	0.70	0.49	0.86	0.63	-4.47	0.54	0.31
35.6	22.0	18.1	0.7	50.84	0.75	1.47	0.62	0.82	-4.46	0.51	0.78
32.1	22.0	19.1	0.8	59.50	0.80	1.24	0.69	0.87	-4.46	0.60	0.78
28.0	21.9	17.0	0.7	60.71	0.78	0.84	0.78	0.78	-4.45	0.61	0.55
30.0	21.9	13.0	0.9	43.33	0.64	1.03	0.73	0.59	-4.45	0.43	0.48
25.5	21.9	19.6	0.7	76.86	0.88	0.68	0.86	0.89	-4.45	0.77	0.61
23.3	21.9	17.0	0.8	72.96	0.83	0.20	0.94	0.78	-4.45	0.73	0.22
24.0	21.7	16.9	0.8	70.42	0.82	0.36	0.90	0.78	-4.44	0.70	0.32
29.4	21.7	15.0	0.8	51.02	0.71	0.98	0.74	0.69	-4.44	0.51	0.53
25.7	21.4	13.0	0.5	50.58	0.67	0.59	0.83	0.61	-4.42	0.51	0.34
27.9	21.0	16.1	0.8	57.71	0.76	0.94	0.75	0.77	-4.39	0.58	0.58
28.1	21.0	15.3	0.6	54.45	0.73	0.95	0.75	0.73	-4.39	0.54	0.55
24.7	20.5	17.9	0.8	72.47	0.86	0.75	0.83	0.87	-4.36	0.72	0.62
24.9	20.5	14.9	0.9	59.84	0.76	0.65	0.82	0.73	-4.36	0.60	0.44
29.4	20.5	19.2	0.7	65.31	0.85	1.26	0.70	0.94	-4.36	0.65	0.87
32.0	20.3	17.0	0.7	53.13	0.76	1.41	0.63	0.84	-4.34	0.53	0.78
24.0	20.1	11.3	0.7	47.08	0.64	0.57	0.84	0.56	-4.33	0.47	0.31
28.4	20.0	14.3	0.7	50.35	0.71	1.11	0.70	0.72	-4.32	0.50	0.60
20.3	20.0	9.5	0.8	46.80	0.61	-0.04	0.99	0.48	-4.32	0.47	0.03
34.5	20.0	13.8	0.6	40.00	0.65	1.69	0.58	0.69	-4.32	0.40	0.70
22.9	19.9	16.5	0.6	72.05	0.84	0.54	0.87	0.83	-4.31	0.72	0.47
23.0	19.8	12.3	0.9	53.48	0.69	0.47	0.86	0.62	-4.31	0.53	0.30
23.9	19.8	13.8	0.7	57.74	0.74	0.62	0.83	0.70	-4.31	0.58	0.41
22.0	19.7	14.1	0.7	64.09	0.77	0.36	0.90	0.72	-4.30	0.64	0.29
26.9	19.5	13.9	0.8	51.67	0.72	1.03	0.72	0.71	-4.29	0.52	0.57
22.0	19.3	16.8	0.9	76.36	0.87	0.55	0.88	0.87	-4.27	0.76	0.52
21.8	19.3	10.9	0.6	50.00	0.66	0.37	0.89	0.56	-4.27	0.50	0.23
25.0	19.3	16.1	0.8	64.40	0.81	0.91	0.77	0.83	-4.27	0.64	0.64
26.4	19.1	15.2	0.7	57.58	0.77	1.05	0.72	0.80	-4.26	0.58	0.65

A-axis	B-axis	C-axis	Roundness	Flatness	Sphericity	OP-index	b/a	c/b	B-axis phi	c/a	a-b/a-c
20.9	19.0	14.1	0.8	67.46	0.79	0.31	0.91	0.74	−4.25	0.67	0.28
22.9	19.0	16.0	0.7	69.87	0.84	0.71	0.83	0.84	−4.25	0.70	0.57
26.4	19.0	12.7	0.8	48.11	0.69	1.05	0.72	0.67	−4.25	0.48	0.54
21.1	18.9	12.0	0.7	56.87	0.71	0.33	0.90	0.63	−4.24	0.57	0.24
26.4	18.9	16.9	0.9	64.02	0.83	1.15	0.72	0.89	−4.24	0.64	0.79
24.3	18.8	13.0	0.9	53.50	0.72	0.83	0.77	0.69	−4.23	0.53	0.49
25.7	18.8	12.2	0.9	47.47	0.68	1.00	0.73	0.65	−4.23	0.47	0.51
21.5	18.8	11.9	0.9	55.35	0.70	0.41	0.87	0.63	−4.23	0.55	0.28
20.0	18.7	12.8	0.8	64.00	0.76	0.17	0.94	0.68	−4.22	0.64	0.18
25.9	18.7	15.3	0.7	59.07	0.78	1.07	0.72	0.82	−4.22	0.59	0.68
20.3	18.6	11.7	0.6	57.64	0.71	0.24	0.92	0.63	−4.22	0.58	0.20
22.0	18.5	15.0	0.7	68.18	0.82	0.63	0.84	0.81	−4.21	0.68	0.50
21.0	18.5	13.1	0.7	62.38	0.76	0.41	0.88	0.71	−4.21	0.62	0.32
23.9	18.4	13.9	0.9	58.16	0.76	0.86	0.77	0.76	−4.20	0.58	0.55
23.1	18.3	16.9	0.7	73.16	0.88	0.95	0.79	0.92	−4.19	0.73	0.77
20.0	18.3	12.0	0.8	60.00	0.73	0.25	0.92	0.66	−4.19	0.60	0.21
22.9	18.3	11.9	0.9	51.97	0.70	0.72	0.80	0.65	−4.19	0.52	0.42
21.9	18.3	12.7	0.8	57.99	0.74	0.58	0.84	0.69	−4.19	0.58	0.39
22.8	18.3	16.0	0.9	70.18	0.85	0.84	0.80	0.87	−4.19	0.70	0.66
19.2	18.2	13.2	0.6	68.75	0.79	0.12	0.95	0.73	−4.19	0.69	0.17
22.5	18.1	12.2	0.7	54.22	0.71	0.70	0.80	0.67	−4.18	0.54	0.43
19.0	18.1	11.3	0.8	59.47	0.72	0.09	0.95	0.62	−4.18	0.59	0.12
35.0	18.1	14.9	0.7	42.57	0.71	1.92	0.52	0.82	−4.18	0.43	0.84
21.3	18.0	13.9	0.7	65.26	0.80	0.58	0.85	0.77	−4.17	0.65	0.45
20.7	18.0	13.0	0.9	62.80	0.77	0.45	0.87	0.72	−4.17	0.63	0.35
27.9	18.0	13.7	0.6	49.10	0.72	1.35	0.65	0.76	−4.17	0.49	0.70
29.4	18.0	8.9	0.8	30.27	0.53	1.76	0.61	0.49	−4.17	0.30	0.56
22.0	18.0	14.3	0.8	65.00	0.80	0.70	0.82	0.79	−4.17	0.65	0.52
22.0	17.9	14.3	0.9	65.00	0.80	0.72	0.81	0.80	−4.16	0.65	0.53
21.1	17.9	12.3	0.7	58.29	0.74	0.53	0.85	0.69	−4.16	0.58	0.36
23.8	17.9	11.9	0.7	50.00	0.69	0.91	0.75	0.66	−4.16	0.50	0.50
27.1	17.9	13.2	0.9	48.71	0.71	1.28	0.66	0.74	−4.16	0.49	0.66
19.9	17.9	11.7	0.7	58.79	0.73	0.31	0.90	0.65	−4.16	0.59	0.24
25.0	17.8	15.0	0.8	60.00	0.80	1.12	0.71	0.84	−4.15	0.60	0.72
34.2	17.8	13.9	0.8	40.64	0.68	1.93	0.52	0.78	−4.15	0.41	0.81
20.5	17.7	13.2	0.8	64.39	0.78	0.49	0.86	0.75	−4.15	0.64	0.38
21.0	17.7	14.9	0.9	70.95	0.84	0.65	0.84	0.84	−4.15	0.71	0.54
19.9	17.7	12.0	0.9	60.30	0.74	0.36	0.89	0.68	−4.15	0.60	0.28
27.0	17.7	16.9	0.9	62.59	0.84	1.39	0.66	0.95	−4.15	0.63	0.92
22.9	17.6	13.0	0.7	56.77	0.75	0.85	0.77	0.74	−4.14	0.57	0.54
22.9	17.5	12.1	0.8	52.84	0.71	0.86	0.76	0.69	−4.13	0.53	0.50
30.3	17.3	14.9	0.9	49.17	0.75	1.65	0.57	0.86	−4.11	0.49	0.84

A-axis	B-axis	C-axis	Roundness	Flatness	Sphericity	OP-index	b/a	c/b	B-axis phi	c/a	a-b/a-c
23.5	17.3	8.7	0.6	37.02	0.57	1.04	0.74	0.50	−4.11	0.37	0.42
20.5	17.3	13.5	0.8	65.85	0.80	0.59	0.84	0.78	−4.11	0.66	0.46
22.9	17.3	11.1	0.9	48.47	0.68	0.89	0.76	0.64	−4.11	0.48	0.47
22.1	17.3	15.1	0.7	68.33	0.84	0.90	0.78	0.87	−4.11	0.68	0.69
22.9	17.2	12.9	0.8	56.33	0.75	0.92	0.75	0.75	−4.10	0.56	0.57
25.5	17.2	12.1	0.7	47.45	0.69	1.23	0.67	0.70	−4.10	0.47	0.62
23.1	17.2	12.3	0.7	53.25	0.72	0.94	0.74	0.72	−4.10	0.53	0.55
19.9	17.1	15.0	0.9	75.38	0.87	0.62	0.86	0.88	−4.10	0.75	0.57
21.1	17.1	13.0	0.9	61.61	0.78	0.70	0.81	0.76	−4.10	0.62	0.49
22.5	17.1	11.2	0.9	49.78	0.69	0.87	0.76	0.65	−4.10	0.50	0.48
30.0	17.1	12.9	0.7	43.00	0.69	1.69	0.57	0.75	−4.10	0.43	0.75
19.4	17.0	11.0	0.8	56.70	0.72	0.40	0.88	0.65	−4.09	0.57	0.29
21.9	17.0	10.1	0.8	46.12	0.65	0.81	0.78	0.59	−4.09	0.46	0.42
25.3	17.0	11.9	0.7	47.04	0.69	1.24	0.67	0.70	−4.09	0.47	0.62
19.0	17.0	11.9	0.8	62.63	0.76	0.34	0.89	0.70	−4.09	0.63	0.28
20.0	17.0	12.8	0.8	64.00	0.78	0.54	0.85	0.75	−4.09	0.64	0.42
18.1	16.9	9.9	0.8	54.70	0.68	0.16	0.93	0.59	−4.08	0.55	0.15
18.5	16.9	14.1	0.7	76.22	0.86	0.33	0.91	0.83	−4.08	0.76	0.36
21.0	16.9	12.9	0.8	61.43	0.78	0.72	0.80	0.76	−4.08	0.61	0.51
18.9	16.9	12.1	0.9	64.02	0.77	0.34	0.89	0.72	−4.08	0.64	0.29
26.0	16.9	13.2	0.8	50.77	0.73	1.32	0.65	0.78	−4.08	0.51	0.71
21.3	16.9	13.9	0.8	65.26	0.81	0.81	0.79	0.82	−4.08	0.65	0.59
25.3	16.9	11.3	0.8	44.66	0.67	1.26	0.67	0.67	−4.08	0.45	0.60
26.5	16.9	12.4	0.8	46.79	0.70	1.38	0.64	0.73	−4.08	0.47	0.68
23.4	16.8	15.0	0.8	64.10	0.83	1.13	0.72	0.89	−4.07	0.64	0.79
19.0	16.7	11.2	0.7	58.95	0.73	0.39	0.88	0.67	−4.06	0.59	0.29
19.7	16.6	11.0	0.8	55.84	0.72	0.54	0.84	0.66	−4.05	0.56	0.36
20.2	16.5	14.9	0.9	73.76	0.87	0.82	0.82	0.90	−4.04	0.74	0.70
18.5	16.5	12.1	0.8	65.41	0.78	0.36	0.89	0.73	−4.04	0.65	0.31
23.4	16.4	13.1	0.7	55.98	0.76	1.13	0.70	0.80	−4.04	0.56	0.68
18.4	16.4	12.9	0.8	70.11	0.82	0.39	0.89	0.79	−4.04	0.70	0.36
30.2	16.4	11.1	0.8	36.75	0.63	1.89	0.54	0.68	−4.04	0.37	0.72
20.0	16.4	12.0	0.7	60.00	0.76	0.65	0.82	0.73	−4.04	0.60	0.45
19.8	16.4	12.9	0.7	65.15	0.80	0.65	0.83	0.79	−4.04	0.65	0.49
17.9	16.3	15.5	0.8	86.59	0.94	0.53	0.91	0.95	−4.03	0.87	0.67
22.0	16.3	9.0	0.8	40.91	0.61	0.98	0.74	0.55	−4.03	0.41	0.44
21.3	16.3	14.3	0.7	67.14	0.84	0.96	0.77	0.88	−4.03	0.67	0.71
20.4	16.3	10.4	0.8	50.98	0.69	0.71	0.80	0.64	−4.03	0.51	0.41
20.9	16.3	12.0	0.9	57.42	0.75	0.80	0.78	0.74	−4.03	0.57	0.52
18.5	16.2	13.2	0.7	71.35	0.83	0.48	0.88	0.81	−4.02	0.71	0.43
18.0	16.2	12.6	0.8	70.00	0.82	0.34	0.90	0.78	−4.02	0.70	0.33
23.5	16.2	15.1	0.7	64.26	0.84	1.26	0.69	0.93	−4.02	0.64	0.87

A−axis	B−axis	C−axis	Roundness	Flatness	Sphericity	OP−index	b/a	c/b	B−axis phi	c/a	a−b/a−c
22.0	16.2	10.4	0.7	47.27	0.67	0.97	0.74	0.64	−4.02	0.47	0.50
18.7	16.2	12.0	0.5	64.17	0.78	0.47	0.87	0.74	−4.02	0.64	0.37
22.7	16.1	13.0	0.8	57.27	0.77	1.10	0.71	0.81	−4.01	0.57	0.68
21.3	16.1	12.4	0.8	58.22	0.77	0.91	0.76	0.77	−4.01	0.58	0.58
21.8	16.0	13.2	0.9	60.55	0.79	1.02	0.73	0.83	−4.00	0.61	0.67
20.9	16.0	10.1	0.7	48.33	0.67	0.84	0.77	0.63	−4.00	0.48	0.45
17.5	16.0	12.1	0.8	69.14	0.81	0.27	0.91	0.76	−4.00	0.69	0.28
19.0	16.0	13.0	0.9	68.42	0.82	0.61	0.84	0.81	−4.00	0.68	0.50
19.2	15.9	10.8	0.8	56.25	0.73	0.59	0.83	0.68	−3.99	0.56	0.39
18.3	15.9	12.9	0.8	70.49	0.83	0.50	0.87	0.81	−3.99	0.70	0.44
17.5	15.9	13.8	0.6	78.86	0.88	0.38	0.91	0.87	−3.99	0.79	0.43
23.7	15.9	11.4	0.9	48.10	0.70	1.23	0.67	0.72	−3.99	0.48	0.63
20.8	15.9	13.0	0.7	62.50	0.80	0.90	0.76	0.82	−3.99	0.63	0.63
18.8	15.9	9.6	0.7	51.06	0.68	0.51	0.85	0.60	−3.99	0.51	0.32
20.6	15.9	14.0	0.8	67.96	0.84	0.94	0.77	0.88	−3.99	0.68	0.71
18.5	15.9	14.7	0.7	79.46	0.90	0.70	0.86	0.92	−3.99	0.79	0.68
21.8	15.8	13.5	0.8	61.93	0.81	1.07	0.72	0.85	−3.98	0.62	0.72
16.2	15.8	10.9	0.8	67.28	0.77	−0.03	0.98	0.69	−3.98	0.67	0.08
20.0	15.8	14.9	0.7	74.50	0.89	0.97	0.79	0.94	−3.98	0.75	0.82
24.3	15.8	12.0	0.8	49.38	0.72	1.32	0.65	0.76	−3.98	0.49	0.69
20.0	15.7	10.9	0.7	54.50	0.72	0.77	0.79	0.69	−3.97	0.55	0.47
19.5	15.7	11.8	0.7	60.51	0.77	0.71	0.81	0.75	−3.97	0.61	0.49
19.4	15.7	11.8	0.8	60.82	0.77	0.69	0.81	0.75	−3.97	0.61	0.49
20.5	15.7	12.0	0.7	58.54	0.76	0.86	0.77	0.76	−3.97	0.59	0.56
20.0	15.7	12.3	0.7	61.50	0.78	0.80	0.79	0.78	−3.97	0.62	0.56
18.3	15.6	12.7	0.9	69.40	0.83	0.57	0.85	0.81	−3.96	0.69	0.48
18.0	15.5	10.0	0.9	55.56	0.71	0.45	0.86	0.65	−3.95	0.56	0.31
20.5	15.5	8.0	0.8	39.02	0.59	0.92	0.76	0.52	−3.95	0.39	0.40
20.8	15.5	13.2	0.6	63.46	0.81	1.00	0.75	0.85	−3.95	0.63	0.70
17.8	15.4	13.5	0.8	75.84	0.87	0.58	0.87	0.88	−3.94	0.76	0.56
19.2	15.4	12.1	0.8	63.02	0.79	0.74	0.80	0.79	−3.94	0.63	0.54
23.8	15.2	12.0	0.8	50.42	0.74	1.36	0.64	0.79	−3.93	0.50	0.73
17.9	15.2	13.0	0.8	72.63	0.85	0.62	0.85	0.86	−3.93	0.73	0.55
18.3	15.2	13.3	0.9	72.68	0.86	0.72	0.83	0.88	−3.93	0.73	0.62
18.1	15.2	12.0	0.7	66.30	0.81	0.59	0.84	0.79	−3.93	0.66	0.48
16.9	15.1	8.1	0.7	47.93	0.64	0.31	0.89	0.54	−3.92	0.48	0.20
17.0	15.1	7.6	0.9	44.71	0.61	0.33	0.89	0.50	−3.92	0.45	0.20
19.9	15.0	11.8	0.9	59.30	0.78	0.92	0.75	0.79	−3.91	0.59	0.60
30.2	15.0	13.1	0.9	43.38	0.72	1.98	0.50	0.87	−3.91	0.43	0.89
16.0	15.0	11.0	0.7	68.75	0.80	0.15	0.94	0.73	−3.91	0.69	0.20
20.7	15.0	10.7	0.8	51.69	0.72	1.01	0.72	0.71	−3.91	0.52	0.57
23.9	15.0	11.2	0.9	46.86	0.70	1.41	0.63	0.75	−3.91	0.47	0.70

A-axis	B-axis	C-axis	Roundness	Flatness	Sphericity	OP-index	b/a	c/b	B-axis phi	c/a	a-b/a-c
18.3	15.0	12.7	0.7	69.40	0.84	0.72	0.82	0.85	-3.91	0.69	0.59
18.4	15.0	10.9	0.8	59.24	0.76	0.65	0.82	0.73	-3.91	0.59	0.45
19.2	15.0	10.2	0.7	53.13	0.71	0.77	0.78	0.68	-3.91	0.53	0.47
26.2	15.0	11.2	0.8	42.75	0.68	1.67	0.57	0.75	-3.91	0.43	0.75
16.1	15.0	10.8	0.9	67.08	0.78	0.17	0.93	0.72	-3.91	0.67	0.21
18.3	15.0	9.9	0.8	54.10	0.71	0.62	0.82	0.66	-3.91	0.54	0.39
19.5	15.0	8.7	0.7	44.62	0.64	0.83	0.77	0.58	-3.91	0.45	0.42
19.1	15.0	11.2	0.8	58.64	0.76	0.78	0.79	0.75	-3.91	0.59	0.52
17.7	15.0	14.0	0.6	79.10	0.90	0.75	0.85	0.93	-3.91	0.79	0.73
19.5	15.0	8.9	0.8	45.64	0.65	0.83	0.77	0.59	-3.91	0.46	0.42
21.5	14.9	9.5	0.8	44.19	0.66	1.15	0.69	0.64	-3.90	0.44	0.55
21.8	14.9	8.8	0.8	40.37	0.62	1.22	0.68	0.59	-3.90	0.40	0.53
16.8	14.9	9.1	0.9	54.17	0.69	0.34	0.89	0.61	-3.90	0.54	0.25
22.2	14.9	12.0	0.6	54.05	0.76	1.23	0.67	0.81	-3.90	0.54	0.72
18.3	14.9	10.3	0.9	56.28	0.73	0.64	0.81	0.69	-3.90	0.56	0.43
19.0	14.9	10.5	0.9	55.26	0.73	0.77	0.78	0.70	-3.90	0.55	0.48
20.6	14.9	11.7	0.6	56.80	0.76	1.03	0.72	0.79	-3.90	0.57	0.64
16.2	14.8	11.0	0.9	67.90	0.80	0.25	0.91	0.74	-3.89	0.68	0.27
16.1	14.8	8.5	0.8	52.80	0.67	0.20	0.92	0.57	-3.89	0.53	0.17
24.0	14.8	13.5	0.9	56.25	0.80	1.47	0.62	0.91	-3.89	0.56	0.88
16.3	14.7	9.9	0.9	60.74	0.74	0.28	0.90	0.67	-3.88	0.61	0.25
22.2	14.7	11.5	0.7	51.80	0.74	1.26	0.66	0.78	-3.88	0.52	0.70
16.8	14.7	12.9	0.9	76.79	0.88	0.53	0.88	0.88	-3.88	0.77	0.54
18.8	14.7	11.1	0.9	59.04	0.76	0.79	0.78	0.76	-3.88	0.59	0.53
19.4	14.6	11.1	0.9	57.22	0.76	0.91	0.75	0.76	-3.87	0.57	0.58
15.3	14.5	9.4	0.9	61.44	0.74	0.08	0.95	0.65	-3.86	0.61	0.14
17.9	14.5	11.9	0.8	66.48	0.82	0.73	0.81	0.82	-3.86	0.66	0.57
15.9	14.5	8.3	0.7	52.20	0.67	0.23	0.91	0.57	-3.86	0.52	0.18
17.9	14.5	11.2	0.8	62.57	0.78	0.69	0.81	0.77	-3.86	0.63	0.51
17.3	14.5	11.3	0.8	65.32	0.80	0.59	0.84	0.78	-3.86	0.65	0.47
16.7	14.3	9.2	0.8	55.09	0.71	0.46	0.86	0.64	-3.84	0.55	0.32
16.0	14.3	9.4	0.8	58.75	0.73	0.31	0.89	0.66	-3.84	0.59	0.26
16.0	14.3	9.2	0.8	57.50	0.72	0.31	0.89	0.64	-3.84	0.58	0.25
21.7	14.3	13.2	0.9	60.83	0.82	1.33	0.66	0.92	-3.84	0.61	0.87
19.1	14.3	12.2	0.7	63.87	0.82	0.98	0.75	0.85	-3.84	0.64	0.70
15.0	14.2	8.9	0.7	59.33	0.72	0.08	0.95	0.63	-3.83	0.59	0.13
20.9	14.2	12.0	0.9	57.42	0.79	1.21	0.68	0.85	-3.83	0.57	0.75
18.3	14.1	10.3	0.8	56.28	0.74	0.82	0.77	0.73	-3.82	0.56	0.53
15.9	14.1	12.7	0.8	79.87	0.90	0.51	0.89	0.90	-3.82	0.80	0.56
17.2	14.1	9.8	0.9	56.98	0.73	0.62	0.82	0.70	-3.82	0.57	0.42
17.2	14.1	11.0	0.8	63.95	0.79	0.66	0.82	0.78	-3.82	0.64	0.50
16.1	14.1	8.9	0.8	55.28	0.70	0.38	0.88	0.63	-3.82	0.55	0.28

A-axis	B-axis	C-axis	Roundness	Flatness	Sphericity	OP-index	b/a	c/b	B-axis phi	c/a	a-b/a-c
16.5	14.0	10.6	0.7	64.24	0.79	0.53	0.85	0.76	−3.81	0.64	0.42
19.9	14.2	14.0	0.8	70.35	0.89	1.25	0.71	0.99	−3.83	0.70	0.97
21.2	14.0	11.8	0.6	55.66	0.78	1.28	0.66	0.84	−3.81	0.56	0.77
16.9	14.0	11.0	0.9	65.09	0.80	0.62	0.83	0.79	−3.81	0.65	0.49
17.8	14.0	10.5	0.8	58.99	0.76	0.77	0.79	0.75	−3.81	0.59	0.52
18.5	14.0	11.7	0.8	63.24	0.81	0.93	0.76	0.84	−3.81	0.63	0.66
22.2	14.0	10.2	0.8	45.95	0.69	1.40	0.63	0.73	−3.81	0.46	0.68
20.0	13.9	12.4	0.8	62.00	0.82	1.19	0.70	0.89	−3.80	0.62	0.80
17.5	13.9	10.0	0.8	57.14	0.74	0.72	0.79	0.72	−3.80	0.57	0.48
16.4	13.9	11.1	0.7	67.68	0.81	0.56	0.85	0.80	−3.80	0.68	0.47
21.0	13.9	9.9	0.8	47.14	0.70	1.26	0.66	0.71	−3.80	0.47	0.64
15.7	13.9	8.4	0.9	53.50	0.69	0.33	0.89	0.60	−3.80	0.54	0.25
16.2	13.9	9.8	0.9	60.49	0.75	0.46	0.86	0.71	−3.80	0.60	0.36
16.9	13.8	12.7	0.9	75.15	0.88	0.82	0.82	0.92	−3.79	0.75	0.74
19.8	13.8	12.3	0.7	62.12	0.82	1.18	0.70	0.89	−3.79	0.62	0.80
16.8	13.8	9.5	0.8	56.55	0.73	0.61	0.82	0.69	−3.79	0.57	0.41
17.3	13.8	10.3	0.8	59.54	0.76	0.72	0.80	0.75	−3.79	0.60	0.50
17.9	13.8	10.8	0.8	60.34	0.78	0.84	0.77	0.78	−3.79	0.60	0.58
14.4	13.8	11.3	0.7	78.47	0.86	0.04	0.96	0.82	−3.79	0.78	0.19
14.0	13.7	9.1	0.9	65.00	0.76	−0.06	0.98	0.66	−3.78	0.65	0.06
16.3	13.6	11.9	0.7	73.01	0.86	0.68	0.83	0.88	−3.77	0.73	0.61
18.9	13.5	11.2	0.7	59.26	0.79	1.07	0.71	0.83	−3.75	0.59	0.70
18.0	13.5	12.0	0.8	66.67	0.84	1.00	0.75	0.89	−3.75	0.67	0.75
15.2	13.3	11.2	0.8	73.68	0.85	0.47	0.88	0.84	−3.73	0.74	0.47
14.9	13.3	11.9	0.9	79.87	0.89	0.46	0.89	0.89	−3.73	0.80	0.53
16.5	13.2	11.9	0.8	72.12	0.87	0.84	0.80	0.90	−3.72	0.72	0.72
18.2	13.2	12.7	0.8	69.78	0.88	1.17	0.73	0.96	−3.72	0.70	0.91
16.0	13.2	11.8	0.8	73.75	0.87	0.74	0.83	0.89	−3.72	0.74	0.67
16.8	13.2	11.5	0.8	68.45	0.84	0.85	0.79	0.87	−3.72	0.68	0.68
20.9	13.2	8.5	0.6	40.67	0.64	1.43	0.63	0.64	−3.72	0.41	0.62
18.2	13.1	12.0	0.9	65.93	0.85	1.13	0.72	0.92	−3.71	0.66	0.82
16.0	13.1	8.9	0.8	55.63	0.72	0.61	0.82	0.68	−3.71	0.56	0.41
16.3	13.1	10.4	0.9	63.80	0.80	0.72	0.80	0.79	−3.71	0.64	0.54
16.9	13.1	11.8	0.7	69.82	0.86	0.93	0.78	0.90	−3.71	0.70	0.75
17.9	13.0	9.2	0.8	51.40	0.71	0.98	0.73	0.71	−3.70	0.51	0.56
19.5	13.0	10.1	0.7	51.79	0.74	1.23	0.67	0.78	−3.70	0.52	0.69
21.0	12.9	10.2	0.8	48.57	0.73	1.45	0.61	0.79	−3.69	0.49	0.75
17.5	12.9	9.2	0.9	52.57	0.72	0.94	0.74	0.71	−3.69	0.53	0.55
18.9	12.9	9.3	0.8	49.21	0.71	1.16	0.68	0.72	−3.69	0.49	0.63
13.9	12.9	10.2	0.8	73.38	0.83	0.18	0.93	0.79	−3.69	0.73	0.27
20.0	12.9	9.0	0.8	45.00	0.68	1.33	0.65	0.70	−3.69	0.45	0.65
16.9	12.9	11.1	0.8	65.68	0.83	0.92	0.76	0.86	−3.69	0.66	0.69

A-axis	B-axis	C-axis	Roundness	Flatness	Sphericity	OP-index	b/a	c/b	B-axis phi	c/a	a-b/a-c
18.2	12.9	11.8	0.9	64.84	0.84	1.16	0.71	0.91	-3.69	0.65	0.83
17.9	12.9	10.0	0.7	55.87	0.76	1.02	0.72	0.78	-3.69	0.56	0.63
19.0	12.8	8.5	0.7	44.74	0.67	1.21	0.67	0.66	-3.68	0.45	0.59
13.8	12.8	10.5	0.8	76.09	0.85	0.20	0.93	0.82	-3.68	0.76	0.30
16.5	12.7	10.3	0.9	62.42	0.80	0.85	0.77	0.81	-3.67	0.62	0.61
16.2	12.6	8.0	0.8	49.38	0.68	0.77	0.78	0.63	-3.66	0.49	0.44
19.4	12.5	12.0	0.8	61.86	0.84	1.40	0.64	0.96	-3.64	0.62	0.93
13.9	12.5	11.3	0.8	81.29	0.90	0.43	0.90	0.90	-3.64	0.81	0.54
13.8	12.5	10.0	0.8	72.46	0.83	0.29	0.91	0.80	-3.64	0.72	0.34
17.2	12.4	11.8	0.8	68.60	0.87	1.16	0.72	0.95	-3.63	0.69	0.89
15.9	12.4	9.0	0.8	56.60	0.74	0.77	0.78	0.73	-3.63	0.57	0.51
13.8	12.3	9.9	0.8	71.74	0.83	0.36	0.89	0.80	-3.62	0.72	0.38
17.9	12.3	10.6	0.8	59.22	0.80	1.18	0.69	0.86	-3.62	0.59	0.77
16.0	12.2	9.5	0.9	59.38	0.77	0.86	0.76	0.78	-3.61	0.59	0.58
16.5	12.2	10.0	0.8	60.61	0.79	0.96	0.74	0.82	-3.61	0.61	0.66
15.0	12.2	11.3	0.7	75.33	0.89	0.83	0.81	0.93	-3.61	0.75	0.76
14.5	12.2	9.0	0.8	62.07	0.77	0.53	0.84	0.74	-3.61	0.62	0.42
14.3	12.1	11.0	0.9	76.92	0.89	0.67	0.85	0.91	-3.60	0.77	0.67
15.4	12.1	10.0	0.7	64.94	0.81	0.80	0.79	0.83	-3.60	0.65	0.61
15.9	12.1	11.2	0.8	70.44	0.87	1.00	0.76	0.93	-3.60	0.70	0.81
12.2	12.1	8.7	0.9	71.31	0.80	-0.16	0.99	0.72	-3.60	0.71	0.03
14.9	12.1	9.0	0.9	60.40	0.77	0.65	0.81	0.74	-3.60	0.60	0.47
18.2	12.0	9.0	0.9	49.45	0.72	1.25	0.66	0.75	-3.58	0.49	0.67
15.0	12.0	10.4	0.8	69.33	0.84	0.78	0.80	0.87	-3.58	0.69	0.65
15.2	12.0	10.1	0.7	66.45	0.82	0.80	0.79	0.84	-3.58	0.66	0.63
14.9	11.9	9.0	0.7	60.40	0.77	0.70	0.80	0.76	-3.57	0.60	0.51
18.1	11.8	7.3	0.8	40.33	0.63	1.33	0.65	0.62	-3.56	0.40	0.58
17.0	11.8	10.2	0.9	60.00	0.80	1.15	0.69	0.86	-3.56	0.60	0.76
13.7	11.6	8.8	0.8	64.23	0.79	0.51	0.85	0.76	-3.54	0.64	0.43
17.9	11.6	8.8	0.7	49.16	0.72	1.30	0.65	0.76	-3.54	0.49	0.69
14.1	11.6	10.0	0.8	70.92	0.85	0.69	0.82	0.86	-3.54	0.71	0.61
12.0	11.5	10.5	0.9	87.50	0.93	0.00	0.96	0.91	-3.52	0.88	0.33
15.0	11.5	9.1	0.6	60.67	0.78	0.84	0.77	0.79	-3.52	0.61	0.59
12.9	11.5	10.9	0.9	84.50	0.93	0.53	0.89	0.95	-3.52	0.84	0.70
13.7	11.4	9.7	0.8	70.80	0.84	0.64	0.83	0.85	-3.51	0.71	0.57
14.6	11.4	7.9	0.9	54.11	0.72	0.74	0.78	0.69	-3.51	0.54	0.48
24.7	12.8	11.4	0.9	46.15	0.74	1.86	0.52	0.89	-3.68	0.46	0.89
15.9	11.3	10.1	0.8	63.52	0.83	1.11	0.71	0.89	-3.50	0.64	0.79
12.9	11.2	11.0	0.9	85.27	0.94	0.74	0.87	0.98	-3.49	0.85	0.89
15.0	11.2	9.0	0.9	60.00	0.78	0.92	0.75	0.80	-3.49	0.60	0.63
18.7	11.2	10.9	0.9	58.29	0.83	1.54	0.60	0.97	-3.49	0.58	0.96
16.5	11.0	10.1	0.9	61.21	0.83	1.28	0.67	0.92	-3.46	0.61	0.86

A-axis	B-axis	C-axis	Roundness	Flatness	Sphericity	OP-index	b/a	c/b	B-axis phi	c/a	a-b/a-c
13.9	11.0	10.1	0.9	72.66	0.87	0.87	0.79	0.92	-3.46	0.73	0.76
12.7	10.8	8.1	0.8	63.78	0.78	0.48	0.85	0.75	-3.43	0.64	0.41
15.0	10.8	8.8	0.9	58.67	0.78	1.02	0.72	0.81	-3.43	0.59	0.68
13.0	10.8	7.9	0.8	60.77	0.76	0.55	0.83	0.73	-3.43	0.61	0.43
16.0	10.6	8.0	0.8	50.00	0.72	1.23	0.66	0.75	-3.41	0.50	0.68
13.0	10.4	9.8	0.8	75.38	0.89	0.87	0.80	0.94	-3.38	0.75	0.81
12.8	10.4	9.7	0.9	75.78	0.89	0.81	0.81	0.93	-3.38	0.76	0.77
13.9	10.0	9.0	0.9	64.75	0.84	1.07	0.72	0.90	-3.32	0.65	0.80
14.0	10.0	9.2	0.7	65.71	0.85	1.11	0.71	0.92	-3.32	0.66	0.83
13.0	9.8	8.0	0.8	61.54	0.79	0.88	0.75	0.82	-3.29	0.62	0.64
17.5	9.0	8.2	0.9	46.86	0.75	1.84	0.51	0.91	-3.17	0.47	0.91